Exploring the reactivity of Ru-PNP complexes in ionic liquids for small molecule transformations

Piccirilli, Luca

Publication date:
2022

Document Version
Publisher's PDF, also known as Version of record

Exploring the reactivity of Ru-PNP complexes in ionic liquids for small molecule transformations

PhD Thesis

Author

Luca Piccirilli

Supervisor

Martin Nielsen

Co-supervisor

Anders Riisager

March 2022

to Marco and Carlo

Preface

Current developments in Europe demonstrate that we live in a world that continues in pursuing war instead of peace, discrimination instead of tolerance, and economic interests instead of fair conditions for all. In this contest, climate change is not getting the attention it needs, and the necessary green transition seems, to date, very challenging. While fossil fuels still play a crucial role in the worldwide geopolitics, there is the need to provide new energy solutions that are beneficial for the environment and society. In response to the Ukrainian crisis, countries are proposing and adopting different strategies such as the reopening of dismissed and polluting carbon plants. Gladly, many European leaders pointed out the potential of renewable energy and hydrogen-related technologies as a solution to achieve energetic independence and move towards a more sustainable future. The question if it is too late to invert the trend remains unanswered; nevertheless, when looking at the many achievements of humankind, I am positive. It is for sure an interesting time to be alive, be active and participate in this transition.

Renewable energy is already increasing its share of the total energy production, and it will become cheaper and more sustainable if the demand raises. This means that policies and incentives from government and industries should all work altogether pursuing the same objective and moving in the same direction, which is often not the case. The discontinuous nature of renewable energy, hence the necessity of efficiently storing it, are main challenges towards the achievement of an electrified society. In addition, only few countries can afford heavy investment in e.g. wind and solar farms that are still limited to relatively small areas.

The hydrogen economy represents a sustainable and viable solution to mitigate climate change, and likely, it will be a crucial component of the coming green transition. In such a scenario, green hydrogen is produced on-demand using renewable energy by means of water electrolysis. Later, the chemical energy stored in hydrogen can be released in the form of heat and electricity using a fuel cell, with water as the only by-product. However, many hydrogen-related technologies are still accompanied with high costs and infrastructural challenges that are hindering a large-scale commercialization of e.g. fuel cell vehicles.

Catalysis plays a fundamental role in the sustainment of society and our life style. The production of fuels, plastic, medicines, and every-day commodities relies on the extensive use of chemistry and catalysis. Hence, it is likely that new game changing solutions and innovation will come from this field. In this regard, homogeneous catalysis is witnessing a new renaissance, offering several advantages compared to established synthetic routes such as lower energetic costs and higher atom economy. This features are very attractive to industry, hence the great potential of this field of research. In this work, I will use homogeneous metal catalysts for hydrogenation and dehydrogenation reactions in the context of the hydrogen economy, hoping to provide new viable approaches and solutions for both energy storage and distribution technologies.

This thesis is the result of the scientific work that I carried out during my PhD studies from January 2019 until March 2022. The work was conducted under the supervision of Assoc Prof Martin Nielsen, and co-supervision of Prof Anders Riisager at DTU Chemistry, Technical University of Denmark.

Kgs. Lyngby, 31-03-2022

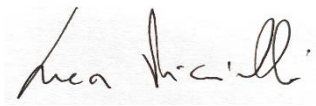

Acknowledgments

I would like to express my sincere gratitude to my supervisor Assoc Prof Martin Nielsen for giving me the opportunity to carry out such an interesting and exciting PhD project(s). I am very grateful for the extreme high-quality research inputs and perspectives that he has provided during the optimization of the processes described in this thesis and throughout the course of my studies. Importantly, Martin has always inspired and pushed me to be more ambitious and eager to obtain rewarding achievements, demonstrating that good work always pays off. Special thanks to my co-supervisor Prof Anders Riisager for all the insightful talks and mentoring since I joined DTU Chemistry for the first time as an exchange student in his group. Finally, I would like to thank my supervisor from Italy, Prof Fabrizio Cavani, for inspiring me towards the direction I have taken.

I would like to thank Dr. Marco Haumann and Prof Peter Wasserscheid for giving me the possibility to perform my external stay at FAU, Erlangen. Despite challenging Covid circumstances resulting in a very short stay of only three weeks, the experience definitely enriched my PhD experience in terms of both scientific contribution and personal gratification. Thanks to Melanie Eßl who let me use her reactor at FAU and for helping with data analysis and every-day problems during my stay.

A special thank goes to all the DTU stuff and colleagues. Thanks a lot to Andreas, for making Chapter 2 possible, for its continuous help in daily lab issues and for the always pleasant conversations in and out his smoking pauses. Similar important contributions were given by Ishak (artisan of autoclaves), Bo and Burak regarding IT support, and Kasper for some very insightful (ss)NMR experiments and related discussions. In addition, thanks to Lars, Jane, Jette, Monica, Kristine, Josephine, Mette, Bodil, Mariusz, and all the people from the DTU stuff who helped me in any way during these three years.

Thanks to my whole research group. Thanks to my mentor and great friend Maria for the useful advices on both work and life matters, the essential guidance during the initial times of my PhD, as well as for the preparation of the papers. Thanks to Dani for always being there for a chat and support, and Brenda who helped me in the final rush with a lot of valuable experiments and some new interesting insights on the projects. Thanks to my office mates Mike, Mathias (who turned my abstract into a resumé), Sakhitha and Alex for always providing a laugh during the challenging and alternating moods of a PhD student. Thanks to Lucas for the extremely nice time in and outside DTU, and Dimitra for all the cigarettes and complaints that we shared, for some TEM fun, and to be such a good friend. Overall, thanks to DTU in general for giving me the opportunity to create relationships that will last in the years to come.

Thanks to the Italian people in Denmark, in and outside DTU, for providing a (northern) taste of Italy. From Irene, who contributed a lot to my extended stay in Denmark, to Vanessa, Elisa, Cecilia, Fabio, Luca etc. Thanks also to all the friends from Italy of course, for always being there.

I would like to express all my gratitude to my family, especially my parents Marcello and Marianna, fro their incondicionate love and for supporting me in all possible ways despite the distance. Finally, thanks to my brother Marco and my grandpa Carlo for always giving me the motivation to be the best person I can be.

Overall, I believe it was a successful PhD, as demonstrated by the highly interesting scientific output, some rewarding personal achievements, and by the fact that I enjoyed writing this dissertation. I hope this work can provide useful insights towards the development of sustainable catalytic processes.

Abstract

Hydrogen release from a Liquid Organic Hydrogen Carrier (LOHC), in synergy with CO_2 capture and utilization (CCU) processes, are of extreme importance for the development of the new hydrogen economy, as well as the decrease of anthropogenic greenhouse emissions in the atmosphere. In this PhD dissertation, I will explore new and unprecedented reactivity modes based on the interaction between organometallic Ru-PNP catalysts dissolved in ionic liquids (ILs). The topics discussed in the thesis are highly attractive from both a societal and industrial point of view, varying from CCU to hydrogen technologies for transportation and renewable energy storage.

Homogeneous transition metal pincer complexes of the type Ru-PNP are known to catalyze hydrogenation and dehydrogenation reactions of a variety of substrates at mild conditions, with high catalytic activity, selectivity and optimal atom efficiency. The main novelty behind this PhD project is represented by their use in combination with an ionic liquid (IL) as the only reaction additive. As such, I will demonstrate that a suitable combination of Ru-PNP catalyst dissolved in IL represents a powerful tool for relevant transformations within sustainable chemistry and catalysis, with hydrogenation and dehydrogenation processes that are at the core of this dissertation. Importantly, the use of ILs avoids the use of both volatile solvents and inorganic bases, maximizing the efficiency of such systems and allowing the obtainment of products without the presence of organic contaminants.

In detail, Ru-PNP catalysts dissolved in ILs catalyze the hydrogenation of CO_2 to the LOHC formic acid without the use of sacrificial CO_2 trapping reagents and already at ambient conditions (1 bar, 25 ºC). The same Ru-PNP/IL mixtures are highly active towards formic acid dehydrogenation as well, offering the attractive possibility to perform efficient hydrogen release at temperatures that are compatible with automotive fuel cell applications (T<100 ºC). After optimization, the Ru-PNP/IL system resulted in the new state-of-the-art for this transformation, with turnover numbers as high as 18 million and a catalyst stability of four months under continuous flow conditions. In addition, the possibility to produce pressurized hydrogen (up to 50 bar) in a closed system has been demonstrated as well.

Based on the results from the single steps of hydrogenation and dehydrogenation, I will discuss an example of a reversible system that stores energy in the form of formic acid, and later releases in the form of hydrogen that is ready to be used in a fuel cell. The stability of such system has been verified by carrying out cycles of hydrogenation and dehydrogenation with no observable loss in catalytic activity.

Ultimately, the efficient dehydrogenation of the LOHC isopropanol has been demonstrated in the presence of Ru-PNP catalysts in IL phase. In this project, the Ru-PNP/IL system was successfully immobilized onto a support material using the Supported Ionic Liquid Phase (SILP) technology. As such, the so-obtained Ru-SILP catalyst showed promising activity in isopropanol dehydrogenation under fixed-bed reaction conditions, usually inaccessible for this type of homogenous species.

Resumé

Som platform for udviklingen af en brint økonomi udgør samspillet mellem teknologier til at frigive H_2 og teknologier til lagring, samt udnyttelse af CO_2, refereret til som Carbon Capture and Utilization (CCU), en central rolle. I denne ph.d.-afhandling udforskes kemien som følge af ruthenium-baseret katalysatorer, såkaldte Ru PNP-komplekser, opløst i ioniske væsker, som demonstrerer reaktivitet uden fortilfælde i frigivelsen af brint fra såkaldte Liquid Organic Hydrogen Carrier (LOHC). De I denne afhandling omdiskuteret emner, er relevante i både et samfundsmæssigt, såvel som i et industrielt perspektiv; fra CCU til brint-baseret teknologier med henblik på dets transport og lagring af bæredygtig energi.

De anvendte ruthenium-komplekser er kendt for, at udvise en høj katalytisk aktivitet og selektivitet i både hydrogenerings samt dehydrogenerings reaktioner af en bred vifte af stoffer. Disse to reaktioner er centrale til arbejdet udført i dette ph.d.-studium, hvor målsætningen har været, at finde den rigtige formulering af katalysatore og ioniske væsker, for at opnå gunstige reaktionsbetingelser. Specifikt har brugen af ioniske væsker medført, at de normalt anvendte opløsningsmidler og additiver fuldstændig kan udelades, resulterende i mere bæredygtige processer.

Kombinationen af ioniske væsker med Ru PNP-komplekser katalyserer hydrogenerings reaktionen af CO_2 til form syre, en LOHC, uden nødvendighed for først at fange CO_2 med et andet reagens, som forløber under atmosfæriske betingelser. Endvidere udviser samme system, en høj aktivitet i frigivelsen af H_2 ved forhøjet temperaturer relevante til transportsektoren i brændselsceller ($T<100$ ºC). Et andet resultat af dette ph.d.-studium er en katalysator formulering som udmærker sig som state-of-the-art i dehydrogenering af form syre; under et kontinuært-flow udviser systemet katalysator stabilitet over fire måneder, turnover number i størrelsesordnen af $18 \cdot 10^6$. Yderligere, er udviklingen af op til 50 bar af H_2 i et lukket system demonstreret.

Som følger af resultaterne fra både hydrogenerings og dehydrogenerings reaktionen, diskuteres et eksempel på form syres anvendelse i et reversibelt system. Specifikt, indledende energi oplagring af H_2 som form syre, efterfulgt af H_2 frigivelse, som direkte kan anvende i brændselsceller. Systemet er robust, bekræftet af intet målbart tab i katalytisk aktivitet over flere cyklusser af hydrogenering efterfulgt af dehydrogenering.

Slutteligt, vises en effektiv frigivelse af H_2 fra isopropanol, og dermed dets anvendelse som LOHC i tilstedeværelsen af Ru PNP-kompleks-ionisk væske kombinationen. Specifikt undersøges konsekvensen af en katalysator formulering immobiliseret på et støttemateriale, ved benyttelsen af Supported Ionic Liquid Phase (SILP) teknologi. Den opnået Ru-SILP formulering udviste lovende aktivitet i dehydrogenering af isopropanol under betingelser hvor lignende metal-komplekser er inaktive.

List of Publications

- Paper I
Piccirilli, L.; Lobo Justo Pinheiro, D.; Nielsen, M. Recent Progress with Pincer Transition Metal Catalysts for Sustainability. Catalysts 2020, 10, 773. https://doi.org/10.3390/catal10070773.
Published (Appendix E)

Planned papers:

- Paper II
L.Piccirilli, B. Rabell, R. Padilla, A. Riisager, M. Nielsen*
Efficient additive-free reversible catalytic hydrogenation of CO_2 and formic acid dehydrogenation under mild conditions
Paper in preparation (Appendix F).

- Paper III
L.Piccirilli, B. Rabell, R. Padilla, A. Riisager, M. Nielsen*
Flexible and robust formic acid dehydrogenation using Ru-PNP complexes and ionic liquids
Paper in preparation (Appendix G).

- Paper IV
L.Piccirilli, M. Eßl, R. Padilla, M. Haumann, A. Riisager, M. Nielsen*
Low-temperature continuous flow isopropanol dehydrogenation using a Ru-SILP catalyst
Paper in preparation (Appendix H).

- Paper V
L.Piccirilli, B. Rabell, R. Padilla, A. Riisager, M. Nielsen*
Reactivity of Ru-PNP complexes in ionic liquids for the hydrogenation of carbon dioxide to formic acid
Paper in preparation (Appendix I).

Dissemination Activities

- 03-11-2019: PhD Symposium, DTU Department of Chemistry, Konventum, Helsingør.
Poster.

- 17-01-2020: CSC-CST New Year Seminar 2020, DTU Department of Chemistry, Lyngby.
Oral presentation.

- 04-11-2021: PhD Symposium, DTU Department of Chemistry, Comwell Borupgaard, Snekkersten.
Oral presentation.

- 08-12-2021: Springboard meeting, DTU Department of Chemistry, Lyngby.
Oral presentation.

Awards

- DTU Discovery Grant (DKK 110.000): Low temperature hydrogen evolution for fuel cell.

- Brødrene Hartmanns Fond (DKK 85.000): Purchase of equipment for low-temperature hydrogen-releaser for fuel cell hydrogen vehicles.

List of abbreviations

CCU = Carbon capture and utilization

IL = Ionic liquid

FC = Fuel cell

LOHC = Liquid Organic Hydrogen Carrier

FA = formic acid

DBT = dibenzyltoluene

SILP = Supported Ionic Liquid Phase

SLP = Supported Liquid Phase

MFC = Mass flow controller

MFM = Mass flow meter

EMIM = 1-ethyl-3-methylimidazolium

EMMIM = 1-ethy-2,3-methylimidazolium

BMIM = 1-buthy-3-methylimidazolium

BMMIM = 1-buthyl-2,3-methylimidazolium

Pyrr = Pyrrolidinium

PIPER = Piperidinium

OTf = trifluoromethanesulfonate

NTf_2 = bis(trifluoromethylsulfonyl)imide

P_{1444} = tributylmethylphosphonium

P_{4444} = tetrabutylphosphonium

TFA = trifluoroacetate

$N(CN)_2$ = dicyanamide

$C(CN)_3$ = tricyanomethanide

DAF = dimethylethanol ammonium formate

DAF-H = 2-Hydroxyethylammonium formate

NHC = N-heterocyclic carbene

HD = Hydrogenation

DH = Dehydrogenation

DBU = 1,8-Diazabicyclo(5.4.0)undec-7-ene

Table of Contents

1. Introduction

This chapter introduces the concepts of hydrogen economy, carbon capture and utilization (CCU), homogeneous catalysis, ionic liquid (IL) as well as supported ionic liquid phase (SILP), which are at the core of the work carried out during my PhD studies. Finally, the chapter will outline the objectives, scientific contents and structure of the thesis.

1.1 The hydrogen economy

Climate change is one of the most challenging tasks that humanity must solve in the near future to ensure a sustainable future for the next generations [1,2]. The urgency of the problem calls for a rapid transition of our current energy system to a sustainable and climate-neutral one [3]. Since the industrial revolution, our society has relied on the extensive use of fossil fuels to satisfy the growing energy demand. As a consequence, the use of such high-carbon energy sources has caused severe emission of greenhouse gases in the atmosphere, namely carbon dioxide (CO_2), methane (CH_4), nitrous oxides (NO_x), as well as several fluorinated gases. In 2018, a total of 55.3 $GtCO_2$ associated with human activities were released in the atmosphere [4]. This has resulted in an increase of the average global temperature of about 1 ºC; as an example, we are measuring extraordinarily out-of-average temperatures in the polar areas more and more often. It is estimated that up to 31.7 billion dollars were used in 2018 to mitigate the effects caused by natural catastrophes, such as fires, storms, floods, and droughts [5]. The Paris agreement aims to limit this increase to 2 ºC by 2100, ideally below 1.5 ºC. Food, water, health, ecosystem and infrastructures are the most affected sectors by the consequences of climate change. Therefore, even if it is estimated that fossil fuels could still provide energy for centuries to come, it is urgent to find sustainable alternatives that are benign for the environment.

The hydrogen (H_2) economy has been proposed as a solution to decrease anthropogenic greenhouse emission in the atmosphere, contributing to accomplishing a completely renewable energy system [6,7]. In the last few decades, hydrogen-based fuels experienced a new interest as potential group of green solutions of the future [8]. Nevertheless, the idea of transforming the chemical energy stored in hydrogen into electricity dates back to 1838, when Sir William Grove proposed the first example of a fuel cell (FC) able to produce power. More recently, hydrogen has been used to propel the first combustion engines, as well as balloons and airships during the last century. Remarkably, hydrogen was the fuel that allowed humanity to reach the moon in 1969.

The demand for pure hydrogen has increased significantly in the last decades, from 28 million tonnes per year in 1970, up to >100 million tonnes in 2018 [7]. The chemical industry already uses pure hydrogen in large amounts, for example in refineries and for the synthesis of ammonia (and fertilizers), taking up to 70 million tonnes per year. Other processes do not require prior purification of hydrogen from gaseous mixtures, for example in the steel industry or for the production of methanol, where the feedstock is the so-called synthesis gas (H_2 + CO). Hydrogen is currently produced from coal or natural gas, hence contributing to the global CO_2 emissions; in particular, 6% and 2% of the total consumption of natural gas and coal is dedicated to hydrogen production, resulting in 830 million tonnes of carbon dioxide emitted per year. Hence, it is crucial that we develop new processes for efficient hydrogen production from low-carbon energy sources such as renewable electricity, biomass or nuclear. In a worldwide contest, solar energy contribution is expected to grow the most, while wind power will probably assess to a minor share of the total energy production [9]. It can be envisioned that both solar, wind, as well as nuclear energy will be extensively used to promote water electrolysis processes for the production of hydrogen, likely playing an important role in the development of a green energy supply chain. In this sense, advances in nuclear fusion technologies might lead to breakthroughs in energy production alternatives.

As depicted in Figure 3.1, the chemical energy stored in hydrogen (33.3 kWh/kg) can be transformed into electricity and heat using a fuel cell (FC), with water (from which hydrogen was produced) as the only by-product [10,11]. In detail, hydrogen is oxidized at the anode using oxygen coming from air; protons travel through the electrolyte solution towards the cathode, while electrons are collected in an external circuit. The nature of both the electrolyte, as well as the ions moving through it, affects the operative conditions of a FC and the type of feed. For example, the first FC built by Grove was composed by zinc and platinum electrodes on porcelain plates, and a solution of sulphuric acid as the electrolyte. Later in 1932, Bacon invented the alkaline FC, still one of the most widespread FC technology used e.g. in space applications, where the electrolyte is an aqueous solution of KOH. Typically, FCs operating at temperatures above 600 ºC (molten carbonates and solid oxide FCs) allow direct feed of hydrocarbons, e.g. methane, that undergo reforming producing hydrogen in the FC [12,13]. This approach can be used for e.g. stationary applications such as in factories, buildings and farms. On the contrary, low-temperature FCs such as alkaline, phosphoric acid, and proton exchange membrane (PEM), require an external source of pure hydrogen. Among all the alternatives, PEM-FCs are particularly interesting for automotive applications since they allow short start up times (1 second, up to 10 minutes for solid oxide FCs), low weight, contain non-corrosive membranes, and perform with high energy efficiency. In this case, a semipermeable fluorine-based polymeric membrane permits the moving of protons in one direction.

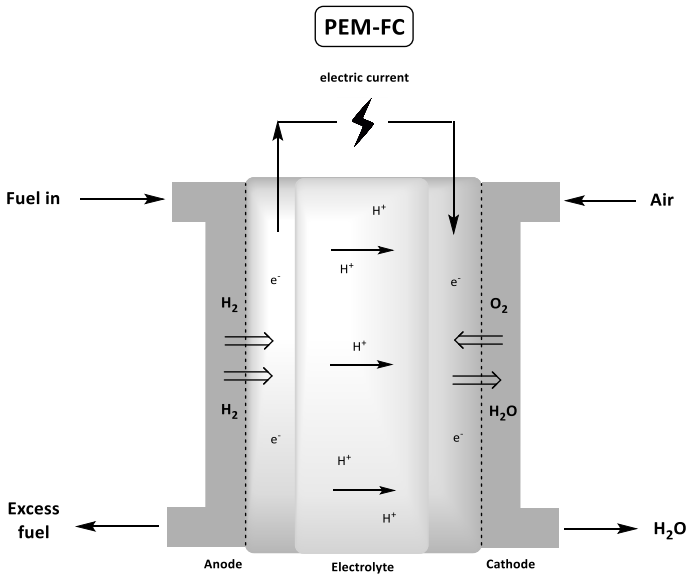

Figure 1.1: Schematic representation of a PEM-FC.

Figure 1.2 shows a schematic and simplified representation of a hydrogen-based energy system. As discussed before, green hydrogen can be obtained via water electrolysis using renewable energy such as wind, solar, geothermic, hydro or nuclear. Importantly, hydrogen would allow the storage of large amounts of electricity circumventing the issue of the imbalance between supply and demand. Later, hydrogen can be transported through pipelines until e.g. fueling stations, or it can be converted into electricity in a FC according to demand, and injected in the electric grid for the powering of houses, industries and farms. Ideally, also fueling stations would be equipped with small-size electrolyzers for the recharging of vehicles in cities and urbanized areas. However, there are still several challenges that prevent the implementation of hydrogen on a large scale. Firstly, the cost of green hydrogen from water electrolysis is not competitive yet with conventional energy sources based on fossil fuels. Moreover, the physio-chemical nature of elemental hydrogen results in a very low volumetric storage density at ambient conditions (3 Wh/L) [14].

For this reason, established technologies for compressed and cryogenic hydrogen apply drastic conditions to increase the volumetric storage density of hydrogen (up to 700 bar and -253 °C, respectively), therefore requiring technically demanding and costly infrastructures that are simply too impractical. In addition, often the sources of renewable energy are far away from industrialized places (off-shore turbines, solar farms etc) rendering even more challenging its storage and transportation. In the next chapter, I will discuss alternatives for hydrogen storage and transportation.

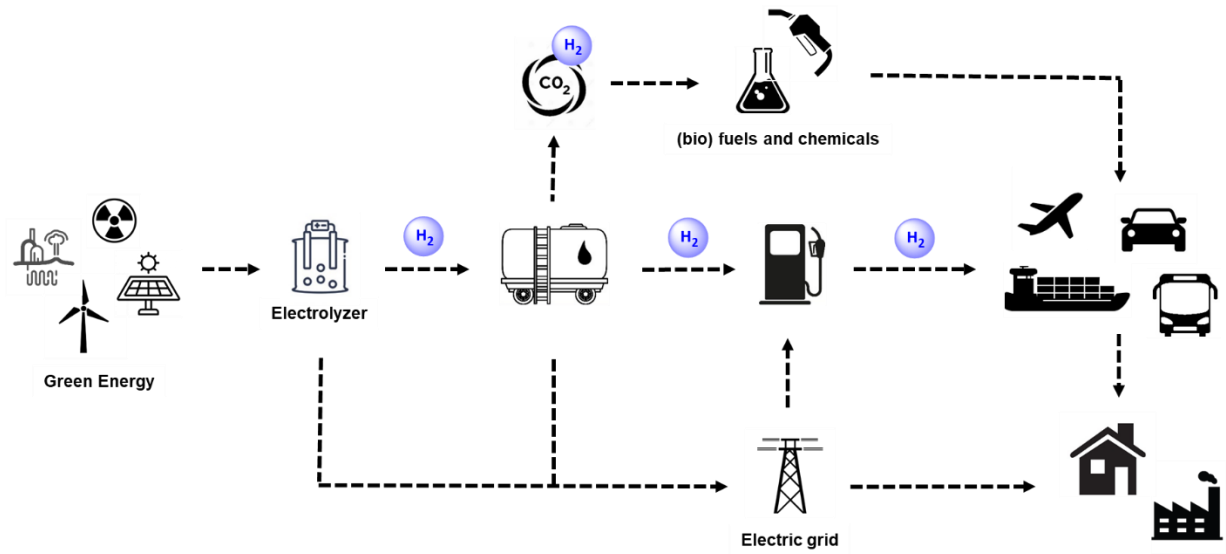

Figure 1.2: Schematic representation of the hydrogen economy.

The report from the International Energy Agency (IEA) from 2019 stated that the cost of hydrogen could drop up to 30% due to the reduced costs of renewables, together with major investment in hydrogen technologies [7]. Recently, the European Union has issued a new strategy to build pipeline systems for efficiently transporting hydrogen across long distances [15,16]. The requirements for the infrastructures are similar to those required for transporting natural gas. Indeed, the blending of H_2 with CH_4 in existing natural gas pipelines has been demonstrated already [17]. It is expected that the production of energy will move from current areas (rich of fossil fuels) to places where renewable energy is highly available. For example, it is envisioned that Europe can import a large amount of energy from future solar farms in North Africa [18]. The same concept applies to places that can exploit the high presence of strong wind, e.g. northern countries or Australia. In this sense, Denmark has reached approximately 50% of the total energy production using wind power already in 2020. Concerning hydrogen distribution, there are eight operative hydrogen fueling stations in Denmark (estimated cost of 15 mil DKK, including water electrolysis plant), with less than 100 FC vehicles.

Besides other uses in the chemical industry discussed above, one of the most attractive utilizations of hydrogen is represented by onboard automotive applications in FC vehicles. In fact, on-board hydrogen technologies represent a particularly promising concept that would provide a zero-emission mobility system. Today, only ≈12000 hydrogen cars are on the roads, a very small proportion of the more than 1 billion cars circulating globally (2 billion expected in 2050). The use of hydrogen has several advantages when compared to e.g. electric vehicles; for instance, FC vehicles are not limited by the size of the engine, being hydrogen continuously fed to the FC similar to a conventional combustion engine, meaning that FC vehicles can extend from small cars up to container ships and airplanes. On the contrary, large size battery-powered vehicles require an increase in size of the battery, with obvious drawbacks in terms of space requirement, weight and costs. However, the low operative temperature of PEM-FC requires the use

of a catalyst, and the high loading of precious metal required (40-50 g of platinum in each fuel, 41% of the total FC cost) is currently unsustainable for a worldwide commercialization of FC powered vehicles [19,20]. In this sense, the scientific community is trying to find cheaper alternatives for the construction of electrodes using e.g. N-doped transition metals catalysts [21] supported on graphene [22].

In summary, hydrogen technologies are still at their early stages, hence the urgency for novel and sustainable solutions. It has to be noticed that the scenario depicted in Figure 1.2 is only a part of the expected new global energy system. In fact, the hydrogen economy will not be the only solution to climate change. It is likely that a green transition will be possible with an optimized combination of new green and sustainable processes, each possessing a share in the future energy production.

1.2 Liquid organic hydrogen carriers

The desired green transition should provide sustainable economic development and viable solutions. Hence it is appropriate, when possible, to use existing infrastructures and facilities to reduce costs and accelerate the process. As introduced above, hydrogen storage and transportation still represent a challenge towards the large-scale implementation of hydrogen technologies; to overcome this issue, the concept of LOHC has been proposed [23,24]. The currently employed technologies (hydrogen compression and/or liquefaction) are accompanied with drawbacks in terms of practicality and scalability on a worldwide scale. In addition, on-board hydrogen storage (700 bar, 5.7 wt% of H_2) is associated with energy loss due to compression, liquefaction and dispersion of H_2. Researchers have tried to investigate the possibility to store interstitial hydrogen in different support materials [25]. This includes e.g. metal hydrides [26], metal organic frameworks (MOFs) [27] as well as specifically designed carbon nanomaterials [28].

LOHC	H_2 wt%
Formic Acid	4.4
Isopropanol	3.3
Methanol	12.6
Ethanol	12
Formaldehyde	6.6
Glycerol	9.6
Sugar Alcohols	8.9–9.3
N-ethylcarbazole (NEC)	5.8
Dibenzyltoluene (DBT)	6.2
1,2-BN-cyclohexane	7.1
BuPy	3.14
MePHI	5.76
Compressed H_2	5.7

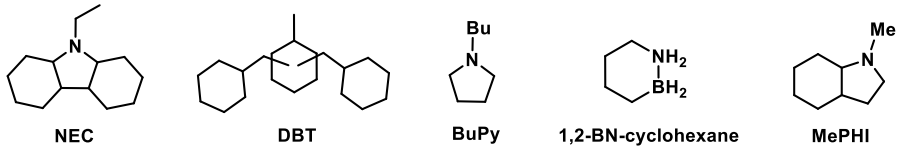

Table 1.1: Hydrogen weight percentage stored in some representative liquid organic hydrogen carriers (LOHCs). The molecules are shown in their H_2-rich form.

On the contrary, in a typical LOHC system hydrogen is chemically stored into a molecule that is liquid and safe to handle at ambient conditions, avoiding energetic costs associated with hydrogen compression [29–33]. Many types of LOHC candidates have been proposed, ranging from small molecules such as methanol [34,35], formic acid (FA) [36], ammonia [37], ammonia- and amine-boranes [38], as well as aromatic compounds such as N-ethylcarbazole [39] or dibenzyltoluene (DBT) [40,41]. The latter are currently the most promising solutions due to their high hydrogen content, as well as their high stability towards cycles of hydrogenation and dehydrogenation under ambient conditions. Table 1.1 provides an overview of representative LOHCs and their hydrogen storage capacity.

Several studies evaluated the use of LOHCs from an economical and practical point of view, assessing and promoting their potential as efficient energy carriers [42,43]. For example, the LOHC would allow moving and distributing hydrogen exploiting existing e.g. pipelines, tracks and cargo ships. In addition, the handling of hydrogen in form of liquids also builds on the public confidence in a global market and society that is already used to liquid fuels. Figure 1.3 represents an extract from Figure 1.2; in this scenario, hydrogen produced in the electrolyzer is stored and distributed as a LOHC until final use in a FC vehicle, where it is extruded from the liquid carrier by means of e.g. catalytic dehydrogenation reaction. Later, the discharged LOHC is reloaded at the filling station or at any place where green hydrogen is available at suitable cost, closing the LOHC storage cycle. Using this approach, the German company *Hydrogenious* is currently promoting the commercialization of LOHC technologies using toleuene-based molecules such as DBT (Table 1.1).

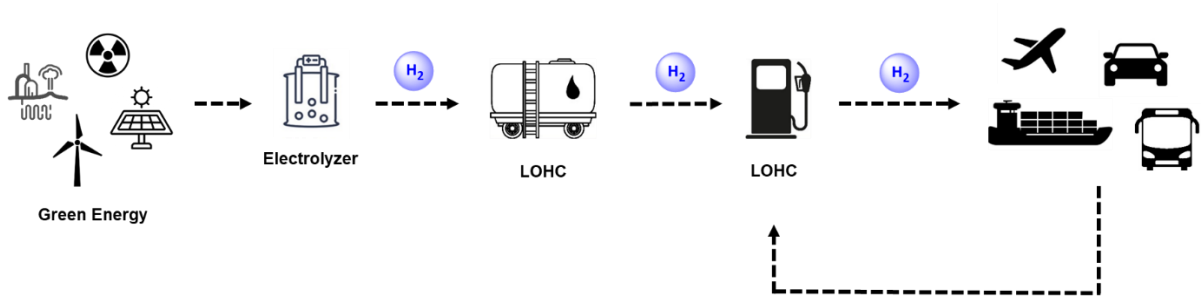

Figure 1.3: Schematic representation of hydrogen production and distribution using a LOHC.

While the LOHC technology is mature in most of the steps in the supply-chain, the main shortfall is that hydrogen can only be released from the LOHC at high temperatures (>250 ºC). This aspect is currently hindering the large commercialization of LOHC fuels for example in the automotive sector [32]. In fact, the on-board use of LOHCs requires that the hydrogen release step is performed at the operative temperature of the used FC, in order to maximize the overall efficiency of the engine. Being PEM-FC the state-of-the-art technology for automotive applications, this means that hydrogen release from the LOHC has to be realized at temperatures 80 ºC≤T≤120 ºC to ensure complete heat-integration [44]. Therefore, the development of efficient catalytic systems for the dehydrogenation of LOHCs at low temperature has the potential to play an important role in the implementation of LOHC technology on a large scale.

In this thesis, my work focuses mostly on the use of the LOHCs formic acid (see Chapters 5 and 6), and the couple isopropanol/acetone (see Chapter 7). Imagining a mobile application, both isopropanol and FA can be considered very attractive LOHC systems if the required hydrogen release is achieved under heat-integrated conditions with the FC. While the high volatility of acetone might represent a challenge towards an effective LOHC recycling, in the case of FA the cycle would be closed by capturing the CO_2 released in air, and recycling it into FA or other useful compounds, as described in the next section.

1.3 Carbon capture and utilization

The level of CO_2 in the atmosphere has increased dramatically due to the extensive use of fossil fuels to satisfy the global energy demand [45]. At the current rates of emissions, it is expected that the CO_2 level in the atmosphere will exceed 600 ppm before the year 2050. In order to mitigate such effect, the scientific community is trying to develop new processes to counteract the CO_2 environmental impact and relative economic consequences. Carbon dioxide has the potential to become a viable, cheap, and safe building block for the synthesis of a wide range of industrially relevant platform molecules [46] and fuels [47]. Thus, carbon capture and utilization (CCU) technologies can reduce our dependence on petrochemicals substituting commonly used fossil-derived sources such as the toxic carbon monoxide (CO), methane (CH_4) or coal [48,49]. Considering the huge scale and impact of the automotive sector on CO_2 emissions in the atmosphere, the possibility to produce fuels directly from CO_2 could dramatically help in mitigating climate change, therefore it has attracted a lot of interests from both academia and industry [50–52]. To date, up to 110 MT per years of CO_2 are currently used for the production of chemical commodities such as urea, carbonates, methanol and salicylic acid. From a practical and economic perspective, the proposed catalytic approaches using CO_2 have to compete with established synthetic routes based on the more reactive carbon monoxide, obtained from reforming of natural gas resulting in the so-called synthesis gas ($CO + H_2$). Direct carbon capture has been investigated using many strategies, both from the atmosphere as well as from industrially relevant gases mixtures such as biogas and flue gas [53,54]. Underground storage in geological formations or empty fossil reservoirs (natural gas) represent a temporary solution for the sequestration and storage of CO_2 [55,56]. The use of amines is by far the most widespread approach towards CO_2 capturing processes [57]; usual routes include the use of amine-based absorbents such as aqueous solutions of triethanolamine (TEA), diisopropanolamine (DIPA), or methyldiethanolamine (MDEA) [58]. However, these methods are usually accompanied by high energetic costs associated with CO_2 compression/decompression, as well as amine regeneration.

Due to the high stability of the molecule (ΔH^o = -400 kJ/mol), whatever transformation involving CO_2 is extremely challenging from an energetic point of view. In this sense, catalysis can provide a solution to the problem of CO_2 activation and promote its further transformation into valuable chemicals. Diverse catalytic methods have been used to perform CO_2 reduction, including photochemistry [59], electrochemistry [60,61] as well as catalytic hydrogenation [45,62–65]. An attractive pathway for CO_2 utilization is represented by the (reversible) water gas shift reaction where CO_2 can be converted into the more reactive CO that can later undergo further transformations (Scheme 1.1) [66].

$$CO_2\,(g) + H_2\,(g) \rightleftharpoons CO\,(g) + H_2O\,(l) \qquad (1)$$

$$CO_2\,(g) + H_2\,(g) \rightleftharpoons HCO_2H \rightleftharpoons CO\,(g) + H_2O\,(l) \qquad (2)$$

Scheme 1.1: Reaction scheme for the water-gas shift reaction of CO_2 to CO [66].

Among the possible products obtainable from CO_2, LOHC molecules are highly attractive targets, as highlighted by the early works from Leitner [67] and Olah [68,69], for FA and methanol, respectively. The methanol economy proposed by Olah has the potential to greatly contribute to the future energy scenario, and many groups are investigating both the hydrogenation of CO_2 to methanol [70,71], as well as the reverse steam reforming reaction to release the three equivalents of hydrogen stored [72]. For case of brevity, this solution will not be discussed in this thesis, but it is in close vicinity with the concepts expressed for the system CO_2/FA.

The other hydrogenation pathway leads to the formation of FA (discovered already in 1670 as the poison produced by the red ant Formica rufa) [73]. The main demand of FA comes from the chemical (pharmaceutical, polymer) and textile industries, as well as from agriculture, with a total production of about 950.000 tonnes per year in 2018 [74]. Scheme 1.2 illustrates the current industrial method employed for the synthesis of FA, where the overall carbonylation of H_2O proceeds promoted by methyl formate as the intermediate. It is possible to notice that CO, which is currently produced starting from fossil fuels, represents the carbon source for the production of FA. In addition, the downstream isolation of FA from H_2O is energy demanding due to formation of an azeotrope mixture with water. Hence, the possibility to obtain FA directly from CO_2 is highly attractive, also considering the toxicity of CO.

$$CH_3OH + CO \underset{NaOMe}{\overset{cat}{\rightleftharpoons}} HCO_2CH_3 \qquad (3)$$

$$HCO_2CH_3 + H_2O \rightleftharpoons HCO_2H + CH_3OH \qquad (4),$$

Scheme 1.2: Reaction scheme for the industrial production of FA [73].

The hydrogenation to FA is an exothermic reaction (-31.5 KJ/mol, Scheme 1.3) but strongly restricted thermodynamically due to entropic limitations (two gaseous molecules combined to give one liquid product). This means that the higher temperatures usually required to overcome kinetic limitations are unfavorable for this transformation, rendering it even more challenging.

$$CO_2\,(g) + H_2\,(g) \longrightarrow HCO_2H\,(l) \qquad (5)$$

$$\Delta G°_{298} = 32.9\ KJ/mol$$
$$\Delta H°_{298} = -31.5\ KJ/mol$$
$$\Delta S°_{298} = -216\ KJ/mol$$

Scheme 1.3: Reaction scheme for the hydrogenation of CO_2 to FA.

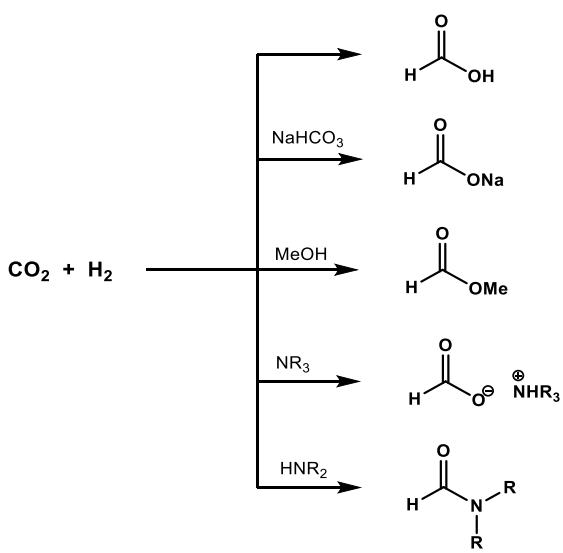

Scheme 1.4: Different strategies for CO_2 capture and hydrogenation to formic acid or formate adducts.

Researchers have used many strategies to lower the thermodynamic barrier and perform the transformation at milder reaction conditions. This involves for example the use of inorganic bases that favor the precipitation of formate salts, or amines as CO_2 trapping reagent, shifting the equilibrium towards the formation of carbamate and formamide derivatives (Scheme 1.4) [57]. The solvent can also play an important role since it can favor higher yields via solvation of both substrate and the produced FA [75]. Other sustainable alternatives include FA production from biomass [74,76], eventually combined with further transformation of FA into syn gas followed by Fischer-Tropsch synthesis of hydrocarbons [77]. Importantly, FA decomposition can lead to the formation of CO and H_2O, representing a potential intermediate to achieve water gas shift reactions avoiding the production of CO from fossil sources (Scheme 1.1).

In Chapter 4, I will demonstrate the possibility to perform CO_2 hydrogenation to FA at very mild conditions (25 ºC, 1 bar) with promising results for further optimization. The reaction is possible using a suitable combination of a transition metal catalyst and an ionic liquid, which will be introduced in the following sections. In addition, Chapters 4 provide a more extensive overview on state-of-the-art CO_2 capture and valorization processes with releavnt examples based on the catalytic systems used in this study.

1.4 Catalysis

The chemical industry already relies on the extensive use of catalysis for the production of almost everything that surrounds us. In the last few decades, there has been a continuous need of developing new catalytic systems that are cheaper and more sustainable. According to the IUPAC definition, a catalyst is “a substance that increases the rate of a reaction without modifying the overall standard Gibbs energy change in the reaction” [78]. Hence, a catalyst allows the obtainment of the desired product but with lower activation energy thanks to the formation of one or more reaction intermediates. During the reaction, the catalyst is regenerated after every catalytic cycle allowing the use of small quantities of it. There are three main types of catalysis: heterogeneous, homogeneous and bio-catalysis. In the former, the catalyst and the substrates/products are present in different phases, usually gas/solid or liquid/solid. On the contrary, in homogeneous catalysis all the reactants are in the same liquid phase, similar to bio-catalysis that is performed in solution by microorganisms and enzymes.

The presence of a transition metal that promotes catalytic transformations is common to both heterogeneous and homogeneous systems. When compared to heterogeneous routes, the main advantages of homogeneous catalysts are represented by milder reaction conditions and higher selectivity of the reactions. This translates to improved atom efficiency and E-factor, as well as lower costs associated with the process, highly attractive concepts for the chemical industry. At the same time, heterogeneous catalysts are more robust and practical, but less active and selective than homogeneous species, therefore requiring harsher reaction conditions in order to perform efficiently. In a typical homogeneous catalyst, a tunable scaffold of organic and/or inorganic ligands surrounds a transition metal. This means that is possible to perform targeted tuning of the steric and electronic properties around the metal selectively for each specific application. In addition, being all reagents in one phase, the direct observation (and sometimes the isolation) of reaction intermediates and catalyst-substrate adducts provides a deep understanding of the reaction mechanisms involved, usually difficult to achieve with biphasic heterogeneous systems.

Many homogeneous processes are still associated with severe drawbacks such as catalyst stability over long times, as well as product separation hence recyclability of such systems. Nevertheless, homogeneous catalysis already contributes largely to the production of bulk chemicals and commodities. The Ziegler-Natta polymerization of terminal alkenes (with Ti and Zr homogeneous complexes) contributed greatly to the development of low-cost plastics such as (low- and high-density) polyethylene,

polypropylene, polybutene, and many other co-polymers. Other relevant examples of homogeneous processes are represented by the oxidation of ethylene to acetaldehyde using $PdCl_2$ (Wacker process), the hydrogenation of olefins catalyzed by the Wilkinson´s catalyst $Rh(PPh_3)_3Cl$, as well as the hydroformylation of alkenes using cobalt pre-catalysts in the presence of phsosphine (Shell) or carbonyl (BASF-oxo) ligands. Other successful examples include metathesis, carbonylation, hydroformylation, as well as oxidation reactions.

Typically, expensive and rare metals such as ruthenium, iridium, platinum, palladium and rhodium are at the core of the best performing homogeneous and heterogeneous systems reported in the literature. In the optic of a more sustainable production of chemicals, a sustainable transition towards the first-row metals is highly desirable due to their major abundance, reflected in reduced costs and environmental impact [79,80].

1.4.1 Homogeneous pincer-type catalysis

The careful choice of the ligand scaffold is of crucial importance for the control of both the activity and the selectivity of the resulting homogeneous catalyst. In fact, steric and electronic properties given by selected ligands can affect deeply the course of a reaction by influencing transition states and reaction intermediates. Typically, a pincer ligand consists of a coplanar chelating structure able to bind the metal center in a tridentate fashion [81]. The constricted geometry given by the rigidity of the ligand results in improved thermal stability of the resulting organometallic complex, avoiding e.g. leaching of the metal in solution [82,83]. In 1976, Moulton and Shaw reported the first example of a pincer ligand with a $^tBu_2PCP$ structure [84]. Since then, a wide range of pincer ligands bearing different heteroatoms have been synthetized and fully characterized [85]. It has been showed that often the pincer structure offers the best solution in homogeneously catalyzed transformations due to an optimal compromise between activity, selectivity and stability of the catalysts. Based on their reported activity towards both hydrogenation and dehydrogenation reactions, this work discusses mainly the use of a selected sub-family of pincer complexes (Ru-PNP), as shown in Figure 1.4.

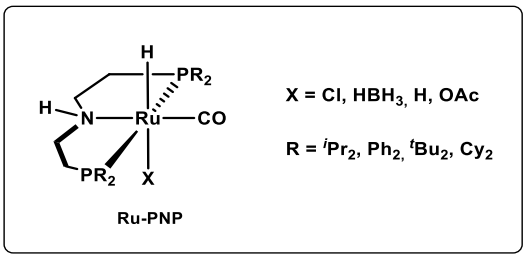

Figure 1.4: Examples of Ru-PNP complexes used in this study.

Two phosphorous arm donors and a central nitrogen bearing an amino proton surround a central ruthenium atom in the oxidation state 2+. Changing the substituents on the phosphorous arms can lead to differences in the catalytic activity based on the degree of electron density donation to the metal center. In addition, the steric properties of the pincer structure have an effect on e.g. solubility of the catalyst and favorable coordination of the substrate. Finally, two X-type ligands and a spectator ligand (CO) complete the octahedral coordination sphere of the catalyst. As discussed in Chapter 3, one of the key aspect using this family of catalysts is represented by their need of activation prior to substrate coordination. In the example shown in Figure 1.4, abstraction of the X ligand is required to start any catalytic transformation. Importantly, several Ru-PNP complexes are very robust and commercially

available at a relatively low price. In this study, I have performed minor modifications on the ligand scaffold, mostly focusing on the effect of the X and R groups (Figure 1.4) on the overall catalytic activity.

Importantly, the pincer structure is often considered to be co-responsible of the resulting catalytic behavior of the organometallic species due to chemical interactions with the substrates [86,87]. This is the case for the Ru-PNP catalysts used in this study, where the amino proton on the PNP structure is often found co-responsible of the resulting catalytic behavior due to hydrogen bond interactions that stabilize reaction intermediates and favor substrate´s coordination to the metal. Hence, fine tuning of the tridentate ligand scaffold results in organometallic species able to catalyze a plethora of chemical transformation with high selectivity and chemical stability. In this sense, the review work in Appendix E provides a wide overview of the many different pincer structures that have been proposed in the past two decades, with high focus on hydrogenation and dehydrogenation reactions in the optic of the hydrogen economy [88].

Acceptorless alcohol dehydrogenation (AAD) is a highly attractive process in hydrogen-related technologies since it provides a green route for efficient hydrogen release from alcohols. In particular, isopropanol (*i*PrOH) has been used extensively as a model substrate to demonstrate the feasibility of such methods [89]. This is also because the dehydrogenation of secondary alcohols is easier than primary ones, due to higher stability of the resulting ketone compared to aldehydes. The first example of homogeneously catalyzed acceptorless dehydrogenation of alcohols is as old as 1967, when Charman showed isopropanol dehydrogenation using a rhodium chloride catalyst [90], later improved by the addition of tin [91]. Later, Robinson demonstrated the dehydrogenation of different alcohols under refluxing conditions using the ruthenium catalyst $[Ru(OCOCF_3)_2(CO)(PPh_3)_2]$ [92]. Sugi in 1981 reported the dehydrogenation of isopropanol mediated by light irradiation using the Wilkinson catalyst $RhCl(PPh_3)_3$ at room temperature [93]. In 1985, Shvo reported the formation of esters from primary alcohols using a ruthenium catalyst [94]. Relevant improvements to the field were provided by the works of Cole-Hamilton who reported ruthenium [95] and rhodium [96,97] catalysts for the dehydrogenation of different alcohols. In 1983, Saito showed that the addition of triphenylphosphine to a solution of $[Rh_2(OAc)_4]$ unlocks catalytic activity towards isopropanol dehydrogenation [98].

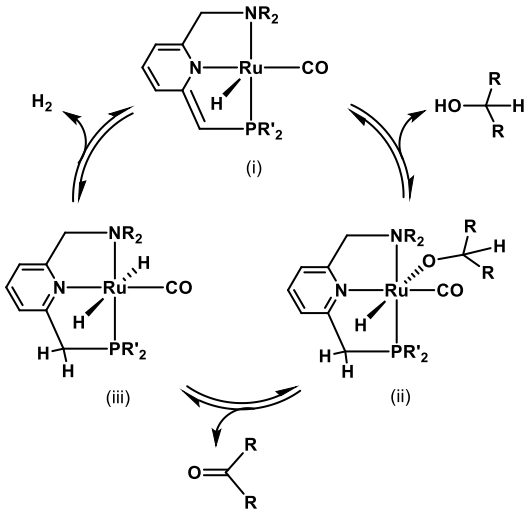

Scheme 1.5: Milstein´s first generation catalysts showing metal ligand cooperation based on aromatization-dearomatization of the pincer ligand.

Many reports will follow, including the use of light irradiation as promoter, but the field did not see particular improvements until the beginning of this century, when the groups of Milstein [99,100] and Beller [101] revolutionized the field using pincer-type homogeneous complexes and showing evidences of metal-ligand cooperation. Scheme 1.5 shows an example of the first generation catalysts developed by Milstein based on aromatization and dearomatization of a pyridine-based PNP ligand [102–105]. On the contrary, Beller started by testing the influence of several phosphine ligands on the activity of in-situ formed ruthenium catalysts, including the same family of PNP pincer discussed in this study. Later, selected configurations of Ru and PNP ligands were synthetized and successfully characterized including crystal structures [106,107]. The pincer catalysts developed by Beller belong to the so-called Noyori-type pincer scaffold [108]. This requires that the amino proton is in a *syn* configuration with respect to the hydride ligand, providing stabilization of the substrate via hydrogen bonding (Scheme 1.6).

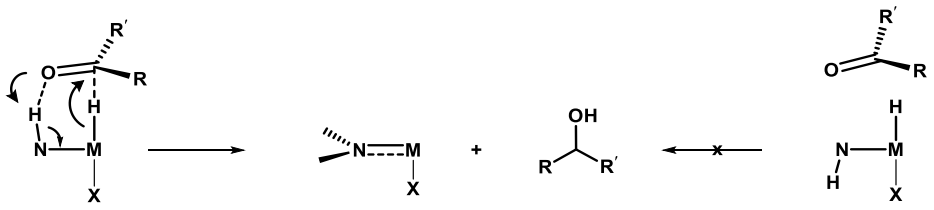

Scheme 1.6: Noyori-type reactivity of pincer complexes used in this study.

Since these seminal works by the two authors, pincer-type catalysts have been widely reported to promote facile hydride transfer between substrates and hydrogen gas, avoiding the use of sacrificial Meerwein-Ponndorf-Verley reagents. Concerning the Ru-PN^{H}P complexes used in this study, the outer sphere mechanism depicted in Scheme 1.7 is usually the main pathway invoked [108].

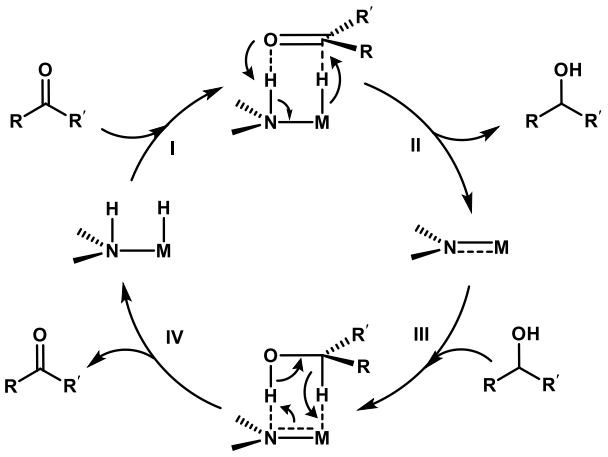

Scheme 1.7: Schematic representation of acceptorless (de)hydrogenation reaction using metal pincer complexes.

The first step of a hydrogenation reaction consists in a nucleophilic attack of the hydrido ligand to the substrate carbonyl group (I). In this conformation, the metal complex performs a concerted hydrogen transfer to the substrate involving both the amino proton and hydride ligand (II), resulting in the formation of the corresponding alcohol. The so-obtained amido complex can be considered the catalytic active specie for dehydrogenation reactions, where an alcohol can coordinate the metal complex via hydrogen bonding

and C-H --- M interaction (III). Finally, the carbonyl substrate leaves the complex (IV) that can either deliver pure hydrogen (in dehydrogenation reactions), or undergo another hydrogenation cycle. The described outer sphere mechanism presents some advantages compared to the inner sphere alternative. For example, it does not require prior activation of the substrate (e.g. deprotonation of alcohols) as well as the presence of two vacant sites on the metal center preferably *cis* to each other. Nevertheless, is has been demonstrated that both mechanisms involve the presence of the same mono- and di-hydride Ru-species as the main catalytically active species (see Chapter 3) [107]). Many mechanistic investigations have been trying to elucidate the mechanisms involved with this type of complexes and the non-innocence of pincer-type ligands [106,109–112].

After the breakthrough reported by the groups of Milstein and Beller, pincer complexes have been successfully applied for a plethora of relevant chemical transformations. Important was the contributions from Gusev using both Ru-PNP for dehydrogenations [113], as well as Ru-SNS pincer catalysts for the hydrogenation of esters [114]. Leitner and Klankermayer have provided relevant contributions to the field highlighting the potential of carbon dioxide capture and utilization [115–118]. The same topic was investigated by Himeda and Fujita using iridium pincer complexes for the reversible hydrogen storage in FA and methanol [119–122]. Ru-PNP complexes used in this study were reported as active catalysts for efficient hydrogen release from aqueous ethanol [123], FA [124] and methanol [125]. In addition, Ru-PNP complexes catalyze ethanol transformation to ethyl acetate [126], hydrogen peroxide decomposition to O_2 and H_2O [127], ethanol upgrading to bio fuels [128–131], glycerol-to-lactic acid dehydrogenation [132,133], hydrogen evolution from biomass [134], as well as biomass valorization by means of transfer hydrogenation reactions [135–138]. Pincer complexes also promote formation of high-value products by dehydrogenative coupling of alcohols and amines, resulting in the formation of esters [139–143] and amides [144–148], respectively. Importantly, the group of Nishibayashi contributed reporting active pincer catalysts active towards nitrogen fixation to ammonia as a green alternative to the consuming Haber-Bosch process [149–152].

Promising are the results obtained with first row transition metal complexes, with the vision of a green transition towards the use of cheaper and more abundant metals. In particular, iron and manganese PNP complexes have been reported with moderate activity for both hydrogenation [153–155] and dehydrogenation reactions [156–161]. Beller demonstarted the use of a Mn-PNP catalyst for methanol reforming [162], as well as for the hydrogenation of carbon monoxide to methanol [163]. Hazari, Bernskoetter, Kirchner, Gonsalvi and co-workers investigated the use of iron and obtained promising results using Fe-PNP complexes in the presence of Lewis Acids as reaction additives [164]. The developed systems effectively catalyze methanol reforming [165], FA dehydrogenation [166–168], as well as CO_2 hydrogenation to formate [169,170]. Importantly, in Chapter 5 I will show the promising activity of a Mn-PNP catalyst towards FA dehydrogenation at mild conditions.

Chapters 4 and 5 will provide selected examples of state-of-the-art pincer complexes based on the specific applications discussed in each chapter. The main novelty behind my research project is represented by the combination of such Ru-PNP complexes and ionic liquids, a class of solvents with extremely interesting properties.

1.5 Ionic Liquids

An ionic liquid (IL) is usually defined as a salt that is in the liquid state at temperatures <100 ºC [171]. Toward the design of sustainable chemical transformations, ILs have been proposed as a green alternative to common volatile organic solvents due to their unique properties. To mention some, chemical and thermal stability, recyclability, negligible vapor pressure under ambient conditions (hence no flammability), as well as tunable properties depending on the desired application. Therefore, they can be used for a wide range of applications [172,173], from catalysis [174–176], product separation [177], hydrogen storage (using borohydride ILs) [178,179], and biomass processing [180–184]. Along with their extraordinary properties as solvents, ILs have been reported as active co-catalysts, offering a wide spectrum of possible applications [29–32]. In fact, ILs can chemically interact with substrates and/or catalyst providing unique chemical properties to the resulting solution.

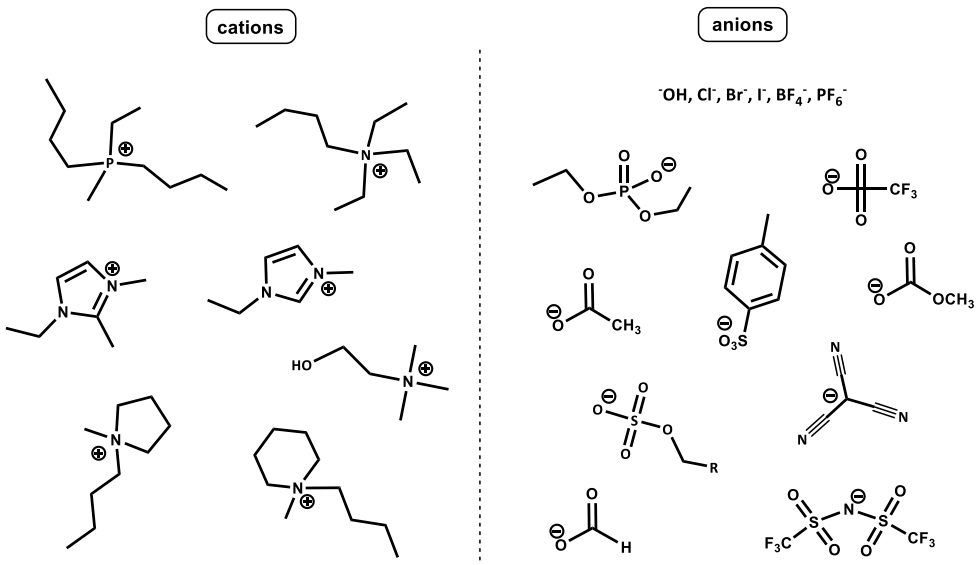

Figure 1.5: Examples of cations and anions of commercially available ionic liquids.

The most used and commercially available ILs are formed by imidazolium, ammonium and phosphonium cations in combination with common anions such as OTf, NTf_2, halogens, acetate, PF_6, BF_4 etc. Figure 1.5 shows some examples of commonly used and commercially available ILs, some of them used in this study. It is possible to imagine that there are almost unlimited combination of cations and anions; in this sense, the possibility of synthetizing task-specific ILs for each desired application is highly attractive from a synthetic point of view. Typically, the anion is considered to be the component affecting chemical properties of the IL such as solvation and overall acidity/basicity of the solution [185,186]. The cation affects other physical parameters such as viscosity, melting point, or density of the IL. The melting point can be influenced by van der Waals interactions, size, charge distribution and symmetry of the ions, as well as hydrogen bonding involved [187]. As an example, bulky and asymmetric cations lead to a decrease in the melting point of the IL. The density of typically employed ionic liquids is usually higher than H_2O, ranging from 1.1 to 1.6 g/ml.

One of the main properties when looking at solvents is their polarity. However, the definition of polarity has always been ambiguous, since it depends on the specific interaction between the solvent and each possible solute [188]. Generally, polarity is affected by multiple factors such as permanent and induced dipole interactions, Columbic interactions, hydrogen bonding, as well

as electron pairs interactions [189]. As a consequence, polarity can not be measured independently for a selected solvent, but only in relation with a solute, and excluding the interactions leading to chemical transformation of the latter. Many studies reported the measurement of the polarity of different ILs in order to find the most suitable solvent for each specific application [188,190]. However, often the used experimental methodologies differ from the standard procedures, resulting in different values that are sometimes difficult to correlate between each other. Generally, this is valid for the measurement of many chemical and physical properties of ILs (acidity, viscosity, density, volatility, as well as degradation pathways etc). The scientific community has achieved considerable advances towards a correct interpretation of the observed behaviour of IL mixtures. Nevertheless, a deeper understanding of the bonds involved between cation and anion, as well as IL and solute, still remain sometimes elusive due to the presence of multiple factors contributing to the overall properties of this fascinating class of solvents [191].

In connection with CCU processes discussed in 1.3, the high solubility of CO_2 in ILs has inspired many groups to carry out investigations on the use of ILs as CO_2 capturing agents [192–197]. Moreover, ILs have been reported to promote photo- [198] and electrocatalytic reduction of CO_2 [199]. The topic will be discussed more in depth in Chapter 4, with examples of reported procedures employing ILs for CO_2 capture and valorization.

In this thesis, I have explored the use of ILs as suitable solvents for hydrogenation and dehydrogenation reactions at mild conditions in the presence of Ru-PNP catalysts. Importantly, besides their use as reaction additives [200–202], organometallic (pincer) catalysts operating exclusively in IL phase are scarcely reported. Hence, I will show that the IL activates Ru-PNP catalysts and stabilizes catalytic active species under a wide range of reaction conditions and for different chemical transformations. As such, it is possible to avoid the use of sacrificial additives and solvents that are usually required for e.g. activation and stabilization of the catalyst, as well as stabilization of substrate and/or product in the catalytic phase. Importantly for the applications discussed in this work, one of the main advantages represented by the use of ILs is the possibility to obtain a clean flow of products without the contamination of volatile solvents. This is a particularly important aspect when considering hydrogen release from LOHC for automotive applications, where the employed PEM-FCs require a clean inlet of hydrogen.

1.6 Supported Ionic Liquid Phase (SILP)

The supported ionic liquid phase (SILP) technology represents an elegant solution to merge the advantages of homogeneous and heterogeneous catalysis, i.e. high selectivity and mild reaction conditions together with increased stability given by the support material [203]. The method was originally proposed in 2003 by Mehnert and Riisager for both hydrogenation [204] and hydroformylation reactions [205–208]. In detail, the procedure consists of immobilizing a homogeneous catalyst onto a support material (SiO_2, Al_2O_3, TiO_2, C…) using an IL as the homogeneous phase where the organometallic complex is dispersed. Figure 1.6 provides a schematic representation of the SILP technology; the catalyst/IL mixture is deposited into the porous support material, therefore creating a thin layer of homogeneous active phase embedded within the pores and the channels of the support.

There are various techniques for the preparation of SILP materials. The most widespread and reliable procedure is represented by incipient wet impregnation, where support, IL and catalyst are dissolved and stirred in a suitable solvent, which is later evaporated under reduced pressure [209]. Other possible modifications involve e.g. binding of the IL covalently to the support material, as well as changes in the morphology of the support such as powder, pellets, and monoliths. For example, the latter shapes are usually preferable in continuous flow fixed-bed reactors in order to avoid pressure drops in the catalyst bed. The three components of a

SILP material operate synergistically: catalyst and IL loading, percentage of pore filling (α), pore size, shape and superficial area of the support, are all features to be considered when preparing a SILP catalyst. Importantly from a sustainable point of view, the loadings of both catalyst and IL are minimized by the high dispersion within the mesoporous support, maximizing the efficiency of each component. This property can help overcoming mass transfer limitations that usually hamper conventional liquid−liquid biphasic processes. Moreover, the low volatility of ILs can facilitate the continuous product separation from the catalytic active phase, usually a severe drawback of traditional homogeneous systems. All of these unique features enable the use of SILP catalysts for e.g. under fixed-bed gas-phase reaction conditions (see Chapter 7), otherwise impossible with organometallic species. Similar concepts based on the use of ILs include supported ionic liquids (SILs), supported ionic liquid films (SILFs), solid catalysts with ILs (SCILs), solid catalysts with IL layer (SCILL), supported ionic liquid catalysis/catalysts (SILC/SILCAs) and supported IL nanoparticles (SILnPs) [210].

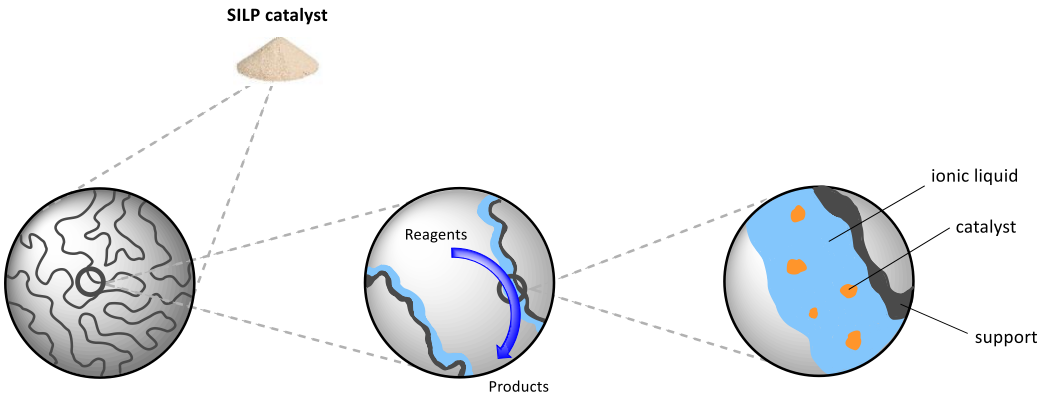

Figure 1.6: Representative scheme of the Supported Ionic Liquid Phase (SILP) technology.

Despite the only 15 years of history, SILP catalysts have been applied successfully to a plethora of gas-phase transformations such as hydroformylation [205,211–214], (chiral) hydrogenation [215–219], Heck reaction [220], hydroamination [221], hydrosylilation [222], carbonylation [223,224], epoxidation [225], alkylation [226], water-gas shift [227–231] as well as for NH_3 adsorption processes [232]. Haumann recently reviewed the potential of SILP materials towards future implementation in large-scale industrial processes, with hydroformylation, asymmetric hydrogenation and water gas shift reactions showing promising results for future optimization [233]. Importantly for the topics discussed in this thesis, and to the best of my knowledge, there are no examples in the literature reporting the use SILP materials for dehydrogenation reactions. In this sense, the only relevant contribution was provided by Haumann who reported the use of Ru-PNP catalysts immobilized on a support material for the low temperature reforming of methanol [234,235].

In Chapter 7, a suitable combination of Ru-PNP catalyst and IL was successfully immobilized into a support material and applied for the gas-phase dehydrogenation of isopropanol at low temperature. In addition, I have carried out a preliminary experiment that demonstrates the activity of Ru-SILP catalysts for the low temperature dehydrogenation of FA as well (see Chapter 8).

1.7. Outlook and contents of the thesis

In this thesis, I have explored the reactivity of homogeneous Ru-PNP catalysts in ILs towards hydrogenation and dehydrogenation reactions for energy storage and distribution processes. This includes dehydrogenation of LOHC molecules such as isopropanol and FA for hydrogen release at low temperature, as well as CO_2 capture and hydrogenation to FA. As an expansion of the introduction provided in this chapter, the review work in Appendix E offers a wide overview of the many applications of pincer complexes within sustainable catalysis, often resulting in the best choice for homogeneously catalyzed processes. In addition, more detailed comparisons with state-of-the-art methods using homogenous catalysts will be provided in the next chapters for each application. Looking at the literature, it is also possible to notice that examples of Ru-PNP operating exclusively in ILs are extremely rare, highlighting the novelty of this PhD project.

In particular, Chapter 2 describes the design and optimization of the different reaction set-ups that allowed me to produce a substantial part of the scientific data presented in this work. The fundamental studies shown in Chapter 3 represent the principles and the foundation of this PhD dissertation, demonstrating new activation and reactivity modes involving Ru-PNP catalysts and ILs. It has been demonstrated that a suitable IL can activate Ru-PNP catalysts, rendering them available to undergo hydrogenation and dehydrogenation reactions. Based on these findings, I have developed the catalytic applications described in the following chapters.

Chapter 4 discloses the hydrogenation of CO_2 to FA catalyzed by Ru-PNP/IL at mild conditions. The IL and the Ru-PNP catalyst act in synergy promoting formation of FA already at ambient conditions. Chapter 5 reports the remarkable activity of Ru-PNP/IL combinations for the continuous flow FA dehydrogenation at temperatures compatible with FC applications. Therefore, Chapter 6 describes a potential application of the Ru-PNP/IL for the reversible CO_2 hydrogenation and FA dehydrogenation, envisioning its development as a potential device for efficient storage and distribution of green energy. Finally, the scientific work presented in Chapter 7 is a result of a collaborative effort with Friedrich-Alexander-Universität (FAU) where I performed my external stay in September 2020. In this project, I investigated the use of Ru-PNP complexes in ILs for the dehydrogenation of another LOHC candidate, isopropanol (*i*PrOH). In addition, the system Ru-PNP/IL was successfully immobilized onto a support material using the SILP technology, demonstrating the applicability of the system for fixed-bed reaction conditions.

The confidentiality of the projects, combined with the possibility of patenting parts of the research output described herein prevented prior publication of scientific results. Appendices F-I contain papers that are currently in preparation and will be submitted to peer-reviewed journals after the publication of this thesis. In this regard, the preliminary studies showed in Chapter 3 will be distributed between the articles based on the topic that is discussed in each work (CO_2 hydrogenation, FA and *i*PrOH dehydrogenation). Similarly, the data obtained for both CO_2 hydrogenation and FA dehydrogenation present obvious overlaps, resulting in multiple choices when it comes to publishing strategy. Moreover, considering the large amount of data and ongoing work in the Nielsen´s group, hopefully more publications will follow.

2. Design and optimization of a reaction set-up for gas phase reactions

This chapter describes the design, construction and optimization of the reaction set-up used in this study for dehydrogenation reactions. I would like to remark the extremely helpful contribution of Andreas Graff Pedersen from the DTU Chemistry workshop who helped in the assembling of the here described equipment.

I have started by designing an allocated fume hood that allows carrying out batch reactions producing mixtures of different gases; as shown in Figure 2.1, it is possible to carry out up to three different reactions. After proper treatment of the downstream gases (condenser and/or cold trap, depending on reaction temperature and type of reaction), the flow is directed to a mass flow meter (MFM). The fume hood is equipped with four different MFMs, each measuring a different range of gas volumes, depending on the reaction scale used, hence gas flow produced. There is the possibility to insert more MFMs in line for example for higher flows of gases (up to 1000 mL/min) which will be done in the next future. Finally, the room has been equipped with H_2 and CO sensor to comply with safety regulations.

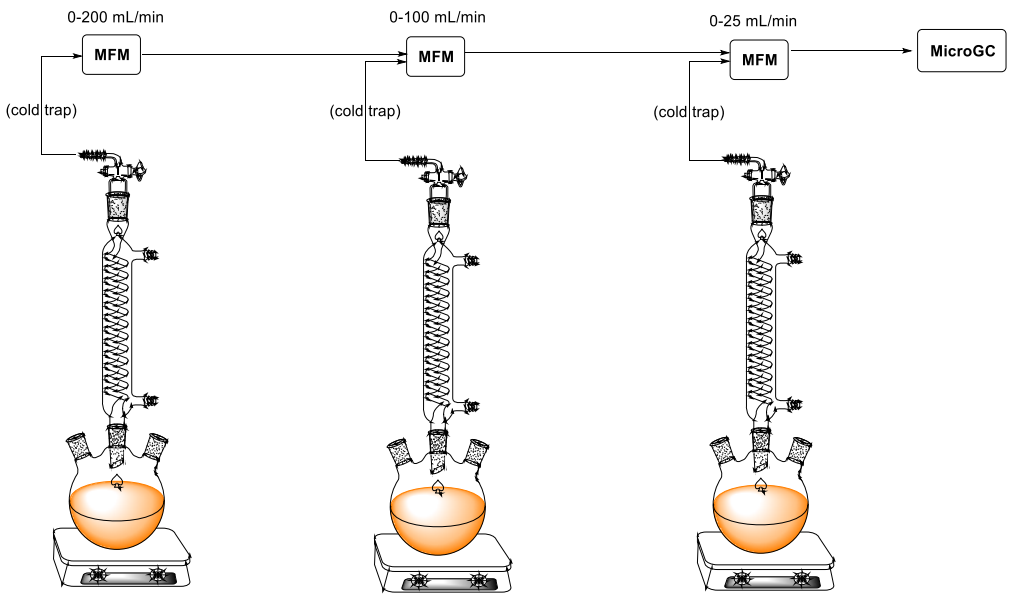

Figure 2.1: Schematic representation of the reaction set-up for batch reactions producing gases at DTU Chemistry**.**

Figure 2.2 shows a real picture of the set-up just described. The fume hood is equipped with a Schlenk line that allows cleaning of the pipes, flushing of condensers and reaction flasks, possibility to conduct reactions under inert conditions, as well as degassing of feeding solutions when needed (A). Manometers at each reaction set-up allows measuring of the total pressure in the system in real time (B), while the MFMs measure the produced flow (C). Finally, it is possible to either vent the downstream in the fume hood or a gas-bag (D), or direct it to the GC for analysis and quantification of the gaseous products (E).

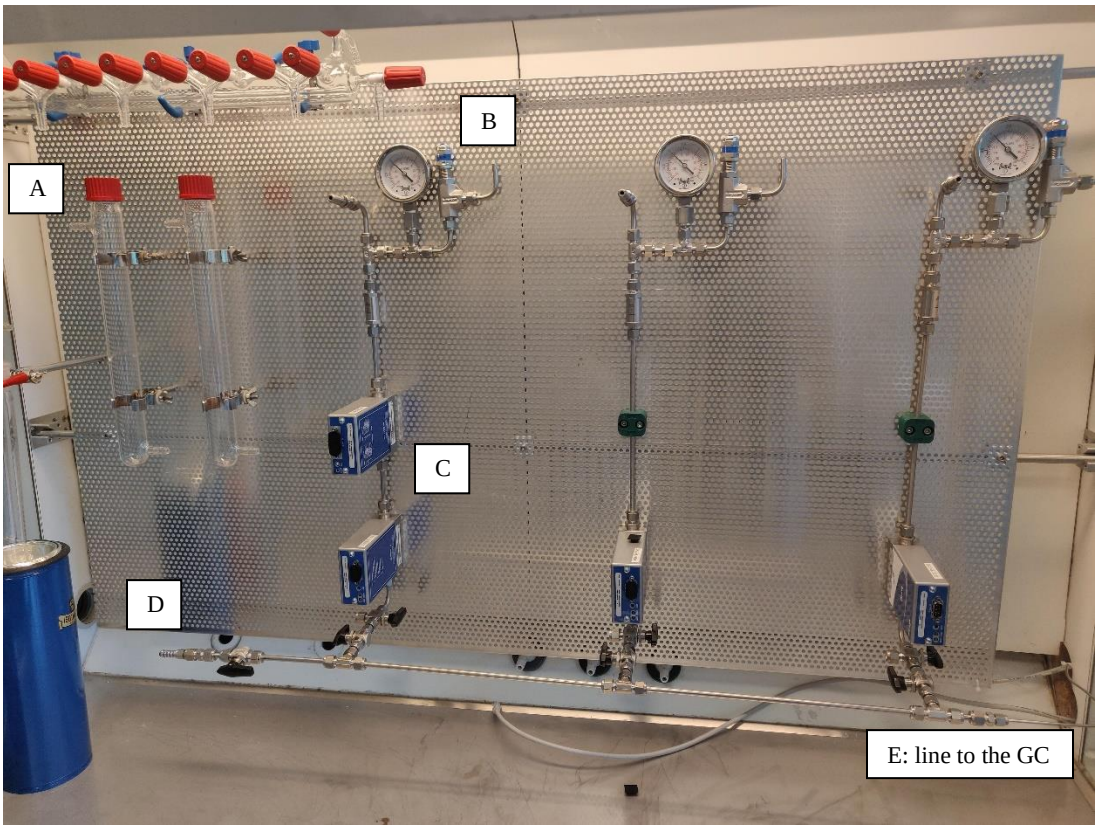

Figure 2.2: Reaction set-up for batch reactions producing gases at DTU Chemistry**.**

Figure 2.3 (up) depicts a schematic representation of the reaction set-up I used to carry out continuous flow FA dehydrogenation reactions as described in Chapter 5. More in detail, Figure 2.3 (down) shows a real image of the same set-up, where two different syringe pumps (with a total of three syringes) were feeding FA to the reaction flask (A). A Findenser was connected to the reaction flask to ensure full FA condensation (B_p = 100.8 ºC) (B). In this example, the off-gases where simply connected to an oil bubbler for a visual observation of the produced flow. As described before, it is possible to direct the downstream flow to the MFM (D) and/or to the MicroGC.

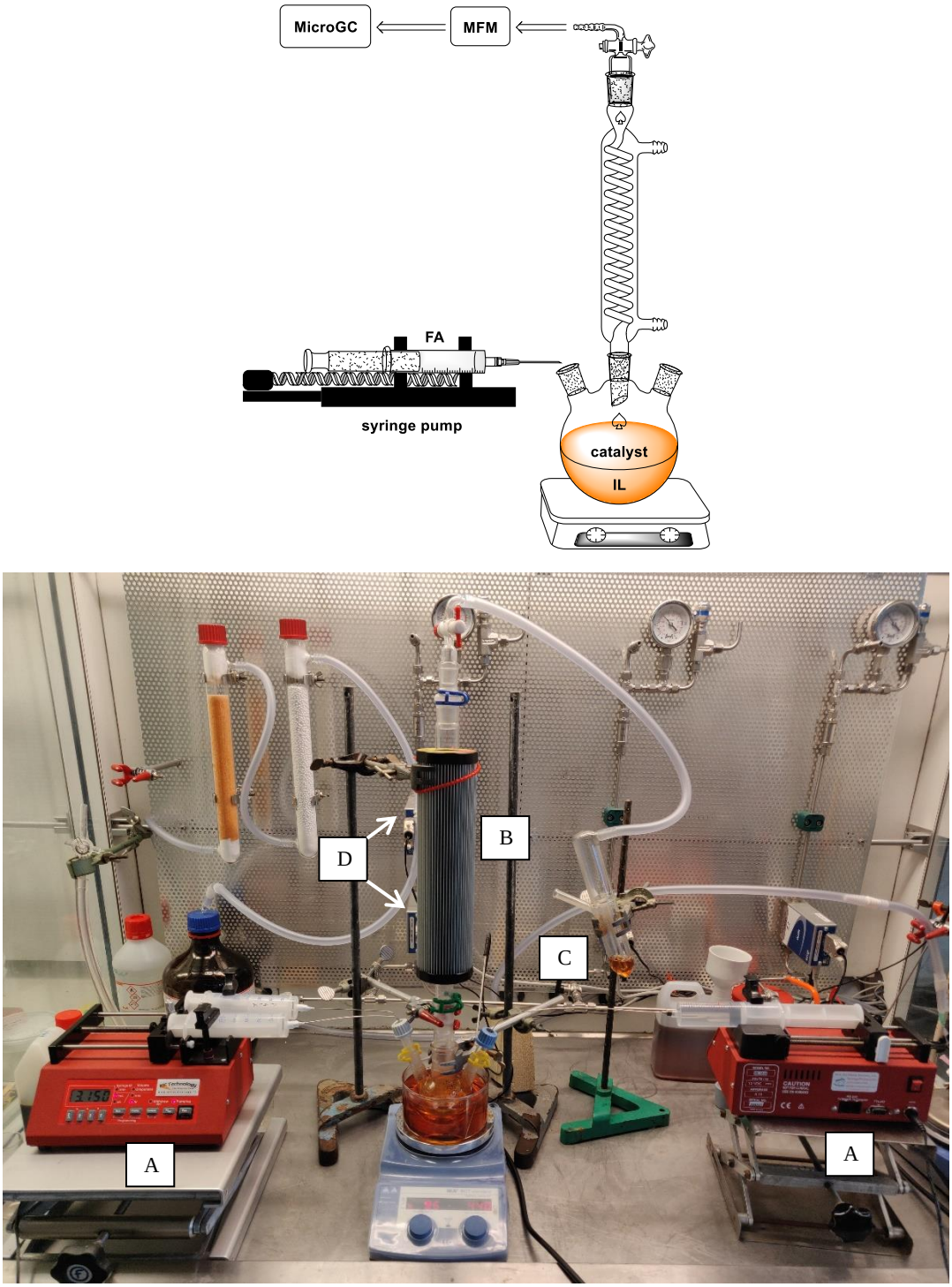

Figure 2.3: Schematic representation (up) and real image (down) of the reaction set-up used for continuous flow FA dehydrogenation (see Chapter 5)**.**

Figure 2.4 shows a picture of the set-up I have designed for gas phase reaction, which can be divided in three sections: upstream, reactor and downstream. In particular, four mass flow controllers (MFCs) control the desired volumetric flow of gases coming from the gas bottles (A), in this case H_2, CO_2 and CO (N_2 and Ar are used as carriers and for flushing/cleaning of the pipes). Importantly, by changing the calibration parameters of the MFCs, it is possible to feed different gases to the system. Particle filters (B) prevent dust and other impurities to reach the MFM and enter the system. A manometer equipped with a safety valve (E) visualizes the total pressure of the system, while a VacPro controller (F) controls the gas flow in real time. After the MFC, one-way valves (C) allow flow in only one direction and minimize pressure drops and fluctuations due to the gas bottles. A closed compartment filled with glass pieces of different sizes ensures proper mixing of the chosen gases (D). Later, three valves direct the flow either to the reaction flask or vessel, or bypass the system for e.g. GC measurements (G). The downstream flow is connected again to the line (H), with possibility to pass the flow through a cold trap (I) before it enters the MFM (L). The latter measures both temperature and volume of the downstream flow, with acquisitions in the order of milliseconds. Finally, the flow is directed to the MicroGC for the precise quantification and full analysis of the gaseous reaction products (M).

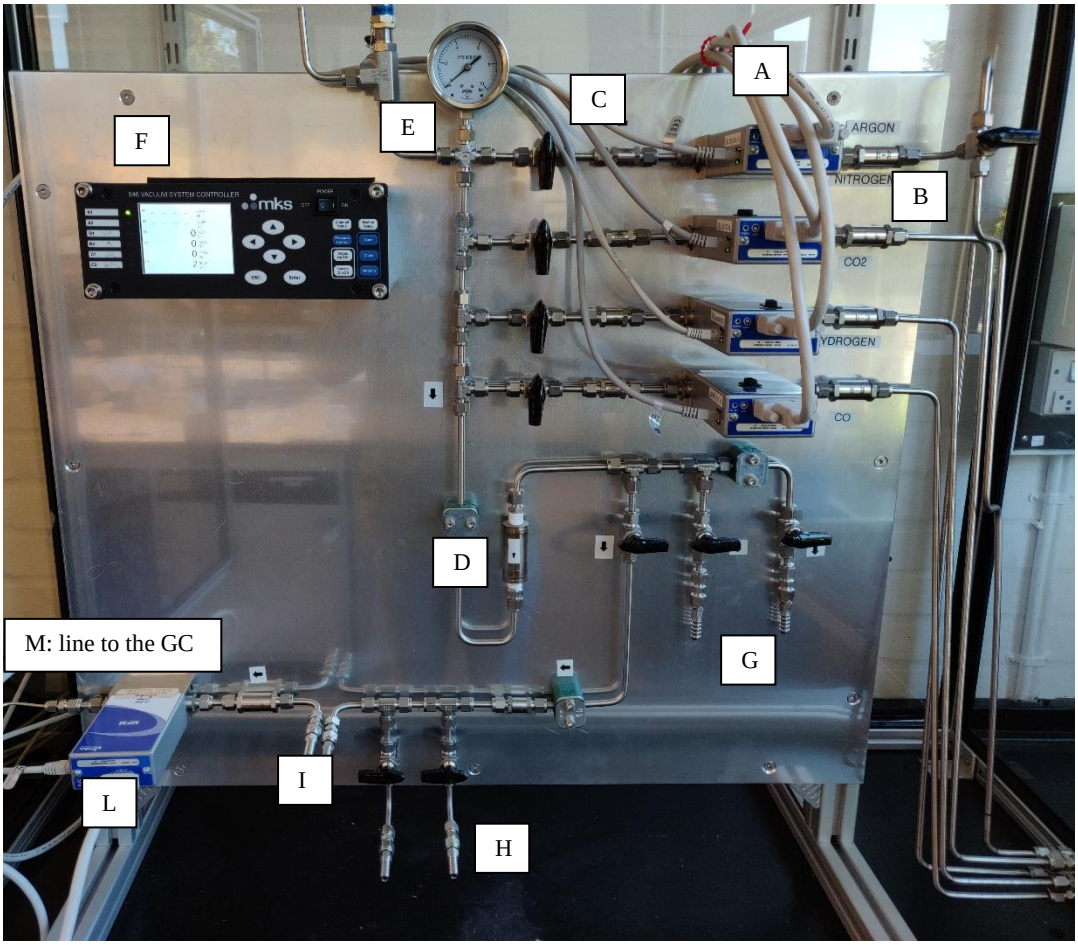

Figure 2.4: Set-up for continuous flow gas reactions optimized at DTU Chemistry**.**

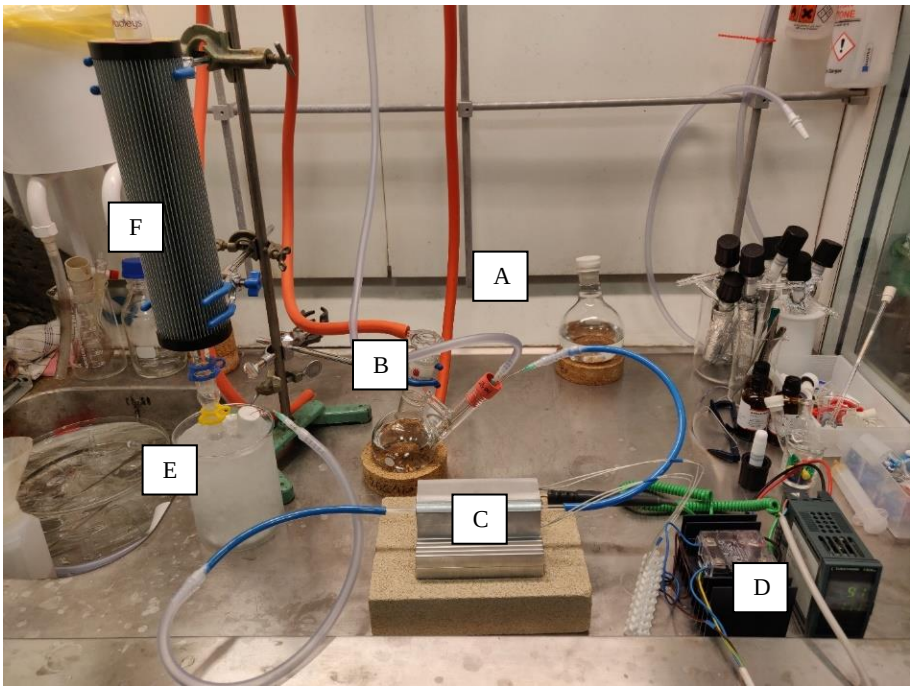

Figure 2.5: Demonstrative set-up for continuous flow gas reactions using a SILP catalyst**.**

Figure 2.5 depicts a demonstrative reaction set-up that I have used at DTU Chemistry to perform preliminary experiments using the prepared SILP catalysts discussed in Chapter 7. Argon gas from the Schlenk line (A) was bubbled through a degassed solution of anhydrous *i*PrOH in order to saturate the argon flow with *i*PrOH (B). Inside the aluminum oven (C), a quartz tube contains the SILP catalyst (2-3 cm reaction bed, 100-250 mg of SILP) that is exposed to the incoming flow of *i*PrOH/N_2. The temperature of the oven is controlled by an electric system composed by thermocontroller, thermocouple, and relay (D). After the reaction oven, the downstream flow is cooled in a cold trap with dry ice (E), and passed through a Findenser (F) to ensure quantitative condensation of isopropanol/acetone. By adding a suitable NMR solvent in the cold trap, it was possible to observe traces of acetone in solution (see Chapter 7).

Later, I have tested such system in the gas-phase set-up described in Figure 2.4. Figure 2.6 shows the overall installation, as well as details of the overall set-up. Importantly, this demonstrative set-up allowed me to observe H_2 via MicroGC, assessing the feasibility of both FA and *i*PrOH dehydrogenation using the SILP technology (see Chapters 7-8). For example, based on the so-obtained preliminary results, I have been able to select targeted SILP materials to test in the pilot plant during the limited time available at FAU, therefore producing most of the results that compose Chapter 7. In detail, it is possible to observe the quartz tube (A) containing the SILP catalyst, resistance elements to heat the aluminum block to the desired temperature (B), as well as a thermocouple measuring the temperature of the oven (C). The lower picture shows the relay (D) and the thermocontroller ensuring constant temperature of the oven (E). As already described before, the downstream flow was directed towards the MFM and the MicroGC, usually after cooling in a cold trap.

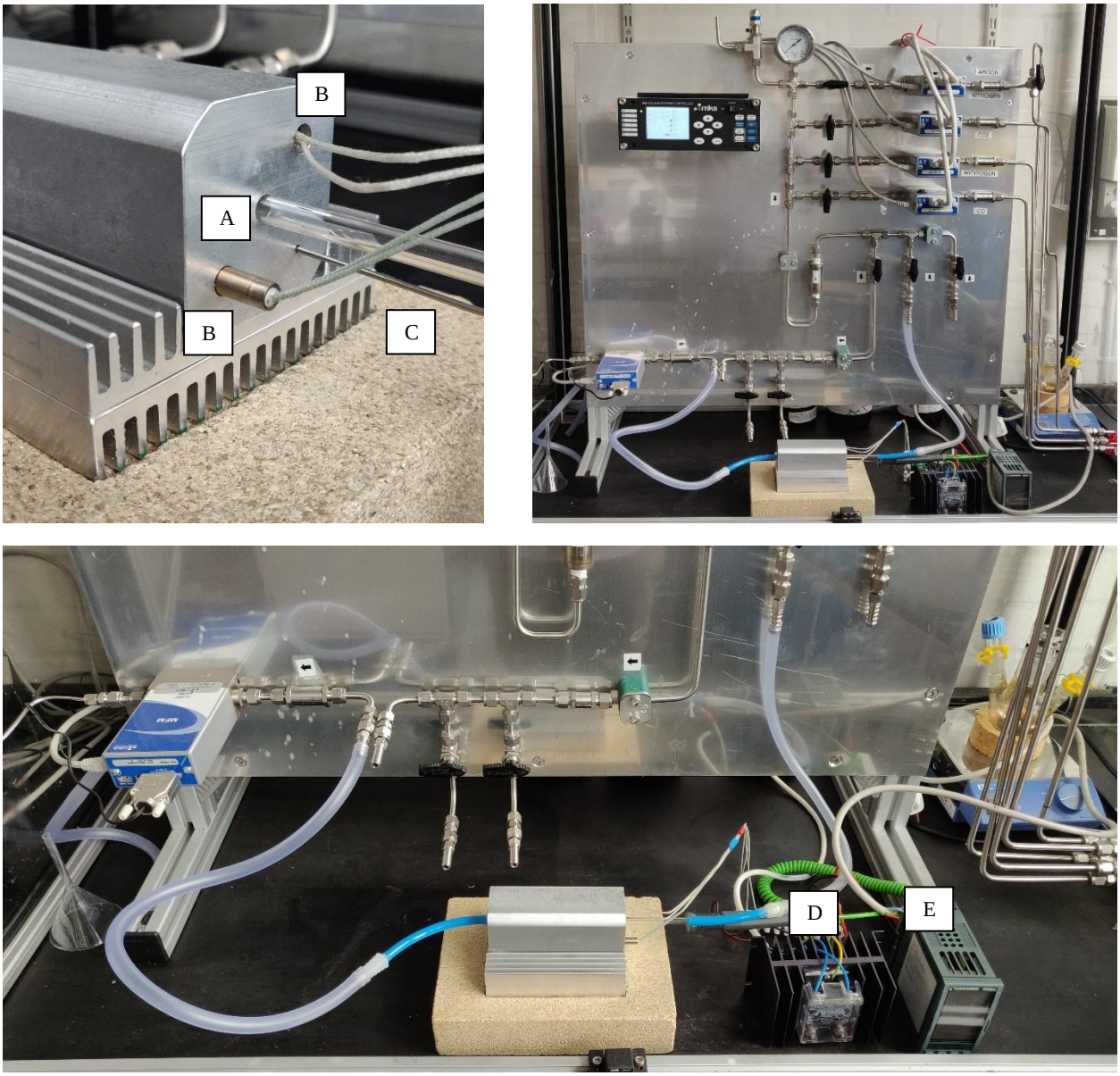

Figure 2.6: Gas-phase reactor prototype at DTU Chemistry.

Figure 2.7 shows the MicroGC that I have used to analyze the gas composition of the produced gases. The installation of the equipment was performed by an Agilent technician during the first months of my PhD studies. A system of valves controls the direction of the downstream flows (passed through cold trap, check-valves and particle filters), hence allowing performing multiple reactions at the same time in the two fume hoods showed before (A). In addition, there is the possibility to analyze gaseous samples that are collected in a gas tight bag, for examples for analysis of reactions in autoclaves. A GenieFilter (B) prevent possible condensated molecules to enter the MicroGC. The MicroGC is equipped with three different channels, each containing a different column and TCD detector (C). In detail, a PoraPLOT Q column allows for separation of hydrocarbons C1–C6, halocarbons, H_2S, CO_2 and SO_2. In this study, such column was used to observe CO_2, acetone and isopropanol. Then, two different Molsieve 5Å

columns permit the separation of H_2, CO, N_2, Ar, O_2 and CH_4. The two columns differ for the carrier gas that is used: in fact, argon is required in order to be able to separate hydrogen, whereas helium is used in the other two columns. The system is completed with traps located at the inlet of the carrier gases, preventing both O_2 and moisture to affect the measurements (D). The system showed in Figure 2.7 will be soon upgraded with new equipment such as a new column to expand the range of substrate that is possible to analyze, as well as a sequencing valve that will allow running multiple reactions, and following GC analysis, in automation.

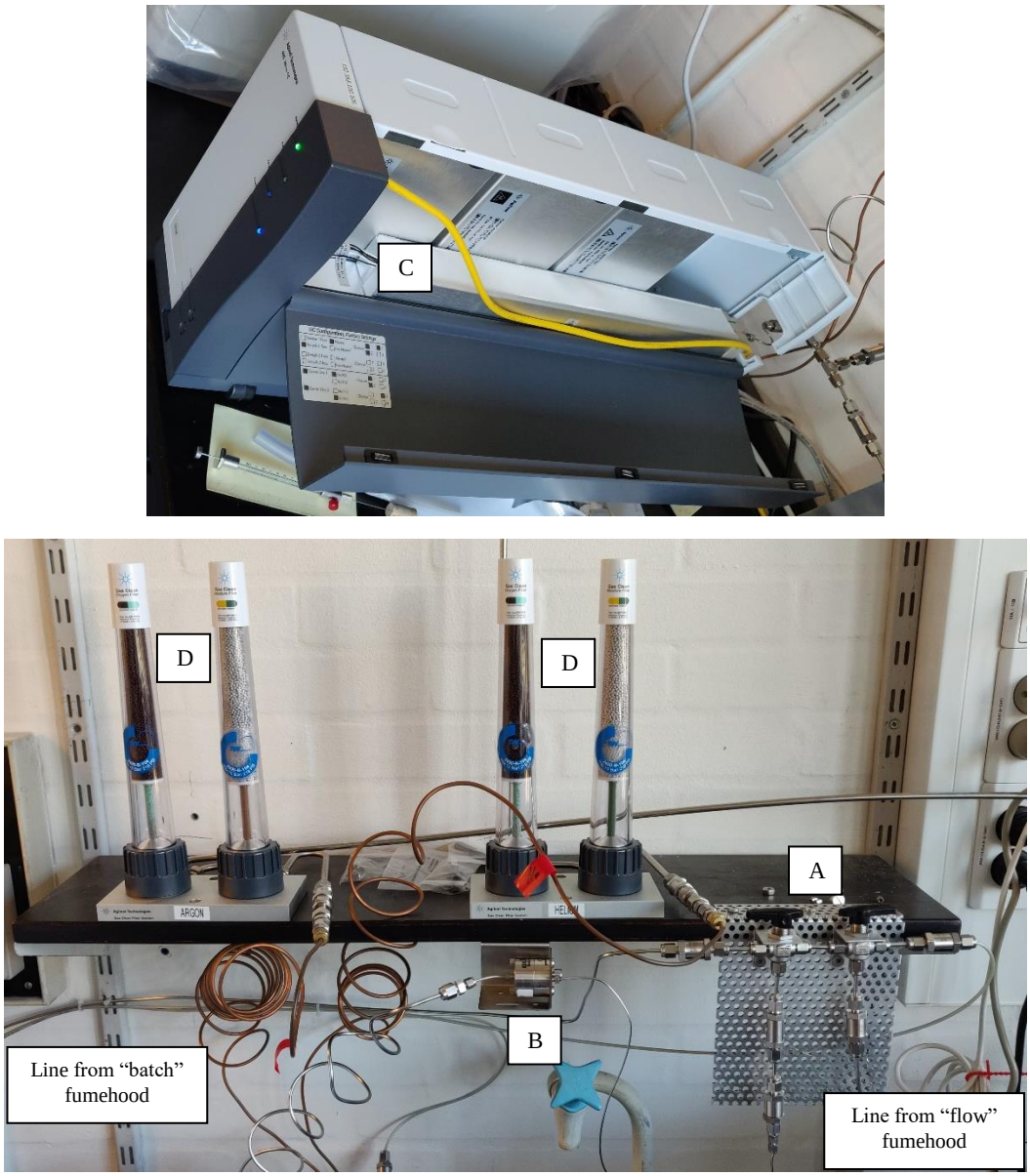

Figure 2.7: MicroGC used for the analysis of the gas-phase samples showed in this study.

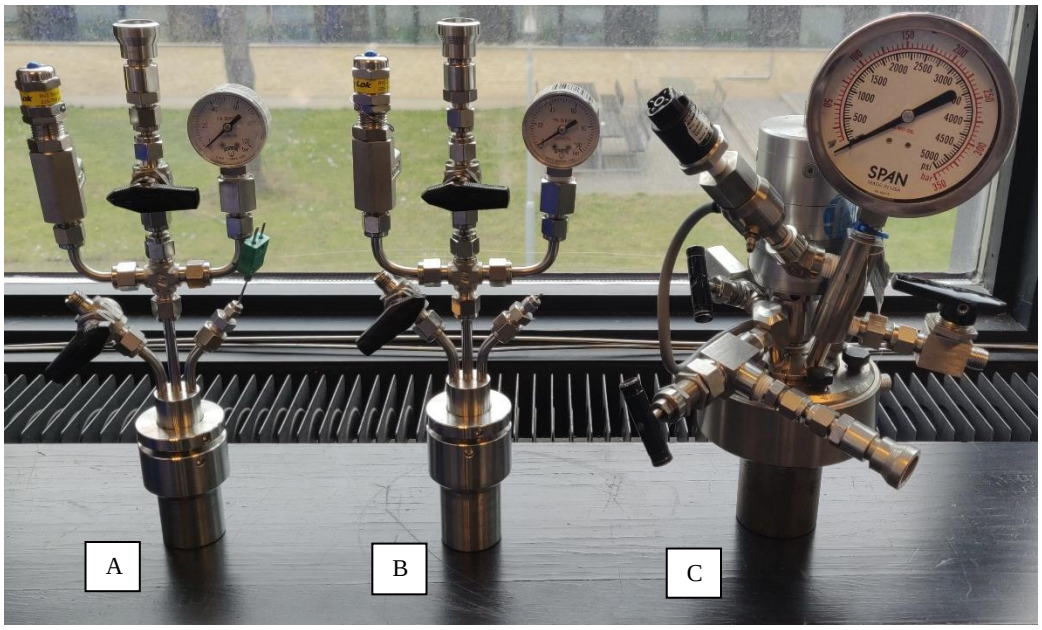

Figure 2.8: Different autoclaves used in this study for reaction under pressurized conditions. DTU Kemi´s garden in the background.

Finally, Figure 2.8 shows the different autoclaves used for reactions under pressure that are discussed in Chapters 4-6. Autoclaves A and B were built by the workshop department here at DTU Chemistry, while autoclave C was purchased from Parr. The sizes of the reaction vessels are 2.5, 5, 22 mL for A, B and C, respectively. Autoclaves A and B were designed to resist pressures up to 40 bar, while autoclave C can operate up to 200 bar and it was used in both CO_2 hydrogenation and FA dehydrogenation scale-up experiments. All of them are equipped with a manometer, a safety valve and a thermocouple.

The funding obtained from DTU Discovery Grant and Brødrene Hartmanns Fond will be used for further optimization of the above-described set-up. In particular, I have purchased a custom-made pump that will be used to control the exact amounts of either *i*PrOH or FA that is fed to the reactor. For example, this will be useful to avoid the use of syringe pumps (Figure 2.3) for long-term dehydrogenation reactions, as well as to perform precise calibration of *i*PrOH and acetone in the GC. In addition, the installation of a specifically designed vaporizer (resistant to FA) after the pump will allow conducting gas-phase reactions using e.g. SILP catalysts in the set-up described in Figure 2.6. In this sense, I have purchased heating bands, thermocouples, thermos-controllers and insulating tapes to ensure constant temperature of both upstream and downstream gases, preventing condensation before MFM and MicroGC measurements. Finally, the system will be upgraded with a new column for the MicroGC able to separate C1-C5 hydrocarbons, of relevance for other projects that are ongoing in the Nielsen´s lab.

3. Reactivity of Ru-PNP complexes with ionic liquids

3.1 Introduction

As already mentioned in Chapter 1, the activation of Ru-PNP pre-catalysts is a fundamental step in order to achieve catalytic activity. Scheme 3.1 shows this activation step performed by a generic base able to extrude the axial –Cl ligand from the pre-catalyst **Ru-2** with consequent formation of the reactive amido complex **Ru-4**. **Ru-1** instead, with two *trans* hydride ligands, is prone to deliver hydrogen readily. In fact, both species are considered key reaction intermediates in all of the catalytic hydrogenation and dehydrogenation transformations described in this work. Importantly, a similar activation pathway is required when using the Milstein´s family of complexes showed in Chapter 1.

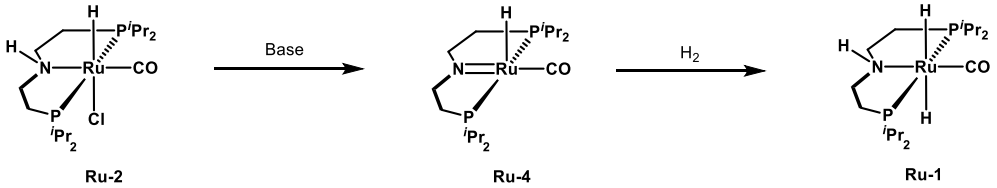

Scheme 3.1: Activation of the pre-catalyst Ru-2 and reactivity towards H_2.

This step is usually carried out with the addition of a sacrificial base in (over) stoichiometric amounts in the presence of a suitable organic solvent. Chapter 4 and 5 will show examples of state-of-the-art of PNP pincer catalysts for hydrogenation of CO_2 to FA as well as FA dehydrogenation, respectively. Indeed, most of the reported procedures in the literature employ sacrificial additives (NaOH, K_2CO_3, $KHCO_3$, EtONa etc.) in combination with an organic solvent (THF, DMF, DCM, 1,4-dioxane, diglyme) to promote catalyst activation and/or stabilization in solution. Despite the low price of conventional bases, the use of such additives is accompanied with decreased atom efficiency, as well as increased costs associated with materials and waste formation. These aspects, combined with the use of (sometimes toxic) organic solvents go against the main principles dictated by the green chemistry guidelines.

As the core of this project, it was speculated that the IL can be a suitable solvent for the homogeneous catalyst, at the same time performing this crucial activation step required in the presence of Ru-PNP complexes. In detail, the basicity given by a suitable IL might promote abstraction of the axial ligand (-Cl in the case of **Ru-MACHO** and **Ru-2**) avoiding the use of sacrificial bases. In addition, depending on its bulkiness and coordination ability, the anion can directly coordinate the metal center leading to the formation of in-situ formed ruthenium species. Therefore, I will demonstrate that acetate and formate ILs effectively activate Ru-PNP catalysts resulting in the formation of Ru-OAc and Ru-OCHO complexes that are stable in solution, and that represent ideal resting states for the catalyst to undergo (de)hydrogenation reactions. As described in the following chapters, this feature allows performing different sustainable reactions without the use of sacrificial additives, but exclusively in the IL as the only solvent.

3.2 Results and discussion

Figure 3.1 provides an overview of the catalysts and ILs that has been used in this chapter.

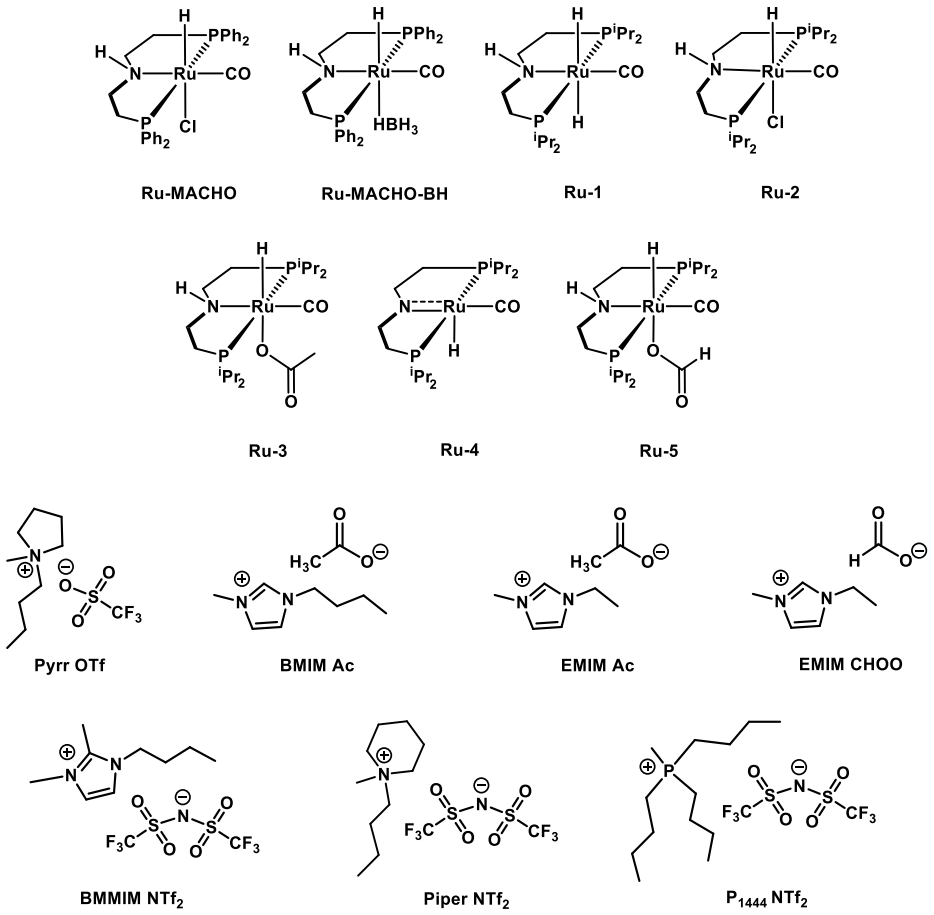

Figure 3.1: Molecular structures of the Ru-PNP catalysts and ionic liquids investigated in this study.

An overview of the basic reactivity of the Ru-PNP complexes reported from literature is provided in Scheme 3.2. Importantly, these reported procedures corroborate the experimental results presented in this thesis via e.g. NMR characterization of the Ru-PNP complexes. Crystal structures were reported for both **Ru-3** [106] and **Ru-5** [107], confirming the presence of hydrogen bonding involved between the carboxylate ligand and the amino proton of the PNP pincer (see 1.4.1). Nevertheless, both configurations of **Ru-3** and **Ru-5** (Figure 3.1 and Scheme 3.2) can be considered valid representations of the molecular structure, and they are likely to coexist in solution depending on the nature of the solvent. Catalysts **Ru-1**, **Ru-2** and **Ru-4** were synthetized according to reported procedures from the –Cl precursor **Ru-2** as shown in Scheme 3.2. In order to confirm our hypothesis on the role of the IL anion in the activation of Ru-PNP catalysts, I have carried out ^{1}H NMR studies of the generated Ru-H species in presence of different ILs.

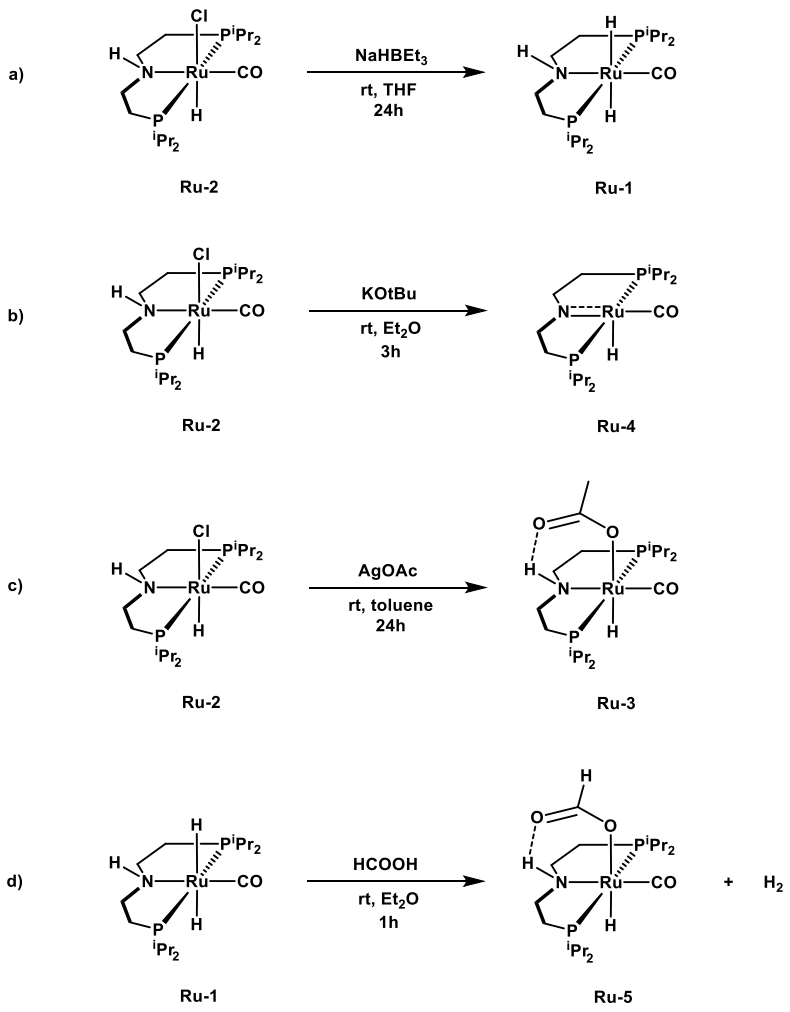

Scheme 3.2: Reactivity of Ru-PNP complexes as reported in the literature. The same methods were used in this study for the preparation of Ru-1 and Ru-4 [236] and Ru-3 [106].

Carboxylate ionic liquids

I have started by monitoring the composition of the reaction mixture of **Ru MACHO** in presence of BMIM Ac. By means of ^{1}H NMR analysis, it is possible to observe Ru-H signals associated with the different Ru species in solution. Typically, each Ru-H signal shows a clear triplet pattern due to coupling between the proton and the two phosphorous atoms on the PNP ligand. It is possible to notice that the main hydride peaks associated with **Ru-MACHO** at -13.87 and -15.15 ppm (Figure 3.2) are lost after addition of BMIM Ac (Figure 3.3). That is explained by the fact that the IL promotes rapid activation of the catalyst, with formation of the acetate complex **Ru-MACHO-OAc** as suggested by the Ru-H peak observed at -17.06 ppm in the hydride region. As visible in Figure 3.3, the addition of the IL makes the identification of other peaks associated with the catalyst impossible. Nevertheless, observing at the hydride region provides a useful tool to monitor the formation of different Ru species in solution. Thus, I will follow this method for most of the NMR characterization that will be discussed in this thesis.

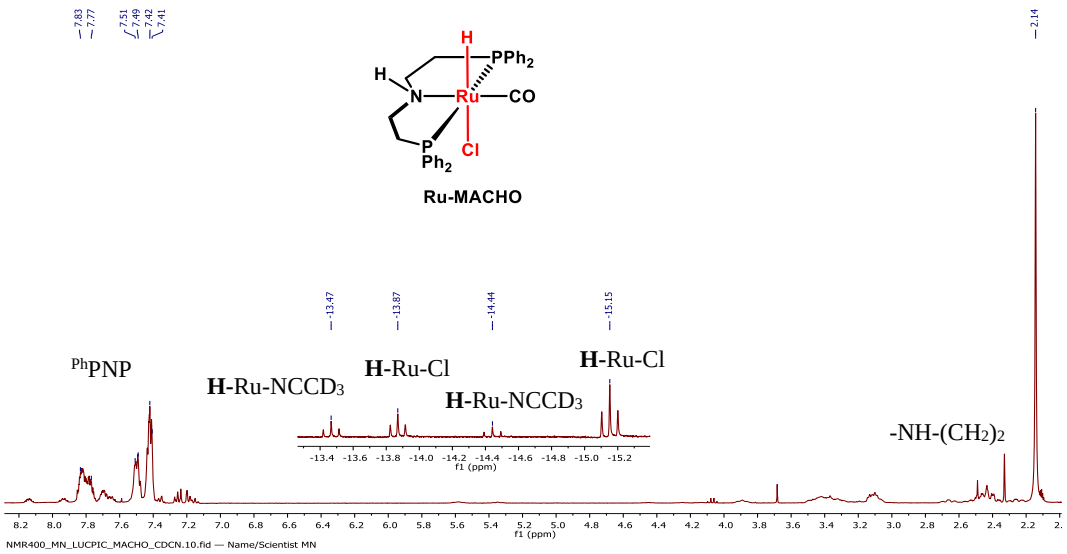

Figure 3.2: ^{1}H NMR spectrum of Ru-MACHO (CD_3CN, 25 °C, 400 MHz). It is possible to notice *trans* and *cis* isomers associated with not fully dissolved starting material. The ^{31}P NMR spectrum is presented in Appendix A, Figure A.1**.**

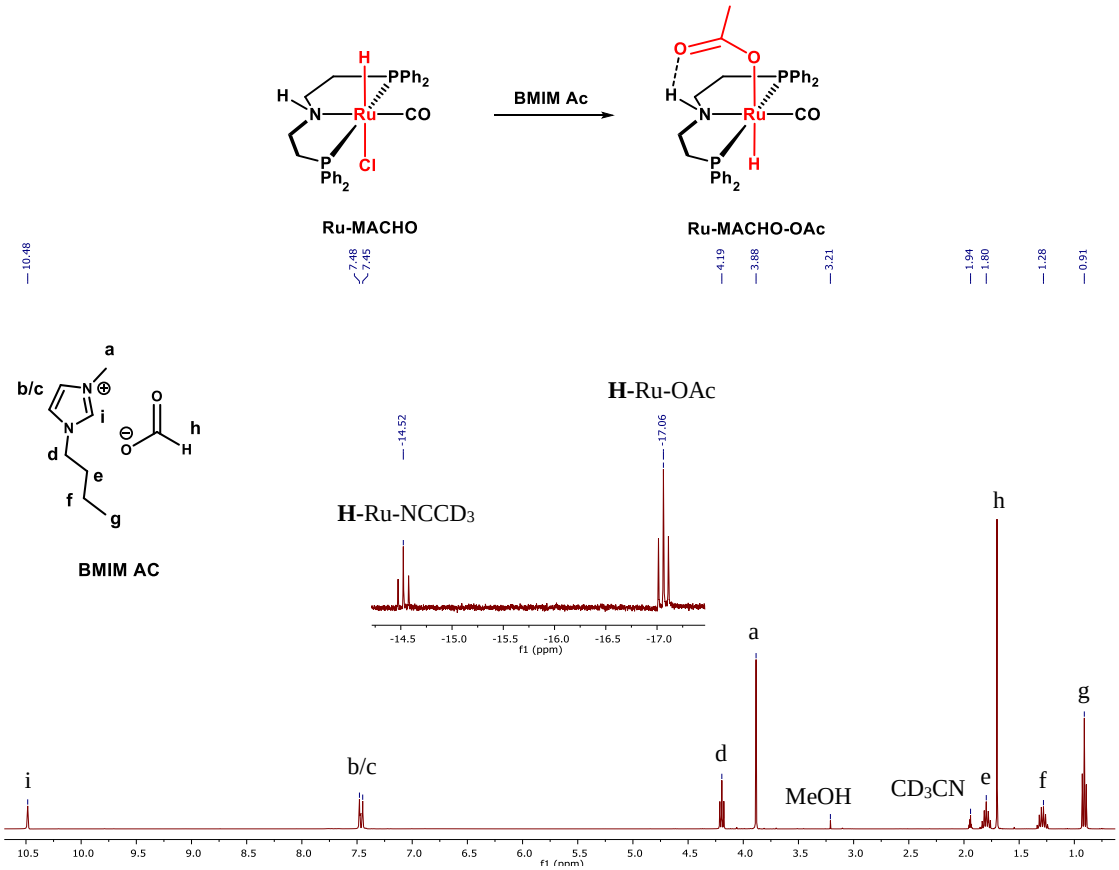

Figure 3.3: ^{1}H NMR spectrum of Ru-MACHO in BMIM Ac (CD_3CN, 25 °C, 400 MHz). Note: MeOH is present as an impurity in the IL (from synthesis procedure). The ^{31}P NMR spectrum is presented in Appendix A, Figure A.2**.**

Figure 3.4 shows in detail the hydride region of the ^{1}H NMR spectrum of **Ru-MACHO** in CD_3CN, staggered with the spectrum of a solution containing **Ru-MACHO** dissolved in BMIM Ac (and CD_3CN). Coordination of *d*-acetonitrile to the ruthenium center explains the presence of multiple hydride peaks due to formation of *cis* and *trans* isomers; however, after addition of BMIM Ac, only one H-Ru-$NCCD_3$ isomer is present at -14.52 ppm. In all the (CD_3CN) spectra showed throughout the work, it has to be noticed that the relative intensities of the Ru-H signals associated with either CD_3CN or the IL anion are the result of manual inconsistency in the preparation of the NMR samples. For example, often the IL mixture after catalytic (de)hydrogenation reactions is very foamy due to high concentrations of gases absorbed, making the preparation of samples with the same concentration difficult. In other cases (see Chapter 4), the reaction mixture is partly solidified due to high concentrations of CO_2 chemisorbed in the IL phase. In addition, solubility of the Ru-PNP catalysts in both NMR solvents and ILs at room temperature is in some cases only partial.

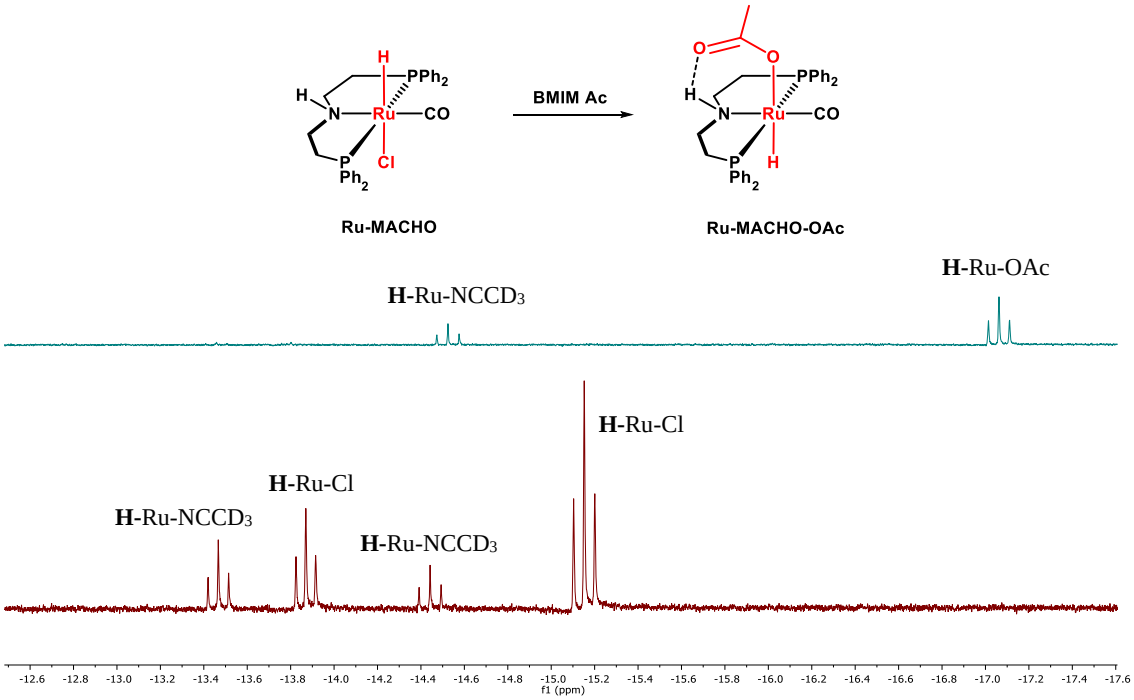

Figure 3.4: ^{1}H NMR spectra of the hydride region for Ru-MACHO (down) and Ru-MACHO in BMIM Ac (up), CD_3CN, 25 ºC, 400 MHz. In the spectrum below, it is possible to notice *trans* and *cis* isomers associated with not fully dissolved starting material.

Ru-MACHO-BH shows similar behavior compared to **Ru-MACHO** in the presence of BMIM Ac, resulting in the quantitative formation of **Ru-MACHO-OAc**. In a benchmark experiment, I have investigated the reactivity of the mixture **Ru-MACHO-BH** and BMIM Ac towards *i*PrOH as a model substrate for dehydrogenation reactions. This was possible thanks to postdoc Maria Padilla, who helped in the design of the experiment, as well as Kasper Enemark-Rasmussen who analyzed the NMR samples that we provided. As such, I have dissolved 0.05 mmol of catalyst in 2 mL of BMIM Ac and added 0.3 mL of *i*PrOH gradually over 4 hours while varying the temperature from 90 to 120 ºC. To our delight, we observed traces of acetone as a result of *i*PrOH dehydrogenation, as it will be discussed in Chapter 7. Importantly for this chapter, the analysis of the reaction mixture was performed by direct ^{1}H NMR analysis of the IL phase, by insertion in the J Young NMR tube of a quartz inner capillary filled with *d*-acetonitrile as the reference (Figure 3.5). This was done in order to observe Ru species exclusively in the IL, at the same time avoiding competitive coordination of the solvent. Importantly, the addition of *i*PrOH leads to the formation of a second hydride

specie at -14.15 ppm, that could be associated with the formation of the complex **Ru-MACHO-OiPr** (Figure 3.5). This experiment has been crucial to demonstrate the suggested reactivity of such Ru-PNP/IL mixtures. Indeed, **Ru-MACHO-BH** will show remarkably high activity in different IL mixtures towards the dehydrogenation of both *i*PrOH (Chapter 7) and FA (Chapter 5).

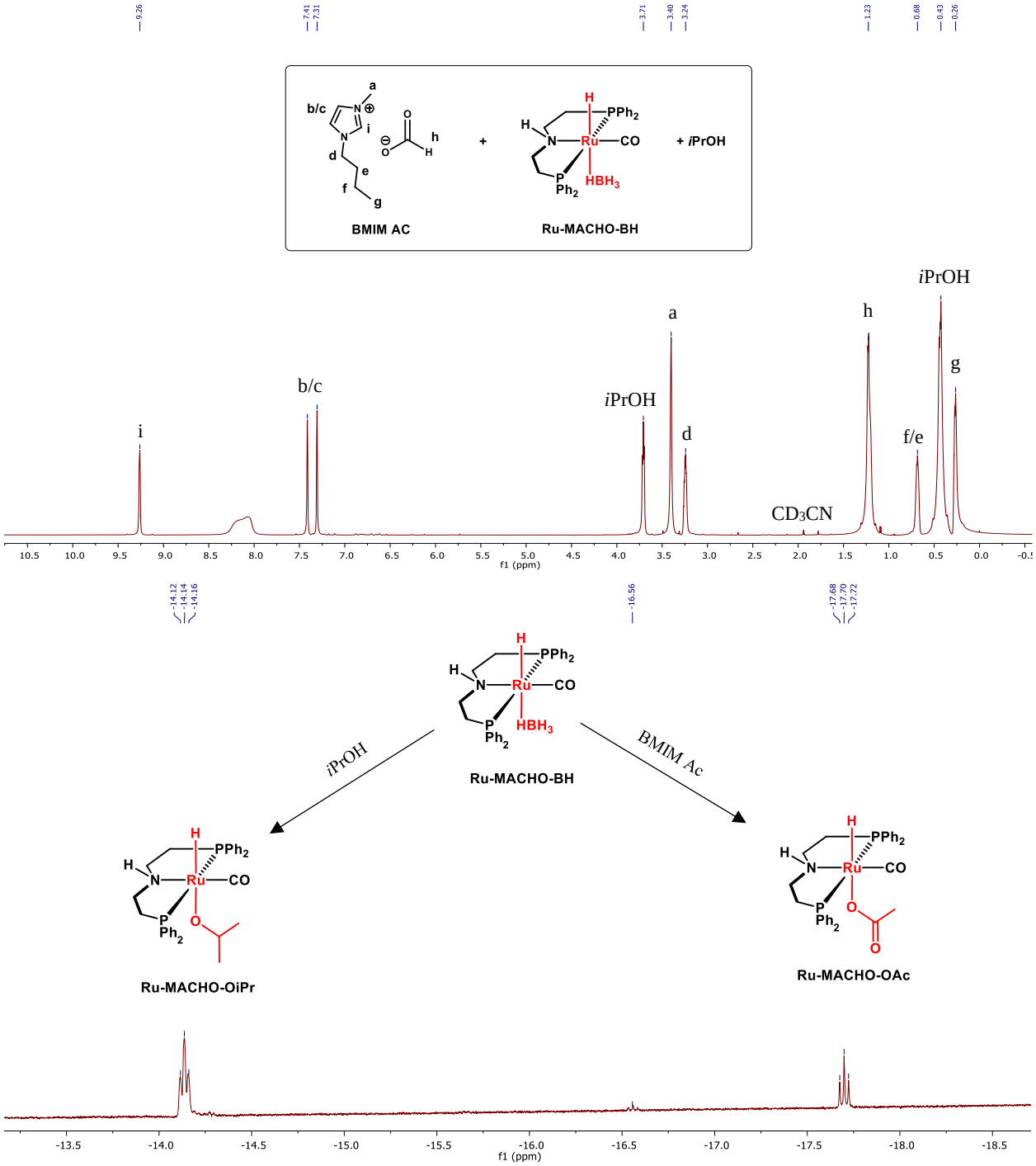

Figure 3.5: ^{1}H NMR spectrum of Ru-MACHO-BH in the presence of BMIM Ac and *i*PrOH (CD_3CN in inner capillary quartz tube to avoid mixing of IL and NMR solvent, 25 °C, 600 MHz).

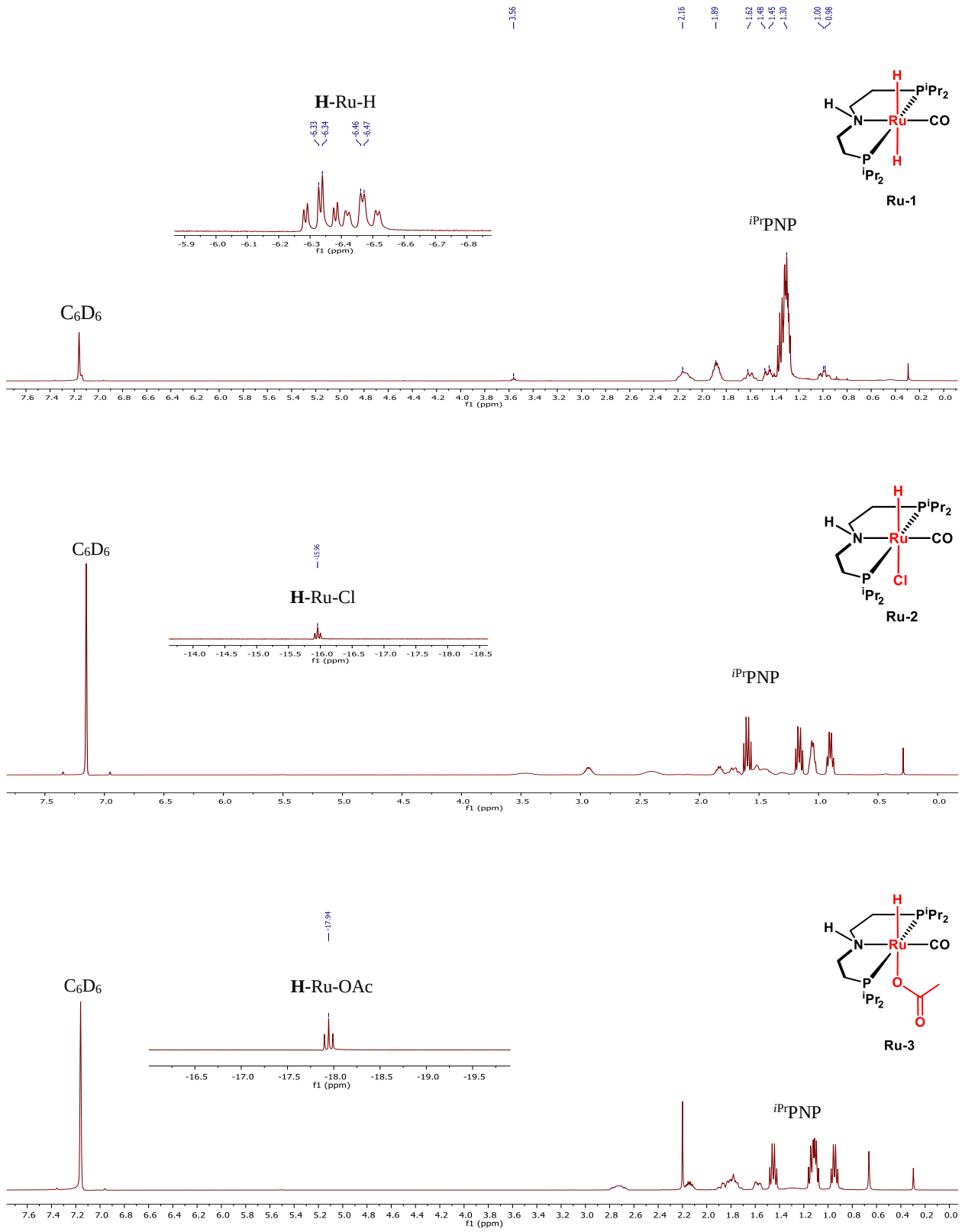

Figure 3.6: ^{1}H NMR spectra of Ru-1, Ru-2 and Ru-3 (C_6D_6, 25 °C, 400 MHz).

Figure 3.6 shows the ^{1}H NMR spectra of the ^{iPr}PNP pincers **Ru-1**, **Ru-2** and **Ru-3** in C_6D_6 with the corresponding hydride signals reported from literature [106,236]. Hence, I have investigated their behavior in the presence of EMIM Ac. Similar to what observed for **Ru-MACHO**, mixing of **Ru-1** and EMIM Ac results in the quantitative formation of the acetate complex **Ru-3**, as indicated by the hydride signal at -17.92 ppm (Figure 3.7).

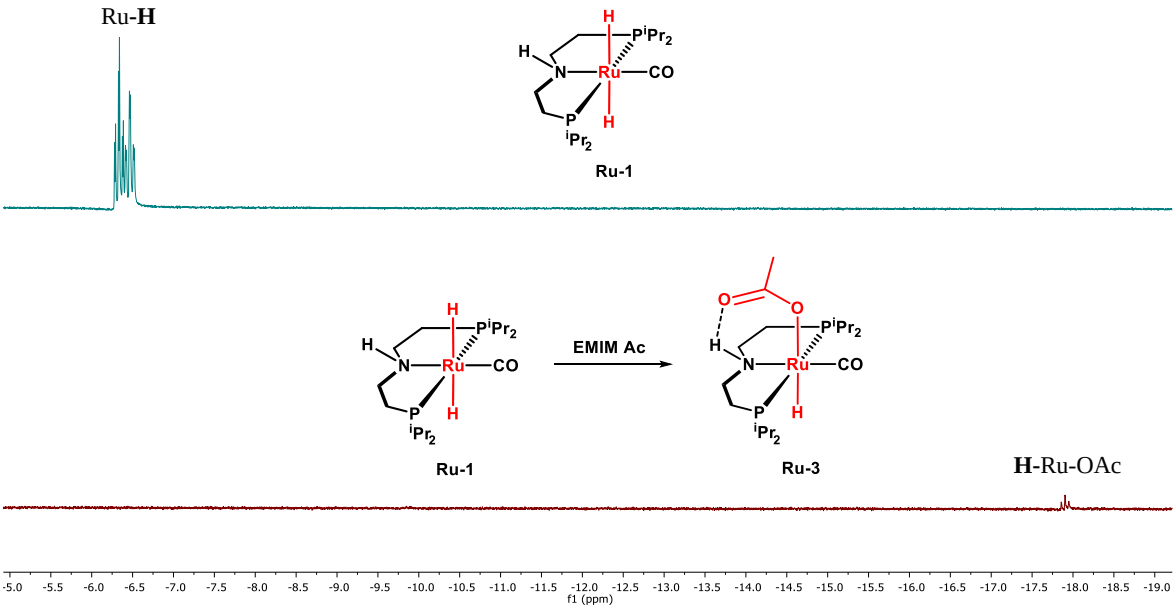

Figure 3.7: ^{1}H NMR spectra of Ru-1 (up) and Ru-1 in the presence of EMIM Ac (down), C_6D_6, 25 °C, 400 MHz.

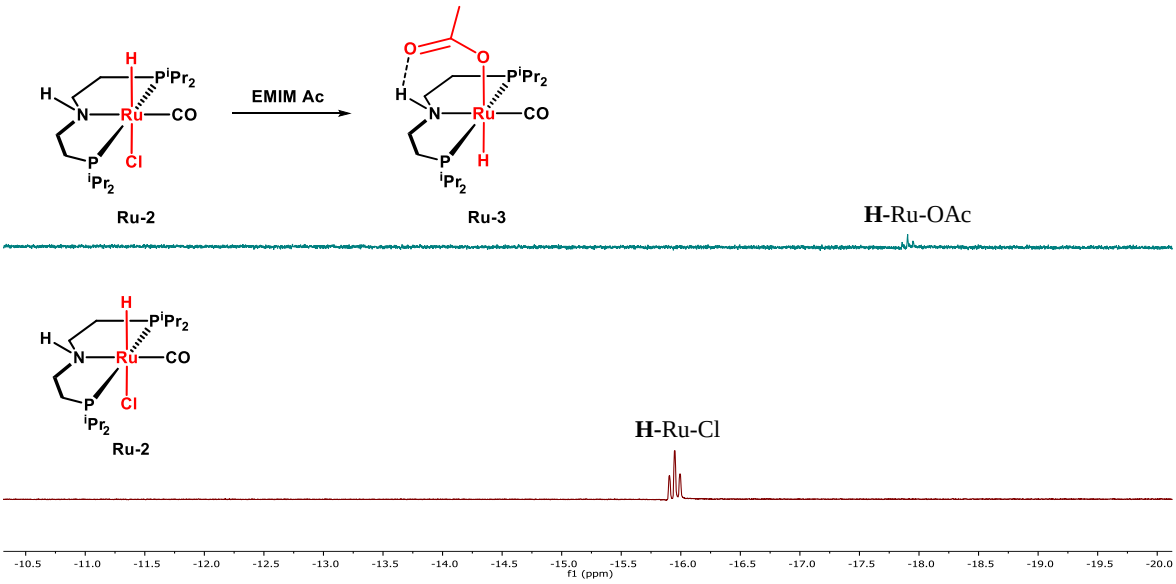

Figure 3.8: ^{1}H NMR spectra of Ru-2 (down) and Ru-2 in the presence of EMIM Ac (up), C_6D_6, 25 °C, 400 MHz.

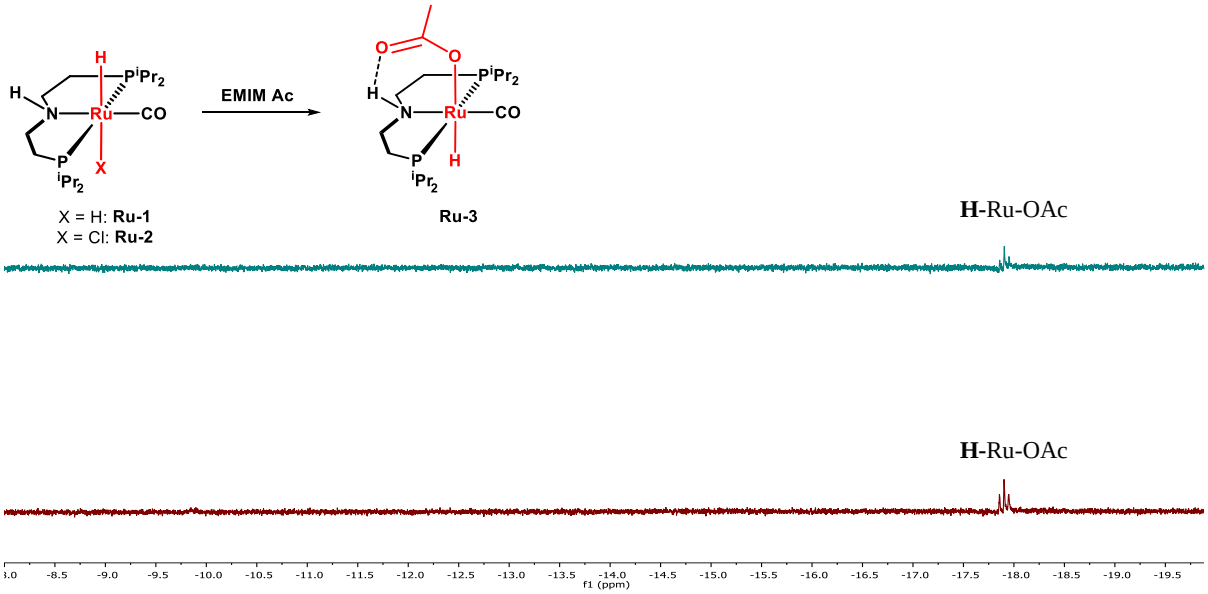

Figure 3.9: ^{1}H NMR spectra of Ru-1 (down) and Ru-2 in EMIM Ac (up), C_6D_6, 25 °C, 400 MHz.

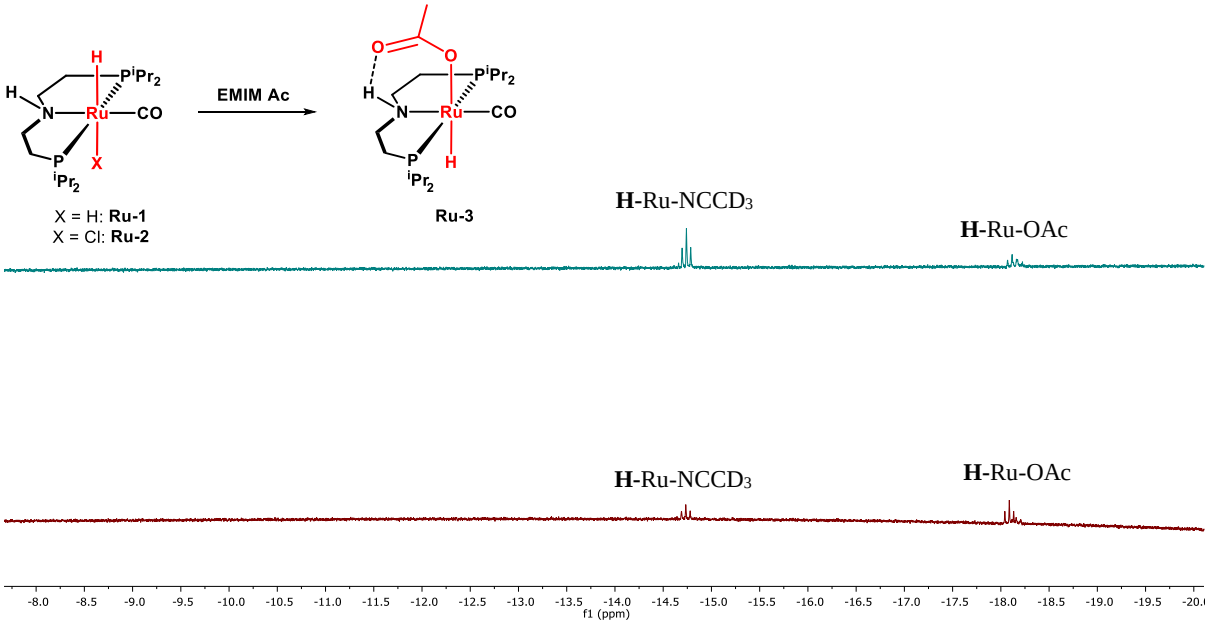

Figure 3.10: ^{1}H NMR spectra of Ru-1 (down) and Ru-2 in EMIM Ac (up), CD_3CN, 25 °C, 400 MHz.

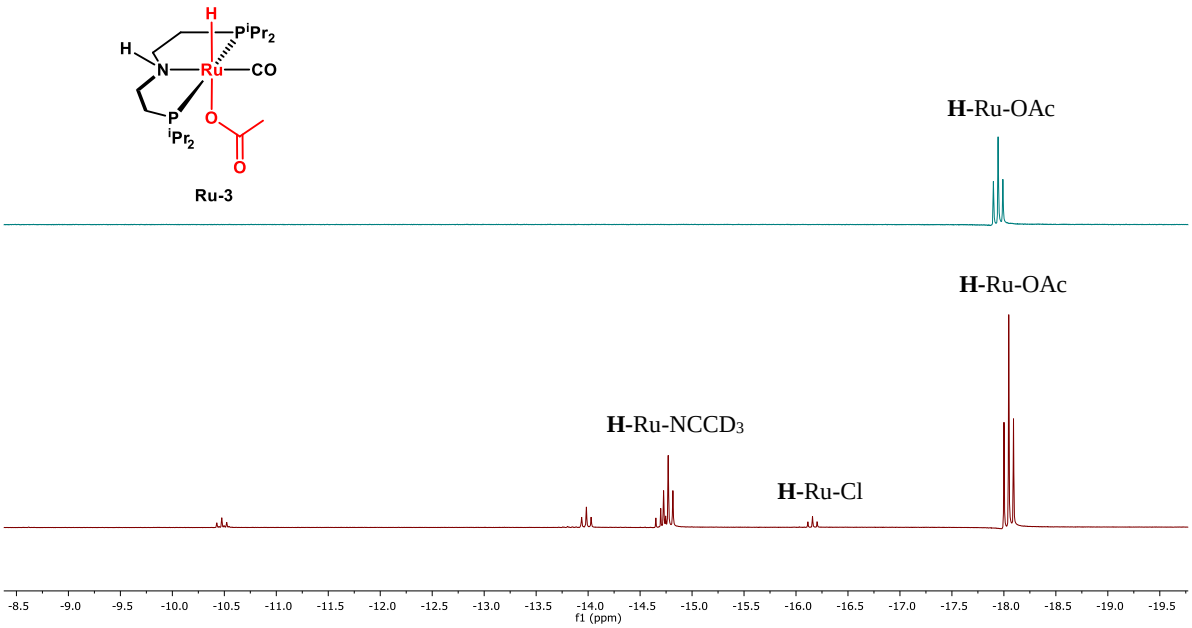

Figure 3.11: ^{1}H NMR spectra of Ru-3 in C_6D_6 (up) and CD_3CN (down). Other peaks observed in *d*-acetonitrile can be explained by the presence of residual Ru-2 after synthesis of Ru-3, *cis* and *trans* H-Ru-NCCD$_3$ isomers, as well as Ru-H$_2$ species at -10.5 ppm. The two spectra belong to different batches of Ru-3 (25 °C, 400 MHz).

As expected, **Ru-2** also results in quantitative formation of **Ru-3** (Figure 3.8), while the ^{1}H NMR spectrum of **Ru-3** in BMIM Ac does not show differences in the hydride region compared to the starting material in CD_3CN (see Figure 3.16). Finally, Figures 3.9 and 3.10 indubitably prove the proposed reactivity, with no visible differences observed between **Ru-1** and **Ru-2** once dissolved in EMIM Ac (see Appendix A, Figures A.3, A.4 and A.5, for ^{31}P NMR spectra). As visible from the previous spectra, the use of *d*-benzene allows for the obtainment of cleaner spectra without the presence of hydride peaks associated with coordination of the solvent. Despite the visible advantages in the observation of Ru-H signals, the poor solubility of ILs in benzene makes the use of the latter unpractical for analysis of the reaction mixture after catalytic reactions. Therefore, *d*-acetonitrile has been used often as the NMR solvent due to complete solubility of both catalysts and ILs, reflected in high resolution of the obtained spectra, as well as absent overlapping with IL signals (which happens in e.g. $CDCl_3$, D_2O). It has to be noted that besides leading to the presence of more Ru-H species, the solvent does not affect the overall observed reactivity between Ru-PNP and ILs in solution.

Considering the application discussed in the following sections, namely FA dehydrogenation and CO_2 hydrogenation to FA, I have explored the possibility to use EMIM CHOO (Figure 3.1) as a suitable IL, being the formate anion a key intermediate in all of the above-mentioned transformations. The synthetic procedure used for the synthesis is depicted in Scheme 3.3.

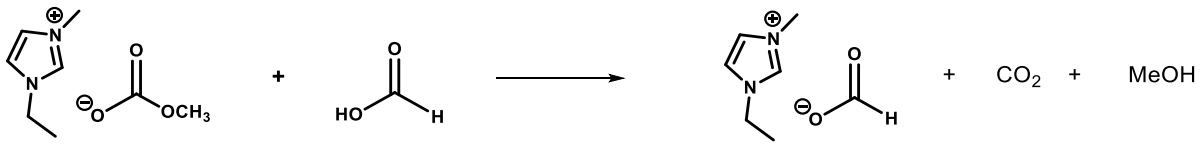

Scheme 3.3: Reaction scheme for the synthesis of EMIM CHOO used in this study.

EMIM CHOO reacts with both **Ru-1** and **Ru-2** in similar fashion as EMIM Ac, resulting in the formation of the formate complex **Ru-5** as shown by the Ru-H signal at -18.04 ppm in C_6D_6 (Figure 3.12) and -18.15 ppm in CD_3CN (Figure 3.13). At least from a qualitative point of view, coordination of *d*-acetonitrile is more pronounced in the presence of EMIM CHOO compared to EMIM Ac (Figure 3.13). This is explained by the known higher reactivity, hence higher instability, of **Ru-5** compared to **Ru-3** [107,125].

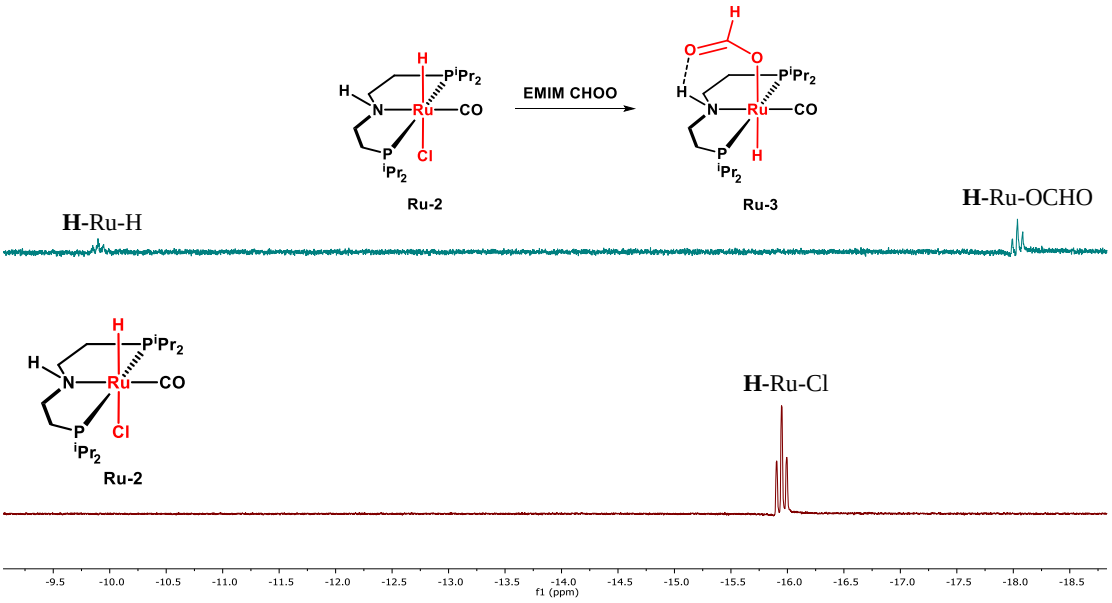

Figure 3.12: ^{1}H NMR spectra of Ru-2 (down) and Ru-2 in EMIM CHOO (up), C_6D_6, 25 °C, 400 MHz.

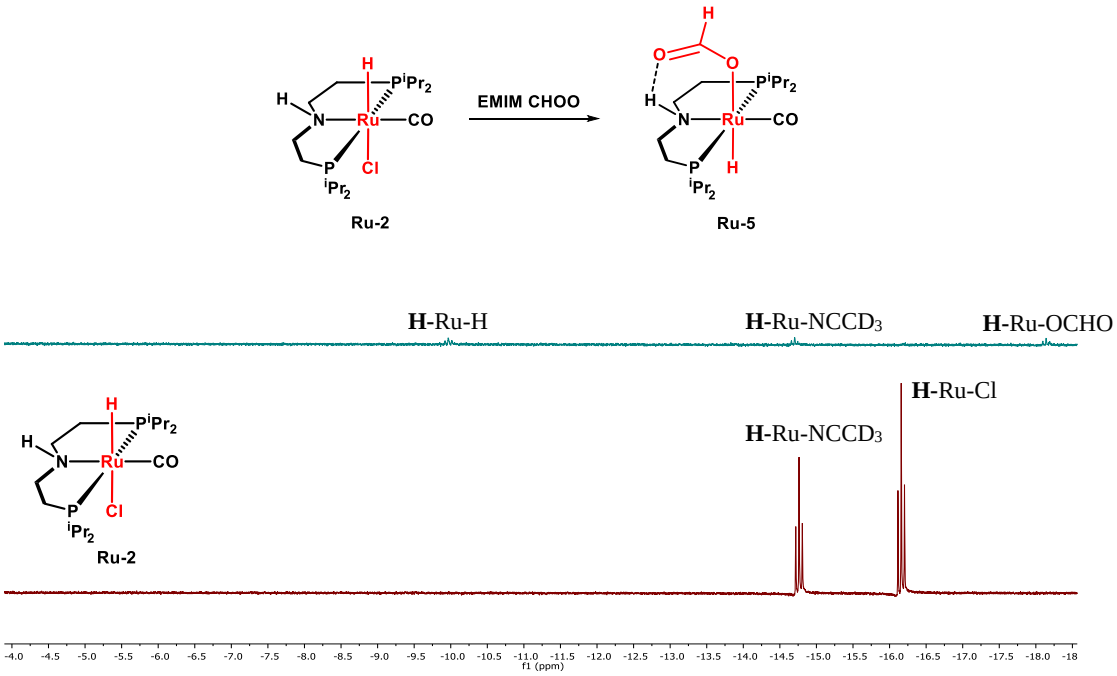

Figure 3.13: ^{1}H NMR spectra of Ru-2 (down), and Ru-2 in EMIM CHOO (up). The experiments were performed at room temperature, hence poor solubility of Ru-2 resulting in the presence of a H-Ru-Cl signal (CD_3CN, 25 °C, 400 MHz).

Figures 3.14 and 3.15 show that **Ru-3** (-17.92 ppm) is distinguishable from **Ru-5** (-18.04 ppm), after mixing of either **Ru-1** or **Ru-2** with EMIM Ac and EMIM CHOO, respectively. Hence, I have mixed EMIM Ac and EMIM CHOO in a 1:1 molar ratio in the presence of **Ru-2**; the peak at -17.92 ppm associated with **Ru-3** is the only hydride signal observed after both 1 and 24 hours, indicating that **Ru-3** is more stable than **Ru-5** (see Figures A.6, A.7 in Appendix A). When using EMIM CHOO, it is possible to notice the presence of a hydride signal at -9.91 ppm, indicating the presence of Ru-dihydride and/or Ru-dihydrogen species. Indeed, the Ru-PNP/EMIM CHOO mixture is highly active for FA dehydrogenation, as will be shown in Chapter 5.

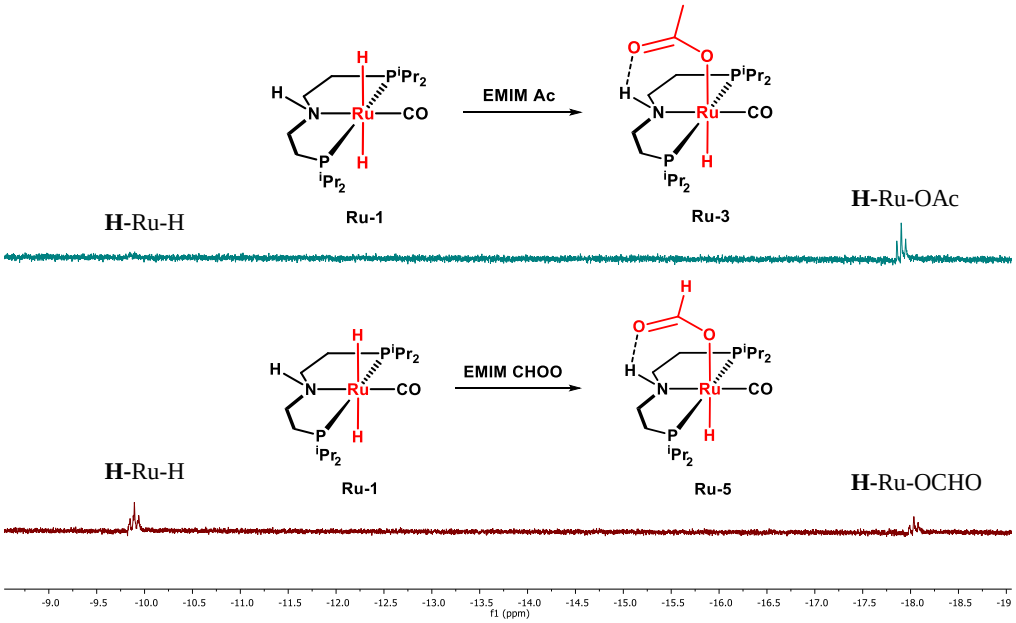

Figure 3.14: ^{1}H NMR spectra of Ru-1 in EMIM CHOO and EMIM Ac (C_6D_6, 25 °C, 400 MHz).

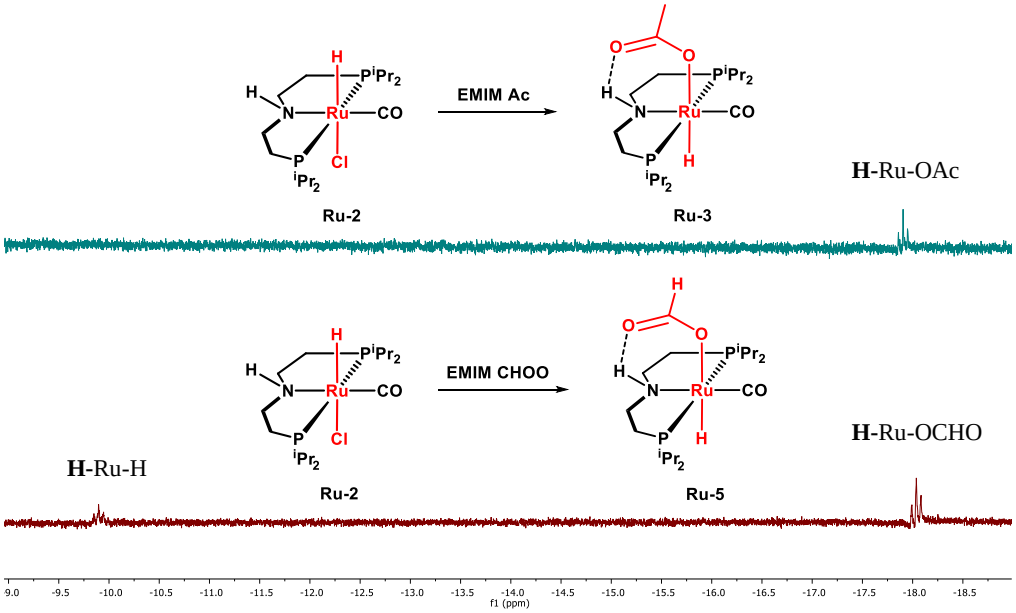

Figure 3.15: ^{1}H NMR spectra of Ru-2 in EMIM CHOO and EMIM Ac (C_6D_6, 25 °C, 400 MHz).

Finally, Scheme 3.4 provides a schematic overview of the activation modes described so far using Ru-PNP complexes in the presence of Ac and CHOO ILs.

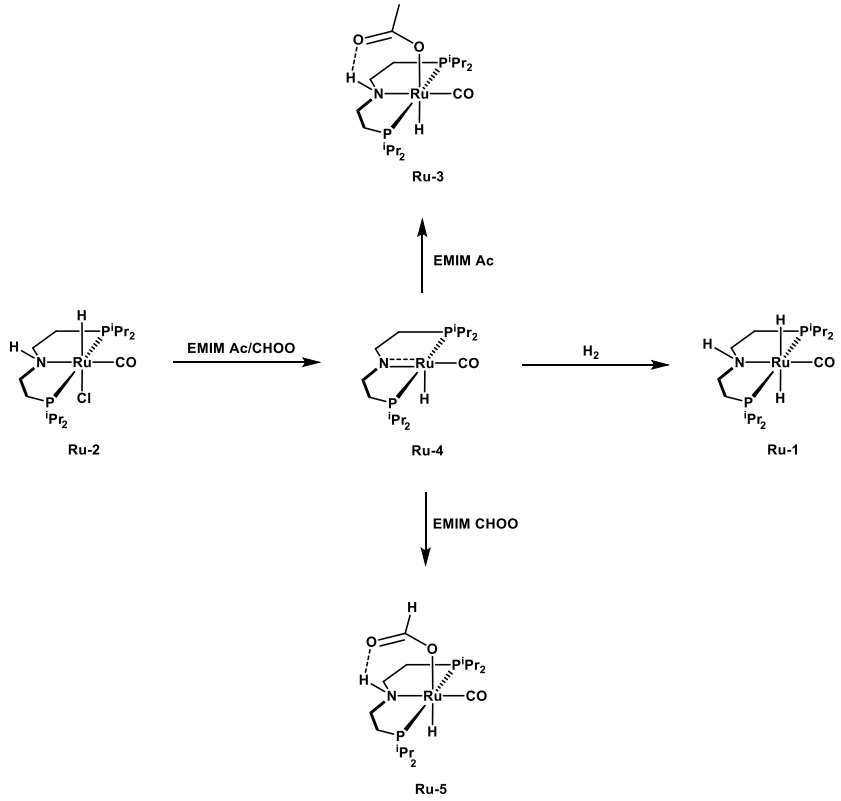

Scheme 3.4: Overall representation of the reactivity between Ru-PNP and acetate/formate ILs described so far. The same is observed with ^{Ph}PNP ligands.

Sulphur-containing, non-coordinating anions

In this section, I have tested the reactivity of Ru-PNP complexes towards other type of anions such as triflate (OTf) and bistriflimide (NTf_2). In the presence of such anions, ^{1}H NMR analysis shows no presence of newly formed Ru-H species. This shows that triflate and bistriflimide anions do not activate Ru-PNP catalyst by coordination to the metal center at room temperature, which happens with both formate and acetate anions. Differences in basicity, as well as size, of these ILs likely explain the observed behavior.

To comprehend further the nature of the main resting species of the organometallic complexes in solution, I have mixed **Ru-3** with BMIM Ac, BMMIM NTf_2, Pyrr OTf as well as the model substrate for dehydrogenation reactions *i*PrOH. Figure 3.11 shows the ^{1}H NMR spectrum of **Ru-3** in *d*-acetonitrile as reference for the spectra that will follow. When using BMIM Ac, the intensity of the signal associated with **Ru-3** increases compared to those associated with CD_3CN coordinated to Ru, in agreement with the observation from the previous section (Figure 3.16). On the other hand, it is clear that the catalyst is not affected by the presence of either BMMIM NTf_2 or Pyrr OTf.

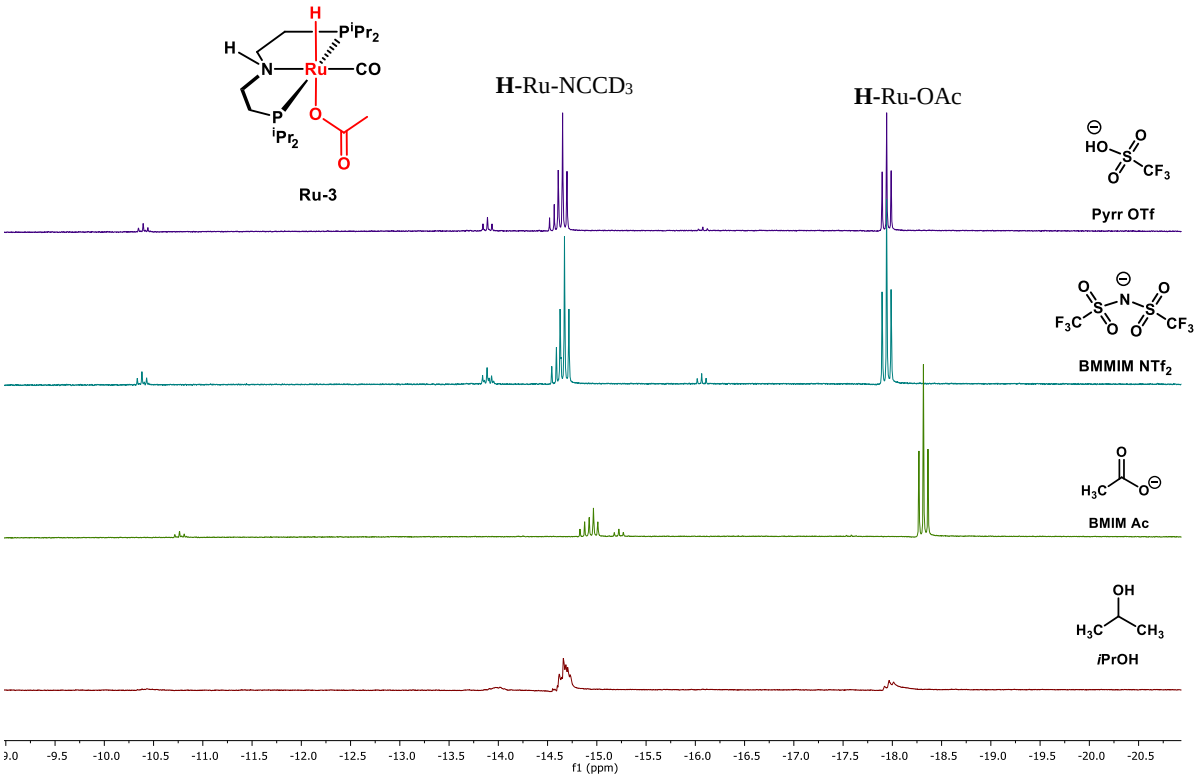

Figure 3.16: ^{1}H NMR spectra of Ru-3 in different media: *i*PrOH, BMIM Ac, BMMIM NTf_2 and Pyrr OTf (CD_3CN, 25 °C, 400 MHz). Only the IL anion is shown for simplicity.

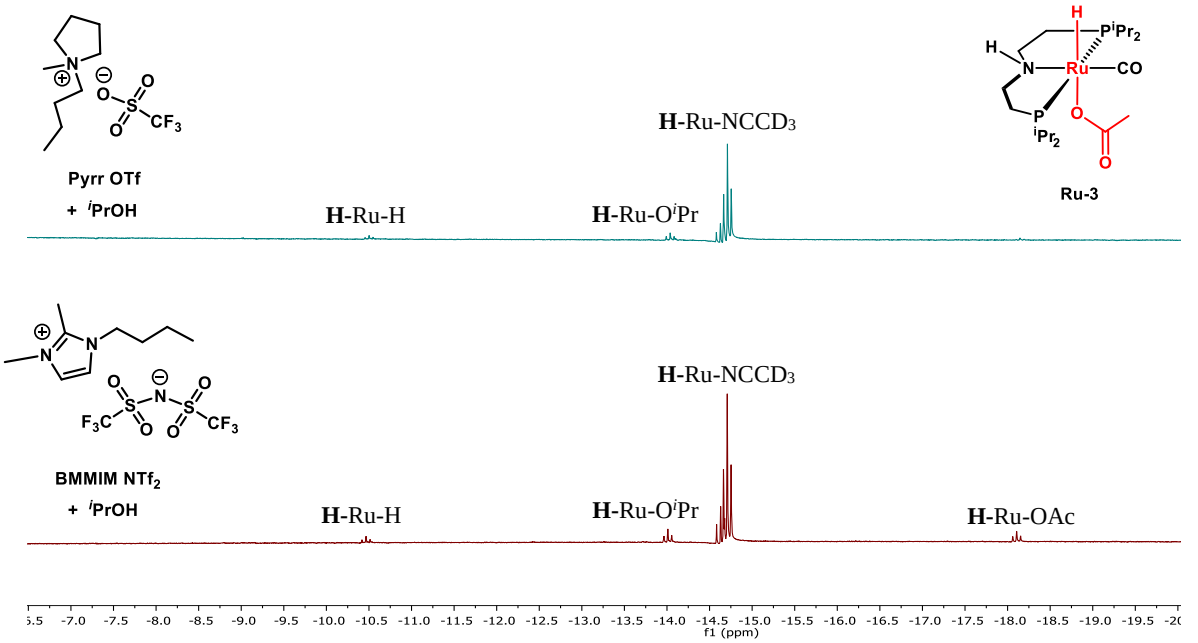

Figure 3.17: ^{1}H NMR spectra of Ru-3 with the IL/*i*PrOH mixtures indicated (CD_3CN, 25 °C, 400 MHz).

Nevertheless, the addition of *i*PrOH to such solutions results in lower amount of **Ru-3** is solution that can be explained by the competitive formation of Ru-O^{i}Pr species (Figure 3.17). This is an agreement with the observations from Figure 3.5 using **Ru-MACHO-BH** and *i*PrOH, where the ambiguity due to *d*-acetonitrile coordination was excluded experimentally. In addition, the peaks at -10.4 ppm are a clear evidence of the presence of hydride and dihydrogen species that might be involved in dehydrogenation reactions of isopropanol.

To conclude, I have investigated the behavior of **Ru-MACHO-BH** in the presence of NTf_2 ILs. Figure 3.18 shows the ^{1}H NMR spectrum of **Ru-MACHO-BH** in *d*-dichloromethane as reference. No visible differences in the resulting mixtures were observed by varying the cation of the tested ILs (BMMIM, Pyrr, Piper, and P_{1444} NTf_2). Figures 3.19 and 3.20 shows that the addition of both P_{1444} NTf_2 as well as *i*PrOH results in the retention of the main Ru-H signals associated with the starting material. This is also reflected by the fact that the catalyst is not fully dissolved at room temperature, as indicated by a turbid appearance of the solution. As already understandable from what described in this chapter using the model substrate *i*PrOH, catalytic activity is still possible using such ILs. In fact, even if OTf and NTf_2 are not active in abstracting -Cl and -OAc ligands, they still succeed in the stabilization of the active species in the presence of catalysts that are activated by external factors, e.g. temperature. This will be the case for e.g **Ru-1**, **Ru-4** and **Ru-MACHO-BH** for both FA dehydrogenation (Chapters 5) as well as dehydrogenation of *i*PrOH (Chapter 7).

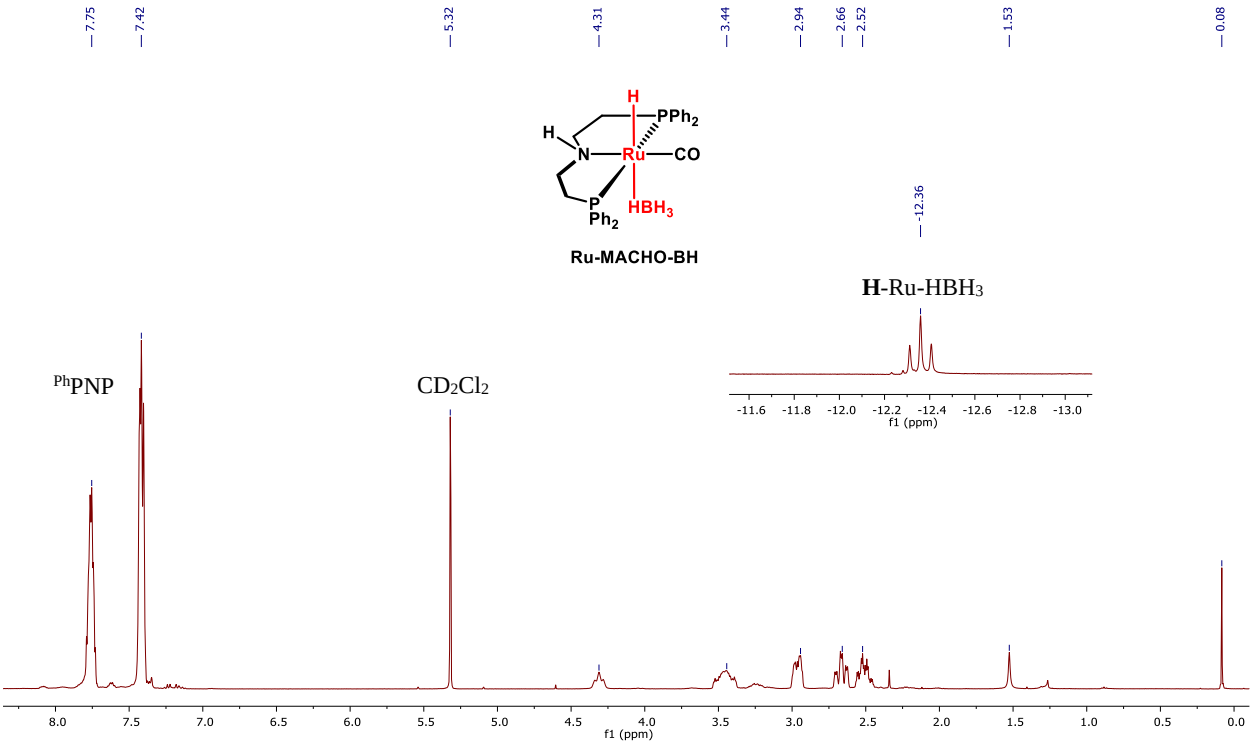

Figure 3.18: ^{1}H NMR spectrum of Ru-MACHO-BH (CD_2Cl_2, 25 °C, 400 MHz).

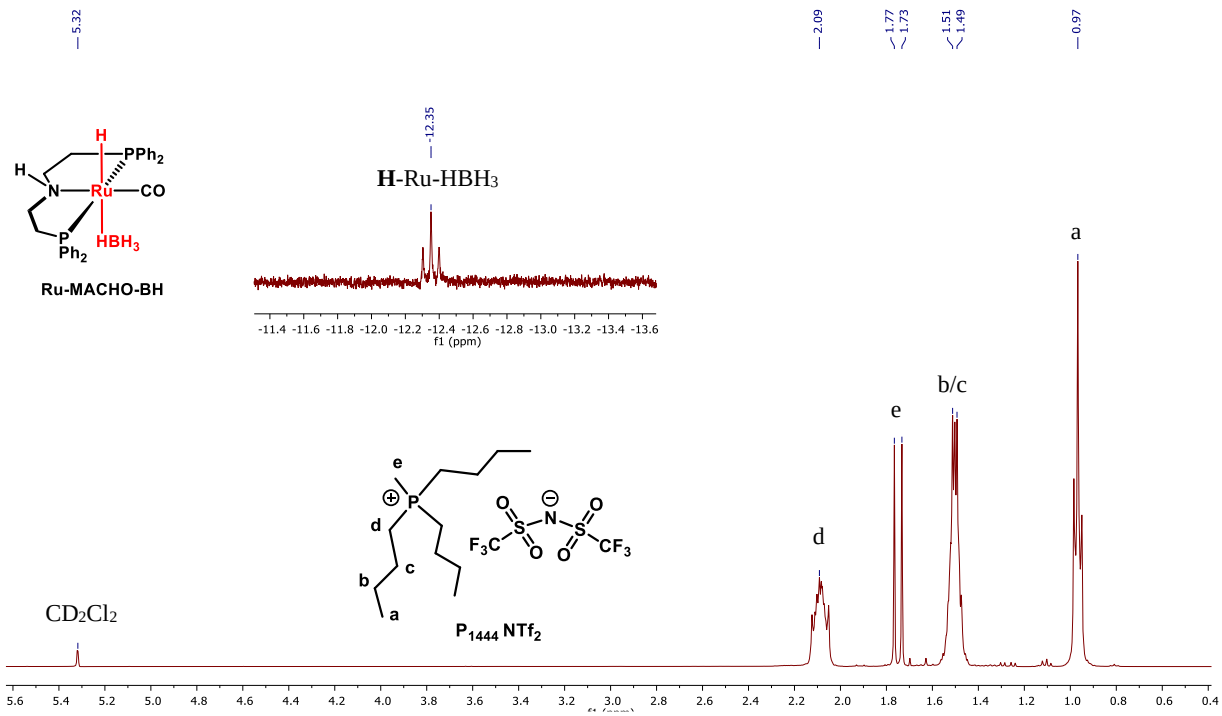

Figure 3.19: ^{1}H NMR spectrum of Ru-MACHO-BH with P_{1444} NTf_2 (CD_2Cl_2, 25 °C, 400 MHz).

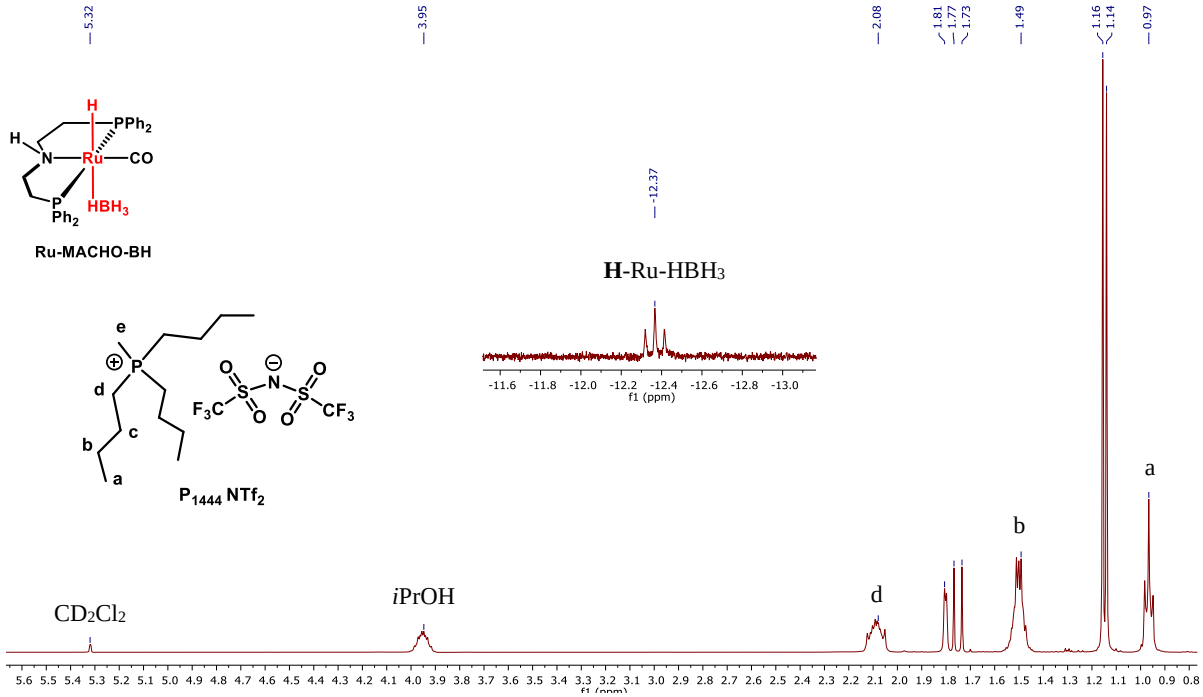

Figure 3.20: ^{1}H NMR spectrum of Ru-MACHO-BH in P_{1444} NTf_2 and *i*PrOH (CD_2Cl_2, 25 °C, 400 MHz).

3.3 Summary

In this chapter, I have demonstrated that a suitable IL can promote the in-situ activation of Ru-PNP catalysts without the need of an external base. At the same time, the ionic liquid stabilizes the catalyst in solution thanks to the formation of stable Ru-acetate and Ru-formate complexes. Importantly, the reactivity observed with acetate and formate ILs is corroborated by the observation of the same complexes already in the literature. The novelty of the reactivity modes showed herein between Ru-PNP and ILs is one of the key aspects of this dissertation. Based on the exploratory work conducted in this chapter, it has been possible to set the foundation for the development of the catalytic applications that will be discussed in this thesis. For example, performing experiments with the model substrate *i*PrOH, I have observed traces of acetone in solution that led us towards the optimization process of *i*PrOH dehydrogenation under continuous flow (see Chapter 7). In this regard, more stoichiometric studies of different Ru-PNP catalysts and substrates in the presence of ILs can easily lead to new possible applications and further expand on the remarkable reactivity of these mixtures.

The NMR characterization provided in this chapter is a clear evidence of the observed behavior of Ru-PNP in ILs. Some examples of ^{31}P NMR analysis are provided in Appendix A and confirm the proposed reactivity. However, a detailed investigation on understanding phosphorous NMRs have not been carried out in this study. Considering the nature of PNP ligands, it is certain to imagine that targeted ^{1}H, ^{13}C, ^{31}P, ^{15}N as well as 2D-NMR analysis can provide useful information on coordination, orientation and space occupation of the IL around the Ru-PNP complex. In this regard, the method used in Figure 3.5 allows to investigate hydride species directly in IL without solvent´s perturbation, hence providing much more insight on the chemical bonds and reactions involved with Ru-PNP, ILs, and potential substrates. Moreover, temperature-profile NMR experiments could provide more information on the solubility and reactivity of these systems at different temperatures. Indeed, it is also possible to envision the in-situ study of catalytic species also in operative conditions (different atmospheres, 25-100 ºC, 1-10 bar).

4. Carbon dioxide hydrogenation to formic acid catalyzed by Ru-PNP complexes in ionic liquids

4.1 Introduction

The use of carbon dioxide is expected to grow and replace common synthetic routes based on petrochemicals for the bulk synthesis of both chemicals and fuels [50]. Green hydrogen from renewable energy (solar, wind) will promote CCU processes connecting both the chemical and the energy sectors. In this regard, catalytic hydrogenation of CO_2 is an atom-efficient, sustainable route for such transformation, as it does not produce stoichiometric waste as in the case of conventional reducing agents. As described in the review work in Appendix E, homogeneous catalysis has accomplished several achievements in the field of hydrogenation of CO_2 to either FA or methanol. However, the use of CO_2 trapping agents in stoichiometric amounts still limits the possibilities offered by this approach. Scheme 4.1 shows examples of classic approaches for CO_2 capture using hydroxide bases or amines. The trapped CO_2 is stabilized by formation of carboxylates or carbamates that are later hydrogenated to e.g. formate adducts. This step usually requires harsh conditions in terms of both pressure and temperature, making such methods unsustainable. When using amines, the uncontrolled formation of different products can lead to degradation after consecutive cycles of utilization. In addition, regeneration of either the amine or the hydroxide trapping agent is associated with high energetic costs. Using this approach, solutions of bicarbonates or formates are reported to promote formate salts formation in the presence of ruthenium and iron catalysts [237–241].

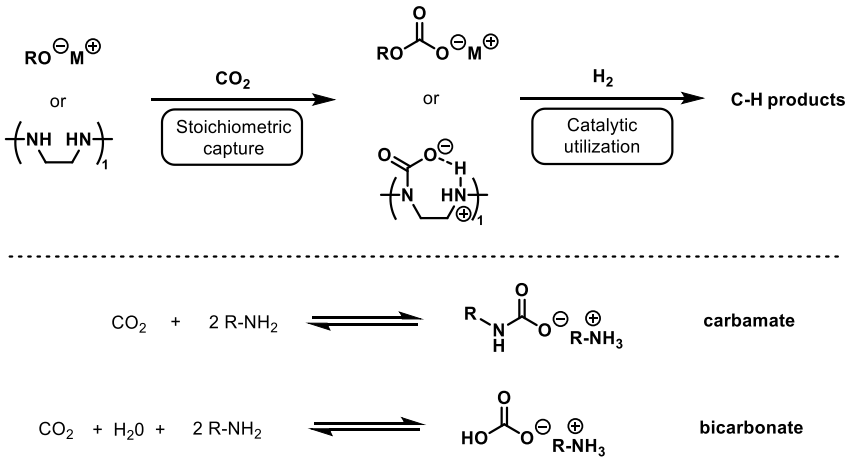

Scheme 4.1: Known strategies for CO_2 capture with hydroxides and amines.

Several review works covered the topic of CO_2 valorization catalyzed by organometallic pincer complexes, including photocatalytic [242] and electrocatalytic [243,244] CO_2 reduction. Concerning catalytic hydrogenation, the Ir-PNP complex **Ir-2** showed by Nozaki represents the state-of-the-art of CO_2 to formate, with TON as high as 3500000 (Table 4.1, Entry 2) [245]. However, the system employs harsh conditions (200 ºC, 80 bar) and KOH to shift the equilibrium towards the formation of potassium formate. Using a similar approach, Hazari reported the use of the water soluble **Ir-3** in aqueous solution for the production of HCOOK affording a TON = 348.000 (Table 4.1, Entry 3) at 185 ºC [246]. Entries 4 and 6 in Table 4.1 provide other examples of efficient iridium catalysts bearing a different ligand scaffold, hence not discussed in this thesis.

Important were the contributions from Milstein using the Fe-PNP analogue of **Ru-6**, **Fe-1** (Scheme 4.2a) [154]. The catalyst afforded a TON = 788 and a TOF of 156 h^{-1} for the production of sodium formate in the presence of a 10:1 mixture of H_2O/THF and 2 M NaOH at 25 ºC. Importantly, the same iron catalyst was also active for FA dehydrogenation [161]. Sanford used the Milstein´s catalyst **Ru-6** to hydrogenate carbon dioxide to potassium formate, remarking the suggested aromatization/dearomatization pathway as the reaction mechanism involved when using this class of catalysts (Scheme 4.2b) [247]. The same catalyst was reported by Pidko to hydrogenate carbon dioxide to HCOOK in the presence of DBU (or $NHex_3$) affording TOF >1000000 at 120 ºC (Scheme 4.2c) [248].

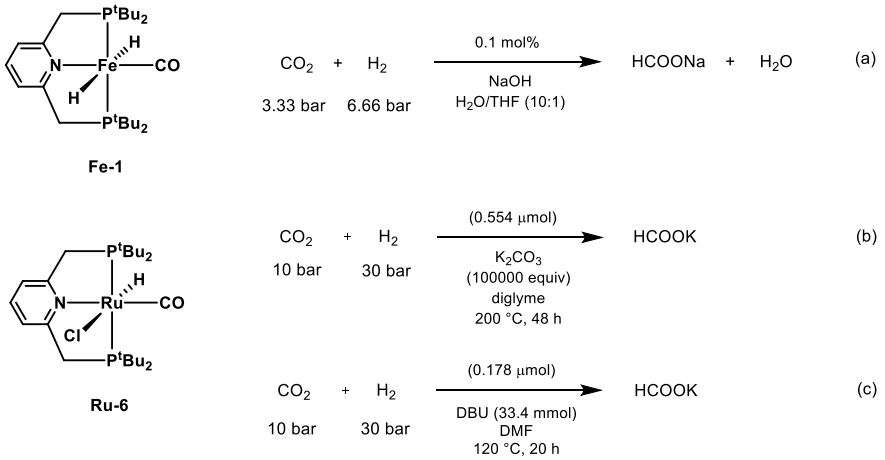

Scheme 4.2: CO_2 hydrogenation studies reported by Milstein (a) [154], Sanford (b) [247] and Pidko (c) [248].

Returning to the Noyori-type PNP catalysts discussed in this study, Prakash proposed an interesting method involving capturing of CO_2 and hydrogenation to formate salts, combined with a direct formate FC and with regeneration of the capturing hydroxide base (Scheme 4.3) [249]. The reaction proceeds in the presence of 50 bar of hydrogen, 2-methyltetrahydrofuran and KOH at 80 ºC, resulting in a TON = 2710 using **Ru-7**. The catalyst remained active for up to 6 cycles of hydrogenation and dehydrogenation.

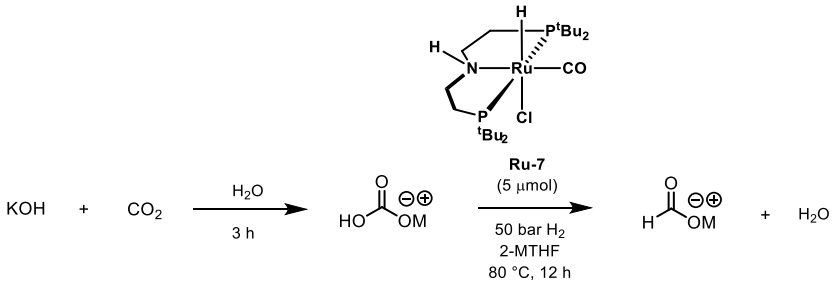

Scheme 4.3: CO_2 hydrogenation promoted by hydroxides as proposed by Prakash [249].

The same author showed a method for CO_2 capture promoted by amines, followed by hydrogenation to formate salts catalyzed by **Ru-MACHO-BH** [250]. Among the screened amines, tetramethylguanidine resulted in better performance, affording a TON = 7375 after 5 consecutive hydrogenations in the presence of 50 bar of H_2, in a mixture of dioxane/H_2O at 55 °C (Scheme 4.4).

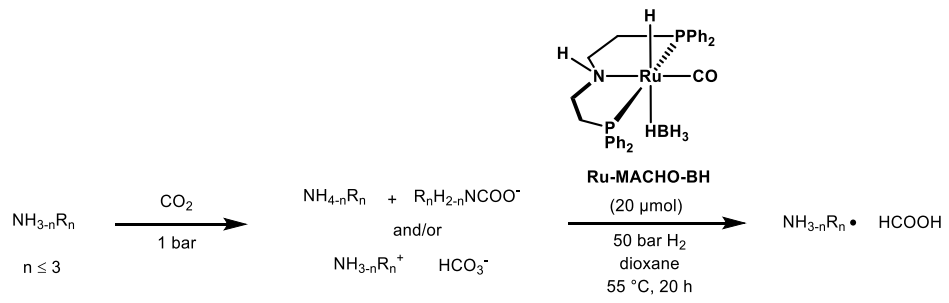

Scheme 4.4: CO_2 hydrogenation promoted by amines as proposed by Prakash [250].

Hazari and Schneider employed a PNP ctalyst **Fe-2** (Table 4.1) for the production of formate affording a TON = 58990 at 80 ºC (Scheme 4.5) [169]. However, the catalyst was active only in the presence of 79600 equivalents of DBU, LiOTf as additive (DBU/LiOTf 5:1), 70 bar of CO_2/H_2 (1:1) and THF as the organic solvent.

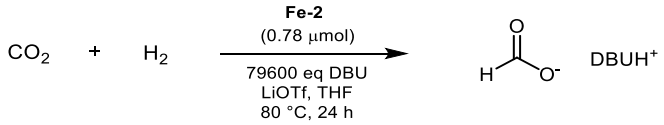

Scheme 4.5: Hazari and Schneider's CO_2 hydrogenation catalyzed by Fe-2 [169].

Beller used **Ru-MACHO**, previously reported as an active catalyst for hydrogenation of esters [251], for the hydrogenation of bicarbonate and CO_2 to formate salts [252]. The method exploits the activity of this catalyst towards methanol reforming to produce the required hydrogen in situ. Using this approach, **Ru-MACHO** afforded a TON of 18000 (a) and 12000 (b) at 150 ºC (Scheme 4.6).

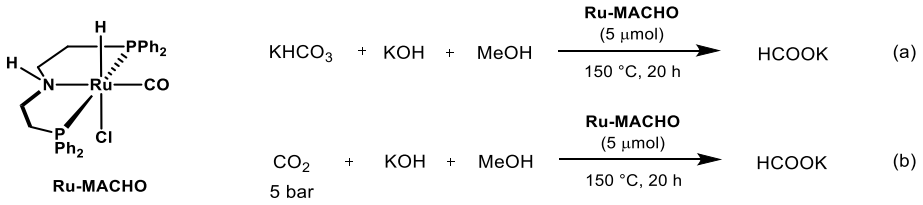

Scheme 4.6: Hydrogenation of carbonates and CO_2 using Ru-MACHO reported by Beller [252].

Table 4.1 offers an overview of the most representative systems reported to be efficient in the hydrogenation of CO_2 to FA. It is possible to notice how in most of the reported procedures there is at least one or two aspects that prevent a real utilization of such systems in real-life applications. This includes the use of volatile and/or toxic solvents, corrosive bases, harsh conditions of temperature and pressure, or inert conditions for the catalysts to operate. For completeness, Table 4.1 contains an example of heterogeneous catalyst composed by Pd nanoparticles supported on carbon is reported as well (Entry 9, Table 4.1) [253]. Interestingly, BMIM Ac was used in this study; the authors claim that the IL performs several roles: it captures and activates CO_2, influences the Pd nanoparticles improving their activity, and stabilizes the generated FA, similarly to what discussed in this chapter.

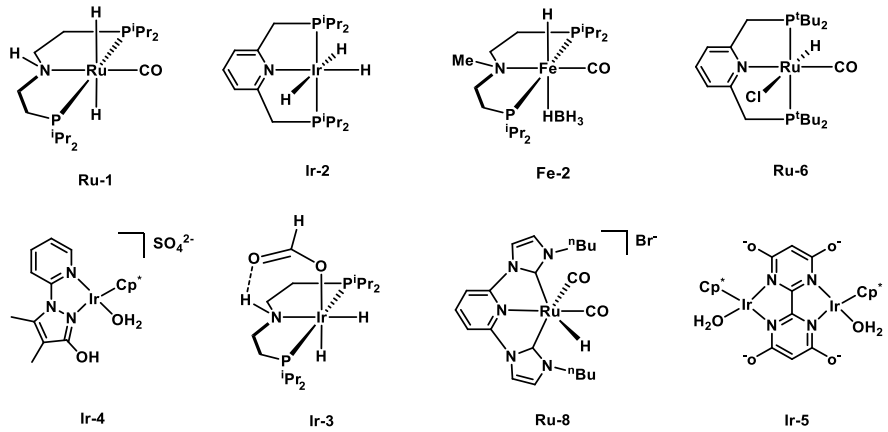

Entry	Corresponding authors	Catalyst	TON	TOF (h^{-1})	T (C) p (bar)	Additives	Comments
1	Nielsen[a]	Ru-1	35.000	1.000	80 60	EMIM Ac	Ambient conditions low p/T Limited TOF
2	Nozaki [245]	Ir-2	3.500.000	150.000	200 80	KOH THF	State-of-the-art Inert conditions Poor stability Volatile solvent
3	Hazari [246]	Ir-3	348.000	14.500	185 55	KOH H_2O	Inert conditions
4	Hull, Himeda, Fujita [254]	Ir-5	79.000	54.000[b]	80 50	$KHCO_3$ H_2O	Inert conditions Volatile solvent
5	Pidko [248]	Ru-6	706.500	1.100.000[b]	120 40	$NHex_3$/DBU DMF	Inert conditions Volatile solvent
6	Himeda [255]	Ir-4	7.850	650	50 10	$NaHCO_3$ H_2O	Inert conditions Volatile solvent
7	Sans [200]	Ru-8	800.000	20.000[b]	120 90	BMMI Ac Dioxane/H_2O	Volatile solvent
8	Hazari et al [169]	Fe-2	59.000	2.500	80 70	DBU THF	First-row metal Low activity Volatile solvent
9	Liu [253]	Pd/C nano	594	25	40 80	BMIM Ac	Heterogeneous

[a] developed in this study. [b] initial TOF.

Table 4.1: Relevant examples of reported active systems for CO_2 hydrogenation to FA in comparison with the Ru-PNP/IL showed in this work. (i) stands for initial TOF.

A different approach to promote hydrogenation of CO_2 to FA under mild conditions is to use the solvation ability of a suitable solvent to shift the equilibrium towards the formation of FA solutions. In particular, mixtures of DMSO/ H_2O have been reported to promote high concentrations of aqueous FA by lowering the entropic penalty in the Gibbs energy of the transformation. As an example, Laurenczy reported the hydeogenation of CO_2 to FA in acidic media catalyzed by a Ru(II) complex bearing water soluble phosphine ligands [256]. In a solution of DMSO and H_2O (10%), the hydrogenation proceeds without other additives affording a

TON = 475 and a concentration of 1.3 M of aqueous FA at 50 ºC. However, high pressure (100 bar, CO_2:H_2 1:1) and long times were necessary. Leitner and Bardow developed a method for CO_2 hydrogenation to FA in a biphasic system with DMSO/n-heptane catalysed by a Rh complex [257]. The highest concentration achieved was 1.3 M FA at 60 ºC in the presence of 40:80 bar of CO_2:H_2. Importantly, the formation of a DMSO/FA azeotrope mixture makes continuous separation of FA challenging. The authors tested various co-solvents, with acetic acid resulting in the best choice for FA separation due to lower energy demand.

Ionic liquids can be used as a suitable alternative for CO_2 capturing materials thanks to their non-volatility, structure-tunability, recyclability, and high CO_2 uptake [258]. One of the first approaches reported for IL-promoted CO_2 capture included the insertion of amine functionalities on either the cation or the anion of the IL [259–262] to produce carbamates. In another examples, ILs have been used in combination with amine blends to increase CO_2 uptake and lower the regeneration temperature of such amine-based adsorbents [263,264]. When compared to other gases such as O_2, N_2 and H_2, CO_2 is soluble in many different ILs to a relatively large extent due to its acidic properties. Usually physisorption processes are involved in CO_2 capture processes [265–268]. However, it was found that in the presence of more basic anions (carboxylates), chemisorption can occur due to interaction between the acidic CO_2 and carbene species that are present in the IL solution [269–274]. Indeed, when considering imidazolium cations, the C2 position of the ring is often responsible of the reactivity of this type of molecules [275]. Following previous reports from Maginn [276] and Dai-Li [277], Rogers showed the chemisorption of CO_2 using 1,3-dialkylimidazolium acetate ILs [278]. Supported by single-crystal X-ray analysis, the authors demonstrated the presence of carbene species able to bind CO_2 selectively and reversibly (see section 4.2.1) [279]. This work by Rogers represents one of the starting point of the project discussed in this chapter; indeed, I have observed the same type of reactivity with the ILs used in this study (EMIM Ac, BMIM Ac, EMIM CHOO, Figure 4.3), and later demonstrated the ability of Ru-PNP to catalyze the efficient hydrogenation of the so-obtained IL-CO_2 adducts to FA. Using a different approach, it is possible to obtain so-called superbasic ILs by combining N-based organobases with different anions [280]. As an example, Dai and Li achieved chemisorption of CO_2 using a mixture of BMMIM NTf_2 and DBU (Figure 4.1a) [281,282]; interestingly, this work present some overlapping with the work presented in this thesis, i.e. CO_2 activation at the C2 position of the imidazolium cation (see 4.2.1). Zhu reported the use of differently substituted DBU-based imidazole ILs that are able to trap reversibly up to 1 mol of CO_2 per mole of IL (Figure 4.1b) [283]. The mechanism involves coordination of the activated CO_2 to the imidazole anion via the nitrogen atom; the authors also showed that different electron donating and withdrawing groups on the anion have a direct effect on the resulting ability of the IL to trap CO_2.

Many studies reported the use of IL as reaction additives that promote CO_2 hydrogenation reactions, especially due to their tunable basic properties. For example, Han employed a heterogeneous ruthenium catalyst immobilized on silica, which was dispersed in an IL (IL-1 in Figure 4.1c) aqueous solution affording a TOF= 103 h^{-1} at 60 °C [284]. Later on, the same author used the same catalyst but a different ionic liquid (IL-2) obtaining a TON = 1059 and TOF = 88 h^{-1} [285]. Leitner and co-workers reported the use of several ruthenium catalysts bearing the Triphos ligand (see **Ru-11** in Figure 4.4) as active species for CO_2 hydrogenation reactions [117]; in this regard, the same author used the precursor [Ru(cod)(methallyl)$_2$] in the presence of tetrabutylphosphonium diphenyl(3-sulfonatophenyl)phosphine (P_{4444} TPPMS) and functionalized ILs as bases (IL-3, IL-4, IL-5 in Figure 4.1d) for the hydrogenation of CO_2 to FA under flow conditions [202]. In addition, Leitner proposed a method for the continuous FA separation promoted by $scCO_2$ in a biphasic system where the ruthenium catalyst is immobilized in the IL phase (see 4.2.3). Sans explored the buffering effect of different ILs in the presence of DMSO/H_2O for FA production from CO_2 and H_2 [201]. The precursor $Ru_3(CO)_{12}$ in the presence of IL-6 (Figure 4.1) afforded a TON=17,000 and a TOF = 100 h^{-1} at 70 °C and 30:40 bar of CO_2:H_2. Later, the same author employed the pincer complex **Ru-8** (Table 4.1 Entry 7) under similar conditions using IL-7 (Figure 4.1), resulting in improved TON = 833800 and TOF=20600 h^{-1} with 15:45 bar of CO_2:H_2 at 120 ºC [200]. Sans also discussed the effect of catalyst

design on the efficiency of this transformation under buffering conditions [286]. It has to be noted that the concentration of FA achievable is usually limited to 1.5 M under the basic conditions described in these studies, similar to the acidic DMSO/H_2O mixtures discussed above.

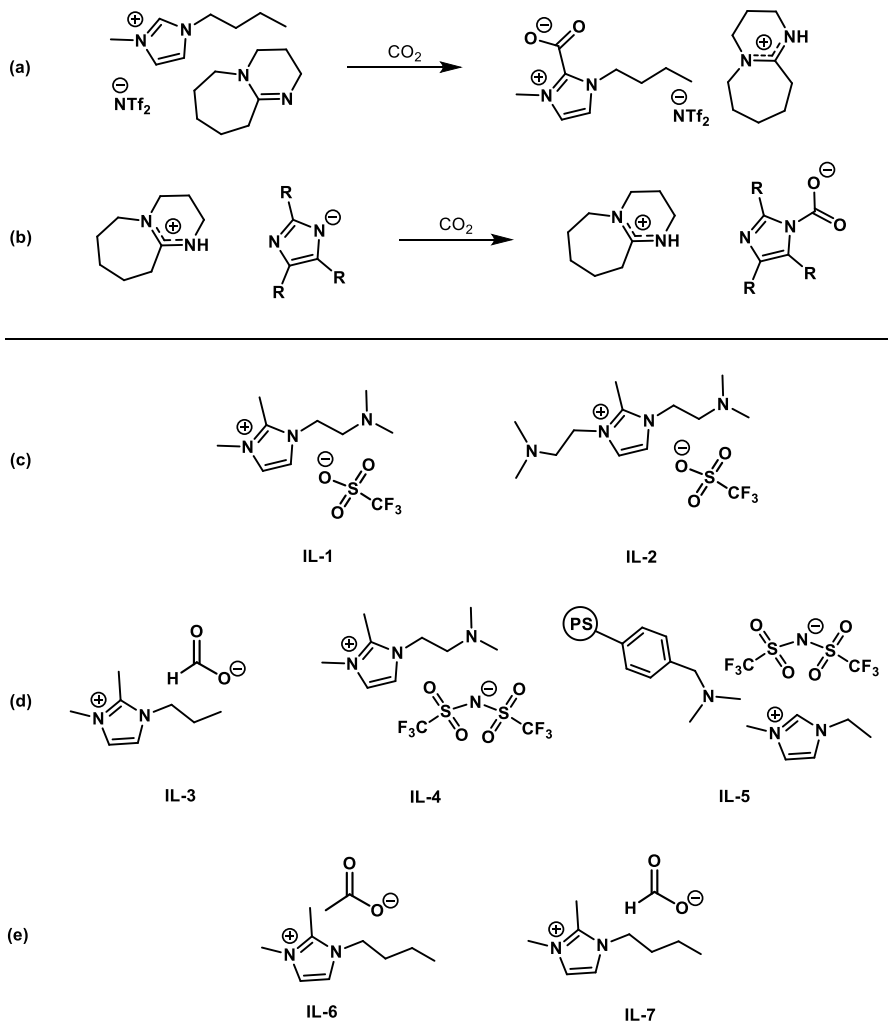

Figure 4.1: Examples of functionlized ILs reported to assist CO_2 capture (up) followed by hydrogenation to FA (down).

In this work, I have explored the reactivity of ruthenium-PNP catalysts for the hydrogenation of CO_2 to FA at mild conditions. I will show that the ionic liquid acts as both CO_2 capturing agent as well as stabilizing solvent for the organometallic complex by interaction of the anion with the metal centre. The hydrogenation of CO_2 proceeds already at 25 ºC and 1 bar under both autoclave and flow conditions leading up to 1.26 equivalents of FA compared to the IL. As a note for the reader, the notation FA has been used to express the product obtained after CO_2 hydrogenation performed in Ru-PNP/IL mixtures throughout this chapter. This has been done for simplicity; however, it will be clear during the discussion that, at least when using acetate ILs, a more correct representation would be "hydrogenation of CO_2 to formate" (see 4.2.3 and 4.2.4).

4.2 Results and discussion

4.2.1 Reactivity of CO_2 with ILs

I have started by investigating the reactivity of EMIM Ac in the presence of CO_2. In agreement with the studies reported by Rogers [279], EMIM Ac readily (and reversibly) traps CO_2 by simple bubbling through the IL solution at room temperature, while more efficient CO_2 trapping is performed under pressure and in shorter times. As visible in Figure 4.2, ^{1}H NMR analysis shows splitting of the signals associated with the imidazolium cation, indicating the formation of EMIM-CO_2. Also in accordance with Rogers, high concentrations of CO_2 trapped result in the formation of a solid precipitate. Hence, I have performed studies on the CO_2 absorption capacity of EMIM Ac at different CO_2 pressures and times. In detail, 1 mL of EMIM Ac was exposed to different CO_2 pressures (1, 5, 10, 15 bar) at different times (5 min, 1h, 2h, 3h, 6h, 18h). Table 4.2 shows an example of such method for experiments at 10 bar. After only 1 hour, the maximum concentration of CO_2 in the IL is achieved (12 mol% of EMIM-CO_2 in EMIM Ac, determined by ^{1}H NMR). In fact, extending the time from 1 to 18 hours resulted in similar molar amounts of CO_2 absorbed (Entry 5, Table 4.2). Importantly, increasing the pressure from 1 to 15 bar did not produce better results in terms of molar CO_2 uptake. The same behavior was observed performing the experiment in a bigger autoclave using 2 mL of EMIM Ac (5 mL volume, B in Figure 2.8). Once again, the IL absorbed up to 12 mol% of CO_2 after 1 hour in the presence of 1-15 bar of CO_2 pressure applied. By measuring the volume of gas released, and quantifying the CO_2 trapped in the IL by ^{1}H NMR analysis, it was possible to derive calibration curves of the molar amount of CO_2 corresponding to different pressures. The same calibration procedure was performed using CO_2/H_2 pressure as well as pure H_2 in order to verify the validity of the method. As such, the so-calculated molar amounts of CO_2 have been used to calculate the FA yield in some of the following experiments.

Entry	Time	CO_2 released[a] (L)	EMIM-CO_2[b] (mol%)	P_{end}	CO_2 trapped[b] (mmol)	CO_2 released[c] (mmol)	tot CO_2 (mmol)
1	5 min	0,13	10	9	0.64	5.33	5.93
2	1h	0,088	12	5	0.77	3.50	4.37
3	2h	0,065	12	5	0.77	2.65	3.43
4	3h	0,072	12	5	0.77	2.94	3.71
5	18h	0,08	13 (s)	5	0.83	3.27	4.11

The reaction were performed at room temperature after flushing the autoclave with N_2. [a] Measured by volume displaced in a graduated cylinder. [b] Measured by NMR. [c] Measured with ideal gas law (PV = nRT).

Table 4.2: Example of the method used for calibration of the autoclaves at different pressures of CO_2.

The mixture shown in Figure 4.2 is the result of a separate experiment, where EMIM Ac (2 mL) was loaded in a 5 mL size autoclave and exposed to 25 bar of CO_2 for 45 min at room temperature. In this example, the CO_2-adduct product is present at 35 mol% relatively to EMIM Ac. At least under the reaction conditions used in this study (pressure of CO_2 max = 25 bar), this is the highest concentration of CO_2 obtainable in EMIM Ac. BMIM Ac performs similarly to EMIM Ac, but with a lower tendency to accumulate CO_2 under the reaction conditions used in this study. This can be explained by the bulkier butyl groups on the imidazolium ring that prevents easy CO_2 coordination. However, this is just a qualitative observation based on the higher catalytic activity of EMIM Ac compared to BMIM Ac towards CO_2 hydrogenation (see 4.2.2), but detailed comparison between the two ILs has not been

carried out in this sense. In addition, it would be interesting to conduct even more studies at different (higher) pressures, temperatures and IL volumes in order to find the optimal CO_2 uptake possible depending on the reaction conditions used.

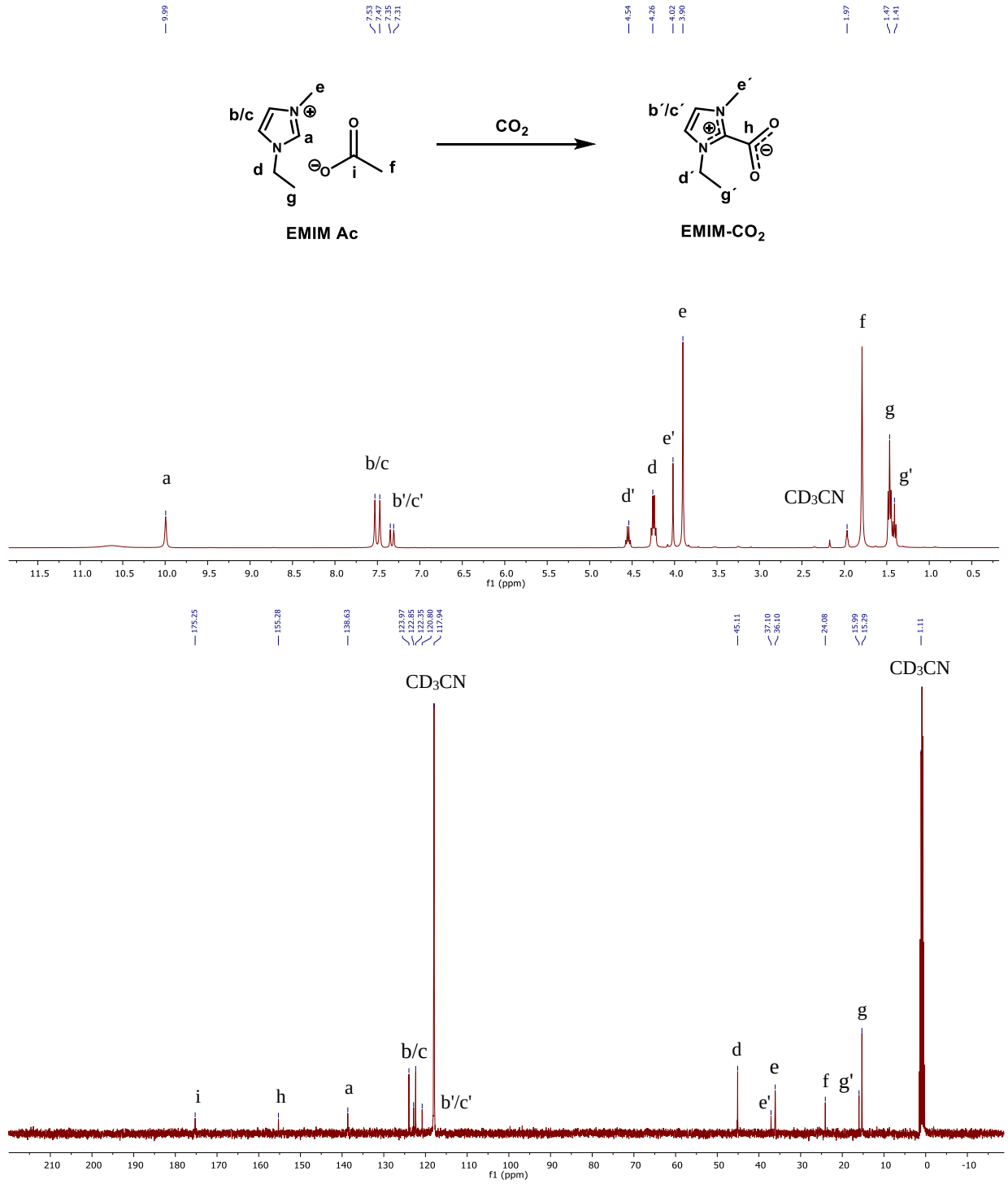

Figure 4.2: ^{1}H NMR (up) and ^{13}C-NMR (down) spectra of EMIM Ac in the presence of 25 bar CO_2 at room temperature for 45 minutes (CD_3CN, 25 ºC, 400 MHz).

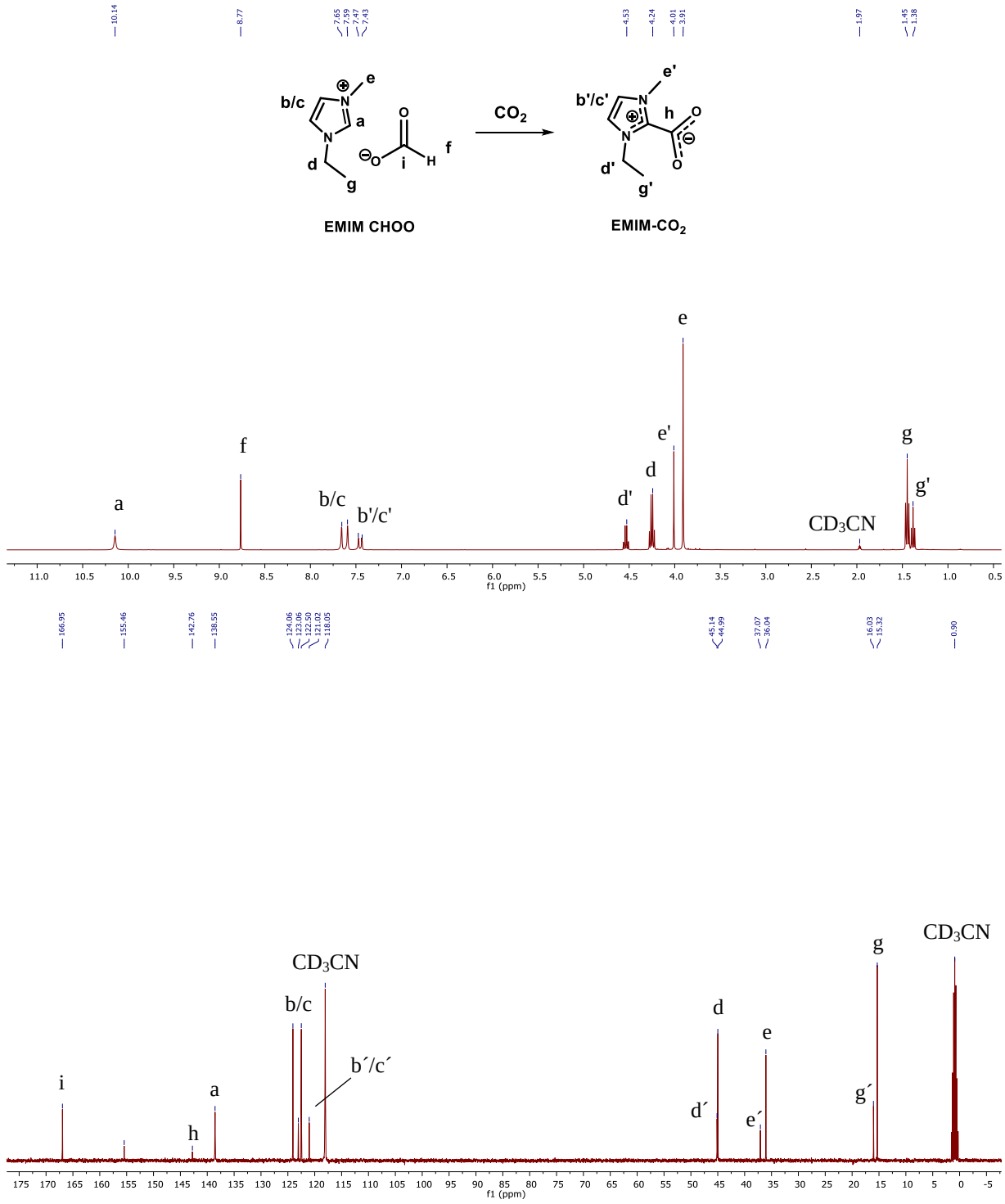

Figure 4.3: ^{1}H (up) and ^{13}C (down) NMR spectra of EMIM CHOO in the presence of 15 bar of CO_2 at 50 ºC for 5 hours (CD_3CN, 25 ºC, 400 MHz).

Later, I have investigated the use of EMIM CHOO. The presence of CO_2 trapped can be noticed already in the isolated IL after the synthesis procedure (Scheme 3.3). Similar to EMIM Ac, Figure 4.3 shows the ^{1}H NMR spectrum of the mixture obtained after

exposing EMIM CHOO to CO_2 at room temperature. Indeed, EMIM CHOO traps CO_2 as effectively as the acetate analogue affording EMIM-CO_2, up to 42 mol% in the example provided in Figure 4.3. In this case, the experiment was carried out at 50 ºC to facilitate liquefaction of EMIM CHOO that is solid at room temperature. Similar to acetate ILs, the formation of carbene species able to bind CO_2 is possible thanks to the stabilization provided by the formation of a FA/formate mixture.

It is possible to observe a qualitative trend towards CO_2 capture in the order EMIM CHOO > EMIM Ac > BMIM Ac, likely explained by the relatively different basicity of the three ILs, following the same order. This trend was particularly evident during my studies on FA dehydrogenation and CO_2 hydrogenation, as it will be discussed in Chapters 4 and 5. In fact, it was during such studies that I have isolated the crystal structure in Scheme 4.8 that clearly indicates activation of CO_2 at the C2 position of the imidazolium ring. The crystal data were compared with literature database, showing that the same crystal was isolated by Rogers while studying novel synthetic procedures with ILs [287]. The presence of water promoting the formation of EMIM HOCOO is explained by the hygroscopic properties of EMIM CHOO and its storage under ambient conditions, as well as water being present as an impurity in the EMIM methylcarbonate precursor used in the synthesis (Scheme 3.3). In this sense, the presence of the unassigned peak at 155 ppm in Figure 4.3 could be attributed to the presence of a bicarbonate specie like EMIM HOCOO. I would like to thank my colleague PhD student Mike S.B. Jørgensen for carrying out the X-ray diffraction experiments and for refining the crystal structure.

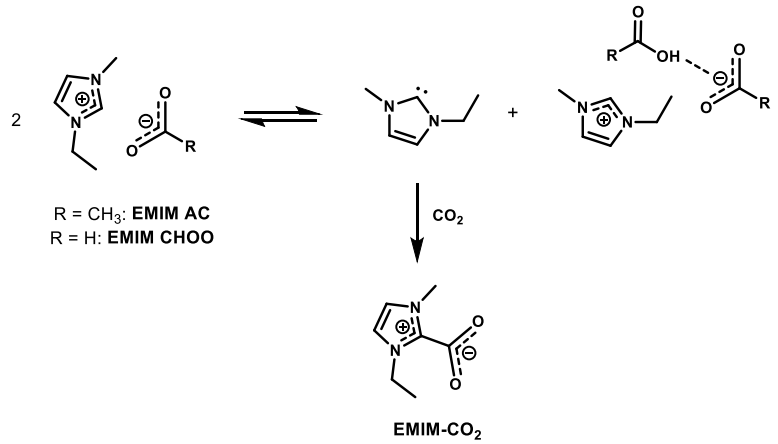

Scheme 4.7: Reaction mechanism for CO_2 activation performed by EMIM Ac and EMIM CHOO (adapted from [279]).

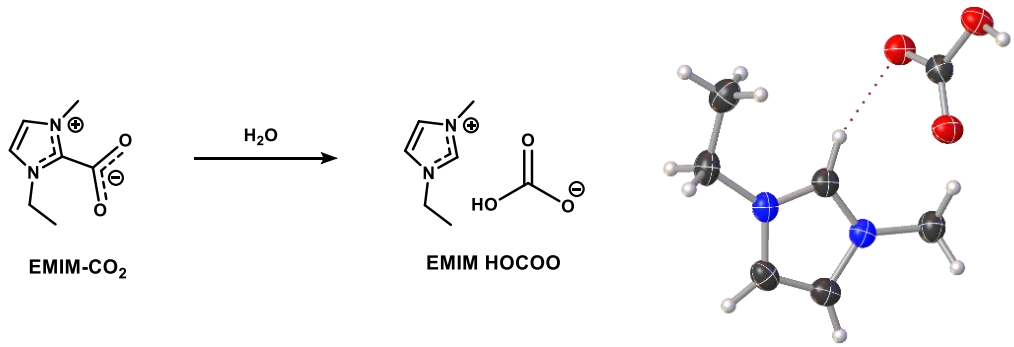

Scheme 4.8: Reaction mechanism for the formation of EMIM HOCOO proposed by Rogers [287].

In summary, the mechanism involved for CO_2 capture when using this type of carboxylate ILs is shown in Scheme 4.7 [279]. The first step consists in the deprotonation of the acidic proton at the C2 position of the imidazolium cation performed by the IL anion. Thus, the so-obtained carbene remains stable in solution due to formation of stable acetic acid/acetate (FA/formate) mixtures [279]. It is important that the corresponding carboxylic acids formed after protonation of the anion remain in solution avoiding degradation of the IL, hence providing a bulk reservoir of free carbene species in solution. Both acetic acid (bp = 118 ºC) and FA (bp = 100.8 ºC) fulfil this requirement due to their relatively low volatility.

4.2.2 Optimization of catalytic CO_2 hydrogenation to FA

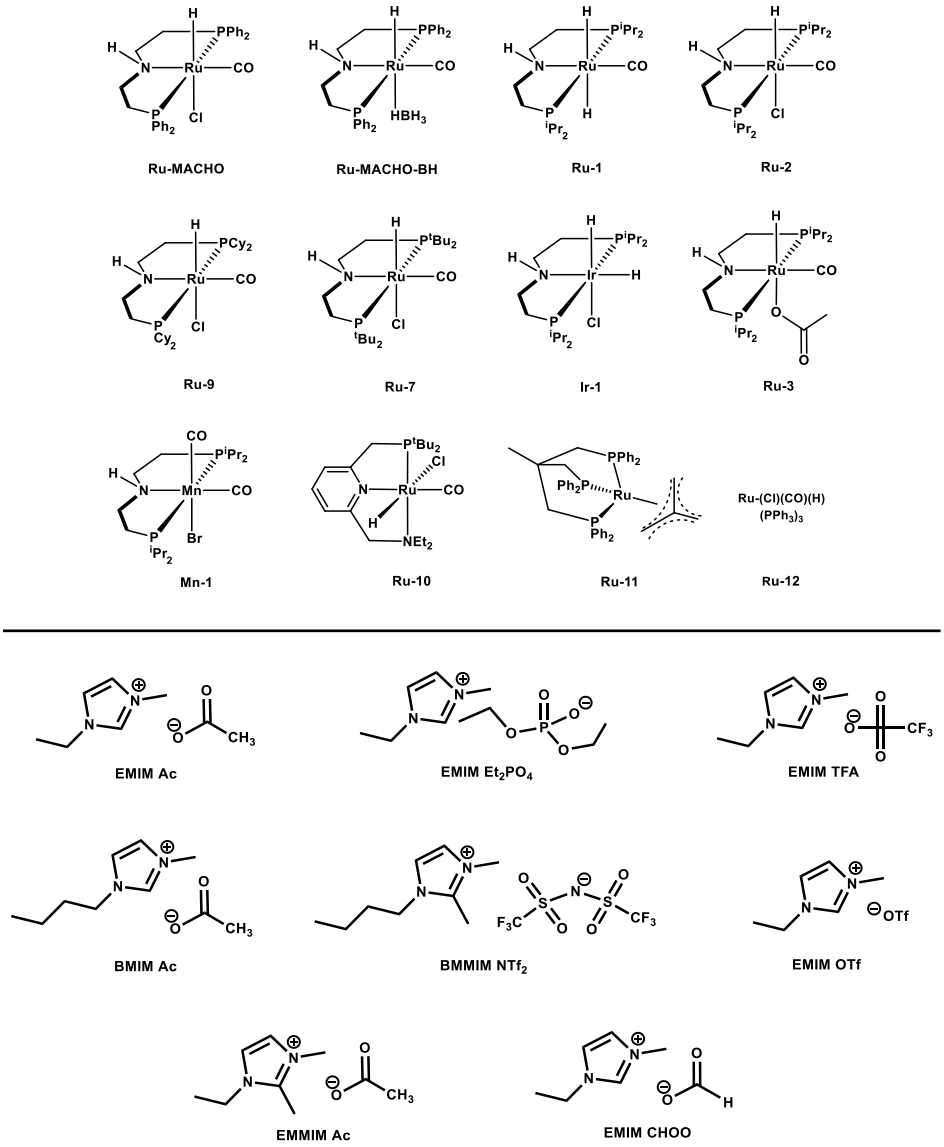

Figure 4.4: Structures and names of catalysts and ionic liquids tested in this chapter.

Encouraged by its high reactivity in the presence of CO_2, I have explored the use of EMIM Ac in combination with a series of ruthenium catalysts for the hydrogenation of CO_2 at room temperature. Figure 4.4 provides a full overview of the catalysts and ILs used in this chapter, while Table 4.3 summarizes the results from the catalyst screening. Based on the easiness of CO_2 chemisorption performed by EMIM Ac, with consequent formation of the solid EMIM-CO_2, I have used H_2 in excess to promote EMIM-CO_2 hydrogenation that is likely the rate determining step in this reaction.

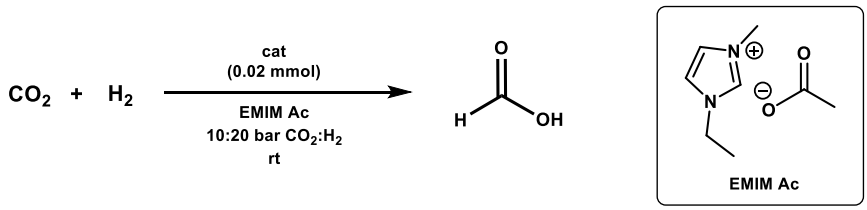

Entry	Catalyst	TON	TOF (h^{-1})	FA yield[a] (%)	FA/IL[b] (mol%)
1	Ru-12	-	-	-	<5
2	Ru-11	-	-	-	<5
3	Ru-10	-	-	-	<5
4	Ru-MACHO	-	-	-	<5
5	Ru-MACHO-BH	-	-	-	<5
6	Ru-9	22	2	11	7
7	Ru-7	66	4	36	22
8	Ir-1	81	4	36	28
9	Ru-3	109	6	61	36
10	Ru-2	106	8	70	35
11	Ru-1	198	10	>99	65
12	Mn-1	-	-	-	-

Reactions reproducible within a 10% error; performed using autoclave A (Figure 2.8, 2.5 mL reaction vessel). [a] Calculated after calibration of CO_2 at different pressures as described in 4.2.1. [b] Determined by ^{1}H NMR.

Table 4.3: Screening of catalysts for the hydrogenation of CO_2 to FA.

In light of their catalytic activity towards hydrogenation reactions, and not to limit the screening to only $P^{H}NP$ pincer ligands, I have evaluated other catalyst candidates including the Milstein´s complex **Ru-10** [100], the Ru-Triphos **Ru-11** [118], as well as the benchmark precursor **Ru-12**. However, none of them promoted visible formation of FA (Entries 1-3, Table 4.3). Also based on previous reports (see Table 4.1), I have tested the active iridium catalyst **Ir-1** that showed moderate activity affording 36% yield in FA and a TON = 81 (Entry 8). However, besides this screening result, the use of iridium catalysts has not been investigated further in this work.

Gladly, **Ru-1** (0.02 mmol) afforded 99% conversion of CO_2 and a TON of 198 at 25 ºC after 18 hours (Entry 11). The -Cl and -OAc analogues **Ru-2** and **Ru-3** showed comparable results, affording a TON of 106 and 109 respectively (Entries 9-10). This is in perfect agreement with the findings from Chapter 3; in fact, it has been demonstrated that both **Ru-1** and **Ru-2** result in the formation of **Ru-3** once dissolved in EMIM Ac, thus explaining the similar catalytic behavior of the three ^{iPr}PNP catalysts towards CO_2 hydrogenation. After the reaction is complete, ^{1}H NMR analysis shows the presence of the acetate specie **Ru-3** as the main resting state in solution (Figure 4.5, see Figures B.1-B.4 in Appendix B for more NMR analysis of reaction mixtures after catalytic CO_2 hydrogenation). The $^{pCy-}$, $^{tBu-}$ and $^{Ph-}$PNP catalysts showed poorer or absent productivity in comparison with the $^{iPr-}$PNP

analogues under the same reaction conditions (Entries 4-7). The differences in solubility between Ru-PNP catalysts in EMIM Ac at room temperature likely explains the observed differences in catalytic activity between **Ru-MACHO**, **Ru-2**, **Ru-7** and **Ru-9**. However, I have not carried out detailed solubility studies at different temperatures in order to validate this hypothesis. Finally, I have explored the use of **Mn-1** that unfortunately proved to be inactive under these conditions, even at higher catalyst loadings.

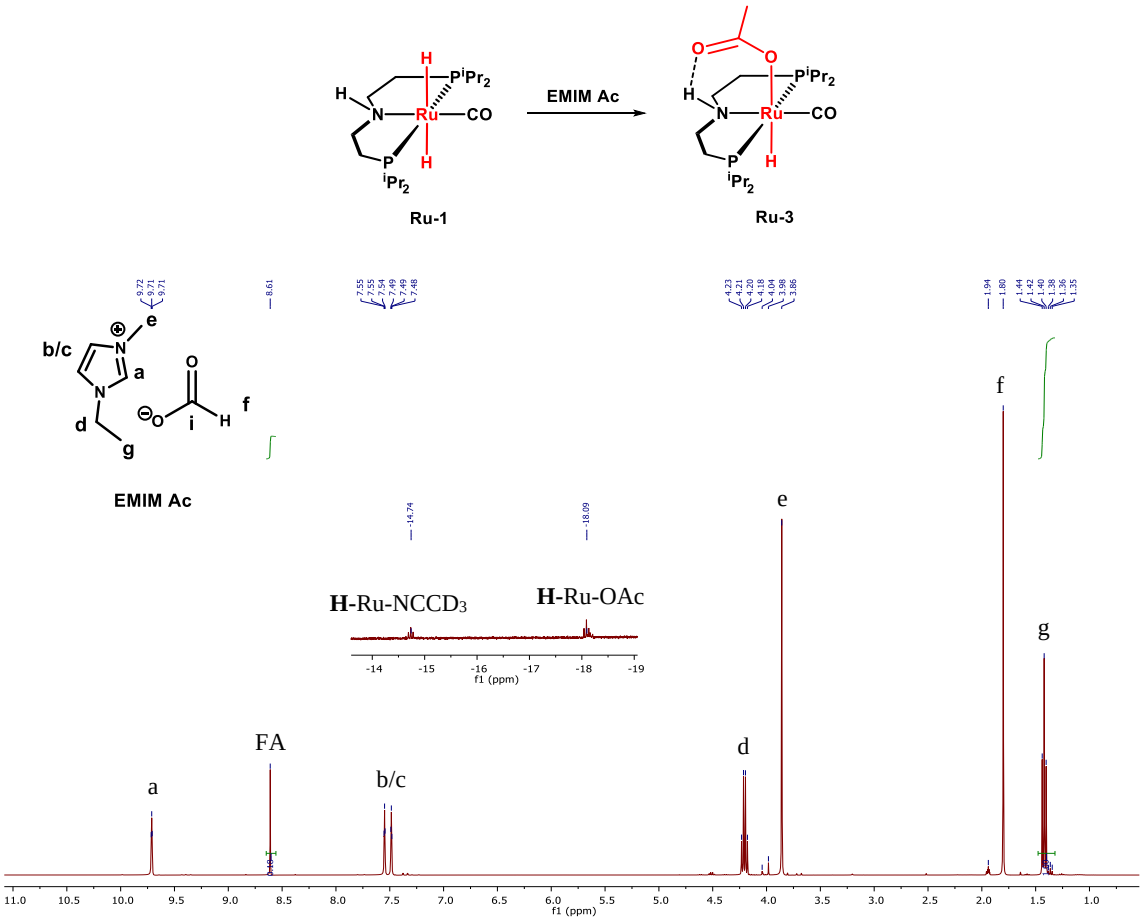

Figure 4.5: ^{1}H NMR of the reaction mixture after catalytic CO_2 hydrogenation to FA (CD_3CN, 25 ºC, 400 MHz). Reaction conditions: Ru-1 (0.02 mmol), EMIM Ac (1 mL), CO_2 (20bar), H_2 (20 bar), rt, 18h. The two integrals shows the peaks that were used for quantifying the FA/IL ratio discussed throughout this chapter.

Later, I have continued the screening process by testing different ILs in the presence of 0.02 mmol of **Ru-2** and 10:20 bar of CO_2:H_2 (Table 4.4, Figure 4.4 for the IL structures). BMIM Ac resulted in lower FA yields compared to EMIM Ac (Entries 6,7). In agreement with what described before in 4.2.1, EMIM CHOO traps CO_2 as effectively as the acetate analogue affording a TON = 130. Accordingly, ^{1}H NMR analysis shows the presence of **Ru-5** as the main specie in solution (see Figure B.4, Appendix B). An experiment with 15:15 bar of CO_2:H_2 and 0.045 mmol of **Ru-2** led to the formation of a 1.2 mol% ratio of FA/EMIM CHOO (determined by ^{1}H NMR, Figure 4.6). After the first hydrogenation step, the reaction mixture was washed with pentane (see 4.2.3), resulting in a decrease of FA lower than the initial EMIM:CHOO ratio in the IL (Figure 4.6). Then, a second cycle of hydrogenation in the presence of 15:15 bar CO_2:H_2 led to a new increase in FA amount (1.1 mol% FA/IL) after 18 h at 50 ºC (Figure 4.6). Encouraged by these results, I have carried out many experiments using EMIM CHOO as the only additive in the presence of either

Ru-2 or Ru-1. Unfortunately, it was not possible to increase the FA:IL molar ratio above 1.4 mol% nor obtain visible separation of FA from the reaction mixtures. This aspect will be discussed more in detail in the next section (see 4.2.3).

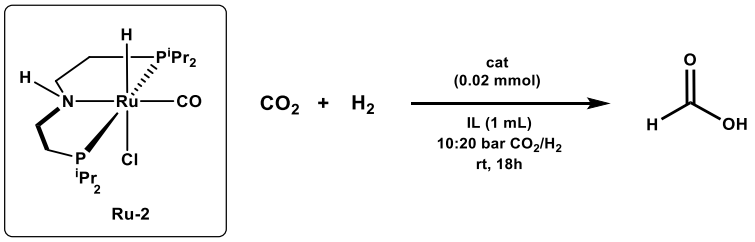

Entry	IL	TON	TOF (h^{-1})	FA/IL[a] (mol%)
1	EMIM TFA	-	-	-
2	EMIM OTf	-	-	-
3	BMMIM NTf_2	-	-	-
4	EMIM Et_2PO_4	-	-	-
5	EMMIM Ac	-	-	-
6	BMIM Ac	60	4	20
7	EMIM Ac	135	8	42
8[b]	EMIM CHOO	130	8	40
9[c]	EMIM CHOO	230	6	40

Reactions reproducible within a 10% error; performed using autoclave A (Figure 2.8, 2.5 mL reaction vessel). [a] Determined by ^{1}H NMR. [b] EMIM CHOO (6.5 mmol), 50 ºC. [c] Ru-2 (0.045 mmol), EMIM CHOO (13 mmol), 15:15 bar CO_2:H_2, 50 ºC; TON value after two runs, as described in Figure 4.6.

Table 4.4: Screening of ionic liquids for CO_2 hydrogenation to FA at room temperature.

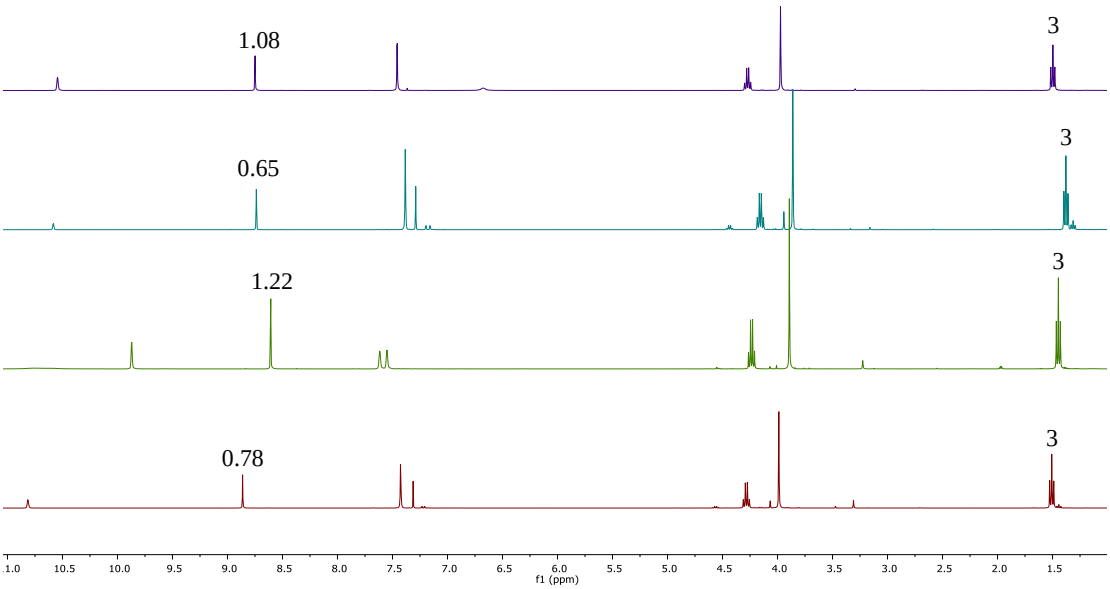

Figure 4.6: Representation of the method used in this study to follow FA production in EMIM CHOO ($CDCl_3$, 25 ºC, 400 MHz). Reaction conditions in Entry 9, Table 4.4.

It has to be noticed that the standard ^{1}H NMR experiments used in this study for the analysis of the reaction mixtures has to be considered only partially quntitative. This is due to multiple reasons: for example, precise measuring of both H_2 and CO_2 pressure was limited by manual regulation of pressure valves that could lead to errors of 1-2 bar between each experiment. In addition, it is known that hydrogen species in (very) small molecules are generally associated with long relaxation times. The measured ^{1}H spectra in this study have employed inter-scan delays of only 1-3 seconds, which is insufficient for a complete recovery of the equilibrium magnetization. Thus, averaging of the signals likely resulted in an underestimation of the true signal intensity. Nevertheless, specifically designed ^{1}H and ^{13}C experiments can certainly afford the desired quantification for example using longer acquisition times or adding an internal standard in solution prior catalytic hydrogenation. In this study, the quantification of FA in solution was achieved using the IL cation as the reference, as depicted in Figures 4.5 (with EMIM Ac) and Figure 4.6 (with EMIM CHOO).

As part of her PhD project, my colleague Brenda Rabell is currently working on optimizing the synthesis procedures of many functionalized (carbene-promoter) ILs. In this sense, she has isolated EMMIM Ac, similar to EMIM Ac, but with a methyl group blocking the C2 position of the imidazolium cation (Figure 4.4). The absent reactivity of such IL can indubitably confirm the reaction mechanism proposed in this study, favored by the presence of carbene species able to activate CO_2 that can later undergo Ru-promoted hydrogenation to FA (see 4.2.4). In this sense, Brenda carried out three experiments using EMMIM Ac, which as expected resulted in no visible FA formation (Entry 5, Table 4.4). However, these results have to be considered unreliable due to the presence of a slight excess of acetic acid from the synthesis procedure that was difficult to remove under vacuum conditions and that can affect the performance of the catalyst.

Nevertheless, there are already strong indications that led to the catalytic cycle proposed in Scheme 4.12. For example, I have tested the presence of water in solution that should result in the full protonation of the C2 position, hence inhibiting carbene formation. As expected, the system showed no catalytic activity towards CO_2 hydrogenation in both EMIM Ac and EMIM CHOO under the reaction conditions showed in Table 4.4 (+0.5 mL of H_2O). Curiously, activity was observed after addition of a 10 vol% solution of H_2O in DMSO (0.5 mL) to a mixture of **Ru-2** (0.02 mmol) and EMIM Ac (2 mL) at 50 ºC, resulting in a TON = 191 and a FA/IL ratio of 30% after 18 hours. Under identical conditions, without the H_2O/DMSO mixture, a TON = 395 and a FA/IL = 65 mol% was observed, confirming that basic conditions are favorable. As also described in the following chapters, the pH clearly has an effect on the resulting activity of the Ru-PNP/IL system in both hydrogenation of CO_2 and dehydrogenation of FA. In this regard, the observed changes in the chemical shift of the peak associated with the C2 proton should indicate changes in the pH of the solution (and/or hydrogen bonding) due to the presence of produced FA.

PhD student Brenda Rabell recently suggested to use Kamlet-Taft parameters to help explaining the observed differences in basicity of the ILs, reflected in different activity towards hydrogenation of CO_2. The Kamlet Taft method allows to estimate a polarity scale by means of three different parameters: hydrogen bond acidity (α), hydrogen bond basicity (β), as well as dipolarity/polarizability effects (π*) [268–271]. In particular, the β parameter can be used to give an indication of the solvent's ability to donate electron density and form hydrogen bonds with the solute, reflected in overall basicity of the IL [272,273]. Looking at reported β values from the literature, it is possible to obtain a qualitative trend of decreasing basicity in the order $^{-}Me_2PO_4$ > ^{-}Ac ≈ $^{-}OCHO$ > $^{-}MeSO_4$ > $^{-}N(CN)_2$, > ^{-}OTf > $^{-}BF_4$ > $^{-}PF_6$ > $^{-}NTf_2$ [189]. More in specific, formate and acetate anions correspond to β ≈ 1, while NTf_2- and OTf-based ILs usually show β ≈ 0-2-0.3. Hence, the considerable highest basicity of acetate and formate would explain the observed higher activity towards CO_2 capture and hydrogenation, favoured by basic conditions. Based on reported β values from the series shown above, it is likely that further optimization should be oriented towards (substituted) carboxylate and phosphate derivatives. Curiously, alkylphosphate anions show similar or higher basicity (β ≈ 1-1.2) than the acetate and formate counterparts do [288].

However, the tested EMIM Et_2PO_4 showed no visible activity under the reaction conditions tested in this study (Entry 4, Table 4.4). As Rogers observed, the formation and stabilization of the carbene species favouring CO_2 activation is the result of complex interactions between cation and anion, with formation of acetic acid/acetate mixtures when using EMIM Ac. In this sense, differences in basicity, bulkiness and electronic properties of Et_2PO_4 compared to Ac/CHOO might explain the observed behaviour (EMIM Et_2PO_4 will show remarkable activity and stability towards continuous flow FA dehydrogenation in the next chapter). It has to be noted that only a limited selection of ILs was tested in this study. Hence, these considerations should be considered purely qualitative and they do not attempt to provide a full explanation of the observed differences in catalytic activity towards CO_2 hydrogenation. Nevertheless, this interpretation based on Kamlet-Taft parameters has been used by Leitner when describing the differences in the reactivity of different ILs towards CO_2 hydrogenation to FA [202]. In fact, the authors found a consistent increase in TON and TOF values in the order of NTf_2 < OTf < CHOO, in complete agreement with the findings showed in this study. In this sense, PhD Brenda Rabell is carrying out more investigations in the Nielsen´s group by e.g. measuring Kamlet-Taft parameters of different functionalized ILs.

Based on this initial screening of catalysts and reaction conditions, I have carried out further investigation on the reaction conditions using EMIM Ac. First, I have investigated the effect of catalyst´s concentration at room temperature. As expected, the yield of FA increases with increasing concentrations of **Ru-2** in EMIM Ac, with quantitative CO_2 conversion achieved at 0.085 M (Figure 4.7). Later, I have investigated the effect of time at different temperatures. Not surprisingly, longer times are required at room temperatures (Figure 4.8, left). This was confirmed in many separate experiments; for example, 0.02 mmol of **Ru-2** in 1 mL EMIM Ac were loaded with 10:20 bar of CO_2 and H_2 respectively. After 1 hour, the FA/IL ratio was only 5 mol%. Reloading the autoclave 10:20 bar for other 2 hours (3 in total) afforded 12 mol% FA/EMIM Ac. Finally, loading a third time resulted in 96 mol% FA/IL and a total turnover number of 295 but only after 72 hours. Higher catalytic activity is possible at 80 ºC, with 50% FA yield obtained after only 3 hours, corresponding to a FA/IL = 60 mol% and a TON = 1050 (Figure 4.8, right). As expected, reactions carried out at 50 ºC shows intermediate results. The beneficial effect of higher temperature was observed in an experiment using **Ru-MACHO-BH**, which was found to be inactive at room temperature (Entry 5, Table 4.3): indeed, in a separate experiment at 120 ºC the catalyst afforded FA/IL = 50 mol% and a TON = 126 using 10:20 bar of CO_2:H_2 after 18 hours. This shows that the ^{Ph}PNP catalysts **Ru-MACHO** and **Ru-MACHO-BH** probably need higher temperature to show relevant catalytic activity. Also in this case, the superior activity of the ^{iPr}PNP catalysts was confirmed by running an experiment using **Ru-2** under identical conditions that resulted in 75 mol% FA/IL and a TON = 210.

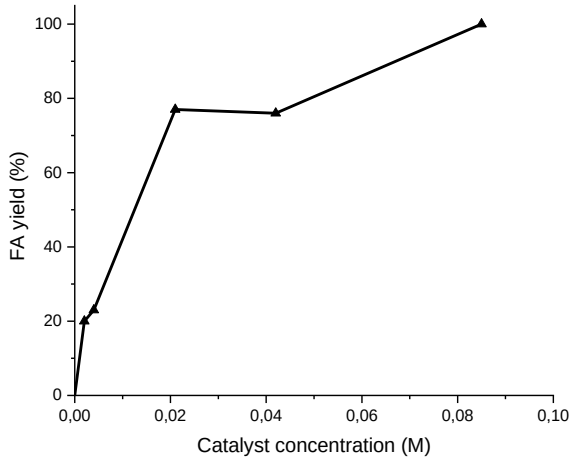

Figure 4.7: Effect of catalyst concentration on the yield of FA. Reaction conditions: Ru-2, EMIM Ac (1 mL), 10:20 bar CO_2:H_2, 25 ºC, 18h.

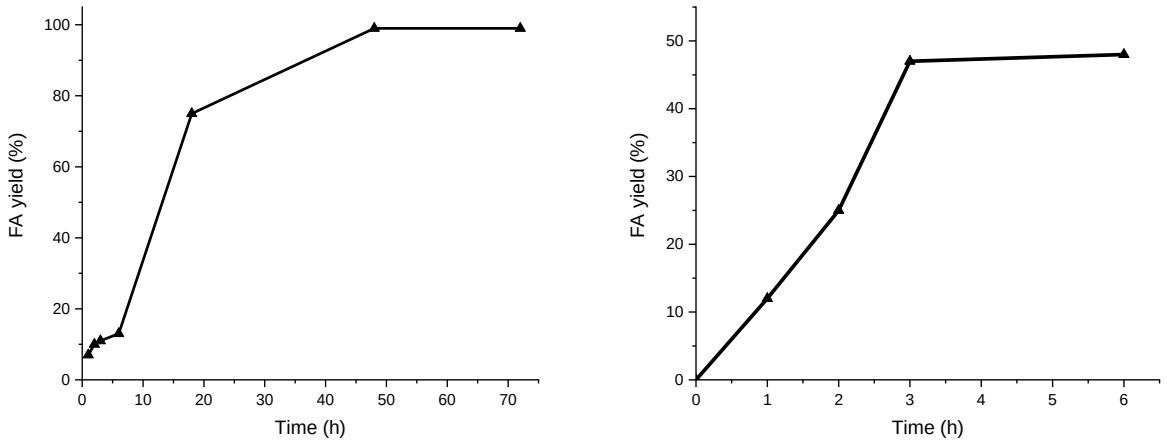

Figure 4.8: Effect of time on the yield of FA. Reaction conditions: Ru-2 (0.02 mmol), EMIM Ac (1 mL), 10:20 bar CO_2:H_2, rt (left); Ru-1 (0.004 mmol), EMIM Ac (1 mL), 15:15 bar CO_2:H_2, 80 ºC (right).

Later, I have investigated the effect of the volume of IL (and catalyst concentration) on the resulting activity using the best catalyst **Ru-1** with EMIM Ac. I have chosen 50 ºC as a compromise between higher catalytic activity compared to room temperature, but still preventing FA dehydrogenation that is favored at 80 ºC. In addition, 5:30 bar of CO_2:H_2 were used with the purpose to ensure full conversion of CO_2. In a first experiment, I have fixed the catalyst loading at 4 µmol while increasing the volume of IL. Figure 4.10 (left) shows how the FA/IL ratio decreases linearly with higher IL volume, with a maximum in FA production at 2 mL of EMIM Ac (0.002 M) after 6 hours at 50 ºC. The same behavior was observed for experiments of 3 hours under otherwise identical reaction conditions (Figure 4.10, right). In a separate experiment, I have increased the IL volume while keeping the catalyst concentration fixed at 0.002 M. Again, the same trend is observed, with maximum activity of the system at 2 mL of EMIM Ac (TON = 967, Figure 4.11).

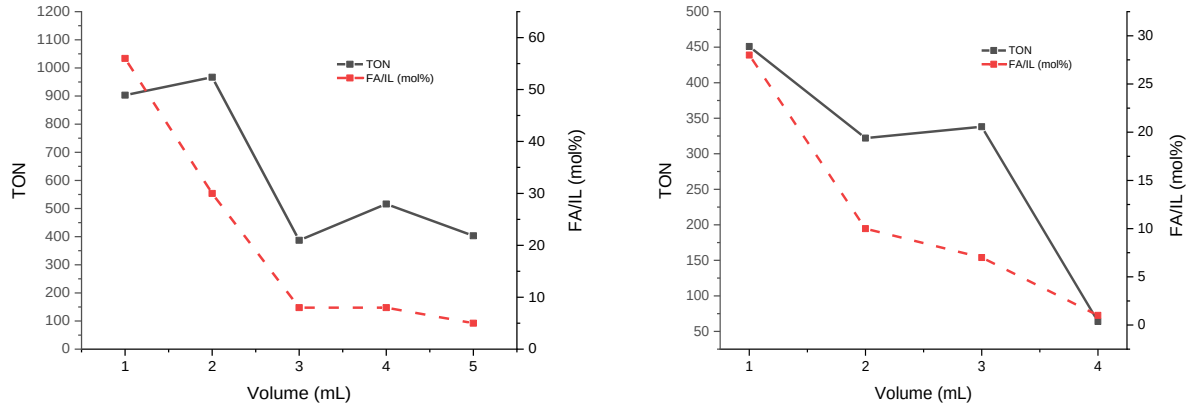

Figure 4.10: Reaction conditions: Ru-1 (0.004 mmol), EMIM Ac (1-5 mL), 5:30 bar CO_2:H_2, 50 ºC, 3h (right), 6h (left).

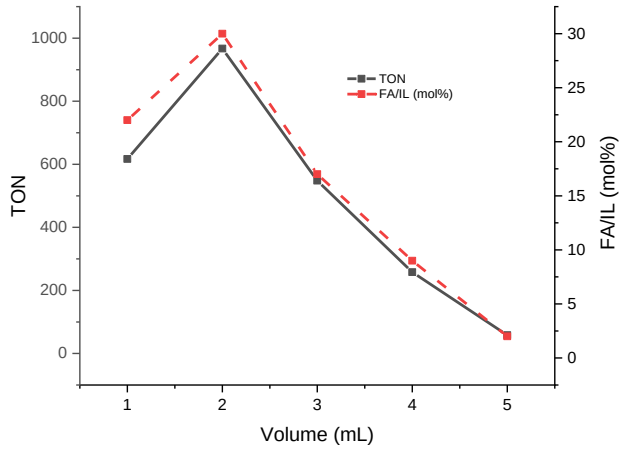

Figure 4.11: Effect of the volume of IL on FA production. Reaction conditions: Ru-1 in EMIM Ac (0.002 M), 5:30 bar CO_2:H_2, 50 ºC, 6h.

The preliminary studies on CO_2 absorption performed with EMIM Ac shows that maximum CO_2 concentration in the IL is achieved after few minutes after the pressure is applied (see 4.2.1). This also indicates that likely the hydrogenation is the rate determining step of the reaction. Therefore, it is intuitive to assume that limited diffusion and low solubility of H_2 in the IL (especially after formation of EMIM-CO_2), as well as low solubility of the catalyst at room temperature likely explain the observed results. Figure 4.9 provides an exhaustive representation of the effect of both temperature and catalyst concentration on the resulting activity of the Ru-PNP/IL system.

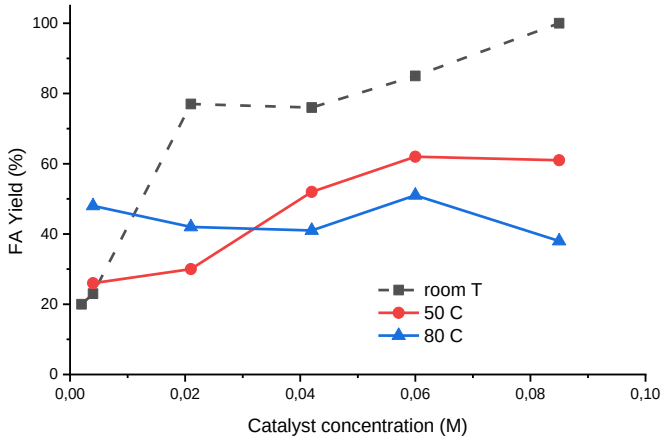

Figure 4.9: Reaction conditions: Ru-2, EMIM Ac (1 mL), 15:15 bar of CO_2:H_2, 6h. Dashed line: Ru-2, EMIM Ac (1 mL), 10:20 bar CO_2:H_2, rt, 18h.

It is possible to achieve higher FA/IL molar ratios at room temperature (and longer times) when compared to 50 ºC and 80 ºC. In contrast, lower catalyst loading is required at higher temperatures to observe catalytic activity; especially at 80 ºC, it is possible to notice that 0.002 M of catalyst in the are sufficient to produce 50% FA yield, while increasing the concentration does not bring any benefit to the reaction. This behavior can be explained by the reversible FA dehydrogenation that is favored at higher temperatures and high catalyst loadings (see Chapter 5). Nascimento and Alves performed computational studies on the thermodynamic of CO_2

hydrogenation to FA and MeOH using the IL EMMIM NO_2: similar to what described here, higher conversions were obtained at low temperatures (<30 ºC) independently from the pressure applied [289]. In addition, the use of hydrogen gas in excess was found to facilitate its diffusion in the IL at high concentrations of the CO_2-EMMIM NO_2 adduct, which become more favorable at higher temperatures, as described below.

Additional optimization of reaction conditions using **Ru-1** and EMIM Ac is described in Table 4.5 for experiments at room temperature. Based on the previous results on reaction parameters such as time, catalyst concentration and temperature, only experiments of 18 hours were performed in this screening. Confirming the observations showed so far, CO_2 and H_2 relative pressures play a major role (Entries 1-6, Table 4.5); it is beneficial to use H_2 in excess to facilitate its diffusion within EMIM Ac, which tends to solidify when high amount of CO_2 are trapped at room temperature. The stirring rate is also important to avoid accumulatinon of the solid EMIM-CO_2 and facilitate H_2 diffusion within the viscous IL phase. Confirming the trend, loading of the autoclave with 10:20 or 15:15 led to similar results in terms of FA/IL achieved (Entries 4-5) but higher EMIM-CO_2 content in the IL when using 15:15 bar. Further increasing the pressure to 20:20 bar of CO_2:H_2 resulted in only 35 mol% FA/IL, with visible accumulation of unconverted EMIM-CO_2 (Entry 6). Nevertheless, of great importance for an energy storage device, it is possible to reload the system by simply applying additional CO_2:H_2 pressure resulting in an over stoichiometric amount of FA/IL = 1.26 after 3 different loadings. Finally, Entries 7 and 8 confirm the observations discussed above on the beneficial effect of both time and higher concentration for reactions at room temperature.

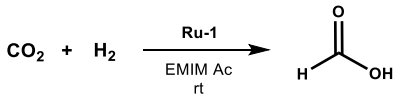

Entry	Cat. Loading (mmol)	Conc (M)	CO_2/H_2 (bar)	Time (h)	TON	TOF (h^{-1})	FA/IL[a] (mol%)
1	0.02	0.02	5:5	18	16	-	5
2	0.02	0.02	5:10	18	26	-	8
3	0.02	0.02	10:10	18	71	4	22
4	0.02	0.02	10:20	18	198	10	75
5	0.02	0.02	15:15	18	184	10	70
6	0.02	0.02	20:20	54	113 (18 h) 358 (36 h) 405 (54 h)	7	35 111 126
7	0.04	0.04	10:20	18	141	8	92
8	0.002	0.004	15:15	18	280	15	2

Reactions reproducible within a 10% error. The reactions were performed using autoclave A (Figure 2.8, 2.5 mL reaction vessel). [a] Determined by ^{1}H NMR.

Table 4.5: Screening of reaction conditions for the hydrogenation of CO_2 at room temperature.

Similarly, Table 4.6 summarizes the reactivity of **Ru-1** at higher temperatures, also reflecting all the trends described so far. Increasing the temperature allows for lower catalyst loading, higher catalytic activity towards hydrogenation, as well as higher solubility of Ru-PNP, CO_2 and H_2 in the IL. As observed in the preliminary studies in 4.2.1, using a bigger autoclave results in improved catalyst activity due to higher molar amount of CO_2:H_2 available. This is reflected in Entries 4-7 for experiments at 50 ºC, and Entry 15 for a final scale-up experiment at 80 ºC. Thus, I have used the biggest autoclave available (C in Figure 2.8) employing 15 mL of EMIM Ac and 60 bar of CO_2:H_2 to facilitate gas-diffusion and mass transport within the IL phase. 0.002 mmol of **Ru-1** afforded a TON of 18886, which raised up to 32411 when additional 60 bar of CO_2:H_2 were applied after 18h at 80 ºC

(Entry 12, Table 4.6). However, loading the autoclave a third time resulted in only a small increase in the FA/IL ratio (67 mol% to 71 mol%), probably explained by the competing FA dehydrogenation at 80 ºC in the presence of high concentrations of FA in the IL. It is important to mention that all manipulations were performed at ambient conditions, indicating the high stability and robustness of the Ru-PNP complexes in the IL.

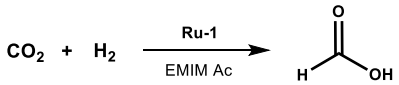

Entry	Cat. Loading (mmol)	Conc (M)	CO_2/H_2 (bar)	T (ºC)	Time (h)	TON	TOF (h^{-1})	FA/IL[a] (mol%)
1	0.004	0.002	10:20	50	6	903	150	28
2	0.004	0.004	10:20	50	6	612	102	38
3	0.004	0.002	15:15	50	18	1515	84	47
4[b]	0.004	0.002	10:20	50	18	2354	131	73
5[b]	0.004	0.0015	10:20	50	18	3241	180	67
6[b]	0.004	0.001	10:20	50	18	3095	172	48
7[b]	0.004	0.0075	10:20	50	18	1935	108	24
8	0.004	0.004	15:15	80	1	258	258	16
9	0.004	0.004	15:15	80	6	1052	175	65
10	0.004	0.002	15:15	80	18	1935	107	60
11	0.002	0.0004	15:15	80	18	3085	171	22
12[b]	0.002	0,0001	30:30	80	36	32411	1000 (18 h) 900 (36 h)	67

Reactions reproducible within a 10% error [a] Determined by ^{1}H NMR. [b] 22 mL reaction vessel (autoclave C, Figure 2.8); all the other experiments in autoclave B (5 mL reaction vessel).

Table 4.6: Screening of reaction conditions for the hydrogenation of CO_2 at 50 ºC and 80 ºC.

Scheme 4.9 provides an overview of the methods used for CO_2 hydrogenation to FA in one-pot reactions. Summarizing the results discussed above, it was possible to obtain turnover numbers in the order of 10^4 and turnover frequencies up to 10^3. It has been shown that the system is flexible under a wide range of operative conditions, from temperature (25-120 ºC), pressure (1-60 bar), as well as catalyst concentration in the IL.

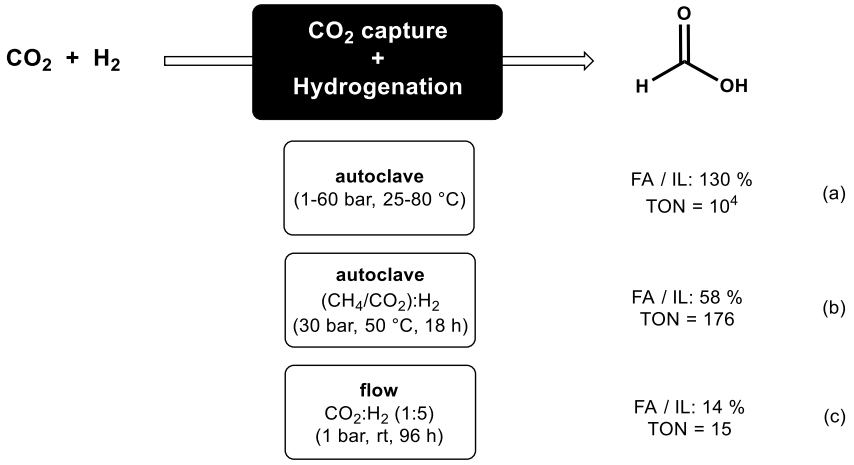

Scheme 4.9: Possible alternatives for CO_2 transformation to FA in one pot.

In addition, I have carried out preliminary experiments using biogas as the source of CO_2. As such, applying 0.02 mmol of **Ru-2** in 1 mL of EMIM Ac in the presence of biogas and H_2 afforded a TON = 164 at 50 ºC after 18 hours using 10:20 bar of biogas:H_2. In another experiment, using 15:15 bar, **Ru-2** provided a TON = 176 and a FA/IL = 58 mol% under the same reaction conditions (Scheme 4.9b). The presence of CH_4 does not affect the catalytic activity of Ru-PNP catalysts, as demonstrated by the presence of the expected **Ru-3** in the reaction mixture, hence the possibility to perform another cycle.

I have also tested the possibility to perform flow reactions in the presence of EMIM Ac. Bubbling directly a mixture of CO_2:H_2 (1:5 volumetric ratio) at ambient conditions in a solution of EMIM Ac containing 0.07 mmol of **Ru-1**, it was possible to achieve 14 mol% of FA/IL (TON = 15) after 96 h (Scheme 4.9c). Further attempts under flow conditions using EMIM CHOO will be discussed in the next section.

Finally, I have examined the possibility to carry out CO_2 capture and subsequent hydrogenation to FA in two different steps. Applying 25 bar of CO_2 in the presence of 2 mL of EMIM Ac resulted in 34 mol% of CO_2 trapped (with respect to the IL) after 45 minutes (Figure 4.2). Later, the gas was released, and 0.02 mmol of **Ru-2** and 25 bar of hydrogen were added, affording a TON = 359 after 18h (Scheme 4.10a). The hydrogenation step was performed at 50ºC to ensure fast liquefaction EMIM-CO_2 hence full dissolution of the catalyst. In a similar fashion, it is possible to simply bubble CO_2 in EMIM Ac for 48h at ambient conditions (1 bar, 25 ºC), followed by addition of 0.02 mmol of **Ru-2** and hydrogen pressure in autoclave (25 bar). In such way, the system afforded a TON of 156 and a FA/IL = 38 mol% at 50 ºC (Scheme 4.10b). Finally, bubbling of CO_2 through 1.5 mL of EMIM Ac resulted in 10 mol% of CO_2 trapped after 24 h. Addition of **Ru-1** (0.02 mmol) and switching the atmosphere to hydrogen with a balloon at ambient conditions resulted in 12 mol% of FA/IL and a TON = 58 after 96 h (Scheme 4.10c). As already showed by Rogers, bubbling is less effective than applying pressure, thus it is more convenient to perform CO_2 capture under (low) pressures but faster. Importantly, once the catalysts were transferred from the glove box, all the following manipulations were performed under air conditions, again demonstrating the increased stability of Ru-PNP complexes in the presence of ILs.

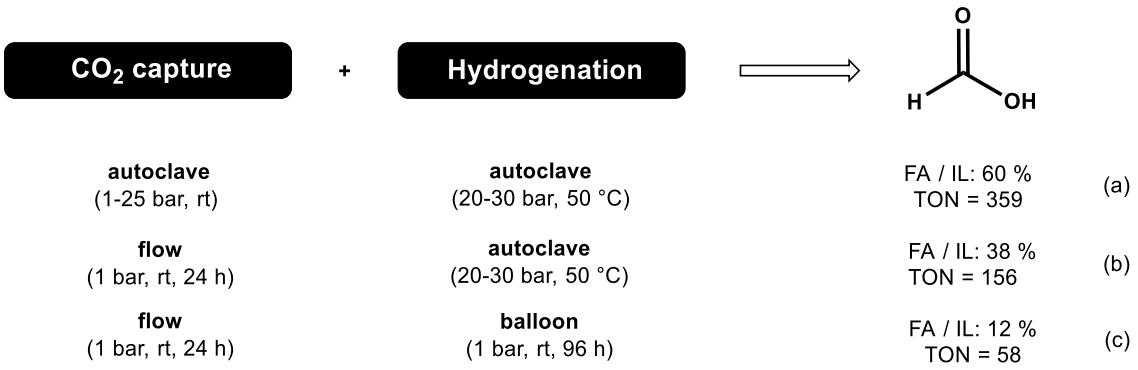

Scheme 4.10: Alternatives for CO_2 capture and hydrogenation under different reaction conditions.

Attempts for one-pot hydrogenation of CO_2 to methanol

Ru-PNP complexes of the type used in this study are widely reported for the hydrogenation of CO_2 to methanol (MeOH) in the presence of reaction promoters [290]. Relevant contributions were provided by the group of Prakash using **Ru-MACHO-BH** in combination with amine and hydroxide CO_2 capturing agents as discussed in the introduction [291–296]. Hazari and Bernskoetter reported the use of Fe-PNP pincer complexes in the presence of Lewis acids to promote the formation of both FA [169] and methanol [297]. Cantat showed Ru-Triphos complexes similar to **Ru-11** (Figure 4.4) invoking FA disproportionation to MeOH [298]. Following on previous studies using Ru-Triphos catalysts [118], Letner investigated the effect of Lewis Acids for the hydrogenation of CO_2 to methanol in the presence of Mn-PNP catalysts (see **Mn-1**, Figure 4.4) and alcohols to promote formation of formate esters [299]. In this study, the role of Mn-OCHO intermediates in the reaction mechanism was investigated in depth, with observed formation of a carboxylate complex as a limiting resting state. Using either $Ti(O^iPr)_4$ or $Sc(O^iPr)_3$ as the Lewis acid, and MeOH/dioxane mixtures, the system afforded decent TON (<100). Byers and Tsung reported an interesting multicatalytic system that combines Ru-PNP complexes of the Milstein´s family with a metal-organic framework (MOF) catalyst for the cascade hydrogenation of CO_2 to methanol [300]. In detail, the first Ru-PNP catalyst promotes hydrogenation of CO_2 to FA, followed by esterification to formate esters catalyzed by the MOF material. Finally, a second Ru-PNP catalyzes the hydrogenation of formate esters to MeOH.

As showed later in Scheme 4.14, after the initial hydrogenation of the CO_2-adduct, it is possible to envision the selective formation of a formyl adduct that can undergo esterification reaction pathways in the presence of a suitable co-catalyst and/or reaction additive. This could lead to catalytic cascade reactions resulting in the formation of formaldehyde and ultimately MeOH. Hence, I have explored the possibility using **Ru-MACHO-BH** and **Ru-2** in the presence of EMIM CHOO and suitable additives to promote formation of formate esters [301]. This included EtOH and MeOH as the alcohol sources, in combination with different Lewis Acids based on Li^+, Zn^{2+}, Sc^{3+} (Ac, CHOO, NTf_2, OTf), as well as *tert*-butyl nitrile [302], to promote the formation of either methyl or ethyl formate. The first intuitive step was to increase the reaction temperature to 120 ºC and apply 1:3 (or higher) CO_2:H_2 pressures. However, it was not possible to observe any visible MeOH formation, nor improve FA formation significantly. Nevertheless, traces of MeOH were observed in the hydrogenation of methy formate using Ru-2 and EMIM CHOO under 30 bar of H_2 at room temperature; this clearly assesses the feasibility of such approach as long as the esterification reaction is promoted efficiently. Indeed, Ru-PNP complexes are known to be efficient catalysts for the hydrogenation of different esters to alcohols under the reaction conditions used in this study.

I have carried out only ≈20 preliminary experiments in this regard, but it is indeed possible to imagine a successful catalytic hydrogenation to MeOH after a full screening and optimization of reaction conditions that I could not perform during my PhD studies. For example, the addition of a co-catalyst or a co-IL, as well as combinations of homogeneous and heterogeneous catalysts are promising solutions to maximize the efficiency of each step by working in synergy.

Effect of NEt_3 on catalytic CO_2 hydrogenation.to FA

As it will be discussed in the next section, the use of amine is widely reported to assist FA formation, as well as to promote FA separation from the catalytic active phase. In addition, amine-functionalized ILs have been reported to increase the catalytic activity of many homogeneous systems (see Figure 4.1). In this sense, I have carried out few preliminary experiments to explore the effect of amines in the reaction mixture using NEt_3 as a model additive. The results from the screening are listed in Table 4.7.

It appears cleat that the addition of NEt_3 leads to improved FA formation using both EMIM Ac (Entries 1-2) and EMIM CHOO (Entries 3-4) already at room temperature. In addition, it is likely that NEt_3 facilitates diffusion of gases in the IL by decreasing the overall viscosity of the mixture (IL and NEt_3 are miscible at the ratios used in Table 4.7). Experiments at 50 ºC confirmed the observed beneficial effect, especially in the presence of a IL/ NEt_3 ratio of 2:1. Current investigations in the Nielsen´s group will further explore this possibility e.g. by varying the IL/NEt_3 ratio, as well as trying the effect of other amines that are e.g. bulkier, branched, secondary, tertiary etc. Importantly, the use of amines might represent a solution for the isolation of FA from the IL mixtures that could not be achieved in this study (see 4.2.3).

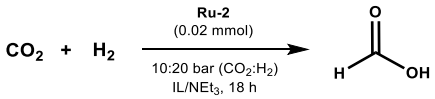

Entry	IL (mL)	IL:NEt_3 (mol)	T (ºC)	TON	TOF (h^{-1})	FA/IL[a] (mol%)
1	EMIM Ac	-	rt	135	8	42
	EMIM Ac	2:1	rt	220	12	68
2	EMIM CHOO	-	rt	130	8	40
3	EMIM CHOO	2:1	rt	234	13	80
4	EMIM Ac	1:1	50	258	14	80
5	EMIM Ac	2:1	50	322	18	100
6	EMIM CHOO	2:1	50	300	17	100
7	EMIM CHOO	0.5:1	50	180	10	60
8	EMIM CHOO	1:1	50	210	11	70

Reactions reproducible within a 10% error. The reactions were performed using autoclave A (Figure 2.8, 2.5 mL reaction vessel). [a] Determined by ^{1}H NMR.

Table 4.7: Screening of reaction conditions for the hydrogenation of CO_2 to FA in the presence of NEt_3.

4.2.3 Separation of FA from IL mixtures

The continuous separation of the desired product from homogeneously catalyzed mixtures has been challenging since the infancy of this type of catalysis and continues to be one of the main drawbacks of otherwise excellent systems [303]. In the process of CO_2 hydrogenation to FA, it is essential to separate the product continuously. In this work, that is both for practical implementation of the system, as well as for possible deactivation of Ru-PNP catalysts in the presence of carboxylic acids or low pH of the solution [125]. Indeed, I have found that high concentrations of FA in mixtures containing Ru-PNP and ILs result in the deactivation of the catalysts (see Chapter 5).

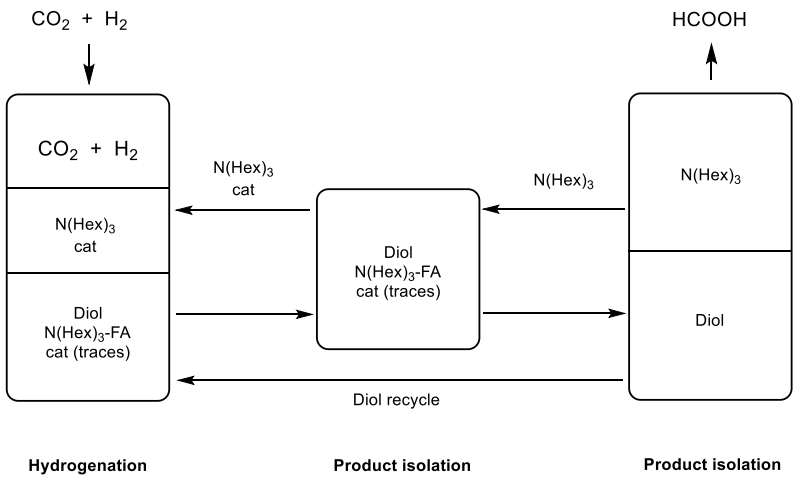

Figure 4.12: FA synthesis and separation promoted by amine-diol mixtures.

Many approaches has been investigated, consisting of active homogeneous species in combination with functionalized supported ligands and dendrimers, soluble polymers, (supported) ILs, $scCO_2$, biphasic systems or combinations of them [303]. Schaub and co-workers developed a method, later patented by BASF, for the synthesis of FA in the presence of $H_2Ru(P\mathit{n}Bu_3)_4$ as the catalyst, high boiling diols and trihexylamine ($NHex_3$) as a promoter for FA formation [304,305]. The system operates under 30 bar of CO_2:H_2 in a 1:3 ratio and 50 ºC, reaching a final concentration of 8.7% in the diol phase (Figure 4.12). However, it is possible to imagine high energetic costs associated with FA separation and amine/diol recycling.

As already mentioned in section 4.1, Leitner proposed a method for the continuous flow separation of FA promoted by the use of $scCO_2$ as the mobile phase, and an amine-functionalized IL in which the catalyst is dissolved as the stationary catalytic phase [202]. Figure 4.13 depicts the concept; likely, solvation of FA in $scCO_2$ is the driving force towards FA formation and separation from the IL mixture. The authors achieved moderate TON = 485 at 50 ºC and 200 bar of pressure after 190 hours under flow. However, the system requires high pressures and large amounts of $scCO_2$, again resulting in high energetic costs associated with the process that only a much higher activity could justify.

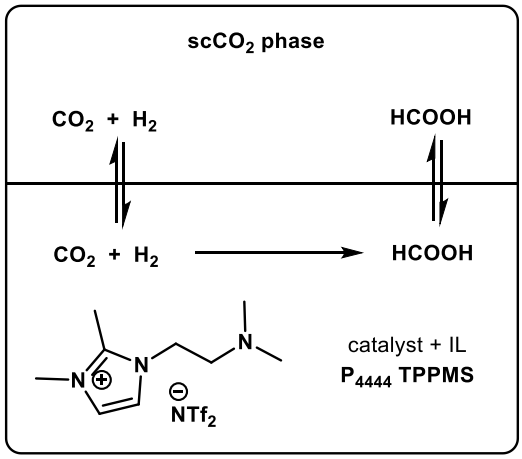

Figure 4.13: Example of continuous flow hydrogenation of CO_2 to FA using immobilized ILs and $scCO_2$ as proposed by Leitner [202].

The same author also proposed a method for the aqueous phase production of FA from CO_2 again involving the formation of amine-FA adducts (Figure 4.14) [306]. The catalyst is the common precursor cis-[Ru(dppm)$_2$Cl$_2$] and the amines belong to the same class of compounds used for CO_2 scrubbing. The biphasic system is composed of a hydrophobic phase for catalyst immobilization, and an aqueous phase promoting the continuous extraction of the produced FA. Other reported examples include the use of acetic acid to promote separation from DMSO/H_2O mixtures [257], as well as longer alcohols such as 1-hexanol and 1-heptanol, reported by Albert to favor separation of FA from aqueous mixtures [307].

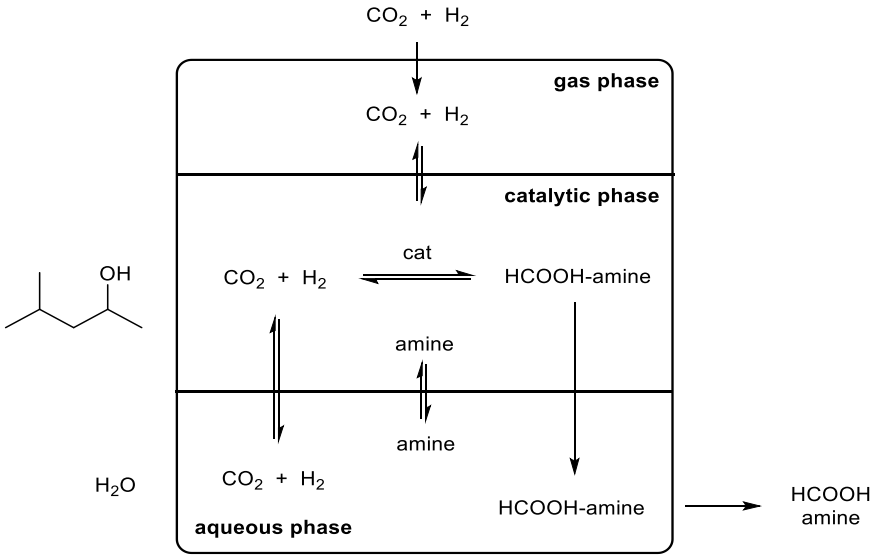

Figure 4.14: Continuous separation of amine-FA products favored by formation of a biphasic system.

In this section, I have explored the possibility to extract FA from the IL mixtures used in this study after performing CO_2 hydrogenation under either autoclave or flow conditions. However, after several attempts, the isolation of observable amounts of

FA has not been successful. In a simple demonstrative experiment, I have added an excess of FA in EMIM Ac and applied vacuum afterwards. ^{1}H NMR analysis shows that the acetate peak is completely replaced by formate, resulting in the formation of EMIM CHOO (Scheme 4.11). The same will be observed in Chapter 5, where after the long-term exposure of BMIM Ac to a continuous flow of FA over time, the resulting IL at the end was indeed BMIM CHOO. This is explained by the difference in basicity of the two anions, reflected in the pKa values of the corresponding carboxylic acids (pKa = 3.74 for FA, pKa = 4.7 for acetic acid). Hence, I further investigated the use of EMIM CHOO hypothesizing that the presence of the formate anion might favor the formation of free FA with possibility of continuous isolation of the product. As shown in Figure 4.6, ^{1}H NMR analysis shows visible formation of FA as shown by the increased intensity of the signal associated with FA. Another confirmation is represented by the fact that EMIM CHOO (solid at rt and with CO_2 absorbed) is always liquefied after catalytic hydrogenation of CO_2, indicating over stoichiometric amounts of FA/IL. However, I have not succeeded in isolating FA from the cat/EMIM CHOO mixtures, nor increasing the final FA/IL molar ratio above ≈1.4.

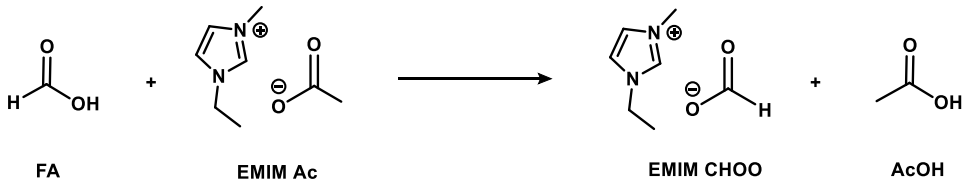

Scheme 4.11: Reaction scheme for the reaction between EMIM Ac and FA.

Initially, I have tried to extract FA by washing the IL mixture obtained after catalytic hydrogenation using different solvents (acetic acid, toluene, benzene, hexane, pentane, diethyl ether). Other techniques used to try to isolate FA from ILs included distillation and vacuum distillation, as well as distillation with pentane using a Dean-Stark apparatus. It has to be noted that only relatively small-scale reactions were carried out in this study. For example, the calculated amount of FA produced in a benchmark experiment with 1-2 mL of IL is <0.1 mL, rendering very challenging its isolation using standard analytic techniques. Scaling up of the reaction by increasing the volume of IL results in lower FA yields, hence higher difficulties in achieving successful isolation. Moreover, in the case of the work presented here, the use of a solvent that does not dissolve the IL limited the available choices to a selected group of (apolar) solvents. After many unsuccessful attempts, Figure 4.12 shows the ^{1}H NMR analysis of the pentane phase after washing of EMIM CHOO (see experiment described in Figure 4.6); indeed, it was possible to observe small amount of what is presumably FA at 8.18 ppm, accompanied by a decrease in the formate signal in the IL solution. It is important to mention that pentane and FA form an azeotrope mixture with B_p = 34.2 ºC. In a similar fashion, I have tried to add pentane in the autoclave prior to catalytic hydrogenation, but no observable FA was present in the pentane phase after cooling of the system.

Encouraged by the result showed in Figure 4.15, I have investigated the possibility to promote FA separation under flow conditions. This was done by bubbling different mixtures of CO_2:H_2 through a solution of EMIM CHOO in the presence of either **Ru-2** or **Ru-1** at relatively high catalyst loading (0.02-0.1 mmol) and temperatures <50 ºC to prevent FA dehydrogenation. Unfortunately, it was not possible to observe traces of FA in the cold trap placed after the reaction. Hence, I have tried to chemically trap FA by bubbling the downstream flow through (deuterated) solutions of H_2O, toluene, DMSO, and DMSO/H_2O, either at room temperature or -78.5 ºC using dry ice, again with no success in the observation of FA.

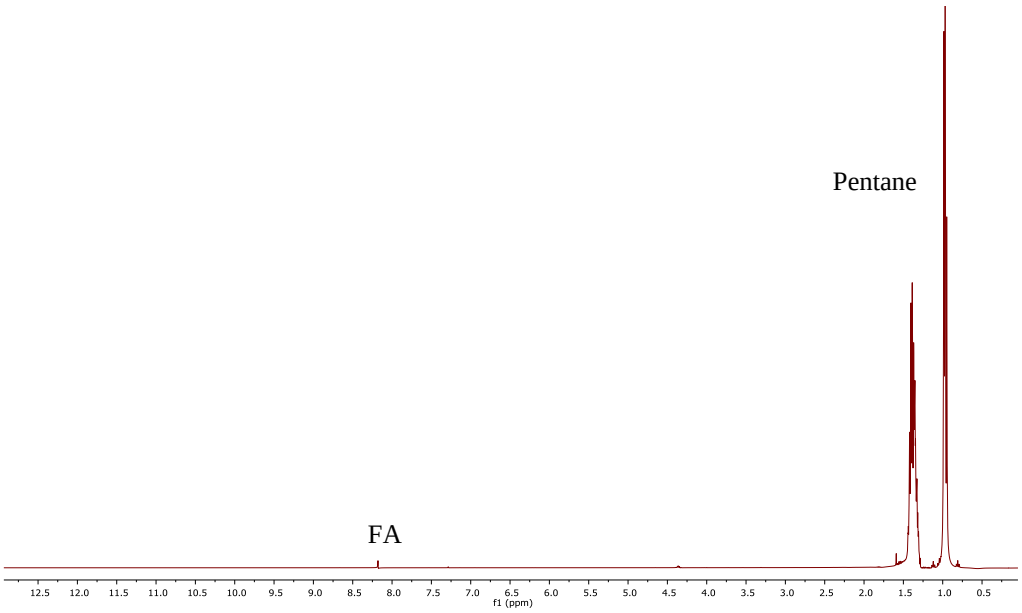

Figure 4.15: Pentane phase after washing of the FA/IL solution after the catalytic hydrogenation cycle described in Figure 4.6 ($CDCl_3$, 25 ºC, 400 MHz).

Later, I have tried to bubble a saturated mixture of CO_2/H_2 with pentane through a solution of **Ru-2** (0.04 mmol) and EMIM CHOO (0.01 mol) at 50 ºC. Bubbling of pentane results in the creation of a biphasic system where pentane is present on top of the IL based on the reaction temperature, hence pentane volatility. Again, no observable FA was detected in the pentane phase in both cases. Finally, I have bubbled the downstream flow (saturated with pentane) through a 2 M solution of NaOH in H_2O, and analyzed the resulting mixture using D_2O as the reference solvent. Indeed, it was possible to observe traces of FA at 8.18 ppm (Figure 4.13)

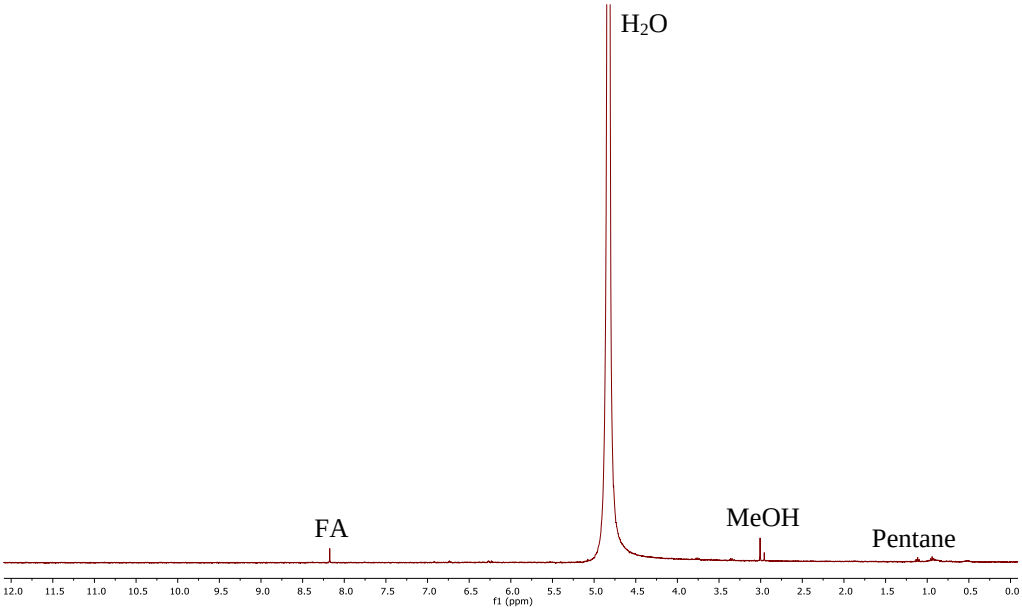

Figure 4.16: Pentane phase bubbled through a 2M NaOH aqueous solution. Note: MeOH is present as an impurity in the IL (from synthesis procedure).

When the reactions under flow conditions are carried out at T >40 ºC, a slow but constant decrease of the formate content in EMIM CHOO is observed, indicating no quantitative formation of FA from CO_2, but instead a slow consumption of the anion over time. This was confirmed by increasing the temperature to >80 ºC, resulting in consequent degradation of the IL. This is in agreement with the high activity of this same system towards FA dehydrogenation, certainly making the isolation of FA from such IL even more challenging. Finally, I have noticed that if pentane is bubbled through EMIM CHOO for long times, it results in the degradation of EMIM CHOO and loss of any catalytic activity. Further ^{1}H and ^{2}D NMR investigations led to the conclusion that what observed in Figures 4.12 and 4.13 might be a product resulting from the degradation of EMIM CHOO into an unknown product that was not possible to identify from the obtained spectra.

As discussed in Chapter III, the solidification of EMIM Ac at high CO_2 concentrations is a factor that affects the diffusion of hydrogen in the IL phase, therefore easiness of hydrogenation performed by the Ru-PNP catalyst. Curiously, for all the reactions at room temperature it was necessary to set the temperature of the reaction plate to 25 ºC in order to avoid irreproducibility of the experiments between e.g. summer and winter due to variable formation of EMIM-CO_2. In particular, when the temperature of the room was <20 ºC, the efficient hydrogenation of CO_2 was prevented by fast formation of a solid mixture within the first minutes of reaction where the catalyst could not be dissolved. This represent an important aspect (drawback) towards possible practical applications of this technology. Hence, I have investigated the possibility to use a co-IL to facilitate mass transport and gas diffusion through EMIM Ac. I have chosen BMMIM NTf_2 because of its low viscosity and inertness towards carbene formation (the C2 position is methylated) and coordination to the metal center.

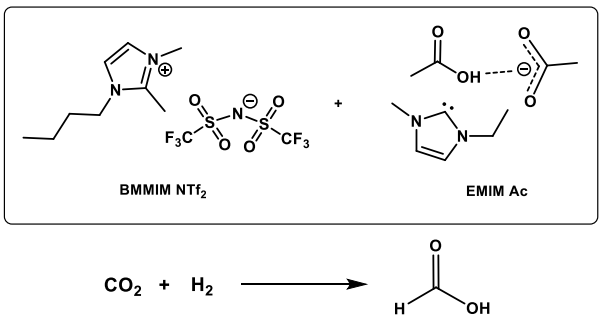

Entry	Catalyst	Cat. Loading (mmol)	IL[a] (mL)	CO_2 (bar)	H_2 (bar)	T (ºC)	Time (h)	TON	TOF (h^{-1})	FA/EMIM Ac[b] (mol%)
1[c]	Ru-2	0.02	2	10	20	25	18	280	16	46
2[c]	Ru-2	0.02	1+1	10	20	25	18	207	12	68
3	Ru-1	0,002	5	20	40	50	18	5160	287	32
4	Ru-1	0,002	5+5	20	40	50	18	9997	555	62
5	Ru-1	0,002	15	30	30	80	18	16477	915	34
6	Ru-1	0,002	10+5	30	30	80	18	20962	1165	65

Reactions reproducible within a 10% error. [a] EMIM Ac (+ BMMIM NTf_2). [b] Determined by ^{1}H NMR. [c] 5 mL reaction vessel (autoclave B, Figure 2.8); all the other experiments in autoclave C (22 mL reaction vessel).

Table 4.8: Optimization of CO_2 hydrogenation using mixtures of EMIM Ac and BMMIM NTf_2.

As shown clearly in Table 4.8, the use of BMMIM NTf_2 is beneficial to achieve higher FA concentration in the IL mixture (Entries 1-2, 3-4, 5-6). This can be explained by lower viscosity of the resulting mixture due to complete dissolution of EMIM-CO_2, hence easier diffusion of both substrates and FA in solution. In addition, BMMIM NTf_2 might have a positive impact on the stabilization of the produced FA by solvation effect. Similar to what described before, I have tried to isolate FA from the EMIM Ac (or EMIM CHOO) - BMMIM NTf_2 mixtures by means of solvent extractions, bubbling of pentane and/or argon, as well as vacuum distillation, but with no success.

In this section, I have carried out only preliminary extractions methods; however, due to the intrinsic basicity of the ILs used in this study, it is difficult to envision direct FA separation without the addition of a co-solvent or co-IL. As a qualitative note, the difficulties observed in the removal of FA from the IL mixture were observed also with MeOH, present as an impurity as it is the solvent for most of the synthesis procedures involving carboxylate ILs. In fact, neither high vacuum nor bubbling of argon for 1 week through a solution of EMIM Ac changed the amount of MeOH present in the IL. In a similar fashion, during the synthesis of EMIM CHOO, it is necessary to apply high vacuum and 40-50 ºC in order to remove methanol or FA if added in over stoichiometric amounts compared to the EMIM methylcarbonate precursor (Scheme 3.3).

In conclusion, the possibility of mixing two different ILs represents an interesting aspect that could e.g. improve the long-term stability of the Ru-PNP/IL system as well as promote FA separation from the catalytically active IL phase. For example, it is possible to envision the use of EMIM Ac (efficient in promoting CO_2 capture) down to catalytic amounts, and use an optimized co-IL that favors continuous FA separation, at the same time avoiding the gradual loss of the volatile acetic acid (see Chapter 5). Further perspectives and possible optimization related to the separation of FA will be provided in the summary in section 4.3.

4.2.4 Mechanistic studies

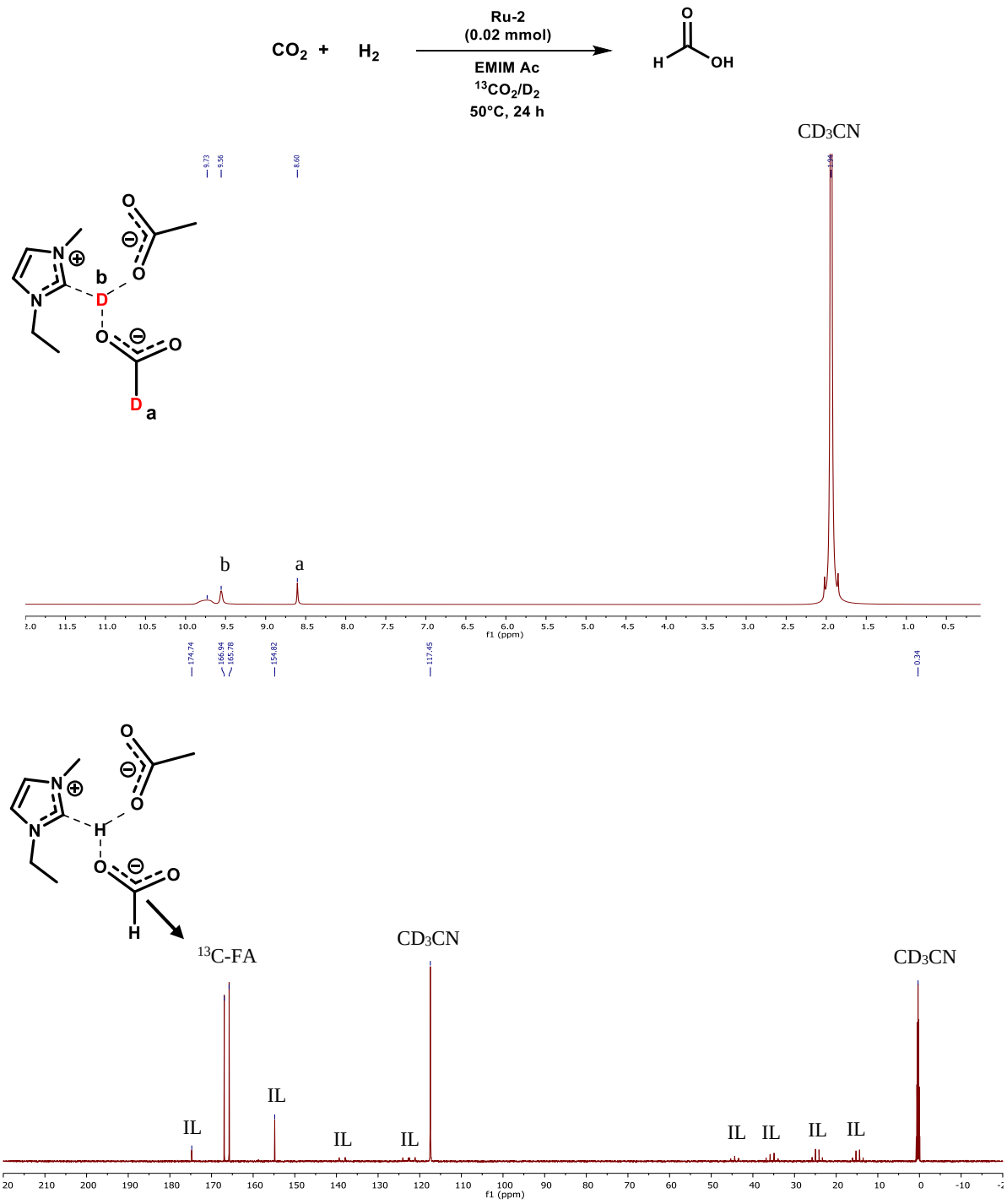

Figure 4.17: Labeling experiments with ^{2}H (up) and ^{13}C (down) using EMIM Ac (CD_3CN, 25 ºC, 600 MHz). Reaction conditions: Ru-2 (0.02 mmol), EMIM Ac (1 mL), 5:15 bar of CO_2:D_2 (up), 1:15 bar of $^{13}CO_2$:H_2 (down), 50ºC, 24h. The ^{13}C is shown without ^{1}H decoupling. See Appendix B for other labeled NMR spectra using EMIM Ac and EMIM CHOO.

I have investigated the mechanism of the reaction performing labeling experiments with both ^{2}H and ^{13}C NMR in the presence of EMIM Ac and **Ru-2** (Figure 4.14). In detail, I have performed the experiments and later provided the NMR samples of the resulting reaction mixtures to Kasper Enemark-Rasmussen who gently performed the experiments at the NMR Center DTU. In a straightforward way, the resulting spectra confirm the proposed mechanism for CO_2 activation via carbene, and subsequent hydride transfer from the catalyst to the trapped CO_2 resulting in a mixture of FA/formate (Scheme 4.7). As shown in the ^{2}H NMR spectrum in Figure 4.14, a formate peak is present at 8.60 ppm, together with another deuterium atom (9.55 ppm) that is exchanged at the C2 position of the imidazole ring. Accordingly, the ^{13}C spectrum shows the expected peak at 166 ppm accompanied by splitting of the signal due to coupling with a proton that confirms the presence of produced ^{13}FA.

I have performed similar experiments using EMIM CHOO (see Appendix B for other ^{2}H and ^{13}C NMR spectra). Similar to what observed with EMIM Ac, deuterium is exchanged at the carbene position of EMIM CHOO, with the other deuterium atom observed as a formate specie. Standard ^{1}H NMR analysis shows the presence of **Ru-5** after the reaction is complete (Figure B.6). The ^{13}C NMR spectrum in the presence of EMIM CHOO also shows visible CO_2 absorbed already at 1 bar, in agreement with what discussed in the beginning of this chapter.

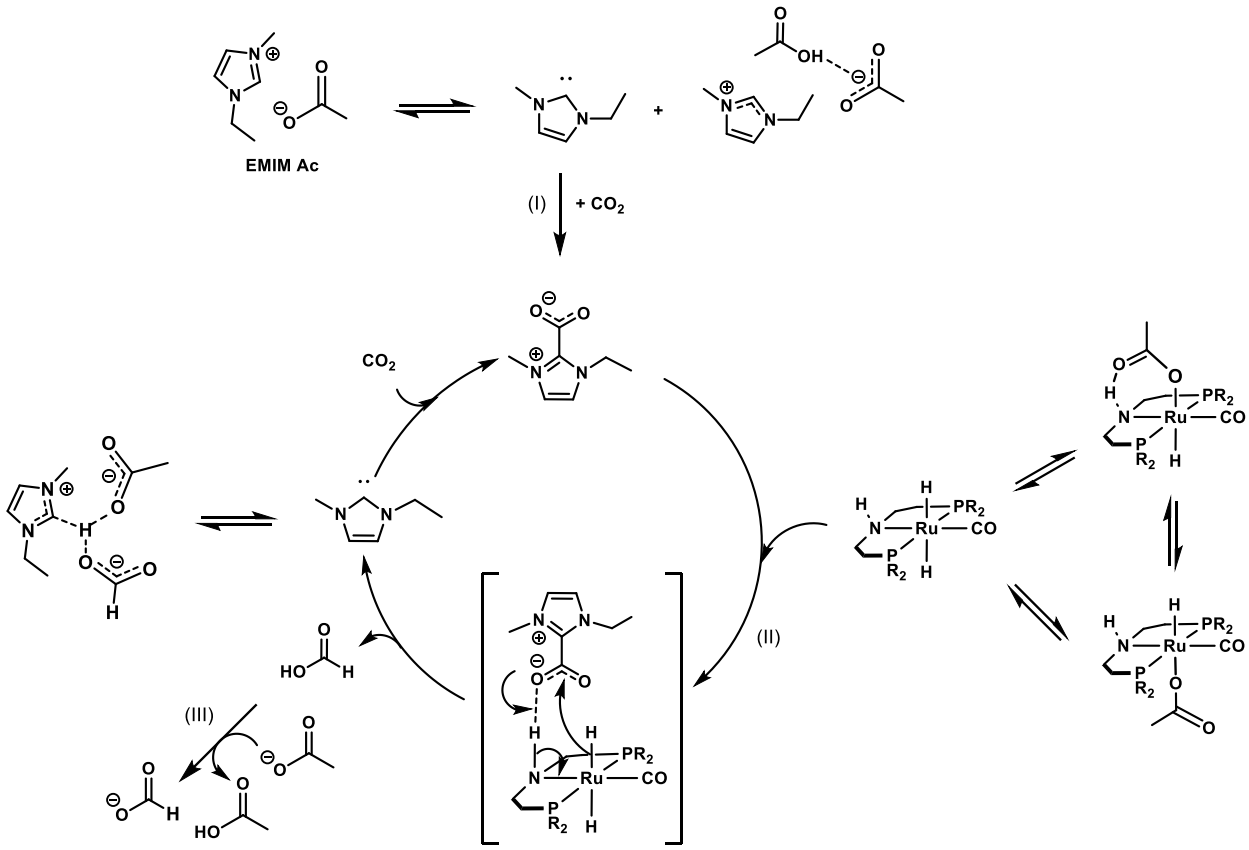

Scheme 4.12: Suggested mechanism for CO_2 activation via carbene specie followed by Ru-PNP catalyzed hydrogenation to FA.

Based on these studies, the catalytic cycle in Scheme 4.12 has been proposed; CO_2 activation is promoted by the IL (I), followed by outer sphere hydrogenation of the so-formed carboxylate performed by the Ru-PNP catalyst (II) and sequestration of the produced FA as a formate anion in equilibrium with acetic acid/acetate mixtures (III). As opposed with other methods for CO_2 activation (see 4.1), here the IL performs this step with high efficiency and does not require the presence of neither hydroxide bases nor amines. Scheme 4.13 shows a complete overview of the different species that are likely to be present in the presence of either EMIM Ac or EMIM CHOO under the conditions used in this study.

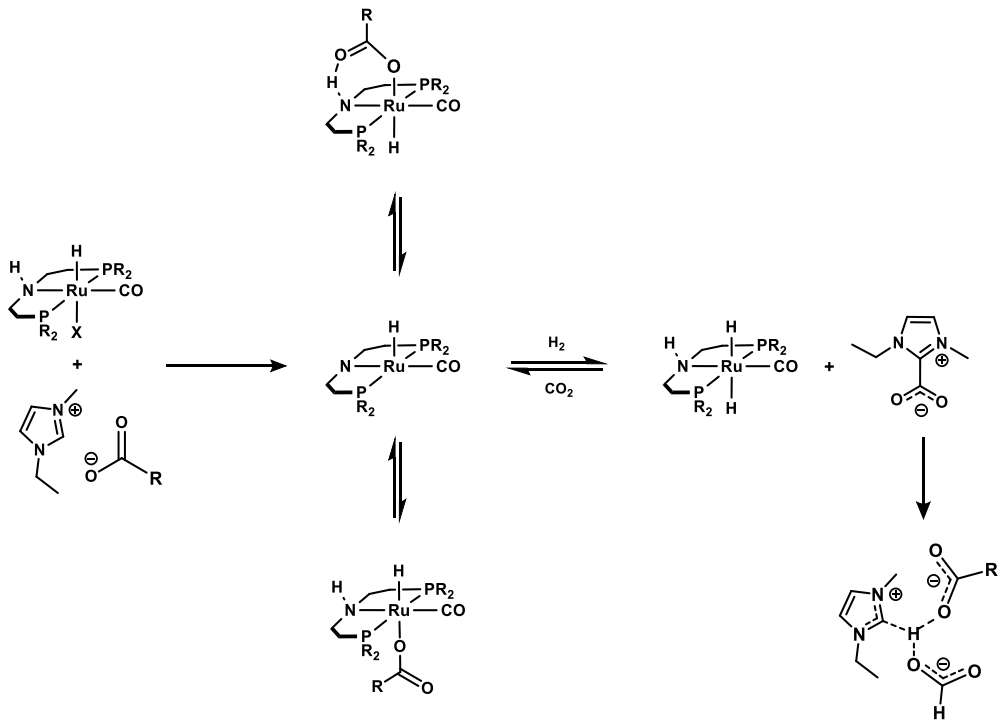

Scheme 4.13: Overall representation of the main species in solution using Ru-PNP catalysts in the presence of imidazolium acetate and formate ionic liquid. R = CH_3 (EMIM Ac), R = H (EMIM CHOO), X = H, Cl. OAc.

Each component of the catalytic system (carbene IL and Ru-PNP) can be selectively tuned to favor higher selectivity in each of the proposed step. Likely, the hydrogenation step depicted in Scheme 4.14 is the key transformation that affects selectivity towards FA. The Ru-PNP catalyst provides hydrogen to the activated CO_2 resulting in a tetrahedral intermediate that collapses to FA. However, it is also possible to imagine the formation of a formyl adduct that can be further hydrogenated to e.g. formaldehyde and eventually methanol. Hence, changing the substituents on the imidazolium cation will reflect in different acidity and electron donation ability of the carbene position, thus leading to different stabilization of the CO_2 adduct and eventually different reaction pathways. Indeed, using this approach, it is possible to envision the possibility to further hydrogenate CO_2 to high value products. Curiously, imidazolium carbene ligands are widely report to provide strong interactions in the presence of transition metals resulting in the formation of particularly stable species [308]. This was not observed in this work, but further investigations should consider this aspect. The type of reactivity described in this thesis is still at its early stages, hence further (computational and experimental) studies could be extremely useful to predict activation energies, reaction intermediates and promote a targeted optimization of both catalyst and IL components of this remarkably active system.

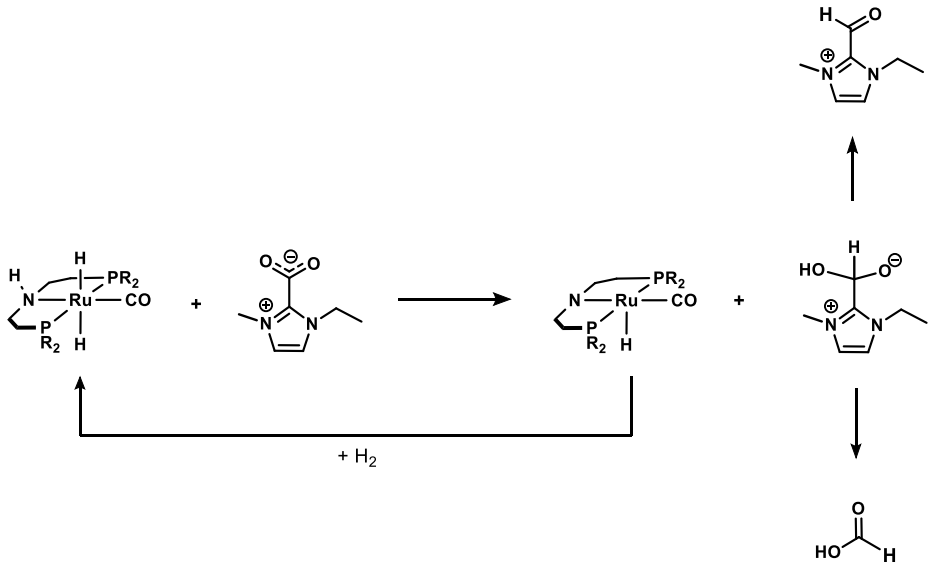

Scheme 4.14: Possible alternatives after initial hydrogenation of EMIM-CO_2.

4.3 Summary

Opposed to most of the reported methods where CO_2 capture and hydrogenation are two different processes, here I have demonstrated the synergistic effect of Ru-PNP and IL performing both steps contemporarily at very mild reaction conditions. The IL plays a crucial role in activating the otherwise unreactive CO_2 and stabilizing the catalytic active species through anion coordination to the metal center. In addition, the basic and polar environment (H bonds) of the IL likely plays a role in the stabilization of reaction intermediates and represents a driving force towards the formation of FA (formate) mixtures.

The steric hindrance and electron-donating properties around the carbene position might lead to substantial differences in the easiness of CO_2 coordination, as well as orientation of the resulting carbonyl adduct. In a similar way, such modifications might lead to major improvements in the catalytic activity in the more challenging hydrogenation step. In this regard, a small difference in activity towards CO_2 hydrogenation has been observed in this study simply varying from EMIM to BMIM Ac. Interestingly, Holloczki and Nyulaszi proposed the formation of different EMIM-CO_2 adducts where CO_2 is coordinated at the C4 and C5 positions of the imidazolium ring. The authors also suggested that such CO_2 products can be obtained in the presence of carbene-less imidazolium cations as long as the necessary basicicty is provided by the IL [273]. Targeted synthesis of task-specific ILs can lead to substantial new insights on this type of catalysis, and current investigations in this sense are ongoing in the Nielsen´s group carried out by PhD student Brenda Rabell. For example, other types of substituents on the imidazolium ring (functionalized alkyl groups with –OH and/or NR_3 groups) might lead to beneficial electronic perturbations that can affect both the efficiency of CO_2 trapping as well as the stereoselectivity of the hydrogenation reaction.

Equally important is the fine-tuning of the organometallic pincer complex. This includes donor arms, backbone linker of the pincer, central donor atom, spectator ligand, as well as the axial ligands affecting the trans influence hence easiness of substrate/product coordination. All of these perturbations can dramatically change the overall steric and electronic properties of the metal complex, hence its tendency to readily deliver activated H_2 to the captured CO_2.

Based on these results, it is also possible to envision direct CO_2 capture from air after appropriate scaling up and optimization of the IL mixture. Not only air, CO_2 can be obtained from other relevant industrial sources such as biogas and flue gas. The composition of biogas may vary according to the sources, but it typically involves a 40:60 volume ratio between CO_2 and CH_4. In this work, I have demonstrated the hydrogenation of a 1:1 mixture of CO_2:CH_4 resembling biogas that produced visible FA formation at mild conditions (Scheme 4.9). As a curiosity, these experiments were the last performed during my studies, to provide even more future perspective to an already exciting project.

Separation of FA, as well as kinetic/thermodynamic limitations hindering higher FA concentrations represent the main challenges to be overcome. From the examples and discussion provided in 4.2.3, it is clear that amine, alcohols, and formation of biphasic systems represent viable solutions for the desired isolation of FA from the IL. The use of amines and/or amine-functionalized ILs seems a promising pathway; the preliminary experiments showed in Table 4.7 show that the addition of NEt_3 is beneficial to achieve higher FA/IL ratios. From a qualitative point of view, NE_3 is soluble in the IL, but it is possible to notice the formation of a biphasic system when NEt_3 is present in larger amounts (>3:1 in volume) compared to either EMIM Ac or EMIM CHOO. The literature is already rich with studies on the solubility of both amine mixtures and ILs, and further investigations in this sense could provide a solution. Functionalization of (immobilized) ILs and use of branched or higher boiling amines are other viable approaches. In this sense, few examples of (reported) potential ILs were provided in Figure 4.1. In all of these cases, it has to be noticed that the separation of FA from either amine or alcoholic mixtures is always associated with energetic costs due to distillation of the so-

obtained FA mixtures. This is why the use of a non-volatile IL can be particularly interesting for this type of transformation. In this regard, it is also possible to envision the use of a SILP catalyst to perform the task under either batch or gas-flow (pressurized) continuous flow conditions (see Chapters 7 and main conclusions).

As already mentioned in Chapter 3, I would like to remark that I see great potential in NMR spectroscopy to be a very useful technique to investigate the reactivity of the Ru-PNP/IL system towards CO_2 hydrogenation. For example, selected ^{1}H and ^{13}C NMR experiments under (labeled) CO_2:H_2 pressures and different temperatures could shed light on the molecular interactions and stereoselectivity involved between Ru-PNP, IL and substrates, guiding future optimization strategies. Furthermore, ^{1}H NMR experiments could help assessing the acidity of the C2 proton of different substituted imidazolium ILs, hence their propensity towards carbene formation and stabilization of the CO_2-adduct during catalytic hydrogenation.

5. Highly efficient formic acid dehydrogenation catalyzed by Ru-PNP complexes in ionic liquids

5.1 Introduction

The use of a Liquid Organic Hydrogen Carrier (LOHC) allows moving of renewable, high-density energy across long distances and in a safe manner. At the same time, LOHCs represent viable solutions for the storing of energy from discontinuous renewable sources such as solar and wind power. FA is considered a viable LOHC candidate as it is liquid and safe to handle at ambient conditions, avoiding energetic costs and safety issues associated with hydrogen compression [309]. It has a hydrogen capacity of 4.4 wt%, corresponding to an energy density of 1.77 kW·h/L, higher than commercial 70 MPa hydrogen tanks (1.4 kW·h/L) [310]. This clearly indicates that FA may be suitable for automotive and mobile applications. When considering the state-of-the-art technology PEM-FCs, it is essential that hydrogen is released from the LOHC at temperatures <100 ºC to ensure full heat-integration [12]. In addition, the flow of hydrogen gas should be free of contaminants such as volatile solvents and carbon monoxide that could irreversibly damage the FC. Another approach is the electrocatalytic oxidation of FA used in direct formic acid fuel cells (DFAFCs) [311].

The literature is rich with examples of homogeneously catalyzed hydrogen evolution from FA, and many excellent review works provide an extensive overview [312–316]. It is also clear that homogeneous catalytic FA dehydrogenation is much more developed than CO_2 hydrogenation. Importantly, many promising studies reported the use of first-row transition metals [160,161,317–321], albeit with the notorious lower activity and stability when compared to Ru and Ir catalysts. Table 5.1 shows examples of reported catalysts for FA dehydrogenation selected based on catalytic activity, stability and overall practicality of the method. Himeda showed an iridium Cp^* complex (**Ir-2**) that afforded a TON = 10 million for the continuous flow dehydrogenation of 20 M of FA (aq) at 70 ºC [255]. Milstein recently reported a Ru-acridine pincer complex (**Ru-13**) that dehydrogenated neat FA affording a TON = 1.7 million [322]. The same work also addressed the possibility to produce hydrogen under pressure, with **Ru-13** that afforded up to 100 bar of CO_2:H_2 in less than 1 hour. The best reported system for hydrogen evolution under pressurized conditions was reported by Kawanami in 2016 using **Ir-3** [323]. The system produced up to 115 MPa, corresponding to >120 L of hydrogen released. Later, the same author further investigated the process exploring the influence of both solvents [324] and ligands [325].

As already discussed in the previous chapters, also in the case of FA dehydrogenation, many of the reported methods employ bases (amines, formates, DBU) to e.g. control the pH of the reaction, deprotonate FA, or avoid catalyst deactivation. The use of volatile and toxic organic solvents (THF, dioxane, DMF) is also widely reported and it goes against practical requirements of PEM-FCs. The possibility to release H_2 from FA without the use of reaction additives allows full energy storage potential and the production of a clean H_2 flow without the contamination of organic molecules vapors. Other studies reported the dehydrogenation of variously diluted aqueous FA mixtures. This not only lower the overall energy storage potential, but leads to the presence of vapor in the H_2 gas stream. Therefore, the possibility to dehydrogenate neat FA is of great industrial interest. At the same time, small amounts of H_2O and other impurities should be tolerated by a candidate catalytic system for every-day applications. Finally, the possibility to produce pressurized hydrogen is a useful feature for industrial implementation in hydrogen storage and delivery.

In this chapter, I have investigated the activity of Ru- and Mn-PNP complexes in the presence of different ILs for FA dehydrogenation in both batch and flow conditions. After optimization, the combination of **Ru-MACHO-BH** and BMIM Ac

resulted in the best result reported to date for continuous flow hydrogen release from FA under heat-integrated conditions for FC applications (Entry 1, Table 5.1).

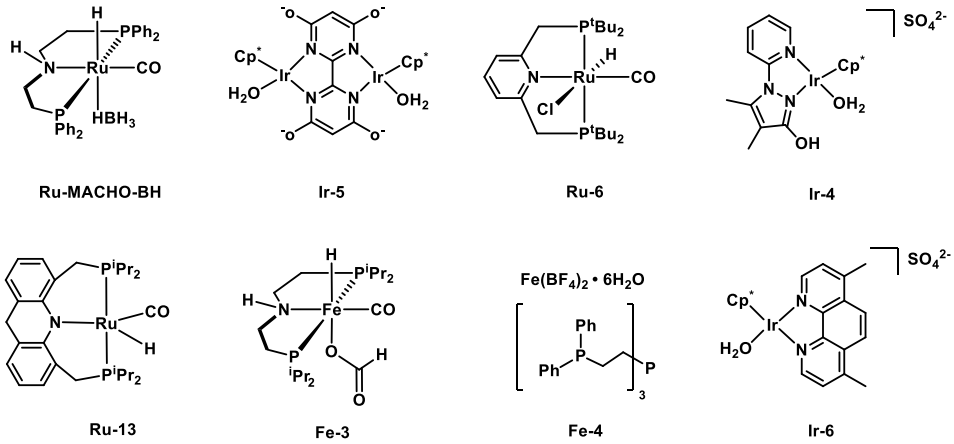

Entry	Corresponding authors	Catalyst	TON	TOF (h^{-1})	T (ºC)	Additives	Comments
1	Nielsen[a]	Ru-MACHO-BH	15.000.000	8.000 (av)	95	BMIM Ac (BMIM CHOO)	State-of-the-art No vapors No inert precautions Batch and flow
2	Hull, Himeda, Fujita [254]	Ir-1	308.000	158.000 (i)	80	NaOCHO/H_2O	Low pH
3	Pidko [248]	Ru-6	310.000	93.000 (257.000 max with NEt_3)	90	DBU, DMF	flexible, inert conditions additives and volatile/toxic solvent
4	Himeda [255]	Ir-2	10.000.000	13.000 (av)	70	H_2O	Degassed FA Flow conditions Volatile solvent
5	Milstein [322]	Ru-13	1.700.000	3.000 (max)	95	-	Inert conditions Flow conditions pressurized FA
6	Beller [326]	Fe-4	92.000	9.500	85	PC	Low activity
7	Hazari et al [166]	Fe-3	983.642	196.728	80	$LiBF_4$ dioxane	Volatile solvent
8	Kawanami [323]	Ir-6	320.000	62.900 (30 min)	99	H_2O (4 M FA)	Low pH pressurized FA

[a] developed in this study

Table 5.1: Relevant examples of reported active systems for FA dehydrogenation in comparison with the Ru-PNP/IL system showed in this work.

5.2 Results and Discussion

5.2.1 Batch

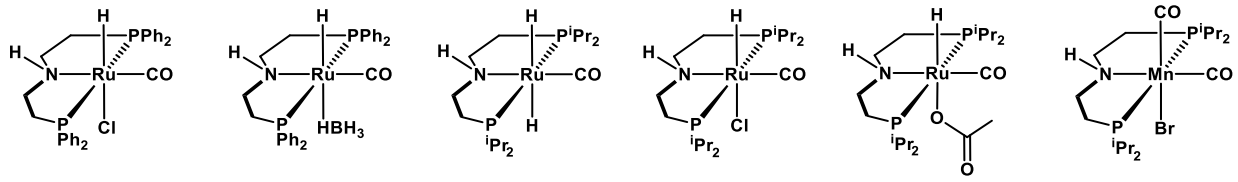

Ru-MACHO Ru-MACHO-BH Ru-1 Ru-2 Ru-3 Mn-1

Entry	Catalyst	IL	Conversion (%)
1		EMIM Ac	Full conversion
2		BMIM Ac	Full conversion
3		EMIM CHOO	Full conversion
4		BMMIM NTf_2	<10%
5		BMIM OTf	<10%
6	Ru-MACHO	EMIM TFA	<10%
7		Choline Ac	Full conversion
8		EMIM Et_2PO_4	Full conversion
9		BMIM $C(CN)_3$	<10%
10[b]		EMIM $N(CN)_2$	<10%
11[b]		EMIM $EtSO_4$	<10%
12	Ru-MACHO-BH	BMIM Ac	Full conversion
13	Ru-3	BMIM Ac	Full conversion
14	Ru-2	BMIM Ac	Full conversion
15[a]	Ru-MACHO	BMIM Ac	<10%
16[a]	Ru-MACHO-BH	BMIM Ac	<10%
17[a]	Ru-2	BMIM Ac	<10%
18	Ru-3	BMMIM NTf_2	Full conversion
19	Ru-1	BMMIM NTf_2	Full conversion
20[c]	Ru-MACHO-BH	DAF	Full conversion
21[d]	Ru-MACHO	DAF(H)	Full conversion

Reaction conditions when not specified: Cat loading (0.1 mol%), IL (0.5 mL), FA (6.6 mmol), 80ºC, 3h. [a] Cat loading (0.05 mol%), FA (13.25 mmol). [b] IL (1 mL), FA (13.25 mmol). [c] Cat loading (0.2 mol%), IL (2 mL), FA (23.25 mmol), ramp 25-80 ºC, 72h. [d] IL (1 mL), FA (26.5 mmol), 60 ºC, 24h.

Table 5.2: Preliminary screening of catalysts and ionic liquids for FA dehydrogenation in high-pressure vials.

Table 5.2 shows the initial screening of catalysts and ILs that was used to discard ILs that did not show any gas evolution. In fact, a clear indication towards possible IL candidates was visible already during this initial screening (Entries 1-10). In particular, the ILs that showed full conversion are able to activate **Ru-MACHO** and stabilize the mixture in the presence of the acidic FA. It appears that, similar to CO_2 hydrogenation, ILs with basic properties are favorable for FA dehydrogenation as well. Clear hydrogen evolution was observed at temperatures >50 ºC in the presence of BMIM Ac, EMIM Ac, EMIM Et_2PO_4, Choline Ac, BMMIM NTf_2 (but only with **Ru-1** and **Ru-3**), as well as the DAF and DAF-H (Table 5.2).

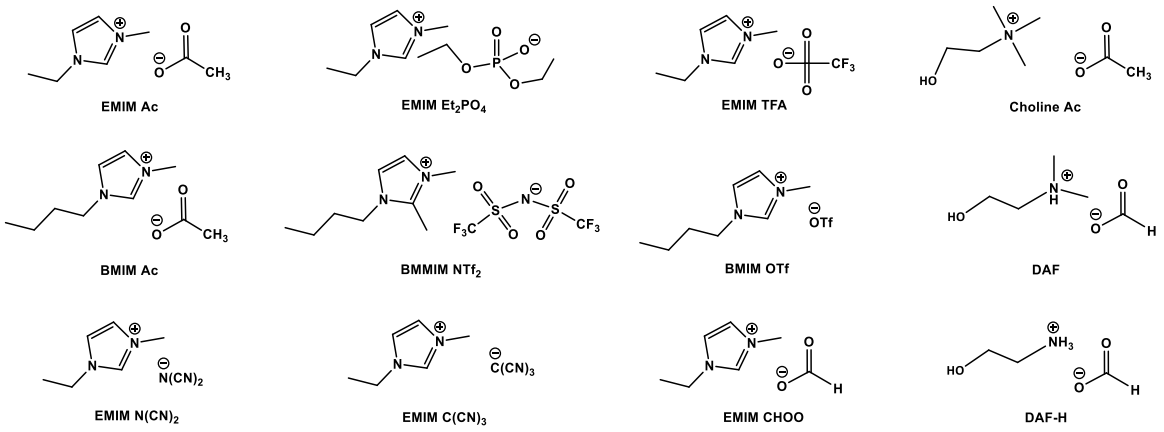

Figure 5.1: Different ILs screened in this chapter for FA dehydrogenation.

While DAF-H was purchased from Iolitec, DAF is obtained by simple mixing of 2-(dimethylamino)ethan-1-ol and FA in stoichiometric amounts followed by stirring at room temperature for 24 hours. Both DAF, DAF-H and Choline Ac (solid at rt) were found to be very active with visible hydrogen evolution observed already at T<50 ºC. However, the solutions of catalyst and such ILs appear very turbid at room temperature, with formation of a thick layer of foam when H_2 and CO_2 are released from the mixtures. In the case of DAF and DAF-H, increasing the temperature to >80 ºC led to visible degradation of the IL resulting in a sub-stoichiometric amount of formate compared to the ammonium cation (see Figure C.1 in Appendix C). Increasing the reaction time to 72 h resulted in the complete disappearance of the formate anion (Entry 20, Table 5.2). For these reasons, I have decided to exclude this family of ILs from further screening due to their instability, besides one example with Choline Ac provided in Table 5.4. Nevertheless, **Ru-MACHO-BH** in DAF also showed the presence of a Ru-H signal associated with the presence of Ru-OCHO resting states (Figure C.1).

Based on the results shown in Table 5.2, I have performed a further screening of catalysts using BMIM Ac as the only solvent. The gas evolution was measured via MFM and its composition analyzed with a MicroGC (see Chapter 2 for experimental details); Table 5.3 summarizes the so-obtained results. In the presence of BMIM Ac, all the screened catalysts reached full conversion within 2 hours (Entries 1-5, Table 5.3). Lowering the catalyst loading to 0.025 mol% led to a higher turnover number of 3780 (Entry 6), while an increase of the initial FA loading resulted in deactivation of the catalyst (Entry 7). This shows that high FA concentrations in the mixture should be balanced with higher IL volumes, so to reduce the increasing acidity of the resulting mixture thanks to the buffering effect of the IL. After optimization in this sense, a TON of 12050 was obtained at 95ºC after 18 hours with 0.008 mol% of **Ru-MACHO-BH** in 3 mL of BMIM Ac (Entry 8). In a similar experiment, two aliquots of FA were added at different times resulting in an overall TON of 16750 (Entry 9). Importantly, the system is also active in the presence of an 89 wt% FA solution in H_2O, reaching full conversion of FA after 3 hours (Entry 10). This is an important aspect, since water presence is usually difficult to avoid in large-scale operations. Of great importance towards more sustainable applications of such system, the manganese complex **Mn-1** also showed moderate catalytic activity at higher catalyst loading, affording a TON = 351 and 77% FA conversion after 3 hours (Entry 12, Table 5.3).

As depicted in Figure 5.2, after completeness of the reaction, it is possible to notice the presence of 15 mol% (relative to the IL) of CO_2 being trapped in BMIM Ac, however to a lower extent than what observed with e.g. EMIM CHOO (Figure 5.3). Gladly, the presence of **Ru-3** (with Ru-1 and EMIM Ac) and **Ru-MACHO-OCHO** (with Ru-MACHO-BH and EMIM CHOO respectively)

as the main species in solution after catalytic dehydrogenation is in agreement with previous findings on catalyst´s stabilization promoted by the IL (Chapter 3).

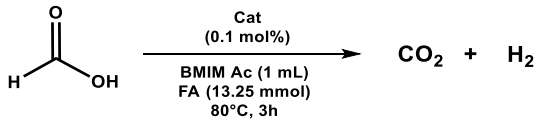

Entry	Catalyst	TON	TOF (h^{-1})	Conversion (%)
1	Ru-MACHO	1000	500	>99
2	Ru-2	1000	500	>99
3	Ru-3	1000	500	>99
4	Ru-1	1000	500	>99
5	Ru-MACHO-BH	1000	500	>99
6[b]	Ru-MACHO-BH	3780	1260	>99
7[c]	Ru-MACHO-BH	-	-	-
8[d]	Ru-MACHO-BH	12050	502	90
9[e]	Ru-MACHO-BH	16750	930	95
10[f]	Ru-MACHO-BH	610	200	>99
11	Mn-1	219	73	26,5
12[g]	Mn-1	351	120	77

[a] EMIM AC. [b] Ru-MACHO-BH (0.025 mol%). [c] Ru-MACHO-BH (0.006 mol%), FA (53 mmol). [d] Ru-MACHO-BH (3 µmol), BMIM Ac (3 mL), FA (39.8 mmol), 95 ºC, 18h. [e] Ru-MACHO-BH (3 µmol), BMIM Ac (3 mL), FA (26.5x2 mmol), 95 ºC, 18h (second addition of FA after 5h). [f] 89% FA in H_2O (12.9 mmol). [g] Ru-MACHO-BH (0.2 mol%).

Table 5.3: Screening of catalysts for FA dehydrogenation in batch conditions.

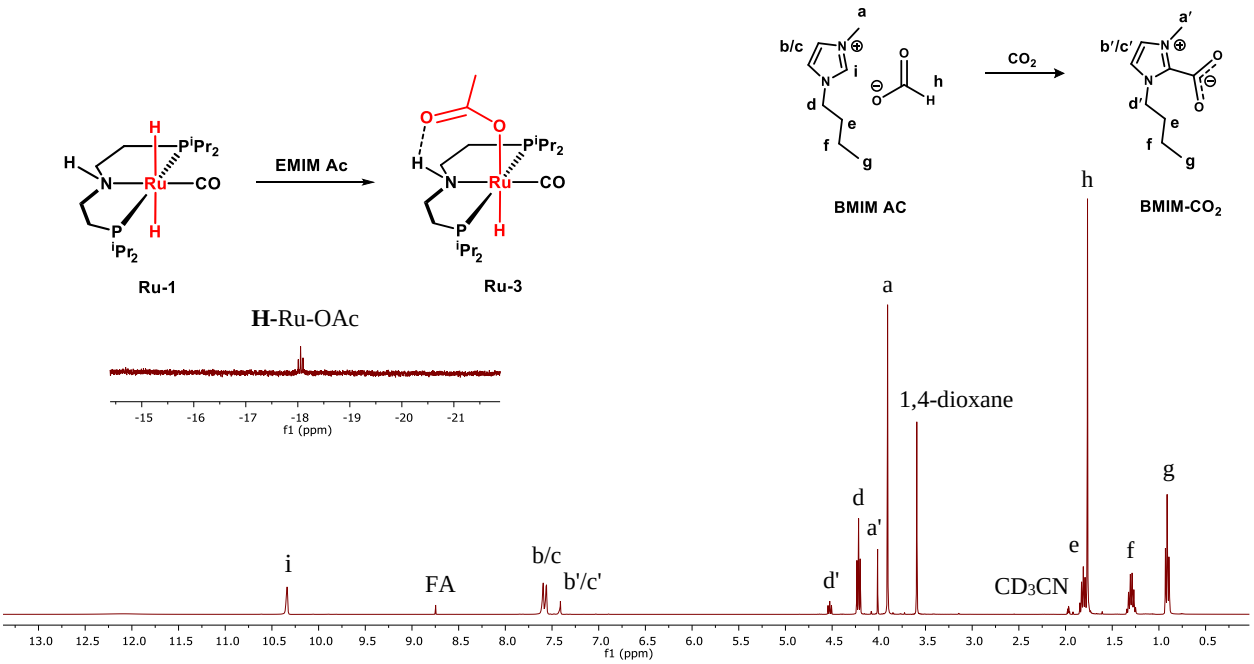

Figure 5.2: ^{1}H NMR of the reaction mixture after catalytic dehydrogenation of FA; reaction conditions in entry 4, Table 5.3 (CD_3CN, 25 ºC, 400 MHz).

Later, I have tested the influence of different ILs based on the preliminary screening showed in Table 5.2; the results are summarized in Table 5.4. As expected, no clear differences were observed between BMIM Ac and EMIM Ac (Entry 1). In the presence of BMMIM NTf_2, **Ru-MACHO-BH** resulted in poor activity, in agreements with the findings from Chapter 3, where it has been demonstrated that NTf_2 is not effective in activating Ru-PNP catalysts. The observed activity is likely explained by simple thermal activation of the catalyst at >80 ºC, with higher temperatures that would probably improve this result. In order to confirm this hypothesis, I have carried out reactions using BMMIM NTf_2 in the presence of the more reactive precursors **Ru-1** and **Ru-3**. Indeed, **Ru-1** resulted in TOF = 333 h^{-1} after 3 hours, while **Ru-3** afforded full conversion within 2 hours (TOF = 500 h^{-1}) at 80 °C (Entries 3,4). This can be explained by the higher propensity of –OAc and –H to be activated by coordination of FA at high temperatures, while in this case the NTf_2 IL has a more conventional role as a stabilizing solvent. However, I have excluded NTf_2 and OTf ILs for further screening due to their lower basicity when compared to acetate and formate anions.

Ru-MACHO-BH (0.1 mol%) in the presence of EMIM CHOO afforded full conversion of FA after 2 h (Entry 5, Table 5.4). As already observed for BMIM Ac (Table 5.3), doubling the initial loading of FA (26.5 mmol) resulted in slower rate of reaction, with a TOF= 100 h^{-1} after 18h (Entry 6, Table 5.4) at 80 ºC. Increasing of the temperature from 80 to 95 ºC led to full FA conversion after 5 hours (Entry 7); the addition of a second aliquot of FA resulted in an overall turnover number of 4000. EMIM Et_2PO_4 also proved to be a suitable solvent for this transformation, affording 99% conversion after 2 h using **Ru-MACHO-BH** under the same reaction conditions (Entry 8, Table 5.4). Increasing by two times the amount of FA with higher catalyst loading (0.16 mol%) resulted in complete FA consumption in only 1 hour (Entry 9). When compared to the formate analogues DAF and DAF-H, Choline Ac shows higher stability towards decomposition of the anion. Under the reaction conditions tested in Table 5.4, the system afforded 75% conversion of FA and a TON = 730 (Entry 10). Importantly, no CO was detected by MicroGC under the reaction conditions used in this study (detection limit <100 ppm, Figure C.4).

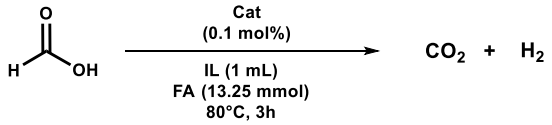

Entry	Catalyst	IL (mol)	TON	TOF (h^{-1})	Conversion (%)
1	Ru-MACHO-BH	EMIM Ac	1000	500	>99
2	Ru-MACHO-BH	BMMIM NTf_2	600	200	60
3	Ru-3	BMMIM NTf_2	1000	500	>99
4	Ru-1	BMMIM NTf_2	1000	333	>99
5	Ru-MACHO-BH	EMIM CHOO	1000	500	>99
6[a]	Ru-MACHO-BH	EMIM CHOO	2000	110	>99
7[b]	Ru-MACHO-BH	EMIM CHOO	4000	166	>99
8	Ru-MACHO-BH	EMIM Et_2PO_4	1000	500	>99
9[c]	Ru-MACHO-BH	EMIM Et_2PO_4	615	615	>99
10[d]	Ru-MACHO-BH	Choline Ac	730	245	75

[a] Cat load 0.05 mol%, EMIM CHOO (6.5 mmol), FA 26.5 mmol, 18h. [b] Cat load 0.05 mol%, EMIM CHOO (6.5 mmol), FA (26.5x2 mmol), 95 ºC, 24h. [c] Cat load 0.16 mol%, FA 26.5 mmol. [d] IL: 1.5 g.

Table 5.4: Screening of catalysts and ionic liquids for FA dehydrogenation in batch conditions.

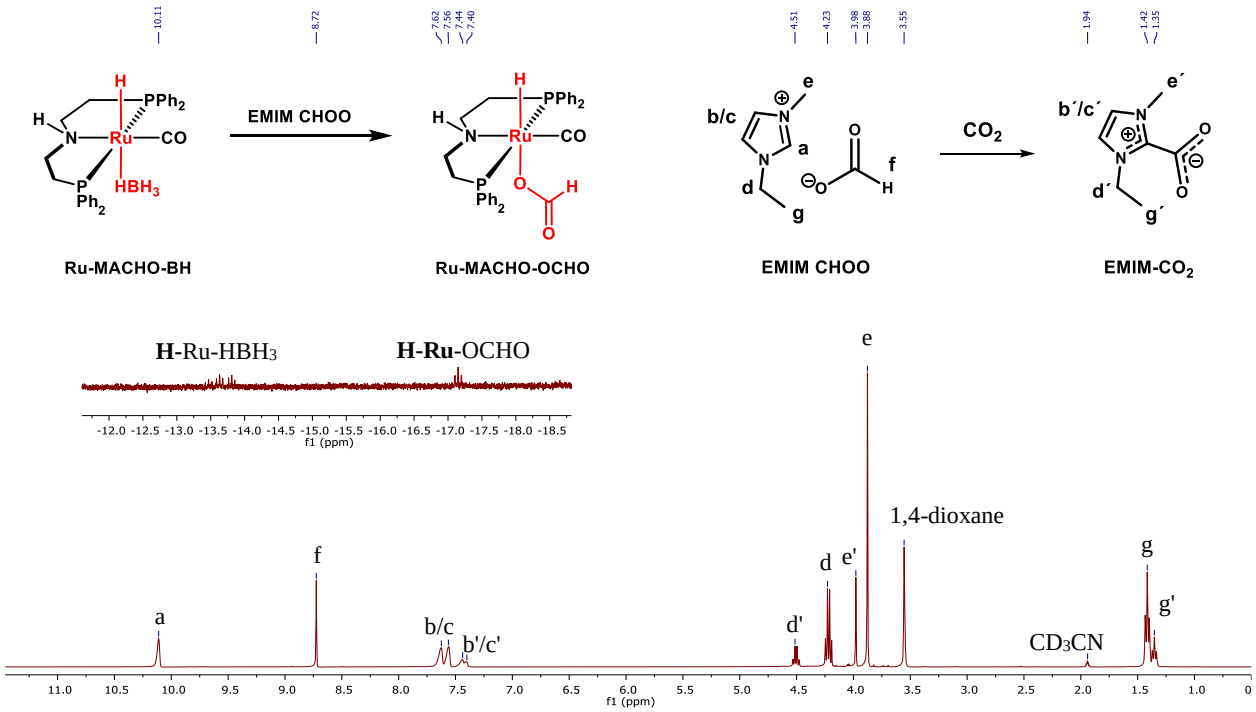

Figure 5.3: ^{1}H NMR spectrum of the reaction mixture after FA dehydrogenation. Reaction conditions in Entry 5, Table 5.4 (CD_3CN, 25 °C, 400 MHz).

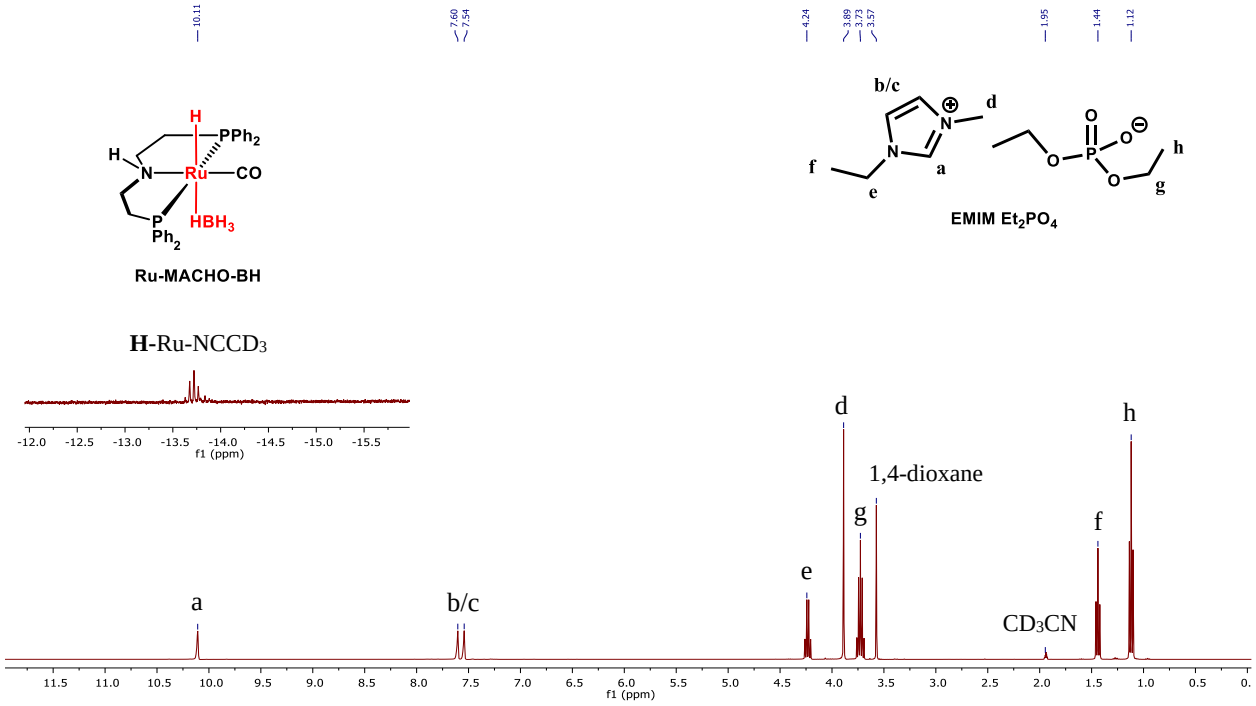

Figure 5.4: ^{1}H NMR spectrum of the reaction mixture and M-hydride region after FA dehydrogenation. Reaction conditions in Entry 8, Table 5.4 (CD_3CN, 25 °C, 400 MHz).

The ^{1}H NMR analysis of the reaction mixture after FA dehydrogenation showed the presence of up to 35 mol% of CO_2 trapped when using EMIM CHOO (Figure 5.3). The presence of hydride signals indicates the presence of catalytically active species, with the hydride peak at -17.2 associated with the **Ru-MACHO-OCHO** complex formed after coordination of the IL anion. Also in the case of EMIM Et_2PO_4, the ^{1}H NMR spectrum shows the presence of resting Ru-species coordinated with *d*-acetonitrile (Figure 5.4), confirming the stability of Ru-PNP catalysts also in the presence of non-coordinating anions. In addition, EMIM Et_2PO_4 does not show any evidence of chemisorbed CO_2 that could lead to degradation of the system over time (see 5.2.2).

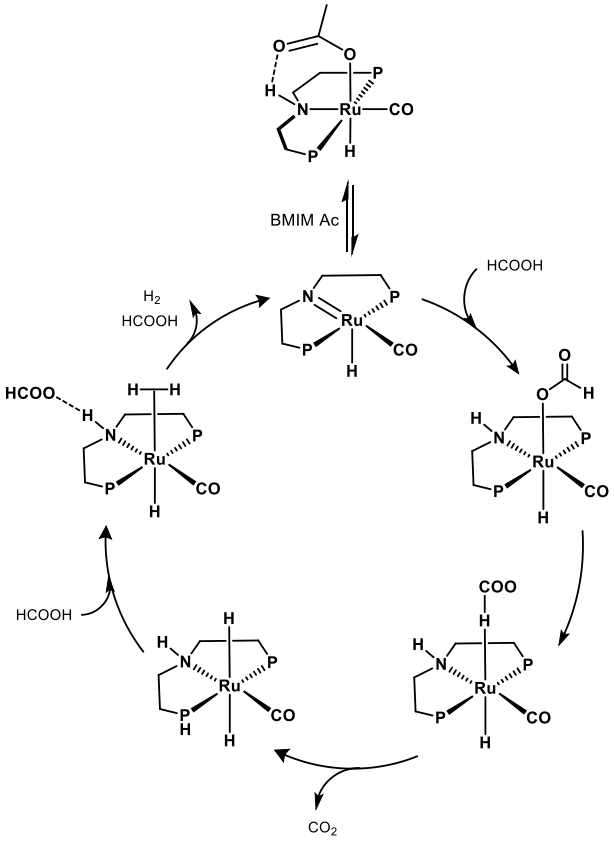

Scheme 5.1: Reaction scheme for Ru-PNP catalyzed FA dehydrogenation proposed (and adapted) by Beller [327].

Regarding the reaction mechanism, I will only refer to previous mechanistic studies performed by the group of Beller using the same family of Ru-PNP catalysts shown herein [107,327]. Importantly, the authors investigated the difference in reactivity between *N*-Me vs *N*-H PNP complexes for both FA dehydrogenation [327] and methanol reforming [107] catalyzed by **Ru-2** and its *N*-Me analogue. Interestingly in the case of FA dehydrogenation, the *N*-Me catalyst possesses comparable or even superior catalytic activity compared to the *N*-H analogue under all the reaction conditions tested in the study. This certainly opens questions on the reaction mechanism invoked for dehydrogenation reactions and the role of the amino-PNP proton. Scheme 5.1 illustrates the proposed cycle for reactions using the $P^{H}NP$ showed in this study. The authors proposed that the protonation of complex **Ru-4** with consequent formation of **Ru-1** is the rate determining step for this transformation. In addition, the formate complex **Ru-5** and the dihydride complex **Ru-1** were the only observable species in solution, in agreement with the findings from this study. The authors also found that the best performance of the system was obtained under acidic conditions. It is possible to imagine that each of the

catalytic active species shown in Scheme 5.1 benefit from the stabilizing effect given by the IL, especially in the presence of coordinating anions (Ac and CHOO). However, ILs represent such a different reaction media (triglyme was used by Beller for the studies described above) compared to normally used solvents that can lead to significant differences in reaction mechanism and activation energies involved. More insightful mechanistic studies on the reactivity between Ru-PNP complexes and ILs for FA dehydrogenation are beyond the scope of the experimental work described in this thesis.

As shown in Figure 5.5, the gas evolution profile of a typical batch experiment appears very rapid as soon as the FA is added to the mixture of IL and catalyst, and slowly decreases until all FA is consumed. This observation is corroborated by simple eye inspection of the reaction mixture when adding FA, indicating the presence of high (initial) turnover frequencies. In addition, it is possible to add more FA with the gas evolution showing the same behavior (Figure 5.5, final TON = 2548). This clearly shows that the reaction is highly dependent on the rate at which FA is added, hence that high values of TON and TOF are obtainable by keeping the IL/FA ratio at an optimal level, while deactivation of the catalyst occurs at high FA concentrations in the IL. In addition, I have observed that a mixture containing **Ru-MACHO** and BMIM Ac was active after 4 weeks of simple storage at ambient conditions and retained the same catalytic activity when more FA was added after heating at 80ºC. The same was observed for EMIM Et_2PO_4, with catalyst activity retained after storage under air for 2 months. Encouraged by these observations, I have evaluated the robustness and stability of the system under continuous FA feed, simulating possible applications such as in automotive FC technologies.

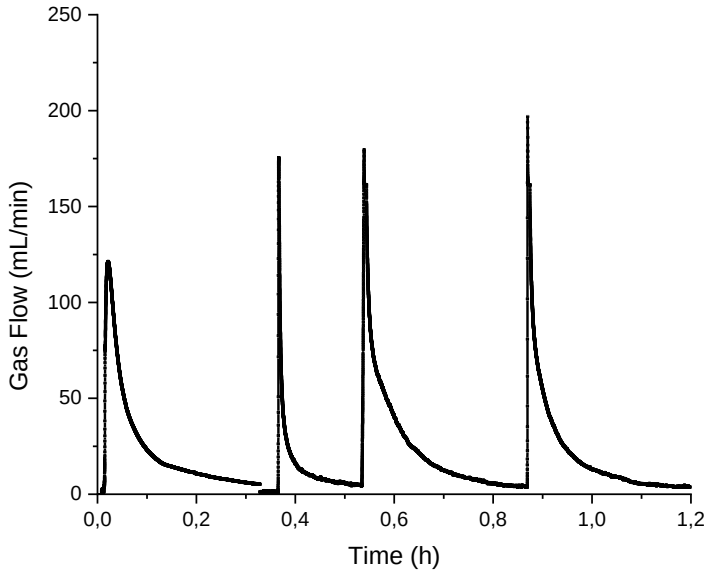

Figure 5.5: Gas evolution for FA dehydrogenation in batch. Reaction conditions: 0.013 mmol Ru-MACHO-BH (0.1 mol%), BMIM Ac (1 mL), FA (13.25 mmol), 80 ºC. Three more addition of FA of 0.25 mL each.

5.2.2 Continuous Flow

I have tested the Ru-PNP/IL system for continuous FA dehydrogenation using a syringe pump for manual control of the FA feed (see Chapter 2, Figure 2.3 for experimental details). Increasing the temperature from 80 ºC to 95 ºC allows the use of higher FA rates, still being within the temperature range of a PEM-FC off-heat (Entries 1-2, Table 5.5). The ^{iPr}PNP catalysts showed lower stability towards high FA addition rates. Under the same reaction conditions, **Ru-1** and **Ru-2** reached a maximum TOF of 7288 h^{-1} before visible accumulation of FA in the IL mixture that immediately ceased gas evolution (Entries 2,3, Table 5.5). On the contrary, **Ru-MACHO** and **Ru-MACHO-BH** could bear FA flows up to 10 mL/h, corresponding to a maximum turnover frequency of 10600 h^{-1} (Entries 4-5, Table 5.5).

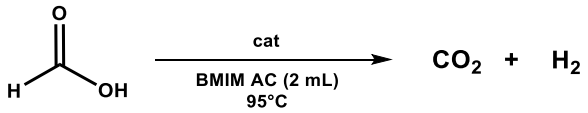

Entry	Catalyst	Cat loading (mmol)	TOF_{max}[a] (h^{-1})
1[b]	Ru-MACHO-BH	0.027	4908
2	Ru-1	0.020	7288
3	Ru-2	0.020	7288
4	Ru-MACHO	0.020	10800
5	Ru-MACHO-BH	0.025	10600

[a] measured at the last FA feed rate before visible FA accumulation; starting rate at 2 mL/h FA [b] 80ºC

Table 5.5: Screening of Ru-PNP catalysts for the dehydrogenation of FA under continuous flow.

Later, I have screened different ILs using **Ru-MACHO-BH** as the reference catalyst. Besides the above-described higher stability compared to ^{iPr}PNP, the choice was justified by the fact that **Ru-MACHO** would lead competitive -Cl coordination, likely resulting in lower turnover frequencies (for the same reason I have not tested common imidazolium halides ILs throughout this thesis). The results are summarized in Table 5.6.

As expected from the findings under batch conditions, BMMIM NTf_2, EMIM TFA and BMIM OTf were completely inactive under continuous flow conditions, leading to fast FA accumulation and no visible gas evolution (Entries 1-3, Table 5.6). On the contrary, EMIM CHOO afforded a maximum turnover frequency of 11990 h^{-1}, corresponding to a FA rate of 9.5 mL/h at 95 ºC (entry 4, Table 5.6). ^{1}H NMR analysis shows that the FA amount in solution remains constant going from 8 to 9.5 mL/h of FA added, indicating quantitative consumption (Figure 5.6). Increasing the flow of FA from 8 mL/h to 10 mL/h led to visible accumulation of unconverted FA followed by deactivation of the catalytic system. The same was observed setting the FA flow at high rates since the beginning (Entry 5, Table 5.6). In fact, a gradual ramp is required to reach the optimal conversion rate (e.g., 1 mL/h increase every 15/20 min approx.) and this was observed for all the Ru-PNP/IL mixtures tested in this study. Doubling the loading of EMIM CHOO to 0.026 mol (4 g) did not lead to improved catalytic activity (Entry 6, Table 5.6). Finally, also EMIM Et_2PO_4 proved to be a suitable solvent for continuous flow FA dehydrogenation (Entry 8, Table 5.6), affording the maximum turnover frequency achieved in this study. The use of such IL will be discussed later in this section.

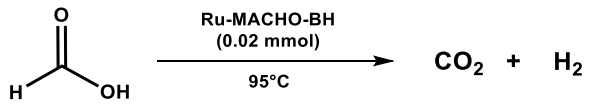

Entry	Ionic Liquid	Ionic Liquid (mol)	TOF_{max}[a] (h^{-1})
1	BMMIM NTf_2	0.007	-
2	EMIM TFA	0.013	-
3	BMIM OTf	0.013	-
4	EMIM CHOO	0.013	11990
5[b]	EMIM CHOO	0.013	-
6	EMIM CHOO	0.026	10720
7[c]	EMIM Et_2PO_4	0.009	-
8	EMIM Et_2PO_4	0.013	12620

[a] measured at the last FA feed rate before visible FA accumulation; starting rate at 2 mL/h FA otherwise specified. [b] Start at 8 mL/h of FA. [c] Start at 5 mL/h of FA.

Table 5.6: Screening of ionic liquids for the dehydrogenation of FA under continuous flow.

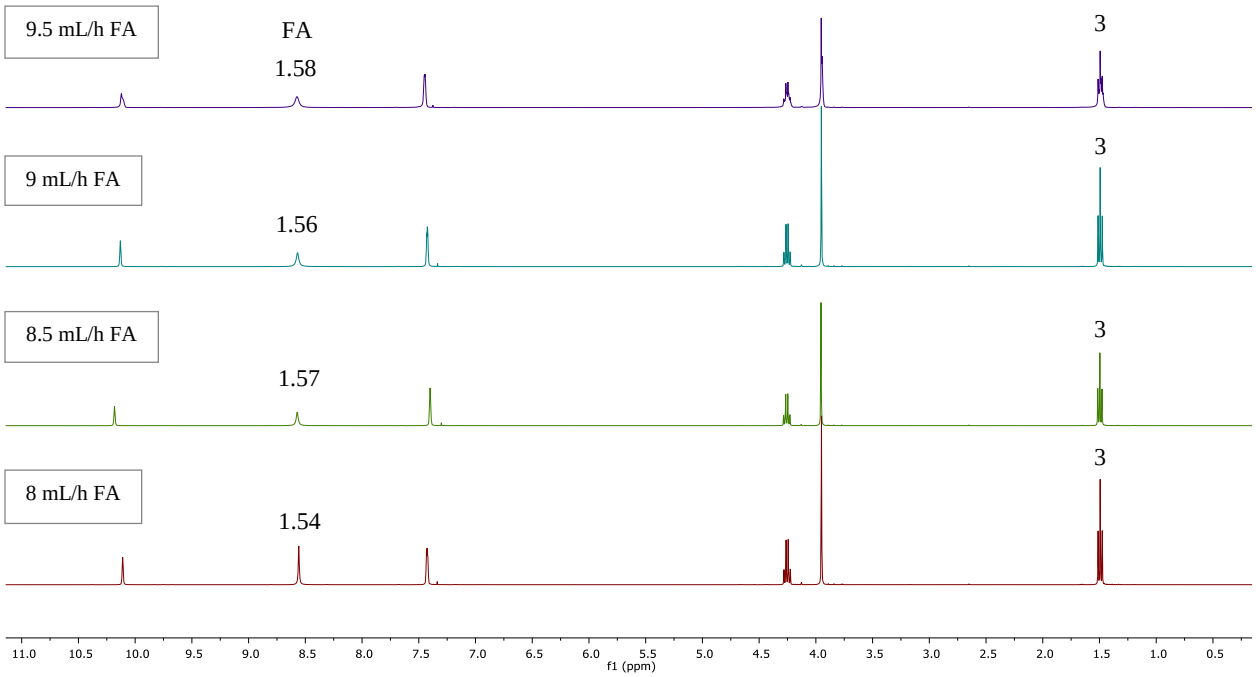

Figure 5.6: ^{1}H NMR spectra of the reaction mixture at different FA addition rates (Entry 4, Table 5.6). The numbers indicate the relative amounts based on NMR integration using the IL as reference ($CDCl_3$, 25 °C, 400 MHz).

When the system **Ru-MACHO-BH**/EMIM CHOO is left overnight at 95 ºC without any FA being added, it results in the formation of considerable amounts of EMIM-CO_2, with CO_2 that is trapped up to 60 mol% (Figure 5.7). If the reaction mixture is cooled to room temperature, off-white crystals precipitates in the reaction flask. Single-crystal X-ray diffraction analysis of such crystals led to the identification of the bicarbonate IL EMIM HOCOO structure showed in Chapter 4.2.1. Indeed, CO_2 chemisorption is always

present under these conditions, with an observed propensity towards CO_2 capture in the order EMIM CHOO > EMIM Ac > BMIM Ac. Stirring rate is also important based on the shape and the size of both magnet and reaction flask, as well as the volume of IL. That is due to formation of a dense layer of foam when FA is added at high rates, with consequent formation of high flows of CO_2/H_2 released (200-300 mL/min). For these reasons, I have always set the stirring rate at the maximum allowed value to allow higher turbulence hence easier gas release from the IL.

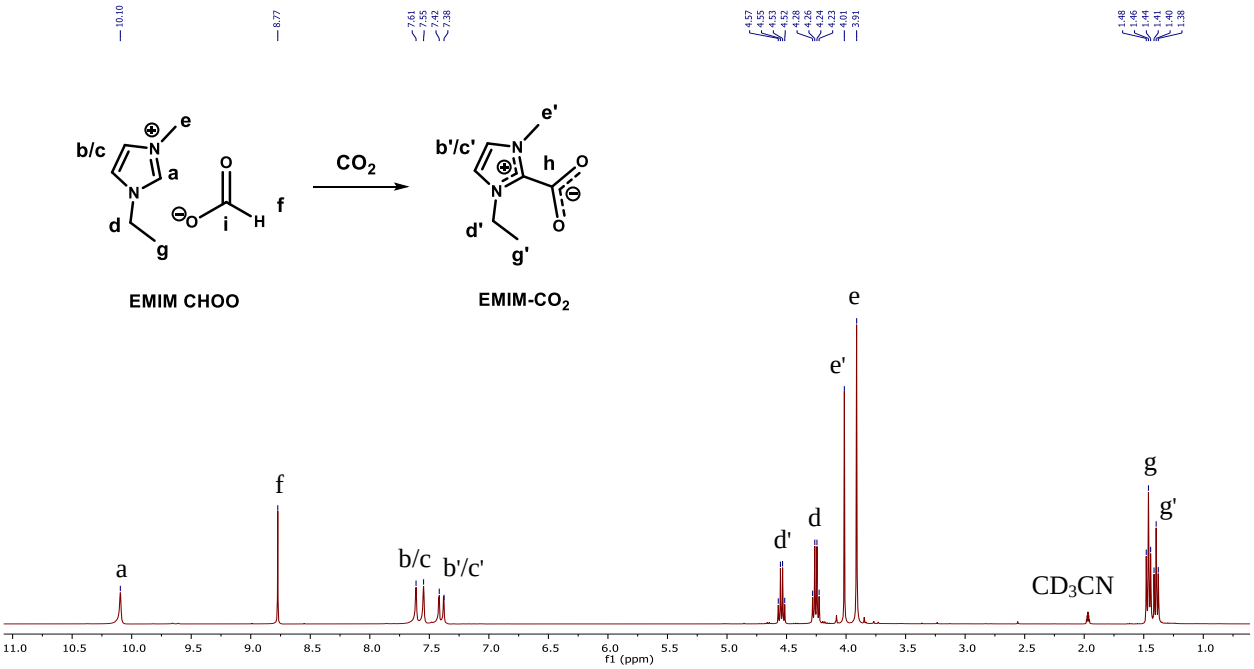

Figure 5.7: ^{1}H NMR spectrum of the reaction mixture left at 95 ºC overnight. Reaction condition in Entry 6, Table 5.6 (CD_3CN, 25 °C, 400 MHz). The crystal structure of EMIM HOCOO showed in Scheme 4.8 was obtained in this experiment.

Initially, I have chosen BMIM Ac for long-term dehydrogenation experiments under continuous flow. Lowering the catalyst concentration resulted in higher stability of the mixture reflected in the possibility to achieve higher turnover frequencies (Table 5.7). This is likely attributed to the increased buffering effect given by the IL towards high FA concentration, resulting in improved stability over prolonged times. As shown in Figure 5.8, the gas evolution profile follows the changes in FA rate, confirming the initial hypothesis of optimizing the system under continuous flow conditions.

Entry	BMIM Ac (mL)	Concentration (M)	TON	TOF_{med} (h^{-1})
1	2	0.01	980.000 (9 days)	4.500
2	3	0.007	2.171.653 (15 days)	6.030
3	4	0.005	15.143.315 (79 days)	7.986

Table 5.7: Optimization of FA dehydrogenation under flow conditions using Ru-MACHO-BH (0.02 mmol) at 95 ºC.

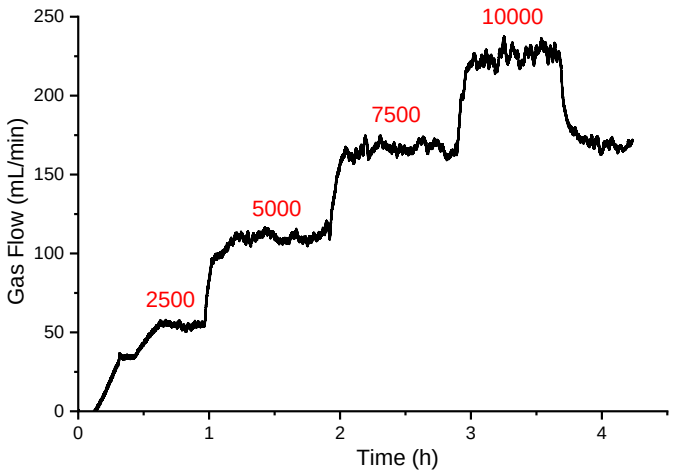

Figure 5.8: Gas evolution profile of continuous flow FA dehydrogenation. Reaction conditions: Ru-MACHO-BH (0.02 mmol), BMIM Ac (3 mL), 95 ºC; turnover frequencies for each FA rate are expressed in red; final TON = 2.171.653 (Entry 2, Table 5.7).

In a final long-term experiment (Entry 3, Table 5.7), I applied 0.02 mmol of **Ru-MACHO-BH** in BMIM Ac (4 mL) at 95 ºC. As such, it was possible to dehydrogenate up to 14.5 liters of FA (FA/IL > 3600 in volume) at an average rate of 8000 h^{-1}, resulting in a turnover number of 18.1 million after 112 days (Figure 5.9).

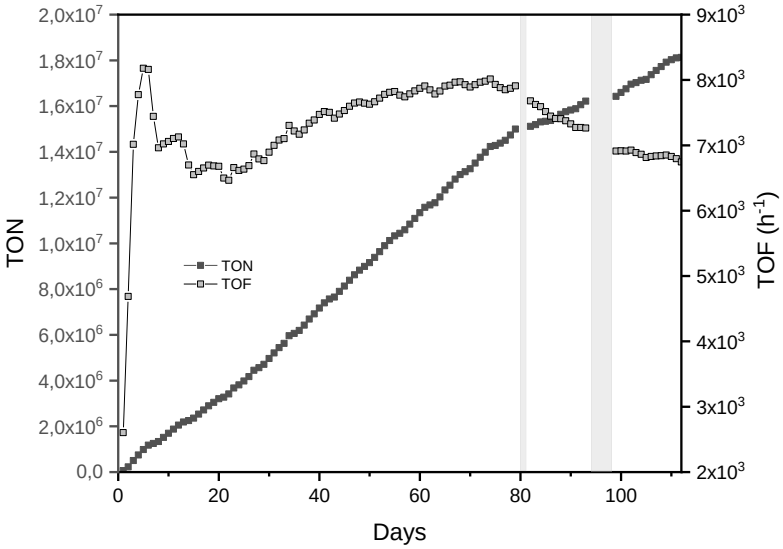

Figure 5.9: Gas evolution profile of long-term continuous flow FA dehydrogenation. Reaction conditions: Ru-MACHO-BH (0.02 mmol), BMIM Ac (4 mL), 95 ºC (Entry 3, Table 5.7).

The maximum FA addition rate was 8.4 mL/h, corresponding to a TOF = 10050 h^{-1} and a gas evolution fluctuating between 230-250 mL/min. Figures C.2 and C.3 in Appendix C provide more examples of the measured gas flow at random days over the course of the almost four months of reaction. In addition, it was possible to stop the system, which was cooled at room temperature for 4 days, and start it again by heating at 95 ºC and restoring the FA feed (second gray bar in the graph).

After 79 days, FA started to accumulate in the reaction flask with consequent decrease in the gas flow measured by the MFM (first gray bar in the graph, Figure 5.9). Hence, I have removed the excess of FA and restarted the reaction. However, it was not possible to achieve the same rate in activity, but only its 80%. Figure 5.10 (compared with Figure 5.8) clearly shows that the system could not tolerate the initial FA addition rate (8 mL/h, TOF = 10000 h^{-1}). Nevertheless, the system remained stable at an average rate of 7950 h^{-1} (FA rate of 6 mL/h – 160 mL/min gas flow) until day 112 when the reaction was stopped on purpose (Figure 5.9). Similar to batch conditions, no CO was detected in the various measurements over the 108 days (Figure C.7). Importantly, once the maximum flow tolerated by the system is determined, it is possible to change the FA feed between the allowed values as the user wants, hence controlling the amount of hydrogen that is released by the system (Figure S6). In addition, proper scaling up of the Ru-PNP/IL mixture allows to control the overall H_2 output obtainable. This can be done by proper adjustment of the catalyst concentration in the IL, and overall size of the catalytic phase. Importantly, it was possible to restart the reaction by simply restoring the FA feed, both if the system is kept at 95 ºC or cooled to room temperature and heated again. All of these features are of extreme importance for practical application of the technology, e.g. for FC technologies.

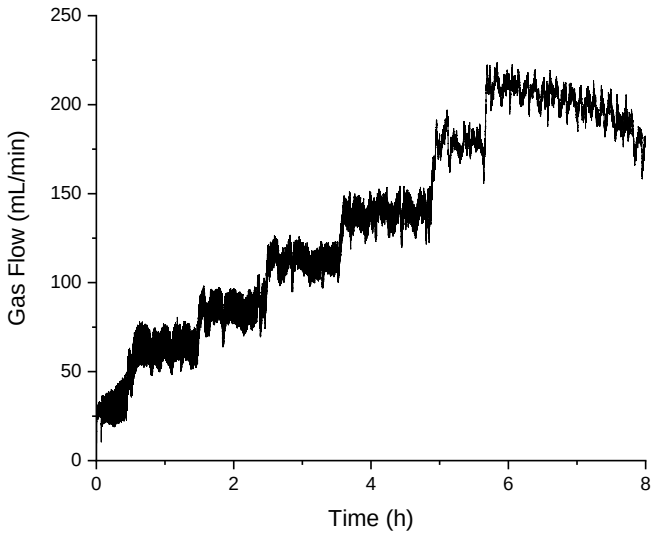

Figure 5.10: Gas evolution after reactivation of the system (Figure 5.9, day 84).

^{1}H NMR analysis of the reaction mixture revealed that the acetate anion had been replaced quantitatively by formate over the 3 months of reaction, resulting in the formation of the corresponding BMIM CHOO IL (Figure 5.11). Importantly, during the reactivation attempts (day 80), I have added 1 mL of BMIM Ac in order to decrease the viscosity of the solution and partially restore its basic properties. From the ^{1}H NMR analysis performed at the end of the reaction (day 108), the newly-added acetate was quantitatively replaced by the formate anion as well, in agreement with what described in 4.2.3. Proton signals around 2.75-3.5 ppm might indicate degradation of the IL and/or accumulation of impurities. Indeed, the integration was found to be unreliable for the main peaks associated with the initial BMIM structure. As visible from Figure 5.11, the reaction mixture appears as a dark-brown, viscous liquid, very different than BMIM Ac before use.

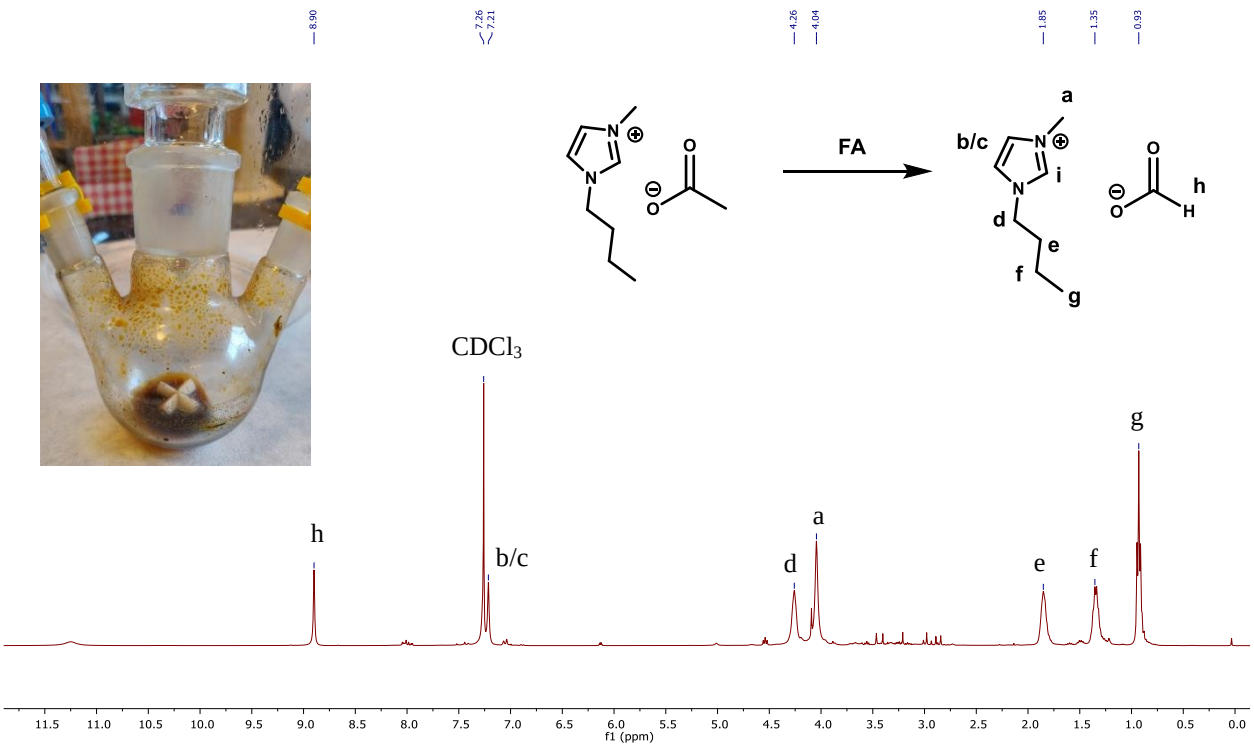

Figure 5.11: ^{1}H NMR spectrum (and picture) of the reaction mixture after the long-term experiment (day 105) in Figure 5.9 (CD_3Cl, 25 ºC, 400 MHz).

The feed of FA was changed during the course of the experiment, varying from commercial grade FA 96% that was distilled before utilization, to 98-100% FA (from Supelco) that was used without prior distillation. In addition, FA was kept under an argon atmosphere to avoid increasing level of moisture in the feed. However, it is likely that even low concentrations of impurities in the feed (at ppm levels) might lead to significant detrimental effects over such long reaction times. It has to be noted that no NMR samples were taken during the first 108 days of experiment in order not to perturbate the catalyst concentration in the IL. Further optimization should target to e.g. monitoring of the exact composition of FA, eventually adding selected impurities to investigate the effect of each of them on possible deactivation pathways, and continuous analysis of the reaction mixture by GC, NMR, or IR. For example, data from the suppliers of FA indicate the presence of both cations (K^+, Ca^{2+}, Al^{3+}, Fe^{2+}, Mg^{2+}, Na^+) as well as anions ($C_2O_4^{2-}$, Cl^-, SO_4^{2-}, SO_3^{2-}) that can lead to deactivation of the system due to formation of inactive Ru species. In addition, the ILs were used without prior purification from e.g. water and halides that are present in <1% (from Iolitec).

Later, I have explored the long-term stability of EMIM Et_2PO_4 hoping for a more stable reaction solvent. Similar to what described for the other ILs, starting the reaction with a high FA feed (5.5 mL/h) resulted in rapid deactivation of the system (Entry 7, Table 5.6). Hence, I have increased the volume of IL and started another experiment with gradual ramp from 2 to 10 mL/h. Applying 0.02 mmol of **Ru-MACHO-BH** in 3 mL of EMIM Et_2PO_4, the system afforded a TON of 684.000 after 5 days, with a maximum turnover frequency of 12620 h^{-1} (10 mL/h of FA) at 95 ºC (Entry 8, Table 5.6). At this point, I have tried to further increase the FA rate (from 10 to 12 mL/h) but it resulted in rapid accumulation of FA. ^{1}H NMR analysis of the reaction mixture after accumulation of FA shows retained stability of the anion liquid, with stoichiometric amount of cation/anion after 5 days at 95 ºC (Figure 5.12).

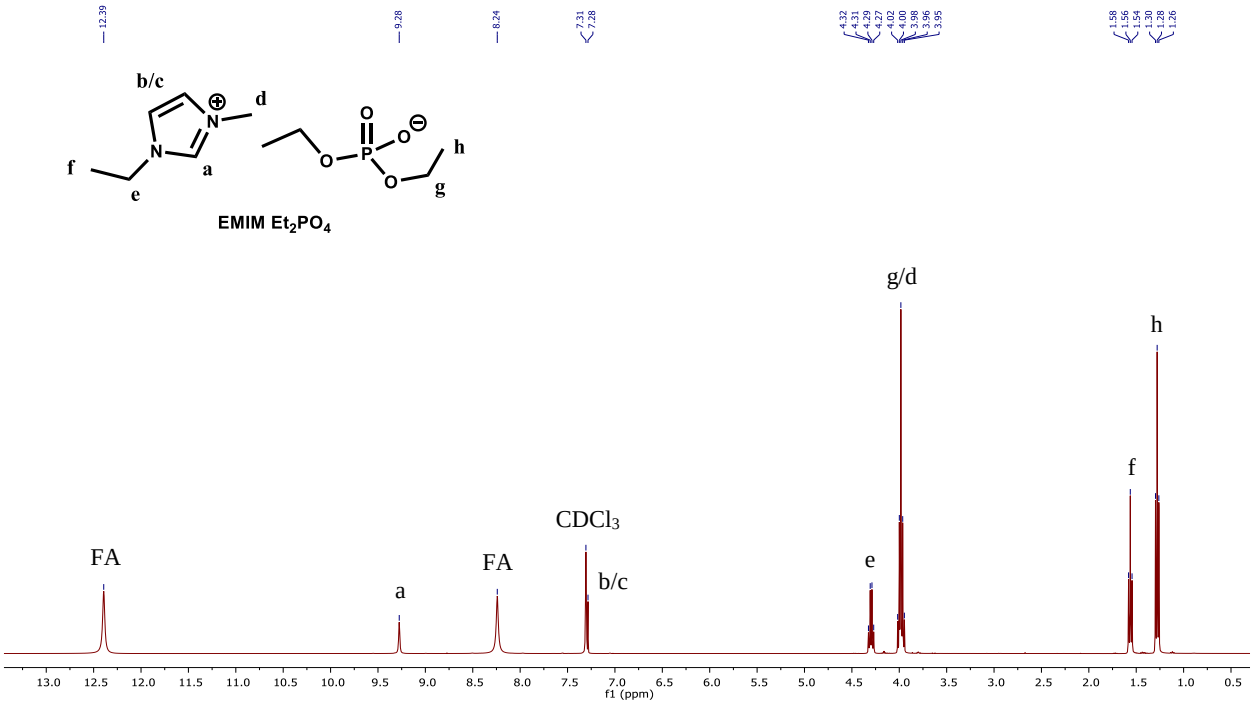

Figure 5.12: ^{1}H NMR spctrum of the reaction mixture after the continuous flow FA dehydrogenation shown in Entry 8, Table 5.6 ($CDCl_3$, 25 °C, 400 MHz).

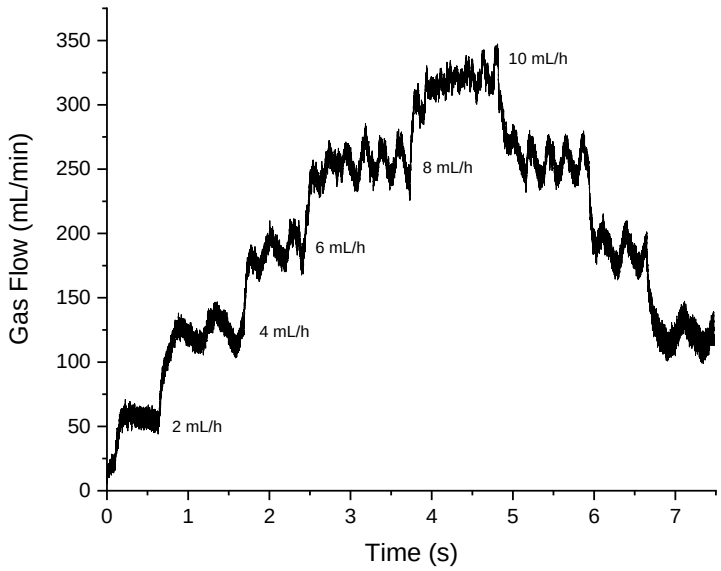

Figure 5.13: Gas flow evolution of continuous flow FA dehydrogenation at different FA rates; reaction conditions in Entry 8, Table 5.6.

In a final long-term experiment, I have increased the volume of EMIM Et_2PO_4 to 4 mL in order to increase the buffering properties of the mixture; **Ru-MACHO-BH** (0.02 mmol) afforded a TON = 3.600.000 after 29 days of reaction at 95 ºC, before FA started to accumulate in solution. I would like to express my gratitude to PhD student Brenda Rabell who has been of great help during these long-term experiments that required almost a daily control. As an example of her contribution, she measured the gas-flow profile at different FA addition rates depicted in Figure 5.13.

As observed before in Chapter 4, it appears evident that the control of the pH is an aspect of extreme importance in such transformation. This is because the IL is crucial to buffer the solution and retain catalytic activity, reflected in higher stability of the mixture towards high FA addition rates. I was not able to perform precise analysis of the pH of IL solution due to lack of equipment. However, the observed experimental basicity reported in literature follows the order $^-Me_2PO_4$ > ^-OAc ≈ $CHOO^-$ >> $^-N(CN)_2$, > ^-OTf > $^-NTf_2$ [189]. In this study, the highest activity in terms of turnover frequency observed was in the order $^-Et_2PO_4$ > ^-OAc ≈ $CHOO^-$, clearly confirming the beneficial effect of basic ILs on the resulting reactivity of the mixture. In fact, EMIM Et_2PO_4 afforded the best TOF reported in this study for FA dehydrogenation (12620 h^{-1}), slightly higher than what observed with EMIM Ac and EMIM CHOO. In addition, we noticed that when using EMIM Et_2PO_4, it is possible to perform larger variations in the FA addition rate without consequent deactivation of the catalyst (for example from 4 to 10 mL/h), which was not possible with EMIM CHOO and BMIM Ac.

Based on these observations, it is possible to envision that an optimized mixture of one or more (functionalized) ILs might lead to substantial increase in the stability of the system described herein. As an example, the use of bulkier carboxylate anions should lead to increased stability of the solution due to the lower volatility of the corresponding carboxylic acids. In addition, the experiments with EMIM Et_2PO_4 shows that using phosphate-based anion it is possible to avoid competitive CO_2 capture processes that result in increased viscosity and/or degradation of the solution. Also in this case, different functionalities on the phosphate anion might be beneficial to increase the stability of the solution. Again, it is clear that the basic properties of the IL mixture clearly affect the catalytic activity of Ru-PNP catalysts, with possibility to adjust the required acidic-basic properties based on the desired application. This represents another prove of the extraordinary potential given by the tunable properties of such a Ru-PNP/IL system.

5.2.3 Dehydrogenation of FA in a closed system

In this section, I have investigated the possibility to produce pressurized H_2 in closed systems using sealed autoclaves as described in Chapter 2. To my delight, simply applying 0.02 mmol (0.08 mol%) of **Ru-MACHO-BH** in the presence of EMIM CHOO at 80 ºC resulted in full conversion of FA and 35 bar of a 1:1 CO_2:H_2 pressure produced after only 2 hours, importantly with no CO detected (Entry 1, Table 5.8). Similar to continuous flow conditions, the reaction mixture solidifies after cooling at room temperature, with 14 mol% of CO_2 trapped (Figure 5.14). Decreasing the catalyst loading to 0.05 mol% and 0.02 mol% resulted in 35 and 20 bar of pressure produced after 18h respectively using a bigger autoclave (22 mL, Entries 2,3). Later, I have tried to mix **Ru-MACHO-BH** and **Ru-2** in a 1:1 molar ratio (Entry 4) considering the higher activity of ^{iPr}PNP towards CO_2 hydrogenation. The addition of **Ru-2** did not change the FA conversion nor the pressure produced, showing that the hydrogenation of CO_2 does not compete with FA dehydrogenation under these conditions. Later, I have scaled up the reaction in order to produce higher H_2 pressures. Entries 5 and 6 in Table 5.8 show that if one wants to obtain high pressures, the increase in FA loading should be followed by an increase in the IL volume to balance the increasing acidity of the mixture, in agreement with the experiments under batch conditions. In addition, longer times allow the obtainment of higher CO_2:H_2 pressures, with a maximum of 125 bar at 90 ºC after 72 h (Entry 7, Table 5.8). The use of BMIM Ac and EMIM Ac (Entries 8-12) leads to similar observations, in particular the need for the IL:FA volumetric ratio to be ≥1 or similar in order to stabilize the catalyst and prevent deactivation. Using BMIM Ac, it was possible to obtain up to 105 bar of H_2/CO_2 after 72 h (Entry 12).

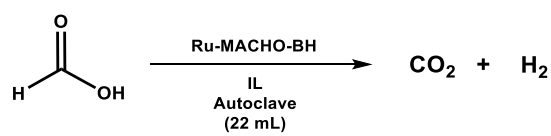

Entry	Cat Load (mol%)	IL	IL (mol)	FA (mmol)	T (°C)	Time (h)	Pressure produced
1[a]- FAD 64	0.08	EMIM CHOO	0.01	26.5	80	2	35
2- FAD76	0.05	EMIM CHOO	0.01	39.7	80	18	35
3 -FAD78	0.02	EMIM CHOO	0.01	79.5	80	18	20
4[b]- FAD77	0.05	EMIM CHOO	0.01	39.7	80	18	35
5- FAD85	0.01	EMIM CHOO	0.025	119.3	90	18	15
6-FAD91	0.01	EMIM CHOO	0.07	159	90	72	65
7- FAD97	0.02	EMIM CHOO	0.05	212	90	72	125
8- FAD87	0.02	BMIM Ac	0.03	79.5	80	18	50
9- FAD88	0.01	BMIM Ac	0.03	132.5	80	18	10
10- FAD96	0.01	EMIM Ac	0.06	159	90	72	90
11- FAD90	0.01	BMIM Ac	0.07	212	90	60	15 (24h) 15 (60h)
12- FAD89	0.01	BMIM Ac	0.06	159	90	72	35 (24 h) 75 (48h) 105[c] (72h)

[a] 5 mL reaction vessel (autoclave B, Figure 2.8) [b] Ru-MACHO-BH + Ru-2. [c] 85 bar when cooled to rt; other experiments did not show such a difference after cooling.

Table 5.8: Optimization for the dehydrogenation of FA under pressurized conditions.

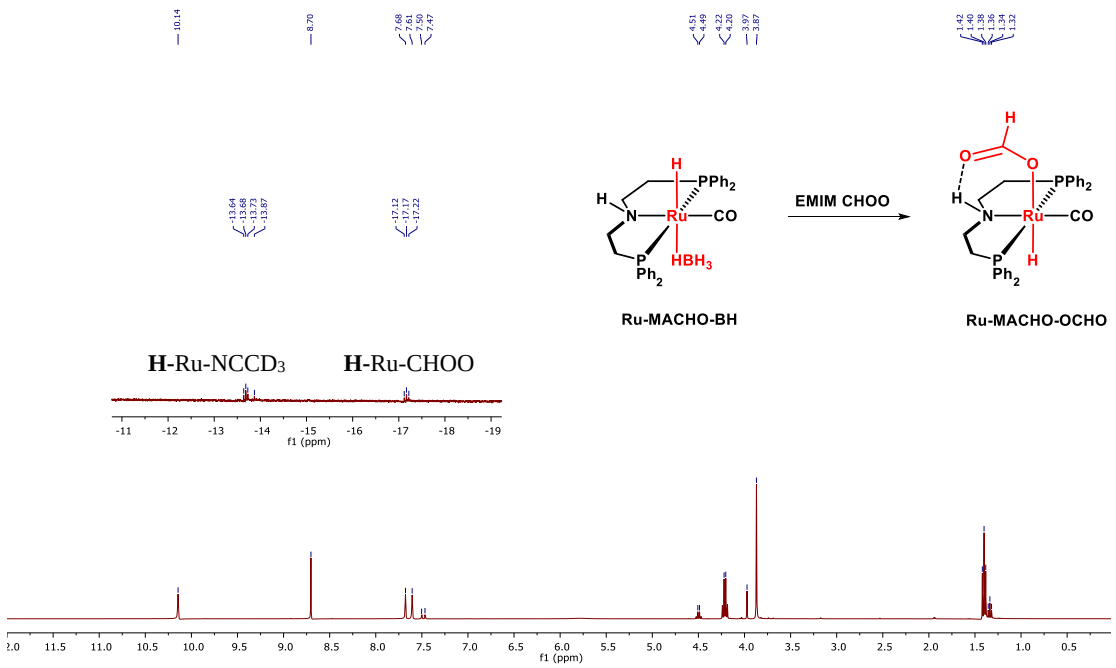

Figure 5.14: ^{1}H NMR spectrum of the reaction mixture after FA dehydrogenation under pressure in Entry 1, Table 5.8 (CD_3CN, 25 °C, 400 MHz).

Unfortunately, MicroGC analysis revealed that long reaction times and high pressures lead to CO production (>100 ppm), indicating that water gas-shift reaction (or FA decomposition) might occur under these conditions (Figure C.9 for the GC report of Entry 7, Table 5.8). The same was observed in the presence of both BMIM Ac and EMIM CHOO. Nevertheless, reactions carried out at lower temperature (Entries 1-5, 8) show no visible CO formation (Figure C.8 for the MicroGC report), indicating the possibility of obtaining clean pressurized hydrogen without the contamination of CO under optimized conditions. In addition, based on the findings from continuous-flow FA dehydrogenation, it is possible to envision a system where FA is added at a rate that produces the desired pressure. Finally, ^{1}H NMR analysis shows the presence of the usual Ru-H signals, therefore the possibility to repeat the operation (Figure 5.14).

5.3 Summary

In conclusion, I have demonstrated that the combination of Ru-PNP and ILs is an effective system for FA dehydrogenation under both batch and continuous flow conditions. The system shows extreme flexibility, stability and reversibility under a wide range of temperatures, pressures, times and catalyst loading. All of these features make the system a promising candidate for energy delivery technologies based on FA as the LOHC. Imidazolium acetate, formate and phosphate ILs are all suitable reaction media for this transformation, offering wide margins for further optimization. Importantly, using the IL as the only solvent provides a clean flow of CO_2:H_2 without the presence of volatile species.

The most important result is the one presented in Figure 5.9, where I have showed the continuous and selective hydrogen release from FA at temperatures below 100 °C, and thus under conditions that enable transfer of off-heat from a PEM-FC. The combination of **Ru-MACHO-BH** and BMIM Ac afforded an overall turnover number of 18 million after 4 months under flow conditions, showing great potential for industrial application. It has to be noted that this result could have been much higher; in fact, the FA flow has been adjusted according to time and size of syringes available, for example slower during nights and weekends. Nevertheless, higher FA flows could lead to faster deactivation of the system; in this sense, further optimization and up-scale reactions are required to assess the robustness of the system for even longer times.

The method presented in this work presents several advantages when compared to other reported procedures (see 5.1). For instance, it is possible to feed FA continuously from a separate compartment, as opposed to other methods were the catalyst is initially dispersed in large amounts of FA. Hence, it is possible to imagine a practical and small unit that simulates the operative conditions of e.g. a hydrogen vehicle, where the LOHC is fed to the FC based on the desired energy output. It is possible to pause and stop the system, feed commercial grade FA, and perform all the relevant manipulations without the need of inert or dry conditions. Importantly, the possibility of using neat FA allows the maximum gravimetric H_2 content of the system, maximizing its energetic and volumetric properties in a reduced scale. All of these features make the Ru-PNP/IL system an ideal candidate for practical implementation within the transportation sector.

Finally, I have demonstrated the possibility of producing pressurized H_2 up to 100 bar. The formation of CO can be avoided by controlling reaction parameters such as temperature and pressure, as well as the concentration of FA in the IL or the presence of water in the reaction mixture. Once again, the basicity of the IL (and the resulting overall acidity of the solution after FA addition) could play an important role in the selectivity towards CO. Nevertheless, the presence of CO indicates possible water gas shift reaction pathways that deserve further investigation. Indeed, FA can be considered an interesting intermediate for the water gas shift reaction between CO_2 and CO (currently produced from fossil feedstock, see section 1.3)

In this study, **Ru-MACHO-BH** showed the best results in terms of both catalyst stability and activity. Nevertheless, despite the lower stability and activity showed by ^{iPr}PNP ligands compared to ^{Ph}PNP catalysts, it can not be excluded that other Ru (and Ir) pincer ligands can be applied for this transformation. For example, N-heterocyclic carbene (NHC) pincer complexes are known for their remarkable stability due to the presence of strong Ru-NHC bonds and could be tested for such application. Importantly, in this work I have showed the promising activity of the manganese catalyst **Mn-1**. It is likely that in the case of Mn, higher catalyst loading are required to reach relevant activity, but the abundancy (reflected in the price) of Mn compared to Ru would mitigate such a requirement. Especially in the case of manganese, the modification of the ligand structure aiming for a better stability of the resulting complex is highly desirable.

To conclude, among all the possible applications of the Ru-PNP/IL system described in this study, the continuous flow FA dehydrogenation is certainly the most robust, displaying several encouraging openings for further optimization in terms of e.g. scaled-up studies, optimization of the IL mixture for higher stability over time, as well as use with other LOHC candidates.

6. A reversible energy storage system based on Ru-PNP complexes and ionic liquids

6.1 Introduction

Hydrogen economy and Power-to-X technologies will likely be main players in the coming green green transition, providing a solution for the discontinuous nature of renewable energy sources [328]. FA is the first CO_2 hydrogenation product and a promising LOHC candidate for the long-term, safe and practical storage of renewable energy (4,4 wt% H_2) [329,330]. It decomposes to a 1:1 mixture of H_2 and CO_2 where hydrogen is converted into electricity, while the released CO_2 is captured and converted back to FA, closing an ideal carbon-free energy cycle (Figure 6.1) [36,309,331–333]. As described in the previous chapters, homogeneously catalyzed hydrogenations and dehydrogenations are two of the main approaches for the reversible interconversion between CO_2 and the LOHC FA [331,334]. In the effort of developing efficient and stable systems, researchers have proposed different strategies for both CO_2 valorization to FA [65,200,202,249,250,335,336], as well as FA dehydrogenation [166,245,255,322,326].

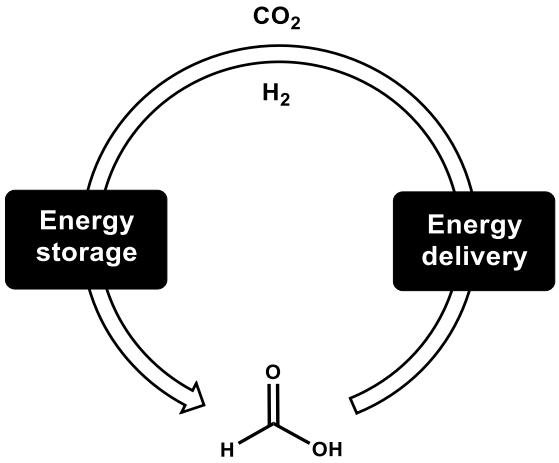

Figure 6.1: Energy storage system based on CO_2/FA.

Nevertheless, there are only few examples of reversible systems reported in the literature that shows promising prospect for real usage [248,254]. For instance, Laurenczy reported the combination of Fe(II) precursors in combination with meta-trisulfonated-tris[2-(diphenyl-phosphino)-ethyl]phosphine (PP_3TS) for the production of FA in aqueous solution [337]. The reaction proceeds with no additives and it is reversible towards hydrogen production. However, as already visible from other examples from Chapter 4.1, the system is limited by the maximum concentration of FA obtainable (0.5 M in this study). Pidko reported the reversible hydrogenation of CO_2 to formate employing **Ru-6** in DMF/DBU mixtures, demonstrating 10 cycles of H_2 storage-release by switching the temperature between 65 ºC and 90 ºC as well as the pressure between 5-40 bar and 1 bar (Entry 3, Table 6.1) [248]. Hull, Himeda and Fujita employed a dinuclear iridium catalyst (**Ir-5**) and sacrificial $KHCO_3$ and H_2SO_4 to switch between CO_2 hydrogenation and FA dehydrogenation [254]. The hydrogenation proceeded at 30 ºC under 1:1 CO_2/H_2 at 1 bar, and the dehydrogenation at 50 ºC (Entry 2, Table 6.1). Likewise, Himeda showed that a pyridyl-pyrazole Cp^*-Ir catalyst **Ir-4** hydrogenates CO_2 in presence of 1.0 M $NaHCO_3$ (aq) under 10 bar of 1:1 CO_2/H_2 at 50 ºC, giving TON = 7850 and TOF = 164 h^{-1} after 48 h [255]. Changing the reaction conditions to 4 M of FA (aq) and 70 ºC, the same catalyst dehydrogenates a continuous

flow of 20 M FA (aq) affording TON = 10 million after 35 days. However, it is unclear whether the source of FA is CO_2 or the bicarbonate, and the authors did not demonstrate cycles of the reversible transformation.

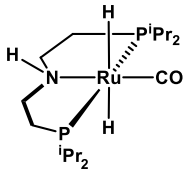

Ru-1

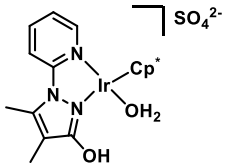

Ir-4

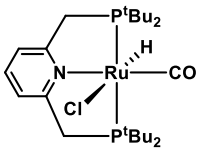

Ru-6

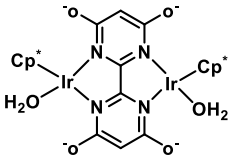

Ir-5

Entry	Corresponding authors	Catalyst	TON	TOF (h^{-1})	T / p (HD)	T (DH)	Additives	Comments
1	Nielsen[a]	Ru-1	50.000	1.000	25-80 1-30 bar	80-95	EMIM Ac	flexible, no inert conditions, stable
2	Hull, Himeda, Fujita [254]	Ir-5	79.000	54.000	30 / 1 (136h)	50	$KHCO_3$ H_2O	inert conditions, volatile solvent pH adjustments ($H_2SO_4/KHCO_3$)
3	Pidko [248]	Ru-6	-	-	65 / 40	95	DBU DMF	flexible, inert conditions, volatile/toxic solvents
4	Himeda[b] [255]	Ir-4	-	-	50 / 10	70	$NaHCO_3$ H_2O	only single steps

[a] developed in this study

Table 6.1: Overview of the most representative systems for the reversible conversion of CO_2 and FA compared to the Ru-PNP/IL catalyst used in this study.

As already described in the previous chapters, the reported systems usually require sacrificial additives (e.g. inorganic bases and solvents) to achieve satisfactory activity and stability, therefore lowering the overall volumetric/gravimetric energy storage potential of a hypothetic reversible system. In addition, such an energy system based on CO_2/FA requires a clean flow of hydrogen gas released, without the presence of any volatile additives that would decrease the H_2 storage capacity and potentially damage the FC. In this sense, the negligible vapor pressure and high chemical and thermal stability of ILs allow the obtainment of a clean flow of hydrogen without any organic contaminants that could damage a FC. Another important aspect for a viable energy system is the ability to operate reversibly under a wide range of pressures and temperatures. As described before, there are only few examples of catalytic systems that fulfill all of these features and are able to perform both steps of energy storage and release without the use of additional additives and by only changing one or two reaction parameters. As showed herein, the Ru-PNP/IL system possesses all the requirements for such application, despite some drawbacks that will be discussed in this chapter.

6.2 Results and discussion

During the studies showed in Chapter 4, immediately I have observed the reversibility of the CO_2 hydrogenation process: by simply applying heat (>60 ºC) in the presence of the catalyst, it was possible to release a 1:1 mixture of H_2:CO_2 from the Ru-PNP/IL mixture restoring the system that could undergo another cycle of hydrogenation. In addition, in Chapter 5 I have showed that FA dehydrogenation is favored at T>50 ºC in the presence of the same catalysts performing CO_2 hydrogenation at low temperatures (**Ru-1** and **Ru-2**). Hence, I have investigated the performance of the Ru-PNP/IL system for cycles of hydrogenation and dehydrogenation, imagining an energy device based on CO_2/FA (Figure 6.1). Importantly, the use of an IL provides clean flow of gases in and out the system during both cycles of hydrogenation/dehydrogenation based on charging and discharge of FA. As shown in the previous chapters, the same concept can be applied to EMIM CHOO, active in both steps.

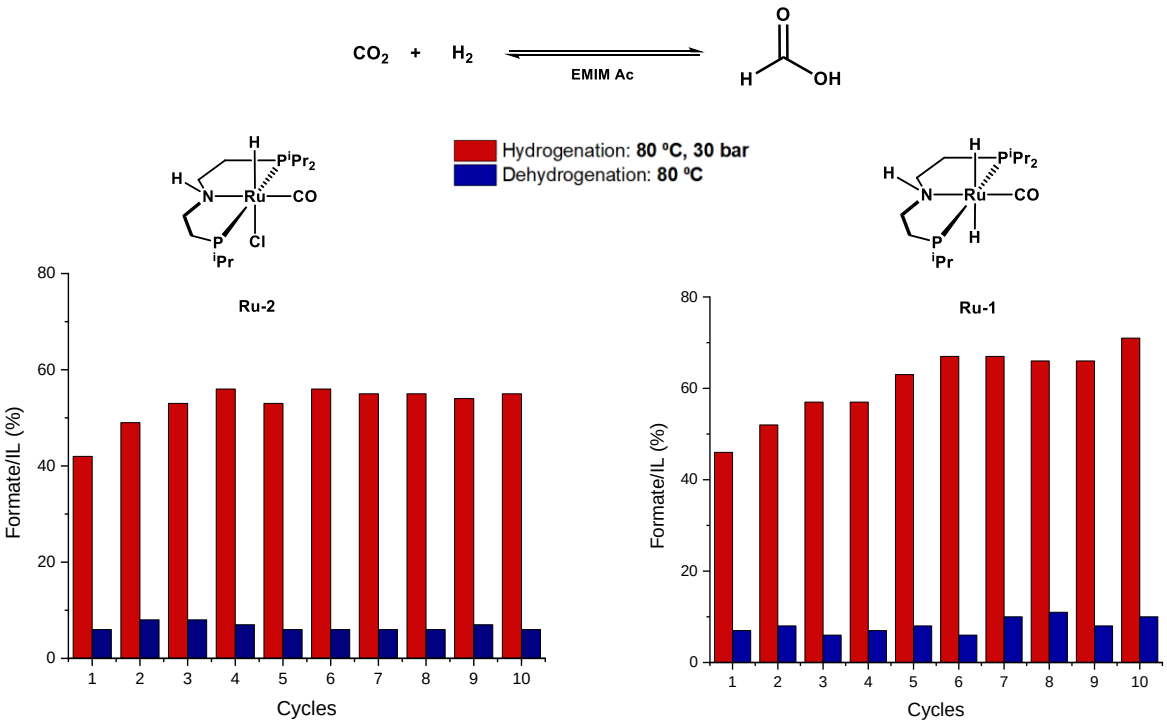

Figure 6.2: Cycles experiment of CO_2 hydrogenation followed by hydrogen release. Reaction conditions: Ru-1 (0.004 mmol), Ru-2 (0.02 mmol), EMIM Ac (3 mL), 80ºC, 18h each cycle. CO_2 (10 bar), H_2 (20 bar) for the hydrogenation, open autoclave for the dehydrogenation.

In a first set of experiments, I have tested the possibility to keep the system at the same temperature of 80 ºC and control the selectivity between the two steps by changing the pressure (Figure 6.2). The amount of FA in the system was determined by ^{1}H NMR relatively to the IL, similarly to what described in the previous chapters (Figure 6.4). In a straightforward way, by a simple pressure switch, it is possible to load the system applying CO_2:H_2 pressure (30 bar), resulting in the formation of FA as described in Chapter 4. Later, the system readily releases the stored hydrogen by keeping the autoclave open at 80 ºC. The results are shown in Figure 6.2 for both both **Ru-1** and **Ru-2**. At a low catalyst loading of 0.004 mmol, **Ru-1** resulted in an overall TON of 51761 after 10 cycles with no indication of catalyst deactivation. The presence of Ru-H species confirm the retained activity of both catalysts after being exposed to cycles of hydrogenation and dehydrogenation. With both catalysts, it is possible to notice some degree of activation of the system during the first 4-5 cycles. However, it was not possible to explain the observed behavior,

considering that solubility of the catalyst should be complete at 80 ºC. However, H_2 diffusion within the IL is much slower than that of CO_2; it is possible that the IL slowly saturated with H_2 during the first cycles and then stabilizes at its maximum productivity, at the same time favoring easier formation of **Ru-1** under operative reaction conditions.

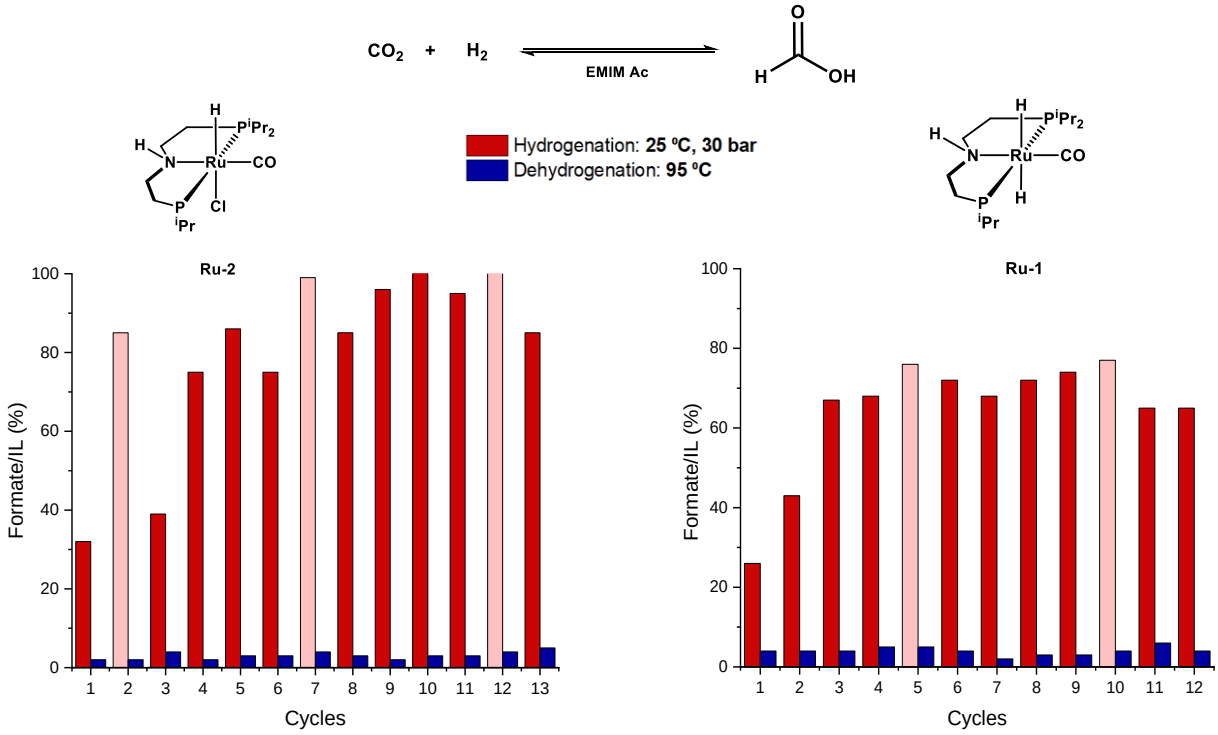

Figure 6.3: Cycles experiment of CO_2 hydrogenation followed by hydrogen release. Reaction conditions: Ru-1 (0.07 mmol), Ru-2 (0.05 mmol), EMIM Ac (2 mL). CO_2 (10 bar), H_2 (20 bar), 18 h (72 h in the lighter bars), 25 °C for the hydrogenation. Open autoclave, 95 °C, 4 h for the dehydrogenation.

In a similar fashion, I have demonstrated that is possible to perform the hydrogenation step at room temperature under 30 bar of 1:2 CO_2:H_2, with hydrogen release favored by heating at 95 ºC (Figure 6.3). Based on the findings from Chapter 4, the catalyst loading was increased compared to the previous experiments where the hydrogenation step was carried out at 80 ºC. In addition, the dehydrogenation temperature was increased to 95 ºC to allow faster hydrogen discharge that was performed in 4 hours under these conditions. Both **Ru-1** and **Ru-2** catalyzed up to 12 cycles (13 for **Ru-2**) of HD/DH without observable loss of catalytic activity. As expected, the catalyst loading can be adjusted accordingly to the temperature chosen for the hydrogenation step. Higher catalyst loadings maximize the energy storage potential by preventing the presence of unconverted CO_2 in the reaction mixture, and allow faster and complete hydrogen release, with a FA/IL ratio always < 5% after the DH step (Figure 6.4). In the experiments in Figure 6.3, **Ru-2** was used in lower catalyst loading compared to **Ru-1**, 0.05 and 0.07 mmol, respectively. When using **Ru-2**, it was possible to obtain loading of FA close to a 1:1 molar ratio compared to EMIM Ac under otherwise identical reaction conditions. Similar to the experiment at 80ºC, it is possible to notice an activation profile during the first 4-5 cycles. This aspect has to be considered when observing at the results discussed in Chapter 4 after only one cycle of hydrogenation. For example, it could explain some problems of irreproducibility that I have observed during the experiments at room temperature. In this regard, the most representative results reported in this thesis were always reproduced at least two times.

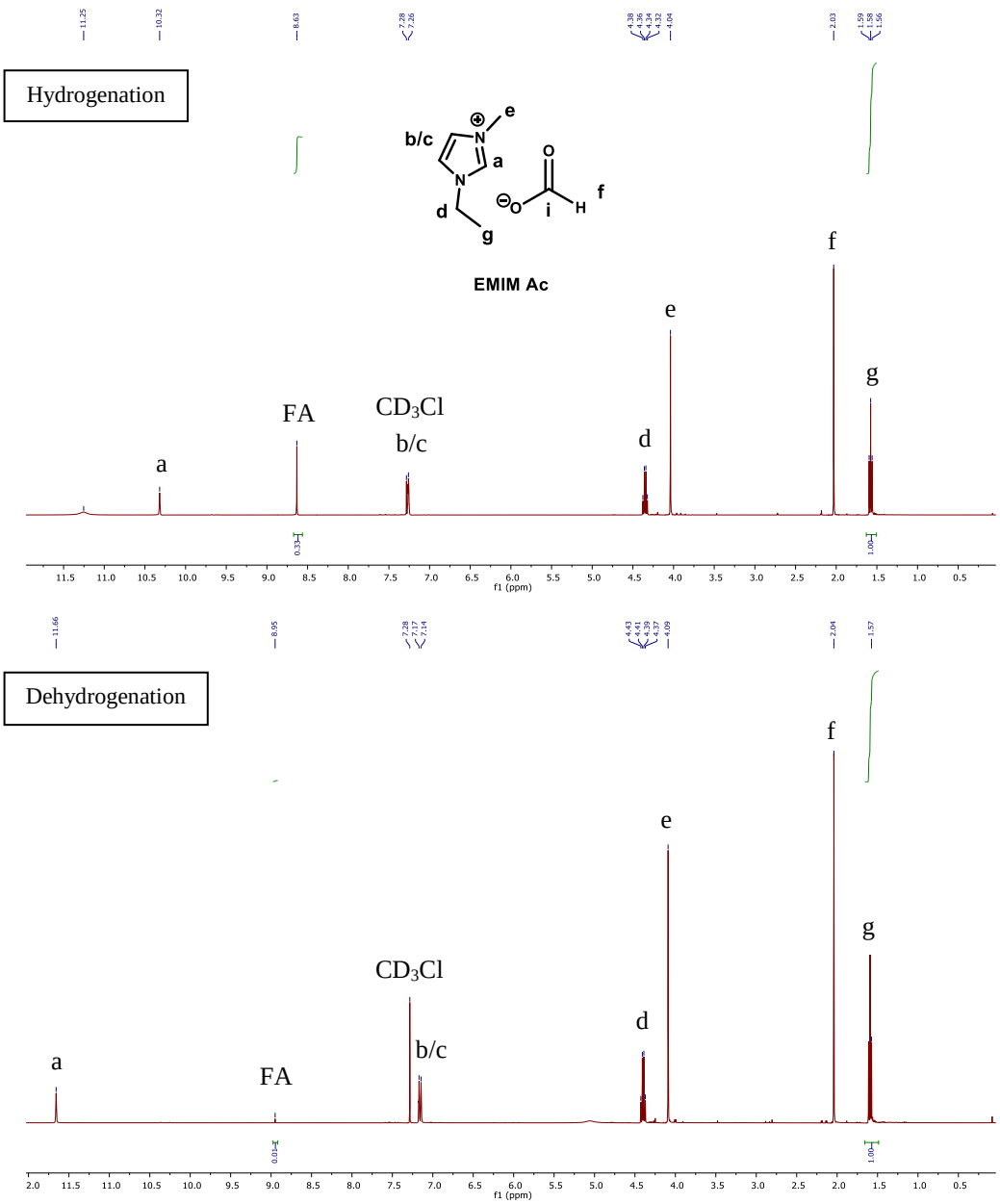

Figure 6.4: ^{1}H NMR spectra after hydrogenation and dehydrogenation cycles (CD_3Cl, 25 °C, 400 MHz).

The lighter bars in Figure 6.3 indicate 72 hours experiments compared to the standard 18 hours for the hydrogenation step. In the experiment with **Ru-2**, the hydrogenation cycle performed over 72 hours at the second cycle leads to much higher FA loading, indicating that it is beneficial to run the first hydrogenation cycle for longer times. Importantly from a practical point of view, it is possible to perform the hydrogen release step by keeping the system closed, resulting in the production of pressurized hydrogen (up to 10 bar in a single dehydrogenation step in Figure 6.3, see 5.2.3).

Figure 6.4 shows the ^{1}H NMR analysis of the IL mixture performed at the ninth cycle of the experiment in Figure 6.3 using **Ru-2**. It is possible to notice the presence of a broad signal at 12.25 ppm after the hydrogenation step that disappears when FA is dehydrogenated. The peak at 12.25 ppm can indicate the presence of –OH carboxylic groups; hence, it can be attributed to the

presence of free FA. As described in Chapter 4, this can be the case when using EMIM CHOO, while EMIM Ac results in the formation of different species in solution, with acetic acid coexisting in combination with acetate and formate anions. Hence, this peak probably arises from such hydrogen bond interactions in the IL phase, still confirming the production of formate in solution. Accordingly, the peak associated with the carbene C2 proton on the imidazole ring shows large changes in chemical shift, probably explained by a change in acidity of the solution depending on the changing FA concentration (Figure 6.3).

6.3 Summary

In conclusion, I have demonstrated a new approach for a reversible, hydrogen-based battery device for the storage of energy in the form of FA. The system is robust, flexible and stable under a wide range of temperatures, pressures, and catalyst concentration in the IL. By simply changing either temperature or pressure, the same system catalyzes up to 13 cycles of hydrogenation and dehydrogenation without any observable loss in activity under ambient conditions. The extreme simplicity and stability of this formate-based hydrogen storage system demonstrate its viable implementation within hydrogen storage technologies. Indeed, the findings discussed in this chapter can be considered as a foundation for the optimization of a reversible system for the storage and delivery of green energy at low operative costs.

Based on what has been described in this study, the system is currently limited by the amount of FA that is possible to accumulate in solution (≈1:1 molar ratio with respect to the IL). The same challenge is the most reported in the literature regarding FA production from CO_2, and a viable solution still has to be provided. Only EMIM Ac was tested in this demonstrative study, but the use of higher (carboxylate) ILs seems to be highly possible based on the results that I have showed for both CO_2 hydrogenation and FA dehydrogenation. In addition, the use of a co-IL might function as a stabilizer, and promote higher concentrations of FA in the hydrogenation step (see section 4.2.3).

In Chapter 5, I have demonstrated that the hydrogen release step of this proposed system is definitely more robust, representing the new state-of-the-art for hydrogen release from FA at temperatures compatible with PEM-FC applications. Therefore, combining the Ru-PNP system showed in this work with future and more efficient catalysts for CO_2 hydrogenation to FA, the likelihood of such a reversible energy system becomes considerable. In addition, I have demonstrated the possibility to perform the hydrogen release step under pressurized conditions according to the desired output. This feature makes the system showed here even more attractive for potential applications.

7. Continuous flow isopropanol dehydrogenation using a Ru-SILP catalyst

7.1 Introduction

Isopropanol offers a hydrogen capacity of 3.3 wt% and an energy storage density of 1.11 kWh/kg (or 0.87 kWh/L). Conventionally, it can be obtained from acetone by catalytic (transfer) hydrogenation step using both homogeneous and heterogeneous catalytic systems [338–340]. Direct *i*PrOH FCs represent a solution that does not require prior hydrogen release from the LOHC, and that does not emit CO_2 as a consequence of the oxidation process [341,342]. In addition, the transfer hydrogenation of acetone has been proposed as a strategy to reduce the temperature required for the dehydrogenation of bigger LOHC molecules such as dibenzyltoluene (see Chapter 8) [343]. The other approach investigated in this study involves the catalytic *i*PrOH dehydrogenation at low temperatures to afford clean hydrogen that can be used in a PEM-FC after it is separated from the by-product acetone. Hydrogenation of the latter closes the LOHC cycle.

Ru-PNP pincer catalysts have been widely reported for the efficient dehydrogenation of several LOHCs candidates such as methanol [125,165], FA [36,166,326], and importantly for this chapter, acceptorless dehydrogenation of alcohols [123,126]. Many excellent reviews cover the topic with focus on hydrogen production from alcoholic substrates, with isopropanol often used as a model substrate [89,313,344–346]. Regarding the use of homogeneous catalysis, Beller in 2012 reported the state-of-the-art system for homogeneously catalyzed dehydrogenation of *i*PrOH using **Ru-1**, which afforded a TOF = 2048 h^{-1} after 2 hours at 90 ºC without the use of basic additives (Scheme 7.1) [236].

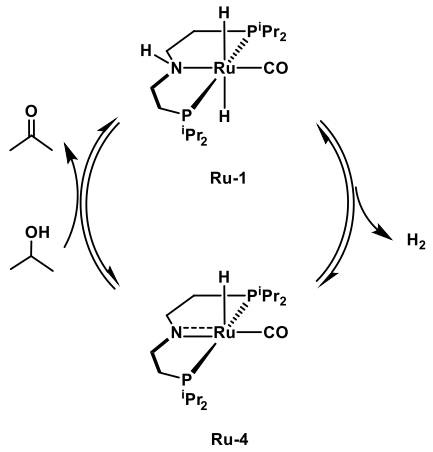

Scheme 7.1: State-of-the-art homogeneous system for *i*PrOH dehydrogenation reported by Beller [236].

As described in Chapter 1.6, the SILP technology allows the obtainment of an active homogeneous catalytic system (with advantages in terms of activity and selectivity) that resembles a robust and convenient macroscopic heterogeneous material in the form of a powder (Figure 7.1). This means that SILP materials can potentially allow product separation from homogeneous phase reactions, and render homogeneous catalysts applicable for continuous flow gas-phase reactions, with hydroformylation being the most predominant example in the literature.

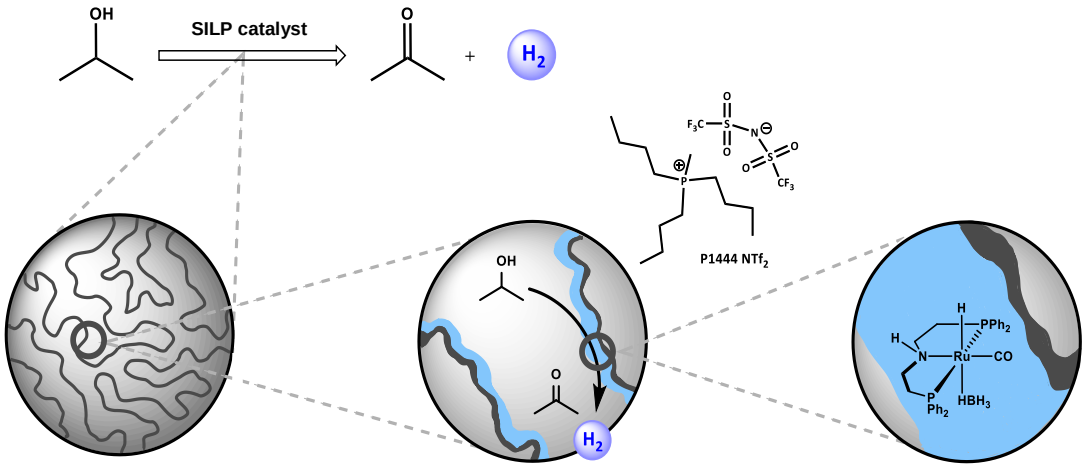

Figure 7.1: Schematic representation of the supported ionic liquid phase (SILP) technology with the catalyst (Ru-MACHO-BH) and IL (P_{1444} NTf_2) used in this study.

Relevant examples of SILP technology that include the use of pincer complexes were reported by Haumann for the reforming of methanol using **Ru-2** [234]. SILP materials were prepared using P_{1444} NTf_2 (Figure 7.2) and P_{1444} $MeOSO_3$ as the IL phase. Curiously, better performance of the system was obtained in the presence of KOH as the only coating material, in the so-called Supported Liquid Phase (SLP). The authors carried out extensive studies on SILP/SLP composition (loading of catalyst, base, and ionic liquid) as well as variation of operative parameters under fixed-bed conditions. In a follow-up work, the activity was improved by addition of the $PN^{Me}P$ analogue of **Ru-2** as a co-catalyst, and CsOH instead of KOH as the coating material [235]. Kirchner and Hoffmann reported Fe-PNP complexes supported on a silica material using the SILP technology for the selective hydrogenation of substituted aldehydes to alcohols obtaining relatively high turnover frequencies (4000 h^{-1}) [216]. The authors performed functionalization of the IL BMMIM NTf_2 with silica groups, creating covalent bonding with the support in order to prevent leaching and favor product separation under autoclave conditions (Figure 7.2). Later, a similar approach was followed using a carbon material as the heterogeneous phase of the system [347]. It has to be noticed that the prepared SILP materials were used under batch conditions, whereas the main advantage of the SILP technology is represented by the possibility to perform gas-phase continuous flow reactions otherwise impossible with conventional homogeneous systems. Most of the reported SILP catalysts in the literature do not use such homogenous pincer-type catalysts as the Ru-PNP used in this study, hence they are not considered in this discussion. Nevertheless, the same concepts expressed in this work can be applied to SILP materials prepared with e.g. common metal precursors.

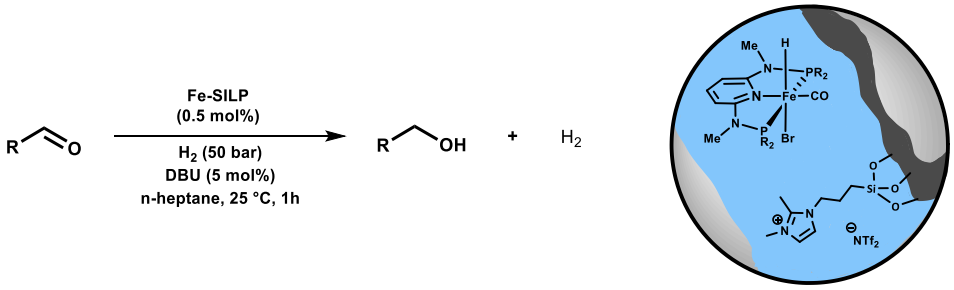

Figure 7.2: Schematic representation of the Fe-SILP catalyst reported by Kirchner and Hoffmann for aldehyde hydrogenation [216].

In this chapter, I have explored the reactivity of Ru-PNP catalysts in ILs applied to the dehydrogenation of the LOHC *i*PrOH under mild conditions and without the use of external additives. After optimization of the reaction in batch conditions, the system was transferred to the SILP technology resulting in a rare example of gas-phase *i*PrOH dehydrogenation using an organometallic catalyst. The system in Figure 7.1 showed stable hydrogen evolution with acetone as the only detectable by-product, and remained active for reaction times up to 100 hours. Following up on the studies performed by Haumann using **Ru-2** for methanol reforming [234,235], I have demonstrated that Ru-PNP complexes can be effectively immobilized on a support material using the SILP technology, affording a macroscopic heterogeneous catalyst retaining its homogeneous features.

7.2 Results and discussion

7.2.1 Batch reactions

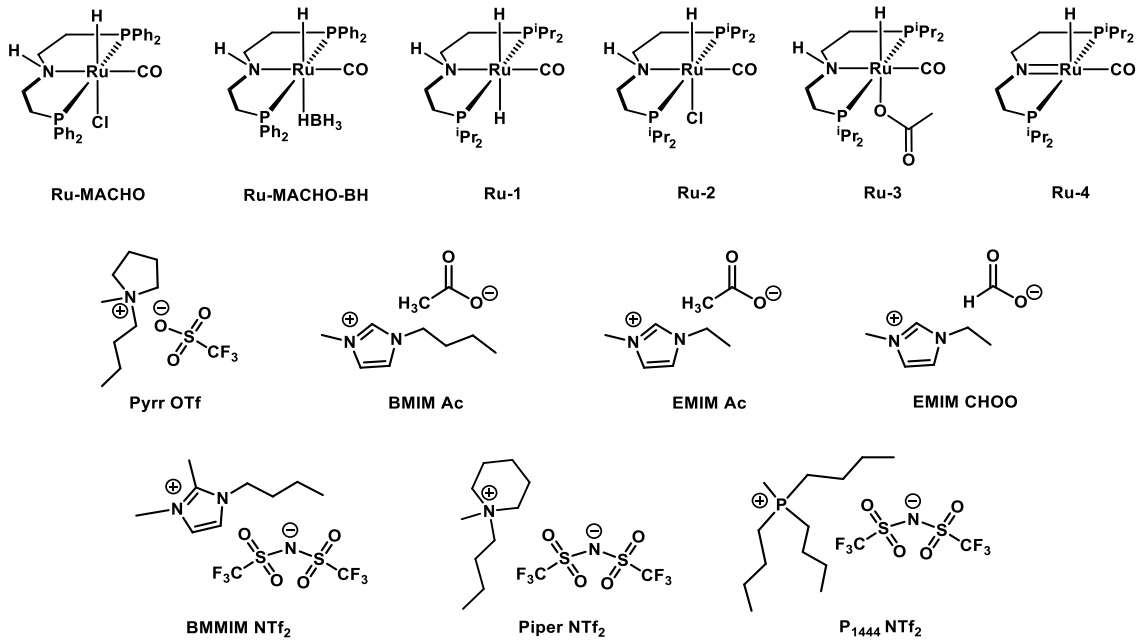

Figure 7.3: Overview of the Ru-PNP catalysts and ILs used in this chapter.

In the previous chapters, I have demonstrated that the anion of the IL plays a major role in the activation and stabilization of the Ru-PNP catalysts used in this thesis. Already in Chapter 2, I have shown the reactivity of Ru-PNP/IL mixtures towards the dehydrogenation of *i*PrOH. Based on the excellent activity showed in the previous chapters towards both CO_2 hydrogenation and FA dehydrogenation, I have investigated in depth the use of BMIM Ac and **Ru-MACHO** hoping that the consequent formation of the more active **Ru-MACHO-OAc** (Figure 3.3) would lead to catalytic activity towards *i*PrOH dehydrogenation. In a benchmark experiment similar to what described in Figure 3.5, I have used **Ru-MACHO** (0.1 mmol), BMIM Ac (4 mL), and added *i*PrOH (9 mmol) at 120 ºC over 2 hours. The subsequent distillation of the liquid mixture showed traces of acetone in solution (determined by ^{1}H NMR in $CDCl_3$ and D_2O, see Figures D.1 and D.2 in Appendix D), albeit with very low conversion (< 1%). Hence, I have

explored the use of reaction additives such as different bases (K^{t}BuO, NaOH, KOH, Et_3N) and Li^+ salts (CHOO, Ac, NTf_2, OTf, BF_4) hoping to trigger catalytic activity. However, it was not possible to observe relevant amounts of acetone formed in solution. It appears evident that the reactivity is completely different from what observed for FA. In this case, the use of acetate ILs does not promote any significant *i*PrOH dehydrogenation (tested until 130 ºC). Likely, the formation of stable Ru-acetate species prevents any reactivity towards *i*PrOH dehydrogenation (see Chapter 3).

Table 7.1 contains examples from the optimization process that clearly shows the observed differences in activity between CO_2/FA and *i*PrOH. Indeed, catalyst **Ru-1** is active in the presence of BMMIM NTf_2, showing visible gas evolution and the presence of acetone in solution after 2 hours at 120 ºC, equal to 10% conversion of *i*PrOH and a TON of 105 (Entry 1, Table 7.1). On the contrary, **Ru-1** in BMIM Ac resulted in only negligible conversion (Entry 2). In agreement with literature reports, it is possible to observe catalytic activity using **Ru-2** if combined with an external base that promotes abstraction of the -Cl ligand; in addition, the use of a base probably leads to a higher degree of *i*PrOH deprotonation, resulting in easier coordination of the isopropoxide anion to the metal center (Entry 3, Table 7.1). However, it was a choice not to explore further the use of such reaction promoters in order to keep the system as additive-free as possible. Finally, the pre-activated amido complex **Ru-4** afforded a TON = 150 after 1.5 hours (Entry 4).

Entry	**Catalyst (mol%[a])**	**Ionic liquid (mL)**	***i*PrOH (mmol)**	**Time (h)**	**T (ºC)**	**TON**	**Conversion[b] (%)**
1	Ru-1 (0.10)	BMMIM NTf_2 (1)	5.2	1.5	90	105	10
2	Ru-1 (0.20)	BMIM Ac (1)	5.2	2	90	/	<5
3[c]	Ru-2 (0.15)	Pyrr NTf_2 (1)	26	1	100	90	14
4	Ru-4 (0.05)	Piper NTf_2 (1)	26	1.5	100	150	7

Reactions reproducible within a 10% error. [a] mol% with respect to *i*PrOH. [b] Determined by ^{1}H NMR. [c] With NaOEt (2 eq with respect to Ru-2).

Table 7.1: Overview of the reactivity of Ru-PNP in ILs towards *i*PrOH dehydrogenation.

Later, I have performed a screening of different Ru-PNP using BMMIM NTf_2; the results are summarized in Table 7.2. **Ru-3** did not produce any observable evolution of hydrogen (Entry 5), confirming the detrimental effect of the acetate anion already at catalytic amounts. In agreement with the observations so far, the -Cl catalysts **Ru-MACHO** and **Ru-2** were found to be completely inactive under these reaction conditions (Entries 1,4). **Ru-MACHO-BH** showed 10% conversion and a TOF = 33 (Entry 2). Indeed, as opposed to the chlorido ligand in **Ru-MACHO**, the -HBH_3 group can be removed by heating of the mixture at 90 ºC. Finally, **Ru-1** (2 μmol) afforded 14% conversion of *i*PrOH and a TON of 91 after 2 hours at 90 ºC (Entry 3), while **Ru-4** produced 15% conversion and a TON = 98 under the same conditions. Indeed, it is likely to imagine that both **Ru-1** and **Ru-4** result in the formation of the same species in the presence of IL/iPrOH/H_2. Indeed, overlapping hydride signals at –9.45 ppm show the presence of catalytically active species after the reaction is completed for both **Ru-1** (Figure 7.4) and **Ru-4** (Figure 7.5). **Ru-4** is a highly sensitive catalyst if exposed to air, but it remain stable in the presence of BMMIM NTf_2, confirming the beneficial effect of the IL in stabilizing active species discussed in this text. However, due to the higher instability of **Ru-4**, I have continued the optimization using **Ru-1** and the slightly less active but more robust, **Ru-MACHO-BH**.

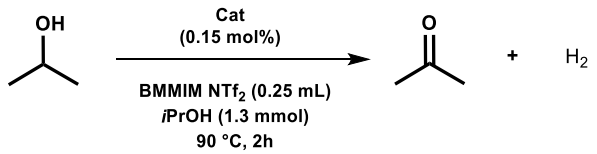

Entry	Catalyst	TON	TOF (h^{-1})	Conversion[a] (%)
1	Ru-MACHO	-	-	<5
2	Ru-MACHO-BH	65	33	10
3	Ru-1	91	55	14
4	Ru-2	-	-	<5
5	Ru-3	-	-	<5
6	Ru-4	98	42	15

Reactions reproducible within a 10% error. [a] Determined by ^{1}H NMR.

Table 7.2: Screening of Ru-PNP catalysts for *i*PrOH dehydrogenation in BMMIM NTf_2.

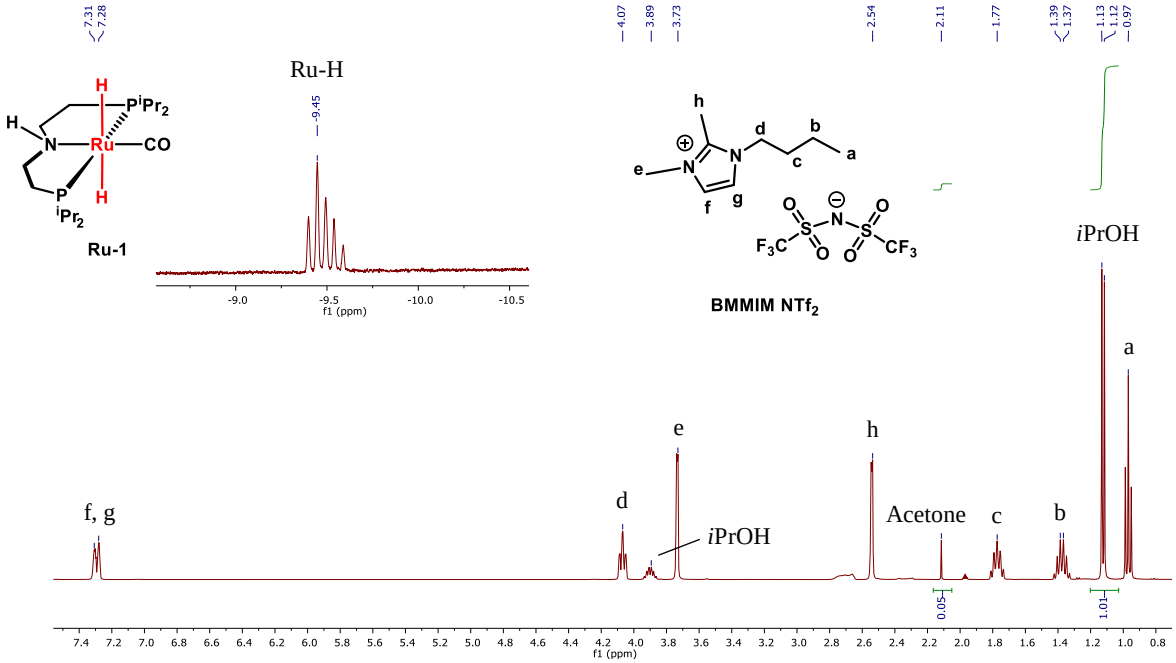

Figure 7.4: ^{1}H NMR spectrum of Ru-1 in BMMIM NTf_2 after *i*PrOH dehydrogenation (CD_3CN, 25 ºC 400 MHz). Reaction conditions in Entry 3, Table 7.2.

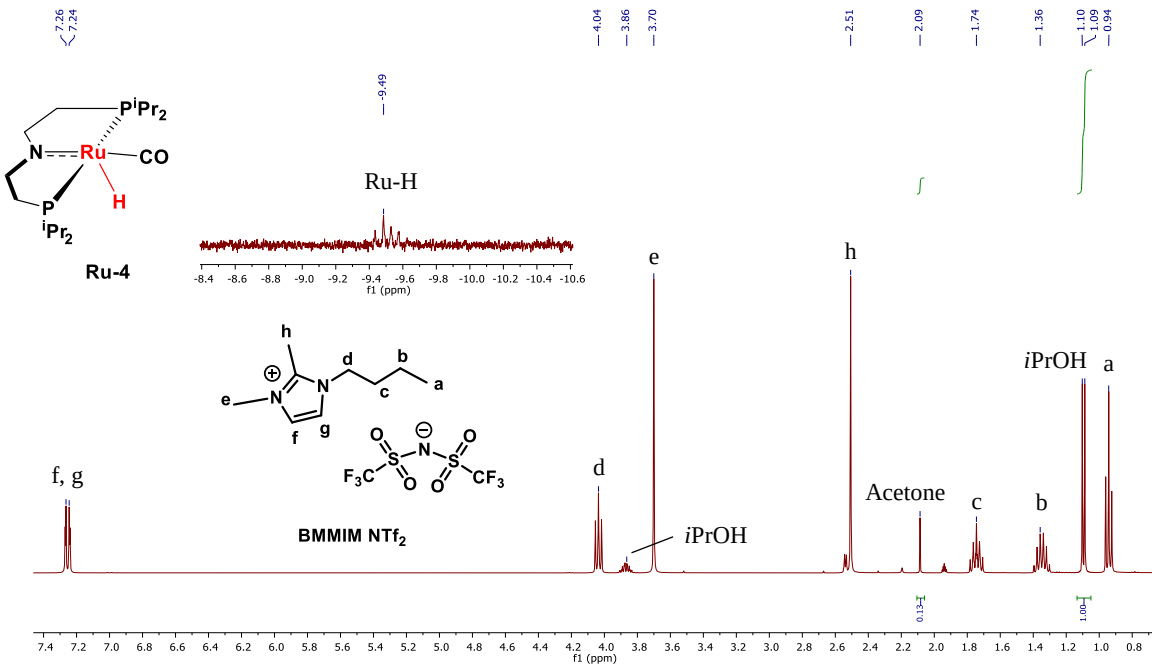

Figure 7.5: ^{1}H NMR spectrum of Ru-4 in BMMIM NTf_2 after *i*PrOH dehydrogenation (CD_3CN, 25 ºC 400 MHz). Reaction conditions in Entry 6, Table 7.2.

Table 7.3 summarizes the optimization of reaction conditions using different NTf_2-based ILs. As a note, the choice of such ILs was justified by the lower viscosity of BMMIM NTf_2 (1.42 g/cm³ at 25 °C) compared to the OTf analogue that has a melting point of 40 ºC (from Iolitec). The opposite is valid for the non-methylated EMIM OTf and EMIM NTf_2: in this case, the viscosity is higher for the NTf_2 (1.52 g/cm³) than the OTf analogue (1.39 g/cm³). However, these ILs were excluded from the optimization due to visible changes in color after catalytic transformations, indicating degradation and/or the presence of carbene species, usually associated with darker shades of orange-brown of the resulting IL mixture. At least from a qualitative point of view, it is possible to observe a very similar behavior between NTf_2 and OTf ILs. Based on these observations, it was a personal choice to continue the optimization using the more stable and practical BMMIM NTf_2, at the same time exploring the use of different cations, as shown in Table 7.3.

Varying the volumetric ratio of IL/*i*PrOH resulted in the same conversion of 10% (Entries 1-3, Table 7.3) indicating that the reaction reaches a thermodynamic plateau. This is also confirmed by the fact that longer reaction times does not lead to increased *i*PrOH consumption; in the experiment showed in Entry 4, Table 7.3, the same conversion (8%) was measured after 5, 10 and 20 minutes and did not improve after prolonged times. The higher catalyst loading used in this experiment might render the reverse acetone hydrogenation even more competitive. In addition, it is possible to notice that the gas evolution is visible only in the first minutes after *i*PrOH is added. I have decided to continue the optimization using an IL/iPrOH ratio of 0.5 that allows for higher turnover numbers (Entry 2), while higher IL/iPrOH ratios seem to decrease catalytic activity. Increasing the temperature from 90 to 120 ºC led to higher conversion (15%) and a TON = 85 (Entry 5). The IL cation seems to have a small influence on the catalytic activities; the saturated pyrrolidinium and piperidinium gave superior results compared to the imidazolium IL (Entries 2, 6, 7), in the order Piper > Pyrr > BMMIM. Even under optimized conditions, it was not possible to increase the conversion of iPrOH above 25%

(Entry 8). Finally, decreasing the catalyst loading to 0.05 mol% provided the best TON = 380 (TOF = 190 h^{-1}) at 100 ºC after 2 hours using Piper NTf_2 (Entry 9).

Entry	Catalyst (mol%[a])	Ionic liquid	*i*PrOH (mmol)	IL (mL)	IL/*i*PrOH (v/v)	Time (h)	T (ºC)	TON	Conversion[b] [%]
1	Ru-1 (0.20)	BMMIM NTf_2	13	1	1	1.5	90	60	10
2	Ru-1 (0.10)	BMMIM NTf_2	26	1	0.5	1.5	90	114	11
3	Ru-1 (0.35)	BMMIM NTf_2	13	2	2	1	90	25	10
4	Ru-1 (1.20)	BMMIM NTf_2	1.3	0.5	5	0.3	90	6	8
5	Ru-1 (0.20)	BMMIM NTf_2	13	1	1	2	120	85	15
6	Ru-1 (0.15)	Pyrr NTf_2	26	1	0.5	2	100	160	23
7	Ru-1 (0.12)	Piper NTf_2	26	1	0.5	1	100	180	21
8	Ru-1 (0.14)	Piper NTf_2	26	1	0.5	18	100	170	23
9	Ru-1 (0.05)	Piper NTf_2	26	1	0.5	2	100	380	19
10	Ru-MACHO-BH (0.15)	Pyrr NTf_2	26	1	0.5	2	100	70	10
11	Ru-MACHO-BH (0.20)	P_{1444} NTf_2	26	1	0.5	2	110	68	13

Reactions reproducible within a 10% error. [a] Mol% with respect to *i*PrOH. [b] Determined by ^{1}NMR.

Table 7.3: Optimization of *i*PrOH dehydrogenation under batch conditions.

Ru-MACHO-BH was also active in the presence of Pyrr NTf_2 and P_{1444} NTf_2, affording a TON of 70 and 68, respectively, after 2 hours (Entries 9 and 10). Also in this case, I have not carried out detailed stability studies but only observing at hydride signals in solution by NMR, it is possible to notice a higher stability of ^{Ph}PNP ligands compared to ^{iPr}PNP analogues. Indeed, **Ru-MACHO-BH** will perform much better under flow conditions, while **Ru-1** will show no visible catalytic activity. However, this is not surprising considering the observed higher stability of ^{Ph}PNP over ^{iPr}PNP ligands throughout this whole dissertation.

Overall, the batch experiments demonstrated that the system Ru-PNP/IL is active for *i*PrOH dehydrogenation at T<120 ºC, reaching equilibrium plateaus that was not possible to overcome. Therefore, I have transferred the most active combinations of Ru-PNP/ILs to the SILP technology for *i*PrOH dehydrogenation under continuous flow conditions.

7.2.2 Continuous flow

In a preliminary experiment, I have prepared a SILP material using **Ru-1** (Ru/SiO_2 = 0.25 wt%), BMMIM NTf_2 and the mesoporous silica 100 as the support material (see Appendix D for BET data). The SILP were tested in the demonstrative set-up showed in the experimental section (Figure 2.6). Gladly, low concentrations of H_2 were observed via MicroGC, confirming *i*PrOH dehydrogenation occurring under flow conditions. A similar experiment was conducted using a SILP catalyst with **Ru-MACHO-BH** instead of **Ru-1**. Similarly, H_2 (5-10 vol% in N_2) was observed in the gas phase by MicroGC. The combination of both batch and flow experiments allowed me to prepare selected SILP materials to be tested in my external stay at FAU University in Erlangen. In detail, I have prepared a number of SILP materials using **Ru-1** and **Ru-MACHO-BH** as the catalysts, Piper NTf_2 as the IL, and screened different Ru/SiO_2 wt% ratios using the mesoporous silica 100 and silica 60 (measured by BET analysis, see Appendix D). I have chosen the percentage of volumetric pore filling (α) to be consistently 20% for all the samples to avoid overfilling and saturation of the pores, as usually done for this type of materials [209]. Table 7.4 shows an overview of the so-prepared SILP catalysts. The percentage of pore filling was measured as follows:

$$\alpha = \frac{m_{IL}/\rho_{IL}}{m_{SiO_2} * Pore\ Vol_{SiO_2}} \qquad (1)$$

Catalyst	silica 100 Ru/SiO_2 wt%	silica 60 Ru/SiO_2 wt%
	~~0,5~~	~~0,35~~
Ru-1	~~1~~	~~0,1~~
	~~0,1~~	~~0,91~~
	0,5	~~0,1~~
Ru-MACHO-BH	**1**	**0,87**
	~~0,1~~	-

Table 7.4: Screening of SILP catalysts for initial tests in fixed-bed reactor at FAU. The SILP catalysts were prepared by wet impregnation as described in chapter 7.3 using Piper NTf_2 (α = 20%). The SILP catalysts that showed activity under continuous flow fixed-bed conditions are shown in red.

The catalytic tests were carried out in a fixed-bed reactor equipped with a MicroGC for the analysis of the gaseous products (see section 7.3 for details and schematic representation of the reaction set-up). I would like to express my gratitude to PhD student Melanie Eßl for training and assistance while using the reactor set-up she designed and optimized during her PhD studies. She also carried out extremely useful experiments after I left Erlangen, providing even more insights for the work that is described here. In addition, she contributed with most of the plots that are shown in this section. Curiously, her project also dealt with the continuous flow of *i*PrOH, but catalyzed by heterogeneous catalysts at higher temperatures than those presented in this study.

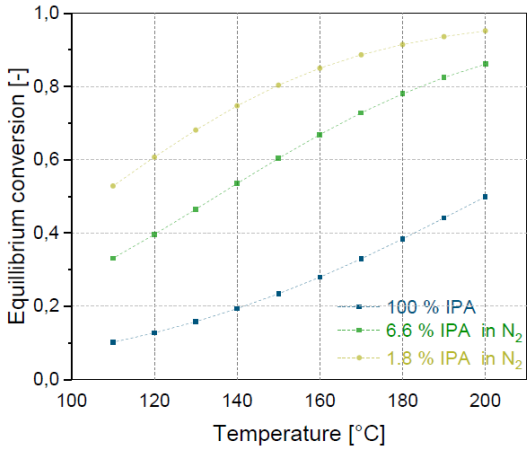

Figure 7.6: Thermodynamic equilibrium conversion vs temperature at different *i*PrOH dilutions in N_2 (provided by FAU).

Opposed to the previous findings in batch conditions, **Ru-1** was inactive when exposed to a gaseous *i*PrOH feed (Table 7.4). Probably, the complex deactivates during the manipulations (placing of the SILP in the catalytic bed, flushing and heating up of the reactor) before the actual reaction starts. On the contrary, the SILP materials containing **Ru-MACHO-BH** (in Ru/SiO_2 ratios >0.5 wt%) produced a stable flow of hydrogen, with the conversion of *i*PrOH that follows the temperature profile in the reactor, very close to the calculated equilibrium conversion during the initial times of reaction. In this regard, Figure 7.6 was provided by FAU and shows the different *i*PrOH conversions that is possible to obtain at different temperatures and *i*PrOH dilutions in N_2. As will be described in this section, continuous flow reactions carried out with diluted *i*PrOH feed shows very poor hydrogen evolution, likely explained by too high dilution of *i*PrOH and too small size of the catalytic bed. Hence, I have used undiluted *i*PrOH for most of the following experiments. Figure 7.6 shows that the expectable conversion at the temperatures used in this study (90-130 ºC) is between 5-15%.

Figure 7.7 shows the conversion profile of an experiment using a SILP catalyst containing **Ru-MACHO-BH** (1 wt% Ru/SiO_2), Piper NTf_2 (α=20% as for all the tested SILPs) and silica 100 as the support. The conversion varies from 3 to 15% according to the changes in temperature, with a selectivity >95% towards hydrogen and acetone and no quantifiable by-products. However, when the temperature was increased again, the conversion did not reach the initial values indicating some degree of deactivation of the SILP catalyst. The same material was reused in a second experiment after simple storage at ambient conditions exhibiting a substantial loss of activity, as shown in Figure 7.7c. A similar deactivation pattern was observed using a SILP catalyst with Ru/SiO_2 = 0.5% with otherwise identical composition (Figure D.3).

Keeping the temperature stable at 110 ºC leads to a similar deactivation profile as the one observed in the temperature ramp experiments, in the presence of both silica 60 and silica 100 (Figure 7.8 for silica 60). It is clear that both supports are suitable for this transformation; however, I have decided to continue the screening using silica 100 that possesses bigger pore size and volume, which should allow easier gas diffusion through the catalyst phase, and lower degree of condensation and accumulation of *i*PrOH and/or impurities in the catalytic bed. In fact, this aspect can explain the higher degree of scattering of data points observed in the experiments with silica 60 due to easier clogging of the pores and/or local condensation of *i*PrOH.

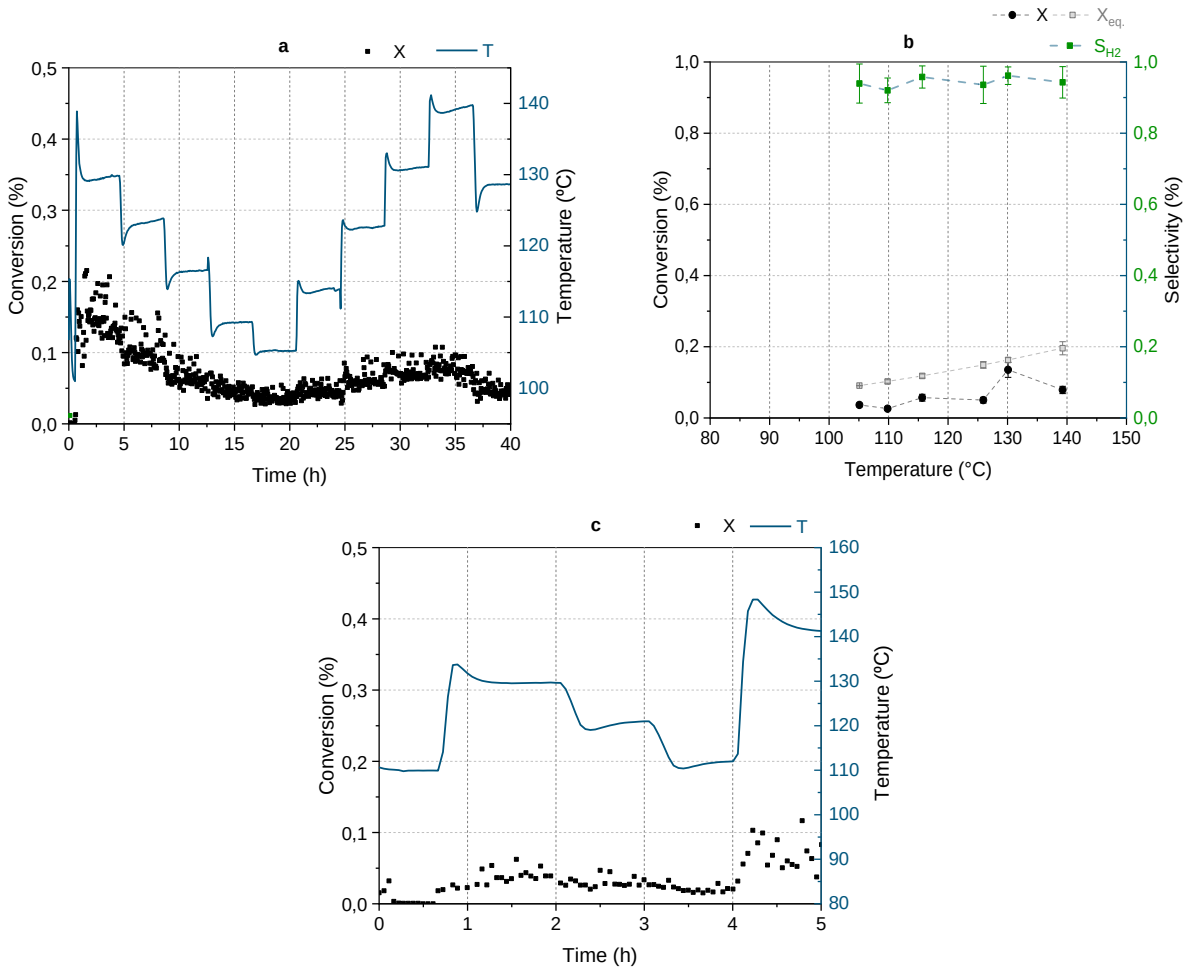

Figure 7.7: Continuous flow *i*PrOH dehydrogenation; Ru-MACHO-BH/SiO_2 (1 wt%), Piper NTf_2 (α = 20%), silica 100.

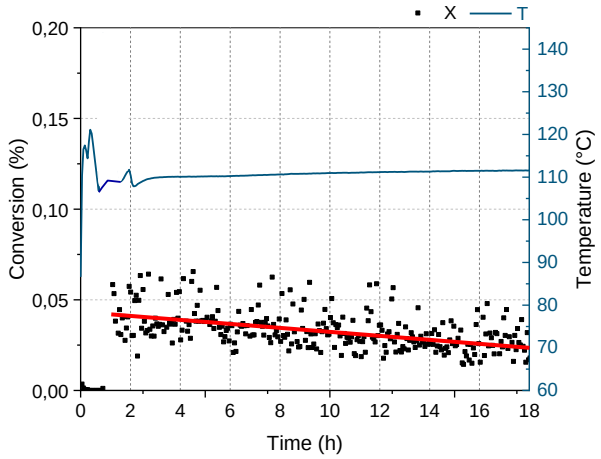

Figure 7.8: Continuous flow *i*PrOH dehydrogenation; Ru-MACHO-BH/SiO_2 = 0.9 wt%, Piper NTf_2 (α = 20%), silica 60. The red line highlights the deactivation profile observed in all the experiments.

Based on these initial testing, I have synthetized more SILP materials during my stay FAU, and screened different bistriflimide ILs varying the cation. In fact, such perturbations can influence parameters such as space occupation, wettability and viscosity of the IL phase in the SILP material. Hence, I have tested BMMIM NTf_2, Pyrr NTf_2 and P_{1444} NTf_2; no clear influence of the cation on the catalytic activity was observed under experimental conditions (Figure D.4).

Later, I have attempted to assess the robustness of the system by feeding a mixture of 25 vol% acetone in *i*PrOH with the purpose of simulating operative conditions where unconverted *i*PrOH is recycled with the presence of acetone in the feed (see Figure 8.4, Chapter 8). As expected, the SILP catalyst with Ru/SiO_2 = 1 wt% and P_{1444} NTf_2 resulted in poorer activity compared to a pure *i*PrOH feed; however, the system was still able to release hydrogen from *i*PrOH, with a stable conversion of 5-7% at 110-130 ºC over 18 hours of experiment (Figure D.5).

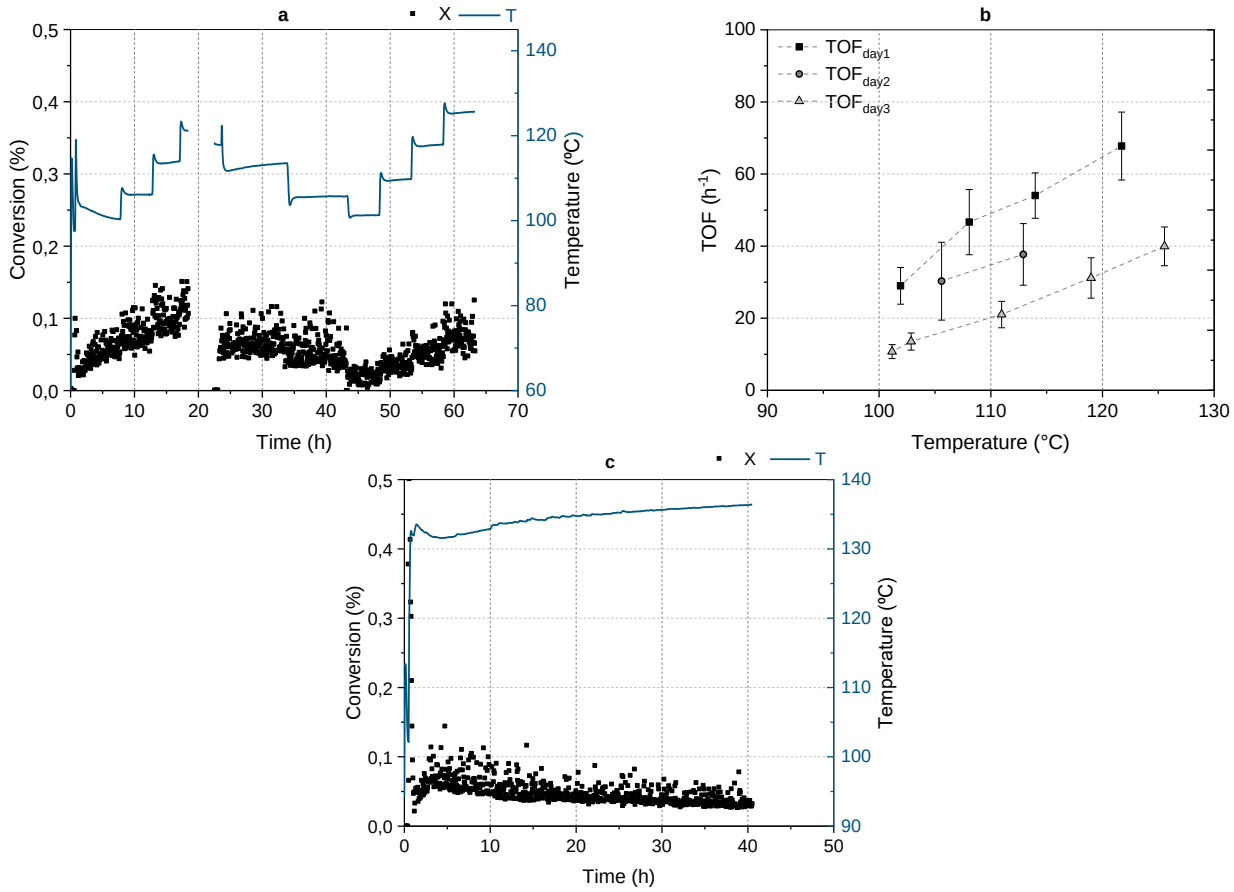

Figure 7.9: Continuous flow *i*PrOH dehydrogenation. a) in the missing space the catalyst was exposed to 25% acetone in *i*PrOH. b) TOF measured at different temperatures over the 3 days of reaction. c) Experiment after 2 months. Ru-MACHO-BH/SiO_2 = 0.9 wt%, P_{1444} NTf_2 (α = 20%), silica 100.

In a following experiment, 4g of the SILP catalyst (Ru/SiO_2 = 0.9 wt%, P_{1444} NTf_2, silica 100) were diluted with 1g of silica 100 to ensure maximum dispersion of the catalytic active phase. The SILP was exposed to changes in temperature and reaction conditions and the reactor stopped overnight for two times over 3 days (Figure 7.9). As shown in Figure 7.9b, it is possible to observe a consistent decrease in the turnover frequencies achieved by the catalyst over the 3 days, with a deactivation profile that

seems to be independent from the different temperatures and reaction conditions used. Nevertheless, in the first 20 h of reaction, the system shows high selectivity and conversion values that are very close to the calculated equilibrium (Figure D.6), affording a maximum turnover frequency of 70 h^{-1} at 120 ºC (Figure 7.9b). In Figure 7.9c, the same SILP catalyst was reused in a second experiment after 2 months of simple storage at ambient conditions. The system was stable for up to 40 h at 130 ºC, showing that catalytic activity is not fully lost. The TOF values were calculated as follows:

$$TOF = \frac{X_{IPA} * \dot{n}_{\text{iPrOH}}}{n_{catalyst}} \qquad (2)$$

In a final long-term experiment, a SILP catalyst containing **Ru-MACHO-BH** (Ru/SiO_2 = 1%), P_{1444} NTf_2 and silica 100 was exposed to changes in temperature, different dilutions of *i*PrOH in N_2, as well as to a 25 vol% acetone/ *i*PrOH mixture as the feed (Figure 7.10). The *i*PrOH feed was diluted with N_2 (80 vol% of *i*PrOH in N_2) to prevent condensation and accumulation of *i*PrOH in the catalytic bed, a potential cause of the decreased activity. Also in this case, the deactivation profile (red line in Figure 7.10) seems to be independent of the different reaction conditions.

Dilution of *i*PrOH with N_2 did not lead to any observable effect on the catalytic activity and stability. In fact, when comparing two experiments using the same catalyst but different dilutions (40 and 80 vol% of *i*PrOH in N_2), similar deactivation profiles occur. The same behavior was observed during acetone dilution (pink bar) and temperature variation (orange bar) experiments, with a consistent decrease in activity that is largely independent of the reaction conditions. Appendix D provides more data related to this experiments in terms of turnover frequency over the 100 hours of reaction (Figure D.7), acetone (Figure D.8) and *i*PrOH dilution (Figure D.9), as well as temperature effect. From basic kinetic calculations, it was possible to deduct that the reaction follows a first order kinetic profile, as shown in Figure 7.11. The calculated activation energy at 80 vol% of *i*PrOH in N_2 was 53.45 KJ/mol.

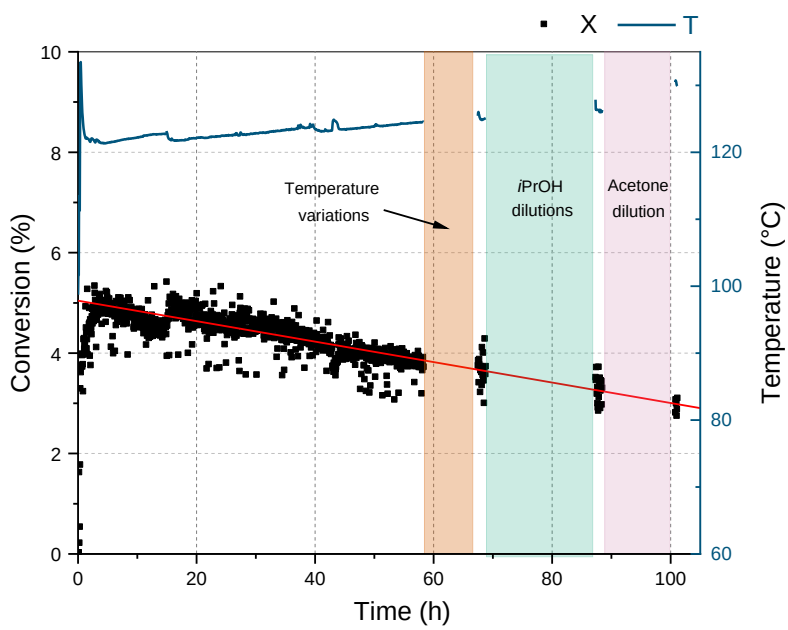

Figure 7.10: Continuous flow *i*PrOH dehydrogenation, long time experiment; Ru-MACHO-BH/SiO_2 = 1 wt%, P_{1444} NTf_2 (α = 20%), silica 100.

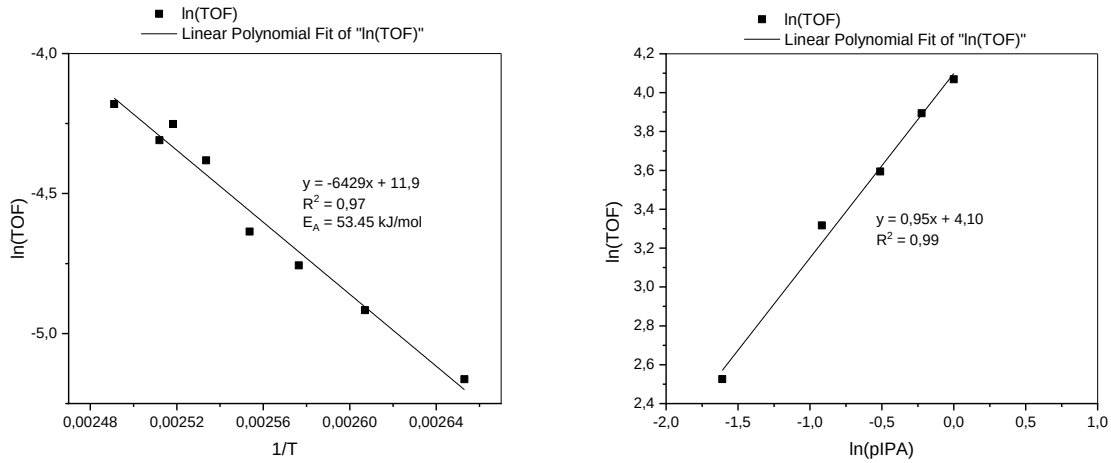

$$\ln(TOF) = \ln(C) + n * \ln(p_{IPA})^2 \qquad (3)$$

$$\ln(TOF) = \ln(C) - \frac{E_a}{RT} \qquad (4)$$

Figure 7.11: Kinetic calculations performed using data from the experiment described in Figure 7.10. Thanks to PhD student Melanie Eßl at FAU.

All of the tested SILP materials (initially white) turned brown after catalytic tests in the reactor tube or if exposed in air for long times, indicating degradation of the IL and/or the catalyst. After extraction of the catalyst/IL phase from the exhaust SILP catalysts with DCM, ^{1}NMR analysis shows the presence of *i*PrOH, acetone and H_2O. These substances may well clog the pores of the porous support, resulting in decreased activity over time, even with possible formation of inactive ruthenium species (Figure 7.12).

I have performed NMR studies in solution to elucidate the stability and possible deactivation explanations of the mixture **Ru-MACHO-BH** and P_{1444} NTf_2. As discussed in Figures 3.18-3.20 in Chapter 3, the corresponding signals of **Ru-MACHO-BH** are still detectable after addition of both P_{1444} NTf_2 and *i*PrOH. Therefore, I have conducted more NMR analysis after extracting the catalytic active phase from a freshly prepared SILP using dry DCM. Figure 7.13 shows the ^{1}H NMR of the extracted Ru-SILP catalyst used under continuous flow conditions containing **Ru-MACHO-BH** and P_{1444} NTf_2. It is possible to observe Ru-H signals indicating the presence of catalytically active species. The same is visible in Figure 7.14, where the ^{1}H NMR spectrum of **Ru-MACHO-BH** (down) is staggered with an extracted (not used) SILP material prepared with P_{1444} NTf_2. Similar to the used SILP, the extracted phase shows the presence of hydride signals. At least from a qualitative point of view, degradation of the aromatic pincer structure might occur, as indicated by the presence of newly formed peaks at 7.1-7.3 ppm.

It has to be noted that commercial grade *i*PrOH without prior purification was used as a feed, which can lead to accumulation of impurities, as well as H_2O, over extended reaction times. In addition to mechanical stress causing leaching of the IL at high gas flows, probably not all the Ru-PNP catalyst is fully dispersed and homogenized in the IL phase. Indeed, the catalytic activity is not fully lost after 100 hours on stream, indicating that part of the homogeneous system is still active, as corroborated by the extracted IL phase containing Ru-H signals.

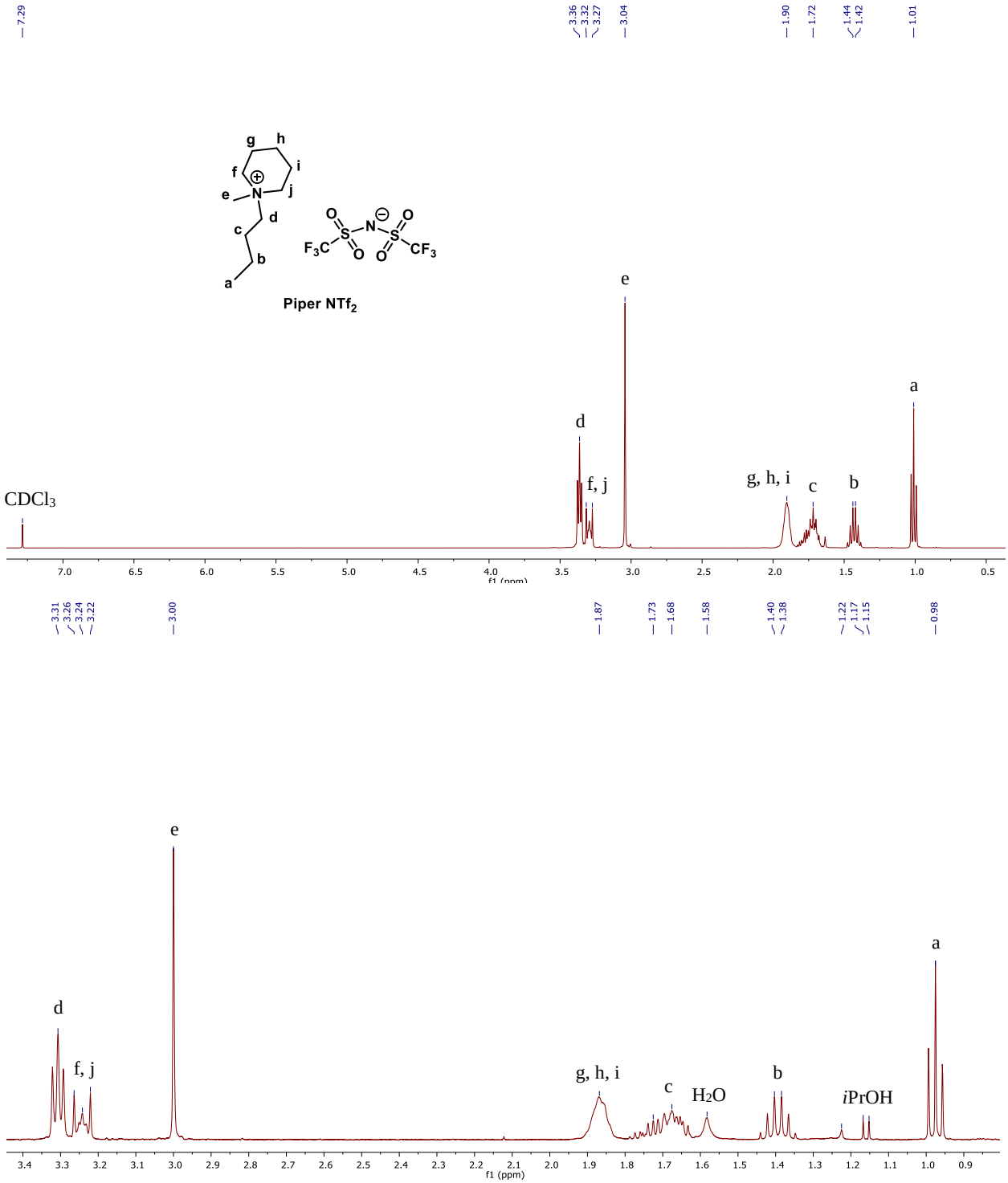

Figure 7.12: ^{1}H NMR spectra of Piper NTf_2 as reference (up) and the extracted SILP catalyst (down) after reaction in the fixed-bed reactor ($CDCl_3$, 25 ^{o}C 400 MHz). Ru-MACHO-BH/SiO_2 = 1 wt%, Piper NTf_2 (α = 20%), silica 100.

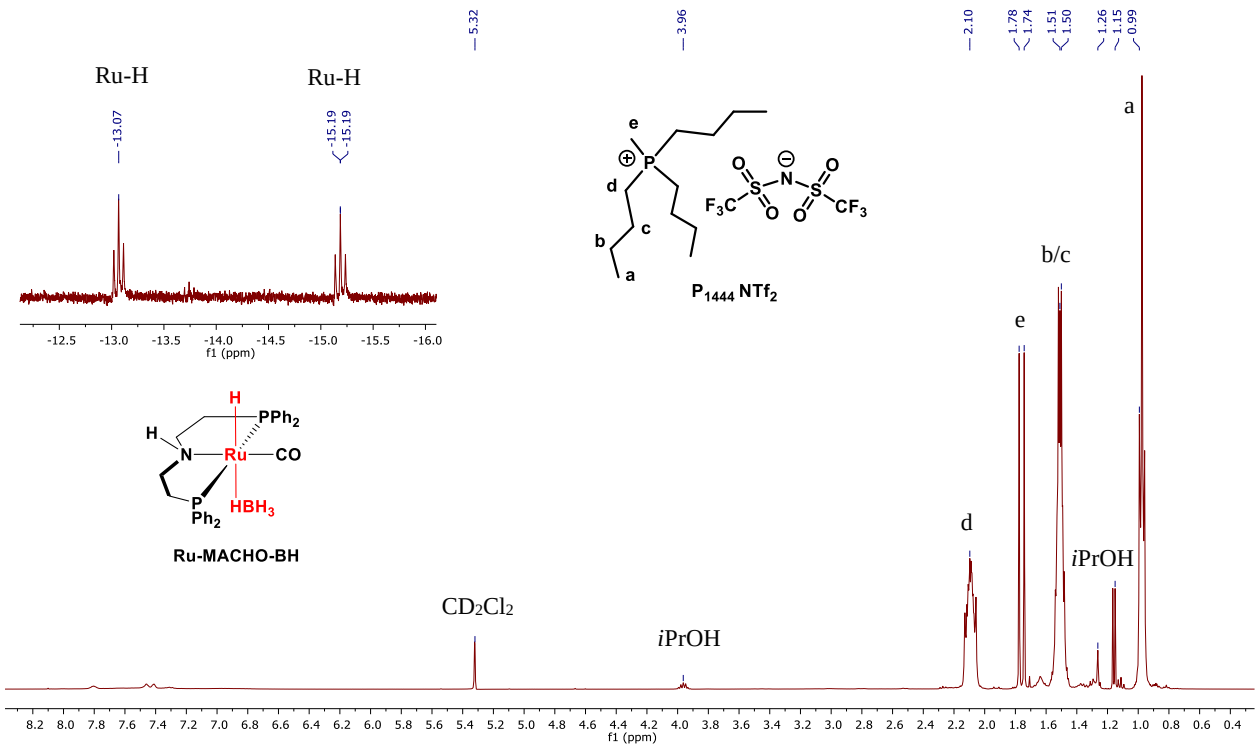

Figure 7.13: ^{1}H NMR analysis of the extract solution from a SILP sample used in the fixed-bed reactor. Ru-MACHO-BH/SiO_2 = 1 wt%, P_{1444} NTf_2 (α = 20%), silica 100 (*d*-DCM, 25 °C, 400 MHz).

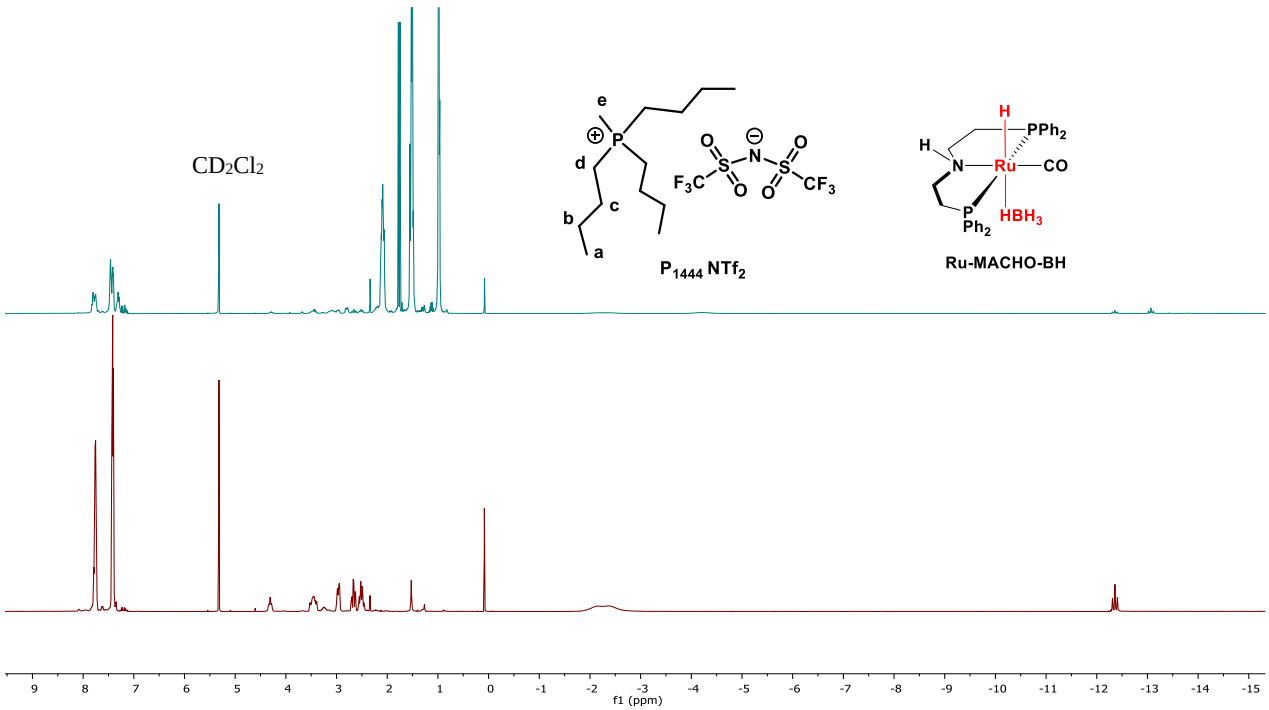

Figure 7.14: ^{1}H NMR of Ru-MACHO-BH in *d*-DCM (down) staggered with a solution of a fresh SILP catalyst that was extracted in *d*-DCM (up). Extracted SILP: Ru-MACHO-BH/SiO_2 = 1 wt%, P_{1444} NTf_2 (α = 20%), silica 100 (*d*-DCM, 25 °C, 400 MHz).

Later, I have investigated the use of solid-state ^{29}Si, ^{31}P, and ^{13}C NMR spectroscopy for the characterization of both fresh and spent SILP materials (reference ^{13}C and ^{31}P NMR spectra of the used P_{1444} NTf_2 are provided in Appendix D, Figure D.11). The experiments were possible thanks to the kind contribution of Kasper Enemark-Rasmussen who analyzed the SILP materials I provided, and helped me with the interpretation of the obtained spectra (see Appendix D for experimental details of the ssNMR analysis).

The ^{29}Si ssNMR spectra for the fresh and spent SILP samples appear very similar, showing that the overall silicate support structure remained intact after catalytic dehydrogenation (Figure 7.15). From a qualitative point of view, the ^{29}Si spectrum for the used catalysts shows a slight reduced intensity around -100 to -105 ppm, indicating a lower amount of superficial Si-OH species. It has to be noted that storage of the used materials under ambient conditions might lead to accumulation of water over time. In fact, such experiments were conducted after many months after use of the SILPs in Germany.

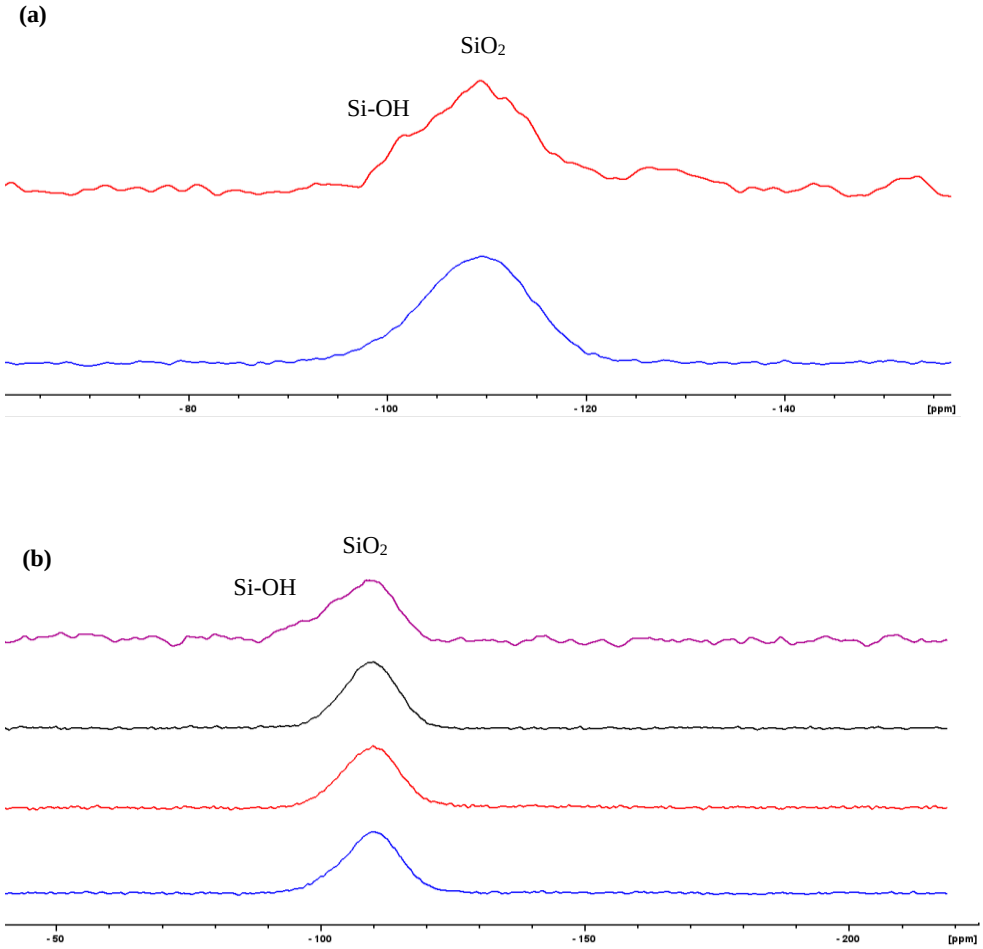

Figure 7.15: (a) ^{29}Si ssNMR spectra of fresh SILP (red line) and used SILP (blue line). (b) ^{29}Si NMR spectra of fresh SILP (purple line) and used SILPs (blue, red and black lines). Ru-MACHO-BH/SiO_2 = 1 wt%, P_{1444} NTf_2 (α = 20%), silica 100 for all the samples.

The ^{13}C ssNMR spectrum for the used SILP sample shows the presence of more signals at 64-67 ppm and 24 ppm compared to the fresh SILP (Figure 7.16a). Both signals can be attributed to the presence of iPrOH trapped in the SILP catalyst after use, thus providing a plausible explanation for the observed (decreasing) activity over time due to clogging of the pores. This behavior appears even clearer from Figure 7.16b: the purple line indicates the fresh SILP as the reference, while the three lines below are the ^{13}C spectra of used SILP in the reactor under different isopropanol dilution in nitrogen.

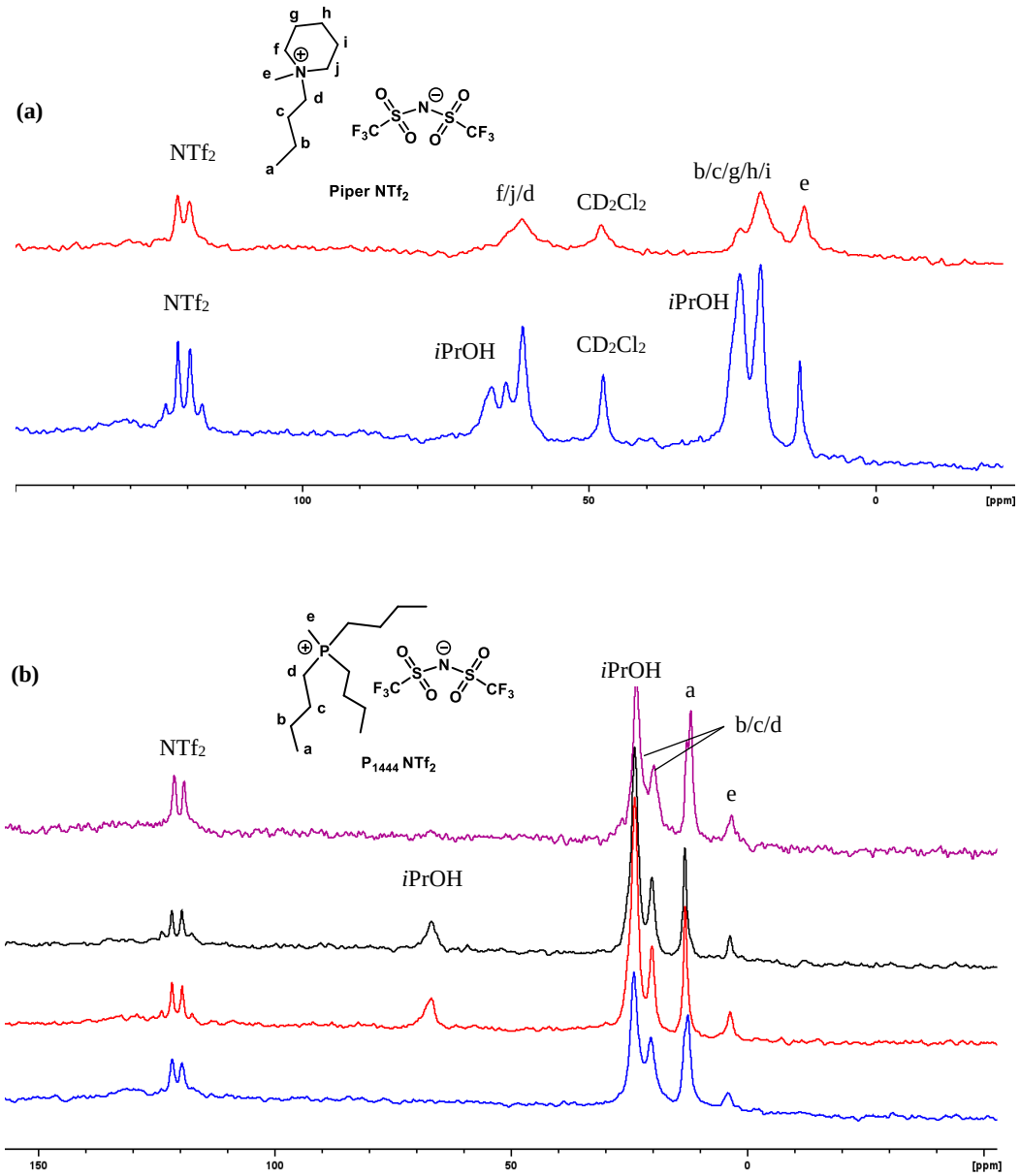

Figure 7.16: (a) ^{13}C ssNMR spectra of fresh SILP (red line) and used SILP (blue line). The presence of DCM can be explained by the synthesis procedure of SILP catalysts (see 7.3). (b) ^{13}C NMR spectra of fresh SILP (purple line) and used SILP (blue, red and black lines) under different reaction conditions. Ru-MACHO-BH/SiO_2 = 1 wt%, P_{1444} NTf_2 (α = 20%), silica 100 for all the samples.

In particular, it is possible to notice that the sample represented by the blue line shows a lower degree of *i*PrOH accumulated. This is easily explained by the fact that this experiment was conducted for shorter times (24 h) using a 40% *i*PrOH in N_2 feed solution, resulting in a lower propensity towards *i*PrOH condensation in the catalytic bed. However, as already described before, diluting the *i*PrOH is not beneficial in the long term; in fact, the red line represents another experiment, also using 40% *i*PrOH but for longer times (40 h). Finally, the black like shows the SILP catalyst used in the long-term experiment depicted in Figure 7.10, where besides *i*PrOH dilutions (green bar in Figure 7.10) the system was tested using 80% *i*PrOH in N_2. Importantly, the signals at 120 ppm (NTf_2), as well as the multiple signals at 0-30 ppm (P_{1444}) indicate that no visible degradation occurred to the IL (as also observed in the NMR analysis in solution showed before).

Finally, the ^{31}P NMR spectra in Figure 7.17 for the fresh and spent SILPs contain similar signal intensities in the same chemical shift region (see Appendix D for ^{31}P NMR spectrum of P_{1444} NTf_2). From a qualitative point of view, the spent SILP results in a more broad and featureless spectrum. However, it is not possible to derive more detailed conclusion based on phosphorous NMR analysis being the the IL´s signals very intense and close to each other.

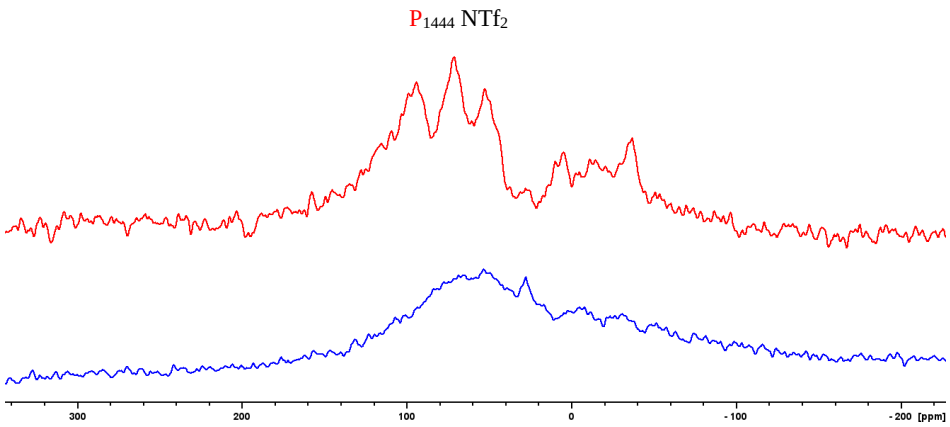

Figure 7.17: ^{31}P ssNMR spectra of fresh SILP (red line) and used SILP (blue line). Ru-MACHO-BH/SiO_2 = 1 wt%, P_{1444} NTf_2 (α = 20%), silica 100.

Very recently, in collaboration with postdoc Maria Padilla, we are exploring the possibility to perform attenuated-total-reflectance (ATR) Fourier Transform infrared (FTIR) studies thanks to the equipment gently provided by Prof René Wugt Larsen at DTU Chemistry. This is a particularly useful technique since it allows the observation of signals that are directly associated with the used catalysts, such as the $–HBH_3$ and the CO ligands in the case of **Ru-MACHO-BH**. Future investigations in this sense could elucidate the nature of the interactions involved between catalyst, IL and support, as well as provide an explanation for possible deactivation pathways.

BET analysis did not provide particularly useful information concerning possible deactivation causes. The differences in pore size and pore volumes between fresh and used SILPs is negligible and does not indicate a substantial clogging of the pores (see Table D.1, Appendix D). Similarly, TGA analysis shows a constant loss in weight when the SILP catalyst is kept at 120 ºC for 16 hours. The loss in weight is relatively small (0.15 mg) and does not explain the catalytic behavior (Figure D.14, Appendix D).

7.3 Experimental part

Procedure for batch isopropanol dehydrogenation

In a typical experiment, the desired amount of catalyst was scaled in a glove box and transferred in a dry two-neck flask. Later, the IL was added and the resulting mixture stirred while heating to the desired temperature until full catalyst dissolution. Finally, anhydrous *i*PrOH was added by means of a syringe in the reaction flask that was set under refluxing conditions with a gentle argon flow to facilitate hydrogen release from the IL. After the reaction was completed, the solution was cooled to room temperature and a sample was taken for NMR analysis for the quantification of the acetone produced.

Preparation of SILP catalysts

All manipulations were performed under Schlenk conditions. The silica precursor was calcined at 600ºC overnight and stored in a glove box. The SILP catalysts were prepared by dissolving the desired amounts of catalyst (Ru/SiO_2) in dry dichloromethane. Later, the ionic liquid was added and the mixture stirred for 10 minutes to allow full catalyst solubility. The support material is then added to the mixture under vigorous stirring for not more than 20 minutes, in order to avoid mechanical stress on the support material. Finally, the solvent is evaporated under vacuum and the SILP material is stored in a glove box until catalytic use.

Continuous gas-phase reactor setup

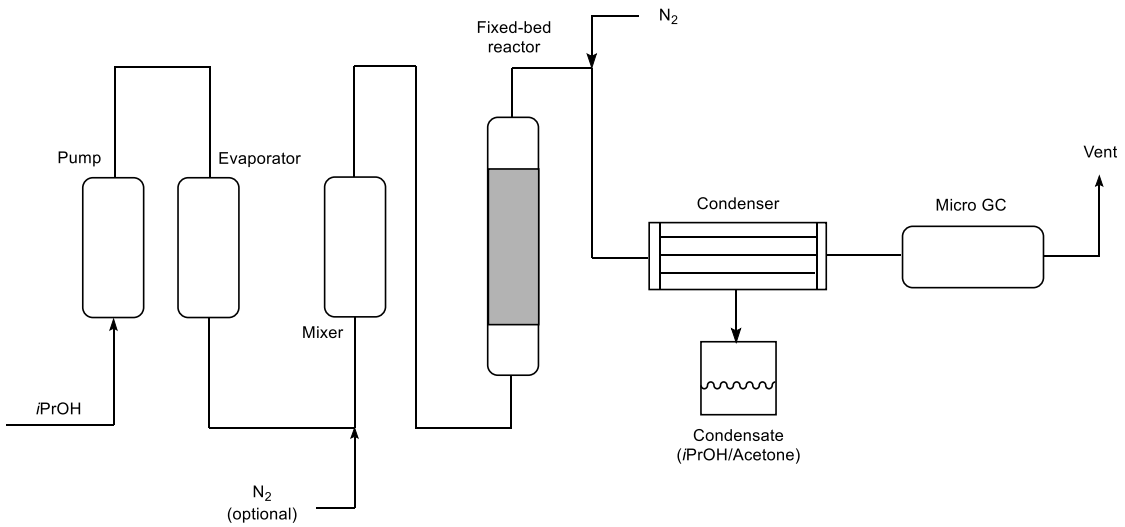

Figure 7.18: Schematic representation of the fixed-bed reactor used at FAU for continuous flow dehydrogenation of *i*PrOH using Ru-SILP catalysts.

The continuous gas-phase *i*PrOH dehydrogenation experiments were conducted the fixed bed reactor set-up available at FAU, of which Figure 7.18 provides a schematic representation. The liquid substrate *i*PrOH was pumped by means of a Techlab HPLC pump and delivered to an Adrop vaporizer. N_2 was used to flush the system during heating of the pipes/reactor or to dilute the *i*PrOH feed when needed. The temperature of the pipes was set at T>120 ºC (and T = 150º in the downstream line) in order to avoid *i*PrOH condensation. However, it was possible to observe fluctuations in the amounts of acetone and *i*PrOH recorded by the

MicroGC, indicating possible creation of *i*PrOH droplets. A temperature gradient between the set temperature and the measured value was always ≈20-30 ºC, due to heat dissipation. A total of five thermocouples controlled the temperature in different parts of the reactor, in particular one in the upstream line, three in the reactor tube, and one in the downstream line. After the reactor, the gas steam was passed through a condenser and the vapor phase continuously analyzed by MicroGC to quantify the H_2, acetone and *i*PrOH volumetric content in the gas phase. The reactor column consisted in a 50x3.3 cm glass tube filled with glass spheres to facilitate gas mixing. The SILP material was placed in the middle of the column between two glass-fiber disks, hence with tunable thickness of the resulting catalytic bed (2-4 cm i.e. 2-5 g of SILP). In some experiments, the prepared SILP materials were diluted with silica to increase the size of the catalytic bed and disperse the catalytically active phase on a larger support area.

7.4 Summary

In conclusion, I have demonstrated a rare example of gas-phase *i*PrOH dehydrogenation using a homogeneous organometallic complex at low temperatures (<120 ºC). Remarkably, the system operates very closely to the upper limit of equilibrium conversion dictated by the universal law of thermodynamics (approximately 8% conversion at 100 ºC). It was possible to start/pause the system, and the catalyst retained its activity when feeding *i*PrOH at different concentrations, as well as in the presence of the by-product acetone. These results are crucial for proving the application feasibility of such system since they model real-life conditions of hydrogen vehicles. Moreover, I have performed several analytic investigations on the used SILP materials that showed how the catalytic active species remains active after 2 months of simple storage at ambient conditions.

It has been demonstrated that thermally activated Ru-PNP catalysts work under the reaction conditions used in this study. The resulting stability of such complexes under fixed-bed conditions due to the beneficial effect of the IL represents a promising starting point for further optimization. The observed differences between batch and flow conditions indicate a synergistic effect of Ru-PNP, IL and support material on the final catalytic performance of such mixtures. In fact, this preliminary study opens up for further optimization concerning every single component (catalyst, IL and support) of such SILP materials for dehydrogenation reactions at mild conditions. Changes in SILP composition (catalyst and IL loading, support nature and porosity), anchoring of the catalyst/IL to the support covalently (Figure 7.2), as well as modifications of the PNP pincer and/or addition of a co-catalyst, represent examples for future screening and optimization. Equally important is the in-depth study of reaction parameters such as gas velocity in the reactor, size of the catalytic bed, mass transport and gas diffusion phenomena within the SILP catalyst, and influence of temperature, pressure, *i*PrOH dilution etc. In fact, *i*PrOH condensation and accumulation in the SILP material is likely the main cause of the (partial) observed deactivation profile. Therefore, it is possible to imagine structural modifications of catalytic bed, reactor size and shape, as well as a more efficient heating system to ensure that the reaction is carried out exclusively in the gas phase.

Usually, degradation of the homogeneous catalyst under operative conditions, as well as leaching of IL/cat outside of the support material are the main drawbacks involved when using SILP and other supported technologies. Indeed, they could both explain the deactivation profile observed in long-term experiments (together clogging of the pores due to condensation). Nevertheless, I would like to remark that the observed drop in activity in not complete. Longer time reactions might demonstrate that the catalytic activity is retained to a certain level, and eventually kept for longer reaction times than those used in this work. Promising indications in this sense are provided by the long-term experiment in Figure 7.10 as well as the recycle experiment after storage under air in Figure 7.8c. In this regard, I have attempted to provide an explanation to the observed deactivation of the Ru-SILP catalysts using

several techniques such as solution and solid state NMR, IR, TGA, and BET. Indeed, NMR spectroscopy clearly shows the presence of active Ru-H species after reactions under continuous flow conditions. Overall, the successful optimization of a SILP-catalyzed dehydrogenation of isopropanol (and other LOHCs) can be a key step towards the consolidation of the LOHC technology applied to the transportation sector.

8. Main Conclusions and perspectives

In conclusion, I have demonstrated that the combination of Ru-PNP complexes and ILs represent a powerful tool to be used in relevant transformations within sustainable catalysis, particularly for hydrogenation and dehydrogenation reactions. In this dissertation, I have attempted to provide a full overview of the potential of such system, from fundamental studies of basic reactivity between Ru-PNP and ILs, up to concrete potential industrial applications. In addition, I have tried to provide an overview of the current employed methods with associated drawbacks and challenges, as well as future perspectives for hydrogen-related technologies.

In Chapter 3, I have set the bases for the catalytic applications of the Ru-PNP/IL system described in the following chapters, showing how such a "simple" combination can lead to many possible catalytic processes. It has been hypothesized and later confirmed that the IL can act as a solvent and at the same time perform the activation step usually required in the presence of Ru-PNP complexes. Indeed, I have demonstrated the unprecedented activation of Ru-PNP pre-catalysts promoted by acetate and formate ILs. The IL provides the needed basic properties, and stabilizes ruthenium active species in solution resulting in catalytic systems with remarkable stability over time. For example, the system does not require inert precautions (manipulation and storage) and the ILs were used as provided from the vendor (Iolitec) without prior purification; these aspects clearly assess the applicability of such solution under real-life conditions.

In Chapter 4, I have demonstrated a new approach for CO_2 valorization to FA based on Ru-PNP pincer organometallic complexes in IL. The system promotes both carbene-assisted activation of CO_2 as well as the hydrogenation of the CO_2-adduct to FA already at ambient conditions (25 ºC, 1 bar). Importantly, CO_2 capture and hydrogenation to FA from biogas mixtures has been showed as well, expanding the possibility for spin-off projects. Currently, low turnover frequencies and the impossibility to separate FA from the IL mixture represent the main drawbacks and challenges to be solved. I envision that the addition of a suitable co-IL can allow the desired FA separation, as well as increase the overall stability and efficiency of the system. For example, it is possible to imagine that the IL active for CO_2 activation is present only at catalytic amounts in combination with the Ru-PNP catalyst, resulting in a real bi-catalytic system. Then, a co-IL would stabilize FA formation in solution, at the same time favoring its separation from the catalytic active phase. The work conducted in this thesis represents a starting point towards this direction. From the results shown in Chapter 4, it is clear that the CO_2 activation is not the main challenge related to this process, and it easily performed by imidazolium carboxylate ILs. Hence, the method proposed here for CO_2 can be exploited for further transformation involving carbon dioxide. For example, changing the hydrogenation catalyst (or adding a co-catalyst to the Ru-PNP) could lead to the formation of other valuable products such as the LOHC methanol.

In Chapter 5, I have showed that the dehydrogenation of FA catalyzed by Ru-PNP/IL proceeds at temperatures compatible with low temperature PEM-FCs (T = 80-95 ºC) with turnover frequencies up to 10^4. The optimized system remained stable for up to 4 months, achieving an overall TON of 18 million, the best result published to date in terms of both catalyst activity and stability over extended reaction times. Thanks to the IL, hydrogen is released with no contamination of vaporized solvents or bases. The system shows extreme flexibility, stability and reversibility under a wide range of temperatures, pressures, times and catalyst loading. These features make Ru-PNP/IL a promising candidate for hydrogen delivery technologies using the LOHC FA. Storage and manipulations were performed under ambient conditions, and the possibility to dehydrogenate neat FA maximizes the atom efficiency and hydrogen gravimetric content of the system. It is possible to pause and restart the device, which could potentially be positioned in a small compartment with FA that is added continuously from a separate container, representing the ideal conditions for practical implementation of the technology in e.g. a FC vehicle. Typically, the minimum amount of hydrogen release for an

adequate hydrogen-to-electricity conversion influences size and weight of such a device, which in turn affects its practical applicability. In this sense, the practical advantages of the Ru-PNP/IL system have been demonstrated in Chapter 5. Importantly, the production of pressurized hydrogen, of great importance for large-scale implementation of hydrogen technologies, has been proven as well.

As a logical consequence of the findings from Chapter 4 and 5, in Chapter 6 I have described an example of reversible CO_2 hydrogenation and FA dehydrogenation performed by the same catalytic system without the addition of external sacrificial additives. Switching between the cycles is favored by changing either pressure or temperature, and Ru-PNP/IL performed up to 13 cycles with retention of the catalytic activity and unchanged stability over time. The findings shown in this chapter represent a starting point towards the possible optimization of a practical device for the renewable storage and release of renewable energy.

Finally, in Chapter 7 I have demonstrated that the Ru-PNP/IL system is also active for the dehydrogenation of isopropanol and can be trasferred into a heterogeneous-like catalytic system by means of the SILP technology. The deposition of the catalyst and the IL system into a porous supporting material provides high activity and selectivity at low temperatures, combined with improved chemical and mechanical stability, recyclability and easy handling. As such, the so-obtained Ru-SILP catalyst dehydrogenated *i*PrOH efficiently under fixed-bed reaction conditions, reaching conversion values close to the calculated thermodynamic equilibrium.

The experimental work presented in Chapter 7 demonstrates that the Ru-PNP/IL system is a suitable candidate for continuous flow (de)hydrogenation reactions using the SILP technology. This means that also the Ru-PNP/IL combinations (and applications) described in Chapter 4, 5 and 6 could potentially be transferred to a SILP material with obvious advantages given by the possibility to perform continuous-flow processes. The SILP technology could provide a solution to the drawbacks encountered during the optimization of CO_2 hydrogenation to FA; for example, immobilization of a suitable mixture of catalyst and IL into a support material could allow for continuous separation of FA from the catalytic active phase. In this regard, highly attractive is the possibility to functionalize ILs with e.g. silicates, and covalently bind them to the support, avoiding leaching and favoring product separation. The support might play a fundamental role; for example, materials with intrinsic basicity (alumina) might enhance the performance of the Ru-PNP catalysts towards both hydrogenation of CO_2 and dehydrogenation of FA, where basic conditions are favorable. Moreover, heterogeneous catalysis is rich with many examples of functionalized silica, alumina, carbon, titania or zeolite materials. Hence, highly attractive is the possibility to use the SILP technology combining known and active heterogeneous materials (Cu-zeolites) with active homogeneous catalysts (Ru-PNP) to perform both hydrogenation and dehydrogenation reactions with great efficiency and mild reaction conditions.

Overall, the organometallic Ru-PNP catalysts are responsible for the great selectivity under extremely mild reaction conditions reported in this work. Fine-tuning of the two components (catalyst and IL) can access a wide range of possible transformations, with hydrogenation and dehydrogenation that have been demonstrated in this study. Knowing the extraordinary flexibility in catalytic applications offered by organometallic pincer complexes (see Appendix E), it is possible to envision the applicability of Ru-PNP/IL using the SILP technology for many reactions that allows both reagents and products to run in the gas-phase. This includes e.g. dehydrogenation of FA, methanol and alohols at low temperature, hydrogenation of CO_2 and CO to different products, (reverse) water gas shift, ethanol valorization to bio-fuels, etc. When it is not possible to vaporize the substrate, the Ru-PNP/IL can be used under batch conditions for e.g. selective valorization of biomass-derived compounds such as glycerol, furanics, and up to carbohydrates and cellulose/hemicellulose. Importantly, the activity of Ru- and Ir-PNP catalysts towards such substrates has been demonstrated already and currently investigated in the Nielsen´s group [348–351]. For example, proper tuning of the ILs properties

(especially in terms of acidity/basicity) can provide the one pot dissolution of biomass and further valorization to relevant monomers and building blocks [352,353]. Hence, the Ru-PNP would perform hydrogenation and/or transfer hydrogenation reactions of the so-obtained monomers producing highly attractive building blocks for the chemical industry. The unlimited possibilities given by task-specific synthesis of ILs make all of the proposed visions at least worth exploring.

Obviously, the choice of the catalyst is not limited to the Ru-PNP complexes showed in this study. The literature is already rich with numerous examples of first row transition metal PNP catalysts being active for the same dehydrogenation and hydrogenation reactions described in this study [354,355]. In particular, iron (same group) is a promising candidate to substitute the expensive and rare ruthenium. The Fe-PNP catalysts reported by Hazari and co-workers possess the same ligand structure as the Ru-PNP catalysts showed here, showing remarkable activity in both hydrogenation of CO_2 as well as FA/MeOH dehydrogenation. Mn-PNP complexes (**Mn-1**) also show promising results in the same transformations. In this perspective, the activity of **Mn-1** for FA dehydrogenation in ILs has been demonstrated in Chapter 5, offering exciting premises for future optimization. Despite the lower activity and stability of iron and manganese compared to e.g. ruthenium and iridium, I envision the possibility to transfer the system Ru-PNP/IL showed in this work to first-row transition metal complexes. In this sense, the use of an IL has the potential to provide a solution to the limited stability showed by these metals.

The attractiveness of the processes discussed in this thesis (and their possible industrial applications) has attracted interest from both the academic and business sectors. This was demonstrated by the funding received from DTU Discovery Grant (DKK 110.000) and Hartmann Fond (DKK 85.000). The money have been used for the purchase of equipment that will contribute greatly to the optimization of the reaction set-ups described in Chapter 2. Such installations will provide high quality and real-time data, and will certainly speed up the optimization process of the catalytic systems investigated in the Nielsen´s group.

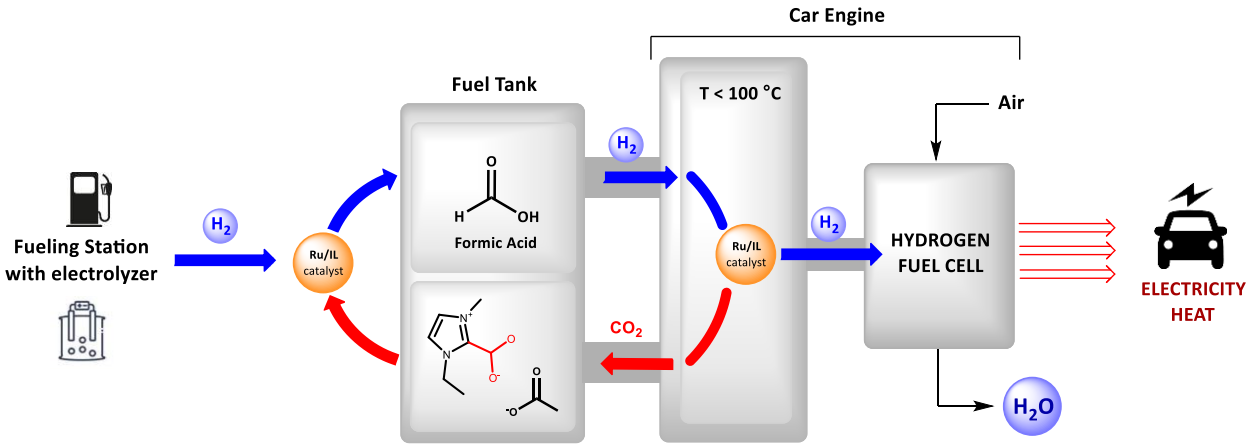

Figure 8.1: Possible implementation of the Ru-PNP/IL system in a FC vehicle using FA as the LOHC.

Figures 8.1, 8.3 and 8.4 show schematic representations of potential industrial applications of the processes discussed in this thesis. In particulatr, Figure 8.1 describes a FC vehicle that uses FA as the LOHC fuel. Based on the results from Chapter 5, it is possible to imagine a compartment of the vehicle´s engine where H_2 is extruded from the LOHC and delivered to the FC using the off-heat provided by the latter. The co-produced CO_2 can be either released in air or separated from H_2 and stored in a different compartment.

This can be done using e.g. a membrane, or an IL absorbent. Potentially, the product could be implemented in the transportation sectors, from small-size cars up to larger vehicles.

Ideally, and the work discussed in this thesis confirms, it is possible to envision a system where the same (or slightly modified) Ru-PNP/IL system can perform both cycles, as depicted in Figure 8.1. Indeed, in Chapter 6 I have demonstrated the reversible HD/DH of CO_2/FA, hence that the system is a suitable candidate for such an application. Importantly, the so-described unit can be envisioned with both liquid solutions as well as SILP configurations of Ru-PNP/IL. In this regard, I carried out a preliminary experiment with a SILP catalyst for the continuous flow gas-phase dehydrogenation of FA using the most active system described in Chapter 5 (Figure 8.2). The SILP material was prepared by wet impregnation depositing **Ru-MACHO-BH** (1 wt% Ru/SiO_2) and BMIM Ac on SiO_2 as described in the experimental part of Chapter 7. The experiment was carried out with the demonstrative set-up showed in Figure 2.5, by saturating a flow of nitrogen gas with FA, and pass the resulting mixture through the SILP catalyst at 120 ºC. To my delight, the system produced a 1:1 mixture of H_2:CO_2, assessing the feasibility of the such solution. In order to avoid condensation of FA in the catalytic bed, the reactor oven was set at 120 ºC. This can explain the presence of CO, in agreement with the findings from 5.2.3 (FA dehydrogenation in a closed system). Nevertheless, the results showed in Chapter 5 confirms that catalytic activity should be observed already at 80-95 ºC, which should avoid the formation of the unwanted CO.

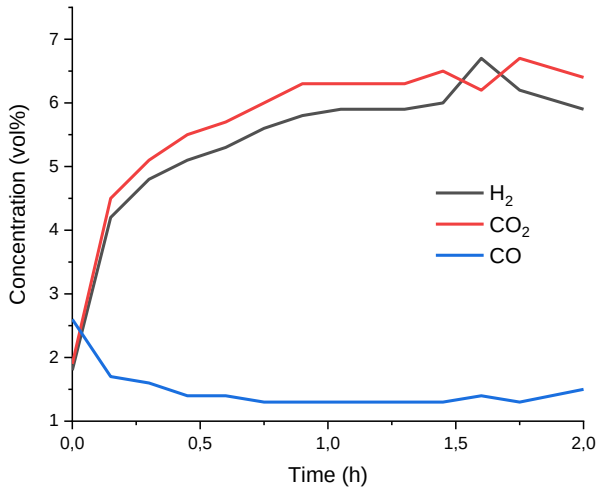

Figure 8.2: Continuous flow gas-phase FA dehydrogenation using a Ru-SILP catalyst. The presence of H_2O as a product is omitted. Ru-MACHO-BH/SiO_2 = 1 wt%, BMIM Ac (α = 20%), silica 100.

Figure 8.3 shows the same concept applied for a FC vehicle where the LOHC system is the couple *i*PrOH/acetone (see Chapter 7). As mentioned in Chapter 7, the couple *i*PrOH/acetone can be used to lower the dehydrogenation temperature of known LOHCs such as dibenzyltoluene (T = 200-300 ºC). Figure 8.4 shows an example of such application using a Ru-SILP as the one described in this thesis. In detail, DBT is passed through a flow of acetone in combination with a heterogeneous catalyst that promotes transfer hydrogenation reaction of acetone. The so formed *i*PrOH reaches the SILP catalyst where it is dehydrogenated providing H_2 to the FC (H_2 and acetone separation can be achieved using e.g. selective membranes). Acetone is then reloaded with H_2 from fresh DBT closing the cycle. Thanks to the low operative temperature of the SILP catalyst, the whole compartment could be able to achieve H_2 extrusion from DBT using the FC off-heat. However, the presence of acetone vapors in the H_2 flow, long-term stability of the

SILP catalyst, overall efficiency of the system, as well as insufficient yields in both hydrogenation/dehydrogenation steps are likely the main challenges of this otherwise clever approach.

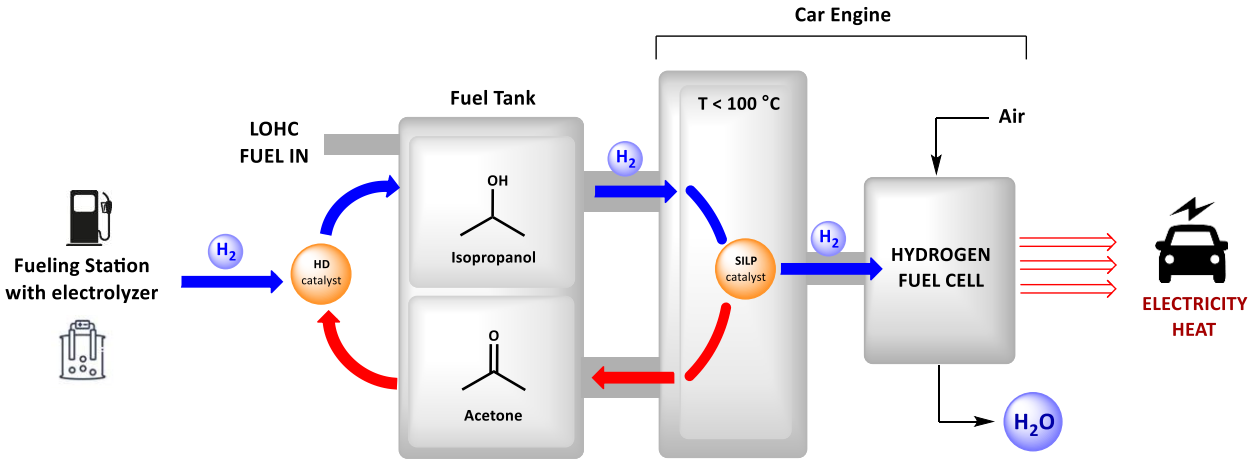

Figure 8.3: Possible implementation of the Ru-PNP/IL system in a FC vehicle using *i*PrOH/acetone as the LOHC.

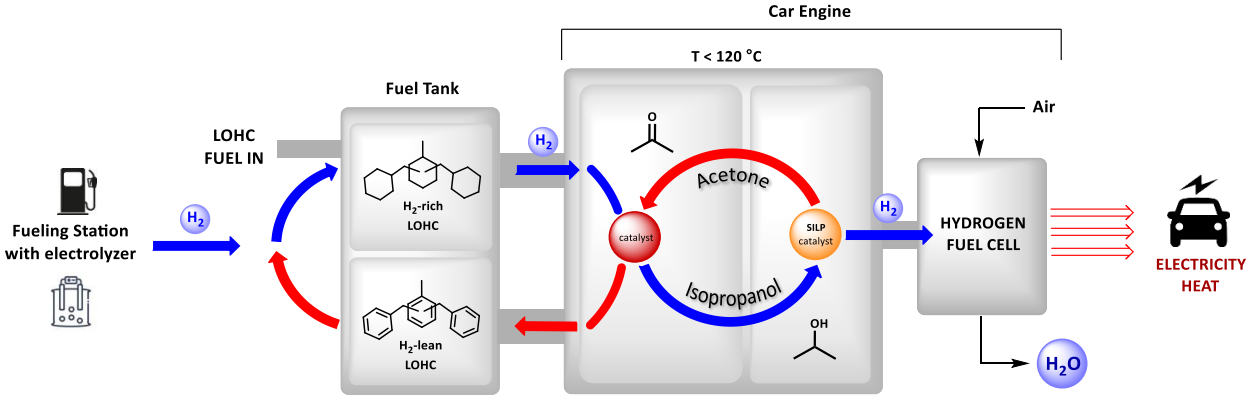

Figure 8.4: Possible implementation of the Ru-PNP/IL system in a FC vehicle using DBT as the LOHC.

To conclude, I hope I could convince the reader of the great potential that I see in the combination of pincer-type organometallic complexes and ionic liquids. I hope this work can contribute to the development of new and efficient catalytic systems aiming for a fast expansion of the hydrogen economy.

Appendix A – Supplementary information for Chapter 3

General information

Most chemicals were purchased from commercial suppliers and used without further purification unless otherwise stated. The ionic liquids were purchased from Iolitec. **Ru-MACHO**, **Ru-MACHO-BH** and **Ru-2** were purchased from StremChemicals and stored in a glove box. **Ru-1, Ru-4** and **Ru-3** were synthetized modifying reported procedures starting from the precursor **Ru-2** [106,236]. *d*-acetonitrile and *d*-benzene for NMR analysis where purchased from Fluorochem. All reactions dealing with air or moisture-sensitive compounds were performed using standard Schlenk techniques or in an argon-filled glovebox. The presented NMR spectra were measured on either a Bruker AVANCE III HD 400 MHz spectrometer, equipped with a 5 mm BBO Prodigy CryoProbe, a Bruker Avance II 400 MHz instrument equipped with a 5 mm BBFO RT probe, or a Bruker Avance III HD 600 MHz equipped with a 5 mm BBFO RT SmartProbe. NMR experiments were carried out at 25 °C using standard pulse sequences from Bruker's pulse sequence library and referenced on the solvent peak.

Entry	Solvent	^{1}H	^{13}C
1	*d*-acetonitrile	1.94	1.32 118.26
2	*d*-chloroform	7.26	77.16
3	*d*-benzene	7.16	128.06
4	*d*-dichloromethane	5.32	53.84
5	D_2O	4.79	-

Table A.1: Reported chemical shifts of the NMR solvents used in this study as reference for the showed spectra [356].

Synthesis of EMIM CHOO

In a typical experiment, 100 g of EMIM $MeOCO_2$ (30% wt in MeOH, 0.2 mol) were stirred vigorously in a round-bottom flask under ambient conditions and FA was added in stoichiometric amount dropwise (Scheme 3.3). After the evolution of CO_2 gas ceased, the mixture was dried in a rotary evaporator to remove the excess of MeOH. Later, the ionic liquid was further dried under high vacuum at 50 ºC overnight until precipitation of white crystals of EMIM $CHOO^-$.

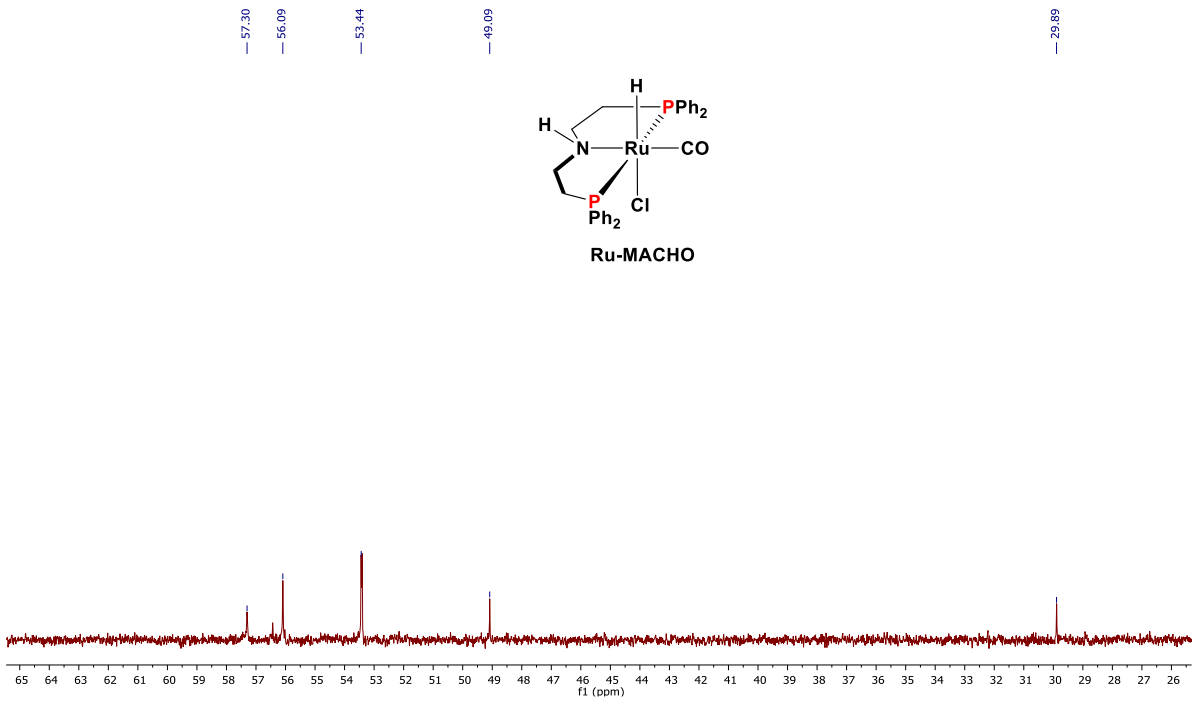

Figure A.1: ^{31}P NMR spectrum of Ru-MACHO. The presence of multiple peaks can be explained by the presence of undissolved and dissolved catalyst, as well as *cis* and *trans* H-Ru-NCCD$_3$ isomers (CD$_3$CN, 25 °C, 400 MHz).

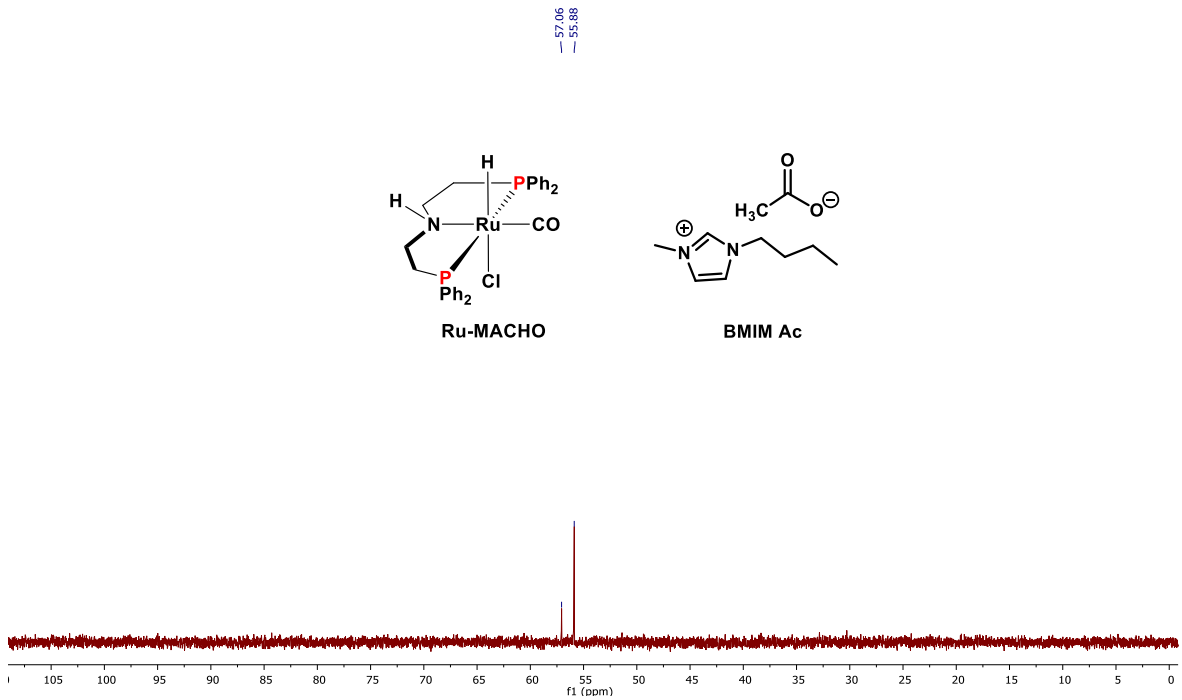

Figure A.2: ^{31}P NMR spectrum of Ru-MACHO in BMIM Ac (CD$_3$CN, 25 °C, 400 MHz). The presence of two peaks can be explained by the presence of H-Ru-NCCD$_3$ and H-Ru-OAc species.

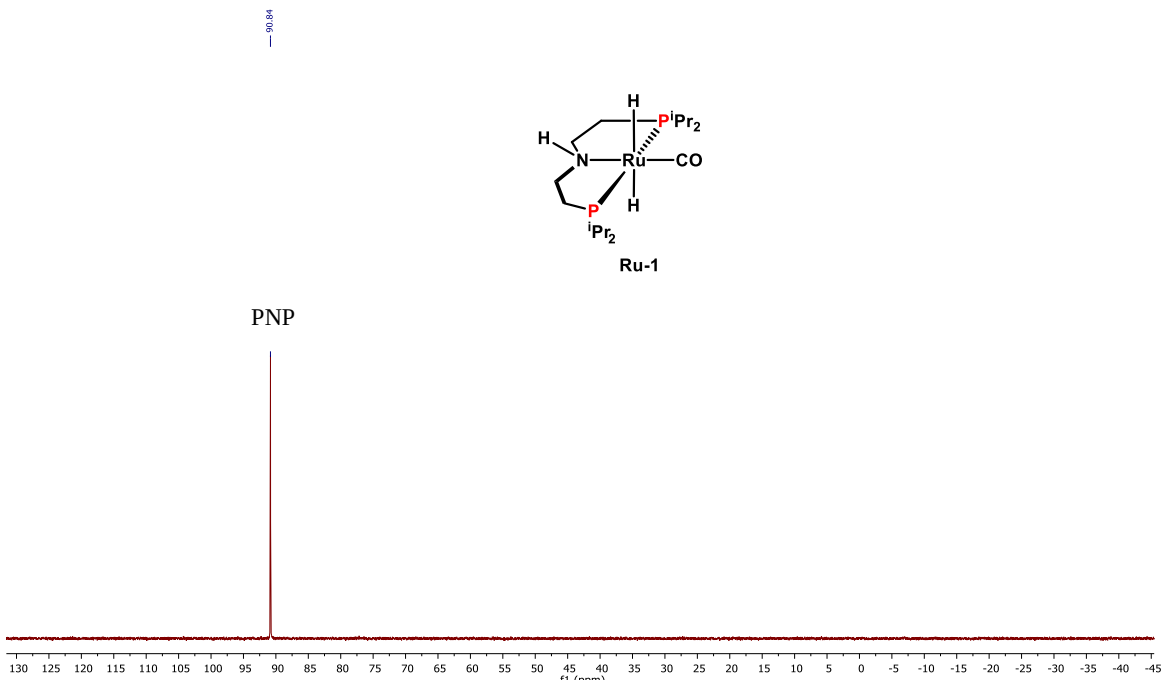

Figure A.3: ^{31}P NMR spectrum of Ru-1 (C_6D_6, 25 °C, 400 MHz).

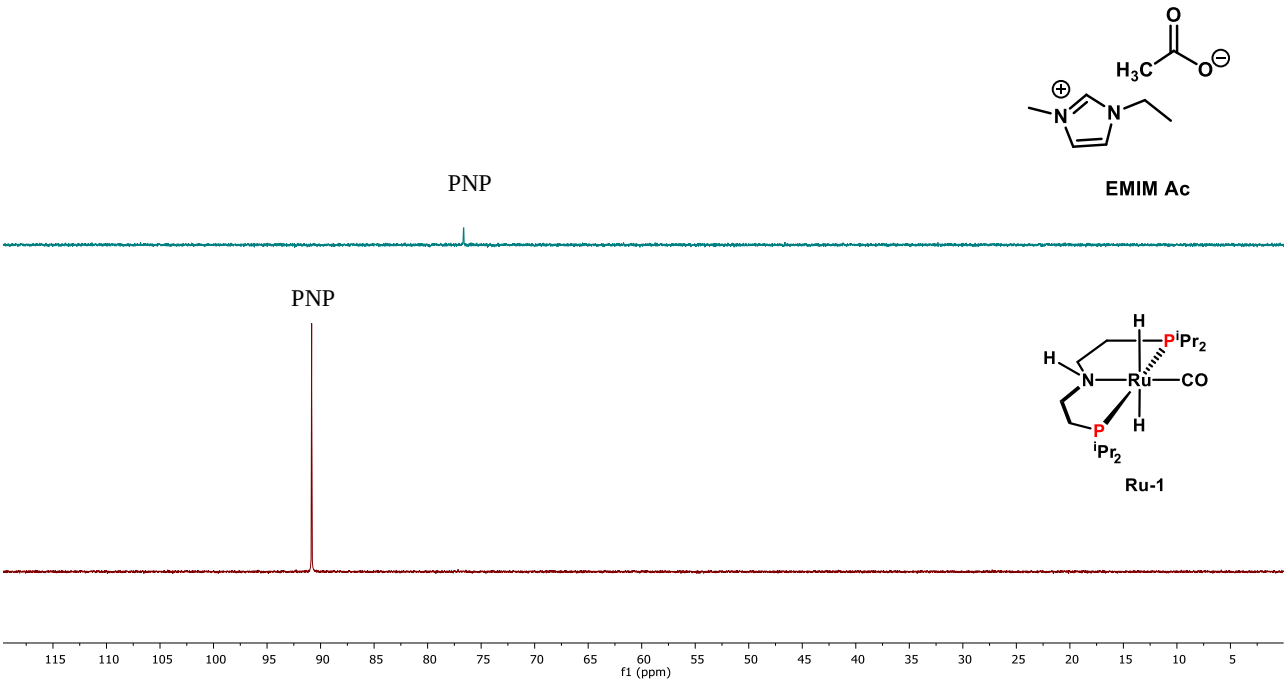

Figure A.4: ^{31}P NMR spectra of Ru-1 (down) and Ru-1 in the presence of EMIM Ac (up), (C_6D_6, 25 °C, 400 MHz).

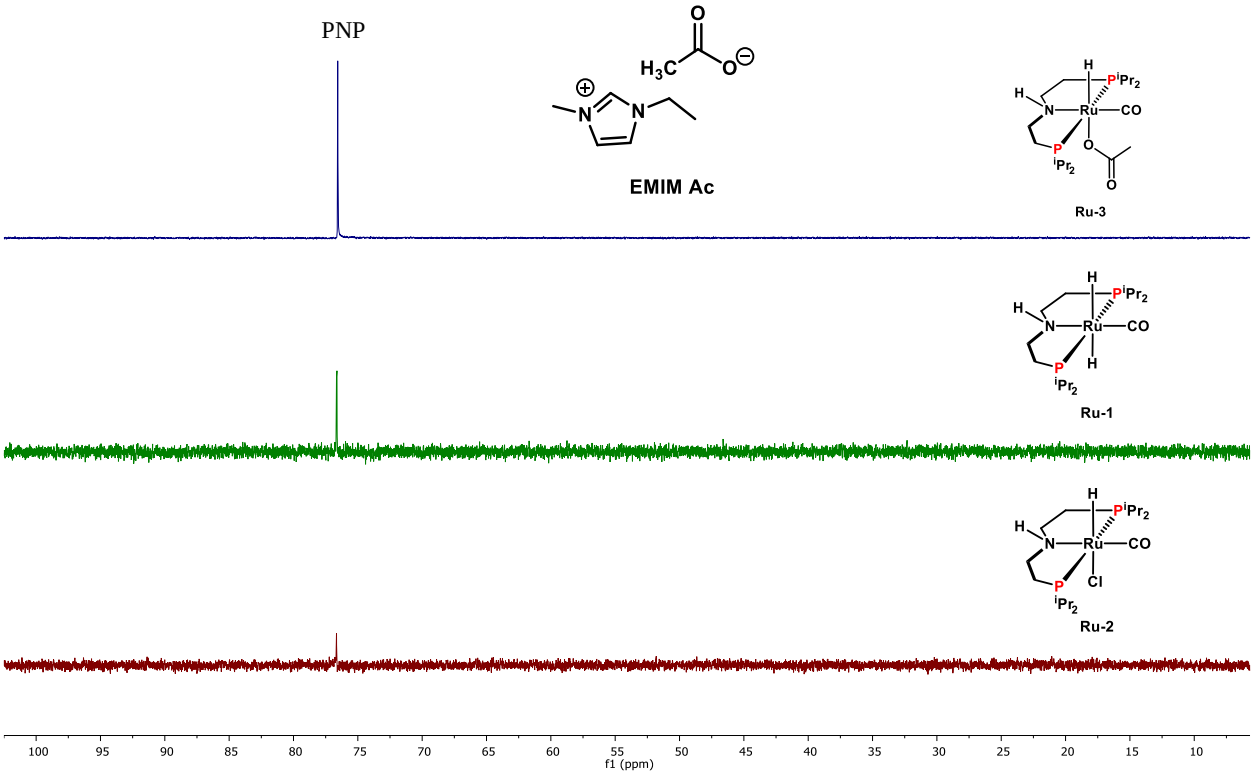

Figure A.5: ^{31}P NMR spectra of Ru-1, Ru-2 and Ru-3 in the presence of EMIM Ac (C_6D_6, 25 ºC, 400 MHz).

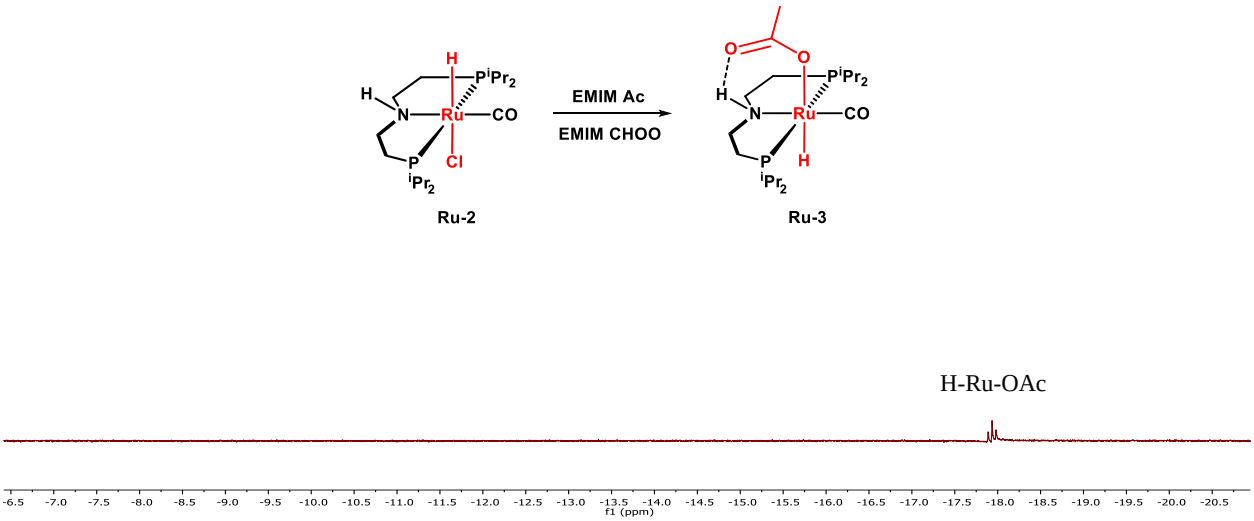

Figure A.6: ^{1}H NMR spectra of Ru-2 in the presence of a 1:1 molar mixture of EMIM Ac and EMIM CHOO (C_6D_6, 25 ºC, 400 MHz).

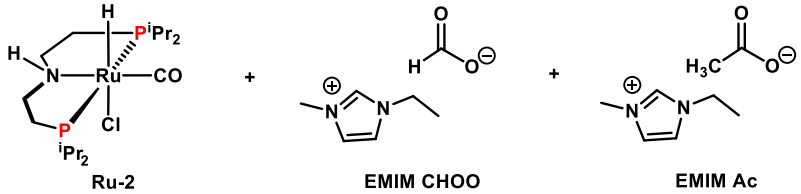

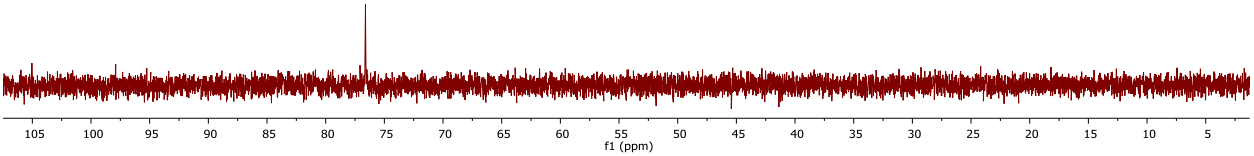

Figure A.7: ^{31}P NMR spectrum of Ru-2 in the presence of a 1:1 molar mixture of EMIM Ac and EMIM CHOO (C_6D_6, 25 ºC, 400 MHz).

Appendix B – Supplementary information for Chapter 4

General information

Most chemicals were purchased from commercial suppliers and used without further purification unless otherwise stated. The ionic liquids were purchased from Iolitec. **Ru-MACHO**, **Ru-MACHO-BH**, **Ru-2**, **Ru-7**, **Ru-9**, **Ir-1**, **Ru-10** and **Ru-12** were purchased from StremChemicals and stored in a glove box. **Ru-1** [236], **Ru-3** [106] **Mn-1** [357] and **Ru-11** [118] were synthetized according to reported procedures. *d*-acetonitrile and *d*-benzene for NMR analysis where purchased from Fluorochem. All reactions dealing with air or moisture-sensitive compounds were performed using standard Schlenk techniques or in an argon-filled glovebox. The presented NMR spectra were measured on either a Bruker AVANCE III HD 400 MHz spectrometer, equipped with a 5 mm BBO Prodigy CryoProbe, a Bruker Avance II 400 MHz instrument equipped with a 5 mm BBFO RT probe, or a Bruker Avance III HD 600 MHz equipped with a 5 mm BBFO RT SmartProbe and and were referenced on the solvent peak. NMR experiments were carried out at 25 °C using standard pulse sequences from Bruker's pulse sequence library and referenced to the solvent peak.

The recorded ^{2}H FID's were detected using the internal lock channel system. ^{1}H and ^{13}C chemical shifts are reported relative to TMS ($\nu_{iso}(^{1}H)$ = 0.0 ppm and $\nu_{iso}(^{13}C)$ = 0.0 ppm) using the residual ^{1}H signal from the deuterated solvent as secondary reference. ^{2}H chemical shifts were referenced to the solvent signal.

Procedure for the hydrogenation of CO_2

In a typical experiment, the autoclave vessel (see Figure 2.8) was loaded with the desired volume of the IL and the catalyst. The autoclave was flushed with CO_2 three times to remove air before applying the desired pressure of CO_2/H_2 and the desired temperature under a stirring of 650-1300 rpm. The reaction was then cooled (when above room temperature), the remaining pressure released, and the reaction mixture was analyzed by ^{1}H NMR using the IL as the reference for quantification of the produced FA (molar ratio by integration). When necessary, the gas contained in the autoclave was released in gas-tight bags that were connected to MicroGC for analysis of the gas mixture composition.

Procedure for the analysis of crystal structure

The crystal structure showed in Scheme 4.8 was analyzed as follows: the crystal was immersed in polybutene oil (Aldrich, > 90%) as a protection against air and moisture. A suitable crystal was collected with a MiTeGen cryo loop and mounted on a goniometer attached to a SuperNova Dual Source CCD-diffractometer. The crystal data were collected using Cu Kα radiation. The structure was solved using Olex2 and SHELXT, and refined using SHELXL refinement package using Least Squares minimization. I would like to express my gratitude to PhD student Mike S.B. Jørgensen for carrying out the measurement and refining of the structure.

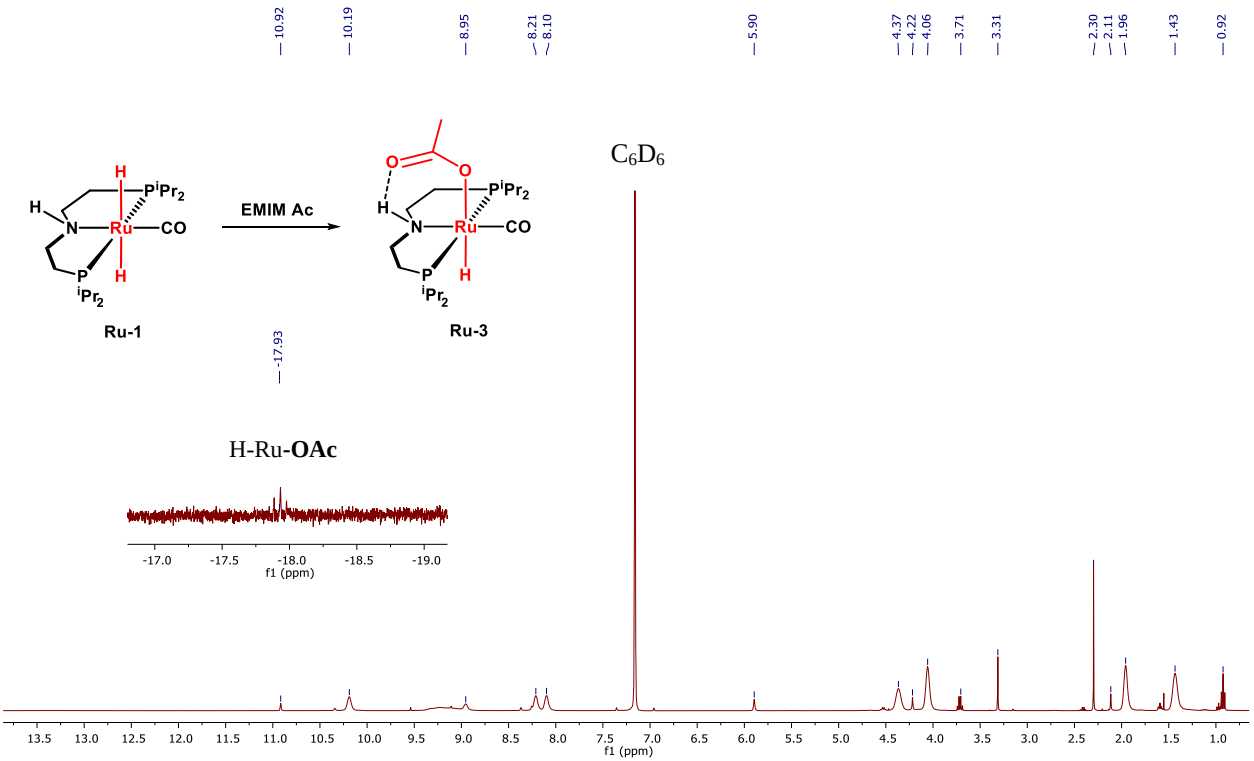

Figure B.1: ^{1}H NMR spectrum of Ru-1 in EMIM Ac after catalytic CO_2 hydrogenation (C_6D_6, 25 ^oC, 400 MHz).

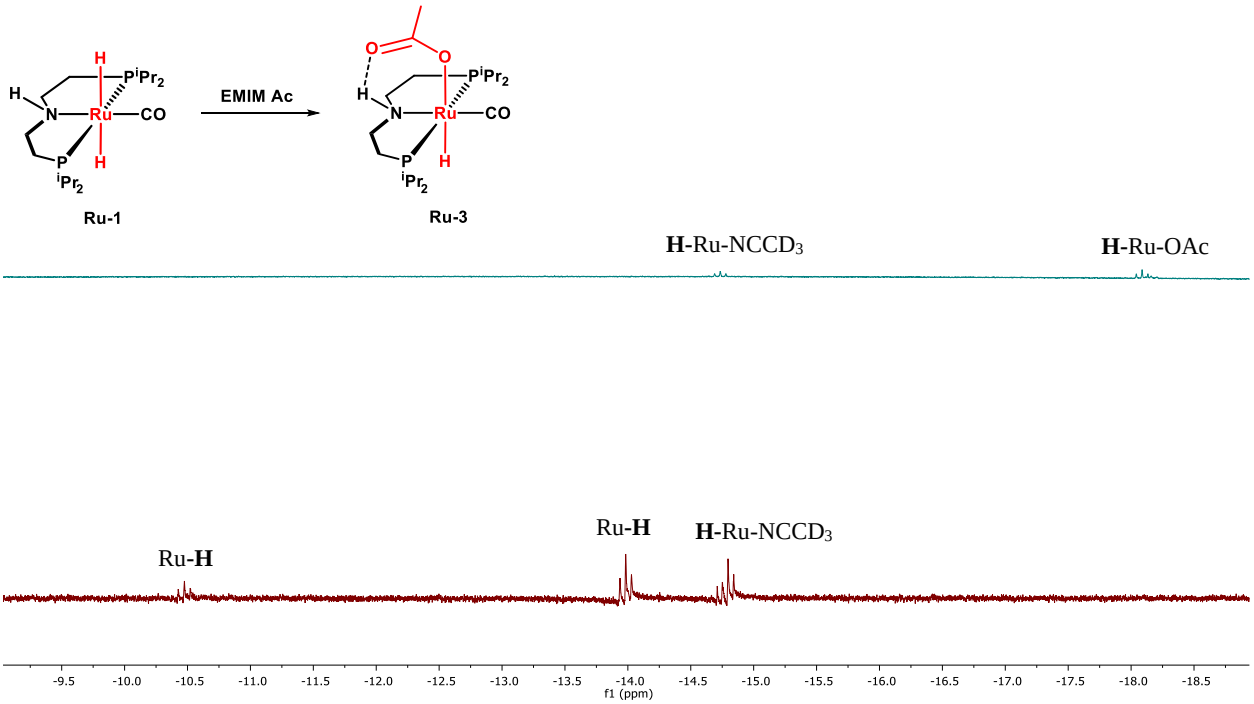

Figure B.2: ^{1}H NMR spectrum of Ru-1 in CD_3CN (down) and Ru-1 after catalytic CO_2 hydrogenation in EMIM Ac (up), (CD_3CN, 25 ^oC, 400 MHz).

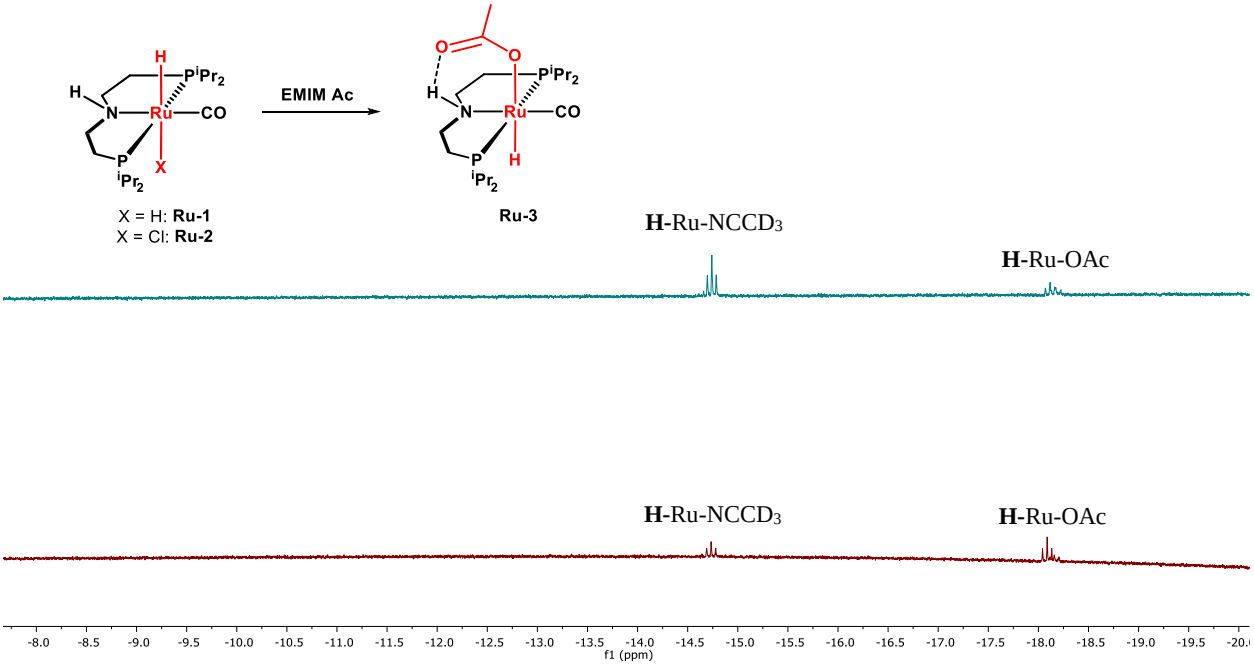

Figure B.3: ^{1}H NMR spectrum of Ru-1 (down) and Ru-2 (up) after catalytic CO_2 hydrogenation in EMIM Ac (CD_3CN, 25 ºC, 400 MHz).

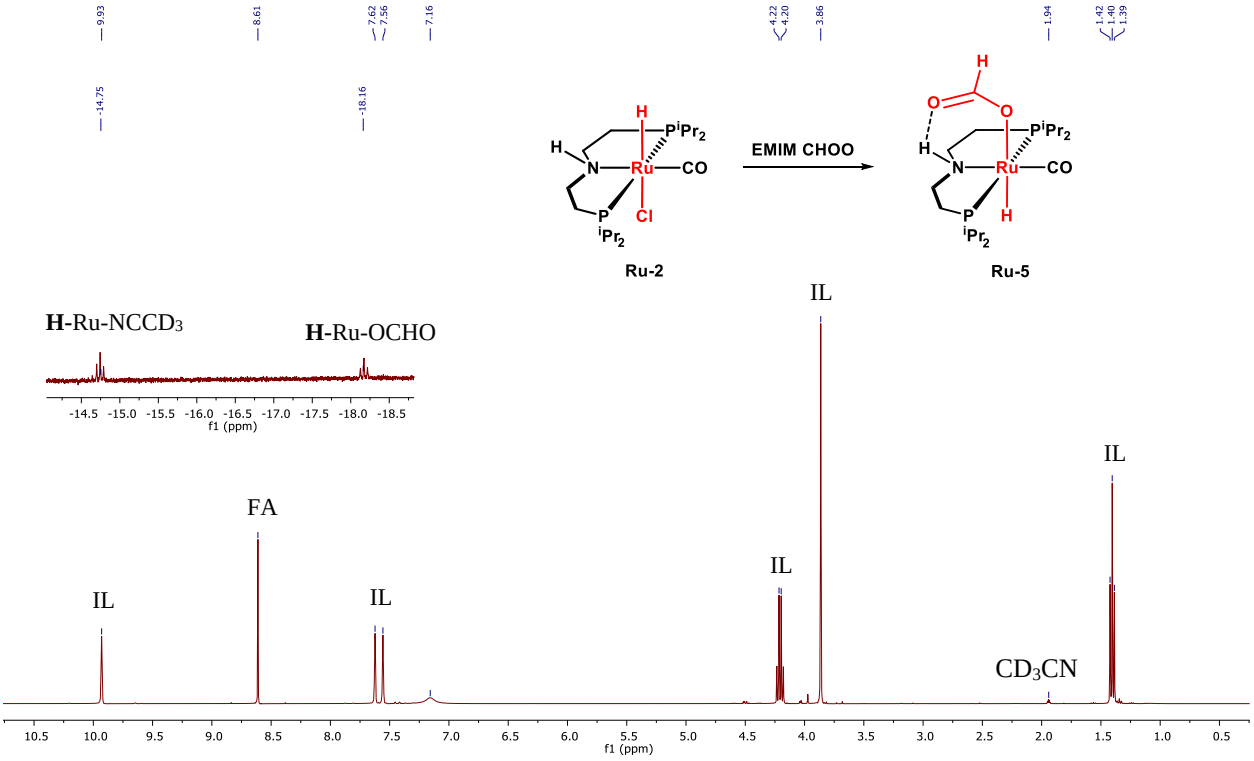

Figure B.4: ^{1}H NMR analysis of the reaction mixture after CO_2 hydrogenation to FA in EMIM CHOO. Reaction conditions: Ru-2 (0.02 mmol), EMIM CHOO (0.0056 mmol), 10:20 bar CO_2:H_2, 50 ºC, 18 h. See Figure 4.3 for assignment of EMIM CHOO (CD_3CN, 25 ºC, 400 MHz).

Labeling experiment with EMIM Ac and $^{13}CO_2/H_2$

^{1}H

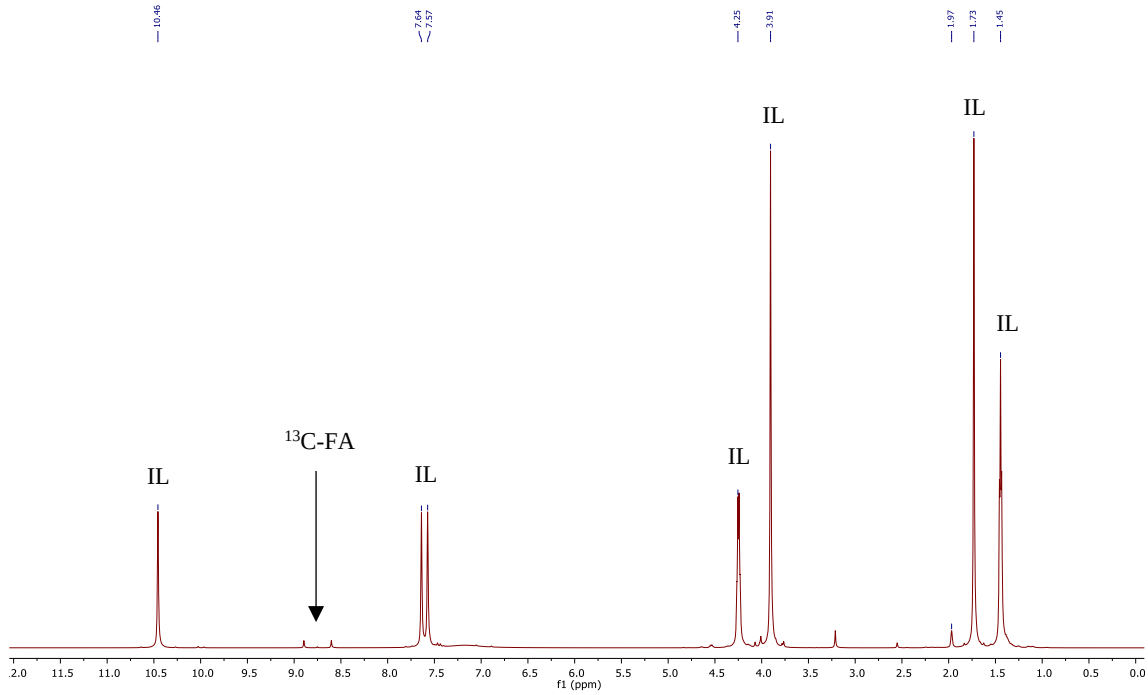

^{1}H with ^{13}C decoupling

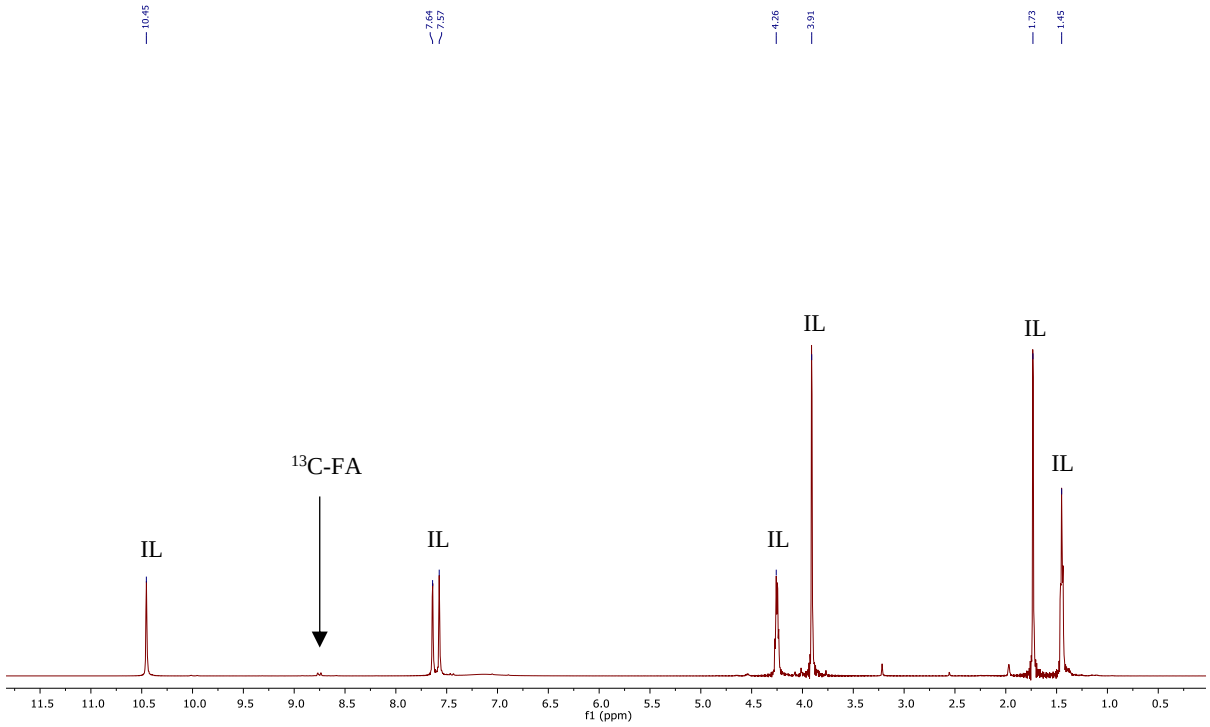

^{13}C w. ^{1}H decoupling

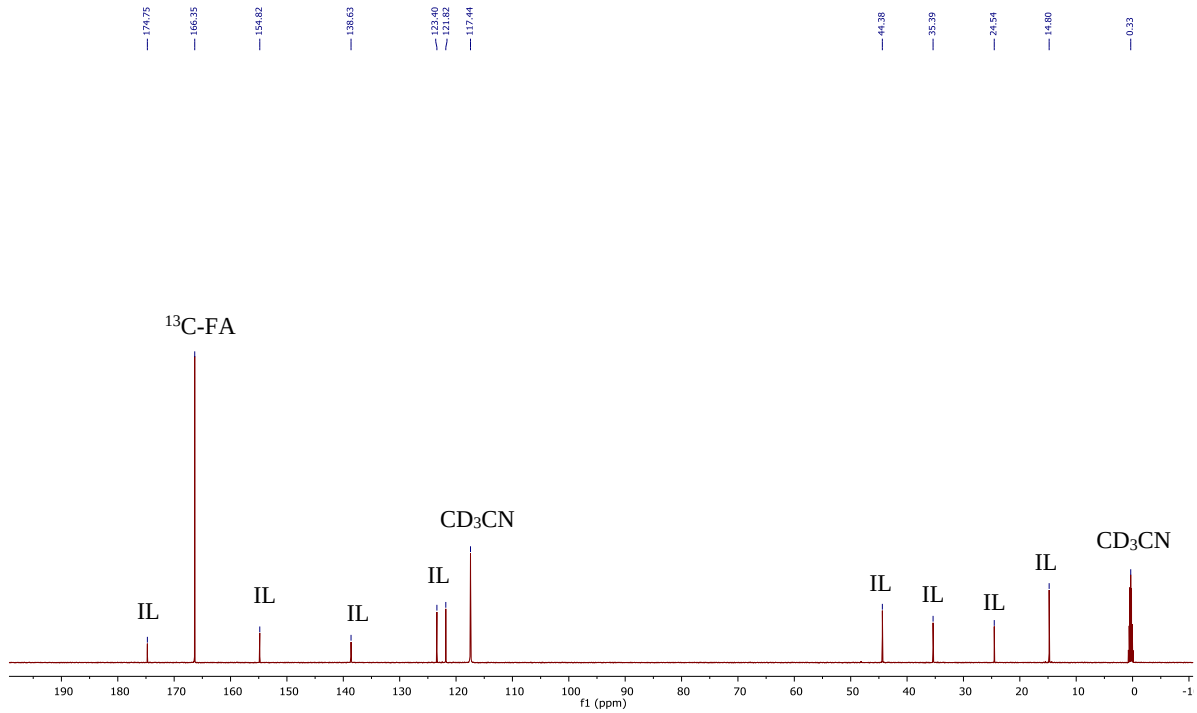

^{13}C without ^{1}H decoupling.

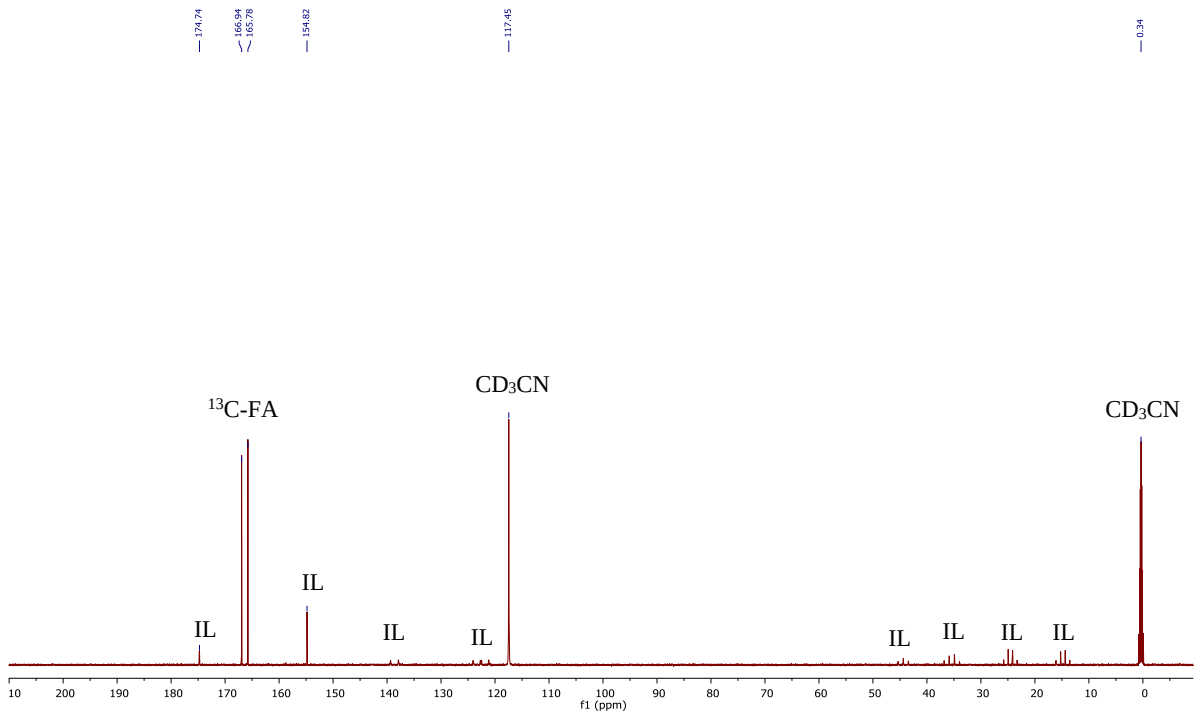

Figure B.5: Labeling experiment with $^{13}CO_2$. Reaction conditions: Ru-2 (0.02 mmol), EMIM Ac (1 mL), $^{13}CO_2$ (1 bar), H_2 (15 bar), 50ºC, 24h. See Figure 4.2 for the assignment of EMIM Ac (CD_3CN, 25 ºC, 600 MHz).

Labeling experiment with EMIM CHOO and $CO_2/^2H$

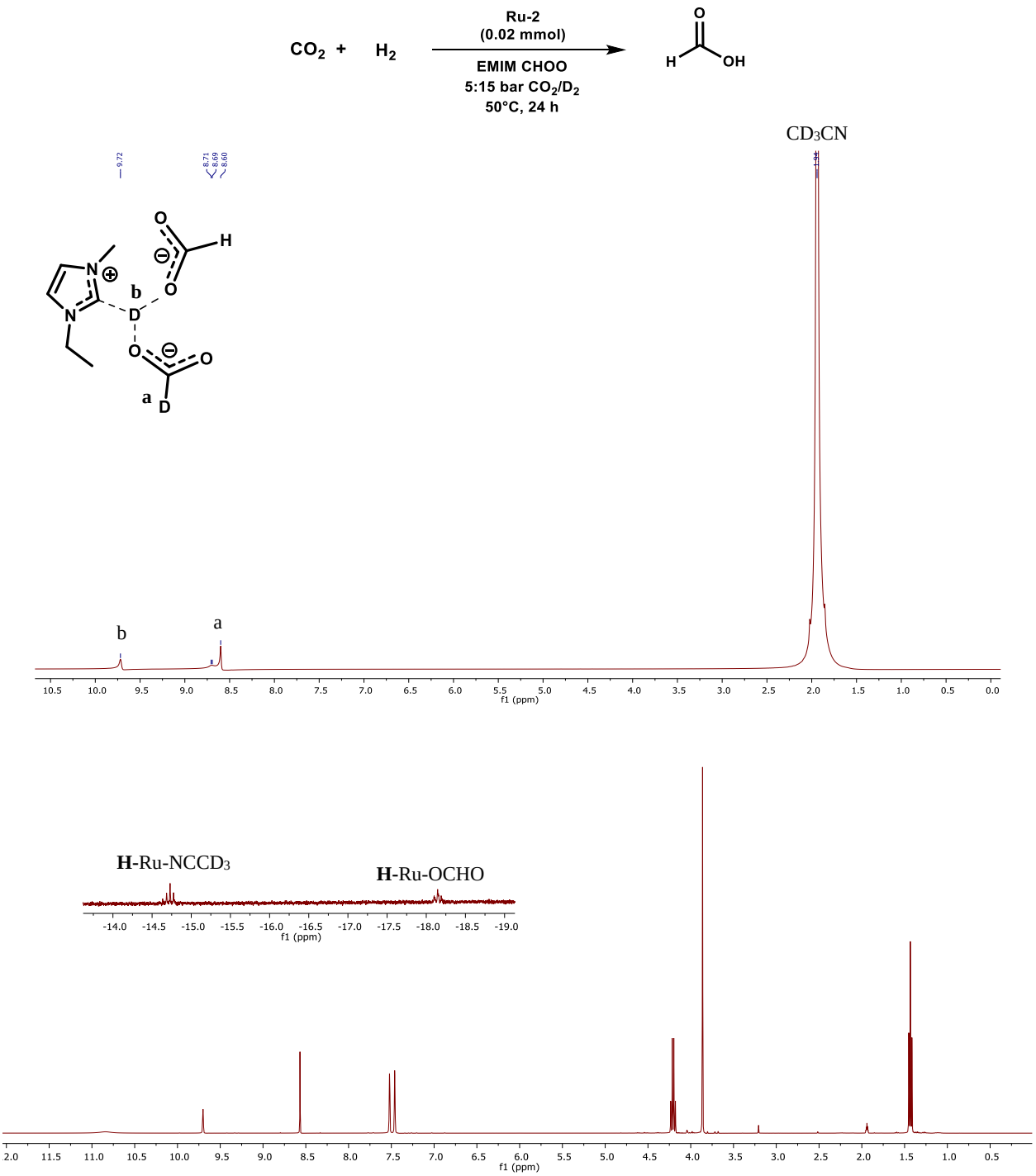

Figure B.6: ^2D (up, CD_3CN, 25 ºC, 600 MHz) and ^1H (down, CD_3CN, 25 ºC, 400 MHz) NMR spectra of the labeling experiment with deuterium and EMIM CHOO. Reaction conditions: Ru-2 (0.02 mmol), EMIM Ac (1 mL), 5:15 bar of CO_2:D_2, 50ºC, 24h.

Labeling experiment with EMIM CHOO and $^{13}CO_2/H_2$

^{1}H

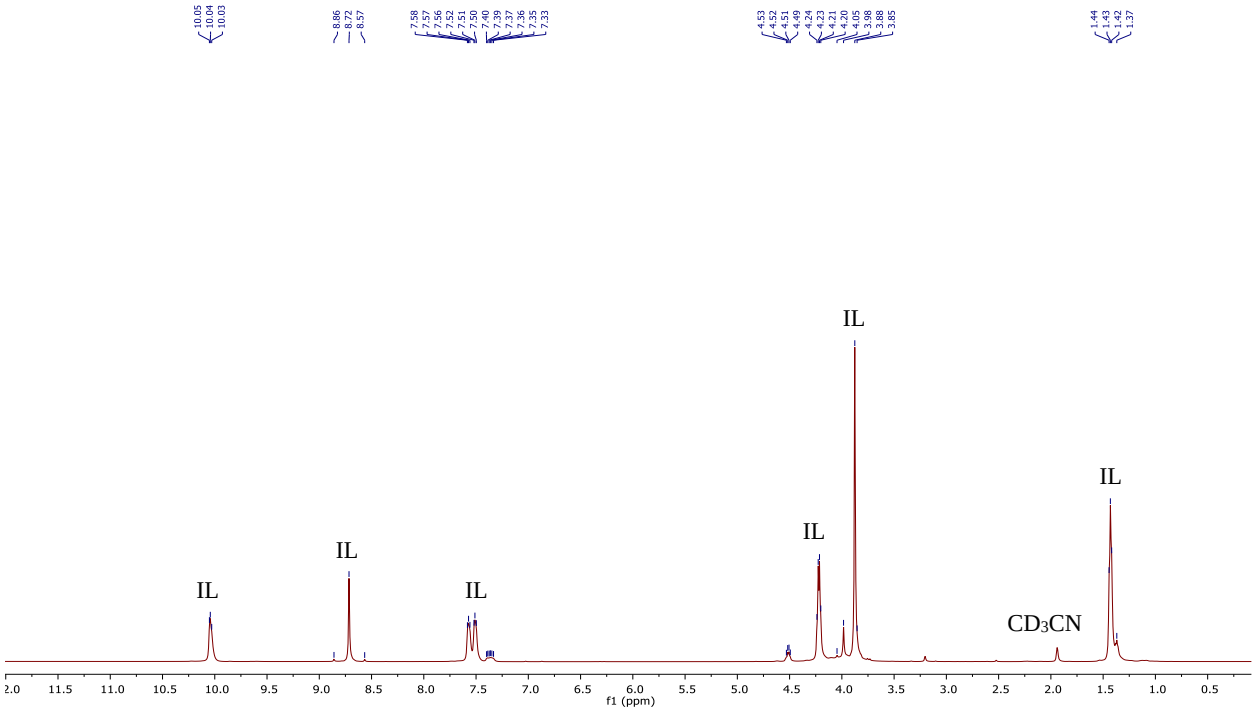

^{1}H w. ^{13}C decoupling

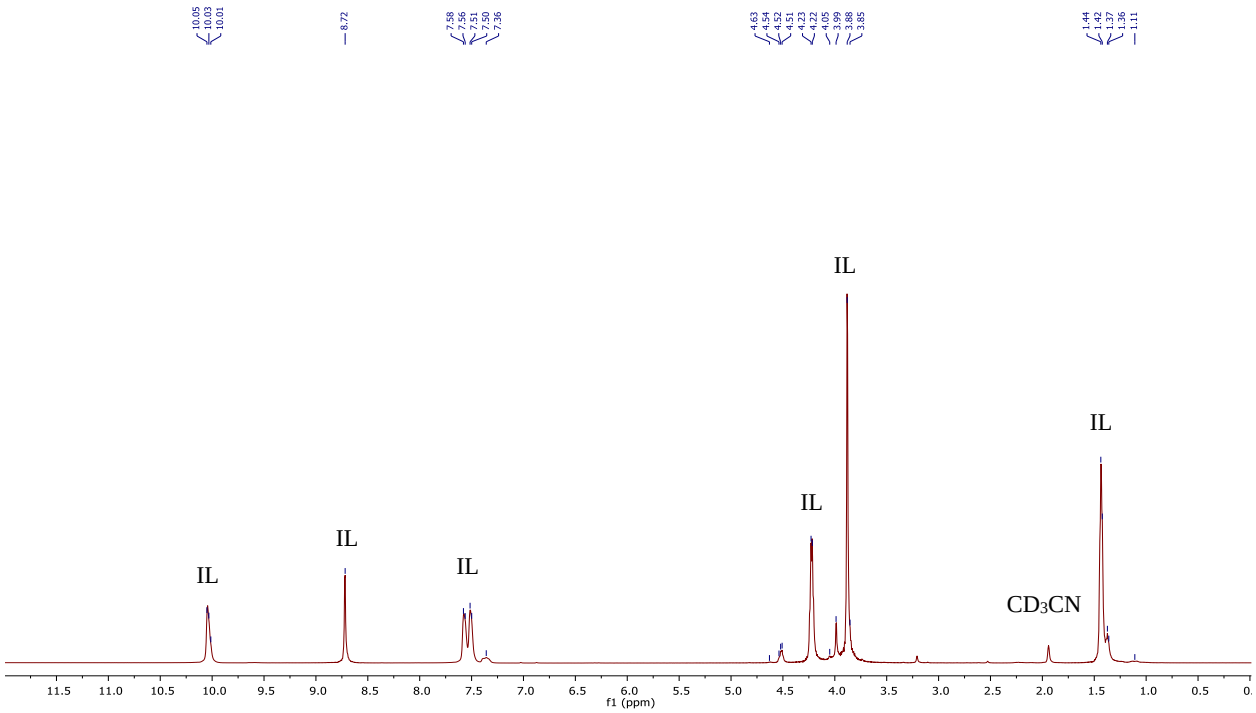

^{13}C w. ^{1}H decoupling

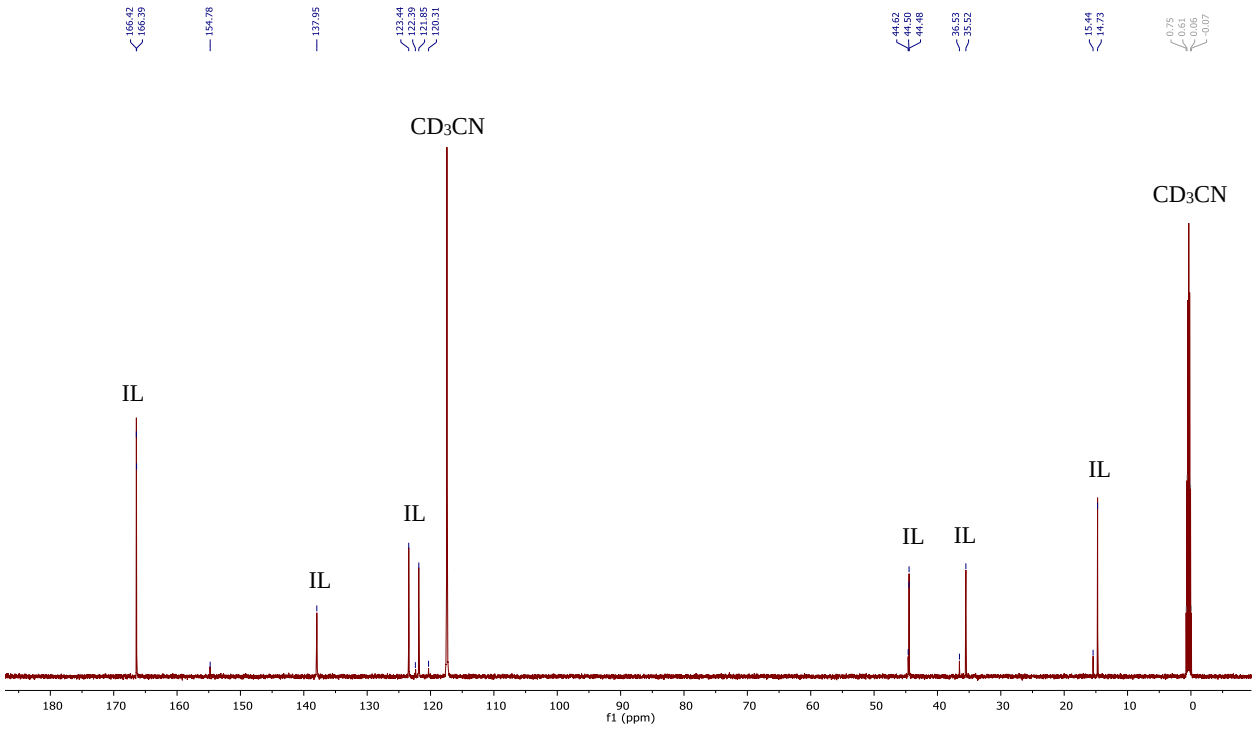

^{13}C without ^{1}H decoupling.

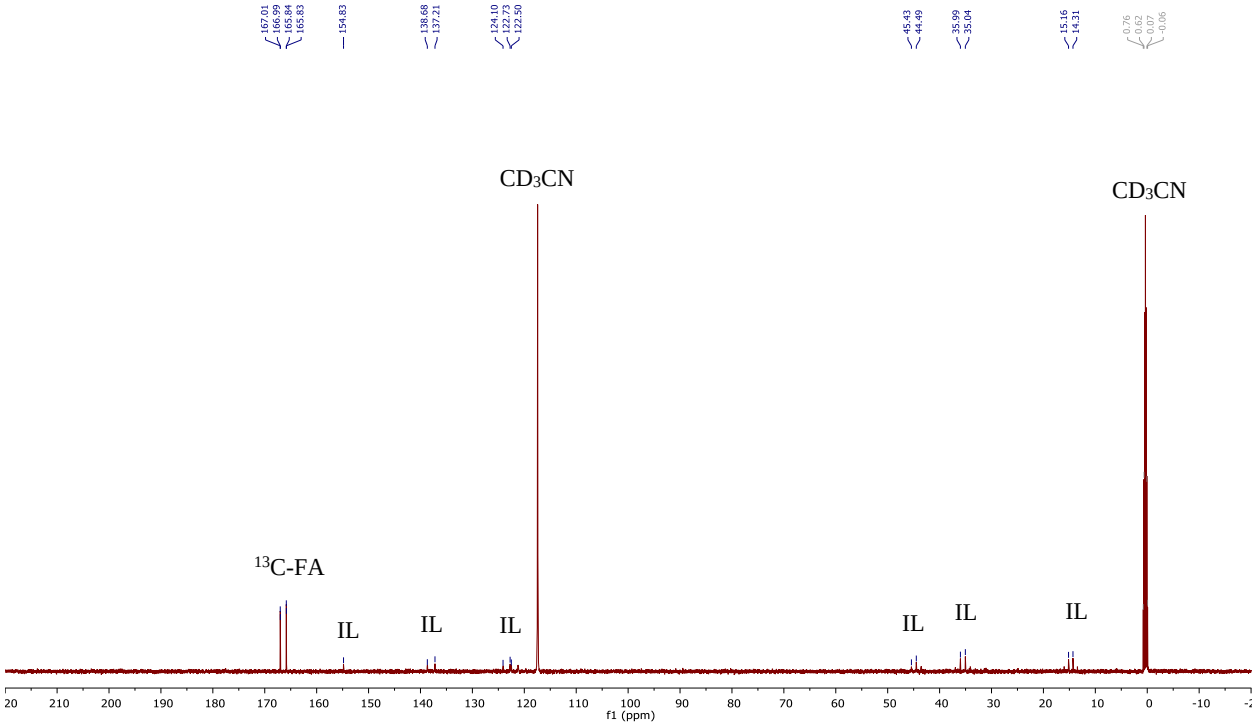

Figure B.7: Labeling experiment with $^{13}CO_2$ (CD_3CN, 25 ºC, 600MHz). Reaction conditions: Ru-2 (0.02 mmol), EMIM CHOO (1 g), $^{13}CO_2$ (1 bar), H_2 (15 bar), 50ºC, 24h. See Figure 4.3 for the assignment of EMIM CHOO.

Appendix C – Supplementary information for Chapter 5

General information

Most chemicals were purchased from commercial suppliers and used without further purification unless otherwise stated. The ionic liquids were purchased from Iolitec. **Ru-MACHO**, **Ru-MACHO-BH** and **Ru-2** were purchased from StremChemicals and stored in a glove box. **Ru-1** [236], **Ru-3** [106] and **Mn-1** [357] were synthetized according to reported procedures. FA 96% was obtained from Merck, while FA 89% and 98-100% were obtained from Supelco. Deuterated solvents where purchased from Merck. All reactions dealing with air or moisture-sensitive compounds were performed using standard Schlenk techniques or in an argon-filled glovebox. The NMR spectra were recorded on a Bruker Avance III 400 MHz spectrometer and referenced on the solvent peak.

Procedure for the dehydrogenation of FA (batch)

In a typical experiment, the catalyst was scaled in a two-necks flask inside the glove box. Later, the desired volume of ionic liquid was added and the mixture stirred at the chosen temperature until complete dissolution of the catalyst. Later, FA was added in the presence of a gentle flow of argon to facilitate hydrogen release. One sample for NMR analysis was taken after 30 min, 1h and 2h to monitor FA consumption. After 3h, the reaction mixture was cooled to room temperature and analyzed by ^{1}H NMR using 1,4-dioxane as the internal standard as follows [358]:

$$\frac{c_i}{c_{IS}} = \frac{Area_i^{1_H} / N_i^H}{Area_{IS}^{1_H} / N_{IS}^H}$$

Procedure for the dehydrogenation of FA (flow)

In a typical experiment, the catalyst was weighted in a glove box and transferred into a three-neck flask. Later, the desired volume of ionic liquid was added. The mixture was stirred at the chosen temperature until complete dissolution of the catalyst. The syringe pumps were loaded with a 60 mL PP syringe. The rate was slowly increased to assess the maximum TOF until visible FA accumulation was observed, determining the end of the reaction. The gas flow evolution was measured by means of a MFM and the gas composition analyzed via MicroGC analysis. See Chapter 2 for more details about the experimental set-up. In the long-term experiments discussed in Chapter 5.2.2, the reaction was prepared as described before, setting the oil bath at 95ºC and the stirring at 650 rpm. The flow was changed accordingly to the time available (for example slower during the weekends).

Procedure for the dehydrogenation of FA (autoclave)

In a typical experiment, the autoclave vessel was loaded with the desired volume of the ionic liquid, catalyst and IL. The autoclave was flushed with nitrogen three times in order to remove air and do not perturb the analysis of the reaction mixture by MicroGC. The reaction was then cooled to room temperature, the remaining pressure released, and the reaction mixture analyzed by ^{1}H NMR. When necessary, the gas contained in the autoclave was released in gas-tight bags that were connected to MicroGC for analysis of the gas mixture composition.

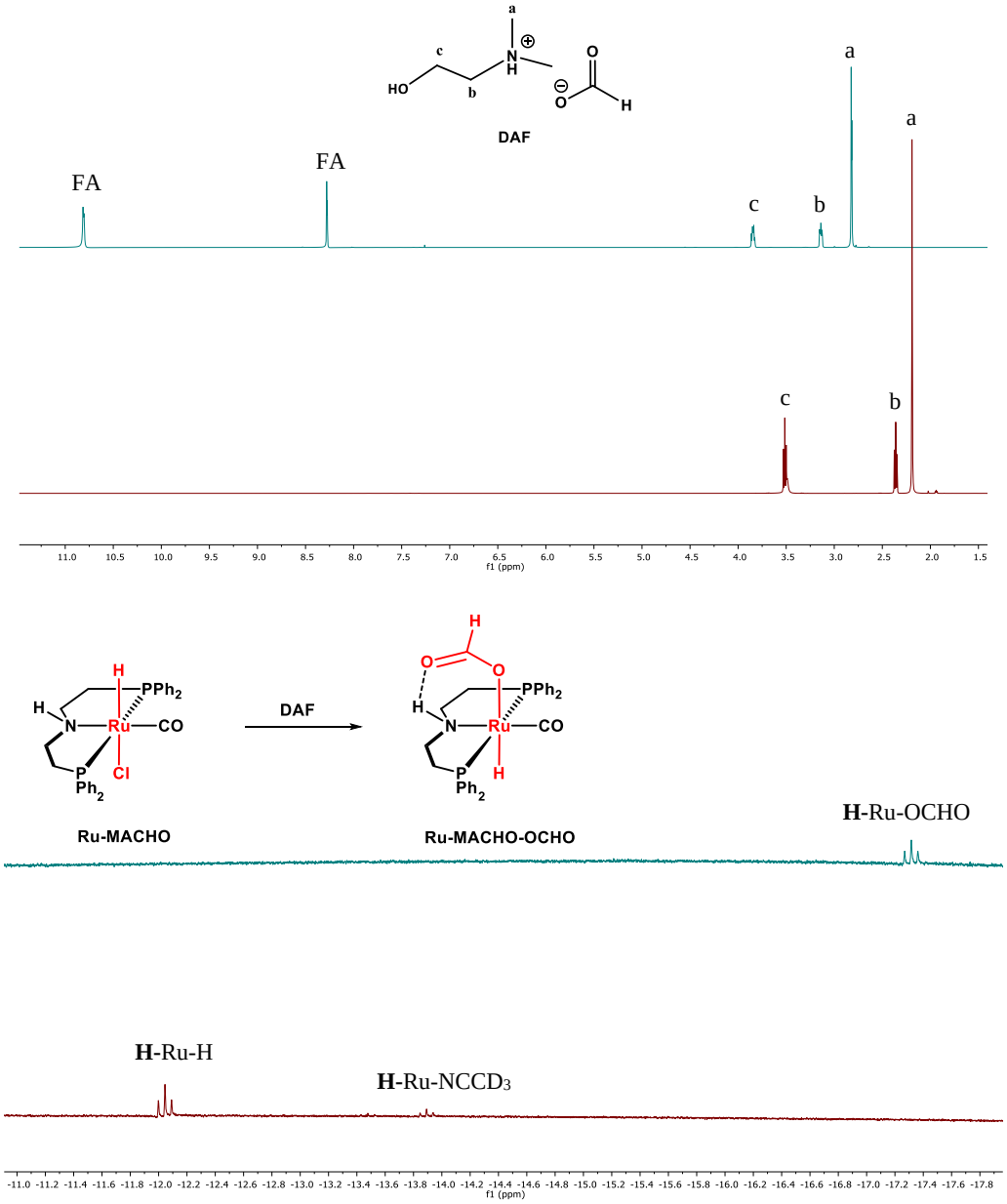

Figure C.1: ^{1}H NMR analysis of the reaction mixture after FA dehydrogenation using DAF. Reaction conditions: Ru-MACHO-BH (0.02 mmol), DAF (2 mL), FA (23.25 mmol), ramp 25-80 ºC, 0-72 h (up-down), Entry 20, Table 5.2. $CDCl_3$, 25 ºC, 400MHz).

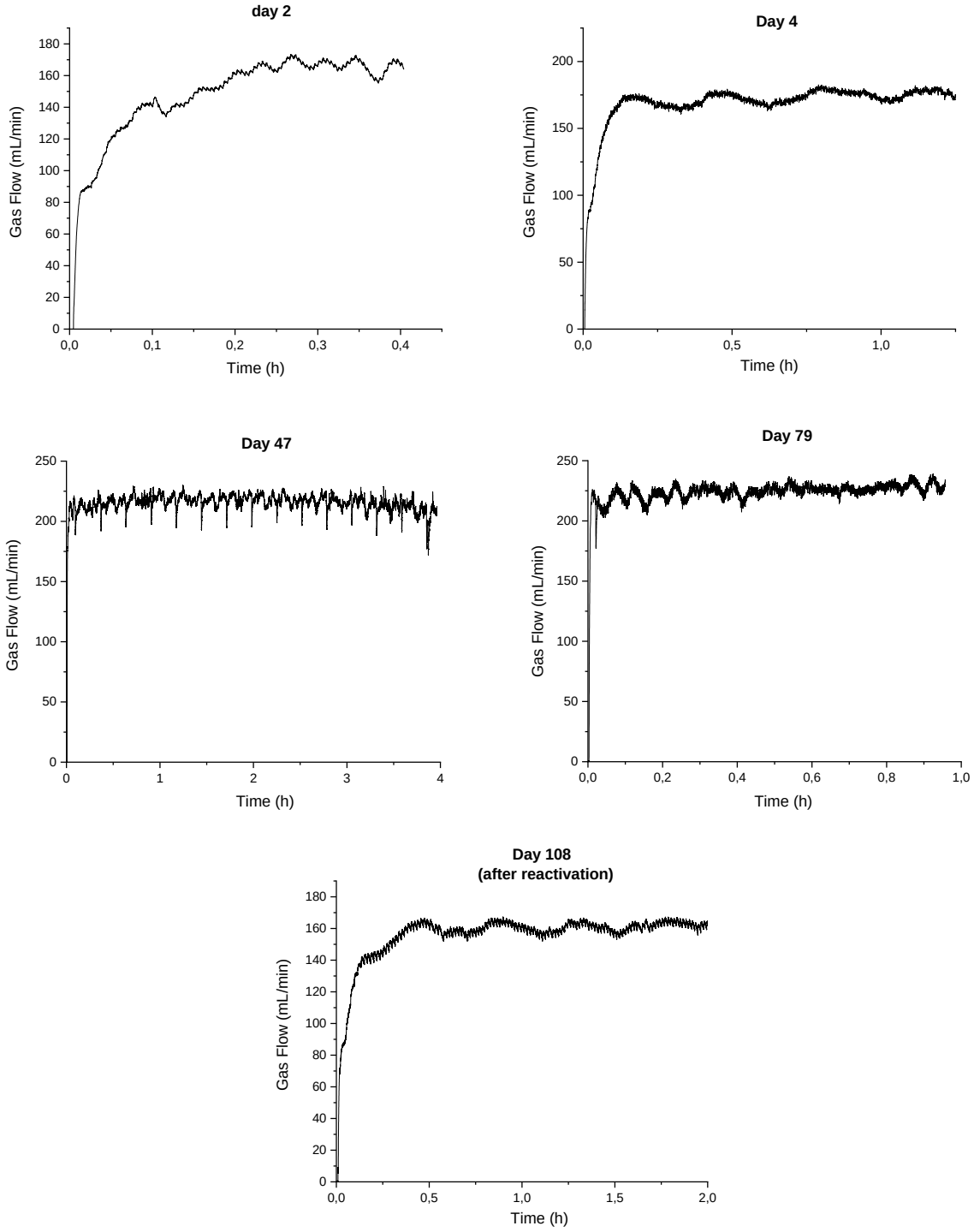

Figure C.2: Gas flow evolution measured over the long-term experiment showed in Figure 5.9. Reaction conditions: Ru-MACHO-BH (0.02 mmol), BMIM Ac (4 mL), 95 ºC.

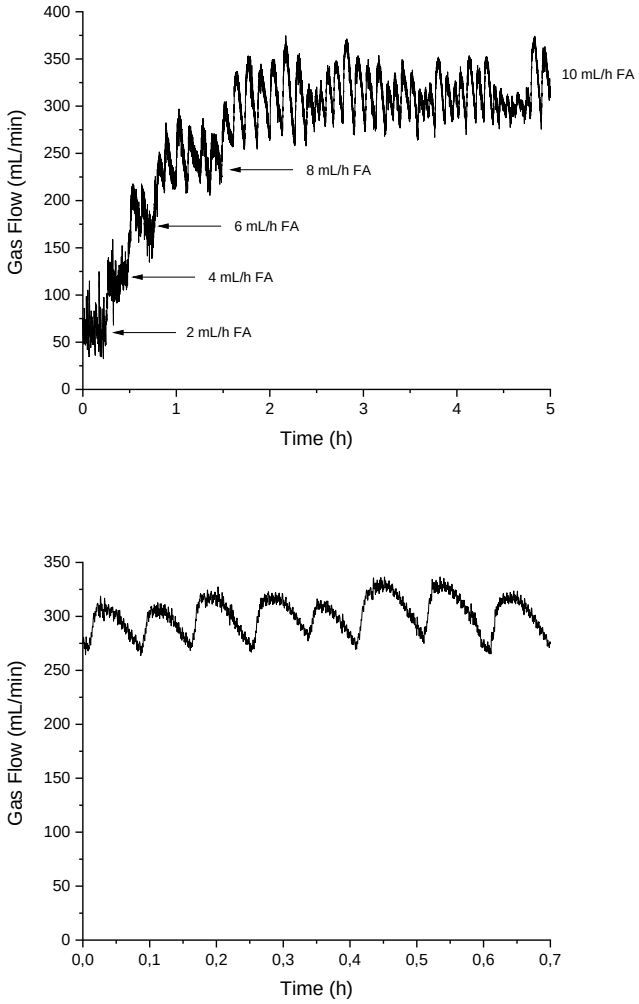

Figure C.3: Gas flow evolution of continuous flow FA dehydrogenation (Entry 8, Table 5.6). Reaction conditions: Ru-MACHO-BH (0.02 mmol), EMIM Et_2PO_4 (3 mL), 95 ºC. Note: the fluctuations are due to the inconstant dropping from the syringes, and passing of the flow through pipes of different sizes that can create local overpressures.

GC report of FA dehydrogenation under batch conditions

External Standard Report

Page 1 of 2

Method Name: C:\Users\Administrator\Agilent\Method\20190717_Luca_Final.met
Data: C:\Users\Administrator\Agilent\Result\161_FAD27-MACHOBH-BATCH_2021-10-20 09-59-48 (GMT +02-00).dat.rslt\161_FAD27-MACHOBH-BATCH_2021-10-20 10-41-35 (GMT +02-00)-Rep6.dat
User: SYSTEM (SYSTEM)
Acquired: 10/20/2021 10:42:22 AM (GMT +02:00)
Printed: 10/28/2021 1:49:58 PM (GMT +02:00)

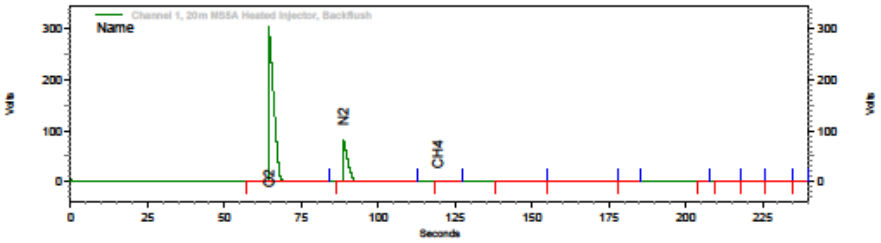

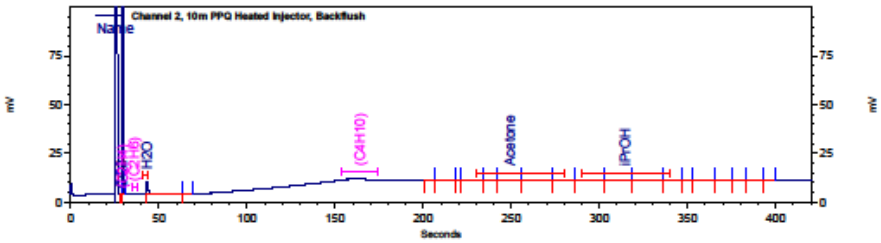

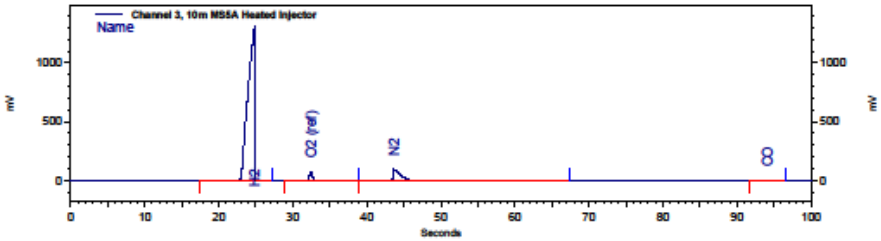

Channel 1, 20m MS5A Heated Injector, Backflush Results

Pk #	Name	Retention Time	Area	Concentration
1	O2	64.5	55408347	**51.5**
2	N2	88.7	14691423	**13.3**
3	CH4	119.4	402	**0.0**
	CO			**0.0 BDL**

External Standard Report

Method Name: C:\Users\Administrator\Agilent\Method\20190717_Luca_Final.met
Data: C:\Users\Administrator\Agilent\Result\161_FAD27-MACHOBH-BATCH_2021-10-20 09-59-48 (GMT +02-00).dat.rslt\161_FAD27-MACHOBH-BATCH_2021-10-20 10-41-35 (GMT +02-00)-Rep6.dat
User: SYSTEM (SYSTEM)
Acquired: 10/20/2021 10:42:22 AM (GMT +02:00)
Printed: 10/28/2021 1:49:58 PM (GMT +02:00)

Totals		70100172	**64.8**

Channel 2, 10m PPQ Heated Injector, Backflush Results

Pk #	*Name*	*Retention Time*	*Area*	*Concentration*
2	CO2	29.0	31956999	**15.6**
	C2H4			**0.0 BDL**
	C2H6			**0.0 BDL**
3	H2O	43.3	727980	**10.7**
	C4H10			**0.0 BDL**
10	Acetone	249.1	2754	**0.0**
14	iPrOH	314.4	3274	**0.0**
Totals			32691007	**26.3**

Channel 3, 10m MS5A Heated Injector Results

Pk #	*Name*	*Retention Time*	*Area*	*Concentration*
1	H2	24.9	139563171	**18.4**
2	O2 (ref)	32.4	3512694	**3.7**
3	N2	43.6	10596593	**14.7**
4	CO	94.1	637	**0.0**
Totals			153673095	**36.7**

Figure C.4: MicroGC report of FA dehydrogenation under batch conditions (Entry 5, Table 5.3 in the main text).

GC reports of FA dehydrogenation under continuous flow (EMIM Et_2PO_4)

External Standard Report **Page 1 of 2**

Method Name: C:\Users\Administrator\Agilent\Method\20190717_Luca_Final.met
Data: C:\Users\Administrator\Agilent\Result\FAD100_2022-02-09 15-01-44 (GMT +01-00).dat.rslt\FAD99_2022-02-09 15-18-12 (GMT +01-00)-Rep3.dat
User: SYSTEM (SYSTEM)
Acquired: 2/9/2022 3:19:00 PM (GMT +01:00)
Printed: 2/14/2022 1:06:21 PM (GMT +01:00)

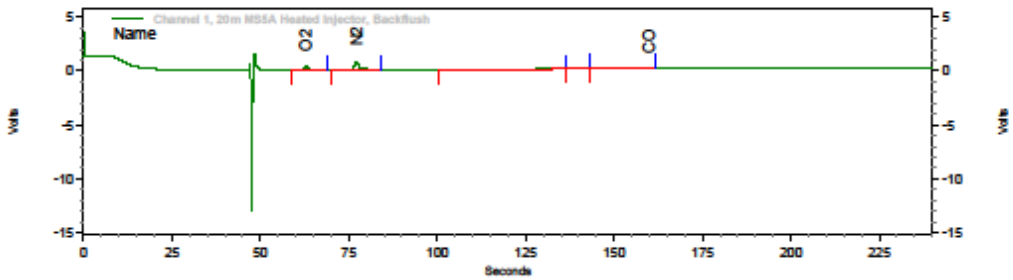

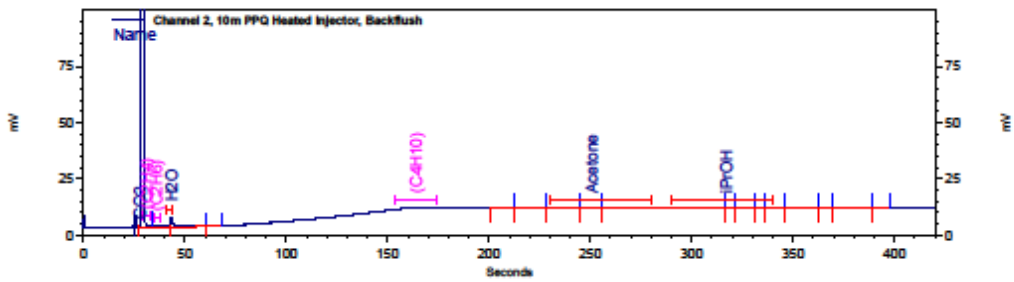

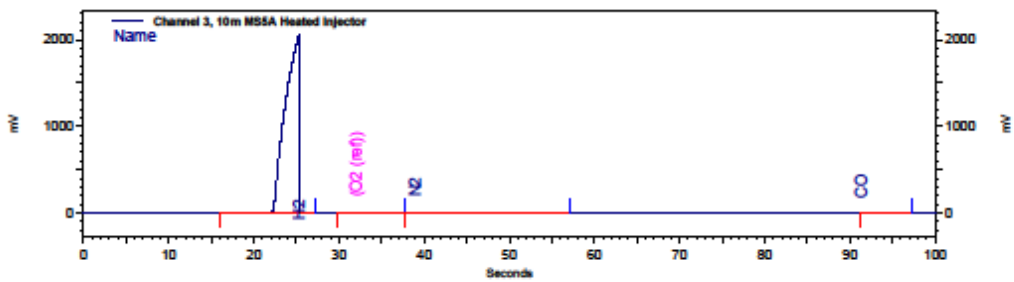

Channel 1, 20m MS5A Heated Injector, Backflush Results

Pk #	Name	Retention Time	Area	Concentration
1	O2	62.8	29388	0.0
2	N2	77.2	103322	0.1
	CH4			0.0 BDL
5	CO	159.8	2547	0.0

External Standard Report

Method Name: C:\Users\Administrator\Agilent\Method\20190717_Luca_Final.met
Data: C:\Users\Administrator\Agilent\Result\FAD100_2022-02-09 15-01-44 (GMT +01-00).dat.rslt\FAD99_2022-02-09 15-18-12 (GMT +01-00)-Rep3.dat
User: SYSTEM (SYSTEM)
Acquired: 2/9/2022 3:19:00 PM (GMT +01:00)
Printed: 2/14/2022 1:06:21 PM (GMT +01:00)

Totals		135257	0.1

Channel 2, 10m PPQ Heated Injector, Backflush Results

Pk #	*Name*	*Retention Time*	*Area*	*Concentration*
1	CO2	27.9	118236927	57.7
	C2H4			0.0 BDL
	C2H6			0.0 BDL
2	H2O	43.4	525658	7.7
	C4H10			0.0 BDL
7	Acetone	250.7	2631	0.0
9	iPrOH	317.0	7663	0.0
Totals			118772879	65.5

Channel 3, 10m MS5A Heated Injector Results

Pk #	*Name*	*Retention Time*	*Area*	*Concentration*
1	H2	25.3	383434795	50.5
	O2 (ref)			0.0 BDL
3	N2	38.9	116368	0.2
4	CO	91.4	11837	0.0
Totals			383563000	50.6

Figure C.5: GC report of FA dehydrogenation under continuous flow (Entry 8, Table 5.6). Note: the given value of H_2O concentration by the instrument is due to no calibration.

GC reports of FA dehydrogenation under continuous flow (EMIM CHOOO)

External Standard Report

Page 1 of 2

Method Name: C:\Users\Administrator\Agilent\Method\20190717_Luca_Final_short.met
Data: C:\Users\Administrator\Agilent\Result\FAD106-EMIMForm_2022-02-22 14-19-10 (GMT +01-00).dat.rslt\FAD106-EMIMForm_2022-02-22 14-19-13 (GMT +01-00)-Rep1.dat
User: SYSTEM (SYSTEM)
Acquired: 2/22/2022 2:19:39 PM (GMT +01:00)
Printed: 2/23/2022 11:52:22 AM (GMT +01:00)

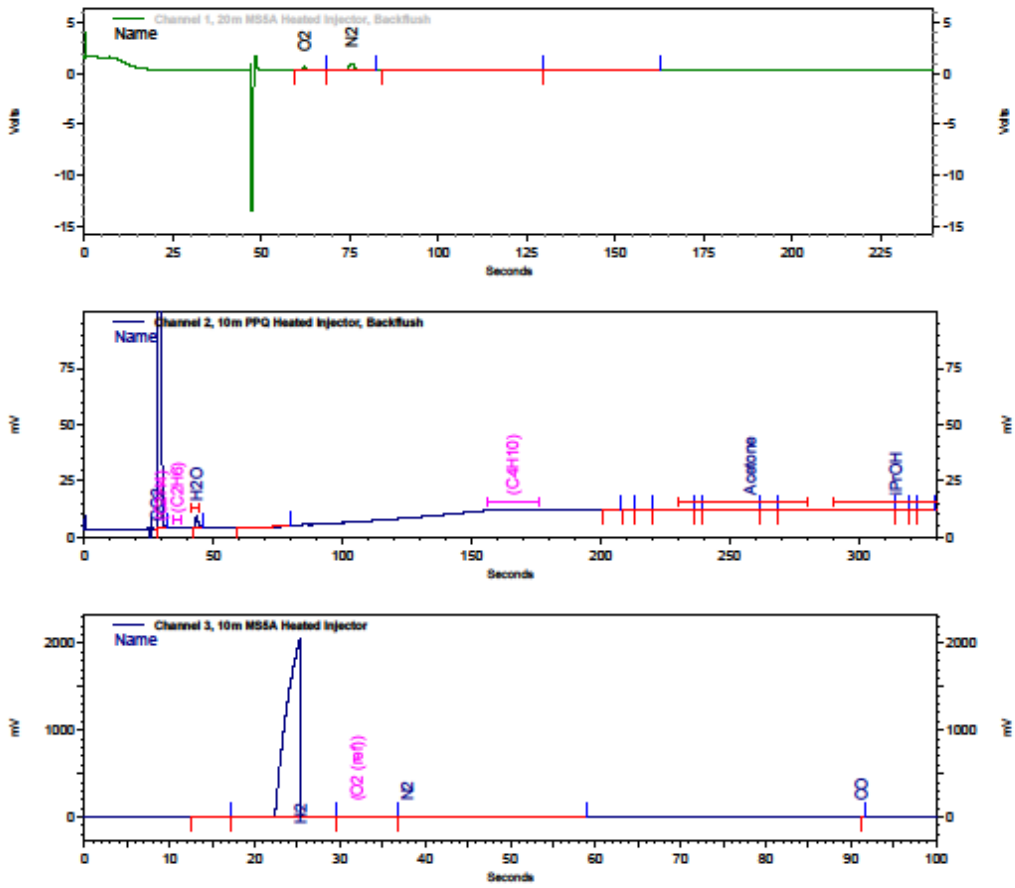

Channel 1, 20m MS5A Heated Injector, Backflush Results

Pk #	*Name*	*Retention Time*	*Area*	*Concentration*
1	O2	62.2	33549	**0.0**
2	N2	75.5	110429	**0.1**
	CH4			**0.0 BDL**
	CO			**0.0 BDL**

External Standard Report

Method Name: C:\Users\Administrator\Agilent\Method\20190717_Luca_Final_short.met
Data: C:\Users\Administrator\Agilent\Result\FAD106-EMIMForm_2022-02-22 14-19-10 (GMT +01-00).dat.rslt\FAD106-EMIMForm_2022-02-22 14-19-13 (GMT +01-00)-Rep1.dat
User: SYSTEM (SYSTEM)
Acquired: 2/22/2022 2:19:39 PM (GMT +01:00)
Printed: 2/23/2022 11:52:22 AM (GMT +01:00)

Totals		143978	0.1

Channel 2, 10m PPQ Heated Injector, Backflush Results

Pk #	*Name*	*Retention Time*	*Area*	*Concentration*
1	CO2	28.0	115252846	56.3
	C2H4			0.0 BDL
	C2H6			0.0 BDL
2	H2O	43.4	538689	7.9
	C4H10			0.0 BDL
9	Acetone	257.9	5991	0.0
12	iPrOH	314.3	3437	0.0
Totals			115800963	64.2

Channel 3, 10m MS5A Heated Injector Results

Pk #	*Name*	*Retention Time*	*Area*	*Concentration*
2	H2	25.4	381086505	50.2
	O2 (ref)			0.0 BDL
4	N2	37.9	129896	0.2
5	CO	91.2	185	0.0
Totals			381216586	50.3

Figure C.6: GC report of FA dehydrogenation under continuous flow (Entry 6, Table 5.6). Note: the given value of H_2O concentration by the instrument is due to no calibration.

GC reports of FA dehydrogenation under continuous flow (BMIM Ac)

External Standard Report **Page 1 of 2**

Method Name: C:\Users\Administrator\Agilent\Method\20190717_Luca_Final.met
Data: C:\Users\Administrator\Agilent\Result\FA syringe pump\159_FAD86_day58_ArFirst_2021-09-28 10-11-15 (GMT +02-00).dat.rslt\159_FAD86_day58_ArFirst_2021-09-28 13-32-49 (GMT +02-00)-Rep25.dat
User: SYSTEM (SYSTEM)
Acquired: 9/28/2021 1:33:42 PM (GMT +02:00)
Printed: 10/28/2021 1:56:57 PM (GMT +02:00)

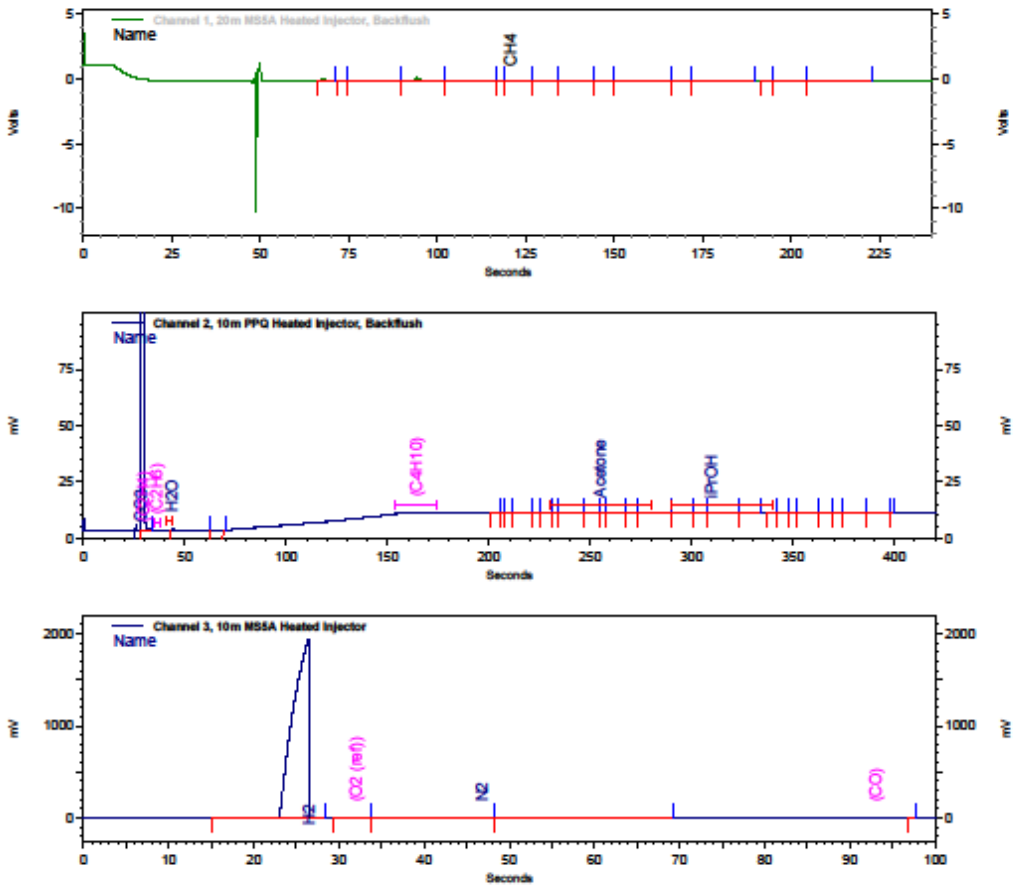

Channel 1, 20m MS5A Heated Injector, Backflush Results

Pk #	Name	Retention Time	Area	Concentration
	O2			0.0 BDL
	N2			0.0 BDL
7	CH4	120.6	3447	0.0
	CO			0.0 BDL

External Standard Report

Method Name: C:\Users\Administrator\Agilent\Method\20190717_Luca_Final.met
Data: C:\Users\Administrator\Agilent\Result\FA syringe pump\159_FAD86_day58_ArFirst_2021-09-28 10-11-15 (GMT +02-00).dat.rslt\159_FAD86_day58_ArFirst_2021-09-28 13-32-49 (GMT +02-00)-Rep25.dat
User: SYSTEM (SYSTEM)
Acquired: 9/28/2021 1:33:42 PM (GMT +02:00)
Printed: 10/28/2021 1:56:57 PM (GMT +02:00)

Totals		3447	0.0

Channel 2, 10m PPQ Heated Injector, Backflush Results

Pk #	*Name*	*Retention Time*	*Area*	*Concentration*
1	CO2	28.0	115218056	56.3
	C2H4			0.0 BDL
	C2H6			0.0 BDL
2	H2O	43.7	90414017	1325.5
	C4H10			0.0 BDL
13	Acetone	254.6	2659	0.0
19	iPrOH	309.6	21079	0.0
Totals			205655811	1381.8

Channel 3, 10m MS5A Heated Injector Results

Pk #	*Name*	*Retention Time*	*Area*	*Concentration*
1	H2	26.4	402568512	53.0
	O2 (ref)			0.0 BDL
3	N2	46.8	147920	0.2
	CO			0.0 BDL
Totals			402716432	53.2

Figure C.7: MicroGC report of FA dehydrogenation under continuous flow (long-term experiment in Figure 5.9, day 58).

GC reports of FA dehydrogenation in a closed system

External Standard Report **Page 1 of 2**

Method Name: C:\Users\Administrator\Agilent\Method\20190717_Luca_Final.met
Data: C:\Users\Administrator\Agilent\Result\FA autoclave\112LPFAD64_autoclave_2021-05-07 09-45-34 (GMT +02-00).dat.rslt\112LPFAD64_autoclave_2021-05-07 11-01-00 (GMT +02-00)-Rep10.dat
User: SYSTEM (SYSTEM)
Acquired: 5/7/2021 11:01:52 AM (GMT +02:00)
Printed: 10/28/2021 1:49:02 PM (GMT +02:00)

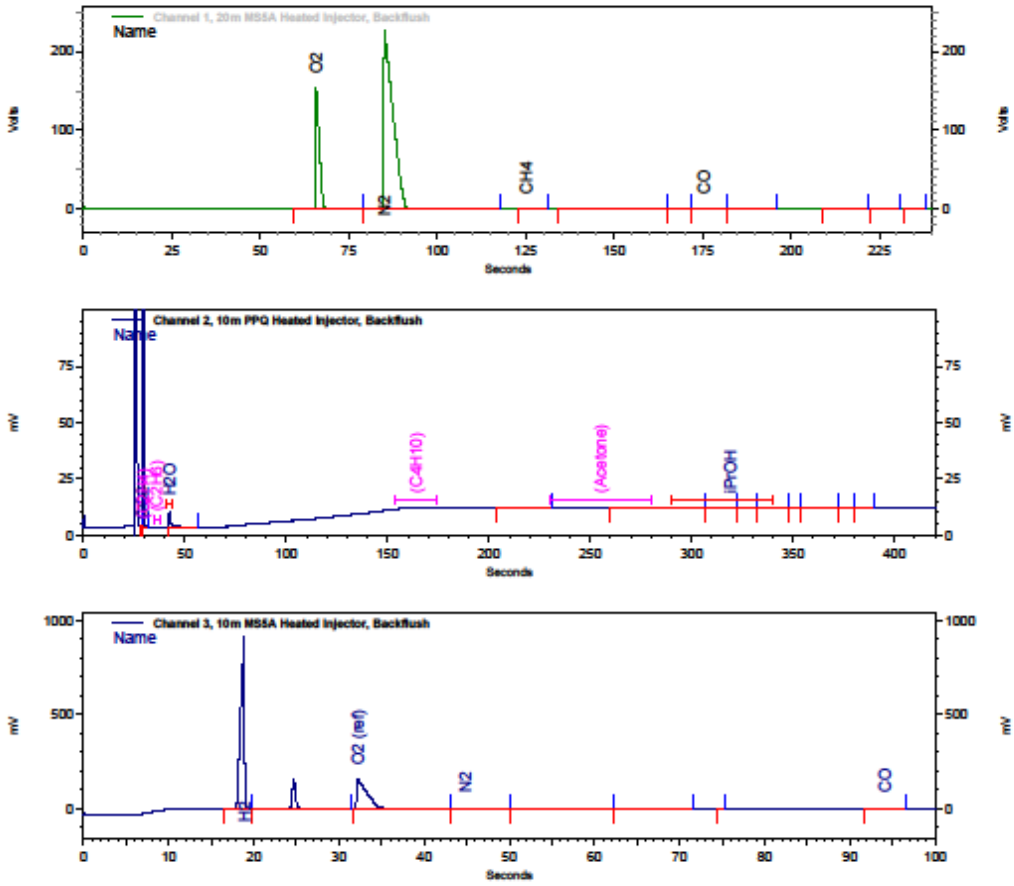

Channel 1, 20m MS5A Heated Injector, Backflush Results

Pk #	Name	Retention Time	Area	Concentration
1	O2	65.8	17875842	**16.6**
2	N2	85.1	66579868	**60.5**
3	CH4	125.1	335	**0.0**
6	CO	175.4	1418	**0.0**

External Standard Report

Method Name: C:\Users\Administrator\Agilent\Method\20190717_Luca_Final.met
Data: C:\Users\Administrator\Agilent\Result\FA autoclave\112LPFAD64_autoclave_2021-05-07 09-45-34 (GMT +02-00).dat.rslt\112LPFAD64_autoclave_2021-05-07 11-01-00 (GMT +02-00)-Rep10.dat
User: SYSTEM (SYSTEM)
Acquired: 5/7/2021 11:01:52 AM (GMT +02:00)
Printed: 10/28/2021 1:49:02 PM (GMT +02:00)

Totals		84457463	77.1

Channel 2, 10m PPQ Heated Injector, Backflush Results

Pk #	*Name*	*Retention Time*	*Area*	*Concentration*
2	CO2	29.2	17977361	8.8
	C2H4			0.0 BDL
	C2H6			0.0 BDL
3	H2O	42.4	709319	10.4
	C4H10			0.0 BDL
	Acetone			0.0 BDL
6	iPrOH	319.1	5670	0.0

Totals		18692350	19.2

Channel 3, 10m MS5A Heated Injector, Backflush Results

Pk #	*Name*	*Retention Time*	*Area*	*Concentration*
1	H2	18.9	46911086	6.2
3	O2 (ref)	32.2	20933122	21.9
4	N2	44.8	68118	0.1
8	CO	94.1	2884	0.0

Totals		67915210	28.2

Figure C.8: GC report of FA dehydrogenation in a closed system without CO detected (Entry 1, Table 5.8). Note: the given value of H_2O concentration by the instrument is due to no calibration.

External Standard Report

Page 1 of 2

Method Name: C:\Users\Administrator\Agilent\Method\20190717_Luca_Final.met
Data: C:\Users\Administrator\Agilent\Result\FA autoclave\153_FAD97_2021-10-11 11-18-05 (GMT +02-00).dat.rslt\153_FAD97_2021-10-11 11-18-07 (GMT +02-00)-Rep1.dat
User: SYSTEM (SYSTEM)
Acquired: 10/11/2021 11:18:34 AM (GMT +02:00)
Printed: 10/28/2021 1:45:54 PM (GMT +02:00)

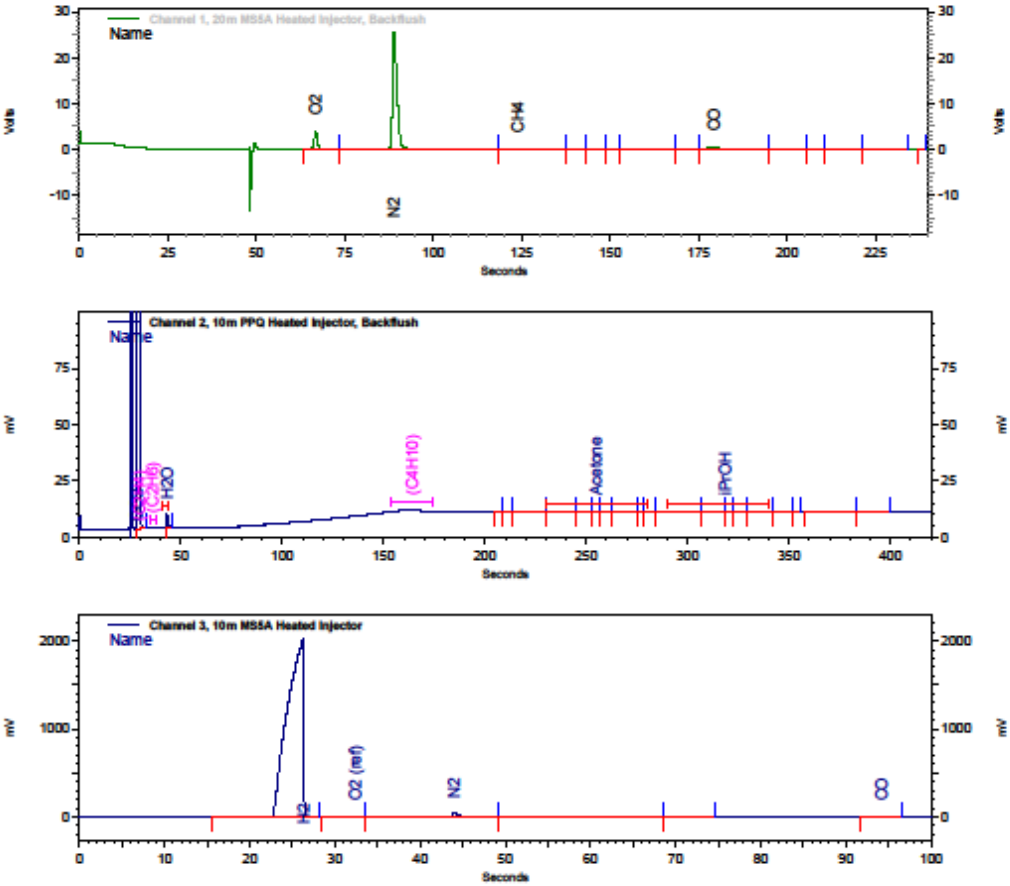

Channel 1, 20m MS5A Heated Injector, Backflush Results

Pk #	*Name*	*Retention Time*	*Area*	*Concentration*
1	O2	66.8	355083	**0.3**
2	N2	88.9	3711443	**3.4**
3	CH4	123.8	1384	**0.0**
9	CO	179.3	88208	**0.1**

External Standard Report

Method Name: C:\Users\Administrator\Agilent\Method\20190717_Luca_Final.met
Data: C:\Users\Administrator\Agilent\Result\FA autoclave\153_FAD97_2021-10-11 11-18-05 (GMT +02-00).dat.rslt\153_FAD97_2021-10-11 11-18-07 (GMT +02-00)-Rep1.dat
User: SYSTEM (SYSTEM)
Acquired: 10/11/2021 11:18:34 AM (GMT +02:00)
Printed: 10/28/2021 1:45:54 PM (GMT +02:00)

Totals		4156118	3.8

Channel 2, 10m PPQ Heated Injector, Backflush Results

Pk #	*Name*	*Retention Time*	*Area*	*Concentration*
1	CO2	28.1	91442313	44.7
	C2H4			0.0 BDL
	C2H6			0.0 BDL
2	H2O	43.1	609539	8.9
	C4H10			0.0 BDL
8	Acetone	254.6	508	0.0
15	iPrOH	318.3	680	0.0
Totals			92053040	53.6

Channel 3, 10m MS5A Heated Injector Results

Pk #	*Name*	*Retention Time*	*Area*	*Concentration*
1	H2	26.3	439299225	57.8
2	O2 (ref)	32.4	356804	0.4
3	N2	44.0	3097630	4.3
6	CO	94.1	62770	0.1
Totals			442816429	62.6

Figure C.9: GC report of FA dehydrogenation in a closed system with CO detected (Entry 7, Table 5.8). Note: the given value of H_2O concentration by the instrument is due to no calibration.

Appendix D – Supplementary information for Chapter 7

General information

Most chemicals were purchased from commercial suppliers and used without further purification unless otherwise stated. The ionic liquids were purchased from Iolitec. **Ru-MACHO**, **Ru-MACHO-BH**, **Ru-2**, were purchased from StremChemicals and stored in a glove box. **Ru-1, Ru-4** and **Ru-3** were synthetized modifying reported procedures starting from the precursor **Ru-2** [106,236]. Deuterated solvents where purchased from Merck. All reactions dealing with air or moisture-sensitive compounds were performed using standard Schlenk techniques or in an argon-filled glovebox.

The NMR spectra were recorded on a Bruker Avance III 400 MHz spectrometer and referenced on the solvent peak. Solid-state NMR spectra were measured on a Bruker Avance III HD 600 MHz spectrometer equipped with a broadband 4 mm CP/MAS probe. ^{29}Si and ^{31}P spectra were measured with a 90º excitation pulse, a spinning frequency of 6 kHz and interscan delay of 30 seconds. The ^{13}C spectra were measured using a ^{1}H-ramped Cross-polarization pulse sequence with a contact pulse of 2 ms, an interscan delay of 3 seconds and spinning frequency of 6 kHz. High-power ^{1}H SPINAL64 decoupling was employed during acquisition (ν_{RF} = 100 kHz) for all spectra. Chemical shifts are reported relative to TMS for ^{13}C and ^{29}Si, and H_3PO_4 (85% in H_2O) for ^{31}P using the most deshielded ^{13}C signal from adamantane as secondary reference shift (ν_{iso} = 38.48 ppm) and calculating the corresponding ^{29}Si and ^{31}P chemical shifts from the IUPAC unified reference scale.

All ex situ TEM studies for this work were performed on a FEI Tecnai T20 G2 microscope operated at 200 keV. A Micrometrics 3Flex physisorption instrument was used to record the nitrogen adsorption-desorption isotherm at 77 K. The total surface area was determined by the BET method, the total pore volume is determined from a single-point read at 0.95 p/p0, the microporous volume is calculated from the t-plot and the pore-size distribution are calculated according to the BJH method. Prior to physisorption analysis, the samples were degassed at 200 °C in vacuum overnight. TGA analysis were carried out using a Mettler Toledo equipment. The SILP material was heated at a rate of 10 °C min/h in air until the desired temperature.

Procedure for the dehydrogenation of *i*PrOH (batch)

In a typical experiment, the catalyst was scaled in a two-necks flask inside the glove box. Later, the desired volume of ionic liquid was added and the mixture stirred at the chosen temperature until complete dissolution of the catalyst. Later, *i*PrOH was added in the presence of a gentle flow of argon to facilitate hydrogen release. After 3h, the reaction mixture was cooled to room temperature and analyzed by ^{1}H NMR.

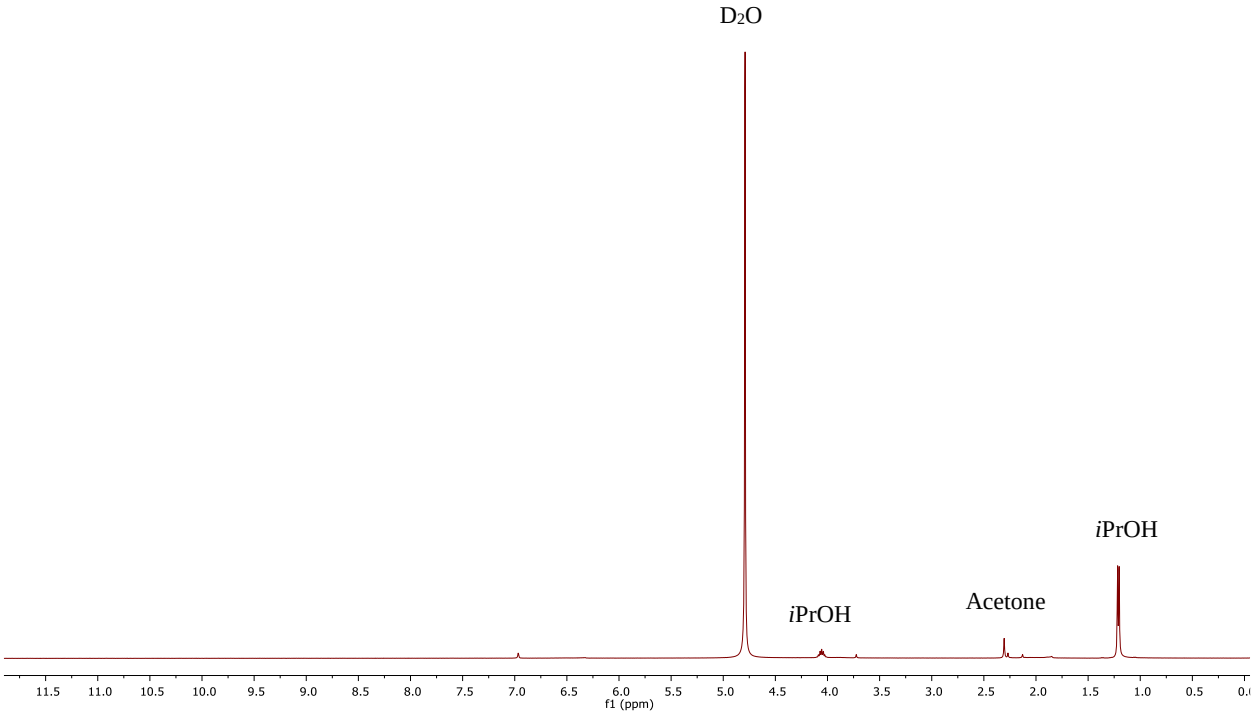

Figure D.1: ^{1}H NMR spectrum of the distillate from *i*PrOH dehydrogenation (D_2O, 25 ºC, 400 MHz).

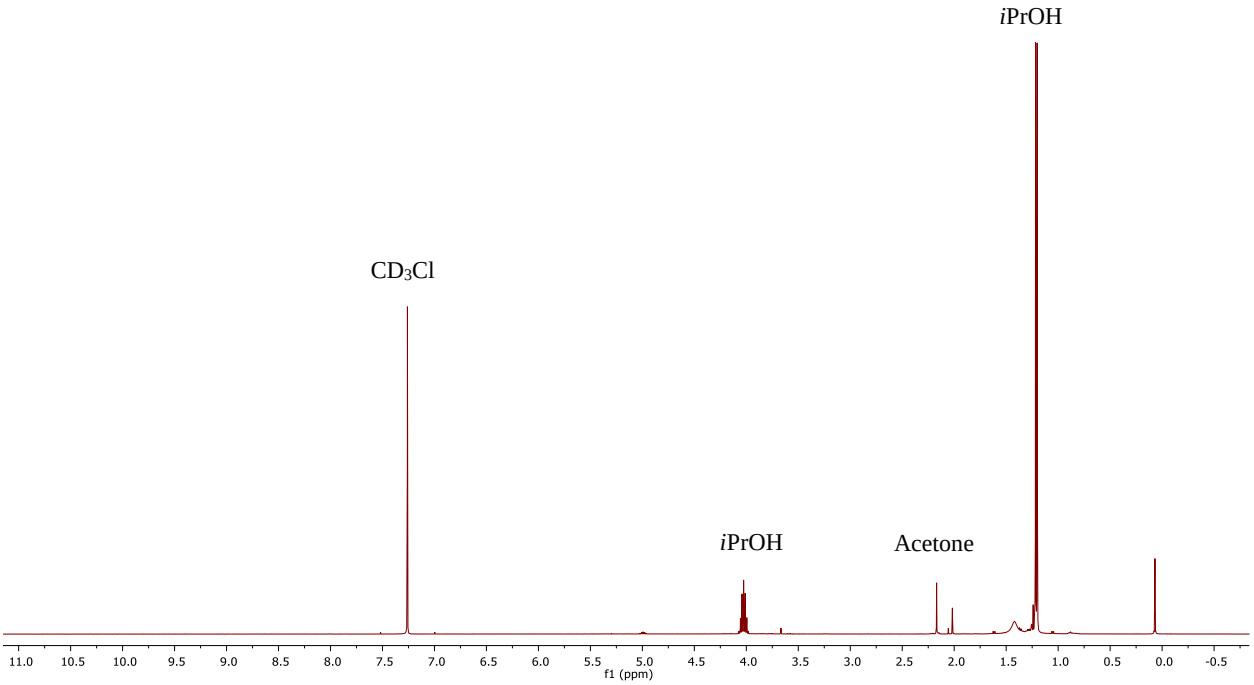

Figure D.2: ^{1}H NMR spectrum of the distillate from *i*PrOH dehydrogenation (CD_3Cl, 25 ºC, 400 MHz).

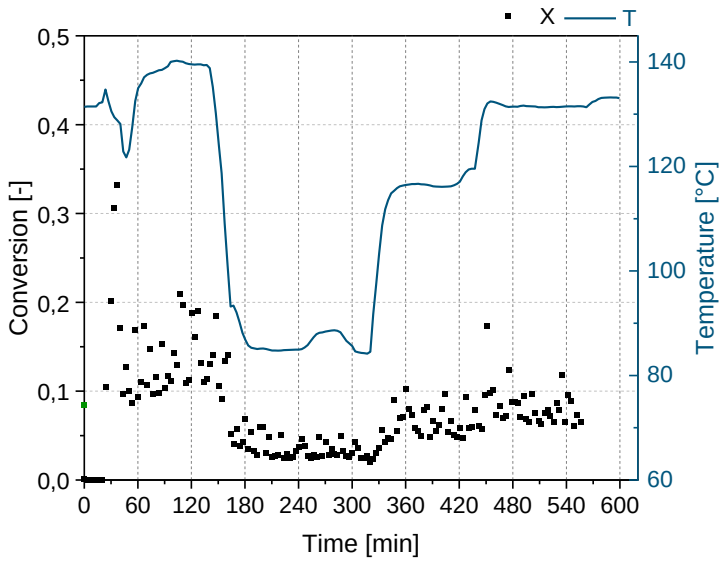

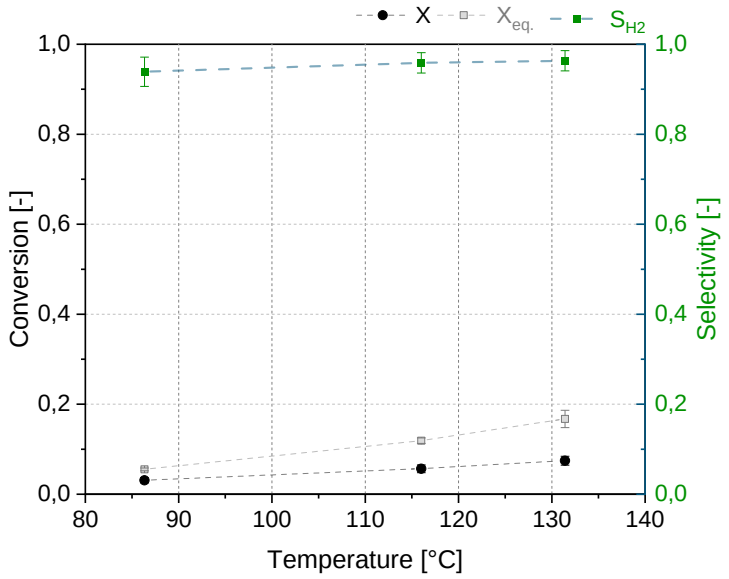

Figure D.3: 0.5 wt% Ru-MACHO-BH/SiO_2, Piper NTf_2 (α = 20%), silica 100.

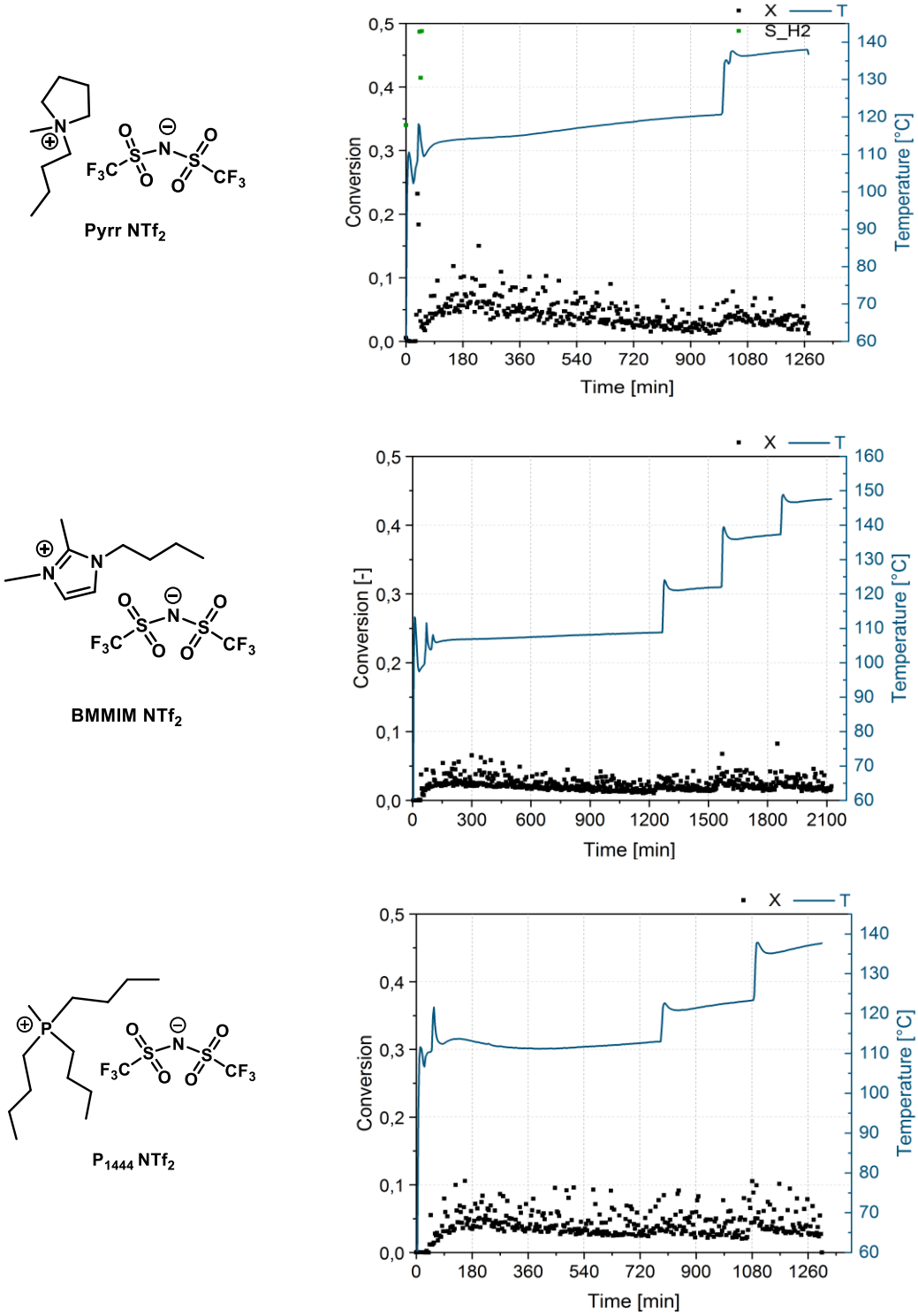

Figure D.4: Screening of different NTf_2-based ILs. Ru-MACHO-BH/SiO_2 = 0.6 wt%, α = 20%, silica 100, undiluted *i*PrOH.

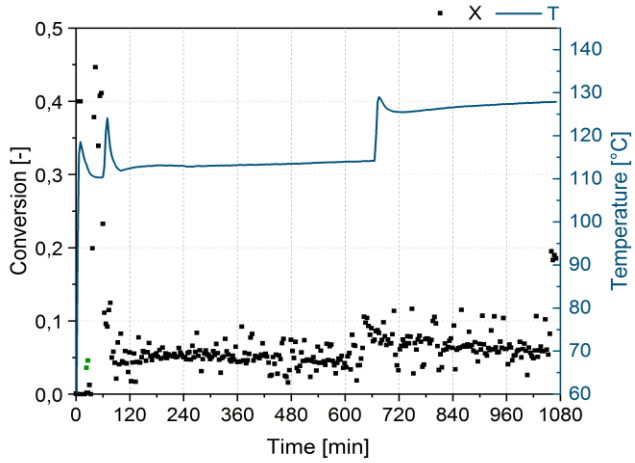

Figure D.5: Acetone – *i*PrOH: 25-75 vol%. Ru-MACHO-BH/SiO_2 = 1 wt%, P_{1444} NTf_2 (α = 20%), silica 100.

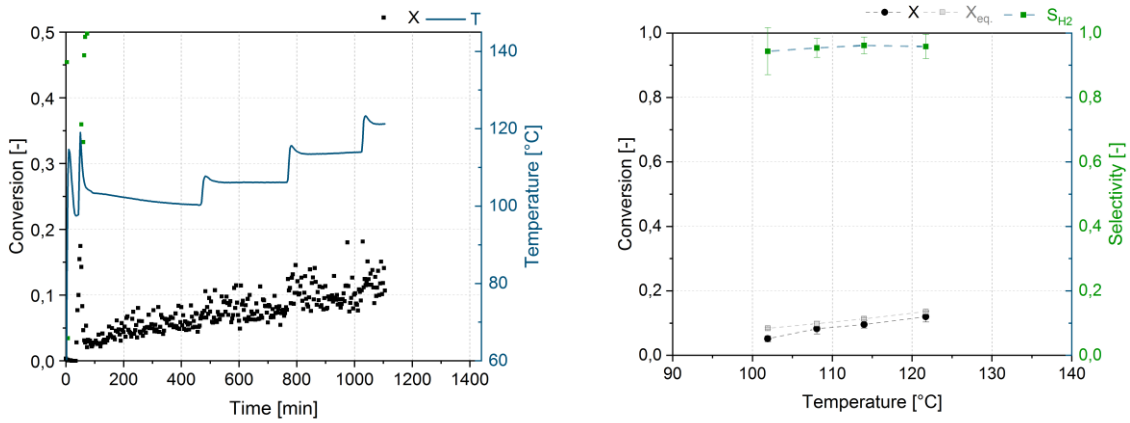

Figure D.6: Ru-MACHO-BH/SiO_2 = 0.9 wt%, P_{1444} NTf_2 (α = 20%), silica 100, α = 20%, undiluted *i*PrOH.

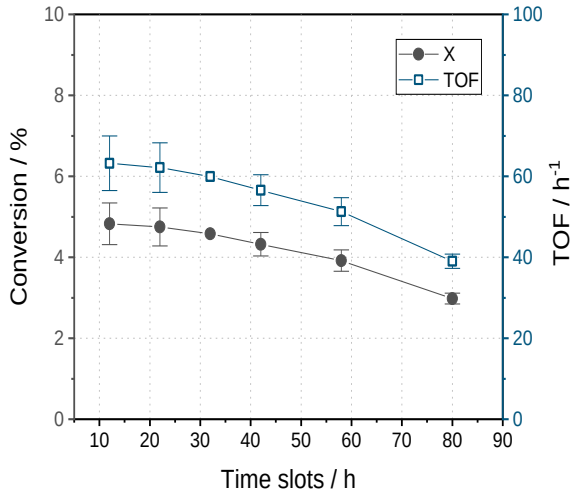

Figure D.7: TOF and conversion trends of tong-term experiment in Figure 7.10. Ru-MACHO-BH/SiO_2 = 1 wt%, P_{1444} NTf_2 (α = 20%), silica 100.

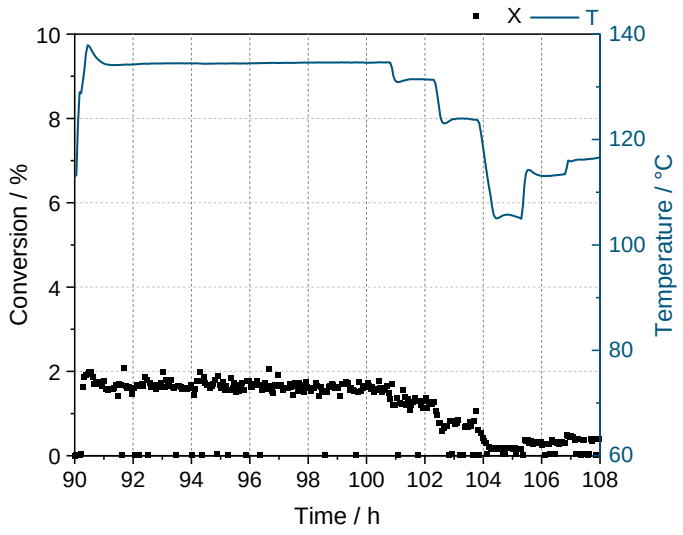

Figure D.8: Long-term experiment in Figure 7.10 (acetone dilution). Ru-MACHO-BH/SiO_2 = 1 wt%, P_{1444} NTf (α = 20%)$_2$, silica 100.

N_2 (vol%)	*i*PrOH (g/h)	N_2 (mL/min)	V_{tot} (mL/min)
0	37.4	0	318
20	30	46	318
40	22.4	93	317
60	15	140	319
80	7.5	187	319
93.4	5	440	644

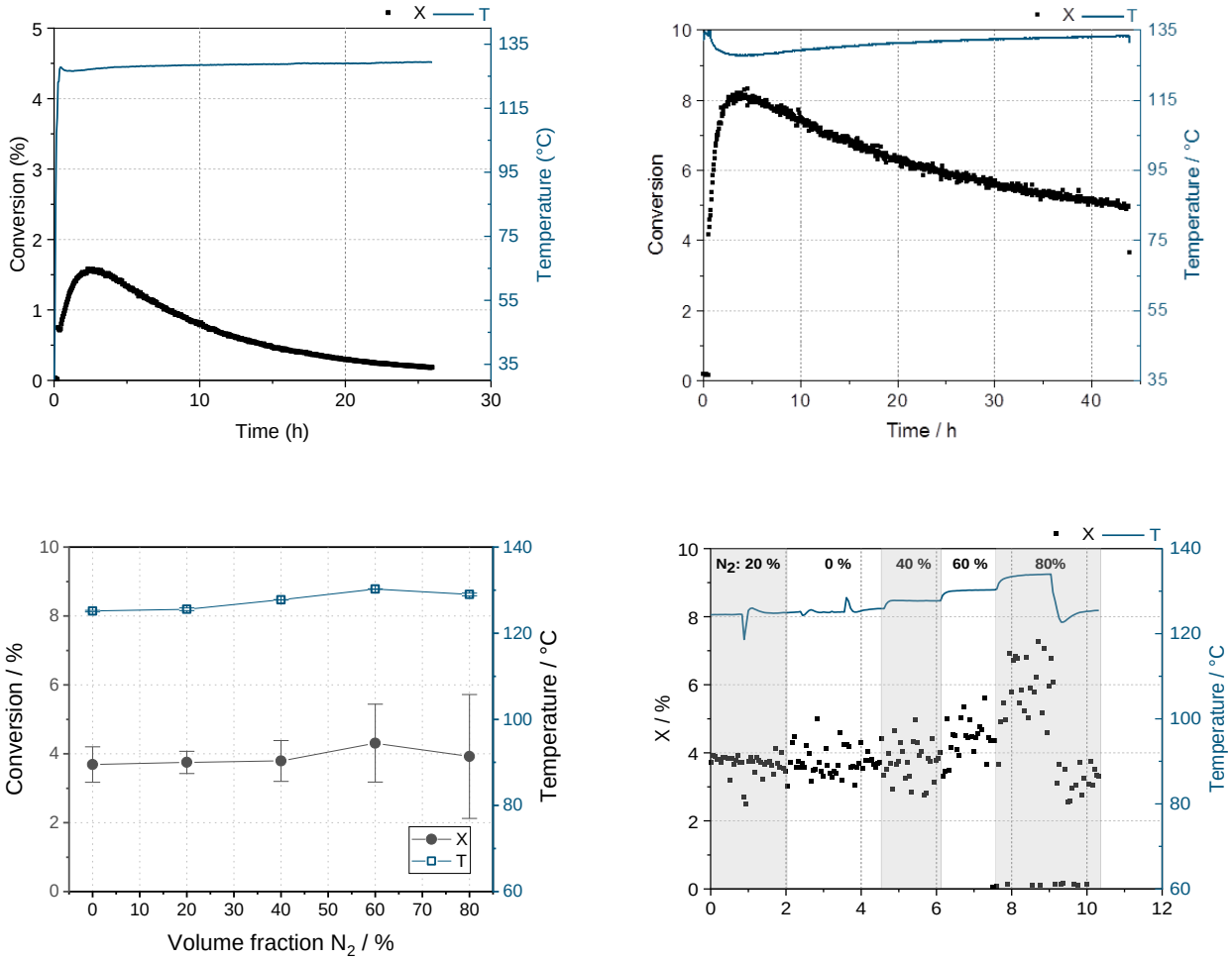

Figure D.9: Long-term experiment in Figure 7.10 (*i*PrOH dilution). Ru-MACHO-BH/SiO_2 = 1 wt%, P_{1444} NTf_2 (α = 20%), silica 100.

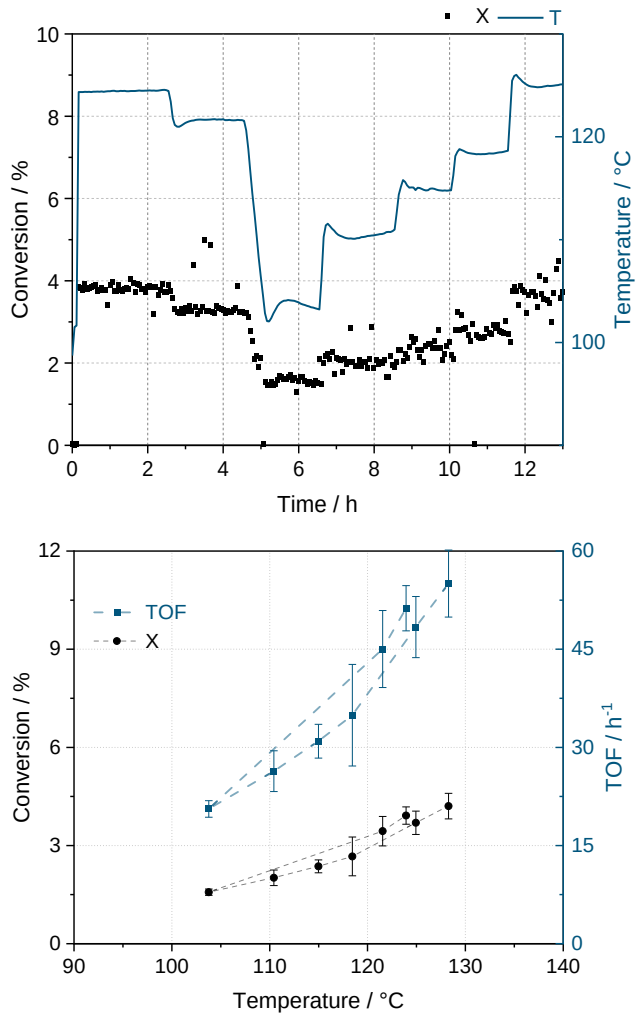

Figure D.10: Long-term experiment in Figure 7.10 (temperature variations). Ru-MACHO-BH/SiO_2 = 1 wt%, P_{1444} NTf_2 (α = 20%), silica 100.

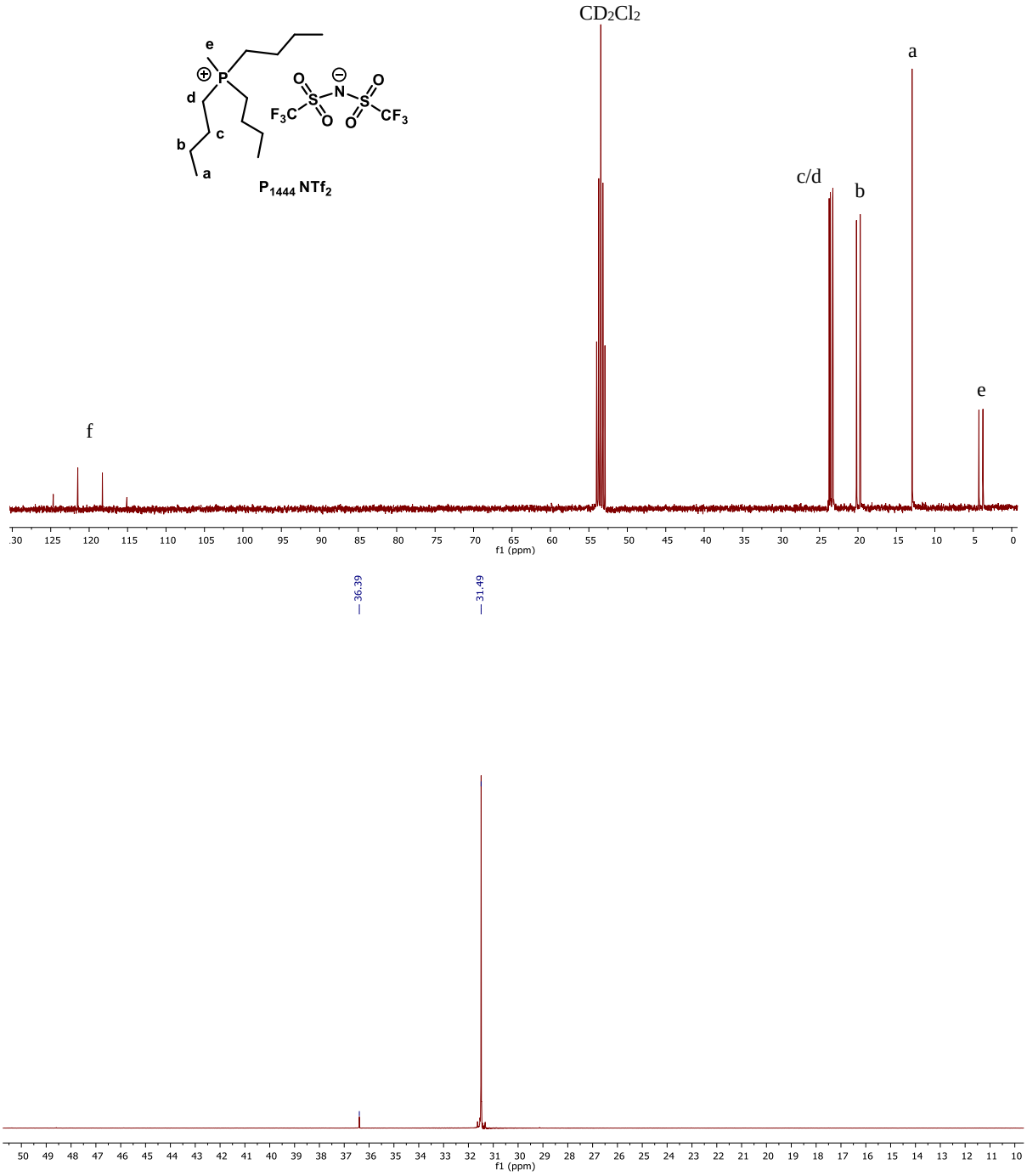

Figure D.11: ^{13}C (up) and ^{31}P (down) NMR spectra of P_{1444} NTf_2 as reference for the solid state NMR studies in Figures 7.15 and 7.16.

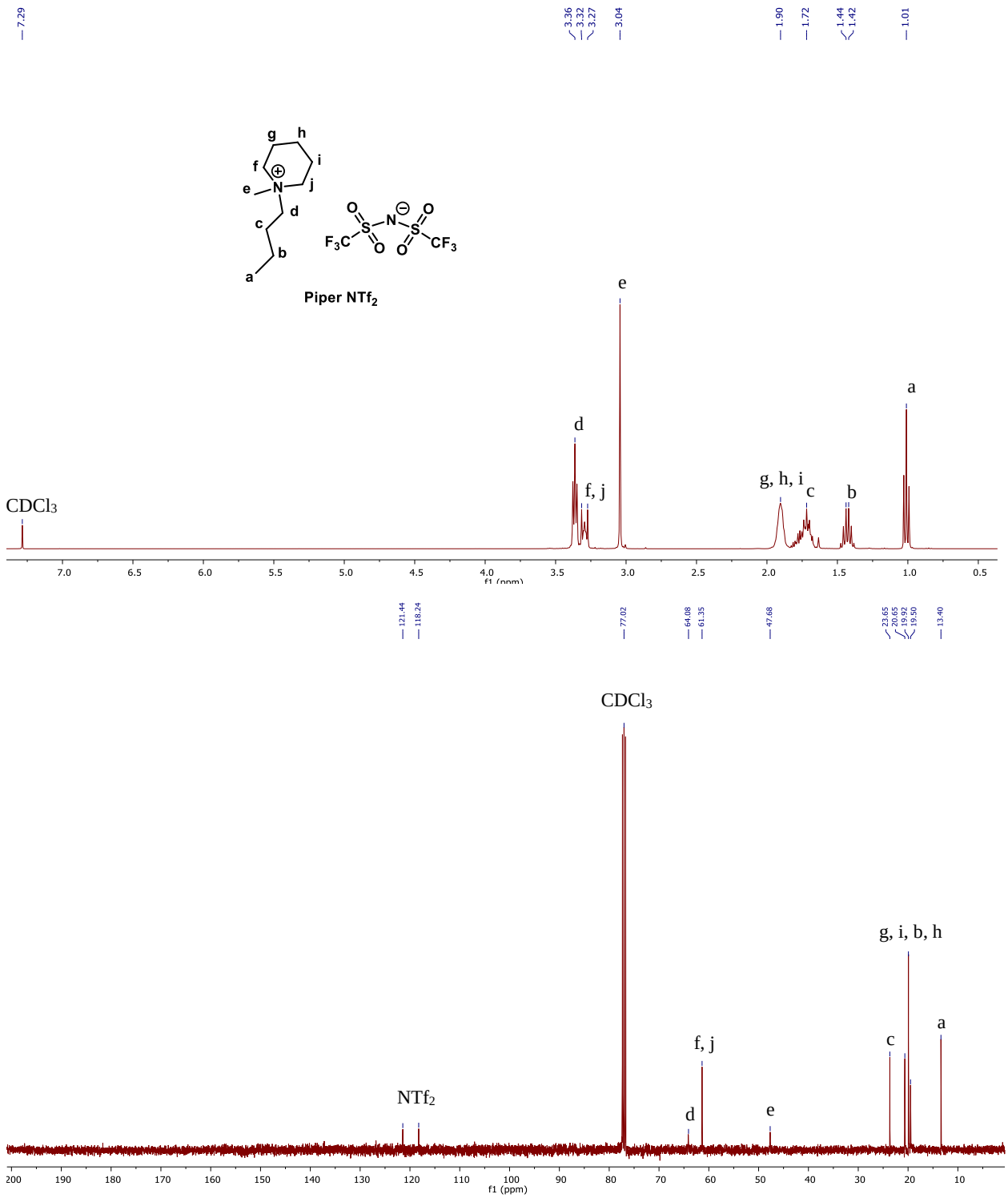

Figure D.12: ^{1}H (up) and ^{13}C (down) NMR spectra of Piper NTf_2 as reference for the solid state NMR studies.

	Total Pore Volume (cm^3/g)	BET surface Area (m^2/g)	Pore size (Å)
SILICA 100	1	305	131
SILP23	0,51	131	137
23 (136)	0,56	170	151
23 (127)	0,53	154	141
23 (133)	0,51	146	141

Table D.1: BET analysis of support, fresh and used SILPs after use in the fixed-bed reactor under different reaction conditions. The SILP composition is the same for the three samples: Ru-MACHO-BH/SiO_2 = 1 wt%, P_{1444} NTf_2 (α = 20%), silica 100.

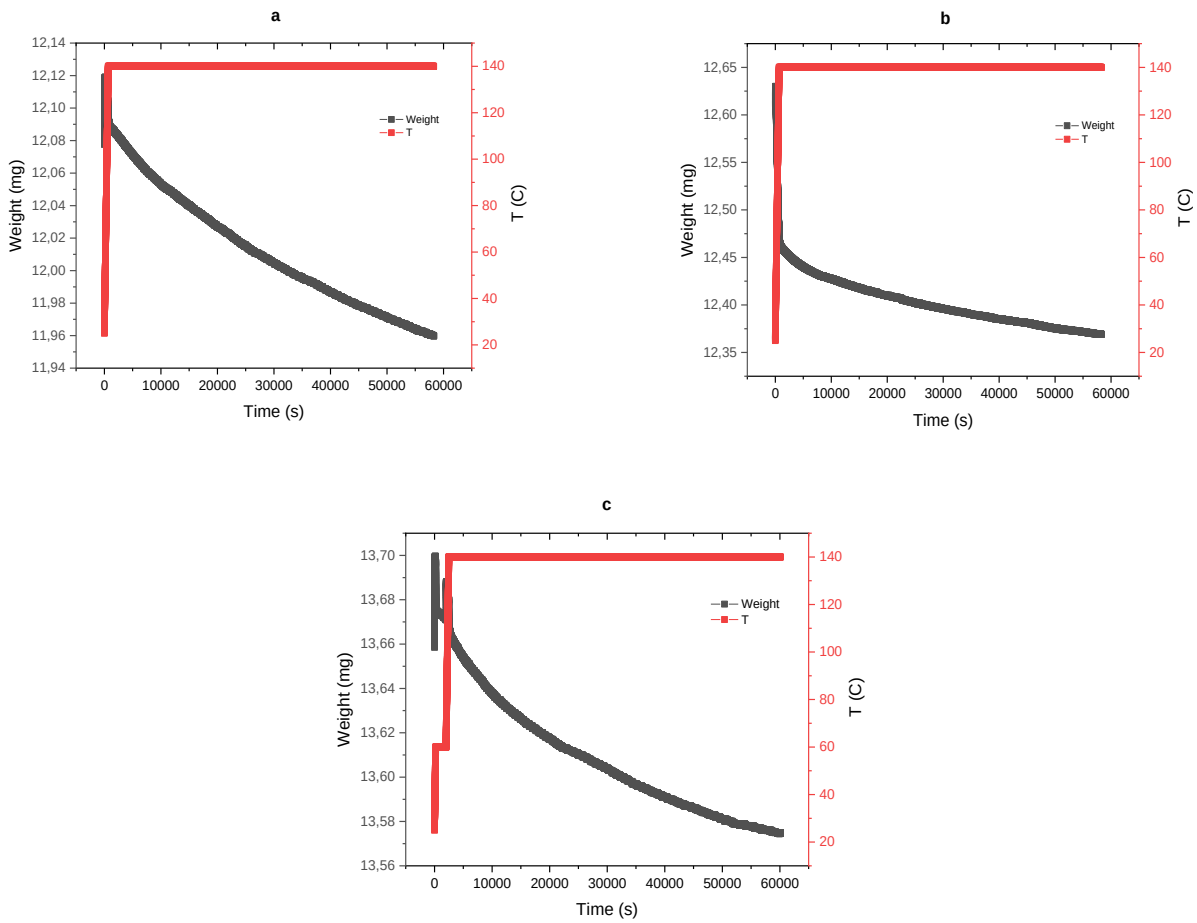

Figure D.13: (a) Fresh SILP. (b) SILP catalyst used in the long-term experiment in Figure 7.10. (c) Fresh SILP with pre-treatment at 60 ºC for 2 hours to remove volatiles.

TEM analysis of SILP materials

Purely for personal interest, I have tried to acquire TEM images of the SILP materials. In this sense, I would like to thank PhD student Dimitra Iltsiou for helping me in the acquisition and processing of the images. Similar to what described in the chapter for NMR and IR characterization, I have tried to compare images of the silica used as support material with new and used SILP. It was not possible to observe any visible differences, at least to the best of my knowledge, between the different samples. The obtained TEM images are showed below

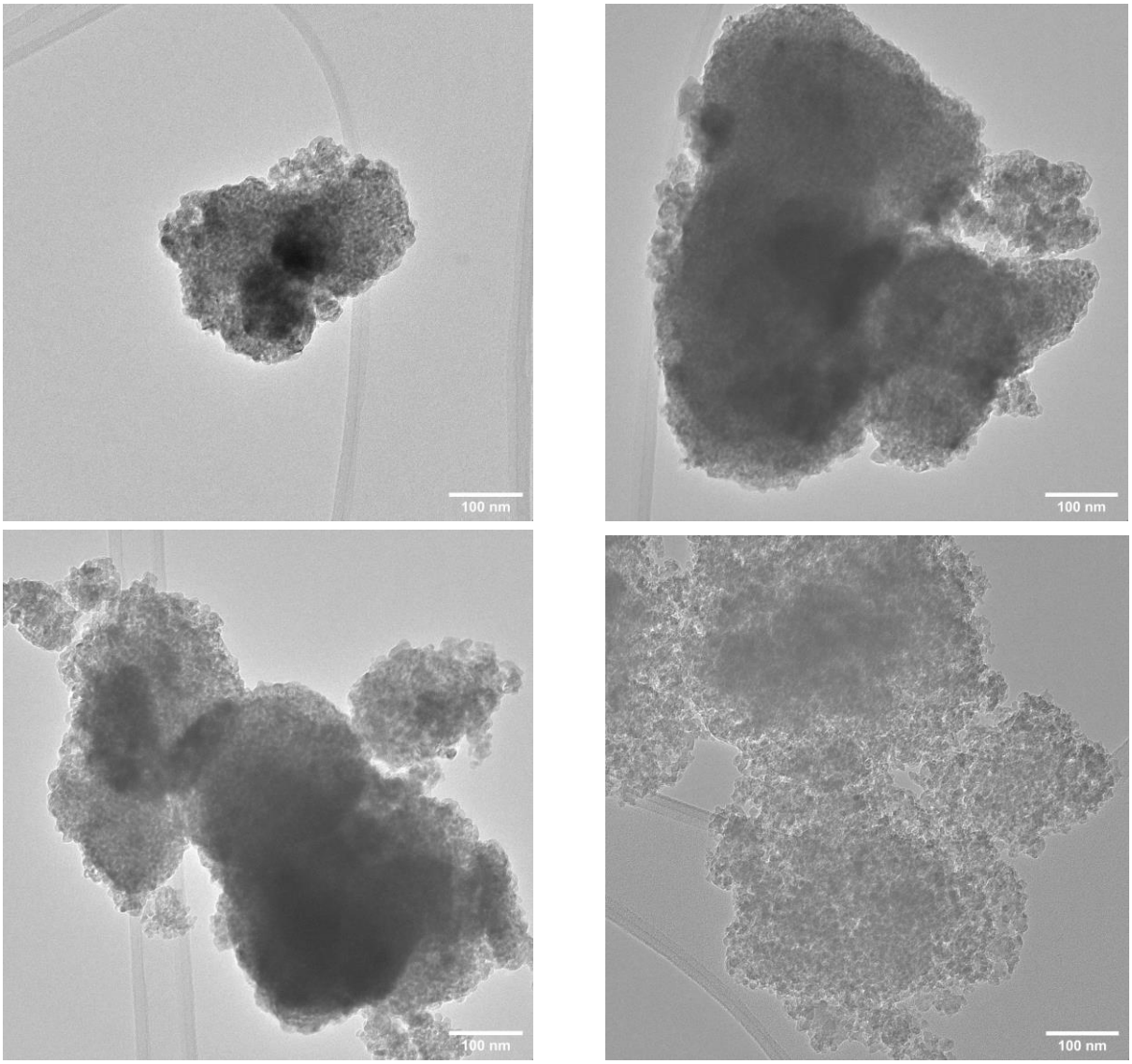

Figure D.14: TEM images of the silica 100 used as support material for preparation of the SILP catalysts discussed in Chapter 7.

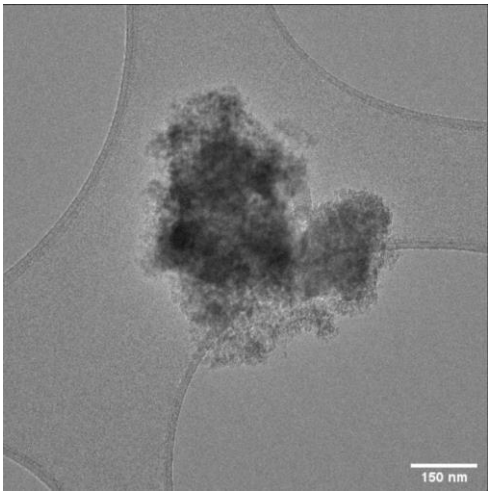
150 nm

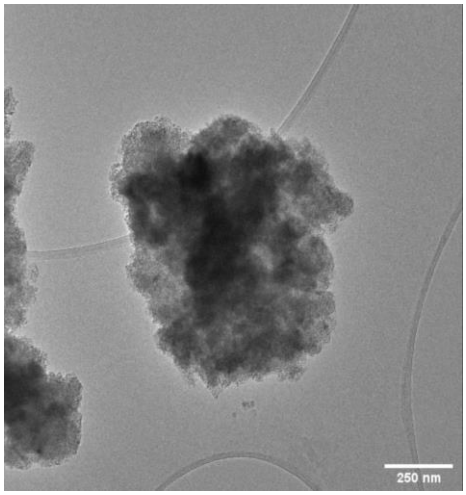
250 nm

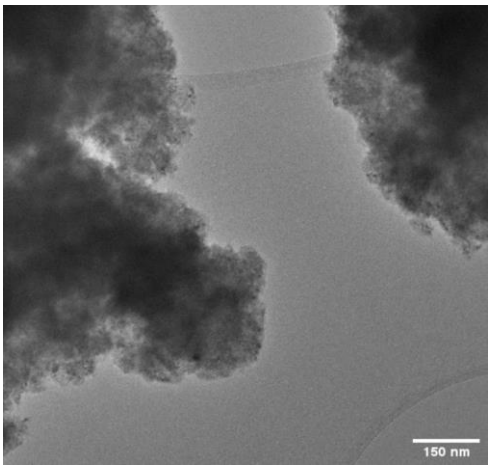
150 nm

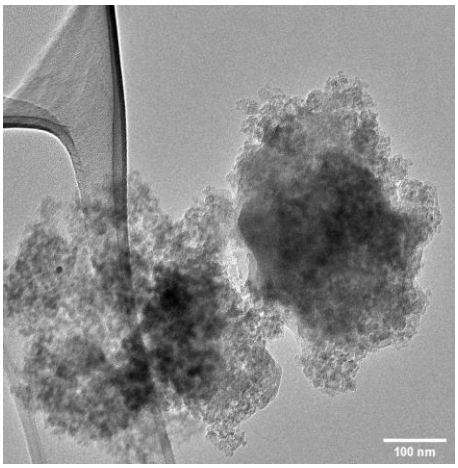
100 nm

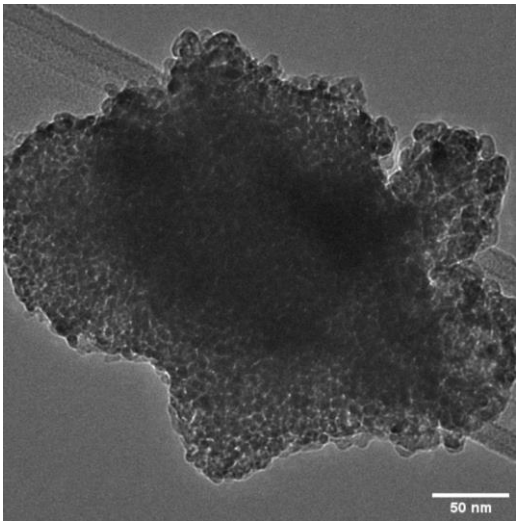
50 nm

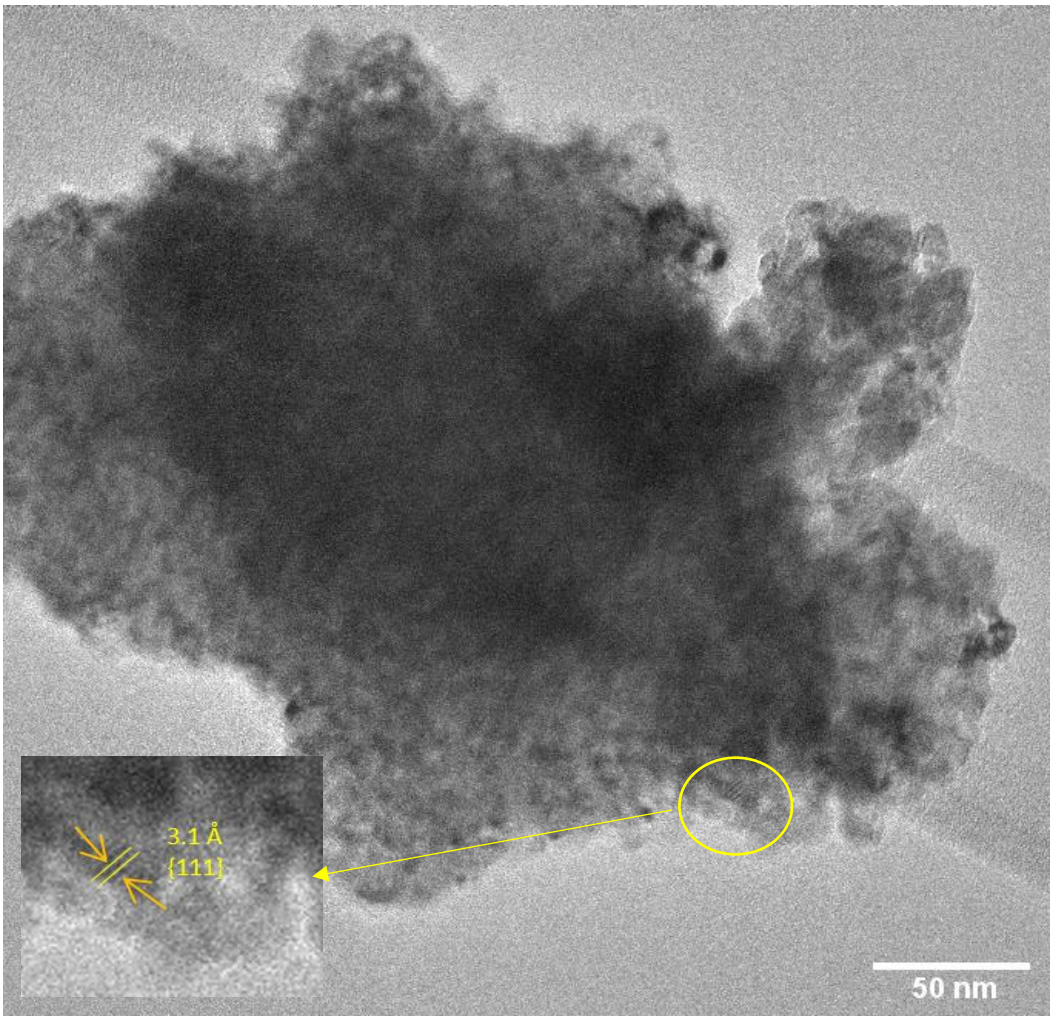

Figure D.15: TEM images of the SILP catalyst before use in the fixed-bed reactor (experiment in Figure 7.8).

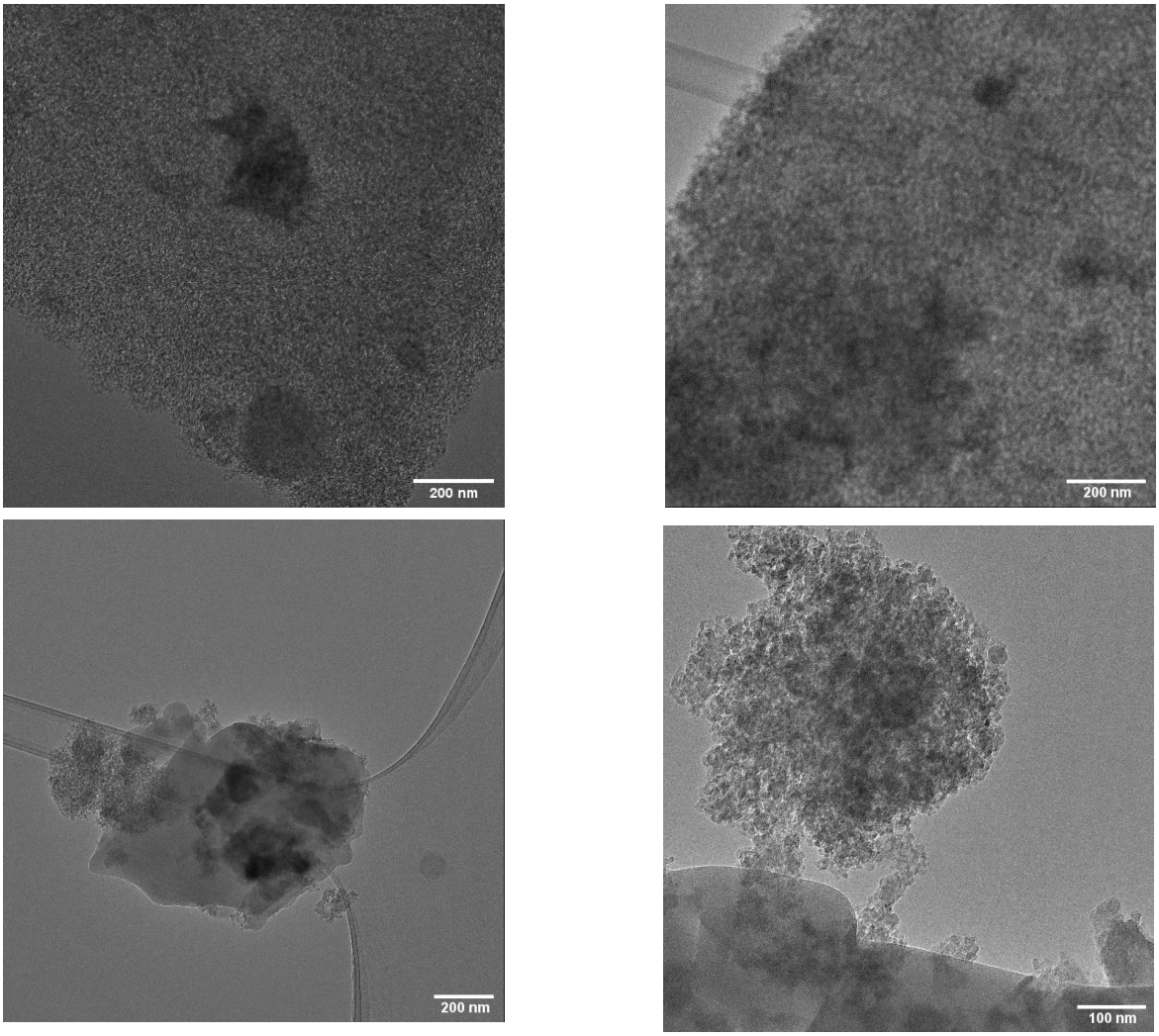

Figure D.16: TEM images of the SILP catalyst after use in the fixed-bed reactor (experiment in Figure 7.8).

Appendix E – Paper I

This review paper was written at the Department of Chemistry at DTU in collaboration with postdoc Danielle Nielsen, and Assoc Prof Martin Nielsen. The work covers the main advances of pincer-type homogeneous catalysts in relevant catalytic transformations within sustainability during the period 2015-2020. It also provides an historical background on the main achievements of pincer chemistry in relevant sustainable reactions, with high focus on H_2- and CO_2-related processes. As an example, dehydrogenation of LOHC molecules such as methanol, FA, and ammonia-borane, CO_2 hydrogenation to FA and methanol, N_2 fixation, as well as valorization of biomass substrates. Of major interest for the reader, the parts on dehydrogenation of LOHCs and CO_2 hydrogenation to FA are the key topics for the experimental work discussed in this thesis.

Published: Catalysts 2020, 10, 773; doi:10.3390/catal10070773

Author´s contribution

LP and MN designed the structure and content. LP and DN found literature and wrote the initial manuscript. LP and MN revised the manuscript.

catalysts

MDPI

Review

Recent Progress with Pincer Transition Metal Catalysts for Sustainability

Luca Piccirilli, Danielle Lobo Justo Pinheiro and Martin Nielsen *

Department of Chemistry, Technical University of Denmark, DK-2800 Kgs. Lyngby, Denmark; lucpic@kemi.dtu.dk (L.P.); dane@kemi.dtu.dk (D.L.J.P.)
* Correspondence: marnie@kemi.dtu.dk; Tel.: +45-24651045

Received: 11 June 2020; Accepted: 6 July 2020; Published: 11 July 2020

Abstract: Our planet urgently needs sustainable solutions to alleviate the anthropogenic global warming and climate change. Homogeneous catalysis has the potential to play a fundamental role in this process, providing novel, efficient, and at the same time eco-friendly routes for both chemicals and energy production. In particular, pincer-type ligation shows promising properties in terms of long-term stability and selectivity, as well as allowing for mild reaction conditions and low catalyst loading. Indeed, pincer complexes have been applied to a plethora of sustainable chemical processes, such as hydrogen release, CO_2 capture and conversion, N_2 fixation, and biomass valorization for the synthesis of high-value chemicals and fuels. In this work, we show the main advances of the last five years in the use of pincer transition metal complexes in key catalytic processes aiming for a more sustainable chemical and energy production.

Keywords: pincer complexes; sustainability; biomass valorization; hydrogen; carbon dioxide valorization; nitrogen fixation

1. Introduction

During the last 15 years, organometallic pincer-type complexes have emerged as a highly promising group of catalysts for numerous processes within sustainable chemistry. They have been applied in energy production through hydrogen generation, dehydrogenative synthesis of high-value chemicals, as well as CO_2 and N_2 hydrogenations for carbon dioxide capture and recycling and a more sustainable ammonia production, respectively. As such, the use of this family of homogeneous catalysts enhances the sustainability of an incredible number of chemical processes. High catalytic activity at mild reaction conditions, low catalyst loading, combined with high selectivity and excellent atom efficiency are the general main advantages. Notably, all these aspects are crucial when considering the sustainability of chemical processes, as dictated by the green chemistry guidelines [1]. Unfortunately, catalyst deactivation and/or degradation are usually the main drawbacks of homogeneous catalysis, otherwise excellent systems in terms of activity, selectivity, and reaction conditions. The currently employed heterogeneous alternatives are more robust and with an established know-how on the processes, but they usually require high temperatures and hence are high-energy demanding. Pincer-type ligations provides increased robustness because of the stabilization of the tridentate coordination, resulting in homogeneous catalytic systems with increased chemical and thermal stability [2–4].

The ligand design of pincer complexes offers numerous possibilities as well as potential catalytic applications [5,6]. For example, the pincer arm can bear an array of different heteroatoms and functionalities. In addition to affording chemical stability, the pincer ligand can take active part of the catalytic cycle by providing a suitable coordination site for the substrate, weakening selected bonds (H-X bonds), or accepting/donating electrons and protons. Moreover, the cooperation between the

central metal atom and the ligand is tunable based on the desired steric/electronic environment and catalytic application.

After the first family of PCP complexes was synthetized by Shaw in 1976 [7], numerous research groups have applied this concept for almost all types of homogeneously catalyzed chemical reactions. A myriad of novel complexes with different pincer arms have been synthetized and characterized, including a vast family of carbene pincers [8–23], PNP [24–29], PNN [30,31], POP [32], PCP [33–38], SNS [39,40], NCN [41], NSiN [42], CNC [43], CNN [44], NNN [45], as well as sulfur- [46–48], silicon- [49,50], selenium- [51,52], and boron-functionalized [53,54] pincer ligands. Indeed, this topic represents one of the most attractive areas in homogeneous catalysis [55–63]. Many of the most promising results in sustainable transformations have been achieved with second and third-row transition metals, such as Ru [40,64–72], Os [73–76], Ir [77–81], Rh [82,83], and Pd [84–89]. Nevertheless, the current trend in the scientific community is to identify cheaper alternatives based on earth-abundant metals such as Fe [90–96], Mn [97–100], Ni [101–105], V [106–108], and Co [109–114]. In particular, iron and manganese PNP pincer complexes show optimal performance in many relevant sustainable transformations in the optic of the hydrogen economy. Several excellent reviews cover this relevant transition toward first-row metals for a more sustainable chemical production [115–124].

More recently, the incorporation of pincer complexes into porous materials acting as supports has been investigated using the supported (ionic) liquid phase catalysis (SILP or SLP) [125,126]. The idea is to combine the excellent activity of homogeneous systems with the robustness given by the heterogeneous nature of the support. Important examples using pincer-type homogeneous catalysts can be found in aldehyde hydrogenation using Fe(II)-PNP complexes [127,128], and continuous-flow alkane dehydrogenation [129].

Furthermore, several groups have been exploring the use of pincer complexes for a wide series chemical transformations, further expanding the applicability of this family of catalysts. Representative examples include olefination [130–132], hydroamination [133–135], hydrocarboxylation [136], hydrovinylation [137], aminomethylation [138], dehydrogenation of alkanes [139–144], alkane metathetis [145], N-formylation of amines [146,147], C-alkylation of secondary alcohols [148,149], α-alkylation of ketones [150,151], and alkylation of amines [152–156] and anilines [157].

The deoxydehydration (DODH) of biomass-derived vicinal diols and polyols has also been explored by employing metal pincer complexes. The reaction proceeds in the presence of a sacrificial reducing agent and results in the formation of alkenes, relevant building blocks for the polymer industry. Some examples using pincer ligation are reported with vanadium [106,107], rhenium [158], as well as molybdenum pincer catalysts [159]. The field is relatively immature and further optimization is necessary. A comprehensive overview of the best catalytic systems for DODH reactions, including the aforementioned pincer complexes, is provided in the detailed reviews of Fristrup [160] and Monbaliu [161].

Remarkably, there are several reports in literature using pincer-type metal complexes as suitable catalysts for water splitting reactions. The process is key for the development of the hydrogen economy that requires green and sustainable hydrogen produced via solar or wind energy. Many groups explored various combinations of metals and pincer ligation [14,162,163]; in particular, several works report the use of Milstein Ru-PNP catalyst **3** for this transformation [164–169].

The purpose of this review is to show the very recent advances in pincer-type catalysis for sustainable chemistry. Research in this area centers on achieving zero-CO_2 emissions and sustainable, eco-friendly chemistry and energy production. Literature is already rich with numerous excellent works reviewing pincer complex chemistry as well as its applications in homogeneous catalysis for sustainable reactions [170–175]. As such, in this review we will confine ourselves to discuss the recent progress in the use of pincer complexes as catalysts for sustainable chemistry. Moreover, we will mainly cover work from the second half of the previous decade, i.e., 2015–2020. Dehydrogenation of bio-resourced substrates, hydrogenation of CO_2 and N_2, processes for the synthesis of high-value

chemicals with lowered waste and enhanced atom efficiency, as well as hydrogen storage systems, are the main areas of interest of this review.

2. Dehydrogenation Reactions

Acceptorless alcohol dehydrogenation (AAD) by homogeneous catalysis represents a powerful and sustainable route for synthetic purposes as well as for energy production/storage [176,177]. Mild reaction conditions, high selectivity, and excellent atom efficiency are the main advantages of the process. The sustainability of homogeneous catalytic AAD relies on the absence of any Meerwein-Ponndorf-Verley type sacrificial reagents, which traditionally promote the Oppenauer oxidation of the alcoholic moiety in transfer hydrogenation reactions. In addition, even when molecules that are more complex are formed, valuable hydrogen is often the only byproduct, which can be directly used in-house to provide energy to the process, perfectly in line with the idea of new integrated bio-refineries. These facets render AAD dramatically more atom- and energy efficient, respectively, compared to conventional synthetic procedures.

In the optics of abandoning fossil feedstock, the dehydrogenation of biomass-derived molecules is one of the explored alternatives. Formic acid, ethanol, glycerol, and carbohydrates already represent an accessible, sustainable source for the production of chemicals and fuels by acceptorless dehydrogenation. Importantly, they are abundant and easily obtainable from biomasses. Hence, this field holds great potential, and the transformation of these substrates into high-value chemicals or direct hydrogen release by homogeneous pincer catalysis is promising.

Pincer-type complexes have been extensively applied for AAD reactions with a plethora of bio-substrates, ranging from ethanol [178–181] to lignocellulose [182], as described in Section 2.1. The applied transition metal complexes generally show good performance in terms of stability and activity, with the advantage of carrying out selective reactions at mild conditions and low catalyst loading. Often, the pincer ligand plays an active part of the catalytic cycle (metal–ligand cooperativity), which seemingly is determinant for the catalyst's stability as well as reactivity. The mechanistic details of AAD are beyond the scope of this review and can be found elsewhere [183–195]. The topic is of great importance and a deeper understanding of the reaction mechanisms is still necessary [196,197]. Nevertheless, some representative examples of catalytic cycles involving pincer ligand participation are provided throughout the review.

2.1. Early Works

The first example of AAD by homogeneous catalysis dates back to 1960s with the work by Charman, using rhodium chloride as catalyst [198]. In the mid-1970s, Robinson described the ruthenium complex $[Ru(OCOCF_3)_2(CO)(PPh_3)_2]$ in combination with trifluoroacetic acid for the dehydrogenation of isopropanol, 1-butanol, ethanol, methanol, and glycerol [199–202]. Several improvements were achieved in the subsequent 20 years, using various type of homogeneous systems in combinations with a range of additives, including light irradiation.

In 2004, Milstein presented the first example of metal–ligand cooperating pincer ligands in AAD for synthetic purposes [203,204]. In a series of ruthenium(II)-based complexes, the PNP pincer bearing a pyridine moiety and various phosphine substituted side arms was found to be very active for the dehydrogenation of simple secondary alcohols. Some examples of the first generations of Milstein's catalysts can be found in Scheme 1a. In most cases, there is a direct participation of the pincer ligands in the catalytic cycle. The pyridine moiety rearranges by aromatization-dearomatization [64,177,205–209], facilitating the coordination of the alcoholic substrate and the subsequent hydrogen release from the dihydride species, as depicted in the catalytic cycle in Scheme 1b. The involvement of the pincer moiety in the catalytic cycle has been investigated by many groups [210–215]. In 2015, Li reported computational mechanistic studies on several reactions using the Milstein PNP and PNN catalysts [216]. The authors recalculated rate-determining steps and investigated the aromatization-dearomatization equilibria. It was found that aromatic PNP and PNN ligands often provide the lowest activation energy

for some steps, whereas for other steps, the aromatization–dearomatization process was not involved in the lowest energy pathway. Very recently, Gusev investigated the mechanism of AAD of alcohols, as well as ester hydrogenation, using catalyst **4**, and identified the dihydrido complex **4-H** (Scheme 1b) as the active species for both dehydrogenation and hydrogenation reactions [217].

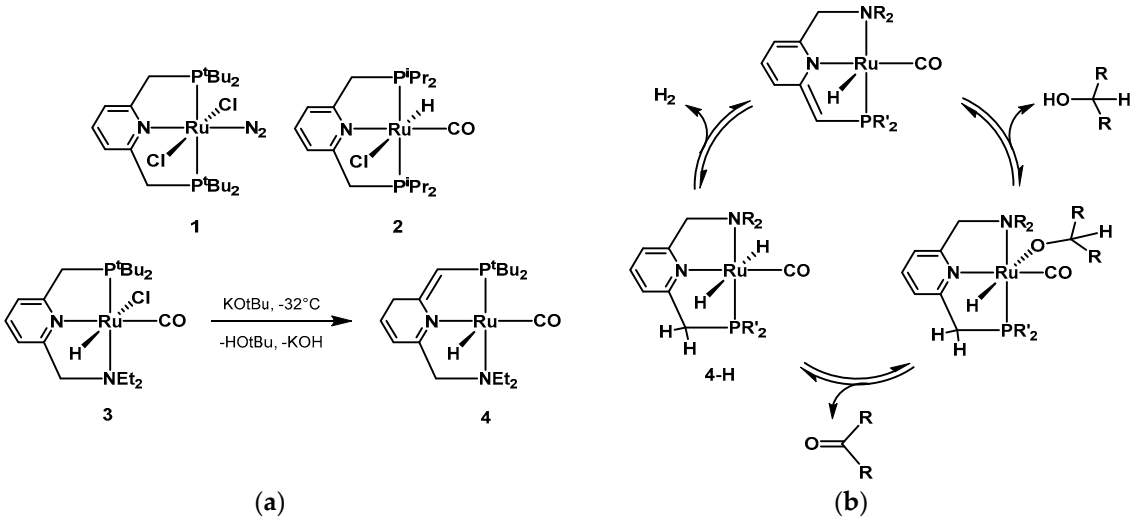

Scheme 1. (**a**) Examples of Milstein's first generation pincer catalysts [204]; (**b**) example of acceptorless alcohol dehydrogenation (AAD) reaction mechanism using Milstein's type PNN pincer complexes based on aromatization/dearomatization of the pyridine moiety.

Simultaneously, the Beller group started exploring the in situ influence of various phosphines and nitrogen containing ligands mixed with ruthenium catalyst precursors for the dehydrogenation of isopropanol [218]. For the first time, they demonstrated the possibility to generate hydrogen from this substrate at temperatures below 100 °C. A dramatic increase in activity was observed with addition of multidentate *N*-ligands, with particularly TMEDA being the most prominent promoter for catalytic activity. Remarkably, the catalyst was active over a period of up to 11 days. The authors applied the same system for ethanol dehydrogenation but no significant H_2 formation was detected.

In a following work from 2011, Beller tested both known catalyst as well as the in situ formation of active species using combinations of Ru-precursors and *N*-containing pincer ligands. They showed that the ruthenium complex $[RuH_2(CO)(PPh_3)_3]$, in the presence of the ^{iPr}PNP ligand **C** shown in Scheme 2, was able to efficiently dehydrogenate isopropanol without the need of any additive [219].

The system showed in Scheme 2 represents the current state-of-the-art of homogeneous isopropanol acceptorless dehydrogenation. The reaction was performed for the first time at mild conditions (90 °C, refluxing isopropanol) and importantly, without additives. The in situ formed active catalyst **10-H** (Scheme 3) resulted in a turnover frequency higher than 8000 h^{-1} using 4 ppm of catalyst.

Almost simultaneously, Gusev presented a range of ruthenium and osmium PNP and POP pincer catalysts for the transformation of alcohols into ketones, widening the applicability of metals to osmium for this type of transformation [73]. The ^{iPr}PNP-Ru-H_2 active dihydrido catalyst **10-H** formed in situ in the work of Beller, was synthetized and characterized starting from the chlorido precursor **10** (Scheme 3). NMR analysis revealed the equilibrium between the dihydrido species and the model substrate isopropanol, and isopropoxo complex **10b** was isolated. Importantly, while the Os-POP catalysts **11** and **11-H** (Figure 1) did not show significant catalytic activity, the Os-PNP complexes **12** and **12-H** demonstrated good air, moisture, and thermal stability, together with outstanding versatility for dehydrogenation of primary alcohols for reactions of transfer hydrogenation, dehydrogenative coupling, and amine alkylation.

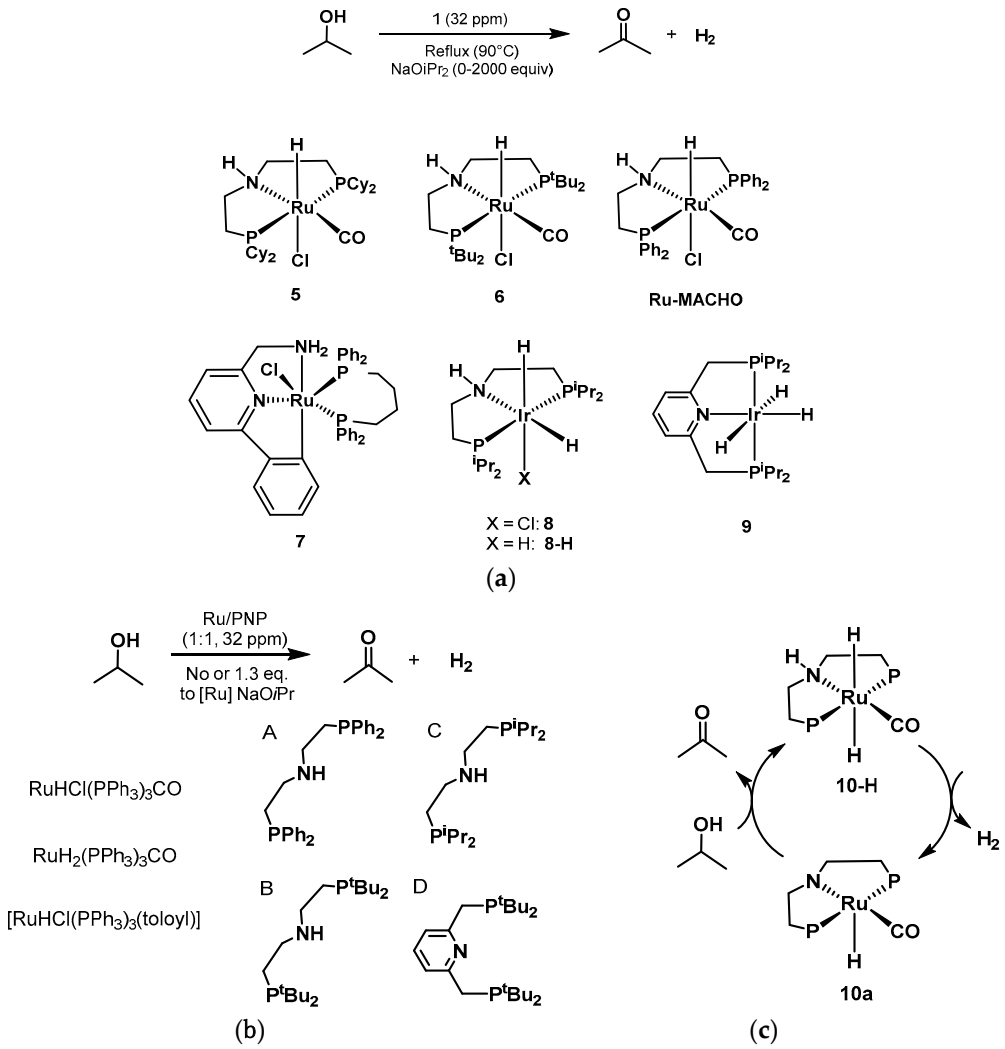

Scheme 2. (**a**) Pincer complexes screened by Beller in 2011; (**b**) low temperature isopropanol dehydrogenation; (**c**) proposed outer-sphere mechanism [219].

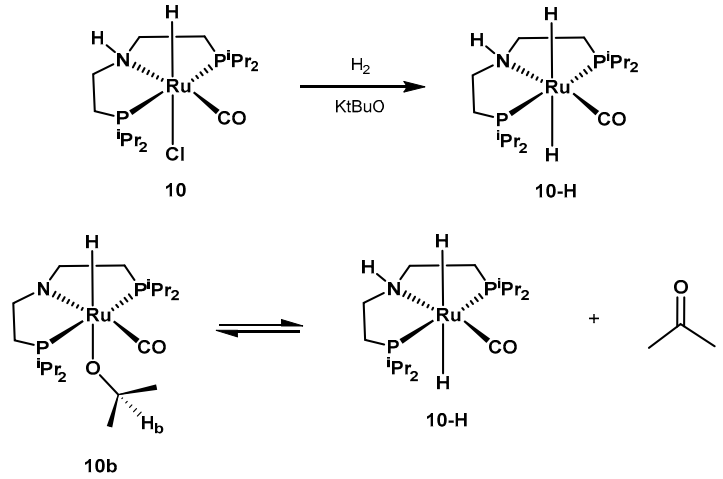

Scheme 3. Ru-^{iPr}PNP catalysts synthetized and characterized by Gusev and equilibrium between **10-H** and **10** [73].

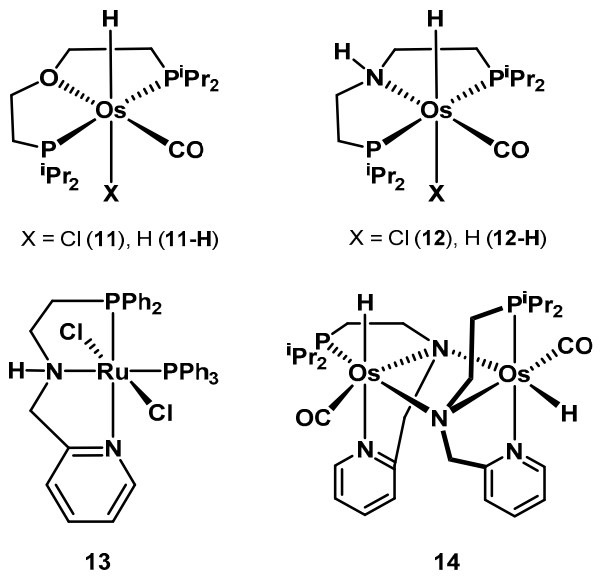

Figure 1. Representative examples of ruthenium and osmium pincer catalysts reported by Gusev [73,178,179].

In 2013, Beller showed the efficient conversion of ethanol into ethyl acetate using **Ru-MACHO**, reported in 2012 to efficiently catalyze ester hydrogenation [220]. The reactions were performed at refluxing conditions and in the presence of NaOEt, necessary for the catalyst activation through Cl^- elimination (Scheme 4) [180]. Furthermore, it was speculated whether the ethoxide plays an active role in driving the reaction further from the acetaldehyde intermediate to the ethyl acetate product. Under optimized conditions, the reaction afforded 77% yield in ethyl acetate (TON = 15,400) using 50 ppm of **Ru-MACHO**, 0.6% mol of NaOEt, at 90 °C, after 46 h. Curiously, in the screening of catalysts, the Ir-PNP catalyst (**8** in Scheme 2) synthetized by Abdur-Rashid [79], as well as the Milstein PNP catalyst **4** [204], were found to be practically inactive for this transformation under the given reaction conditions.

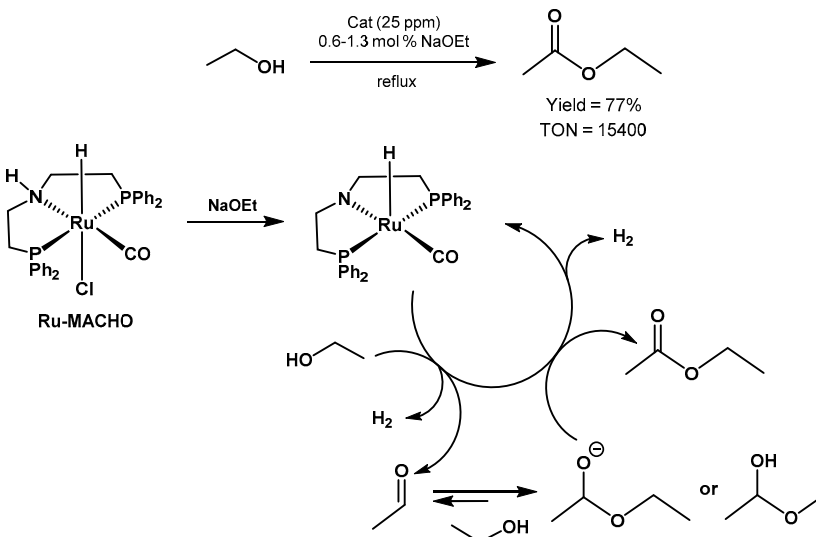

Scheme 4. Ethanol transformation to ethyl acetate using **Ru-MACHO** and proposed reaction mechanism by Beller [180].

The same year, Gusev reported the same transformation catalyzed by the Ru-PNN complex **13** in Figure 1. By applying 50 ppm of **13** in a refluxing solution of EtOH/NaOEt (1 mol%), it was possible to achieve 85% conversion after 40 h [179]. Also the same year, Gusev presented the osmium dimer **14** (Figure 1) as well [178]. This PNN osmium congener to the ruthenium complex **13** is particularly

active in ethanol dehydrogenation into ethyl acetate. As such, the system affords 96% conversion of neat ethanol into ethyl acetate and 2 equivalents of hydrogen after 8 h at 78 °C, with toluene as solvent, 0.5 mol% of KtBuO, and a molar ratio of substrate to metal equal to 1000.

In 2014, Beller showed that it is feasible to generate hydrogen from ethanol/water mixtures as well as from industrial bio-ethanol obtained from fermentation processes, without prior removal of the water content (5%) [181]. Catalyst **10** was active using various water contents (EtOH/H_2O [*v*/*v*] 9:1, 7.5:2.5, 5:5), producing only trace amounts of CO_2 and CO (<10 ppm), of key importance for the direct use of hydrogen in fuel cells. Under optimized conditions, using 25 ppm of catalyst **10** (Scheme 3) and 8 M NaOH, the reaction resulted in TOF of 1707 h^{-1} and 1613 h^{-1} after 1 and 3 h, respectively. A long-term experiment was also carried out, affording 70% yield after 98 h at 88 °C, resulting in a TON as high as 80,000 and 7.8 L of hydrogen gas produced. Remarkably, the system showed comparable activity to the aqueous ethanol solution also when applying real fermented bio-ethanol (TOF = 1770 h^{-1} and 1686 h^{-1} after 1 and 3 h, respectively).

Since their seminal work, the Milstein group has continued exploring novel pincer complexes leading to a series of novel synthetic applications using the AAD methodology [205]. As previously mentioned, the sustainability effect of carrying out dehydrogenation reactions by AAD relies not only on the concomitant production of H_2, but also on the absence of waste, and hence an excellent atom efficiency. The field is extensively growing, and pincer complexes are contributing to the main advances. Several groups have explored new routes for the syntheses of numerous new product types by means of AAD reactions. For example, starting from alcohols and amines, it is now possible to selectively obtain amides [221–225], imines [226–228], imides [229], polyamides [230], pyrroles [231–235], pyridines [236], pyrazines [237–239], pyrimidines [240], hydrazones [241], quinolines [242], or aldimines [243,244]. AAD of alcohols also provide access to clean, efficient routes to carboxylic acids [245–248], ketones or aldehydes [249–251], esters [252–256], acetals [257], alkenes [258], as well as lactones [259–261].

In most of the cited works, homogeneous pincer-type catalysis often provides milder reaction conditions, as well as enhanced atom efficiency compared to the classical synthetic routes. In addition, several of the cited works employ first-row metal complexes, further increasing the sustainability of the processes. The electronic configuration of the metal center, the design of the pincer ligand, together with specific reaction conditions favors the desired reaction mechanism leading to certain products. These possibilities demonstrate the synthetic versatility of AAD and the very high flexibility, selectivity, and activity of pincer catalysts. These complexes might even be considered a privileged family of catalysts [262–266].

2.2. Dehydrogenation Reactions for a Hydrogen Economy

There are many alternatives for continuous hydrogen release from liquid organic hydrogen carriers (LOHCs), such as methanol, formic acid, up to bigger aromatic molecules, and carbohydrates. The topic has been widely reviewed, offering comparison with established energy systems, applicability, and potential impact of LOHCs for the future of energy [267–288]. The H_2 content stored in each of these molecules varies (Table 1), as well as the catalytic pathway involved in their dehydrogenation. In most cases, several reaction mechanisms are competing, each of them releasing different equivalents of hydrogen gas. Together with CO_2 hydrogenation, this topic currently represents one of the more intense research areas within sustainable catalysis.

The dehydrogenation of alcohols in a hydrogen economy perspective has been well-reviewed in the last 10 years by many authors, providing a comprehensive overview of the many possibilities offered by homogeneous catalysis, including pincer-type catalysis [289–293]. The release of hydrogen from LOHCs has been proposed and achieved using different approaches, with either methanol, formic acid, or formaldehyde/water as hydrogen storage systems [294–298]. Methanol and formic acid represent nowadays the most studied technologies for efficient hydrogen release at low temperatures (*vide infra*), hence being promising candidates for acting as LOHCs in the transportation sector, where lower temperatures are required [299–305]. Hydrogen release from methanol, as well as from formic

acid, should be envisioned as part of a wider concept including CO_2 capture and recycling [306,307]. Green hydrogen produced via water electrolysis using e.g., wind- or solar energy can sustain the inverse process of CO_2 hydrogenation to methanol, formic acid, or any favorable LOHC, closing an ideal CO_2-free energy production cycle [308–314].

Table 1. Hydrogen weight percentage stored in some representative liquid organic hydrogen carriers (LOHCs).

LOHC	H_2 wt%
Methanol	12.6
Formic Acid	4.4
Ethanol	12
Formaldehyde	6.6
Glycerol	9.6
Sugar Alcohols	8.9–9.3
N-ethylcarbazole (NEC)	5.8
Dibenzyltoluene (DBT)	6.2
1,2-BN-cyclohexane	7.1
BuPy	3.14
MePHI	5.76

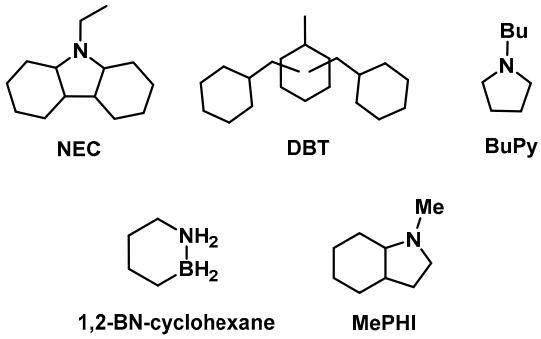

Polyols such as glycerol or carbohydrates might be considered as direct biomass-to-hydrogen suppliers, but their more complicated dehydrogenation pathways as well as lower hydrogen content currently render them unfavorable as hydrogen sources. In this light, Beller screened in 2015 a series of PN^HP-Ru and -Ir complexes (**Ru-MACHO**, **Ru-MACHO-BH**, **5**, **8**, **10**) for hydrogen production from several bio-substrates obtained from biomass [182]. Hydrogen evolution was observed from cellulose, fructose, glucose, lignocellulose, as well as from (used) cigarette filters (cellulose acetate). After optimization, it was possible to release hydrogen at temperatures at 120 °C using ppm amounts of catalyst **8** and stoichiometric amounts of NaOH in a one-pot protocol (Scheme 5). A remarkable TON of about 6000 after 3 h was obtained using 20 ppm of complex **8** in the conversion of cellulose resulting in a 1.00:1.09 mixture of H_2/CO_2.

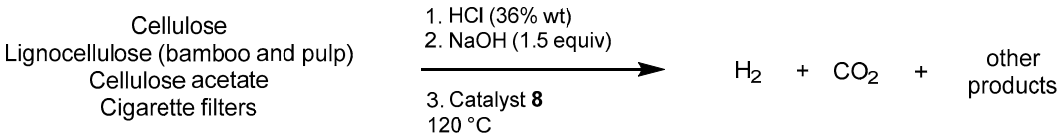

Scheme 5. Conversion of cellulose and other biomass-derived substrates using catalyst 8 in a one-pot protocol proposed by Beller [182].

The same group also proposed a Ru-catalyzed hydrogen production from glycerol accompanied by the selective synthesis of sodium lactate, the monomer for the synthesis of polylactic acid (Scheme 6) [315]. The screening involved the same family of catalysts used in the above-mentioned

work. Using only 2.5 ppm of **Ru-MACHO** and 1.08 eq. of KOH (7.3 M), it was possible to obtain full conversion and 67% yield of sodium lactate.

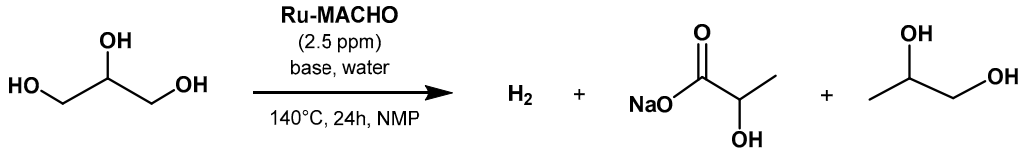

Scheme 6. Beller's glycerol dehydrogenation to lactic acid [315].

Contemporarily, Hazari and Crabtree showed the same transformation applying the family of iron-PNP complexes showed in Scheme 7 [316]. The formate complex **16** showed the highest activity with 24% conversion and 81% selectivity toward sodium lactate. In addition, the authors proposed a transfer hydrogenation of acetophenone to 1-phenylethanol using complex **15**. The yield increase with the amount of KOH vs. substrate, with a maximum of 90% yield after 20 h using 2.5 mol% of **15** and 10 eq. KOH/substrate in *N*-methyl-2-pyrrolidinone. As described later, both complexes **15** and **16** are efficient catalysts for methanol and formic acid dehydrogenations as well. Catalyst **17a**, which is obtained after basic treatment of **15**, was shown to be active in the dehydrogenation of primary alcohols such as 1-butanol to the corresponding esters [317], as well as highly selective urea synthesis by dehydrogenative coupling of methanol and amines, as reported by Hazari and Bernskoetter in 2018 [318].

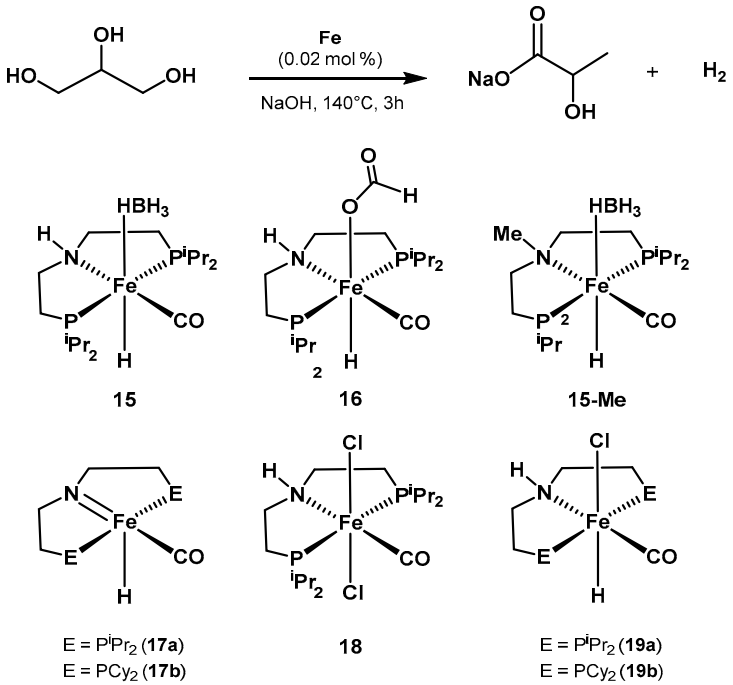

Scheme 7. Screening of iron pincer complexes performed by Hazari and Crabtree for glycerol conversion to lactic acid [316].

Recently, Milstein proposed a reversible and efficient liquid-organic hydrogen carrier using ethylene glycol (EG) [319]. The authors screened various Ru-PNP catalysts bearing different substituents in the *N* and *P* arms (Scheme 8). After optimization, catalyst **23a** reached 97% conversion and 64% yield of H_2. In addition, it was possible to hydrogenate the reaction mixture using the same catalyst and same reaction conditions, resulting in full conversion to ethylene glycol.

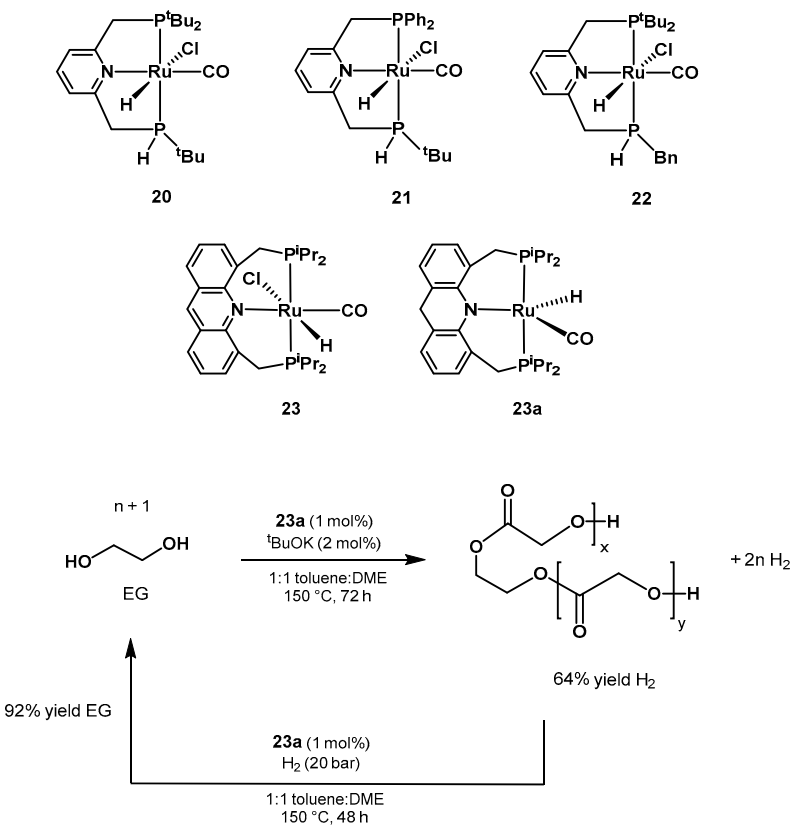

Scheme 8. Hydrogen storage system based on ethylene glycol proposed by Milstein [319].

2.2.1. Methanol Dehydrogenation

The homogeneous dehydrogenation of methanol to H_2 and CO_2 in the optic of a methanol-based economy has been intensively studied over the past decade. The topic has been reviewed by Alberico and Nielsen in 2015 [320], by Prakash in 2018 [321], and very recently by Araya, Liso, Cui, and Knudsen Kær [322]. Importantly, methanol is currently produced from fossil fuels through syngas, hence a sustainable production from biomass or/and atmospheric CO_2 is highly desirable (see Section 3.1.2). The aqueous reforming of methanol involves three consecutive steps yielding three molecule of hydrogen for each molecule of methanol (Scheme 9). The first step is the dehydrogenation of methanol to afford formaldehyde and the first equivalent of hydrogen. Then, formaldehyde reacts with water to form methanediol that can undergo a second dehydrogenation resulting in formic acid. The latter is further dehydrogenated to finally produce CO_2 and the third molecule of hydrogen.

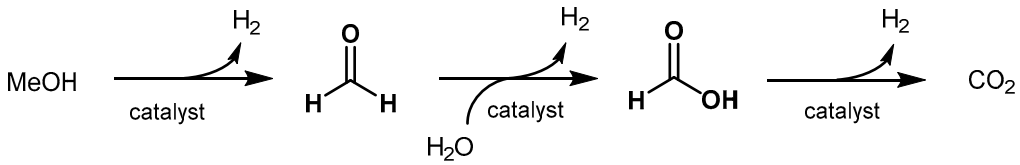

Scheme 9. Reaction pathway of aqueous methanol reforming.

The reforming of methanol to produce hydrogen is currently carried out at elevated temperatures (>200 °C) and pressures (>25 bar) by means of heterogeneous catalysts such as Pt/ Al_2O_3, as well as the less expensive $Cu/ZnO/Al_2O_3$ [323–328]. As discussed below, pincer complexes allow the direct release of hydrogen gas from aqueous methanol at temperatures below 100 °C, with low catalyst loadings as well as promising stability properties.

In 2013, Beller showed that the two catalysts **10** and **Ru-MACHO** are able to efficiently dehydrogenate methanol in a one-pot synthesis toward CO_2 (Scheme 10) [329]. The authors investigated the performance of the known Ru-PNP systems under different natures of the base, its concentration, the water content, and the reaction temperature. After optimization of the amount of base (8.0 M KOH), catalyst **10** showed the best performance affording a TOF = 2,668 h^{-1} in a 9:1 MeOH:H_2O mixture, and a TOF of 4719 h^{-1} in neat CH_3OH, at 91 °C and with 1.6 ppm catalyst loading. The system showed a turnover number of 350,000 after 23 days of continuous reaction. Merely <10 ppm of CO and CH_4 were detected. Because of the highly alkaline nature of the reaction mixture, most of the CO_2 initially produced is trapped as carbonate; hence, the authors performed an experiment with low base loading (0.1 M of NaOH in a 4:1MeOH/H_2O). Indeed, CO_2 was eventually released instead of being trapped, and the expected 3:1 H_2/CO_2 gas composition was observed, indicating a direct correlation between solution pH and the observed gas composition. The authors also proposed a catalytic cycle based on the observed species using in situ NMR experiments; all the catalytic steps were believed to follow a conventional outer-sphere mechanism.

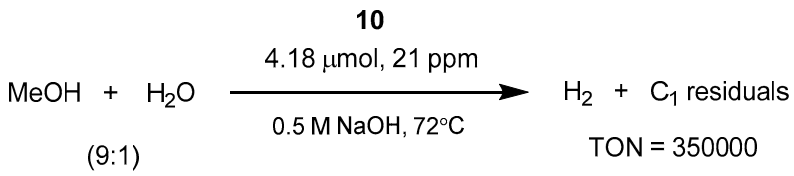

Scheme 10. Ru-PNP catalyzed methanol dehydrogenation showed by Beller [329].

Later, Grützmacher and Trincado reported the homogeneous transition metal complex [K(dme)$_2$][Ru(H)(trop$_2$dad)] for clean hydrogen release from methanol–water mixtures. Total of 0.5 mol% of the ruthenium catalyst at 90 °C achieved up to 80% methanol conversion [330]. In 2015, Yamaguchi demonstrated the low temperature (<100 °C) hydrogen release from methanol-water using an anionic iridium complex bearing a functional bipyridonate ligand [331].

Beller showed that also the iron-^{iPr}PNP complex **15** is able to perform the same transformation in the presence of base [332]. Catalyst **15** dehydrogenated aqueous methanol (9:1 CH_3OH/H_2O) at 91 °C with turnover frequencies of 702 h^{-1} after 1 h (Scheme 11). CO levels < 10 ppm were detected. Lowering the catalyst loading from 4.2 μmol to 1 μmol resulted in a of TOF = 617 h^1 and TON = 10,000 after 46 h. Remarkably, the system was active in neat methanol, as well as without addition of base, although the best performance was obtained in the presence of 8M KOH.

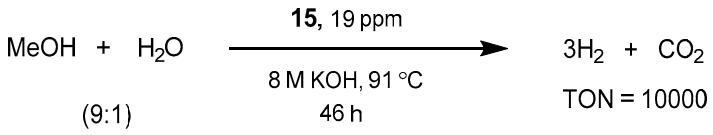

Scheme 11. Fe-PNP catalyzed methanol dehydrogenation showed by Beller [332].

A year later, Milstein applied the Ru-PNN complex **24**, known to be active in the AAD of alcohols to carboxylic acid salts and H_2, for aqueous methanol dehydrogenation as well [333]. Catalyst **24** (Scheme 12) showed promising activity and could be effectively recycled, remaining stable for 1 month and reaching TON values of 29,000. 0.025 mol% of **24** produced an overall H_2 yield of 80% starting from a 1:1 CH_3OH/H_2O mixture, in the presence of 2 equivalents KOH at 100 °C in toluene. Higher water loadings were detrimental for catalytic activity since the formation of a hydroxo complex inhibits the coordination of formic acid in the last reaction step. In order to gain insights on the reaction mechanism, the authors also performed experiments on formic acid dehydrogenation, accompanied by the isolation and characterization of the formic acid adduct by NMR and X-ray crystallography. When ~2 equivalents of NEt_3 were used in the absence of water, 0.09 mol% of catalyst **24** dehydrogenated formic acid with 98% yield of hydrogen at room temperature after 24 h.

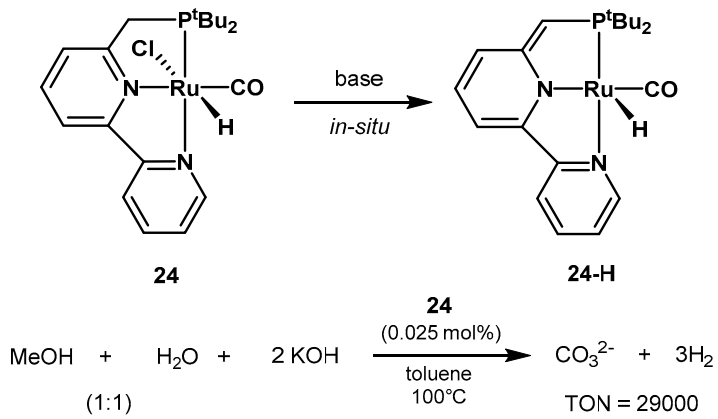

Scheme 12. Ru-PNP catalyzed methanol dehydrogenation showed by Milstein [333].

In 2014, Beller proposed a base-free, bi-catalytic system formed by **Ru-MACHO-BH** and $Ru(H_2)(dppe)_2$ (dppe = 1,2-bis(diphenylphosphino)ethane) as shown in Scheme 13a [334]. The former catalyst is similar to **Ru-MACHO** but, importantly, can be activated by heat instead of by base within the reaction temperature window employed here. The authors screened several co-catalysts in order to improve the step of formic acid dehydrogenation. After optimization, $Ru(H_2)(dppe)_2$ was found to be the optimal option. The authors proposed a synergetic interaction between the two catalysts; indeed, the volume of gas produced by the bi-catalytic system was much bigger than the gas evolution observed with the single catalysts separately, which showed very little gas evolution. The optimized system gave a turnover number >4200 with very low catalyst loading (5 µmol of each catalyst) and only traces of CO impurity (<8 ppm), yielding 26% of hydrogen (based on water).

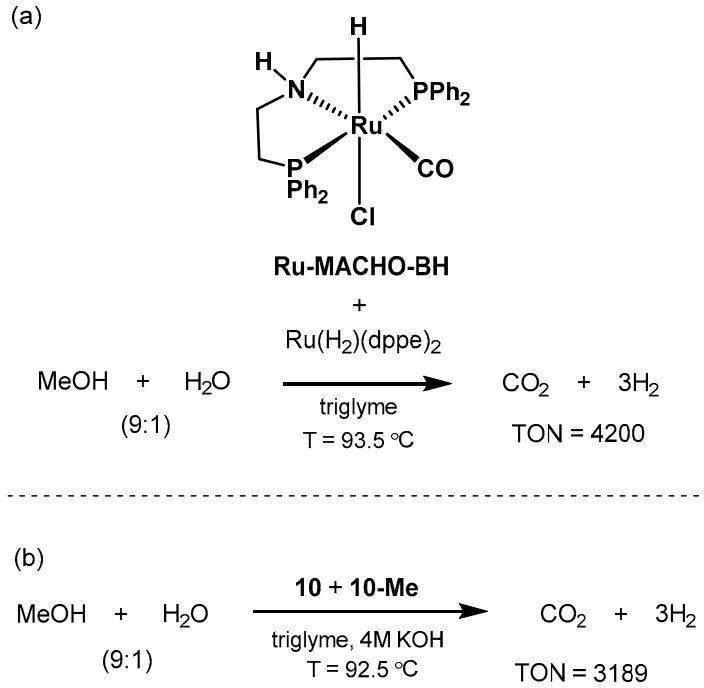

Scheme 13. Beller's bi-catalytic systems for methanol dehydrogenation catalyzed by Ru-PNP complexes [334,335]. (**a**) **Ru-MACHO-BH** + $Ru(H_2)(dppe)_2$ (2014) and (**b**) **10** + **10-Me** (2019).

In 2015, Bernskoetter, Hazari, and Holthausen showed that not only strong basic conditions, but also Lewis acid additives enhance the performance of PNP-based complexes [336]. In this work, the authors screened the same family of catalysts showed in Scheme 7. Using 0.006 mol%, or 60 ppm,

of the iron complex **16** in the presence of 10 mol% $LiBF_4$ in refluxing ethyl acetate, it was possible to convert a 4:1 methanol/water mixture to 3:1 H_2 and CO_2 in 50% yield after 94 h. Increasing the catalyst loading to 0.01 mol% led to full conversion in 52 h. The system produced a turnover number of 51,000, the highest reported for earth-abundant metals (Scheme 14). The work also provides DFT calculations to explain the role of the Lewis acid additive, suggesting that the competitive lithium coordination promotes the rate of formate abstraction, thus resulting in a higher proportion of the catalytically active amido complex.

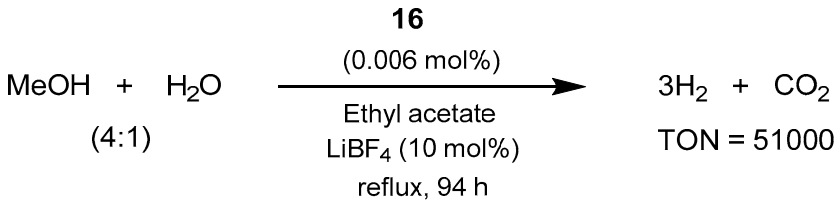

Scheme 14. Iron-catalyzed methanol reforming in the presence of Lewis acids proposed by Bernskoetter, Hazari, and Holthausen [336].

In 2016, Beller investigated the mechanism of aqueous methanol dehydrogenation using the state-of-the-art catalyst under highly alkaline conditions, complex **10**, and compared with its N-Me congener **10-Me**. The proposed catalytic cycle depicted in Scheme 15 was obtained combining experiments, isolation of key intermediates, NMR characterization, single crystal X-ray crystallography, and DFT calculations [337]. Contrarily to the previously invoked outer sphere mechanisms, the authors proposed an inner sphere pathway for the C-H cleavage step, promoted by base. The required amount of base is essential to increase the reaction rate; the authors noted an increase in the ratio of **10″**/**10′**, indicating the "inner-sphere" C–H cleavage, via C–H coordination of the methoxide to the ruthenium center. The lower, but comparable, catalytic activity of **10-Me** with its PN^HP counterpart provides further experimental evidence to the role of the N-H moiety in PNP-catalyzed dehydrogenation reactions [193,338–340].

The same group carried out mechanistic studies on aqueous methanol dehydrogenation using well-defined manganese and rhenium catalysts, under both base-free as well as strongly basic conditions [341]. Fu used DFT calculations to propose a self-catalytic role of methanol in ruthenium PNP-catalyzed dehydrogenation [342]. Several authors have studied the process in depth, using inter alia, DFT calculations, NMR spectroscopy, or Raman-GC techniques [343–345].

In 2017, Beller proposed the structurally defined manganese complex **25** as an active catalyst for aqueous methanol dehydrogenation (Scheme 16) [346]. The optimized conditions resulted in 20,000 turnovers after 900 h at 92 °C, starting from a 9:1 CH_3OH/H_2O mixture in triglyme, with 8M KOH, and in the presence of 10 equivalents of the PNP ligand to the catalyst (2.1 μmol). Moreover, other organic carriers such as ethanol, paraformaldehyde, and formic acid were successfully dehydrogenated as well. Unlike the previous work by Bernskoetter, Hazari, and Holthausen [336], the presence of Lewis acid additives resulted in no observable improved catalytic activity.

The same group showed that, similar to the PNP complexes of ruthenium, iron, and manganese, also the iridium-PNP catalyst **8** is able to promote methanol dehydrogenation under mild conditions albeit with lower catalytic activity [347]. Complex **8** afforded a TON of 1900 after 60 h at 92 °C, showing promising stability over time. In this case too, highly basic conditions were required (8M KOH) for consistent catalytic activity starting from a 9:1 mixture of CH_3OH/H_2O.

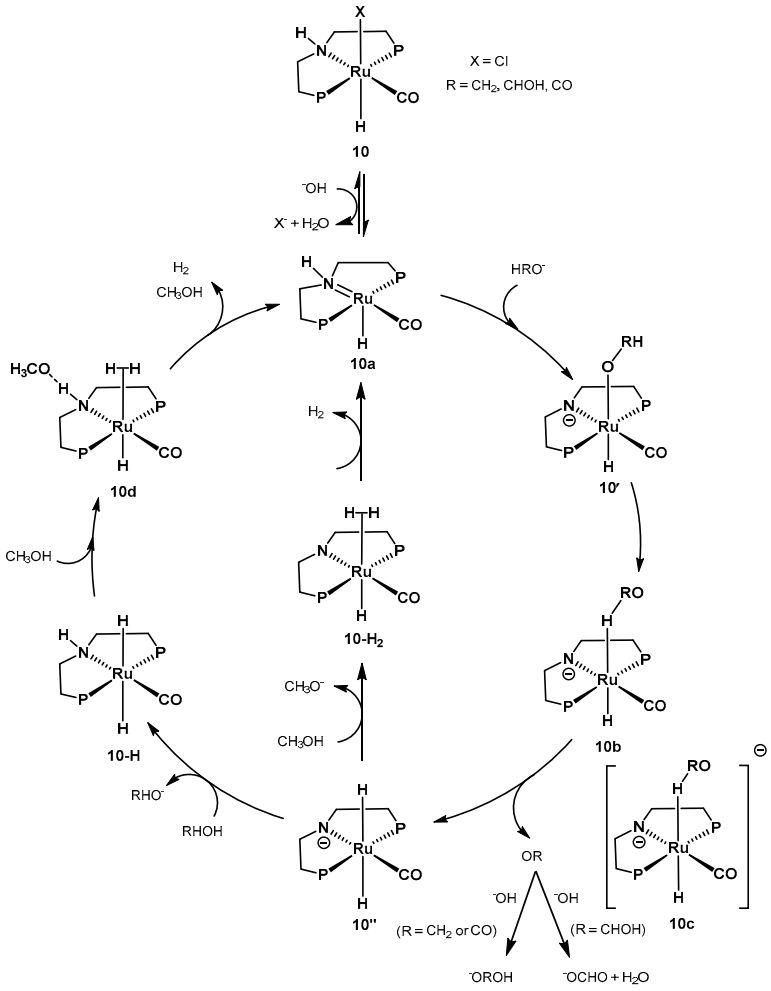

Scheme 15. Proposed inner-sphere catalytic cycle for aqueous methanol dehydrogenation by Beller [337].

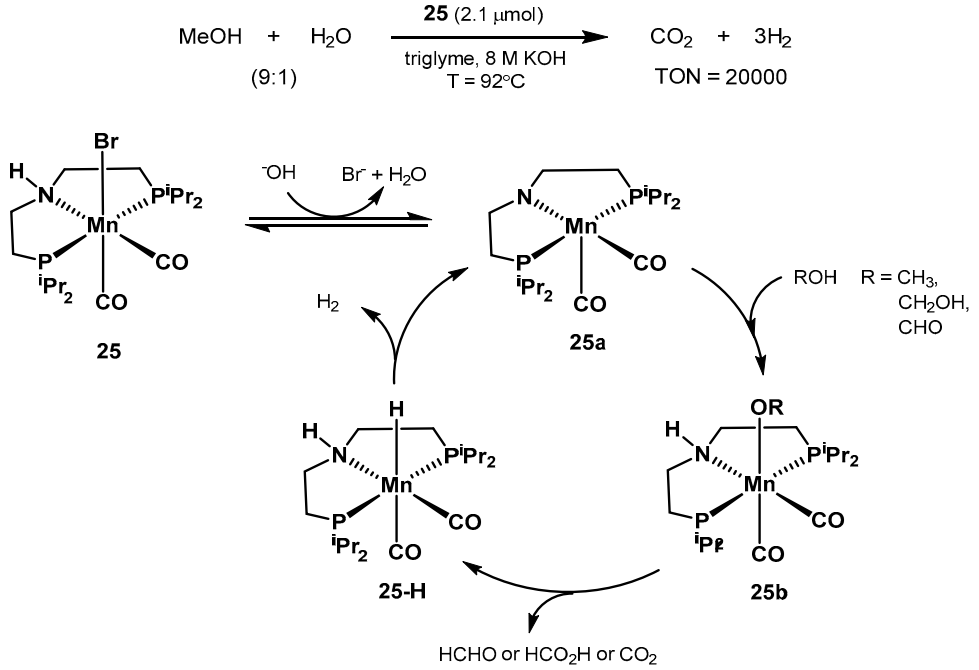

Scheme 16. Manganese-catalyzed methanol reforming and proposed catalytic cycle proposed by the group of Beller [346].

In 2019, Beller improved the performance of Ru-PNP catalysts for methanol dehydrogenation using another bi-catalytic system formed by the catalysts **10**/**10-Me** (Scheme 13b) [335]. Based on observations on the formic acid dehydrogenation step [348], the addition of catalyst **10-Me** promotes the rate of hydrogen release from formic acid in the last step. The combination of the two catalysts together was 1.5 times more active than individually. Employing 8.56–9.62 μmol of **10** + **10-Me** in a 9:1 MeOH:H_2O mixture in triglyme, with 40 mmol KOH at 92.5 °C, afforded a clean 3:1 H_2/CO_2 mixture with TOF = 1063 h^{-1} and a TON = 3189 (calculated based on total amount of catalysts present) after 3 h. This work further shows that applying bi-catalytic systems in cascade reactions is a promising solution to improve the catalytic performance, taking advantage of synergetic effects between two active catalytic species.

The same year, Haumann explored the immobilization of the known ruthenium ^{iPr}PNP catalyst **10** for the continuous gas-phase steam reforming of methanol [349]. Using the supported liquid phase (SLP) technology, the authors investigated the activities of the prepared catalysts using an array of support materials. The best result in terms of activity and stability was achieved using pure KOH deposited onto alumina support. The system was stable for 70 h on stream and only trace amounts of CO were observed.

2.2.2. Formic Acid Dehydrogenation

The use of formic acid as hydrogen carrier and storage system has been widely investigated and reviewed in various works [299,300,350–359]. A variety of both heterogeneous and homogeneous catalytic systems have been applied for its decomposition, including the use of light irradiation [360–381].

In 2011, following previously reported works on iron-catalyzed formic acid dehydrogenation [382,383]. Beller reported the remarkable activity of an iron complex bearing the tetradentate tripodal ligand tris[(2-diphenylphosphino)ethyl]phosphine [$P(CH_2CH_2PPh_2)_3$ (PP_3) [384]. The authors tested both the in situ formation of the active species, as well as various synthesized iron hydride complexes bearing the same PP_3 ligand. The activity of the synthetized catalysts was found to be comparable with that of the in situ formed systems in the presence of 2 equivalents of PP_3 ligand. After optimization, simply applying 5 mmol of $Fe(BF_4)_2{\cdot}6H_2O$ and 2 equivalents of PP_3 to a solution of formic acid in propylene carbonate, afforded a TOF of 9425 h^{-1} and a surprising TON of 92,000 at 80 °C.

Contemporarily, Milstein was also investigating the performance of iron pincer complexes based on the lutidine moiety, reporting suitable catalysts for the hydrogenation of ketones [385,386], as well as CO_2 hydrogenation to formate [387]. In 2013, the group showed a series of iron pincer complexes as active catalysts for formic acid dehydrogenation (Scheme 17) [388]. The dihydrido complex *trans*-[Fe-(^{tBu}PNP)$(H)_2$(CO)] **26** showed the best performance, reaching TON values up to 100,000 at 40 °C in the presence of trialkylamines. 0.001 mol% of **26** in 1,4-dioxane, in the presence of 50 mol% NEt_3, resulted in full conversion of formic acid after 10 days.

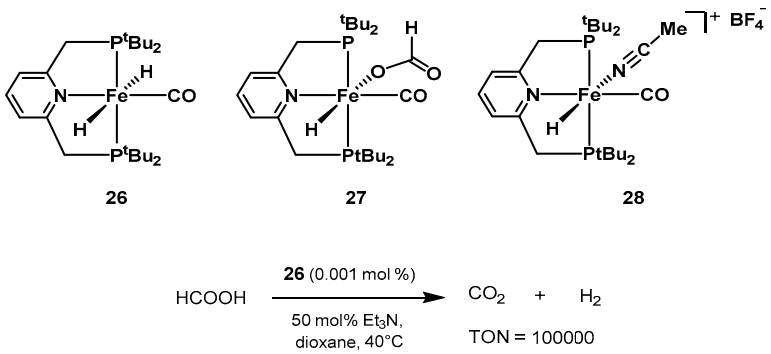

Scheme 17. PNP pincer catalysts screened by Milstein for low-temperature formic acid dehydrogenation [388].

Inspired by the afore-mentioned works carried out by Beller and Milstein using first row transition metals, Schneider and Hazari showed in 2014 that the formate iron-PNP complex **16,** combined with a suitable Lewis acid co-catalyst, is particularly active for formic acid dehydrogenation [389]. As such, employing 0.0001 mol%, or merely 1 ppm, of **16** in the presence of 10 mol% of $LiBF_4$, a TOF of 196,728 h^{-1} was obtained after one hour and a remarkable TON of 983,642 after 9.5 h. As mentioned earlier, the role of the LA is supposed to facilitate the release of formate from the iron formate intermediate, a task usually carried out by basic additives. The reactions were performed at 80 °C in dioxane (Scheme 18). The gaseous products consisted in a 1:1 mixture of H_2 and CO_2 with CO concentration less than 0.5%. The activity of the system showed in this work (TON = 1,000,000) is the highest reported for non-precious transition metals.

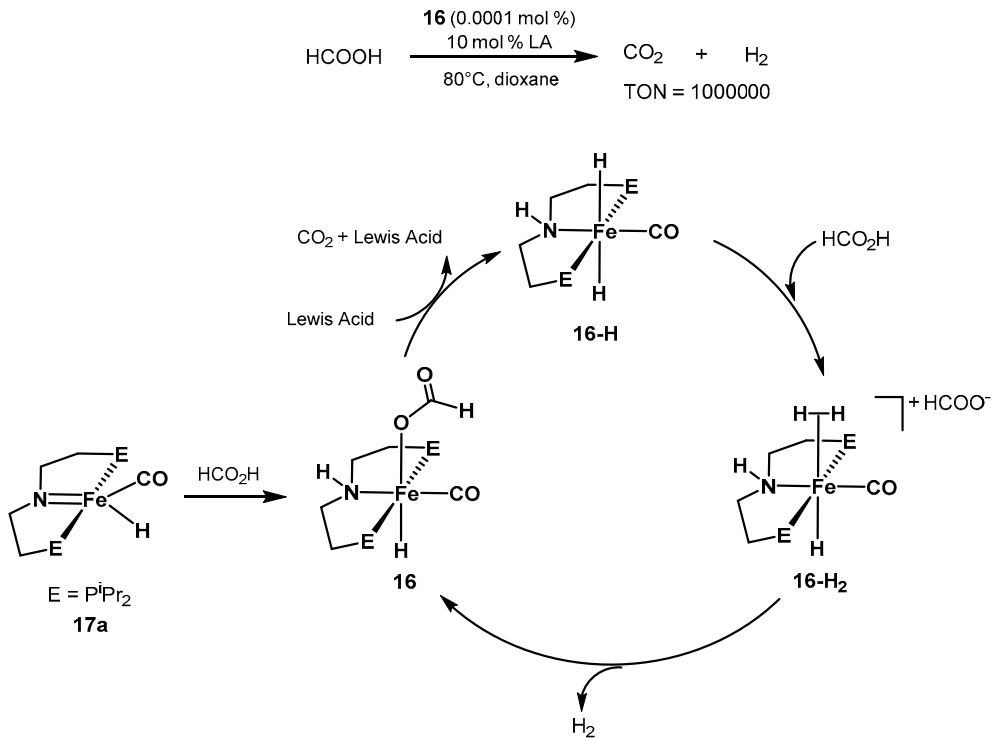

Scheme 18. Schneider and Hazari's Lewis acid assisted formic acid dehydrogenation with the Fe-PNP catalyst **16** [389].

In 2015, Prakash and Olah proposed a remarkable example of CO_2-free energy storage and release based on the formate/bicarbonate couple, which act as both hydrogen carrier and CO_2 storage system [390]. The authors showed a continuous cyclic system of either CO_2 or bicarbonate hydrogenation to formate and subsequent hydrogen release from formate (Scheme 19). The catalyst screening involved the well-known and robust **Ru-MACHO**, **Ru-MACHO-BH**, and the *N*-methylated ^{Me}PNP congener of **Ru-MACHO**. The system is amine-additive free and requires neither pH control nor change of solvent between the cycles; the same catalyst performs in both the hydrogenation and dehydrogenation steps. In a combined experiment, and by simply changing the reaction pressure, it was possible to obtain 90% conversion in both directions with a combined turnover number of 11,500 obtained after six full cycles of hydrogenation/dehydrogenation with **Ru-MACHO-BH**. The possibility of performing both transformation by only changing one parameter, such as pressure, is highly favorable for hydrogen-storage batteries. Importantly, the two *N*-H and *N*-Me PNP catalysts showed similar catalytic activities under the same reaction conditions and for both directions, with the *N*-Me PNP complex being the most active in the dehydrogenation of sodium formate, resulting in a TON of 1000 (TOF = 430 h^{-1} after 2 h) with 0.1 mol% catalyst loading in a 2:1 mixture H_2O:1,4-dioxane as

solvent. A TON of 5000 was achieved lowering the catalyst loading down to 0.01 mol%, albeit with only 50% yield in H_2.

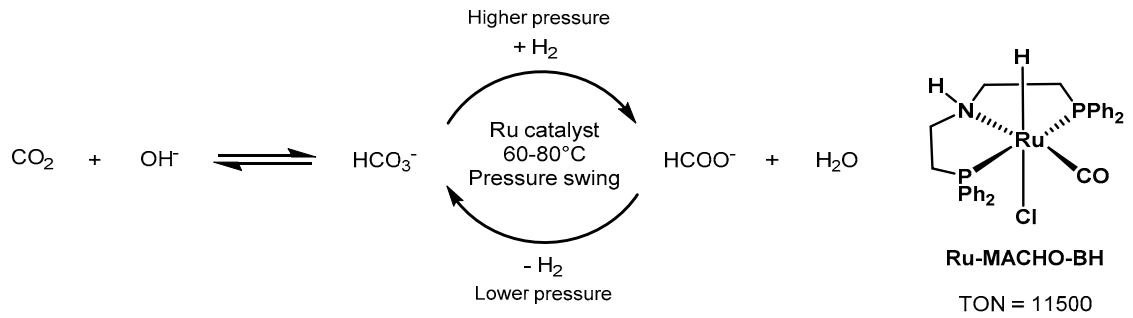

Scheme 19. Reversible formic acid hydrogen release and capture performed by Prakash and Olah using Ru-PNP catalysts [390].

Continuing the exploration of iron pincer complexes, Gonsalvi and Kirchner proposed in 2016 a series of Fe-PNP complexes bearing the 2,6-diaminopyridine scaffold (Scheme 20) [391]. Using propylene carbonate (PC) as solvent and 100 mol% of NEt_3 as base additive, led to full conversion of formic acid into H_2 and CO_2 at 80 °C. A TOF = 2635 h^{-1} after one hour and a turnover number of 10,000 after six hours were achieved using 0.01 mol% of catalyst **29-Me**. Curiously, the authors explored the effect of Lewis acid additives as well. Contrarily to the results reported by Schneider and Hazari using Fe-PNP catalysts [389], this work showed that replacing the base with 10 mol% of $LiBF_4$ resulted in no conversion of formic acid.

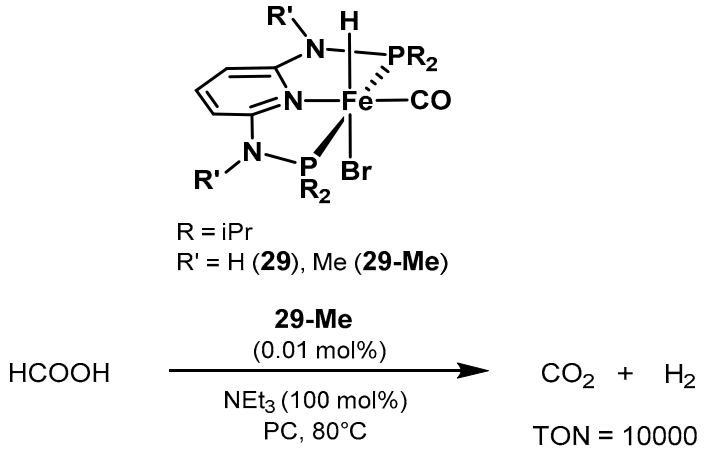

Scheme 20. Iron-PNP catalysts for low-temperature hydrogen release from formic acid reported by Gonsalvi and Kirchner [391].

Also in 2016, Gonsalvi proposed a series of well-defined, in situ formed Ru(II) complexes of the linear tetraphosphine ligand meso-1,1,4,7,10,10-hexaphenyl-1,4,7,10-tetraphosphadecane (tetraphos-1, P4), as shown in Scheme 21a [392]. The system was active for formic acid dehydrogenation in both batch and continuous feed conditions, in the presence of an amine additive. The authors investigated the reaction mechanism using NMR experiments and DFT calculations. The *trans*-[$Ru(H)_2$(meso-P_4)] **32** was found to be the key intermediate in the proposed catalytic cycle, suggesting that formic acid activation occurs on only one of the hydrides of the octahedral specie (Scheme 21b).

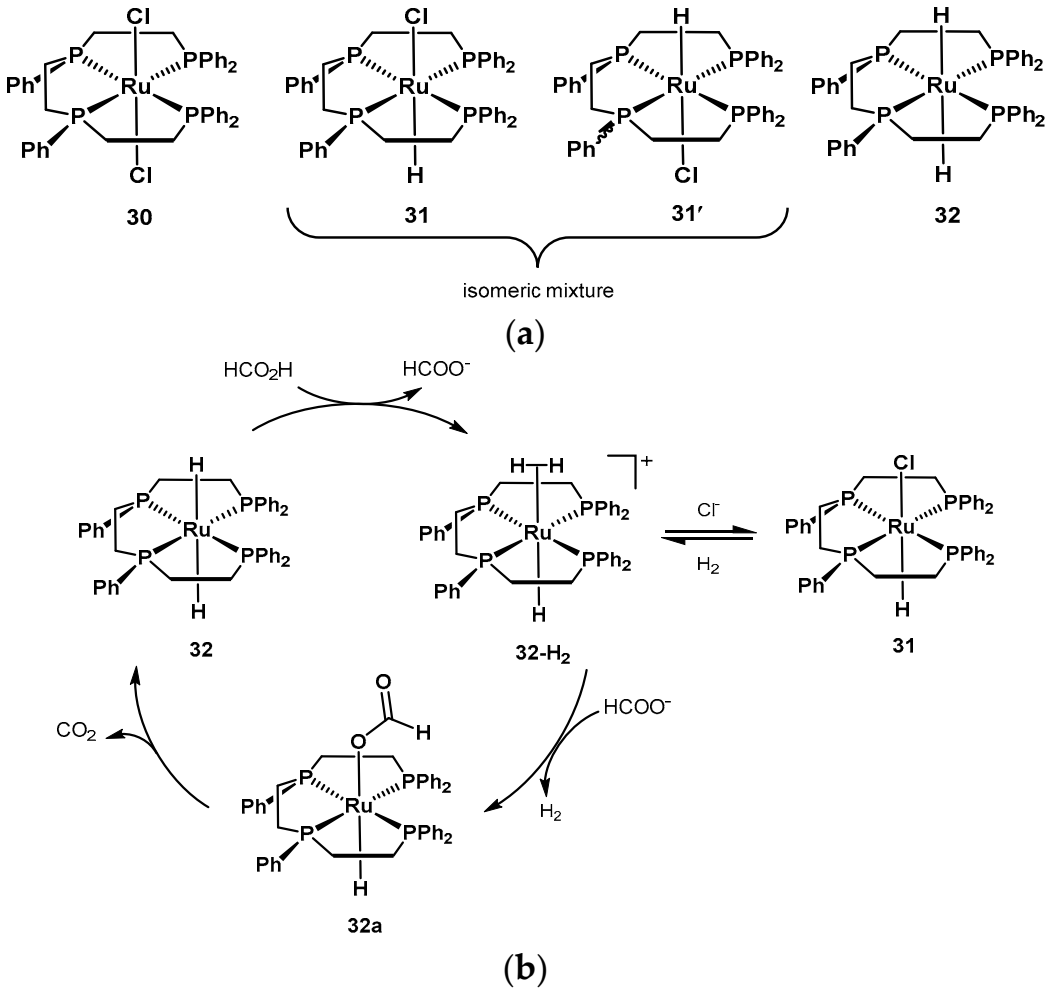

Scheme 21. (**a**) Gonsalvi's ruthenium complexes *trans*-[$RuCl_2$(meso-P4)] (**30**), *trans*-[Ru(H)Cl(meso-P4)] (**31** and **31′**) and *trans*-[$Ru(H)_2$(meso-P4)] (**32**) studied by Gonsalvi; (**b**) proposed reaction mechanism [392].

The same year, Czaun, Olah, and Prakash investigated the in situ formation of active catalytic systems from mixtures of $IrCl_3xH_2O$ and *N*-donor ligands in aqueous solution of formate at temperatures between 90 and 100 °C (Scheme 22) [393]. Among other tested mono- and bidentate ligands, there were the tridentate N,N,N′,N′,N″-pentamethyldiethylenetriamine (PMDETA), and the multidentate 1,3-bis(2′-pyridyl-imino)-isoindoline (IndH) and 1,4-di(2′-pyridyl)aminophthalazine ($PAPH_2$). The catalytic system derived from $IrCl_3$ and IndH in aqueous sodium formate showed the best results in terms of high selectivity and robustness for hydrogen generation. Furthermore, the system remained active under both high and moderate pressure conditions (3–50 bar), used to suppress the formation of CO impurity. Importantly from a practical perspective, neither the precursors (including $IrCl_3{\cdot}H_2O$ and IndH) nor the in situ formed species are air sensitive. The catalyst remains active for up to 20 days, and retains a similar activity even after one year when kept under H_2/CO_2 pressure. The authors also proposed a prototype of an integrated formic acid decomposition and hydrogen–air PEM fuel cell, demonstrating the feasibility of this approach for a continuous hydrogen production and its conversion into clean energy.

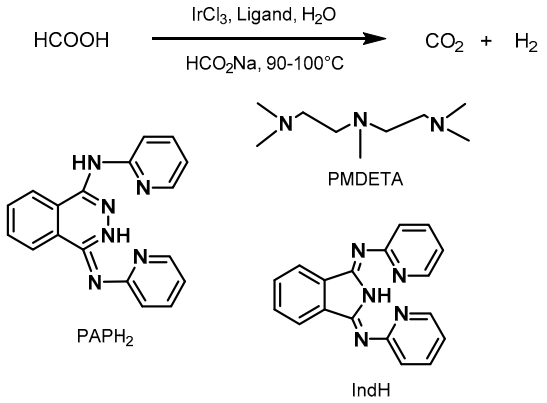

Scheme 22. Screening of ligands and in situ formation of iridium pincer ligands by Prakash [393].

In 2017, Gelman explored a series of new bi-functional iridium-PC$^{(sp3)}$P complexes for the dehydrogenation of formic acid at low temperature (Scheme 23) [394]. Catalyst **33a** (cat/FA = 1:2000) reached a turnover number up to 5×10^5 and a TOF of 2×10^4 h^{-1} (3.8×10^5 and 1.2×10^4 h^{-1} with no additives) in 30 mol% sodium formate in DME and, importantly, under air. Three different pincer ligands with pendant groups of varying basicity were investigated: neutral –OH, basic -NH_2 and acidic -COOH. While the complexes containing –OH and -COOH decomposed through liberation of H_2 at rt < T < 60 °C, the complex bearing the NH_2 group was found to be the most stable and active catalyst showing selective formic acid decomposition to hydrogen and carbon dioxide with no presence of carbon monoxide (by GC-TCD). Supported by experimental studies and quantum chemical calculations, hydrogen is released by protonolysis of the Ir-H bond and formation of a cationic species stabilized by the amine chelation from the amino group in the backbone. Regeneration of the active hydride catalyst is performed via an outer-sphere intramolecular β-H elimination of formic acid while concomitantly forming CO_2.

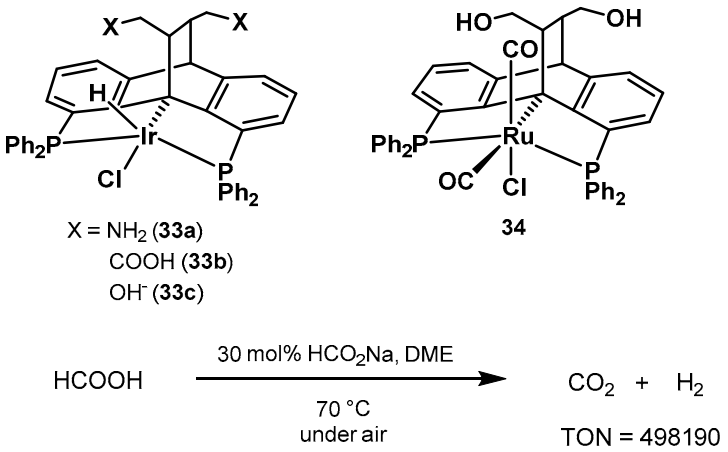

Scheme 23. Iridium-PCP complexes explored by Gelman bearing different outer-sphere pendant ligands [394].

Of the same family of bi-functional PCP complexes, Gelman demonstrated that the ruthenium catalyst **34** is active for the acceptorless dehydrogenative coupling of alcohols and amines [395], as well as the *E*-selective semihydrogenation of alkynes with formic acid [396].

In 2018, Esteruelas demonstrated hydrogen production from formic acid using a trihydridohydroxoosmium(IV)-POP catalyst [397]. The reactions were performed at temperatures between 25–45 °C, yielding turnover number values between 17 and 87 (calculated at 20% conversion). Catalyst **37** is obtained starting from the corresponding chloride complex following the route in Scheme 24. The authors also proposed the catalytic cycle shown in Scheme 24 based on kinetic

analysis of the catalysis, isolation of the intermediates and kinetic analysis of their decomposition pathways, as well as DFT calculations on the rate-determining step. Complex **37a** was fully isolated and characterized. The release of CO_2 was found to occur through complex **37b**, resulting in the formation of **37c** which is protonated by formic acid to give the penthahydrido complex **37d** in equilibrium with **37e**. The liberation of H_2 affords the unsaturated cationic complex **37f**, which can coordinate a new formate anion.

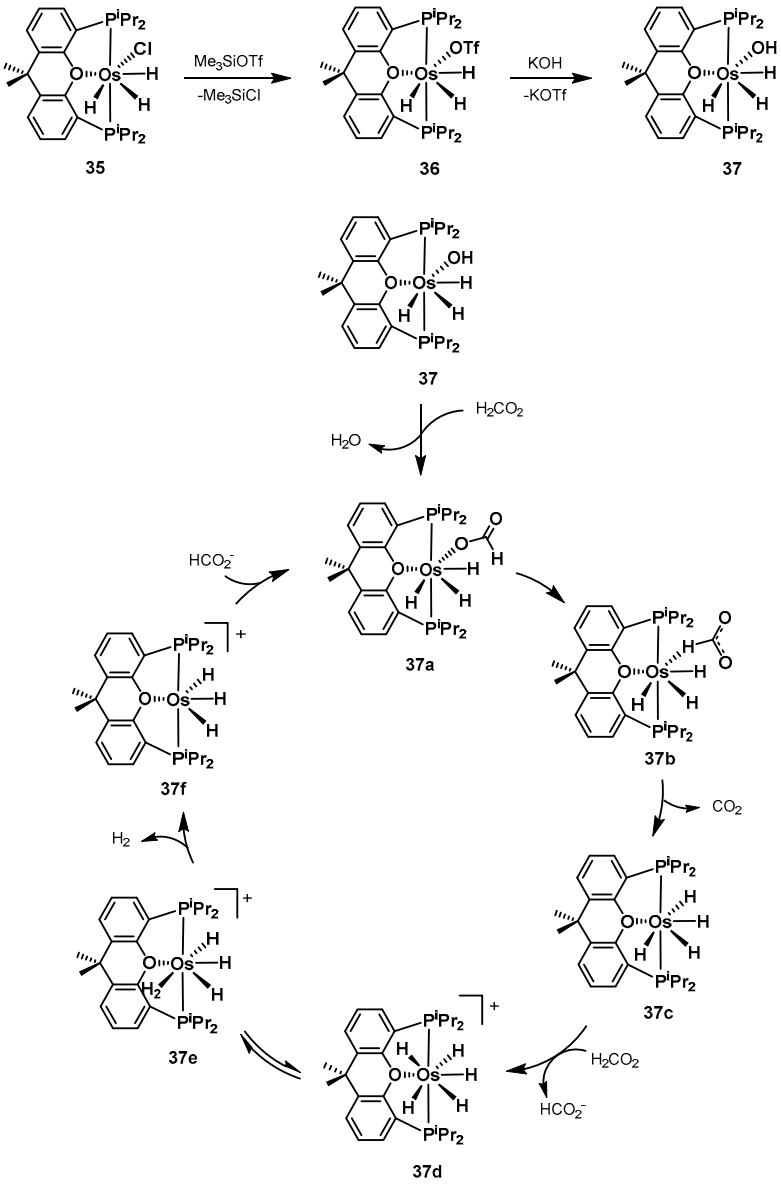

Scheme 24. Synthesis of trihydrido osmium-POP catalysts prepared by Esteruelas as well as their proposed catalytic cycle for formic acid decomposition to H_2 and CO_2 [397].

Zheng and Huang reported a series of new PNP and PNN ruthenium complexes (Scheme 25) as suitable catalysts for formic acid dehydrogenation [398]. The pyridine moiety is dearomatized by deprotonation of one of the arms, leading to an imine functionality, responsible for the catalyst activation/formic acid deprotonation step. Interestingly, the prepared catalysts are both air and water stable. No CO gas is produced together with the CO_2 and H_2. As expected, the performance of the catalyst dramatically increases in the presence of a base such as NEt_3. The system was shown to be active already at 50 °C, but the highest TON of 1,100,000 was obtained at 90 °C, using catalyst **38** in the

presence of triethylenediamine as additive and DMSO as solvent. The same family of catalysts was reported to be active in several promising transformations, i.e., selective dehydrogenation (oxidation) of benzylamines into imines [399], hydrogenation of esters in the presence of water [400], as well as the electrocatalytic reduction of CO_2 to CO and formic acid in aqueous solution with negligible formation of H_2 [401]. In addition, a hydride nickel(I) counterpart of **38** was showed to be active for the cycloaddition of CO_2 and epoxide affording carbonates [402].

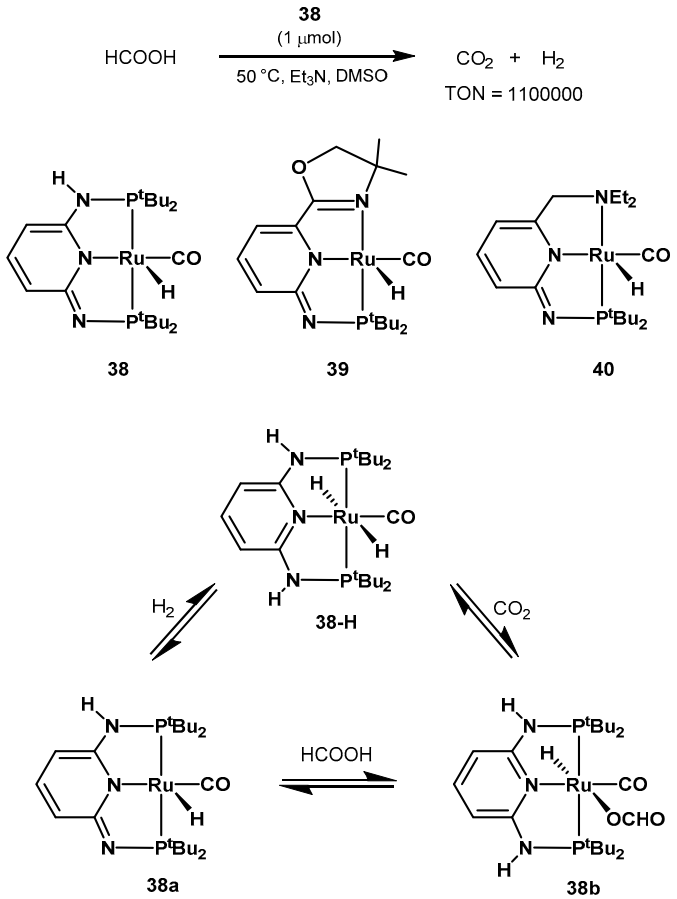

Scheme 25. New PNP complexes studied by Huang and proposed plausible mechanism for hydrogen release from formic acid [398].

With the purpose of increasing the long-term stability of homogeneous catalysis, Lai and Huang recently investigated the immobilization of catalyst **38** knitted into porous organic polymers [403]. The supported catalyst was found to be active for dehydrogenation of formic acid in both organic and aqueous media. The system showed excellent stability affording a turnover number of 145,300 after 50 cycles over a period of three months, using a 1:2500 ratio catalyst to formic acid (calculated by measuring the ruthenium content by ICP). A considerably lower TON (5600) was obtained using the homogeneous analog under the same reaction conditions, because of deactivation of the catalyst.

Kuwata showed a series of ruthenium-NNN pincer complexes bearing protic (trifluoromethyl)pyrazole arms for formic acid dehydrogenation [404]. The complexes were synthetized and characterized, and the impact of the perturbations on the catalytic properties was examined. The authors demonstrated the increased Brønsted acidity given by the *N*-H groups by protonation–deprotonation experiments, whereas the high electron-withdrawing properties of the CF_3 pendants was found to not affect the electron density around the metal center. The NNN pincer complexes **41** and **42** exhibited high catalytic activity; the reaction in the presence of $KN(SiMe_3)_2$ as

additive afforded TONs of 3000 and 3700, respectively (Scheme 26). Importantly, using catalyst **42** the reaction proceeds even without the addition of base additives, resulting in the highest TON of 3700.

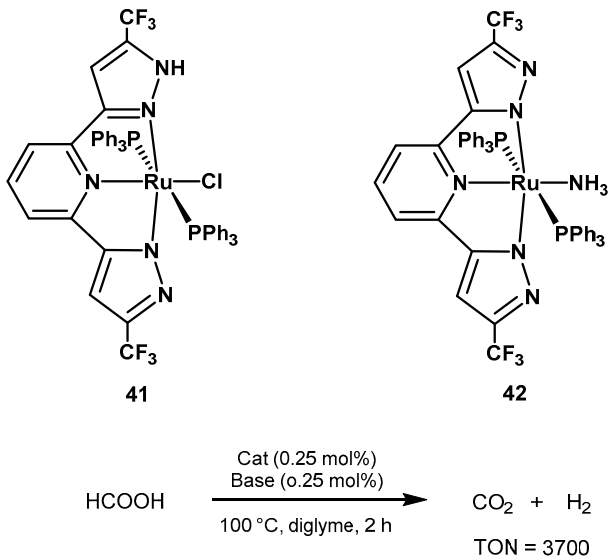

Scheme 26. Novel Ru-NNN catalysts reported by Kuwata for formic acid dehydrogenation [404].

In 2018, Bernskoetter and Hazari proposed three well-defined, single crystal X-ray crystallographically characterized, $PN^{Me}P$ iron pre-catalysts containing isonitrile ligands, in the form of $(^{iPr}PN^{Me}P)Fe(H)(HBH_3)(C{\equiv}NR)$, as shown in Scheme 27 [405]. The catalysts are analogs of the previously showed PNP iron carbonyl complexes, already studied extensively in the literature. A first generation of isonitrile Fe-$PN^{H}P$ catalysts was reported a year before for the hydrogenation of CO_2 to formate [406], albeit showing lower activity compared to the first generation iron carbonyl complexes. In this work, a second-generation $PN^{Me}P$ complexes has been investigated. The new isonitrile catalysts showed to be active in both CO_2 hydrogenation and formate dehydrogenation, although with one-order magnitude inferior activity compared to the corresponding carbonyl complexes. The reaction using 0.1 mol% of **43c**, 50 mol% NEt_3 in 5 mL of dioxane at 80 °C resulted in a TON of merely 140 after 4 h.

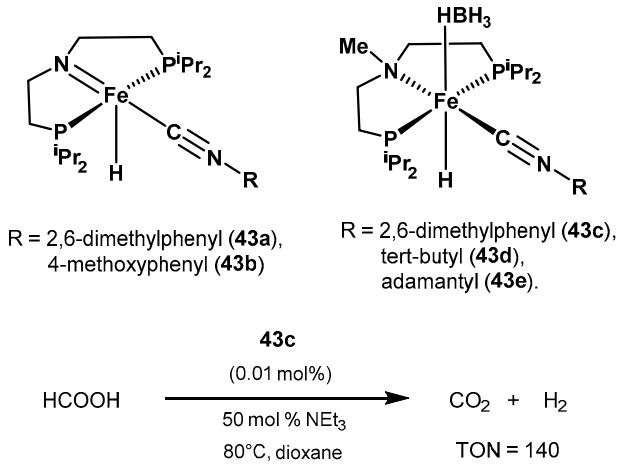

Scheme 27. Isonitrile Fe-$PN^{R}P$ complexes synthetized by Bernskoetter and Hazari [405].

Very recently, the group of Beller studied the effect of the methylation of the nitrogen atom of the PNP pincer, comparing the activities of the active complexes **10** and **10-Me** for the dehydrogenation of formic acid [348]. This work follows a previously reported article by the same group, where the authors unraveled the mechanism of aqueous methanol dehydrogenation (see Section 2.2.1) [337].

The authors screened the two catalysts at various pH values; under all the tested conditions, complex **10-Me** showed superior activity to **10**. In a first screening in basic conditions (pH = 13), catalyst **10-Me** was found to be approximately twice as active as its $PN^{H}P$ congener, with TOF(N^{Me}) = 4251 h^{-1} and TOF(N^{H})=2099 h^{-1} after 1 h. The complexes showed similar activity at neutral pH, while the best activity for both systems was obtained in acidic conditions (pH = 4.5). Catalyst **10-Me** resulted in TOF of 8981 h^{-1} superior to **10** (5263 h^{-1}). In line with the increase in TOF values, the conversion after 3 h also increased: for catalyst **10**, 69% at pH 13 vs 85% at pH 4.5, while catalyst **10-Me** resulted in 82% at pH 13, and in almost full conversion under acidic conditions. After optimization, applying 0.01 mol% of **10-Me** provided a TOF of 6492 h^{-1} after 1 h at 92 °C, with 20 mmol of KOH in a aqueous formic acid solution in triglyme. Extending the reaction time to 6 h resulted in full conversion and a TON = 26,388 after four consecutive additions of formic acid. The authors proposed two different catalytic cycles for the two catalysts (Scheme 28), concluding that in both cases the protonation of the complex resulting in the dihydrogen specie is the key step in formic acid dehydrogenation [337]. Curiously, the effect was different with the Mn-PNP **25**, which showed decreased activity in the presence of the N-Me moiety, but still with increased activity in acidic conditions rather than basic ones.

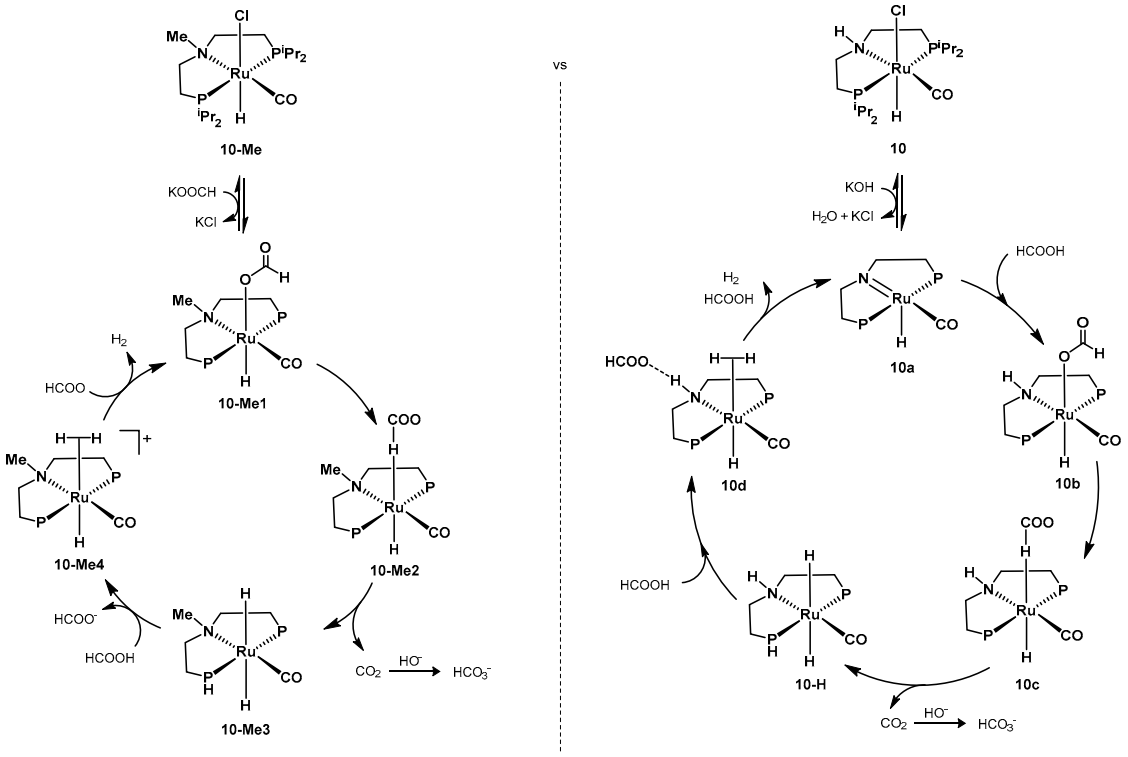

Scheme 28. $PN^{Me}P$ vs. $PN^{H}P$ pincer complexes and proposed catalytic cycle for formic acid dehydrogenation proposed by Beller [348].

In 2018, Beller reported that also the known ruthenium dihydride [$RuH_2(PPh_3)_4$] is a suitable catalyst for the dehydrogenation of aqueous formic acid at low temperature (TOF up to 36,000 h^{-1} at 60 °C in THF) [407]. The catalyst was active for 120 days and it does not require basic additives.

The same group also proposed the cobalt catalyst precursor **44** shown in Scheme 29 for formic acid dehydrogenation in aqueous media and at mild conditions [408]. Reactions were performed at 60–80 °C in the presence of HCOOK. Since the catalytically active species are air-sensitive, the authors investigated the in situ activation of the pre-catalyst **44** in the presence of $NaBEt_3$, resulting in the active hydrido complex **44-H** (Scheme 29). Importantly, under optimized conditions, the benchmark **Ru-MACHO** resulted in scarce H_2 evolution, whereas the manganese catalyst **25** showed no activity in aqueous conditions. The authors proposed an outer-sphere mechanistic cycle similar to the classic

Ru-PNP catalyst, with the amine proton taking active part in the catalytic cycle. The authors concluded that the rate-determining step is the C-H activation resulting in CO_2 release and formation of the amine complex. The work provides useful information for the development of non-noble metal catalysts for formic acid dehydrogenation.

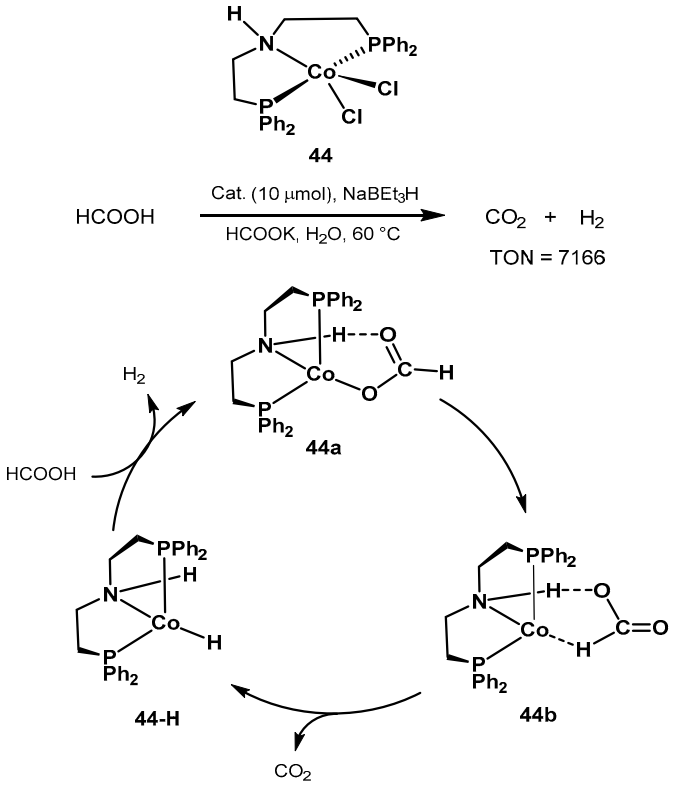

Scheme 29. Novel cobalt-PNP pincer complex for low-temperature formic acid dehydrogenation proposed by Beller [408].

2.2.3. Other Hydrogen Storage Systems

There are other potential solutions for hydrogen storage based on the LOHC technology, where pincer complexes have been applied as well. Some of these include ammonia-borane, amine-borane, hydrazine-borane, as well as pyrrolidine-based liquid organic hydrogen carriers [409–418]. The inverse hydrogenation process of the obtained products has also been explored [419–423]. Several metal catalysts have been investigated for the dehydrocoupling of these hydrogen reservoirs [424–431]; among these, pincer complexes have showed promising features and remarkable activity [432–440]. A comprehensive review on the main progresses in this field can be found in the work of Rossin and Peruzzini [441], whereas Schneider investigated the ruthenium-catalyzed amino-borane dehydrocoupling in 2013 [442]. Herein, we show representative examples of the more recent works from 2015 up to date involving the use of pincer-type catalysts.

In 2015, Schneider proposed the iron-PNP complex **17a** for ammonia-borane dehydrocoupling at room temperature [443]. Ammonia-borane represents a promising hydrogen storage system, storing up to 19.5 wt% of H_2 at ambient conditions [444]. The dehydrogenation proceeds via an aminoborane complex and results in 90% conversion to the linear polyaminoborane polymer (Scheme 30). Catalyst deactivation due to the presence of free BH_3 can be prevented by addition of a simple amine, resulting in high TON up to 350 using 0.2 mol% of **17a** and 0.8 mol% of NMe_2Et. In 2009, the same author showed Ru-PNP catalysts similar to **17a**, but where the CO ligand is exchanged with PMe_3 groups, as active catalyst for the same transformation [445,446].

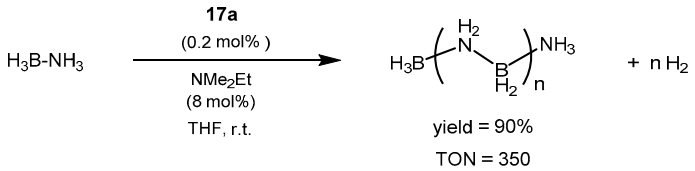

Scheme 30. Iron-catalyzed dehydrogenation of ammonia borane performed by Schneider [443,445].

In 2016, Beweries compared new 3,5-disubstituted cyclometalated iridium(III)-hydrido complexes with the non-substituted counterparts in the dehydrogenation of hydrazine borane (Scheme 31) [447]. All catalysts were active, but when R = COOMe, the derived active species outperformed the other catalysts significantly, resulting in full conversion after 28 s (**47-Cl**) and 18 s (**47-H**) using 2 mol% catalyst loading. In addition, both catalysts **47-H** and **47-Cl** showed promising recyclability properties. The dehydrogenation products were characterized by solid state NMR and FT-IR spectroscopy, while DFT studies were performed using catalyst **45-H** to rationalize the mechanism of hydrazine borane dehydrogenation. The reaction proceeds through coordination of hydrazine borane by either NH_2 or H–BH_2, coexisting in equilibrium; later, the dehydrogenation occurs resulting in a dihydrogen complex and liberation of $H_2B{=}NHNH_2$. Finally, the active specie **45-H** is regenerated after H_2 dissociation.

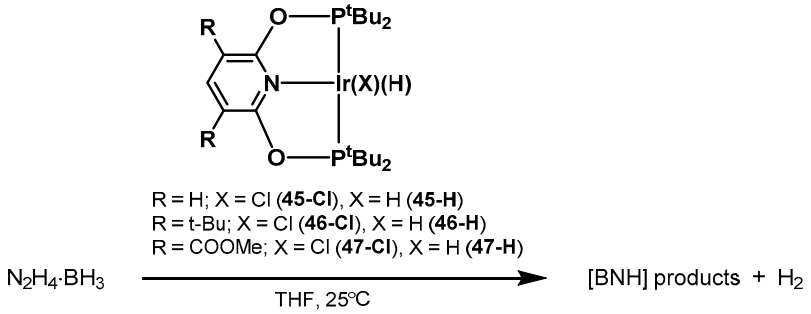

Scheme 31. Dehydrogenation of hydrazine-borane hydrogen storage system by Ir-PNP pincer complexes reported by Beweries [447].

In 2015, Jensen performed kinetic studies on the iridium ^{tBu}PCP complex **48** for the dehydrogenation of several pyrrolidine based LOHCs, such as butyl pyrrolidine (BuPy), *N*-ethylcarbazole (NEC) and methyl perhydroindole (MePHI) (see Table 1) [448]. The authors investigated reaction kinetics in terms of dehydrogenation onset temperatures, activation energies, and frequency factor when catalyst **48** was used in the presence of NaO*t*Bu as additive. The authors concluded that the steric constraints of these LOHCs, rather than the C-H activation at the metal center, represent the main issue preventing higher rates of reaction.

Continuing the exploration of iridium-based pincer complexes, Belkova investigated the mechanism of dimethylamine–borane (DMAB) dehydrogenation using the iridium(III)-PCP complex **49** in Figure 2 [449]. It is possible to use the hydridochlorido complex precursor as precatalyst, which is activated in situ resulting in the active specie **49-H**, as was found for ammonia-borane dehydrogenation by Heinekey and Goldberg in 2006 [450].

In 2016, Esteruelas investigated the monohydride rhodium {xant(P^iPr_2)$_2$} complex **50** for the dehydrocoupling of ammonia-borane, dimethylamine-borane, and a combined system with ammonia-borane dehydrogenation and cyclohexane hydrogenation, as shown in Scheme 32 [451]. Using 1 mol% of catalyst **50** in THF at 31 °C resulted in a TOF of 3150 h^{-1} (calculated at 50% conversion) using BH_3NH_3 and 1725 h^{-1} when employing BH_3NHMe_2. The system releases 1 equivalent of hydrogen via stepwise hydrogen transfer from the substrate to the catalyst, involving the formation of a five-coordinate dihydridorhodium(III) intermediate. Based on DFT calculations, the authors proposed a non-classical dihydrido route for the dehydrogenation step.

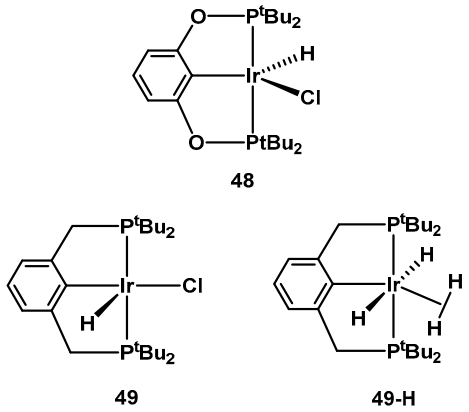

Figure 2. Iridium pincer catalysts investigated by Jensen for hydrogen release from pyrrolidine-based LOHCs [448], as well as dimethylamine–borane dehydrogenation by Belkova [449].

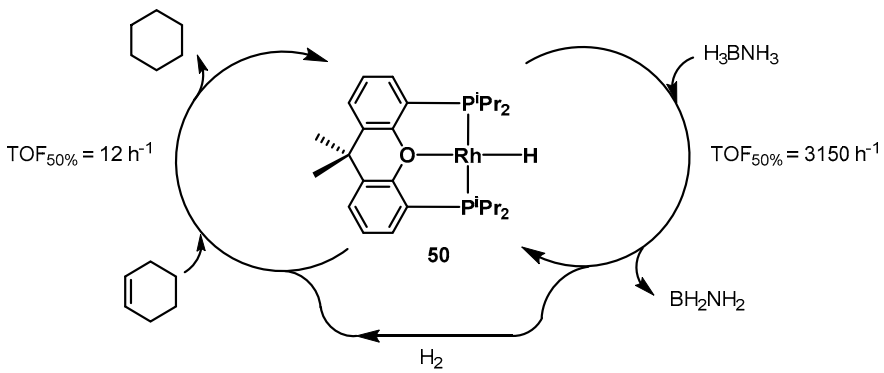

Scheme 32. Rhodium-POP catalyst for the dehydrogenation of ammonia-borane and dimethylamine-borane by Esteruelas [451].

In 2017, Yamashita showed the novel iridium PBP pincer complex **51** in Scheme 33 for the dehydrogenation of dimethylamine–borane (DMAB) [452]. The catalyst is a modification of a previously reported Ir-PBP complex (**52**), active for transfer dehydrogenation of alkanes [453]. In this work, the PBP ligand is modified by changing the benzene ring of the benzodiazaborole with the aliphatic tetramethylethylene functionality, hence decreasing the Lewis acidity on the boron center. The active dihydrido species can be obtained from the chloride precursor after treatment with *n*BuLi at room temperature. The complexes were also characterized by NMR spectroscopy, high-resolution mass spectrometry (HRMS), as well as single-crystal X-ray diffraction analysis. Catalyst **51** catalyzes the dehydrogenation of $Me_2NH{\cdot}BH_3$ to form the cyclic dimer and releasing 1 equivalent of hydrogen. A turnover frequency of 3400 h^{-1} was obtained, with 0.05 mol% of **51** in THF at 60 °C, with a final yield of 87% after 18 h (Scheme 33). Of the same family of PBP catalyst, Peters showed in 2013 that 2 mol% of the cobalt(I)-N_2 complex **53** catalyzes the release of hydrogen from DMAB in 6 h and at room temperature, resulting in full conversion to the cyclic $(Me_2N{-}BH_2)_2$ [437].

Using a different approach, Milstein proposed in 2016 a new hydrogen storage system based on the dehydrogenative coupling of ethylenediamine with ethanol, as depicted in Scheme 34 [454]. Complex **24** was able to perform the dehydrogenation step with a 0.1 mol% catalyst loading, 1.2 equivalents of KO*t*Bu at 105 °C for 24 h resulting in full conversion. Remarkably, the same catalyst was applied for both hydrogenation and dehydrogenation steps; thus, employing 0.2 mol% of **24**, 2.4 equivalents of KO*t*Bu, 50 bar of H_2 in dioxane at 115 °C, it was possible to fully hydrogenate *N*,*N*′-diacetylethylenediamine with 100% yield of ethylenediamine. This result expanded the concept of LOHC systems, paving the way for further optimization as well as applying combinations of amine-alcohol with even higher hydrogen capacity, such as ethylenediamine and methanol.

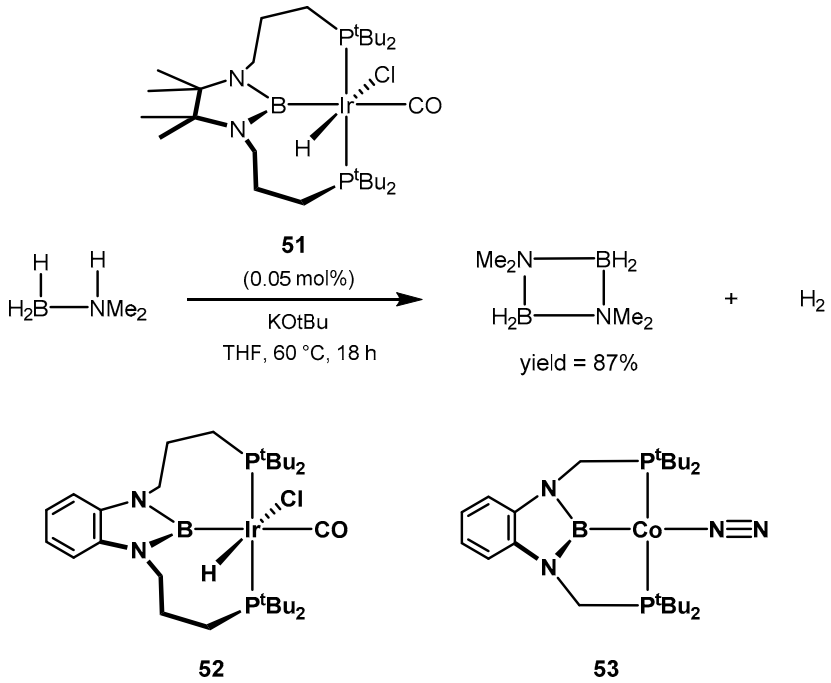

Scheme 33. Yamashita's PBP-Ir and Co- catalysts for hydrogen release from dimethylamine–borane (DMAB) hydrogen storage system [452].

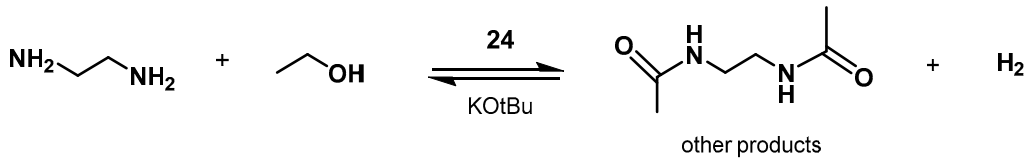

Scheme 34. Hydrogen storage system based on ethylenediamine with alcohol proposed by Milstein, and its reversible (de)hydrogenation catalyzed by complex **24** [454].

Indeed, very recently Milstein demonstrated the hydrogenation of ethylene urea to ethylenediamine and methanol and the reverse dehydrogenative coupling (Scheme 35) resulting in a mixture of ethylene urea, *N*-(2-aminoethyl)formamide and *N*,*N*′-(ethane-1,2-diyl)diformamide [319]. The system is rechargeable and has a high theoretic hydrogen capacity (6.52 wt%). Applying 1 mol% of the Ru-PNN catalyst **54**, 2.2 mol% KO*t*Bu in 1,4-dioxane at 150 °C for 24 h, it was possible to obtain high yields of dehydrogenated products and hydrogen released (>90%). The system was also able to perform the hydrogenation step under the same conditions; by simply applying 50 bar of hydrogen gas, the reaction afforded full conversion to a mixture of ethylenediamine and methanol.

After screening a range of amines, Prakash and Olah demonstrated the same concept using **Ru-MACHO-BH** and dimethylethylenediamine (5.3 wt% H_2) which was successfully dehydrogenated in the presence of methanol resulting in a mixture of formamides [455]. The authors proposed a reversible hydrogen storage system in which both H_2 "loading" and "unloading" can be performed by the same ruthenium pincer catalyst by a simple H_2 pressure swing (Scheme 36). The explorative dehydrogenative reaction using benzylamine in the presence of 1 mol% of **Ru-MACHO-BH** in toluene resulted in 88% yield in *N*,*N*′-dibenzylurea after 24 h at 140 °C, whereas 99% yield was afforded in the inverse hydrogenation of *N*,*N*′-dibenzylurea under 60 bar of hydrogen. The authors then screened other Ru- and Fe-PNP catalysts. Complex **10** combined with dimethylethylenediamine (1:4 molar ratio with respect to MeOH) as substrate and 5 mol% K_3PO_4 as a basic additive afforded 90% yield hydrogen at 120 °C in toluene after 24 h. Importantly, the catalyst retained more than 80% of its catalytic activity after three cycles of reactions. The reverse hydrogenation was carried out using catalyst **10** under 40 or

60 bar of hydrogen resulting in 92% and 95% yield of amine, respectively. Curiously, the *N*-methylated congener of **Ru-MACHO** showed low activity, indicating the presence of an *N*-H assisted outer sphere mechanism. **Ru-MACHO-BH** was also reported by Hong to perform a ruthenium-catalyzed urea synthesis using methanol as the C1 source, with no additive, such as a base, oxidant, or hydrogen acceptor [456].

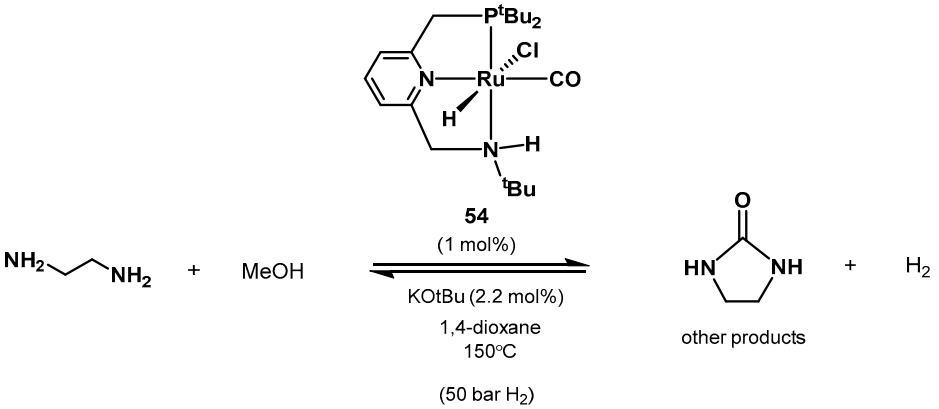

Scheme 35. Reversible hydrogen storage system formed by the couple ethylenediamine and methanol catalyzed by the Ru-PNN complex **53**, as showed by Milstein [319].

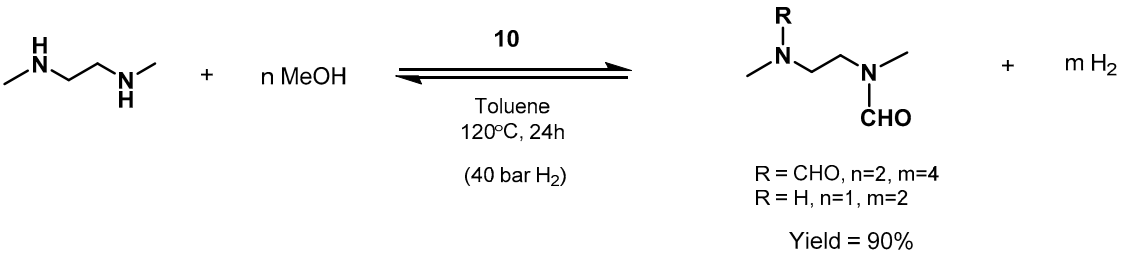

Scheme 36. Dehydrogenation of dimethylethylenediamine hydrogen storage system by **Ru-MACHO-BH** reported by Prakash and Olah [455].

3. Hydrogenation Reactions

For case of brevity, the focus will be on processes involving carbon dioxide and dinitrogen as the main substrates of interests, as well as chemical transformations promoting the valorization of biomass-derived molecules. Nevertheless, pincer complexes have achieved remarkable results in the (transfer) hydrogenation of a wide series of substrates such as ketones [385,457–462], esters [40,179,220,386,400,463–477], aldehydes [478–480], amides [67,481–485], and imines [486,487].

Carbon dioxide is sadly known to be the main responsible for the anthropogenic climate change and global warming [488–491]. At the same time, CO_2 represents an easily accessible C1 building block with the potential to replace the commonly used petrochemical carbon sources in a plethora of useful chemical transformations, dramatically increasing their intrinsic sustainability [492–494]. Several approaches have been investigated for its capture from the atmosphere, as well as from localized emission sources [495–504]. The desorbed CO_2 is subsequently compressed and stored in underground rock formations or utilized in the direct synthesis of value-added products [505–510]. Indeed, the industry already uses several million tons of CO_2 for the production of e.g., urea, salicylic acid, cyclic carbonates, and polypropylenecarbonate [511–513].

In the past decades, the catalytic hydrogenation of CO_2 has gained attention as a powerful tool to store green hydrogen, thereby electrical energy, as introduced by the seminal works by Asinger [514], Leitner [515,516], Noyori [517], as well as Olah [301,518–520]. The process, combined with the aforementioned methanol/formic acid dehydrogenation reactions, has the potential to close

the ideal cycle of CO_2-free energy release and storage. Currently, both methanol and formic acid are industrially produced using fossil feedstock via carbon monoxide, which has lower kinetic and thermodynamic stability compared to CO_2. The direct synthesis from CO_2 is traditionally carried out at high temperatures and pressures with heterogeneous metal catalysts such as $Cu/ZnO/Al_2O_3$ [521–524]. Thus, the sustainability of the direct CO_2-route is strictly dependent on the use of green hydrogen produced without contemporary CO_2 release in the atmosphere, as well as catalytic systems operating efficiently under milder reaction conditions. A variety of homogeneous catalytic systems has been employed for the direct hydrogenation of CO_2 into green fuels [213,214,517,525–535], including first-row metal complexes [536–544]. Pincer-type ligation shows again very encouraging features in terms of stability and mild reaction conditions, with promising possibility of further optimization. In addition, often the same catalyst is active in both directions of hydrogenation and dehydrogenation, expanding the applicability and robustness of this family of catalysts.

One of the most relevant and energy consuming industrial transformations is the conversion of N_2 for the production of ammonia through the Haber-Bosch process, a synthesis that requires harsh conditions and, hence, high operative costs [545–548]. Ammonia is widely used in the global economy as a fertilizer feedstock, industrial and household chemical, as well as chemical precursor in many chemical transformations [549–553]. In addition, it has been considered a future fuel alternative as a hydrogen storage molecule [554–556]. The possibility to perform nitrogen fixation at mild reaction conditions and less energetic costs by means of homogeneous catalysis is of key importance for the future sustainable chemical production, and as discussed in Section 3.2, pincer complexes are protagonists in the development of the best performing homogeneous systems developed to date.

Finally, in Sections 3.3 and 3.4, discuss the main advances in relevant sustainable transformations involving the use of bio-substrates which are already easily accessible from biomasses, representing useful building blocks for the bulk chemical production. In addition, pincer complexes achieved remarkable results also in transfer hydrogenation reactions involving the use of ethanol as the hydrogen source, as well as the upgrading of ethanol to butanol and other C4 molecules to be used as bio-fuel and fuel additives.

3.1. CO_2 Hydrogenation

3.1.1. Early Works

The hydrogenation of carbon dioxide by means of homogeneous catalysis has grown extensively in the last decade. An overview of the best performing systems for CO_2 hydrogenation up to 2010 can be found in the work of Beller [557], while in 2018 and 2019 Prakash reviewed the topic in depth including the use of pincer type complexes [558,559]. In this review, we will focus mostly in CO_2 conversion to formic acid (and/or formate salts) as well as to methanol, both of them representing accessible green fuel and hydrogen carriers.

Up to 2010, the best performing catalytic system was represented by the iridium-PNP catalyst **9** (shown in Scheme 2), reported by Nozaki in 2009, which overcame previously reported Ru [560–563], Rh [564–566], and Ir [567] homogeneous systems. In the work by Nozaki, the reactions were carried out in aqueous KOH, resulting in potassium formate (HCOOK) as the product [568]. Thus, using the trihydridoiridium(III)-PNP complex **6** at 120 °C and 60 bar of 1:1 CO_2/H_2 in 1.0 M aqueous KOH it was possible to achieve excellent TON and TOF values of 3,500,000 and 150,000 h^{-1}, respectively (Scheme 37).

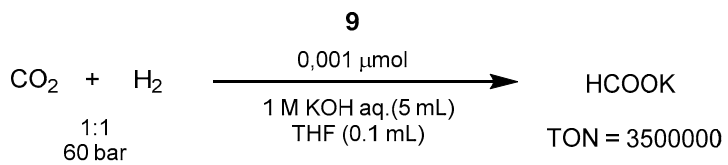

Scheme 37. CO_2 hydrogenation with Ir-PNP catalyst reported by Nozaki in 2009 [568].

The use of iridium pincer complexes was further explored by Hazari in 2011 [569]. The authors were able to isolate the air and moisture stable catalyst **8a**, obtained from **8-H** in the presence of CO_2. Under optimized conditions, the system resulted in yields up to 70% in formate, with TON of 348,000 and TOF of 14,500 h^{-1} (Scheme 38).

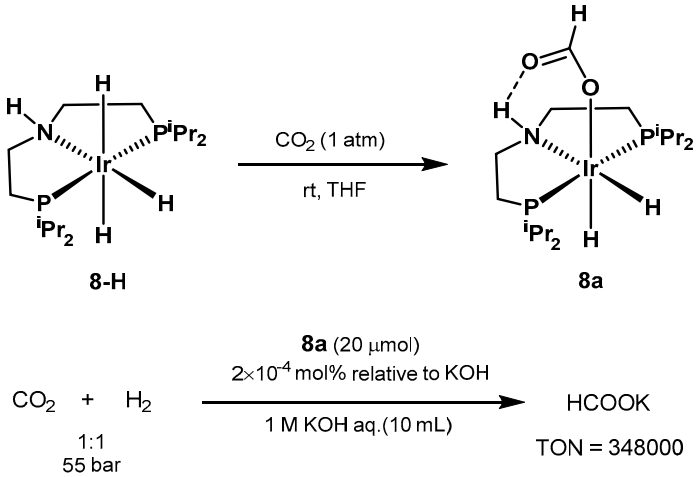

Scheme 38. CO_2 hydrogenation with Ir-PNP catalyst proposed by Hazari [569].

In 2010, Beller and Laurenczy showed the hydrogenation of bicarbonates and carbon dioxide to formates, alkyl formats, and formamides catalyzed by the in situ formed system $Fe(BF_4)_2{\cdot}6H_2O$ and the tetraphos ligand $P(CH_2CH_2PPh_2)_3$ (PP_3) [570]. In the presence of 0.14 mol% of this catalyst at 80 °C with 60 bar of hydrogen, sodium formate was obtained in an excellent yield of 88% with TON of 630 after 20 h.

Encouraged by these findings on iron complexes, Milstein proposed the dihydrido Fe-PNP complex **26** for the low-pressure hydrogenation of carbon dioxide [387]. 0.1 mol% of catalyst **26** (catalyst **27** is formed during the reaction in the presence of CO_2) in a 10:1 mixture H_2O/THF, with 2M NaOH at room temperature, converted CO_2 and H_2 into sodium formate with a TON of 788, TOF of 156 h^{-1}, and 39.4% yield (Scheme 39).

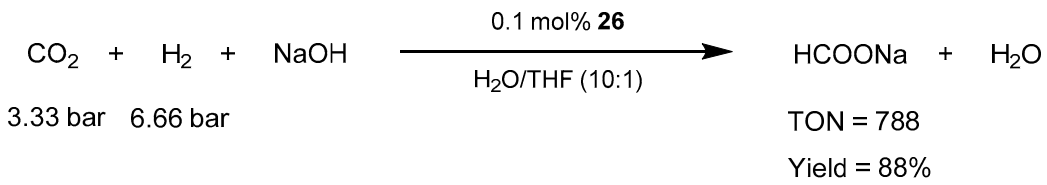

Scheme 39. CO_2 hydrogenation with catalyst **26** proposed by Milstein in 2011 [387].

In 2011, Milstein and co-workers published the first example of hydrogenation of carbonates into alcohols and carbamates into alcohol and amines as an indirect route for the synthesis of methanol from CO_2 [571]. 0.02 mol% of catalyst **24-H** in THF, in the presence of 50 bar of H_2, catalyzed the conversion of dimethyl carbonate into methanol with a TON of 4400, 89% conversion and 88% yield, at 110 °C and after 14 h. With 1 mol% of catalyst **24-H**, in THF and with 10 bar of hydrogen, it was possible to convert *N*-benzyl carbamate into methanol and the corresponding amine with 97% yield, at 110 °C, after 48 h. Finally, the authors tested the hydrogenation of alkyl formates to methanol and the corresponding alcohol. A TON of 4700 and a yield of 94% was achieved applying 0.02 mol% of catalyst **24-H** in THF, 50 bar of H_2, at 110 °C, and after 14 h.

The same year, Sanford proposed a cascade reaction mechanism for CO_2 hydrogenation using the Milstein catalyst **24-H** in combination with other two homogeneous catalysts, i.e., $(PMe_3)_4Ru$-(Cl)(OAc) and $Sc(OTf)_3$ (Scheme 40) [572]. The first two steps consist in the hydrogenation of CO_2 to formic acid,

followed by esterification to generate a formate ester. Later, complex **24-H** catalyzes the hydrogenation of the ester to release methanol. In order to prevent the deactivation of catalyst **24-H** by $Sc(OTf)_3$, the former was placed in the outer vessel of the Parr reactor where it promotes methyl formate hydrogenation to methanol. The protocol was successfully demonstrated resulting in an overall TON of 21 under optimized conditions.

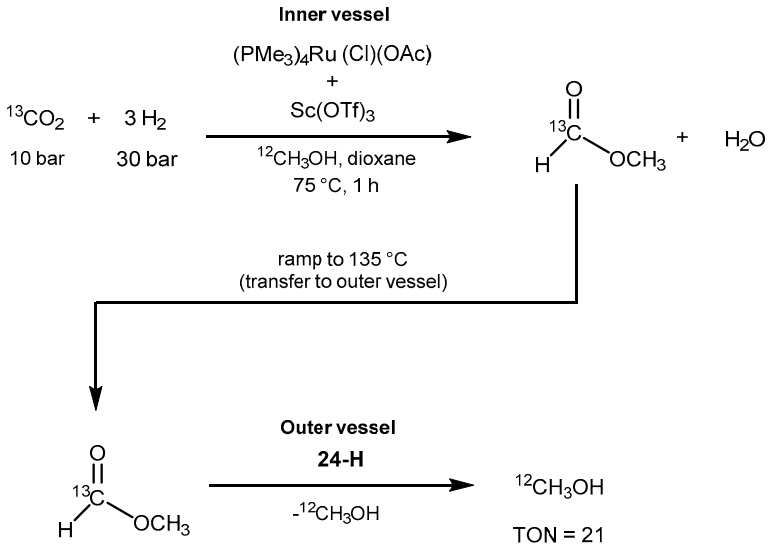

Scheme 40. Cascade reactions promoting CO_2 hydrogenation to methanol using catalyst **24-H** in combination with $(PMe_3)_4Ru$-(Cl)(OAc) and $Sc(OTf)_3$ as showed by Sanford [572].

Catalyst **24-H** was also employed by Milstein to demonstrate the hydrogenation of urea derivatives (easily obtained from CO_2 and amines) to amines and methanol [573]. Catalyst **24-H** promotes the double cleavage of the robust C-N bonds under mild, neutral conditions. 1,3-dimethylurea was used as benchmark substrate to identify the optimized reaction conditions. 2 mol% of catalyst **24-H** in THF, heated at 110 °C and in the presence of 13.8 bar of hydrogen, afforded 96% conversion and 93% yield in methanol after 72 h. With the optimized conditions, the authors screened a wide range of urea derivatives that were converted in good to excellent yields.

In 2011, Leitner performed computational studies on 38 different rhodium pincer alkyl complexes with varied steric and electronic environment for the CO_2 association and insertion into the metal–carbon bond, resulting in the corresponding carboxylate species [574]. Several of the tested catalysts showed insertion barriers with energies that encourage their use within an effective catalytic cycle. The authors pointed out three main features that facilitate CO_2 insertion: (a) the anionic complexes were more reactive than neutral congeners. (b) The activity decreased based on the central donor atom of the pincer arm in the order of $C^- \approx B^- > Si^- > N >$ carbene $> O$. (c) Higher basicity is typically associated with higher reactivity, with the side arm of the pincer that can further tune the electronics around the metal center.

The same author proposed a novel protocol for the direct synthesis of free carboxylic acids via hydrocarboxylation using CO_2 as a C1 building block and simple non-activated olefins [575]. The reactions were carried out in acetic acid using 1:10 $[\{RhCl(CO)_2\}_2]$ and PPh_3 in the presence of 60 bar of CO_2, 10 bar of H_2, CH_3I as a promotor, and *p*-TsOH·H_2O as acid additive. With cyclohexene as a substrate, the reaction afforded full conversion and 92% yield in the carboxylic acid, with only 5% of cyclohexane as the co-product, after 16 h at 180 °C. With optimized conditions, the authors scoped various substrates and it was possible to obtain the corresponding carboxylic acids in good to excellent yields, with only minor amounts of the hydrogenated olefin. After evaporation of the solvent, the authors isolated and characterized the complex $[CH_3PPh_3][RhI_4(CO)(PPh_3)]$ using X-ray crystallographic analysis.

In 2012, Klankermayer and Leitner demonstrated the homogeneous hydrogenation of carbon dioxide to methanol using a catalytic system based on the tripodal PPP Triphos ligand showed in Figure 3 [576]. Both the combination of the precursor $Ru(acac)_3$ and the Triphos ligand, as well as catalyst **55** were active in the hydrogenation of both CO_2 and formate esters. In particular, 25 μmol of catalyst **55**, with 1 equivalent of $HNTf_2$, at 60:20 bar of CO_2:H_2 in THF/EtOH, afforded a TON of 221 after 24 h. Mechanistic studies indicate the active species **57** and **58** as key intermediate in this transformation, with enhanced activity in the presence of weakly coordinating anions [577].

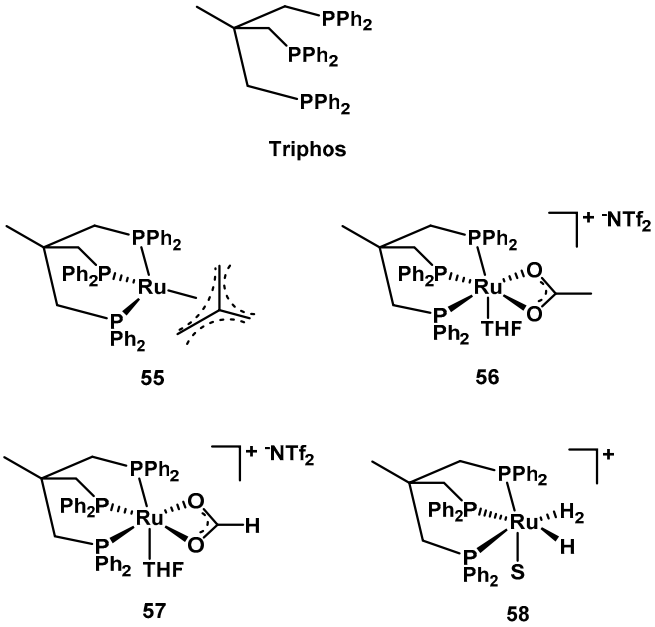

Figure 3. Ruthenium catalysts **55** and **56** based on the triphos ligand, and active formate species **57** and **58** (S = solvent or substrate) [576–579].

In 2015, Leitner employed catalyst **55** for the hydrogenation of CO_2 into methanol without the need of an alcohol additive [578]. Catalysts **55** and **56** were used as pre-catalysts leading to the formation of the active specie **57** under the reaction conditions. Applying only 6.3 μmol of **55**, 1 equivalents of $HNTf_2$, 20:60 bar of CO_2:H_2 in THF, afforded the best TON of 442 at 140 °C after 24 h.

The same group also showed the direct methylation of primary and secondary amines catalyzed by the PPP complex [Ru(Triphos)(tmm)] **55** without the use of reducing agents [579]. The authors found the optimized conditions for the methylation of *N*-methyl aniline, and extended the scope to a wide range of substituted aromatic amines as well as primary anilines. Quantitative yields were obtained for the conversion of *N*-methyl aniline into dimethylaniline by applying 2.5 mol% of [Ru(triphos)(tmm)], 5 mol% of $HNTf_2$, 20:60 bar of CO_2:H_2 in THF at 150 °C.

Meyer and Brookhart proposed the iridium PCP pincer catalyst for the electrocatalytic conversion of CO_2 to formate [580]. The reactions were carried out in acetonitrile with 5% of water. Water promotes the reaction with CO_2 with consequent formation of the cationic specie **59b** coordinated with a formate anion. The electrochemical observations suggest that the catalyst resides largely as **59a** in the electrocatalytic steady state, whereas **59** is the reactive specie (Scheme 41). In 2016, Ahlquist performed computational studies on the electrochemical CO_2 hydrogenation catalyzed by the iridium complex **59**, identifying the in situ reduced cationic iridium(I)-H complex as the active specie for the transformation [581].

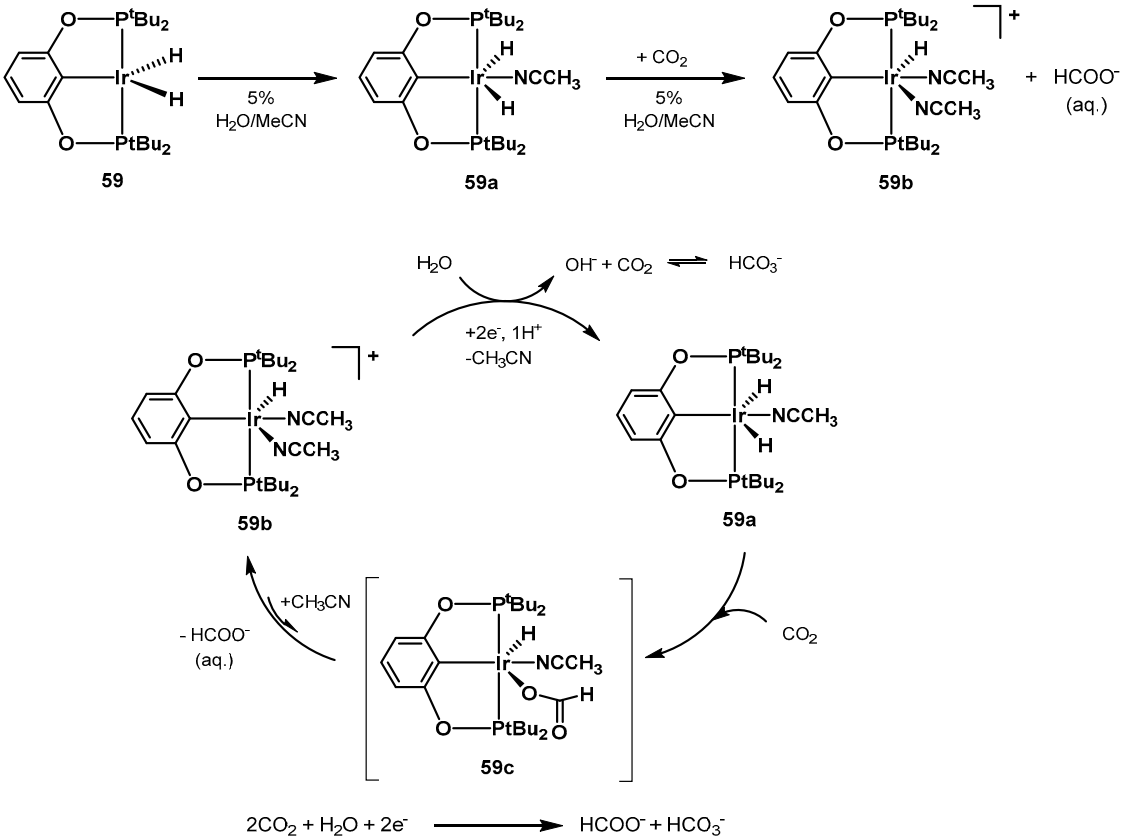

Scheme 41. CO_2 insertion to the Ir-PCP catalyst **59** showed by Meyer and Brookhart [580].

Müller investigated the insertion of CO_2 into metal–phenoxide bonds using homogeneous cobalt and zinc catalysts typically used in the copolymerization of epoxides and CO_2 and shown in Figure 4 [582]. The authors followed the mechanism of insertion resulting in the carbonate species by means of in situ ATR-IR spectroscopy. It was noted that, despite the differences in the two species, the neighboring donor groups of the pincer arm (NO_2 in the case of **60**, amides in the case of **61**) allow the carbonates to remain attached to the ligand sphere, enhancing the nucleophilicity of CO_2, hence favoring the easy transfer to other organic substrates, such as epoxides.

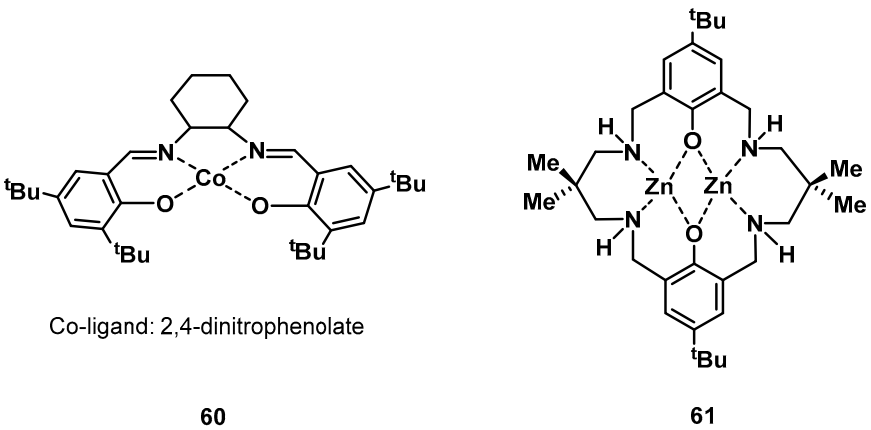

Figure 4. Cobalt and zinc pincer complexes reported to activate carbon dioxide by Müller [582].

In 2013, Milstein synthetized and characterized a series of novel pyridine-based Ni-PNP complexes with the aim of investigating the aromatization/dearomatization equilibria prompted by double protonation-deprotonation of the pincer arm [583]. Complex **64** can be readily prepared starting from

$NiCl_2 \cdot 6H_2O$ and the PNP^R ligand in a cascade reaction as depicted in Scheme 42. Complex **64**, where the negative charge is delocalized in the pincer moiety, was characterized by single-crystal X-ray diffraction studies. In the presence of CO_2, it undergoes electrophilic attack resulting in the anionic specie **64a**, observed by NMR spectroscopy.

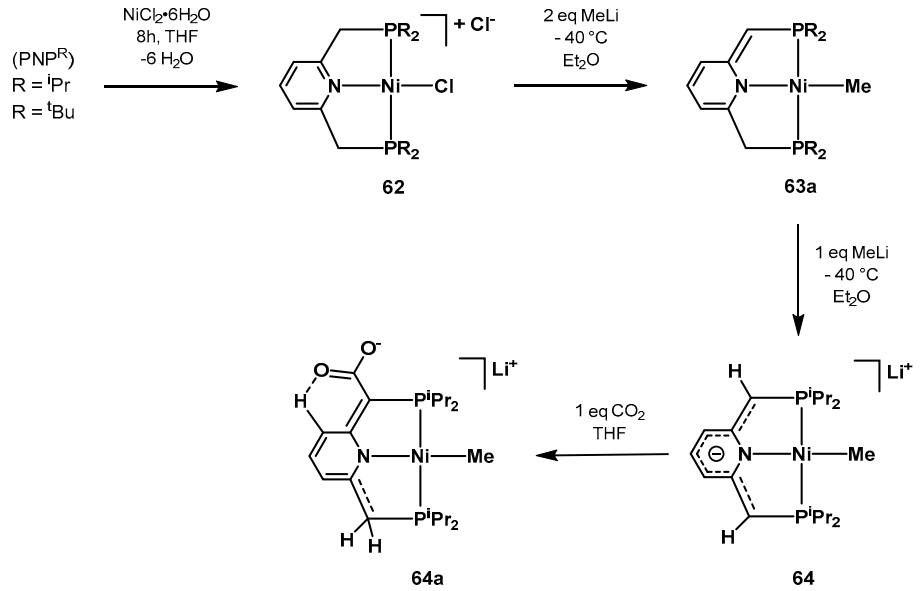

Scheme 42. Synthesis and CO_2 coordination of the Ni-PNP catalyst **64** proposed by Milstein [583].

Goldman performed DFT studies on the hydrogenation of dimethyl carbonate to methanol using the Milstein-type PNN catalyst **4** [215]. The work provided new insights on the mechanism for the C-OMe bond cleavage. The authors proposed an ion-pair-mediated metathesis pathway in which the formed alkoxide C–H bond binds to the ruthenium atom. By simple reorientation of the dimethoxymethanoxide anion formed upon transfer of a hydride to dimethyl carbonate, the methoxy group of the $[OCH(OMe)_2]^-$ anion is in a close proximity to the metal, allowing the C–OMe bond cleavage.

3.1.2. CO_2 Hydrogenation to Methanol

Himeda and Laurenczy reported in 2016 the iridium complex $[(Cp^*)Ir(dhbp)(OH_2)][SO_4]$ (dhbp = 4,4′-dihydroxy-2,2′-bipyridine), already showed for bicarbonate hydrogenation to formate and formic acid dehydrogenation [584], for the production of methanol from CO_2 at room temperature as well [585]. The catalyst was active for both CO_2 hydrogenation to formic acid in acidic media, without additives, as well as formic acid disproportionation into methanol, achieving 98% conversion and 96% selectivity after 72 h. Formic acid was obtained by pressurization of a solution of the catalyst with 20 bar CO_2 and 50 bar H_2 at ambient temperature. Methanol was observed by only increasing the temperature, whereas the addition of an optimized sulfuric acid concentration resulted in the enhanced activity of the system. No carbon monoxide was observed, indicating that decarbonylation of formic acid did not occur.

In 2015, Sanford proposed a ruthenium-catalyzed hydrogenation of CO_2 to methanol with dimethylamine as capturing agent [586]. The reduction proceeds in basic conditions through the in situ formation of dimethylammonium dimethylcarbamate (DMC) as a key intermediate (Scheme 43). **Ru-MACHO-BH** (0.03 mol%) was used as catalyst, in the presence of 2.5:50 bar of CO_2/H_2, and 0.25 mmol of K_3PO_4. The reaction afforded a TON of 550 in methanol and an overall 82% conversion of CO_2 to methanol and a mixture of dimethylformamide and dimethylammonium formate, which raises to 96% total conversion when applying 0.1 mol% of catalyst loading. The work represented a step forward toward the integrated CO_2 capture and direct conversion to methanol.

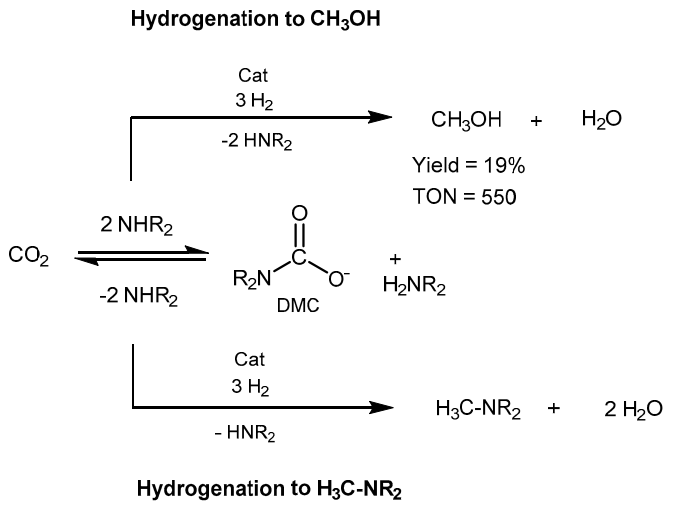

Scheme 43. CO_2 capture and conversion to MeOH proposed by Sanford [586].

The same year, Milstein developed an innovative methodology for indirect CO_2 hydrogenation by means of prior capture by amino alcohols at low pressure followed by the hydrogenation of the generated oxazolidinone to form MeOH (Scheme 44) [587]. Moreover, this approach is inspired by the CO_2 capture industry that uses amino alcohols to capture CO_2 from waste streams [588]. The work provides new possibilities for the use of oxazolidinone, which can be useful for the production of a liquid fuel such as MeOH. Three Ru-NNP complexes (**3**, **24,** and **54**) were tested for this transformation, with complex **24** being the most active catalyst. The authors screened both 2-(methylamino)ethanol and valinol for the first step of CO_2 capture; valinol was chosen considering its ability to capture CO_2 more selectively under only 1 bar of CO_2. Employing Cs_2CO_3 (10 mol%), DMSO as solvent, and at 150 °C under 1 bar of CO_2, for 24 h afforded the oxazolidinone in >90% yield. The product is not purified or isolated and the leftover CO_2 is simply removed under vacuum. Then, the subsequent hydrogenation of the formed oxazolidinone was performed with **24** (2.5 mol%) and KOtBu (25 mol%) under 60 bar of H_2, at 135 °C, for 72 h, producing MeOH and the amino alcohol precursor in 37% and 62% yields, respectively. Remarkably, the process allows direct CO_2 capture with consequent MeOH formation, avoiding the energy-demanding steps of CO_2 regeneration from capture products and subsequent pressurization.

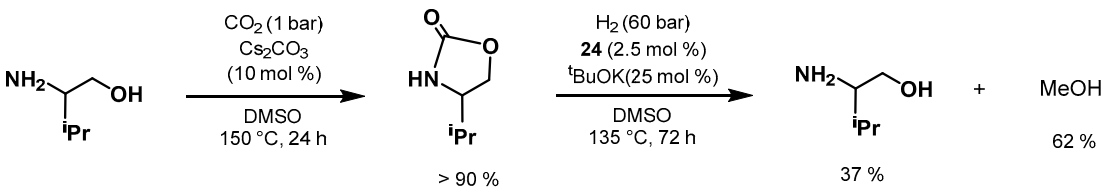

Scheme 44. Milstein's CO_2 capture/hydrogenation to MeOH using amino alcohol [587].

The year after, Olah and Prakash reported an efficient catalytic system for the one-pot CO_2 capture and conversion to methanol, using polyamine and **Ru-MACHO-BH** (Scheme 45a) [589]. The first step of CO_2 capture was achieved by bubbling synthetic air (400 ppm of CO_2 in N_2/O_2 80/20) in an aqueous solution of pentaethylenehexamine (PEHA) for 64 h. **Ru-MACHO-BH** (20 μmol) was applied in the presence of 50 bar of H_2 in triglyme, and 6% of the captured CO_2 (5.4 mmol) was converted into methanol after 55 h in 79% yield (determined by NMR). The authors confirmed the robustness of the method by recycling the catalyst over five consecutive runs of 5 h without significant loss of activity; only 20 μmol of catalyst afforded an overall TON of 2150 at 145 °C under 75 bar pressure of a 1:9 mixture of CO_2:H_2.

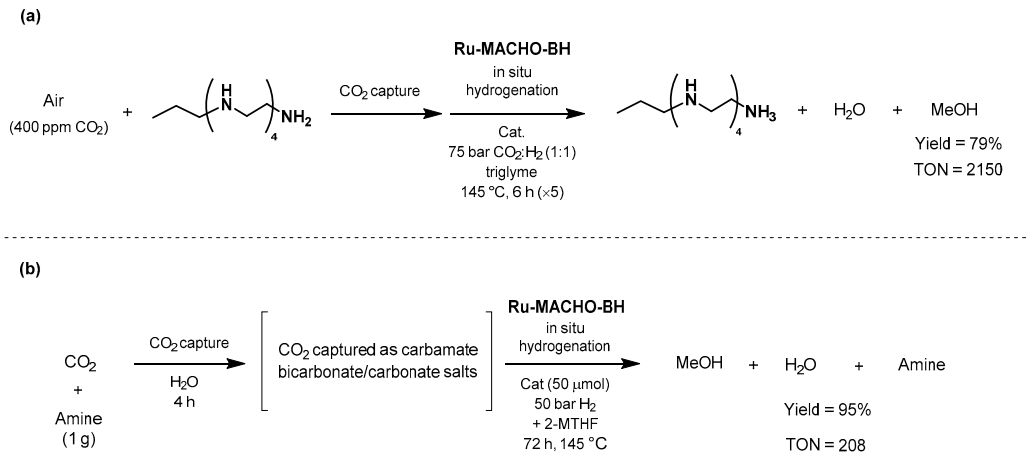

Scheme 45. CO_2-capture and direct conversion to methanol using **Ru-MACHO-BH** as showed by Olah (**a**) and Prakash (**b**) [589,590]

In 2018, Prakash showed another system for the integrative CO_2 capture (trapped in the form of carbamate and bicarbonate salts) followed by hydrogenation to methanol, using a biphasic 2-methyltetrahydrofuran (2-MTHF)/water solvent system, as shown in Scheme 45b [590]. The authors screened known PNP catalysts (**Ru-MACHO**, **Ru-MACHO-BH**, **10**, the Mn-PNP **25**, as well as the iron-PNP congener of **15** where HBH_3 is substituted with Br). Again, the commercially available **Ru-MACHO-BH** was found to be the most active, in combination with PEHA. After 11 mmol of CO_2 was trapped in 0.79 g of PEHA, the system afforded 95% yield of methanol by applying 50 μmol of catalyst in 2-MTHF at 70 bar H_2 at 145 °C for 72 h (TON = 208). Importantly, the biphasic solvent system allows recycling the catalyst, as well as the amine; after the reaction, the amine stays in the bottom aqueous solution, whereas the catalyst remains in the top organic layer. After extracting the methanol, both the amine and catalyst could be reused for three consecutive runs, retaining 90% of the activity in methanol production.

The year after, another approach was proposed by the same author, using amines immobilized onto a solid-silica support as CO_2 capturing agent for the hydrogenation to methanol [591]. The covalently bonded solid-supported amines (SSAs) showed good recyclability properties for CO_2 absorption/desorption, as well as easy separation from the reaction media by simple filtration. The catalyst could be also effectively recycled by vacuum evaporation of the solvent and methanol. One more time, **Ru-MACHO-BH** performed best among the screened Ru- and Mn-PNP catalysts, albeit with lower yields and turnovers compared with the previous reported results. 40 μmol of the catalyst under the reaction conditions in Scheme 46, afforded a yield of ≈5% in methanol after 2 cycles, with a TON of 90 in the first hydrogenation reaction.

Recently, Prakash also investigated the mechanism of ruthenium PNP-catalyzed amine-assisted hydrogenation of CO_2 to methanol [592]. As shown before, **Ru-MACHO** and **Ru-MACHO-BH** are the best catalysts for the transformation, with (di/poly)amines acting as effective reusable additives. In this work, TONs up to 1050 were achieved using PEHA, 10 mmol of **Ru-MACHO-BH$_3$** as catalyst, K_3PO_4 as base, in triglyme, under $CO_2/3H_2$ (75 bar), and at 145 °C for 40 h. A long-term reaction was carried out using **Ru-MACHO-BH$_3$** and PEHA and the catalyst was active for >10 days and TON of 9900 was achieved. The authors also provided mechanistic insight by means of NMR and ATR-IR spectroscopy techniques, as well as single-crystal X-ray diffraction analysis. The proposed catalytic cycle for methanol production through formamide is depicted in Scheme 47; the authors showed a deactivation pathway that leads to the formation of a dicarbonyl complex of **Ru-MACHO**. Under reaction conditions, in the presence of H_2, the resting state is converted back to the active specie by CO dissociation and it was found to selectively catalyze the hydrogenation of the in situ formed formamides resulting in high methanol yields.

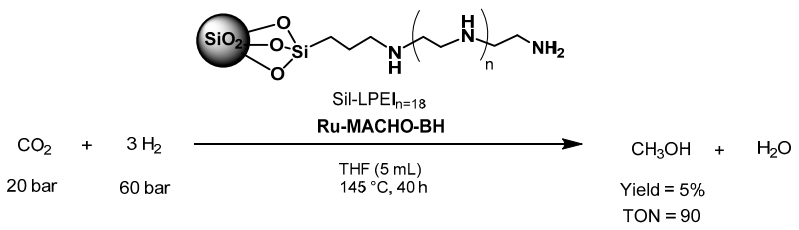

Scheme 46. CO_2 hydrogenation to methanol using **Ru-MACHO-BH** and silica-supported amines as capturing agents proposed by Prakash [591].

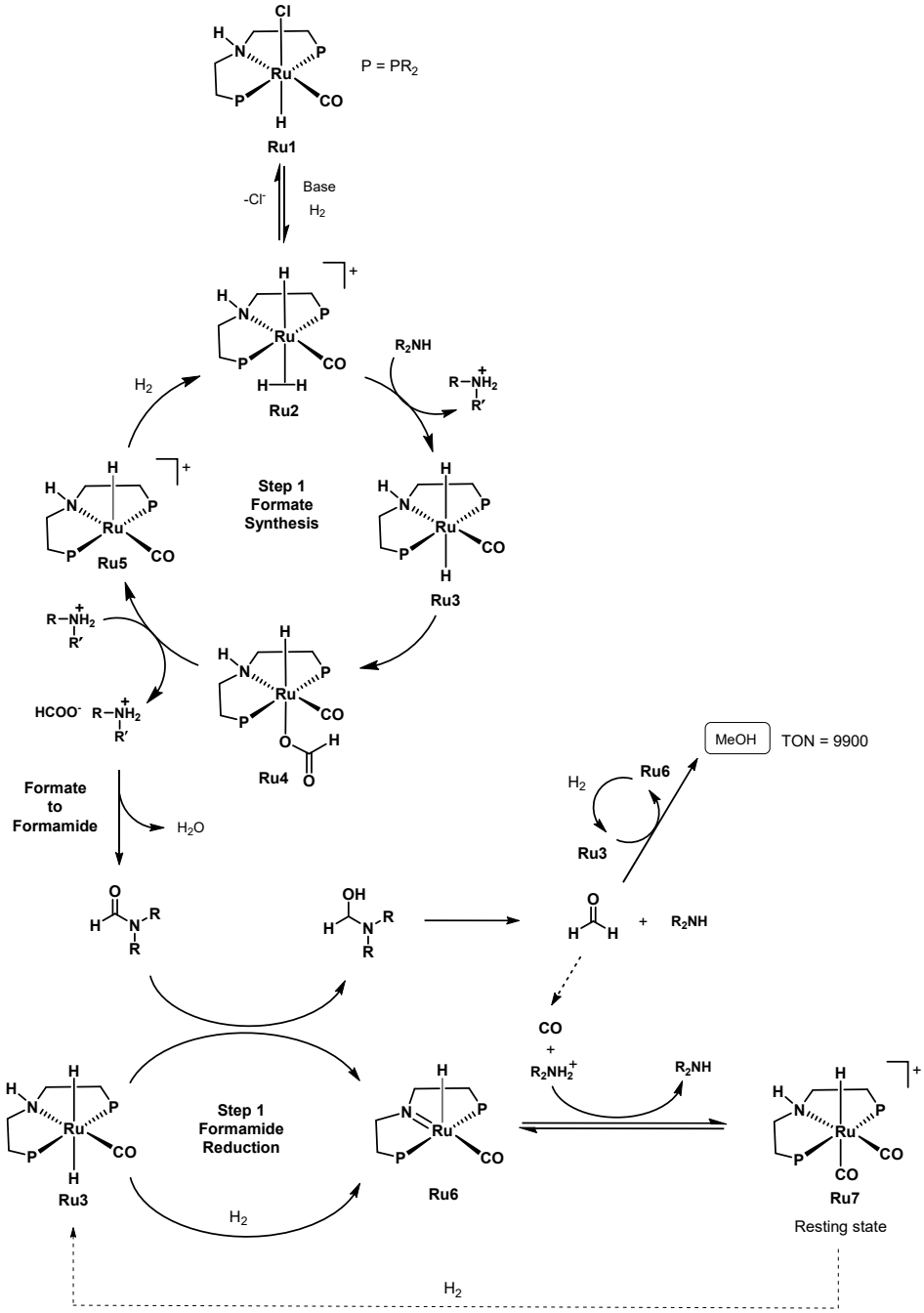

Scheme 47. Proposed catalytic cycle for amine-assisted CO_2 hydrogenation to methanol showed by Prakash [592].

In the last five years, several groups performed studies on the mechanism of CO_2 hydrogenation involving pincer-type catalysis. Pathak studied the base-free CO_2 hydrogenation employing a series of aliphatic Mn-PNP complexes using density functional theory (DFT) calculations [593]. The results suggested that the aliphatic amido PNP complex promotes the heterolytic H_2 cleavage and a proton transfer mechanism, contrarily to other CO_2 hydrogenation pathways promoted by base. Pincer ligands containing σ-donor and π-acceptor functionalities were investigated to explore the steric and electronic effects on the rate-determining step. It was found that both σ-donor, as well as π-acceptor ligands have a pronounced effect on the catalytic activity; in particular, the authors concluded that σ-donor ligands induce hydride transfer mechanism, while π-acceptor ligands promote the heterolytic H_2 cleavage. The same author reported theoretical studies using DFT and microkinetic modelling to study the mechanism of Mn-PNP-catalyzed CO_2 hydrogenation to methanol in the presence of morpholine as a co-catalyst via formamide intermediate [594]. The amidation step increases the overall rate of the reaction, while the *N*-formylmorpholine hydrogenation step could follow two different competitive pathways, both of them showing similar reaction energy barriers for the hydrogenation step.

The Mn-PNP pincer complex **25** was employed by Prakash for the hydrogenation of CO_2 to methanol in a sequential two-step approach [595]. The first step involves the *N*-formylation of an amine resulting in the corresponding formamide, which is further hydrogenated to methanol regenerating the initial amine. The first step was carried out by applying a 1:1 pressure of CO_2:H_2 (60 bar), at 110 °C, for 24 h, in the presence of THF as solvent and K_3PO_4 as base. In the second step, the 1:1 gas mixture was replaced with 80 bar H_2 pressure, at 80 °C, for 36 h. After optimization, the authors proposed a scale up of the process using 0.1 mol% of catalyst **25** combined with benzylamine as trapping agent; the first reduction step afforded 84% yield in formamide, corresponding to a TON of 840. Later, the hydrogenation step was performed under 85 bar of hydrogen, affording 71% yield in methanol with a TON of 36 (Scheme 48).

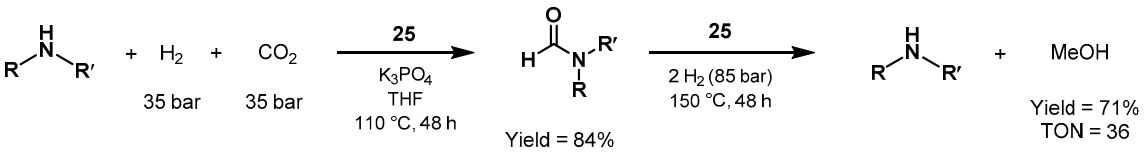

Scheme 48. CO_2 hydrogenation to methanol promoted by the Mn-PNP complex **25** reported by Prakash [595].

Based on a different approach, Prakash proposed this year the first example of hydroxide-based CO_2 capture from air, followed by hydrogenation to methanol [596]. CO_2 was successfully captured in ethylene glycol in the presence of hydroxide bases (NaOH or KOH) simply by stirring at room temperature for 3 h. The obtained bicarbonate and formate salts were later hydrogenated to methanol with high yields in an integrated one-pot system, as depicted in Scheme 49. Under optimized conditions, 0.5 mol% of **Ru-MACHO-BH** hydrogenated the bicarbonate species to methanol at 140 °C under 70 bar of H_2, resulting in 100% yield of methanol after 20 h, with TON of 200. The formed methanol can be easily separated by distillation, with contemporary hydroxide base regeneration. Finally, the authors proposed a one-pot method for direct CO_2 capture from ambient air and direct methanol production; the system afforded 100% yield of MeOH after 72 h with the reaction conditions shown in Scheme 49. Considering the surprising capture efficacy as well as stability of the hydroxide bases, the authors postulated that the hydroxide-based system might be superior to the alternative amine routes for a scalable process.

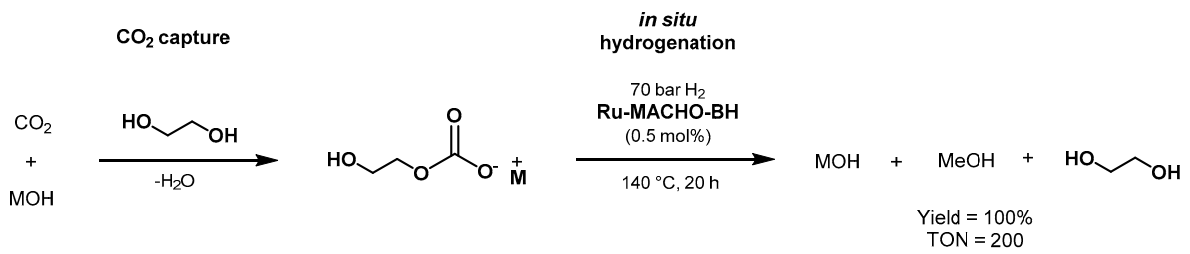

Scheme 49. Hydroxide-based CO_2 capture and subsequent hydrogenation proposed by Prakash [596].

In 2017, Beller reported an efficient cobalt catalyst for the production of methanol from CO_2 [597]. The authors started their investigation based on the $Co(BF_4)_2$/Triphos catalyst proposed by de Bruin for the hydrogenation of esters and carboxylic acids [598]. In this work, the active catalytic specie is formed in situ from either $[Co(acac)_3]$, $Co(OAc)_2{\cdot}4H_2O$, or $Co(BF_4)_2{\cdot}6H_2O$, in the presence of the Triphos ligand and $HNTf_2$. It was found that a 1:3 relationship between [Co]/$[HNTf_2]$ and two equivalents of Triphos with respect to cobalt, afforded the highest activity. The highest TON of 31 was obtained using $[Co(acac)_3]$ as the metal precursor, with the reaction conditions shown in Scheme 50a. The system was later optimized in 2019 [599]; the previous reported results could be improved by either using modified Triphos ligands, as well as by replacing $Co(acac)_2$ with $Co(NTf_2)_2$. After screening of a range of ligands and additives, the authors proposed a new system that is additive free and notably, active below 100 °C (Scheme 50b).

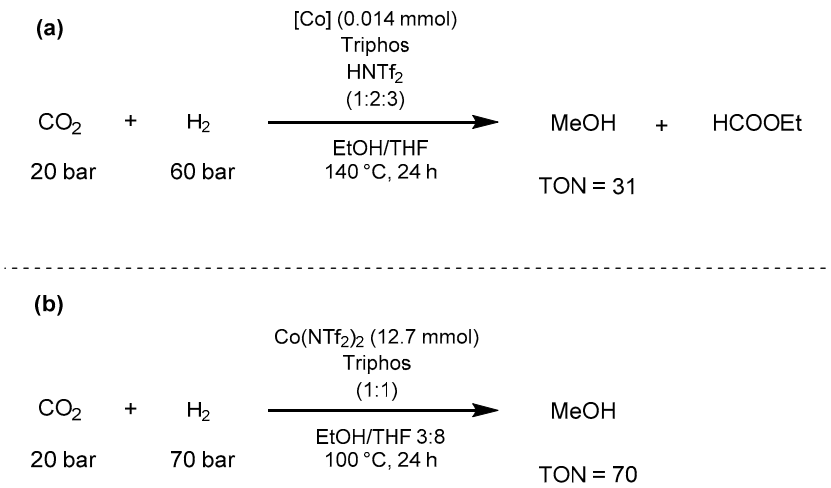

Scheme 50. In situ formed Co-PPP catalysts for carbon dioxide hydrogenation developed by Beller [597,599]: (**a**) First generation systems formed by various Co precursor and Triphos ligand, and (**b**) second generation using $Co(NTf_2)_2$ in combination with Triphos.

In 2017, Klankermayer demonstrated the efficient conversion of carbon dioxide to dialkoxymethane ethers catalyzed by a combination of $Co(BF_4)_2$, the Triphos ligand and $HNTf_2$ as a co-catalyst. The system was optimized for both the transformation of CO_2 to dimethoxymethane (DMM), as well as for the hydrogenation of CO_2 to alkoxy formates (AF) and dialkoxymethane ethers (DAM) in the presence of selected alcohols [600].

In 2018, Milstein showed the hydrogenation of organic carbonates to methanol and alcohols catalyzed by a manganese PNP complex [601]. The catalyst precursor **65** is activated in situ by catalytic amount of base, while the active amido form performs also in the absence of base. The authors demonstrated the efficient hydrogenation of a wide range of symmetrical and unsymmetrical acyclic carbonates and cyclic carbonates, which was possible to convert to methanol and two equivalents of the corresponding alcohols in high to excellent yields (62–99%), as shown in Scheme 51. In addition, the hydrogenation of poly(propylene carbonate) was also investigated as a route for the treatment of

waste plastics. Under the same reaction conditions, catalyst **65** afforded methanol and propylenediol in 59% and 68% yields, respectively, with propylene carbonate as a by-product.

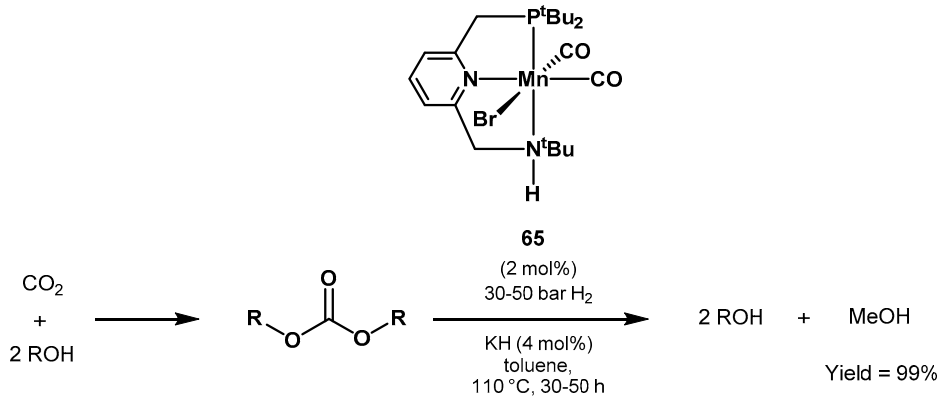

Scheme 51. Hydrogenation of carbonates to methanol and alcohols proposed by Milstein [601].

The same transformation was reported by Cavallo, El-Sepelgy and Rueping using the PNN manganese pincer complex **66** [602]. Several cyclic organic carbonates were successfully hydrogenated to methanol and valuable polyols under the reaction conditions shown in Scheme 52.

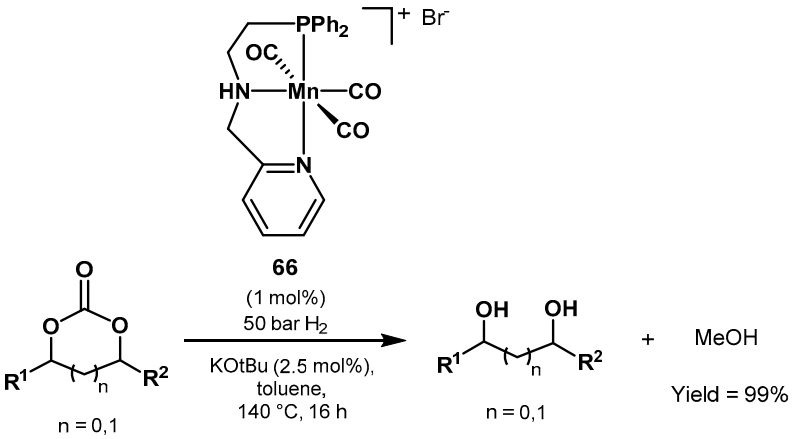

Scheme 52. Manganese-PNN complex **66** catalyzes the hydrogenation of organic carbonates to methanol and polyols as showed by Cavallo, El-Sepelgy, and Rueping [602].

In 2016, Zhang, Chen, and Guan explored the use of bis(phosphinite) pincer ligated Pd thiolate complexes for the hydrogenation of CO_2 [603]. Catecholborane was used to trap CO_2 at room temperature with 1 bar of CO_2, using catalyst **67** (Scheme 53). A TOF of 1789 h^{-1} and a TON of 445 were achieved with this method, being one of the most active systems to date reported for the homogeneous catalytic reduction of CO_2 to methanol or its derivative under mild reaction conditions.

Leitner reported the manganese pincer complex **68** for the reduction of CO_2 and other carbonyl groups using pinacolborane [604]. The system operates using reasonable low catalyst loadings and under solvent-less conditions. The best result was achieved using 0.036 mol% of catalyst **68** and NaOtBu at 100 °C resulting in 96% yield and a TON of 883 after 14 h (Scheme 54). In addition, several cyclic and linear carbonates could be quantitatively converted into the corresponding boronate esters and protected methanol in yields exceeding 95%.

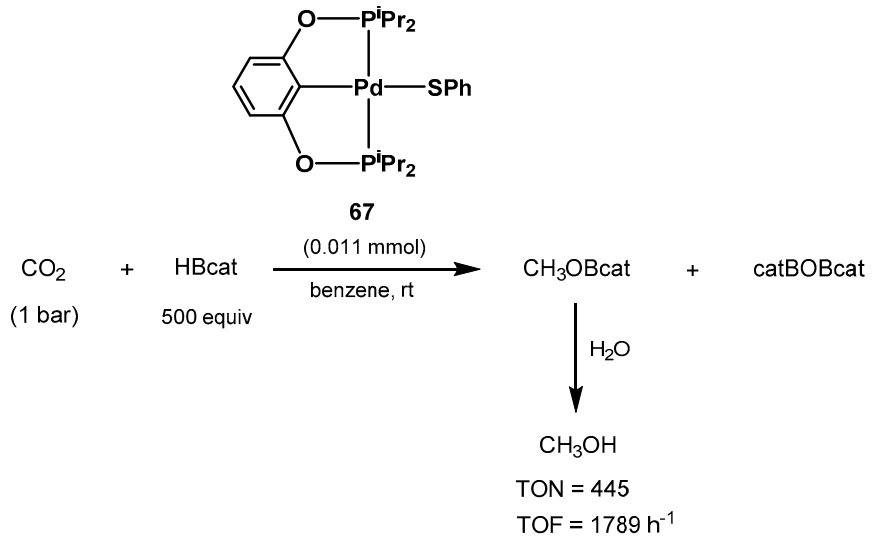

Scheme 53. Catalytic reduction of CO_2 to CH_3OBcat catalyzed by PCP pincer ligated Pd thiolate complexes reported by Zhang, Chen, and Guan [603].

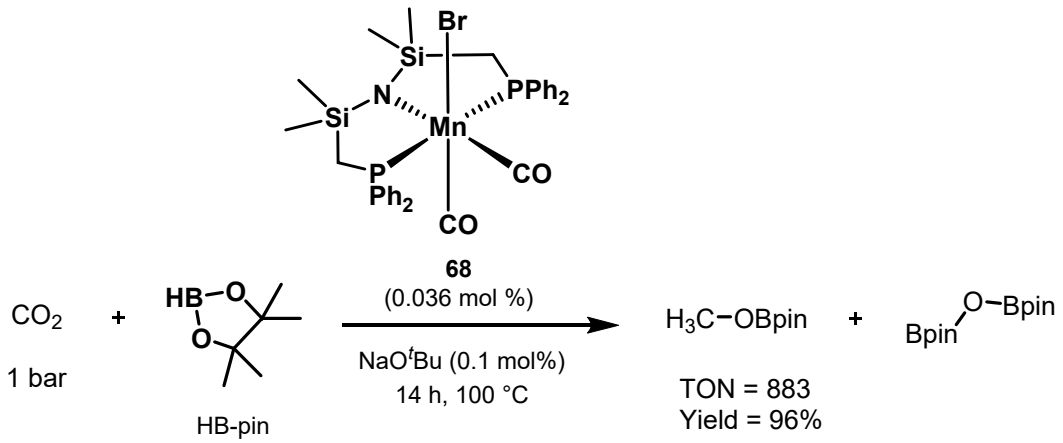

Scheme 54. Leitner's hydroboration of CO_2 using the manganese complex **68** as catalyst [604].

Another method for the capture of CO_2 is its reduction in the presence of silanes, with the formation of strong Si-O bonds as the driving force promoting the transformation. The hydrosilylation of CO_2 has gained much attention in the past decades, with several homogeneous systems reported to catalyze the conversion of carbon dioxide to silyl formates [605–607], as well as to the methoxysilyl derivatives [608–610]. With regard to pincer complexes, important results were achieved in 2010 by Chirik with a Co-PNP complex [611], as well as by Guan using a Ni-PCP catalyst [612].

Gonsalvi and Kirchner showed the Mn(I)-PNP complex **63** as an active catalyst for the selective and efficient reduction of CO_2 to MeOH in the presence of hydrosilanes [613]. The reaction was performed applying 0.014 mmol of the catalyst (10 mol% catalyst to CO_2 and 2 mol% catalyst to Si–H bonds) under mild conditions (80 °C, 1 bar CO_2), in the presence of 5 equivalents of $PhSiH_3$ and DMSO as solvent (Scheme 55). It was possible to achieve 99% yield of methanol, in the form of Si(OMe) derivatives, after 6 h.

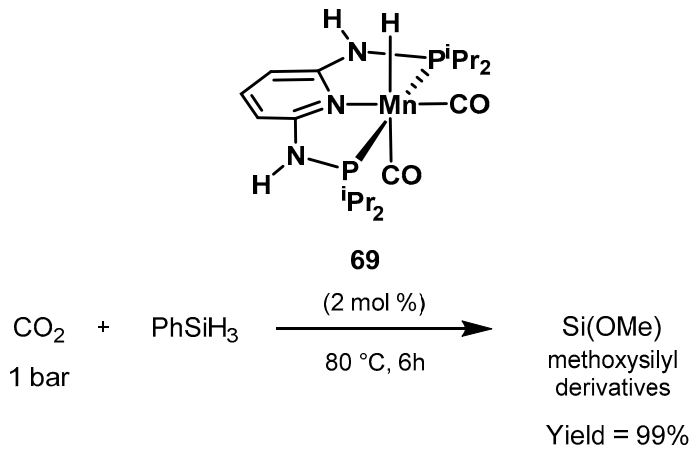

Scheme 55. Hydrosilylation of CO_2 to methoxisilyl derivatives catalyzed by the Mn-PNP **68** reported by Gonsalvi and Kirchner [613].

Abu-Omar developed a method for carbon dioxide reduction into silyl-protected methanol in the presence of an oxo-rhenium PNN pincer complex (Scheme 56) [614]. The reaction employs catalyst **70** (4.5 mol%) with Me_2PhSiH and CO_2 (7 bar), in DCM, at 25 °C to promote the addition of Si-H to Re=O bond affording a complex capable of reducing CO_2 into a silyl formate (95% yield). After 24 h, the silyl formate was reduced to silyl methanol with 53% yield.

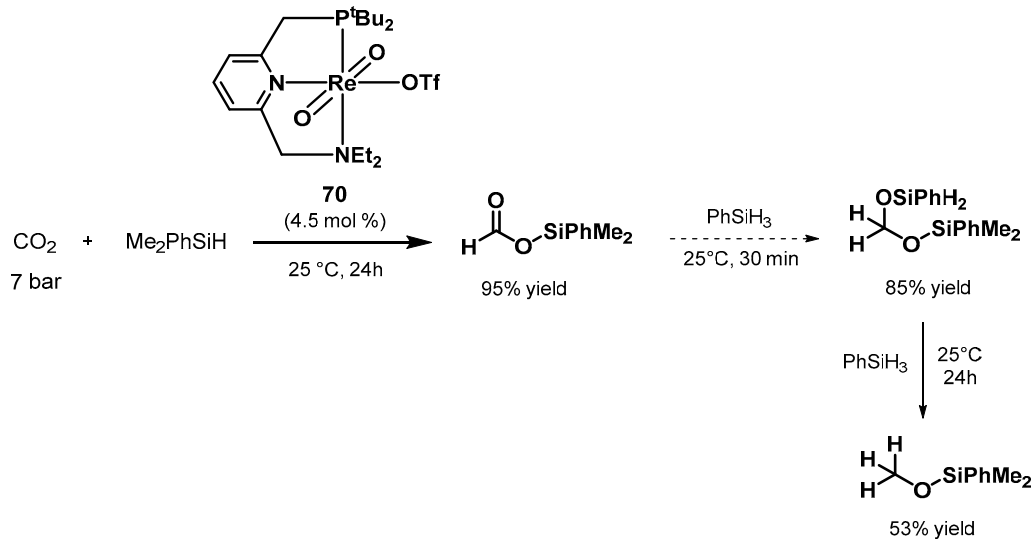

Scheme 56. Abu-Omar's CO_2 reduction to silyl-protected methanol catalyzed by the oxo-rhenium PNN pincer complex **70** [614].

In 2019, Beller and Checinski reported the manganese pincer complex **25** as suitable catalyst also for carbon monoxide hydrogenation to methanol at mild conditions, in the presence of either pyrroles, indoles, or carbazoles as promoter [615]. The reaction performed at 150 °C for 18 h under 1 bar of CO and 40 bar of H_2, using 5 μmol of catalyst **25**, 0.75 mmol of K_3PO_4 as base, and benzene as solvent. This resulted in the formation of methanol with high selectivity and turnover numbers up to 3170. Simultaneously, Prakash reported the same transformation proceeding via formamide catalyzed by **Ru-MACHO-BH** [616]. Both catalysts show promising robustness and tolerance to CO. Similarities and differences between the two proposed catalytic systems for CO hydrogenation can be found in Scheme 57; it is possible to observe how the method proposed by Beller is superior in terms of hydrogen pressure, catalyst loading, as well as reaction time.

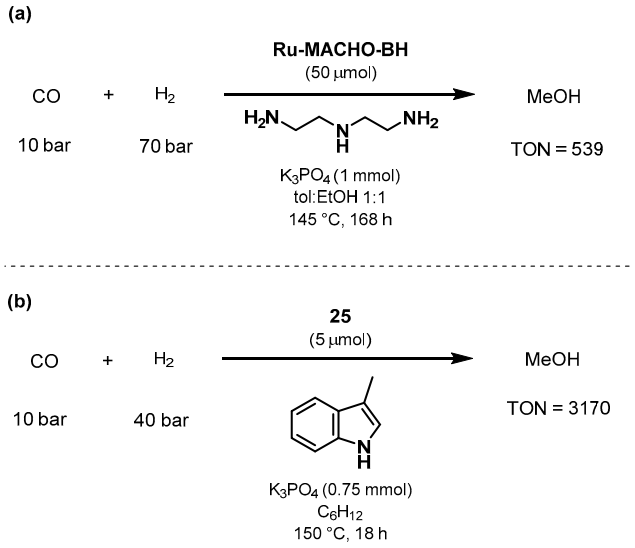

Scheme 57. CO hydrogenation to methanol proposed by **(a)** Prakash and **(b)** Beller [615,616].

In 2018, Schneider proposed a reverse water-gas-shift reaction (WGS) promoted by a nickel pincer complex at ambient reaction conditions [617]. The authors proposed a novel mechanism for CO_2 activation, opposed to the kinetically favored insertion into the catalyst M-H bonds providing formates (Scheme 58a). Under photochemical conditions, the selective formation of the metallacarboxylate was observed [618], consisting in the first step of the proposed WGS, followed by water elimination, CO release, and heterolytic H_2 activation to restore the active hydride specie (Scheme 58b).

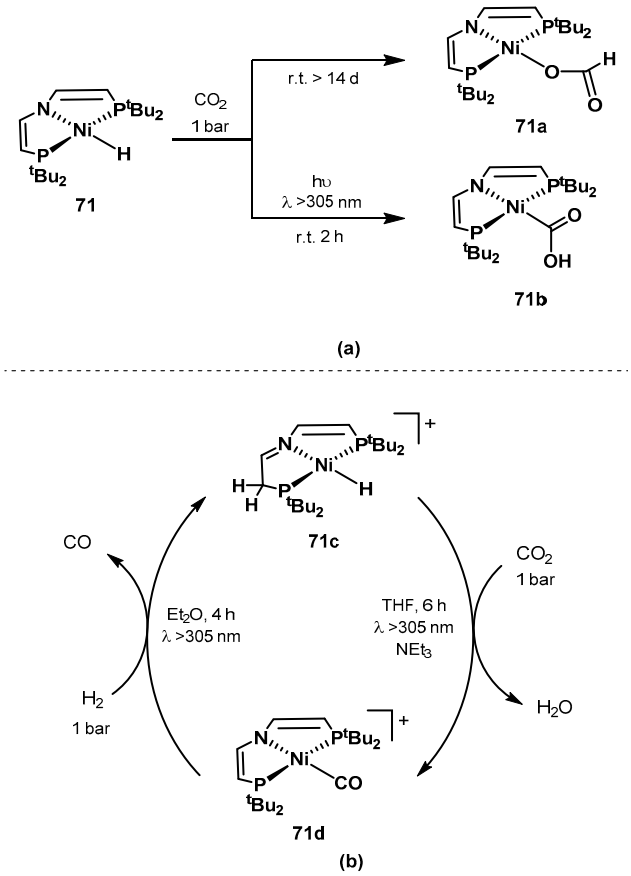

Scheme 58. Water-gas-shift (WGS) reaction of CO_2 to CO and water with a nickel PNP pincer complex proposed by Schneider [617]: (**a**) Reactivity of **71** with CO_2 and (**b**) proposed mechanism.

The iridium-based complexes **72** and **73** reported by Milstein (Figure 5) showed good activity for the reversible activation of CO_2 [619]. Complex **72** is dearomatized at room temperature and reacts with CO_2 in THF or benzene affording two isomers, one where the hydride is trans to the bonded oxygen from CO_2, and a second isomer where the hydride is trans to the pincer ligand. On the contrary, complex **73** reacts with CO_2 at room temperature in the presence of THF, affording only one isomer. The reaction is highly solvent dependent. Under similar conditions, using benzene as solvent, the authors observed a mixture of unidentified products. However, the addition of CO_2 to a pre-heated benzene solution containing **73** at 80 °C resulted in full conversion.

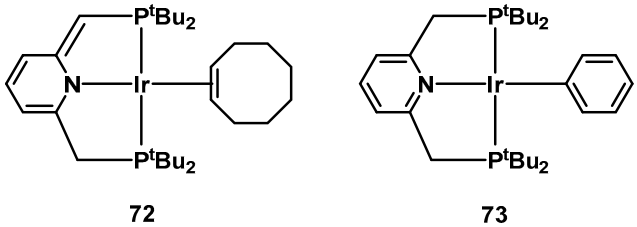

Figure 5. Iridium-based complexes **72** and **73** synthetized by Milstein [619].

The same group showed a stoichiometric CO_2 reductive cleavage to CO and water promoted by a mixture of the two complexes **74** and **75** via metal-ligand cooperation (Scheme 59) [620]. It was suggested that a proton is transferred from the ligand to the activated CO_2 resulting in its cleavage. A reversible 1,3 addition of CO_2 to the benzylic position was also showed by the studies revealing that complex **77** is the kinetic product. Together with the observed, rare example of di-CO_2 metallocycle complex **77a**, both of them are reversibly formed and do not participate in the formation of **76**. The reaction of **74** and **75** with CO results in the formation of dihydrogen and **76**.

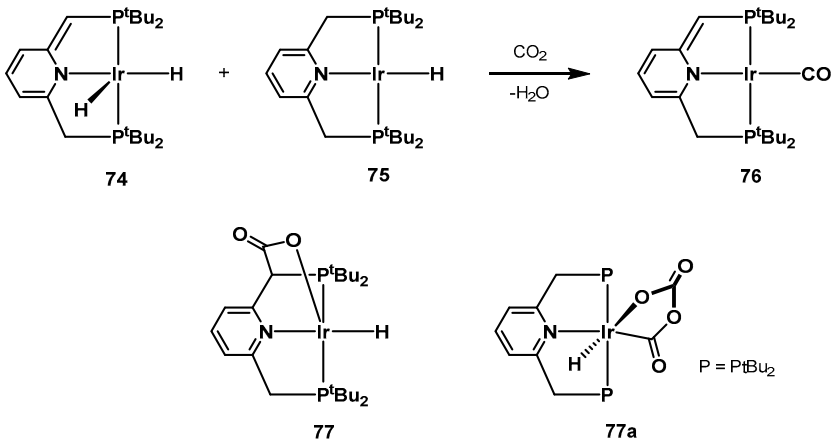

Scheme 59. Reactivity of **74** and **75** with CO_2 showed by Milstein [620].

Milstein also reported that the Rh(I)-PNP pincer complex **78** promotes the splitting of CO_2 leading to the Rh(I) carbonyl complex **78a** that by UV irradiation activates a C-H bond in benzene, followed by the protonation of the benzoyl complex **78b** resulting in a benzaldehyde molecule (Scheme 60) [621].

The reactivity between a square-planar Co(II)-hydrido-PNP complex and small molecules such as CO_2 and CO was investigated by Tonzetich in 2018 [622]. Complex **79** demonstrated a facile migratory insertion of CO_2 producing the formate complex **79b**. The complex was also reacted with nitric oxide, providing the first example of cobalt nitrosyl-hydride complex (Scheme 61).

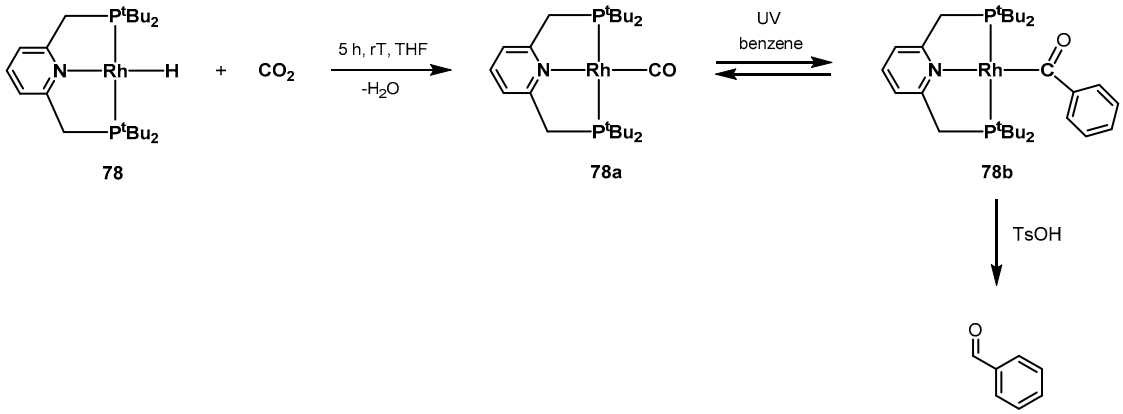

Scheme 60. CO_2 cleavage and photocarbonylation of benzene reported by Milstein [621].

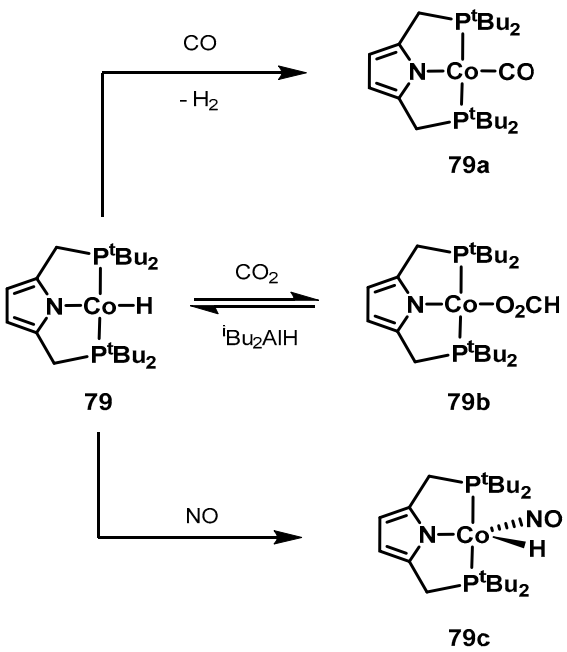

Scheme 61. Square planar Co(II)-hydrido-PNP complex **79** and its reactivity with small molecules showed by Tonzetich in 2018 [622].

3.1.3. CO_2 Hydrogenation to Formate Salts

Several groups explored the homogeneous hydrogenation of CO_2 to give basic formate salts, which can be later acidified to provide formic acid. Various combination of ruthenium complexes bearing phosphine ligands were found to be active in this transformation [623–625]. Important milestones were achieved by Jessop, with Ru-P(Me$_3$)$_3$ catalysts [560,562], Zhang with Ru-P(Ph$_3$)$_3$ species [626], Leitner with the meta-trisulfonated triphenylphosphine ligand (TPPMS) [627], as well as Beller, using [RuCl$_2$(benzene)]$_2$ in combination with the phosphorous ligand bis(diphenylphosphino)methane (DPPM) [628]. In addition, the hydrogenation of bicarbonates (used as CO_2-trapping agents) as an indirect route to provide formates has also been investigated by many groups [629–631]. Important advances in this regard have been achieved by Beller and Laurenczy using again [RuCl$_2$(benzene)]$_2$ and DPPM [632,633], resulting in a formate yield of 61%, and a TON = 2,793 after 20 h at 100 °C in the presence of 50 bar of hydrogen and 35 bar of CO_2 in a sodium bicarbonate solution.

In 2012, the same group showed that not only ruthenium, but also iron and cobalt catalysts are highly active for the hydrogenation of bicarbonates to give formates. In the presence of an iron(II)-fluoro-tris(2-(diphenylphosphino)phenyl)phosphino]tetrafluoroborate complex, obtained

in situ from $Fe(BF_4)_2{\cdot}6H_2O$ and tris(2-(diarylphosphino)aryl)phosphine, the hydrogenation of bicarbonates afforded TON > 7500 and TOF > 750, with 77% yield of sodium formate under 60 bar of hydrogen in methanol at 100 °C [634]. The hydrogenation of CO_2 to formic acid in the presence of methanol and amines was also investigated, resulting in a mixture of formic acid and methyl formate, albeit with only 15% of carbon dioxide conversion.

Using the same approach, the hydrogenation of bicarbonate and carbon dioxide was also demonstrated using an in situ formed cobalt complex [635]. By simply applying 0.028 mol of $Co(BF_4)_2{\cdot}6H_2O$, in the presence of 1 equivalent of the Tetraphos ligand PP_3 ($P(CH_2CH_2PPh_2)_3$), under 1:1 60 bar of H_2/CO_2 at 80 °C, it was possible to obtain 94% yield of sodium formate, with a TON of 645 after 20 h.

Regarding the use of pincer complexes, Beller employed in 2014 **Ru-MACHO** as the catalyst for the combined methanol dehydrogenation and bicarbonate hydrogenation, as well as for the synthesis of potassium formate from carbon dioxide, potassium hydroxide, and methanol [636]. In the first transformation, the reaction afforded excellent TON (>18,000), TOF (>1300 h^{-1}), as well as yield (92% of potassium formate), as shown in Scheme 62. Under the same reaction conditions, with 5 bar of carbon dioxide, the reaction afforded a formate yield of 77%, with a TON of 12308.

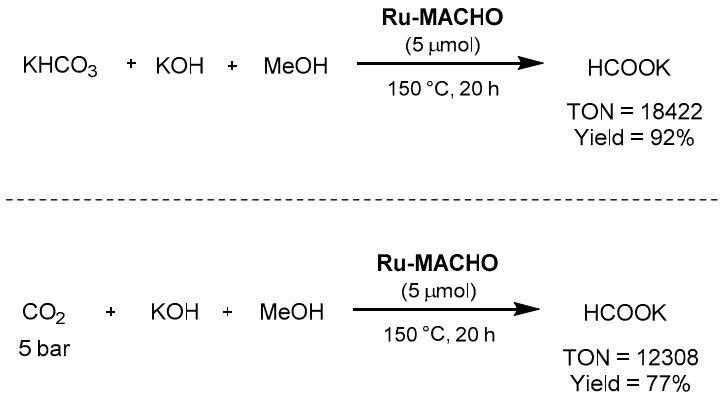

Scheme 62. **Ru-MACHO**-catalyzed hydrogenation of bicarbonate and CO_2 to formate showed by Beller [636].

Sanford showed in 2013 that the Milstein PNN catalyst **3** efficiently catalyze the hydrogenation of CO_2 to formate in the presence of potassium carbonate as base (Scheme 63a) [637]. In addition, the authors performed stoichiometric studies of various organometallic intermediates, showing that the reaction proceeds with a classic ligand-based aromatization/dearomatization pathway. The year after, Pidko showed that another Milstein catalyst, the PNP-pincer **26**, is able to perform the same transformation [638]. With the reaction conditions shown in Scheme 63b, the hydrogenation of CO_2 proceeds in the presence of DBU as base, showing activity already at 65 °C and a TOF of 1,100,000 h^{-1} at 120 °C (Scheme 63b). Importantly for an energetic cycle point of view, catalyst **26** is very active in the reverse formic acid dehydrogenation as well, affording high turnover numbers (1063000) in DMF/NEt_3.

In 2014, Hazari and Schneider demonstrated Fe-PNP complexes as catalysts with a Lewis acid as co-catalyst for the dehydrogenation of formic acid (see Section 2.2.2) [389]. One year later, the hydrogenation of CO_2 catalyzed by the same system was demonstrated by Hazari and Bernskoetter [639]. The catalytic activities of both Fe-PN^HP and Fe-$PN^{Me}P$ complexes were investigated in the study. Both of them demonstrated better results in the presence of co-catalytic amounts of a Lewis acid. The reactions were carried out under 70 bar of CO_2/H_2 (1:1), 79,600 equivalents of DBU to the catalyst, LiOTf as additive (DBU/LiOTf 5:1), THF as solvent, and at 80 °C for 24 h. After optimization, 0.3 μmol of catalysts **15-Me** afforded the best turnover number of 58,990 and 74% yield (Scheme 64). Quantitative yields were afforded when increasing the catalyst loading to 0.78 μmol.

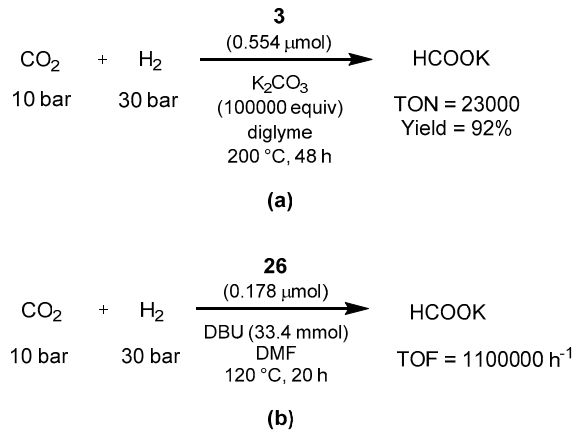

Scheme 63. Hydrogenation of CO_2 to formate using Milstein's catalysts **3** (**a**) and **26** (**b**) as reported by Sanford [637] and Pidko [638].

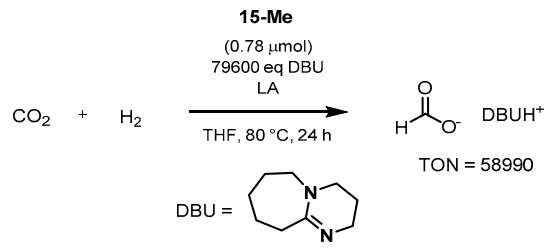

Scheme 64. Hazari and Schneider's CO_2 hydrogenation catalyzed by **15-Me** [639].

In catalytic systems containing a secondary amine ligand, studies via NMR analysis suggested that the key role of the Lewis acid is the weakening of the stability of the hydrogen bond between *N*-H and Fe-O_2CH moieties in **15c** (Scheme 65).

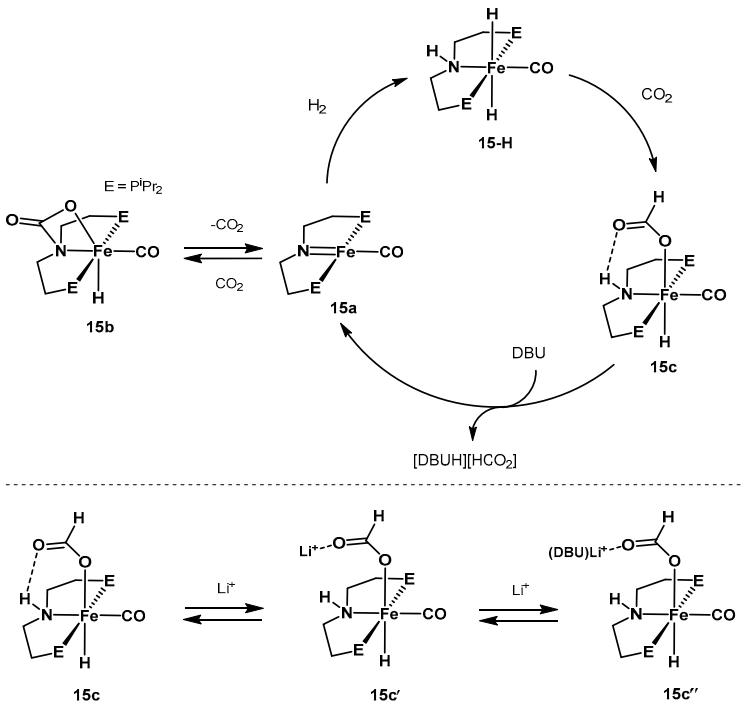

Scheme 65. Proposed mechanism for (^{R}PNP)Fe(H)COLi^{+} catalyzed CO_2 hydrogenation and activation of HCO_2-1a by Li^{+} and DBU as showed by Hazari and Schneider [639].

On the other hand, in the presence of tertiary amine ligand systems, the authors showed that ($^{iPr}PN^{Me}P$)Fe(H)CO(BH_4) is activated by DBU to produce the complex ($^{iPr}PN^{Me}P$)Fe(H)$_2$CO which rapidly captures CO_2 (Scheme 66). Here, the role of the Lewis acid consists in promoting the dihydrogen substitution on the formate complex, generating a transient cationic iron(II) dihydrogen intermediate. DBU deprotonates the dihydrogen complex resulting in the regeneration of ($^{iPr}PN^{Me}P$)Fe(H)$_2$CO. The proposed pathway is believed to improve the reaction rate resulting in turnover frequencies as high as 20,000 h^{-1}. In addition, the authors reported kinetic studies on the influence of solvent and Lewis acid on the insertion of CO_2 metal hydrides. Small and highly charged Lewis acids such as Li^+ provide stabilization of the incipient negative charge on the carboxylate group, hence of the rate-determining step, as long as it is not sequestrated by the solvent via O−···LA^+ interactions.

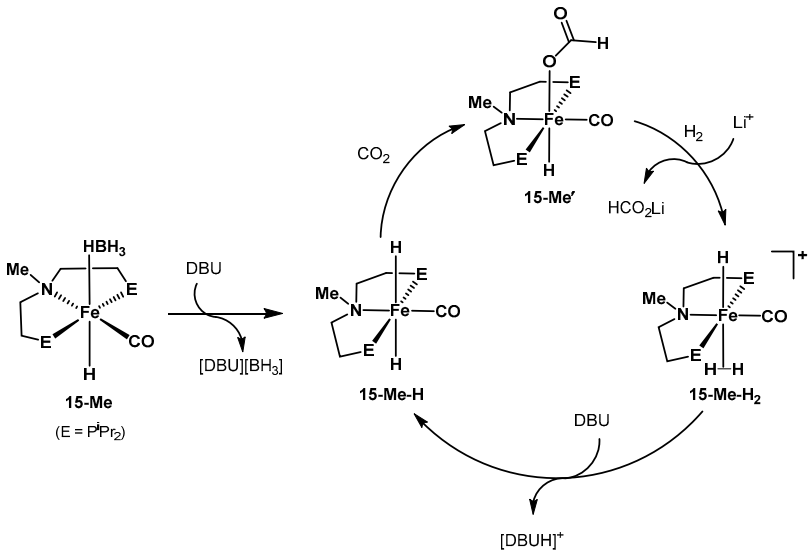

Scheme 66. Proposed pathway for catalytic CO_2 hydrogenation using ($^{iPr}PN^{Me}P$)Fe(H)CO(BH_4) reported by Hazari and Schneider [639].

In 2016, a comprehensive overview of the state-of-the-art for CO_2 hydrogenation, as well as formic acid/methanol dehydrogenation using first-row metal complexes, was published by Bernskoetter and Hazari [640]. The authors provide comparisons between selected iron and cobalt pincers with known Ru-PNP catalysts, and investigate the role of Lewis acid additives in the improvement of these promising base metal catalysts.

The same year, Bernskoetter showed the synthesis, as well as crystallographic characterization, of cobalt(I)-PNP complexes derived from the pincer ligand Me-N[$CH_2CH_2(P^iPr_2]_2$ [641]. The new complexes showed in this work performed better than previously reported $P^{Me}NP$ cobalt pincer catalysts for the hydrogenation of CO_2 to formate. When 0.3 μmol of complex [(^{iPr}PNP)Co(CO)$_2$]$^+$ **80** was paired with 3.2 mmol of the Lewis acidic additive LiOTf, 2.4 mmol of DBU as the base, under 70 bar of 1:1 CO_2/H_2 at 45 °C, a TON near 30,000 and a TOF of 5700 h^{-1} were afforded after 16 h (Scheme 67).

Bernskoetter further investigated the influence of various bifunctional PNP pincer ligands within the same class of low-valent cobalt complexes [642]. Cobalt(I) precatalysts containing tertiary amine ligand showed better activity, as well as improved stability, than those bearing the secondary amine pincer ligand. In this report, the reactions were performed using the same conditions, as shown in Scheme 67. Catalyst **80** achieved a TON of 29,000, while catalyst **81** and **82** achieved TONs of 24,000 and 450, respectively.

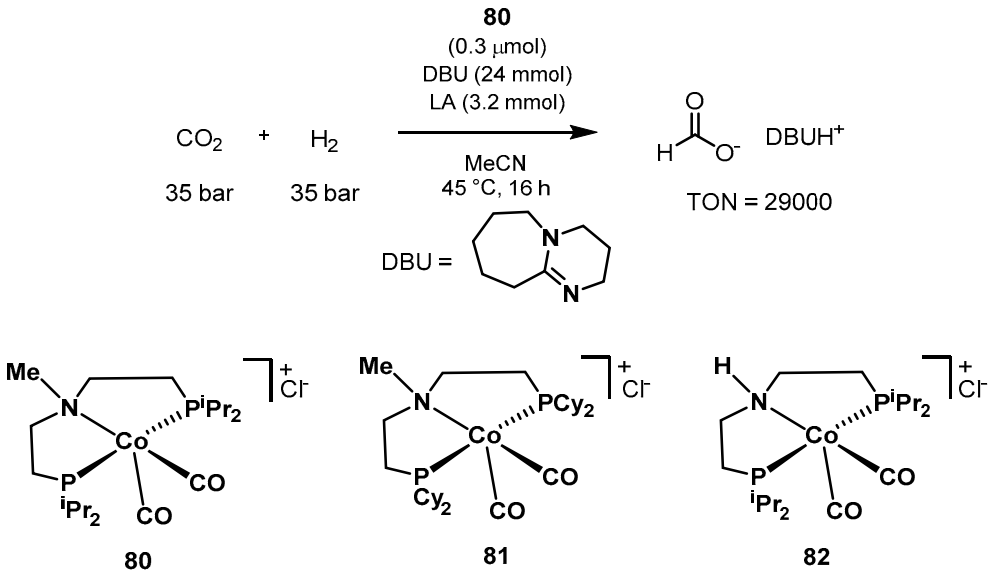

Scheme 67. Co-PNP complexes tested by Bernskoetter for CO_2 hydrogenation to formate with Lewis acid additives [641,642].

Later, Milstein developed Fe-PNP complexes based on the pyrazine backbone (PNzP) [643]. In a similar fashion as the pyridine congener, the PNzP ligand promotes the metal-ligand cooperation by aromatization/dearomatization of the pyrazine ring. Under basic conditions, complex **83** (0.1 mol%) catalyzes the hydrogenation of CO_2 (3.3 bar) to formate salts at low H_2 pressure (6.3 bar) and temperature (55 °C) (Scheme 68a). However, only moderate TON values (up to 388) were obtained. The authors proposed a catalytic cycle for the reaction based on observations obtained with NMR spectroscopy as well as X-ray diffraction. At first, one of the pincer arms is deprotonated to generate a stable dearomatized compound. The so-formed complex reacts with CO_2 and H_2 to afford compounds **83a** and **83-H**, respectively. **83a** reacts with H_2 by formal substitution of CO_2, leading to compound **83-H**. CO_2 is inserted to **83-H** into the hydride-iron bond generating the formate complex **83b**. In the presence of base, **83b** produces the dearomatized complex that reacts with H_2 regenerating the cycle (Scheme 68b).

Gonsalvi and Kirchner reported Fe(II)-hydrido carbonyl complexes supported by PNP ligands with *N*-H or *N*-Me spacers as catalysts for CO_2 and $NaHCO_3$ hydrogenation to sodium formate in protic solvents and in the presence of base [644]. Studies showed that catalyst **29** can work as a bifunctional catalyst in which the *N*-H spacer promotes metal-ligand cooperation. In contrary, the *N*-Me spacer of complex **29-Me** prevents that possibility. Moreover, the authors speculate that the presence of a labile bromide as well as the strongly σ-basic H and π-acidic CO ligands might be ideal for catalytic CO_2 hydrogenation reactions. The hydrogenation of $NaHCO_3$ was catalyzed by **29** (0.05 and 0.005 mol%) under 90 bar of H_2 at 80 °C, and after 24 h of reaction TONs of 1964 (98% yield) and 4560 (23% yield) were achieved, respectively. The use of THF inhibited the reaction suggesting that the use of protic solvents stabilizes the reaction intermediates through hydrogen bonding. The hydrogenation of CO_2 catalyzed by 0.08 mol% of **29** under 80 bar pressure at 80 °C in H_2O/THF proceeded in basic conditions (12.5 mmol NaOH) and resulted in TONs up to 1220 with 98% of yield. The use of NaOH in H_2O/THF in this reaction was fundamental since changing to other bases and solvents resulted in no activity or low conversions. Applying 0.01 mol% of **29-Me**, DBU as base and EtOH as solvent at 80 °C, the reaction afforded 98% yield in sodium formate, corresponding to a TON of 9840. With lower catalyst loading (0.005 mol% of **29-Me**) a TON of 10,275 was achieved, albeit with only 21% yield of formate.

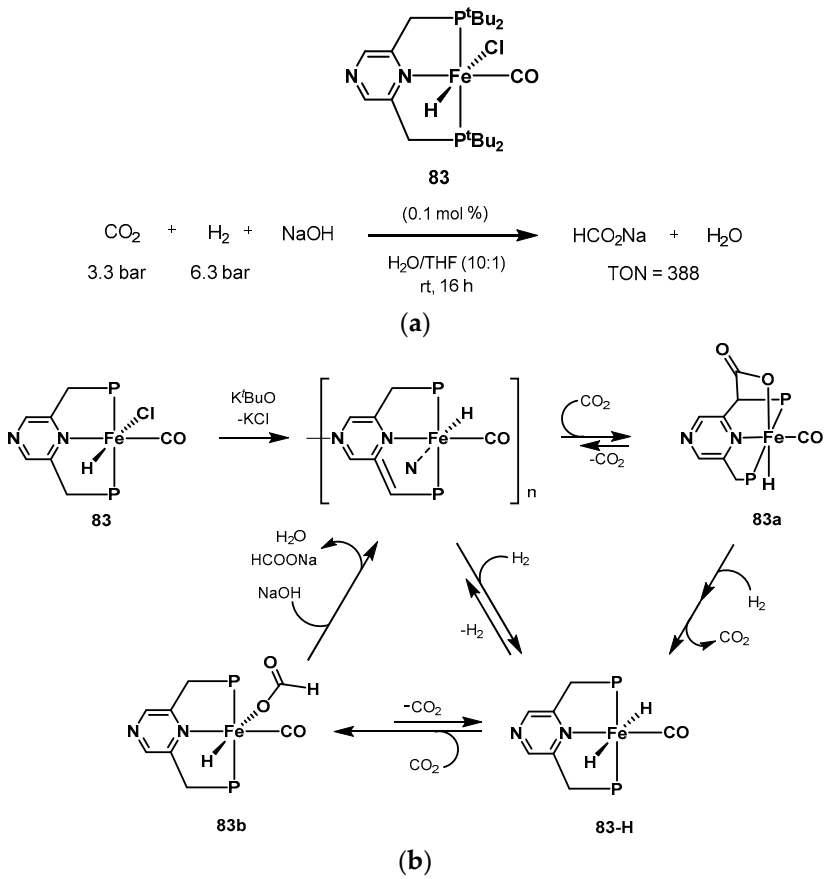

Scheme 68. (**a**) Hydrogenation of CO_2 catalyzed by **83** and (**b**) the proposed mechanism for hydrogenation of CO_2 reported by Milstein [643].

Prakash explored a green and direct procedure for CO_2 capture and its transformation to formate using known Ru- and Fe-PNP pincer complexes without the need of an excess of base [645]. Superbases, such as tetramethylguanidine (TMG), as additives showed the best results for the combined CO_2 capture (15.6 mmol) followed by hydrogenation in aqueous media using 2 µmol of **Ru-MACHO-BH** and 50 bar of H_2 at 55 °C for 20 h in dioxane/water (Scheme 69). It was found that other substrates, such as bicarbonate/carbonates and carbamates, could be converted into formate as well. The catalyst recyclability showed a TON for formate of 7375 in five consecutives hydrogenation steps of 5 h each, by reusing the same organic layer containing the catalyst and with no decrease of the catalytic activity (formate yield = 95%).

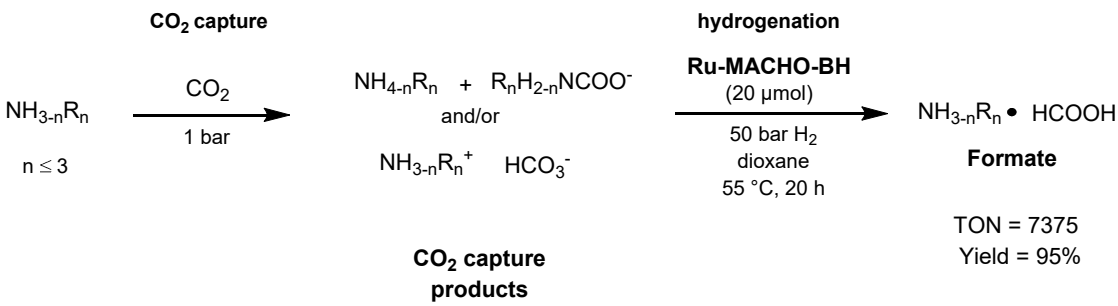

Scheme 69. CO_2 capture and hydrogenation to formate catalyzed by **Ru-MACHO-BH** reported by Prakash [645].

Based on the same approach using hydroxides shown in Section 3.1.2 for the production of methanol, Prakash proposed in 2018 a neutral CO_2 capture and hydrogenation to formate cycle at

low temperatures, with contemporary regeneration of the hydroxide base [646]. Among the screened bases, NaOH, KOH, and CsOH performed best, with the formation of HCOOK being the fastest and completed within 30 min. After the capture of 13.6 mmol of CO_2, the reaction afforded a TON of 2710 and TOF of 5420 h^{-1} using KOH, catalyst **6**, 2-MTHF as the organic solvent, H_2 (50 bar), and at 80 °C (Scheme 70). The obtained formate solution was directly used without any purification in a formate fuel cell, producing electricity with consequent base regeneration, providing a carbon-neutral energy production cycle. The biphasic H_2O/2-MTHF system has again a positive impact on the recycling of the catalyst and the hydroxide base; catalyst **6** retained similar catalytic activity even after five cycles, affording over 90% formate yield in each cycle.

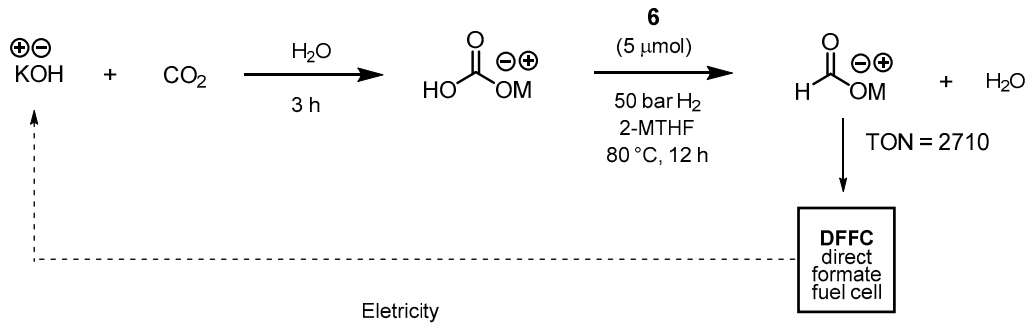

Scheme 70. Capture and hydrogenation of CO_2 combined with a direct formate fuel cell by Prakash [646].

The same year, Treigerman showed a hydrogen storage system based on aqueous sodium bicarbonate and the ruthenium PNP catalyst **Ru-MACHO** (Scheme 71) [647]. The hydrogen charge is performed under mild reaction conditions (70 °C and 20 bar H_2) in isopropanol/water to afford sodium formate, which can be subsequently decomposed to release hydrogen and recycled sodium bicarbonate. **Ru-MACHO** shows again promising recyclability properties, retaining its activity through numerous cycles of the hydrogenations. Simply adding sodium bicarbonate and heating to 70 °C, a TON > 610 was measured in each cycle.

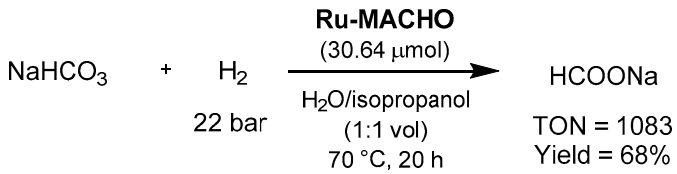

Scheme 71. Hydrogenation of sodium bicarbonate to sodium formate catalyzed by **Ru-MACHO** reported by Treigerman [647].

In 2017, Peng and Zhang reported the syntheses and characterizations of $[RuCl(L1)MeCN)_2]Cl$ **84** and $[RuCl(L2)MeCN)_2]Cl$ **85** (Figure 6) as suitable catalysts for the hydrogenation of CO_2 and bicarbonates to formate salts [648]. Complex **84** (0.1 mol%) showed a good activity and achieved 34% yield (based on NaOH) with a TON of 407 under 30 bar of H_2 and 15 bar of CO_2, using 60 mmol of NaOH and THF/H_2O (1:1) at 130 °C for 24 h. The investigations for the hydrogenation of sodium bicarbonate to sodium formate using **86** (0.05 mol%) showed yield of 77% and TON of 1530 under 30 bar of H_2, using THF/H_2O (1:1) at 130 °C for 24 h.

Kirchner and Gonsalvi reported in 2017 the use of Mn(I) pincer complexes for CO_2 hydrogenation to formate [649]. In this example, the hydride Mn(I) catalyst $[Mn(^{iPr}PNP^{NH})(H)(CO)_2]$ **69** was employed and showed higher stability and activity than its Fe(II) analogue. Thus, using 10 μmol of catalyst **69**, at 80 °C, for 24 h, and 80 bar total pressure (1:1 H_2/CO_2) in THF/H_2O, and in the presence of DBU as base and LiOTf as the co-catalyst, TONs up to 10,000 and yield up to >99% were achieved (Scheme 72). Decreasing the catalyst loading to 0.002 mol%, resulted in TONs up to 30,000. Importantly, the system

is active already at room temperature, and remains active for up to 48 h (TON = 26,600) with an average TOF of approximately 550 h^{-1} indicating a constant rate of reaction.

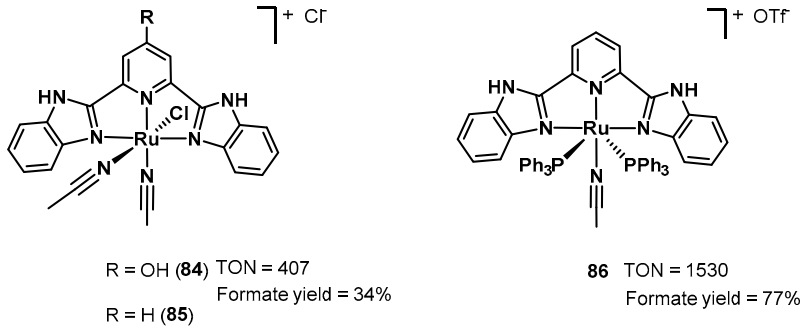

Figure 6. Ru-NNN pincer complexes synthetized and characterized by Peng and Zhang [648].

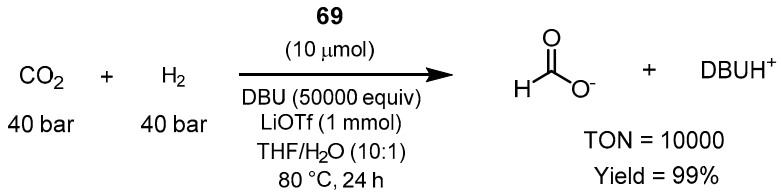

Scheme 72. CO_2 hydrogenation to formate catalyzed by Mn complex **69** reported by Kirchner and Gonsalvi [649].

As discussed before (see Section 2.2.2), Bernskoetter and Hazari reported the synthesis of various iron-PNP complexes with ancillary isonitrile ligands and demonstrated their activity through formic acid dehydrogenation [405], as well as CO_2 hydrogenation to formate salts [406]. The reaction using 0.3 μmol of the catalyst **43a** (containing the isonitrile group C≡NR, with R = 2,6-dimethylphenyl), DBU as base, LiOTf as co-catalyst (7.5:1 DBU/LiOTf), THF, at 80 °C for 24 h achieved a TON of 613. The second-generation isonitrile catalysts, with the methylated amino arm of the PNP pincer, showed better performance, with catalyst **43c** resulting in TON of 5300 under the same reaction conditions (Scheme 73).

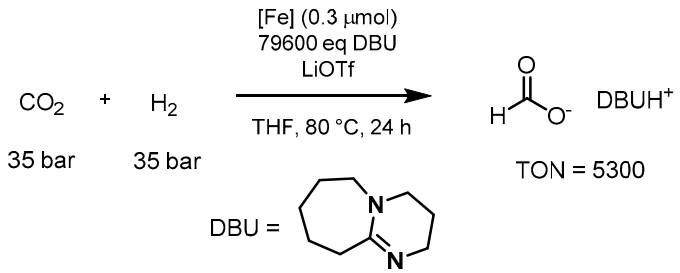

Scheme 73. CO_2 hydrogenation catalyzed by Fe-PNP isonitrile complexes proposed by Bernskoetter and Hazari [405,406].

In 2019, Jagirdar showed the iridium trihydride complex [$IrH_3(PN^HP)$] **87** (Scheme 74) as an active catalyst for the hydrogenation of CO_2 to formate [650]. The reaction was carried out in aqueous 1 M KOH solution, with 0.2 mol% of **87**, at 14 bar of H_2 and CO_2 (1:1). A TON of 144 was afforded at 100 °C for 14 h or 25 °C for 19 h. The highest TOF of 47 h^{-1} was obtained at 80 °C.

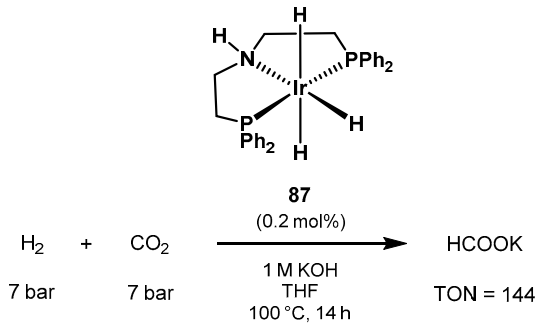

Scheme 74. Ir-PNP catalyst **87** reported by Jagirdar for CO_2 hydrogenation to formate.

Recently, Copéret demonstrated the synthesis of an immobilized lutidine-derived pincer type *N*-heterocyclic carbene ruthenium on a highly ordered silica-based material [651]. Complex **88** was used as catalyst for CO_2 hydrogenation into the corresponding formic acid-base adduct affording a TON of 18,000 in 24 h (Scheme 75). It was demonstrated that the method improves the stability of the catalyst compared to the homogeneous analogue, which afforded a TON of 9250 after 24 h under the same reaction conditions.

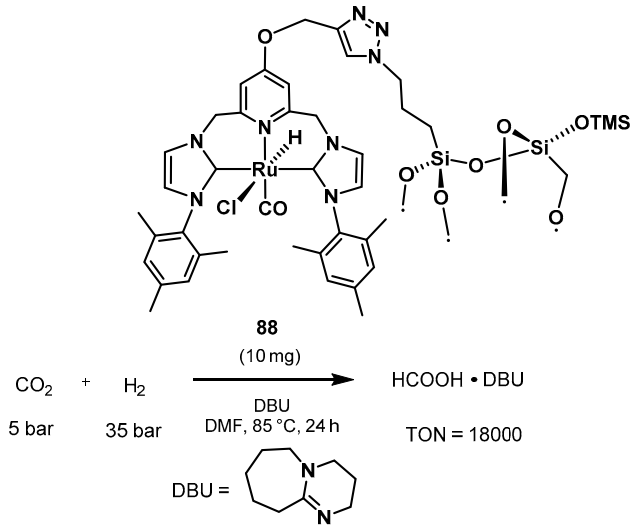

Scheme 75. Catalyst **88** immobilized on silica material for the hydrogenation of carbon dioxide to formate salts showed by Copéret [651].

3.2. Nitrogen Fixation

The homogeneously catalyzed production of ammonia has remained challenging for a long time, and relatively unexplored; in this regard, Minteer, Janik, Renner, and Greenlee recently reviewed the reduction of dinitrogen into ammonia by means of both heterogeneous and homogeneous catalysis [652]. Homogeneous pincer-type catalysis offers the possibility to perform nitrogen fixation under mild reaction conditions albeit significant further improvements are required to reach acceptable industrial relevance. Already in 2007, Leitner explored the potential of pincer complexes of Fe, Ru, and Os as active species for the production of ammonia from N_2 and H_2 [653]. Tuczek [654], Nishibayashi [655–658], Fryzuk [659], and many other authors have reviewed this topic in depth [660–667], with pincer-type ligation being widely employed in the proposed methods.

Back in 1965, the first dinitrogen complex was synthetized by Allen and Senoff [668]; since this report, many studies have focused on the synthesis of novel transition metal dinitrogen complexes and their reactivity with dinitrogen with the purpose of finding alternative approaches for a greener nitrogen fixation process. Several homogeneous systems have been explored for this transformation [669–678],

inspired by the biological nitrogen fixation performed by the active Fe/Mo site of nitrogenase [679,680]. In addition, various works have covered the photochemical activation of molecular nitrogen [681–688].

Only in 2003, Schrock developed the first homogeneously catalyzed production of ammonia using transition metal-nitrogen complexes [689,690]. Eight equivalents of ammonia per catalyst were produced when dinitrogen reacted with a reductant and a proton source at room temperature under 1 bar of N_2 and in the presence of the molybdenum-dinitrogen complex **89** bearing a triamide-monoamine tetradentate ligand (Scheme 76). The mechanism of the reaction was elucidated through isolation of key intermediates; however, they were unsuccessful in improving the catalytic activity of the system.

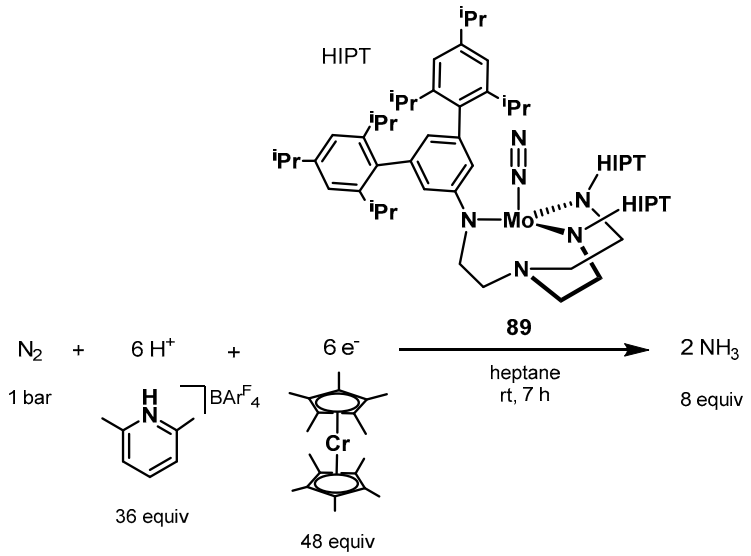

Scheme 76. First example of homogeneous ammonia production by Schrock [690].

In 2011, Nishibayashi showed the molybdenum PNP pincer complex **90** for the second example of catalytic production of ammonia from dinitrogen at ambient conditions [691]. By applying 0.01 mmol of catalyst **90**, 216 equivalents of [LutH]OTf as the proton source, and 288 equivalents of cobaltocene as electrons donor, it was possible to obtain 23 equivalents of ammonia (12 per molybdenum atom) at room temperature (Scheme 77). The mechanistic cycle was elucidated in 2014 in collaboration with Yoshizawa and shown in Scheme 78 [692]. It was shown that the complex maintains a dinuclear character in solution as opposed to the hypothesis that dinitrogen bridges dissociate to the corresponding mononuclear complexes; in case of PNP pincer ligation, the dinuclear specie catalyzes the protonation of the terminal dinitrogen, which is the first step of the catalytic cycle.

In a following paper from 2014, Nishibayashi demonstrated that the catalytic activity can be almost doubled with the introduction of electron-donating groups such as methyl and methoxy groups onto the pyridine ring of the PNP pincer ligand [693]. A shown in Scheme 77, catalyst **91** afforded up to 52 equivalents of ammonia, with 360 equivalents of CoCp and 480 equivalents of [LutH]OTf under 1 bar N_2 at room temperature after 20 h.

The same group later reported the synthesis of other molybdenum-dinitrogen complexes bearing different redox-active substituent on the PNP pincer ligand, with the aim of promoting the reduction step of the transformation [694,695]. The catalysts were then tested for the synthesis of ammonia from molecular dinitrogen. The reactions were performed under 1 bar of N_2 with 0.01 mmol of catalyst, toluene as solvent, at room temperature, for 20 h, and with 288 equivalents of [LuH]OTf and 216 equivalents of $CoCp_2$. The complexes containing ferrocene as a redox-active moiety in the pyridine ring of the PNP ligand showed higher activity for ammonia production, up to 45 equivalents using catalyst **92** (Scheme 77). Electrochemical and theoretical studies showed that the interaction between the Fe atom of the ferrocene moiety and the Mo atom of the catalyst might be fundamental to achieve high catalytic activities.

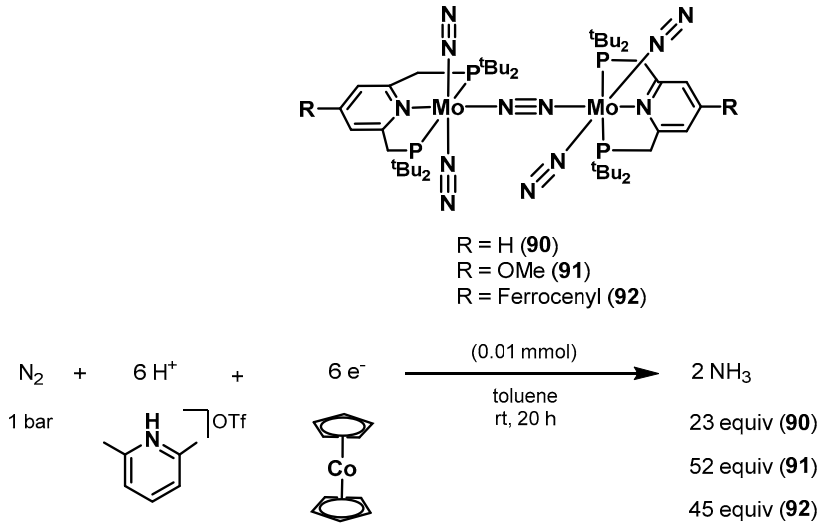

Scheme 77. Molybdenum-catalyzed ammonia production developed by Nishibayashi [691,693–695].

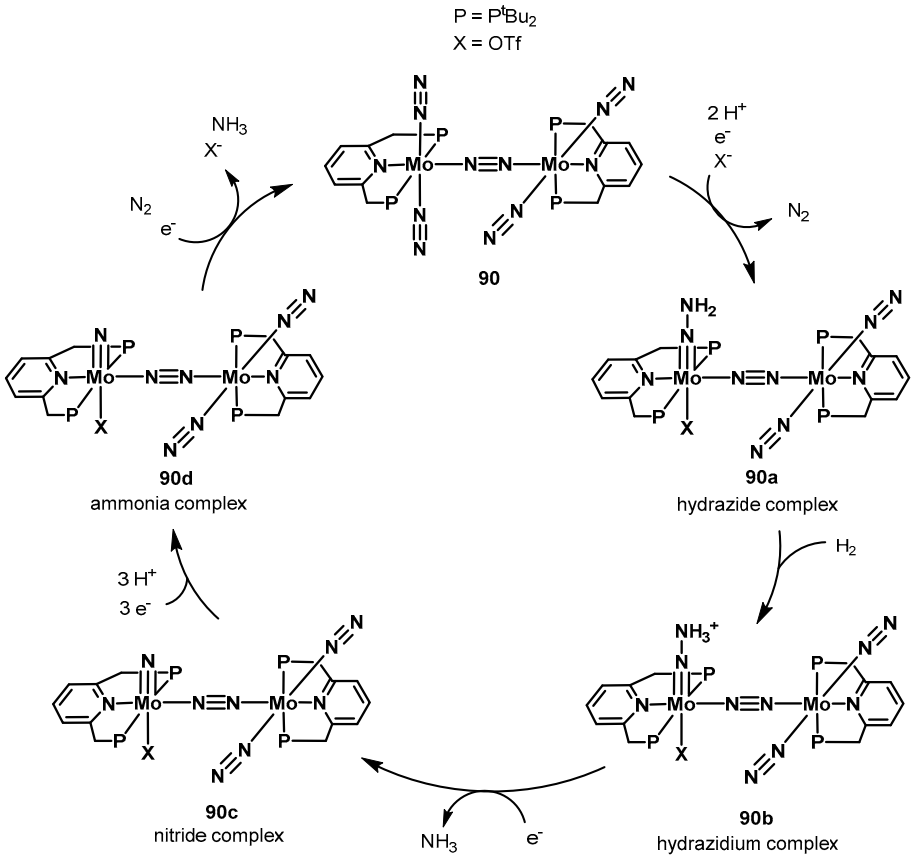

Scheme 78. Catalytic cycle for the dinitrogen-bridged catalyst **90** proposed by the groups of Yoshizawa and Nishibayashi [692].

In 2017, Schneider reviewed in depth the mechanism of N_2 bond activation catalyzed by mid to late transition metal complexes [696]. The same author reported the molybdenum complex **93** and demonstrated the nitrogen activation following the procedure shown in Scheme 79 [697]. The reaction proceeds by reduction of **93** and formation of the diatomic species **93a**, which later undergoes protonation in Brønsted acid conditions, resulting in the formation of two corresponding nitrides (**93b**) and formal dinitrogen cleavage. The authors investigated the mechanism of the reaction in depth by means of DFT calculations, NMR spectroscopy, cyclic voltammetry, MO theory, as well as

X-ray diffraction analysis in order to elucidate the unexpected protonation step as the driving force to nitrogen splitting.

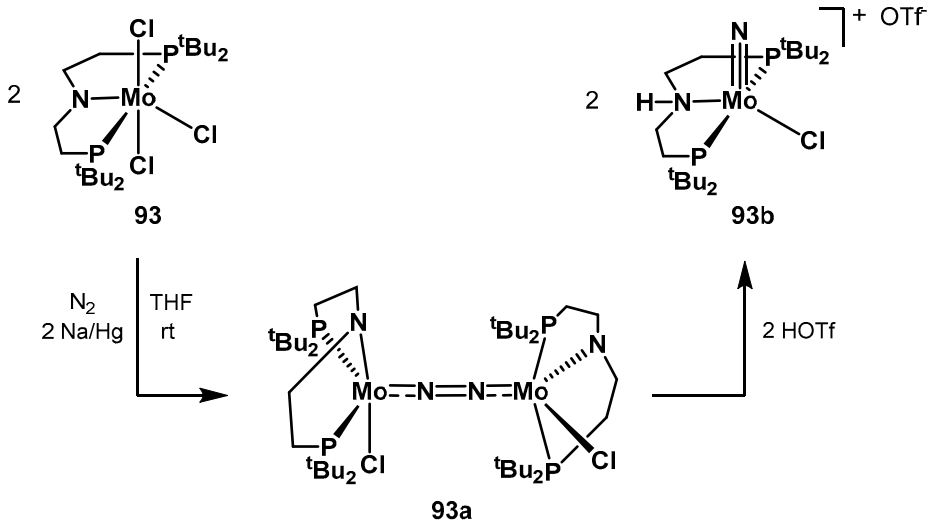

Scheme 79. Molybdenum complex proposed by Schneider for catalytic N_2 splitting [697].

In 2018, the same author performed a systematic investigation on the mechanism of both chemical and electrochemical N_2 splitting, using the rhenium system reported in 2014 [698], and shown in Scheme 80, as an archetypal pincer halide precursor for N_2 cleavage [699]. By means of electrochemical data and computational studies, the authors elucidated the rhenium-catalyzed N_2 activation, up to the final splitting step. The reaction proceeds through formation of the dinuclear species **94a**, which undergoes N-N bond cleavage resulting in two rhenium nitrido complexes. A comproportionation between Re^{I}/Re^{III} states was found to be the driving force of the electrochemical splitting, while a Ru^{II} specie represents the binding state of nitrogen and at the same time cause of the main deactivation pathways. In another work, Schneider reported an innovative approach for the synthesis of acetonitrile using dinitrogen and ethyl triflate catalyzed by complex **94** [700]. The authors demonstrated the feasibility of the catalytic cycle by means of ^{15}N-labeled samples with consequent production of ^{15}N-labeled acetonitrile, accompanied with efficient recovery of the rhenium catalyst. The work offers new insights on the possibility of forming C-N triple bonds after N_2 splitting, expanding the possible applications derived from N_2 splitting to organic transformations.

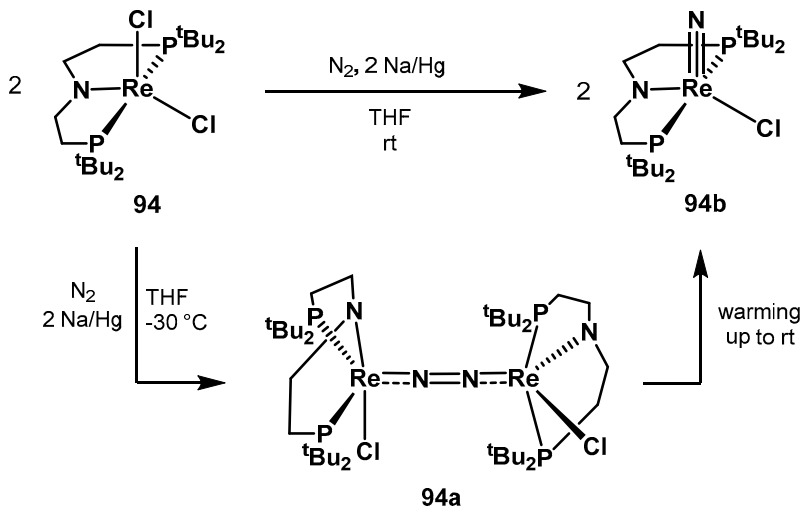

Scheme 80. First example of rhenium-catalyzed ammonia production developed by Schneider [699].

With the purpose of increasing the stability of the first generation Mo-PNP catalyst, Nishibayashi showed new dinitrogen-bridged PPP pincer catalysts for nitrogen fixation [701]. The authors tested new alternatives for the pincer moiety after noticing how the deactivation of the catalyst in the previous reported works was mainly due to the dissociation of the PNP ligand, observed in solution at completed reaction. Using the Mo-PPP catalyst **95**, it was possible to increase the ammonia production up to 126 equivalents, with the reaction conditions showed in Scheme 81. This result represents an improvement with respect to the first Nishibayashi catalyst **90** with five times higher activity.

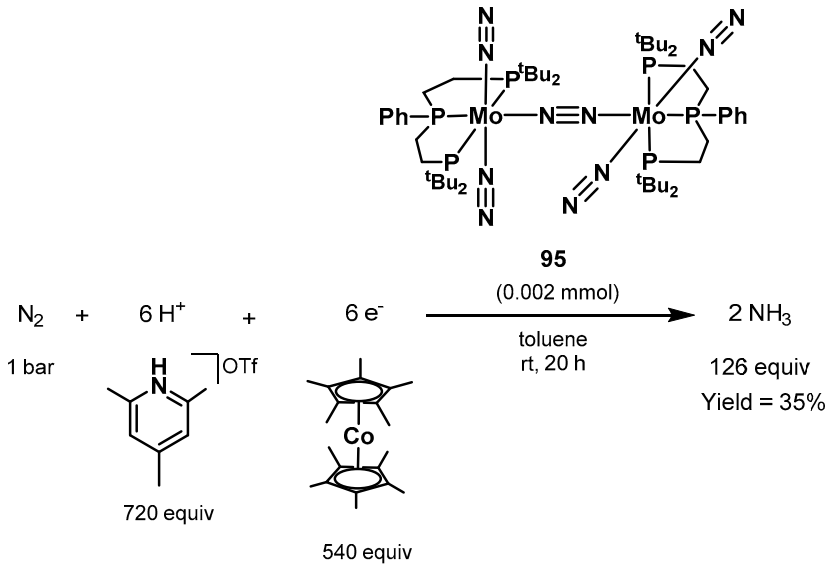

Scheme 81. Mo-PPP dinitrogen complex **95** developed by Nishibayashi [701].

In 2017, the same author reported remarkable activities toward nitrogen fixation by new molybdenum complexes bearing NHC-based PCP-pincer ligands [702]. Both catalysts **96** and **97** resulted in improved catalytic activity; the reaction afforded 200 and 230 equivalents of ammonia using **96** and **97**, respectively. The yield of ammonia was 48% with **97** and 42% with **96**, with yields in H_2 of 18% and 14% (based on CoCp*), respectively (Scheme 82). The authors postulated that the higher performance of **97** is given by an increased back donating ability of the molybdenum centers in the presence of two methyl groups to the benzimidazol-2-ylidene skeleton of the PCP ligand, resulting in enhanced activation of the terminal dinitrogen ligands compared to the previously shown complexes. In addition, the authors performed stability tests in order to compare the first generation Mo-PNP complex **90** with the new PCP ligand synthetized in this study. In this report, the PCP ligand was not observed in solution after the reaction, indicating a higher resistance to dissociation, and the residual presence of the active species. Indeed, after the first 47 equivalents of NH_3 produced, with complex **96** it was possible to feed the reaction adding more CoCp* and [LuH]OTf resulting in further 69 equivalents of ammonia produced after two extra hours. Encouraged by these findings, the authors reported the synthesis of the PCP ligand on larger scale, as well as its consequent complexation with rhodium, nickel, and iridium accompanied by X-ray crystal structure analysis of the obtained complexes [703].

Nishibayashi also showed novel synthesis procedures for the preparation of new molybdenum(V)-nitride complexes as suitable catalysts for nitrogen fixation [704]. In this report, the reaction was performed under ambient reaction temperatures, using toluene as solvent, 0.020 mmol of the catalyst, [LuH]OTf (0.96 mmol) as proton source, and $CoCp_2$ (0.72 mmol) as reductant. The use of **98** and **99** afforded the best results among the prepared catalysts, yielding 6.8 and 7.1 equivalents of NH_3, respectively (Scheme 83).

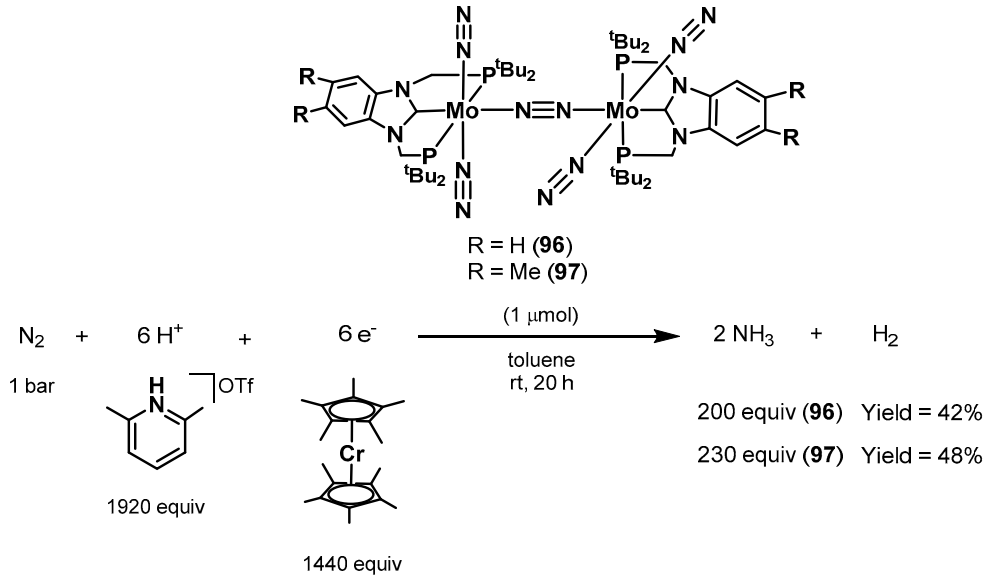

Scheme 82. Mo-PCP dinitrogen-bridged catalysts developed by Nishibayashi [702].

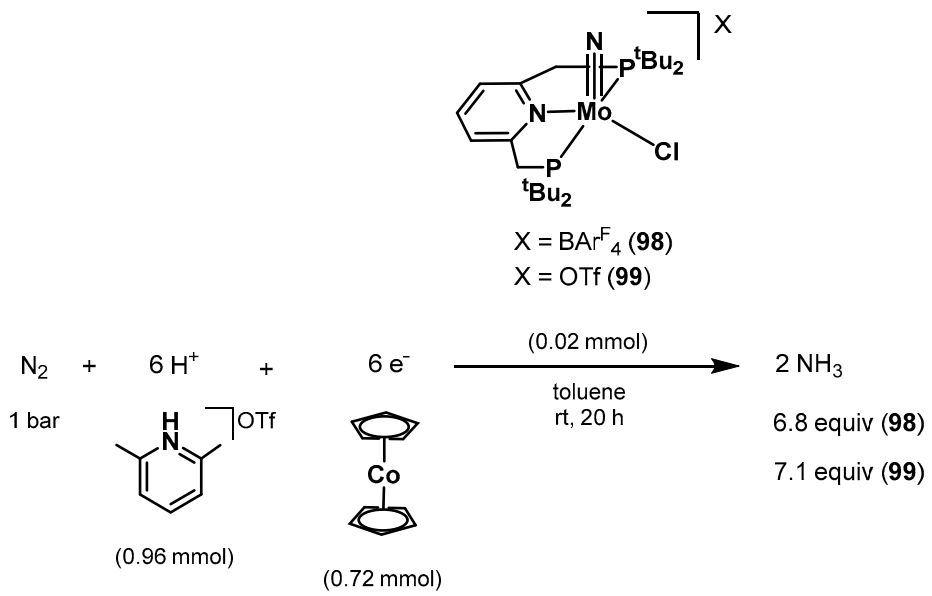

Scheme 83. Catalytic reduction of dinitrogen into ammonia by molybdenum-nitride complexes reported by Nishibayashi [704].

Nishibayashi suggested that in the homogeneous catalytic systems based on the molybdenum complexes showed previously, the bimetallic structure facilitates the dinitrogen conversion into ammonia in comparison to the corresponding monometallic complexes, because of the through-bond interactions between the two metal centers [692]. Tian investigated the chain-like extended models of Nishibayashi's catalyst by computational studies [705]. The effect of the dimension and the types of bridging ligands on the catalytic activities over nitrogen fixation were examined in the study. Polynuclear chains bearing four ($[Mo]_4$) increased the catalytic activity when compared to the mono and bimetallic species, and carbide showed to be a more effective bridging ligand than N_2 regarding electronic charges dispersion between metal atoms, hence favoring the resulting catalytic cycle. The authors concluded that catalytic systems for the conversion of N_2 into NH_3 become more efficient with the extension of the polynuclear chain up to a proper size, combined with a suitable bridging ligand to facilitate charge dispersion between the metal centers.

Inspired by the naturally occurring nitrogen fixation by nitrogenase, Peters investigated in 2013 the ammonia fixation by synthetizing an iron model complex able to produce 7 equivalents of ammonia per catalyst [706]. In 2017 and 2018, an improved catalytic activity was reported by Peters; following the same approach, using the P_3^BFe catalyst **100** showed in Scheme 84 it was possible to achieve NH_3 efficiently and with high turnover numbers [707,708]. The reactions were performed using $CoCp_2$ (54 equivalents) as reductant and $[Ph_2NH_2]OTf$ (108 equivalents) as the acid, in Et_2O as solvent, at −78 °C, and for 3 h yielding up to 72% (for e^- delivery) and 13 equivalents of NH_3 per Fe site. In another experiment, with increased amount of additives, it was possible to achieve a TON of 84 after two further additions of fresh reductant and acid after cooling the mixture to −196 °C (Scheme 84). Freeze-quench Mössbauer spectroscopy under reaction conditions offered insights on the rate of the key step, as well as the formation of a borohydrido-hydrido complex as a resting state. In addition, the prospect of a proton-coupled electron transfer (PCET) under catalytic conditions was further supported by theoretical and experimental studies, demonstrating plausible explanations for the increased efficiency observed.

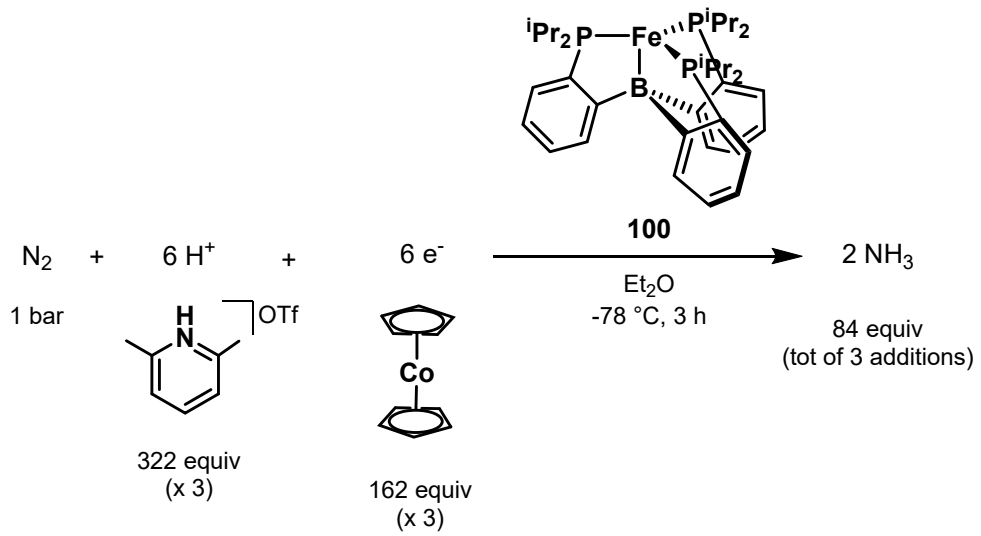

Scheme 84. Iron-catalyzed ammonia production developed by Peters using catalyst **100** [707].

In 2017, Nishibayashi reported the highest catalytic activity for nitrogen fixation using a molybdenum-iodide complex bearing a PNP pincer ligand [709]. The reaction performed under ambient reaction conditions, using 1 bar of N_2, 0.48 mmol of $[Ph_2NH_2]OTf$ as proton source, in toluene, and using $CoCp^*_2$ (0.36 mmol) as reductant and 0.001 mmol of Mo catalysts for 20 h afforded up to 830 equivalents of NH_3 (415 equivalents of ammonia per Mo), as showed in Scheme 85. The generation of a dinitrogen-bridged di-molybdenum-iodide complex in the reaction is responsible for the higher activity due the direct cleavage of the nitrogen triple bond of the bridging ligand in the core (Scheme 85). Curiously, when a stoichiometric amount of iodine was added to the dinitrogen-bridged molybdenum complex **90**, the catalyst showed high catalytic activity, comparable to that of complex **101** and nitride complex **101b**. It was demonstrated that the ammonia is produced by the mononuclear nitride complex **101b**, thus encouraging further studies that resulted in the formulation of the new catalytic cycle depicted in Scheme 86 [709].

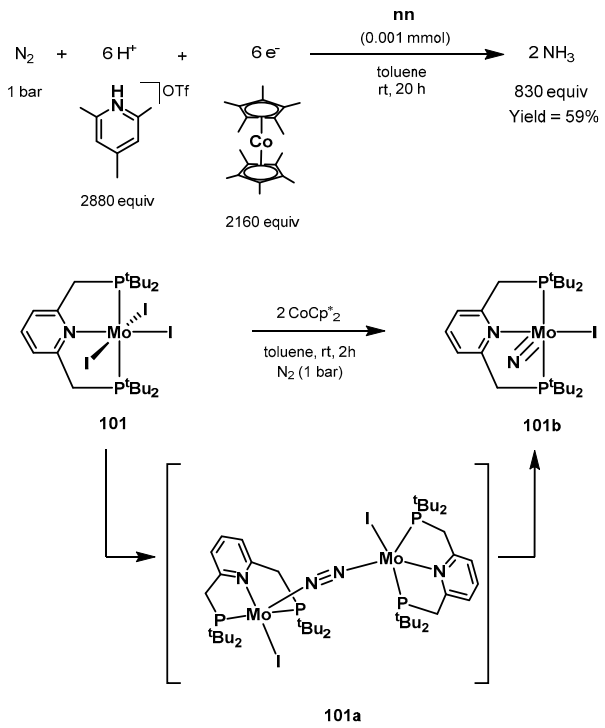

Scheme 85. Molybdenum-iodide complex **101** and conversion to **101b** by generation of the dinitrogen-bridged specie **101a** showed by Nishibayashi [709].

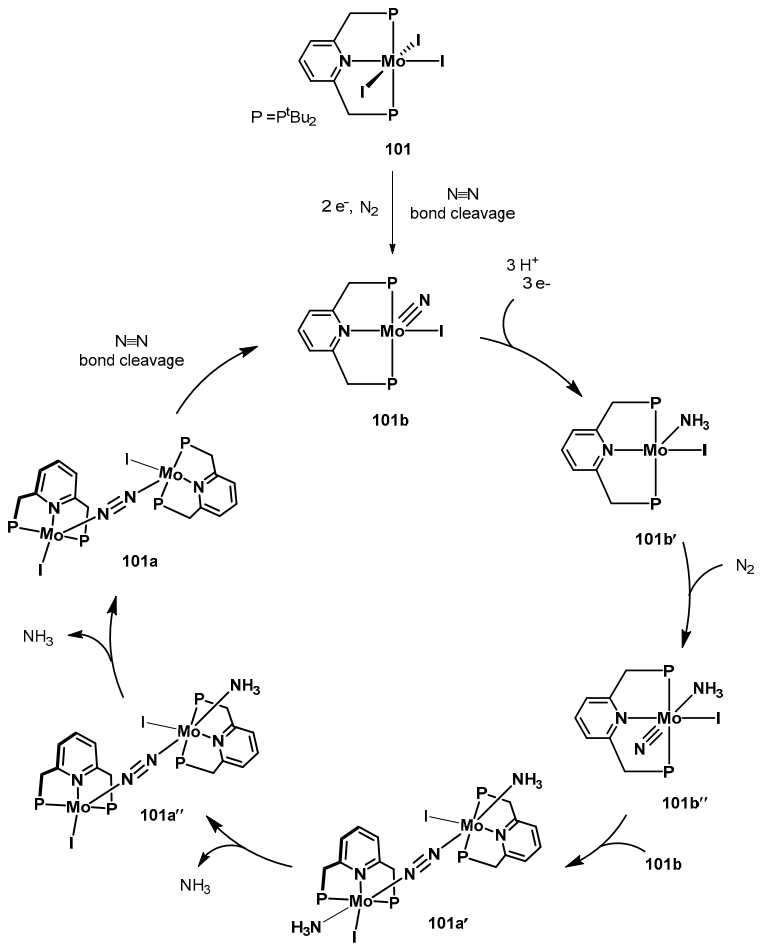

Scheme 86. Proposed catalytic cycle using the nitride complex **101** reported by Nishibayashi [709].

In 2019, Nishibayashi showed the synthesis of new molybdenum triiodide complexes bearing various substituents on the pyridine moiety of the PNP pincer ligand [710]. It was found that the catalytic activity toward nitrogen fixation increases with the introduction of Ph and Fc groups at the 4-position of the pyridine ring because of the electron withdrawing- and redox properties of the so-formed ligands. This observation is in contrast with the experimental results obtained with the afore-mentioned di-nuclear molybdenum species [693]. The work also confirms the preference of molybdenum systems for iodide ligands, performing better than the bromide or chloride congeners. The catalytic activity of the two selected complexes is shown in Scheme 87.

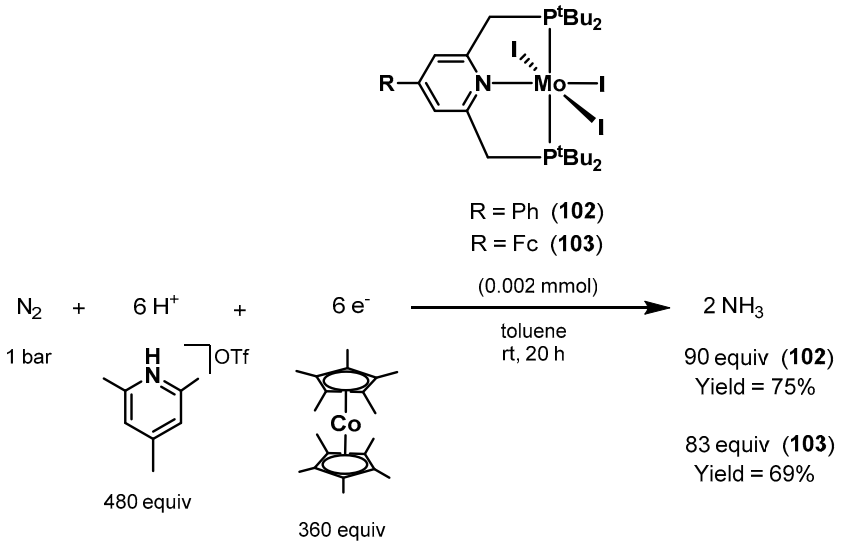

Scheme 87. Molybdenum triiodide complexes bearing various substituted PNP pincer ligands reported by Nishibayashi [710].

Peters also continued his studies on the topic and reported in 2017 an improved catalytic ammonia production employing new ruthenium and osmium complexes [711]. While the ruthenium catalysts tested in the study were found to be poorly active (4.3 equivalents of ammonia produced), using osmium catalyst **104** for the reaction afforded up to 120 equivalents of ammonia with high loadings of $CoCp^*_2$ and $[HNPh_2]OTf$ as reductant and proton source, respectively (Scheme 88). In 2015, Peters explored the same transformation using a cobalt congener of catalyst **104**, which performed scarcely in ammonia production resulting in only 2.4 equivalents of NH_3 [712].

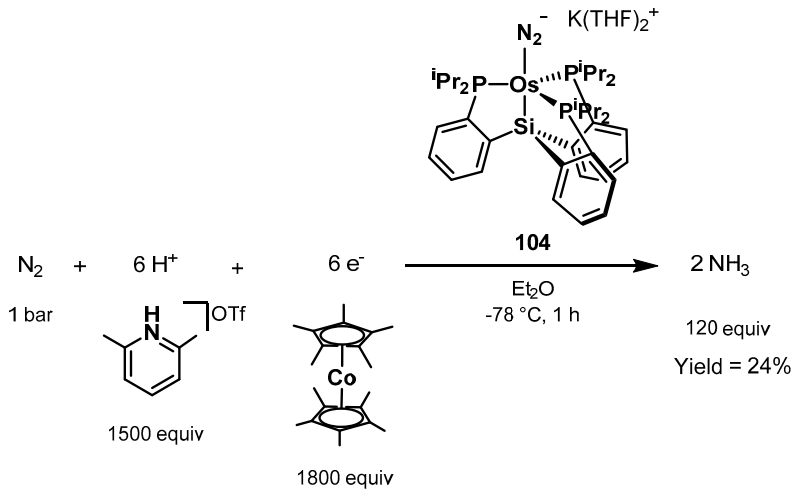

Scheme 88. Osmium-catalyzed nitrogen fixation developed by Peters [711].

After the preliminary works by Peters, Nishibayashi explored the reactivity of iron metal complexes for nitrogen fixation as well, reporting the synthesis of Fe, Mo, and Cr azaferrocene-based PNP-type pincer ligands [695]. In 2017, Nishibayashi proposed iron–dinitrogen complexes bearing an anionic PNP pincer ligand for the catalytic nitrogen fixation producing ammonia and hydrazine [713]. 1 atm of molecular dinitrogen, KC_8 (40 equivalents) as reductant, $[H(OEt_2)_2]BAr^F{}_4$ (38 equivalents) as proton source, 0.010 mmol of catalyst, Et_2O or THF as solvent, and at −78 °C for 1 h were used as conditions for the conversion to ammonia and hydrazine up to 14.3 equivalents and 1.8 equivalents respectively. The best result was obtained using catalyst **105** (Scheme 89). Later, the authors succeeded in improving the catalytic activity of this family of catalysts by proposing a new complex bearing the anionic methyl-substituted pyrrole-bases PNP ligand [714]. As shown in Scheme 89, catalyst **106** afforded 22.7 equivalents of ammonia per catalyst under the same reaction conditions.

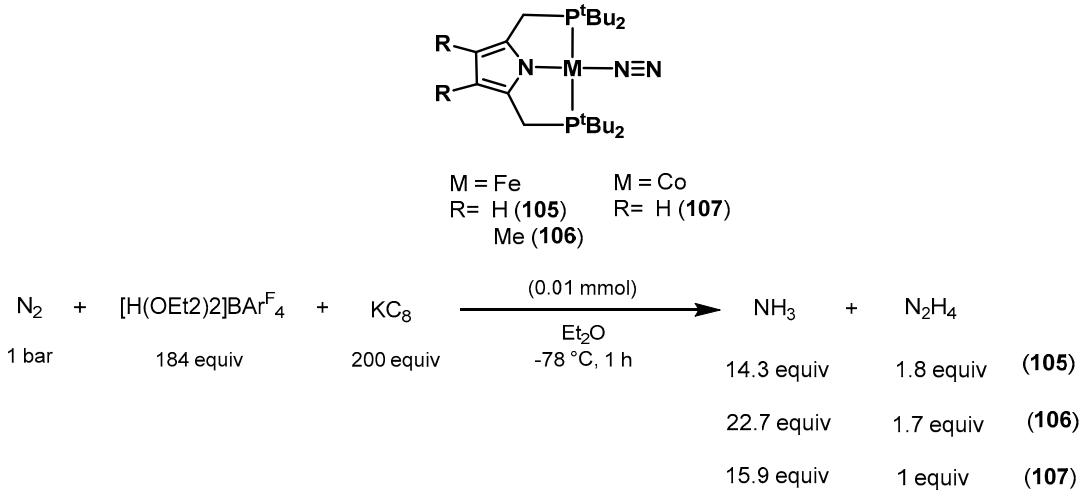

Scheme 89. Nitrogen fixation catalyzed by iron- and cobalt-PNP complexes by Nishibayashi [713–715].

In addition to iron, Nishibayashi also showed the first successful example of cobalt-catalyzed nitrogen fixation [715]. Catalyst **107** showed catalytic activity similar to its iron congener, affording 15.9 equivalents of ammonia under the same reaction conditions (Scheme 89). Interestingly, when a cobalt catalyst bearing a PBP ligand was employed in the transformation, only 0.4 equivalents of ammonia were produced, indicating a relevant contribution of the PNP ligand to the catalytic activity.

In 2018, Nishibayashi designed and prepared novel vanadium complexes containing anionic pyrrole-based PNP pincer complex and aryloxy ligands, and tested them in the direct conversion of molecular dinitrogen into ammonia and hydrazine [716]. The reaction was performed using 200 equivalents of KC_8 as reductant, 184 equivalents of $[H(OEt_2)_2]BAr^F{}_4$ as proton source, Et_2O as solvent, at −78 °C for 1 h. The reaction afforded up to 14 equivalents of ammonia and 2 equivalents of hydrazine when a mixture of catalyst **108** was employed (Scheme 90). Remarkably, this work represents the first example of vanadium-catalyzed nitrogen fixation, a step toward the understanding of the reaction mechanism involving the FeV nitrogenase active site. In addition, the authors synthetized the dinitrogen-bridged version of **108**, which afforded 4.6 equivalents of NH_3 per vanadium.

Contemporarily, the same author also explored the synthesis of novel dinitrogen-bridged species, reporting a new class of dinitrogen-bridged di-titanium and di-zirconium complexes with anionic pyrrole-based PNP pincer complexes for the conversion of dinitrogen into ammonia and hydrazine [717]. The best result was achieved using a mixture of catalyst **109**, with 40 equivalents of KC_8 as reductant, 38 equivalents of $[H(OEt_2)_2][BArF_4]$ as proton source, Et_2O as solvent, and at −78 °C for 1 h yielding up to 1.3 equivalents of ammonia and 0.31 equivalents of hydrazine (Scheme 91). Under the same reaction conditions, catalyst **110** afforded 1 equivalent of ammonia, with no hydrazine.

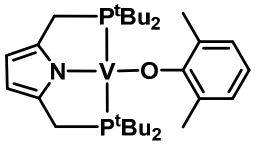

108

N_2 + $[H(OEt_2)_2]BAr^F{}_4$ + KC_8 —(0.01 mmol), Et_2O, -78 °C, 1 h→ NH_3 + N_2H_4

1 bar; 184 equiv; 200 equiv; 14 equiv; 2 equiv

Scheme 90. Vanadium PNP complex for dinitrogen conversion into ammonia and hydrazine reported by Nishibayashi [716].

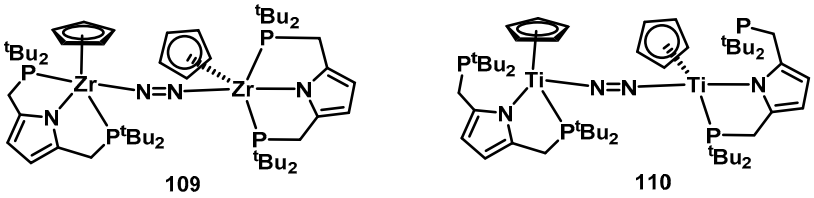

109 **110**

N_2 + $[H(OEt_2)_2]BAr^F{}_4$ + KC_8 —Cat, Et_2O, -78 °C, 1 h→ NH_3 + N_2H_4

1 bar; 38 equiv; 40 equiv; 1.3 equiv; 0.3 equiv (**109**)

1 equiv; 0 equiv (**110**)

Scheme 91. Dinitrogen-bridged di-titanium and di-zirconium complexes bearing pyrrole-based anionic PNP pincer ligands synthetized by Nishibayashi [717].

Improved results using a di-titanium species have been achieved by Liddle using catalyst 111 [718]. After screening reaction conditions and additives, the reaction afforded up to 9 equivalents of ammonia per titanium atom using $[Cy_3PH]I$ as proton source and KC_8 as reductant, notably with higher selectivity and only traces of hydrazine as the co-product (Scheme 92).

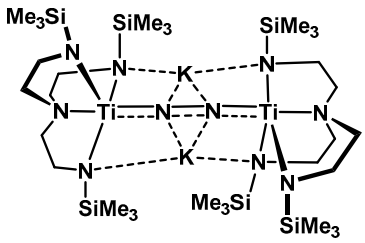

111

N_2 + $[Cy3PH]I$ + KC_8 —(0.01 mmol), Et_2O, -78 °C, 15 h→ NH_3 + N_2H_4

1 bar; 600 equiv; 600 equiv; 17.7 equiv; 0.03 equiv

Scheme 92. Di-titanium catalyst 111 reported by Liddle for nitrogen fixation [718].

Nishibayashi also showed an example of nitrogen fixation using a proton source obtained in situ by means of a ruthenium-catalyzed oxidation of water promoted by a photosensitizer (Scheme 93) [719]. In the proposed method, the oxidation of water occurs using $Na_2S_2O_8$ as a sacrificial oxidizing agent, a suitable ruthenium catalyst for water oxidation (**112**) and $Ru(bpy)_3(OTf)_2$ bpy=2,2′-bipyridine) as the photosensitizer. After 2 h of irradiation of visible light at room temperature, the reaction afforded 99%

conversion into O_2. 2,6-Lutidine and sodium trifluoromethanesulfonate (NaOTf) were added to the reaction in order to obtain $[LutH]^+$ to be used in the following step; $CoCp_2$ was used as the reducing agent to promote the conversion of dinitrogen gas into in the presence of catalyst **90** (0.005 mmol) under ambient reaction conditions, resulting in a total of 6 equivalents of ammonia released.

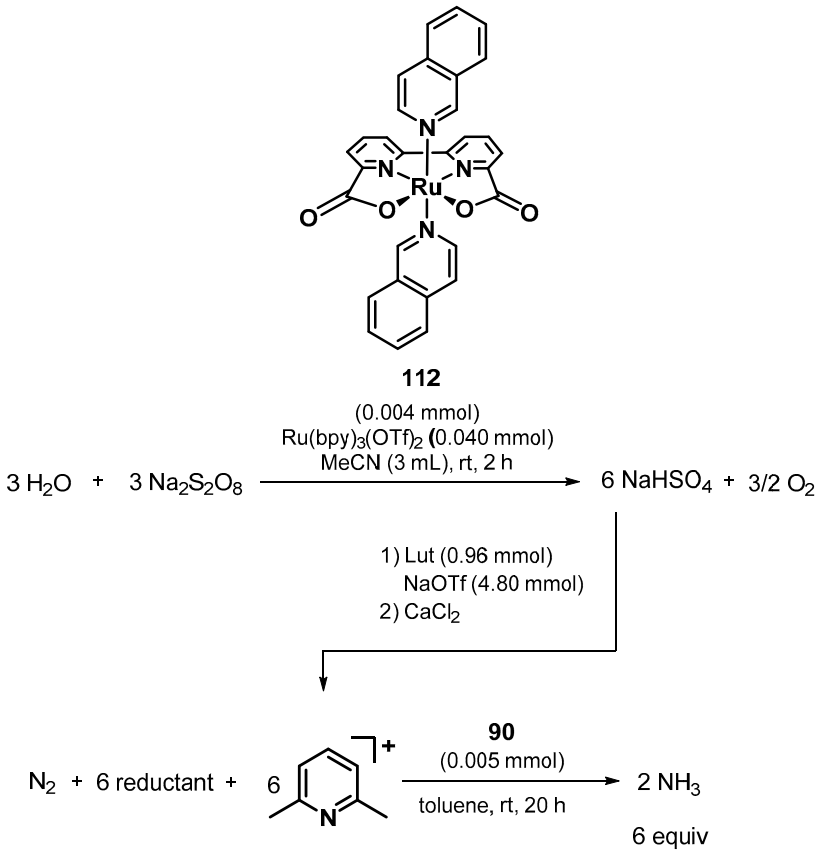

Scheme 93. Nishibayashi's catalytic reduction of dinitrogen into ammonia using an in situ proton source and catalyzed by the molybdenum complex **90** [719].

Nishibayashi reported the synthesis of a range of iron-methyl complexes containing anionic carbazole PNP ligands [720]. Bulkier substituents such as adamantyl groups at the phosphorus atoms showed better catalytic activity toward nitrogen fixation. The reaction using catalyst **113**, 1 bar of N_2, 80 equivalents of KC_8 as reductant, 76 equivalents of $[H(OEt_2)_2]BAr_4^F$ as proton source, in Et_2O, at −78 °C afforded up to 4.8 equivalents of fixed nitrogen as a mixture of ammonia and hydrazine after 1 h (Scheme 94).

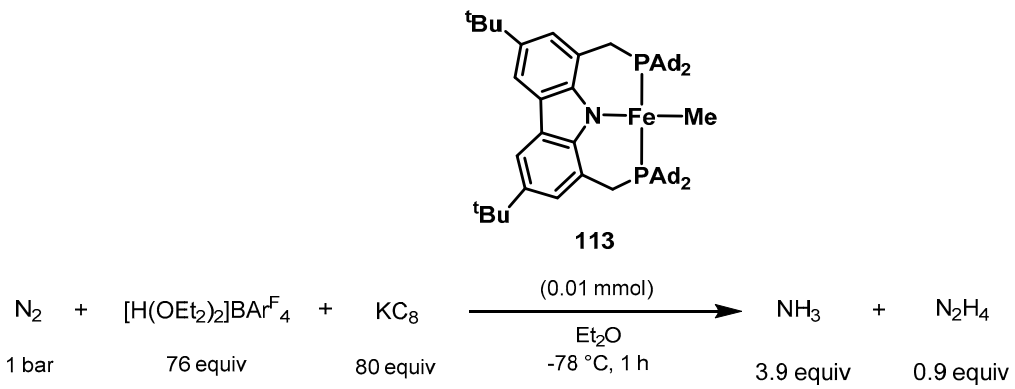

Scheme 94. Nitrogen fixation catalyzed by the iron PNP complex **113** proposed by Nishibayashi [720].

In 2017, Schrock reported the synthesis and the catalytic activity of the $[Ar_2N_3]Mo(OtBu)$ complex **114** as catalyst for the reduction of dinitrogen to ammonia [721]. The reactions were performed in a mixture of **114** in diethyl ether as solvent, 108 equivalents of $CoCp^*_2$ as reductant, 120 equivalents of $[Ph_2NH]OTf$ as proton source, at temperatures between −78 °C and 22 °C, achieving up to 10 equivalents of NH_3 per Mo atom, as depicted in Scheme 95. The authors were not able to demonstrate whereas the tBu group remain intact during the catalytic cycle, or if it is transformed into an OH or an oxo ligand after protonation from $[Ph_2NH]OTf$.

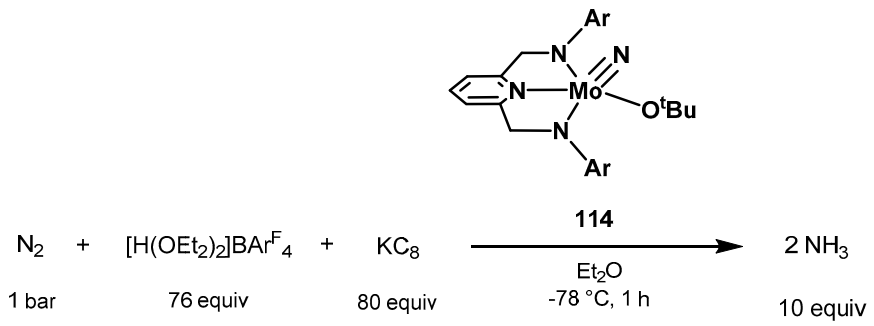

Scheme 95. Dinitrogen conversion into ammonia catalyzed by the Mo-NNN complex **114** showed by Schrock [721].

Szymczak studied the incorporation of two 9-borabicyclo[3.3.1]-nonyl substituents within the secondary coordination sphere of the Fe(II)-NNN pincer complex **115** [722]. The inserted groups act as a Lewis acidic site and allow the coordination of one or two equivalents of hydrazine, as well as stabilization of Fe-NH_2 intermediates (**116** in Figure 7). Later, by addition of $[HNEt_3][Cl]$, a specie with two molecules of ammonia bound to the boron groups was isolated and characterized by single-crystal diffraction studies. Finally, the release of ammonia is achieved with contemporary coordination of a new molecule of hydrazine.

Holland and Mayer studied the protonation, and subsequent reduction of the ruthenium and iridium pincer complexes **117a** and **117b** to investigate their reactivity toward the activation of dinitrogen [723]. The stretching frequencies of N_2 in the complexes **117a** and **117b** showed little activation of the dinitrogen ligand. Later, by means of NMR spectroscopy and cyclic voltammetry, the authors tested the reactivity of the prepared catalysts, however with no positive results in terms of catalytic ammonia production. The protonation, which is a fundamental step in the electrochemical reduction of dinitrogen, results in the formation of cationic metal-hydrides that lose N_2 preventing any further functionalization. Reduction of the metal-hydride with $CoCp_2^*$ also results in fast disproportionation to Ir(II) species, preventing any nitrogen coordination at room temperature (Scheme 96).

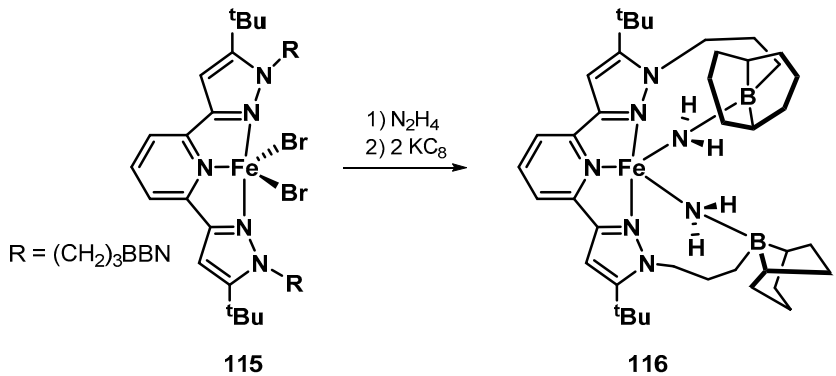

Figure 7. Szymczak's Fe(II)-NNN pincer complex **115** coordinates one to two equivalents of hydrazine [722].

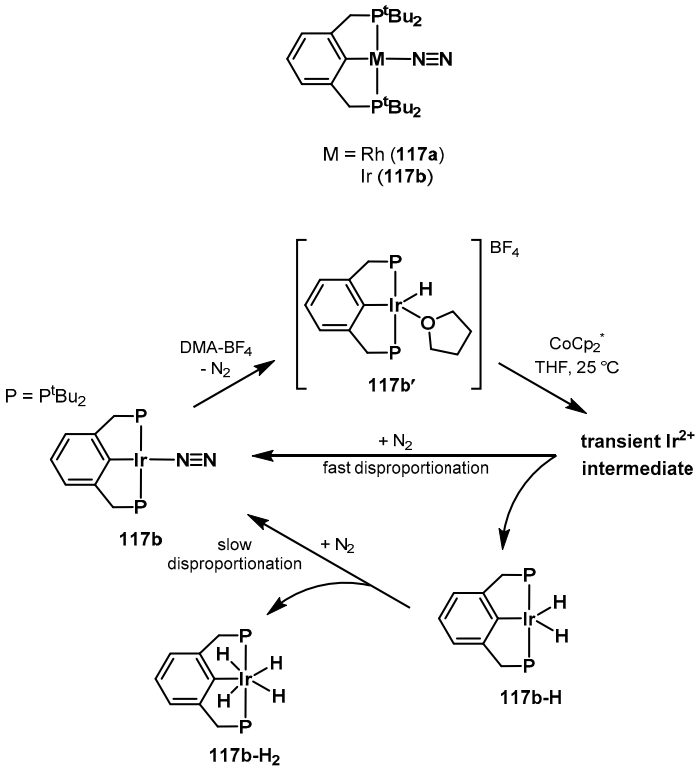

Scheme 96. Ruthenium and iridium PCP pincer complexes tested by Holland and Mayer and reactivity of complex **117b** in the presence of proton source and reducing agents [723].

Tuczek reported in 2018 new molybdenum complexes bearing a PN^3P pincer ligand with various substituents on both metal center and pincer arms [724]. The authors investigated the reactivity with N_2 through the formation of dinitrogen-bridged species based on the classic Nishibayashi Mo-PNP catalysts showed before. It was found that the nature of the substituents has a strong influence on the reactivity toward dinitrogen; the reaction performed with 48 equivalents of [LutH]OTf and 36 equivalents of $CrCp_2$* afforded poor catalytic activity with most of the tested catalyst candidates. Only when 0.01 mmol of complex **118** were applied, it was possible to achieve 3.12 equivalents of ammonia per catalyst (Scheme 97).

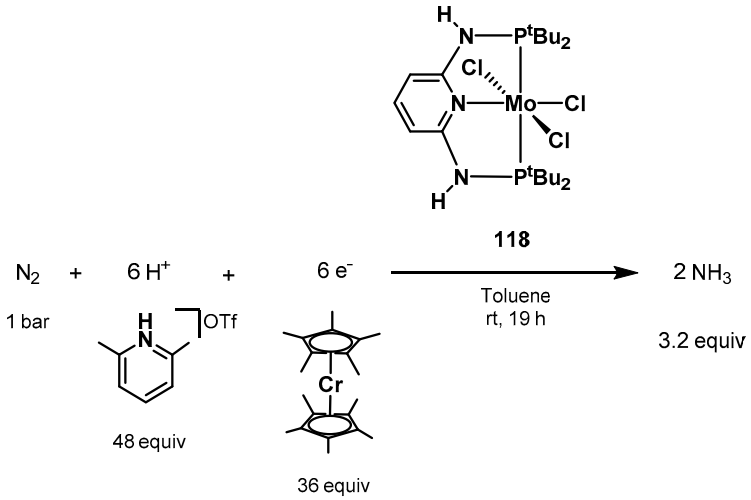

Scheme 97. Catalytic ammonia production catalyzed by complex **118** as showed by Tuczek [724].

Dinitrogen can be also reduced and trapped into in the form of silylamines, from which ammonia can be easily released after hydrolysis. Preliminary studies on the topic date back to 1972 with the work of Shiina [725], and later Hidai in 1989 [726]. Many other reports explored the transformation up to recent days using molybdenum [727], iron [728,729], vanadium [730], titanium [731,732], as well as cobalt homogeneous catalysts [733–737]. A comprehensive review from Nishibayashi recently covered the catalytic silylation of dinitrogen into silylamines as precursors for ammonia production [738].

With regard to the most recent publications involving pincer ligation, Mézailles reported in 2016 the Mo-PPP complex **119** for the reduction of ammonia to silylamines in the presence of silanes [739]. Similar to the previously showed species, catalyst **119** can be obtained starting from a chlorido precursor through formation of a dinitrogen-bridged specie, followed by nitrogen splitting and formation of the nitrido species. Catalyst **119** is then able to react with the bis-silane under mild reaction conditions, resulting in high yields of the corresponding amine (Scheme 98). However, the authors could not achieve the final reduction step from Mo(II) to Mo(I) to regenerate the dinitrogen-bridged specie from **119d**, required to finish a catalytic cycle.

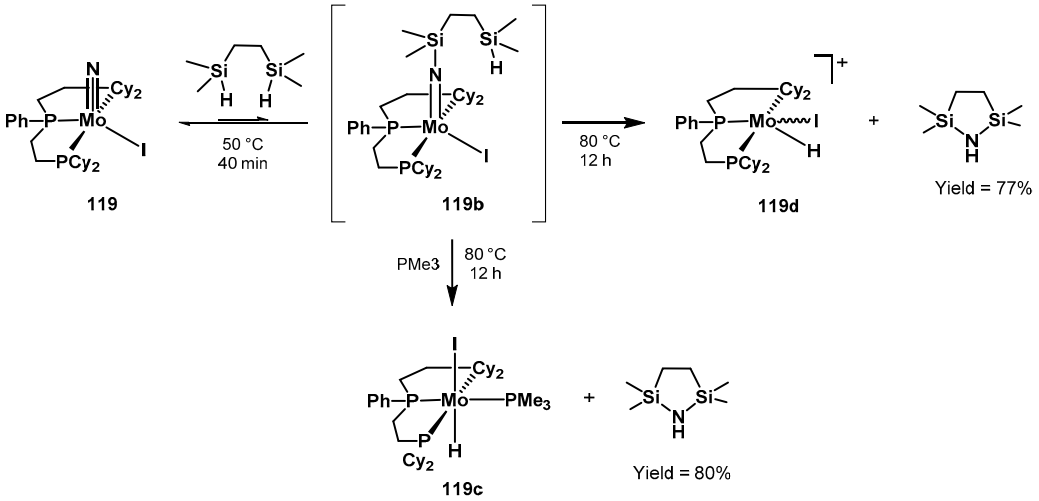

Scheme 98. Catalytic silylation of dinitrogen to silylamine proposed by Mézailles [739].

In 2017, Nishibayashi designed and prepared iron and cobalt-dinitrogen complexes containing a PSiP ligand, and tested them as catalysts for the transformation of dinitrogen gas into silylamine [740]. 1 bar of molecular dinitrogen, 600 equivalents of Na as reductant, MeSiCl (600 equivalents) as silylating reagent in THF at room temperature for 40 h yielded up to 41 equivalents of NH_3 when employing 0.020 mmol of catalyst **120c** (Scheme 99).

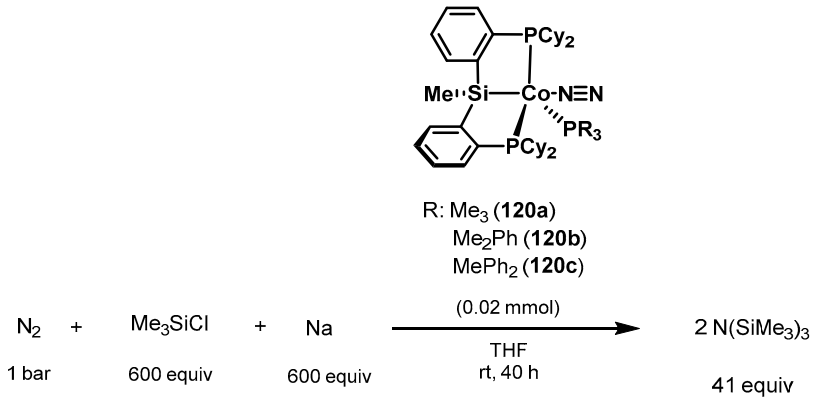

Scheme 99. Cobalt-catalyzed silylation of N_2 reported by Nishibayashi [740].

3.3. Valorization of Biomass-Derived Compounds

Catalytic hydrogenation is a powerful tool for the valorization of biomass-derived compounds into valuable fuels and bulk chemicals for the industry, such as monomers for polymer production, bio-fuels, and additives [741–750]. Among the others, levulinic acid (LA) and γ-valerolactone (GVL) can be readily obtained from biomass by acid treatment of sugar monomers, such as glucose, fructose, and sucrose, representing versatile platform molecules for the bulk industry [751–759], as highlighted by Horvath in 2008 [760]. The use of pincer complexes for this type of transformations is relatively new, but again showing promising performances and allowing the useful hydrogenation of esters, carboxylic acids and aldehydes at mild reaction conditions [761,762].

Various groups reported the use of ruthenium precursors in the presence of different ligands for the hydrogenation of biogenic acids to useful building blocks [763–767]. However, most of the reports use high temperatures (>200 °C) and strong acidic conditions to achieve acceptable yields. Important results using Ru/Triphos combinations were achieved by Leitner [577,768–771], as well as by Beller [772–774] for the hydrogenation of several bio substrates. Milstein employed catalyst **24-H** for the efficient hydrogenation of cyclic di-esters, e.g., biomass-derived glycolide and lactide, to 1,2-diols [775].

The hydrogenation of levulinic acid has been reported by Leitner and Klankermayer [768], Fu [776], and Fischmeister [777], using iridium complexes, as well as by Garcia, who reported the precatalyst [(dtbpe)$PdCl_2$] (dtbpe = 1,2-(bis-di-tert-butylphosphino)ethane) to efficiently catalyze LA hydrogenation, as well as formic acid dehydrogenation to CO_2 and H_2 [778].

In 2015, Singh showed the conversion of several biomass-derived substrates, such as furfural, 5-hydroxymethylfurfural (HMF), and 5-methylfurfural (5-MF), into levulinic acid and diketones, 1-hydroxyhexane-2,5-dione (1-HHD), 3-hydroxyhexane-2,5-dione (3-HHD), and hexane-2,5-dione (2,5-HD) [779]. The reaction proceeds in the presence of formic acid and it is highly dependent on the choice of the ligand, as well as formic acid concentration, reaction temperature and time. The authors screened different Ru(II)-arene catalysts bearing ethylenediamine-based bidentate ligands. Applying 5 mol% of the catalyst, in water at 100 °C, various substrates were quantitatively converted into the corresponding ring-opened products.

With regard to pincer complexes, in 2012 Zhou used the trihydride iridium complex **121** for the hydrogenation of levulinic acid to γ-valerolactone (Scheme 100) [780]. In this sense, Chen used in 2015 density functional theory (DFT) calculations to investigate the mechanism of this transformation catalyzed by Ir-PNP complexes [781].

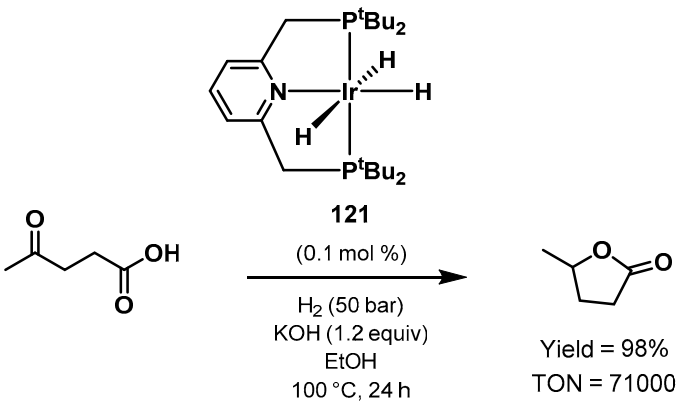

Scheme 100. Iridium-catalyzed hydrogenation of levulinic acid to γ-valerolactone proposed by Zhou [780].

Long and Miller reported the efficient conversion of levulinic acid to either 1,4-pentandiol (PDO) or 2-methyltetrahydrofuran (2-MTHF) using ruthenium complexes bearing a modified Triphos ligand with a nitrogen central atom (Scheme 101) [782]. Catalyst **123** performed best in both transformations,

affording quantitative yields in PDO and 2-MTHF. The active species was formed in situ with 0.5 mol% of [Ru(acac)$_3$] as the metal precursor, 1.0 mol% of N-Triphos, under 65 bar of hydrogen, with no solvent at 150 °C for 25 h. The reaction with these conditions afforded 99% yield of PDO (with 1% of γ-valerolactone). When 5 mol% of HN(Tf$_2$) was added as additive, and THF as solvent, the selectivity of the reaction changed dramatically, resulting in 87% yield in 2-MTHF and 10% in γ-valerolactone.

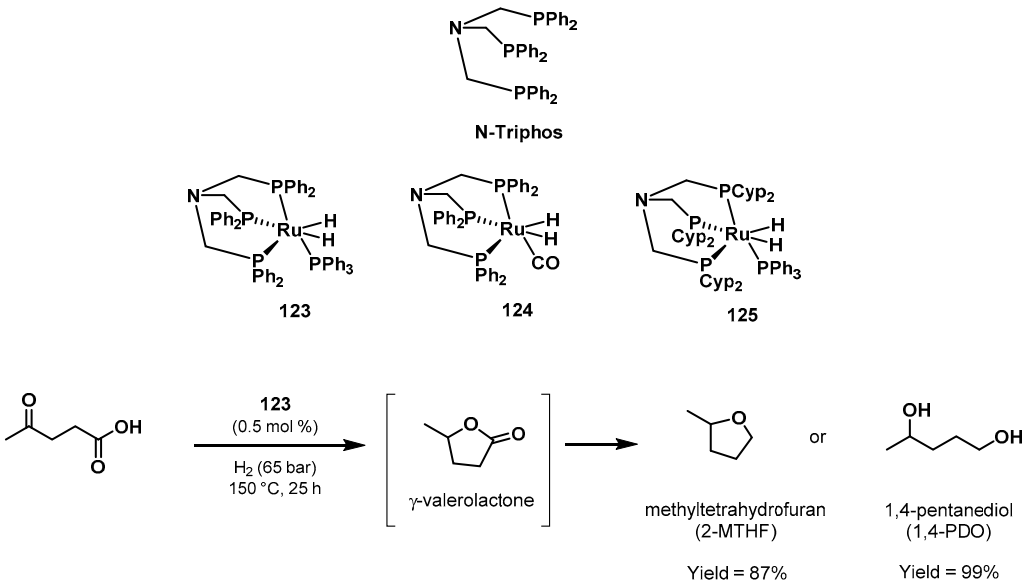

Scheme 101. Hydrogenation of levulinic acid into 1,4-pentandiol (PDO) and 2-methyltetrahydrofuran (2-MTHF) showed by Long and Miller [782].

The year after, Deng and Palkovits showed the same transformations using Ru precursors and a modified version of N-Triphos, where an ethylene linker was substituted in one of the arms [783]. The reactions were performed in THF, with 1.5 equivalents of the novel ligand, 70 bar H_2, 160 °C, for 18 h. The selectivity was found to be highly dependent on the ruthenium precursor used (0.2 mol% Ru loading); when using [Ru(acac)$_3$] as in the previous study by Miller, the reaction afforded 33% yield of GVL and 66% yield of PDO. Surprisingly, both [Ru(acac)$_3$] and $RuH_2(PPh_3)_4$ produced 99% and 95% yield in GVL respectively, when no ligand was added to the reaction mixture, while in the presence of the ethylated N-Triphos ligand, $RuH_2(PPh_3)_4$ afforded 98% yield in PDO. With different combination of a Ru precursor and the new ligand, the authors successfully hydrogenated a series of biogenic acids; among other substrates, fumaric-, succinic-, itaconic-, and maleic acid were converted in high yields into the corresponding lactones at 170 °C and 70 bar H_2 in 48 h.

In 2015, Schlaf showed the synthesis of various ruthenium pincer complexes in the form of ([(40-Ph-terpy)(bipy)Ru(L)](OTf)$_n$ and [(40-Ph-terpy)(quS)Ru(L)](OTf)$_n$ (n = 0 or 1 depending on the charge of L, L = labile ligand, e.g., H_2O, CH_3CN or OTf, bipy = 2,20-bipyridine, quS = quinoline-8-thiolate)) [784]. The authors tested the prepared complexes for the hydrogenation of the biomass derived substrates 2,5-DMF (2,5-dimethylfuran), obtainable from 5-hydroxymethylfurfural, and 2,5-hexanedione, the hydrolysis product of 2,5-dimethylfuran. The reactions were carried out in aqueous acidic medium and temperature between 175 and 225 °C, using complex **126** as the catalyst. It was possible to afford yields of hydrogenated products up to 97% (using 2,5-hexanedione) and 66% using 2,5-DMF. The yield in 2,5-hexanediol was 82% and 78% starting from 2,5-hexanedione and 2,5-dimethylfuran, respectively (Scheme 102).

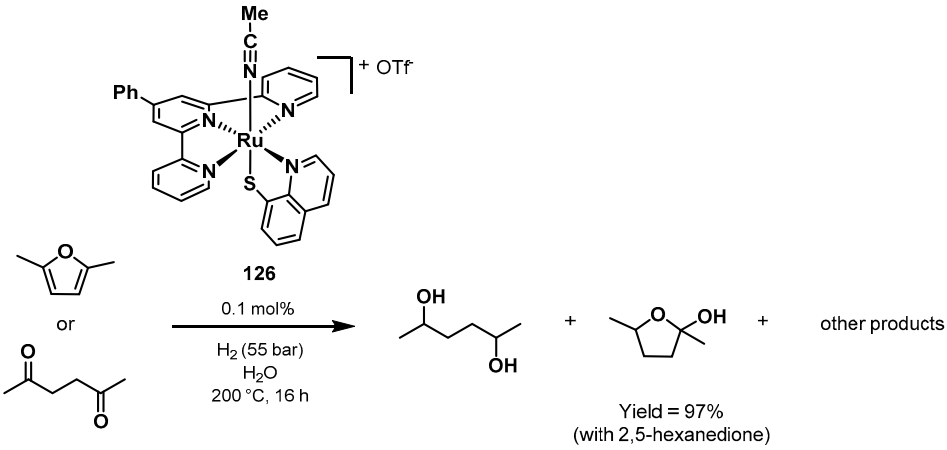

Scheme 102. Water and high temperature stable hydrogenation pincer catalyst for biomass-derived substrates developed by Schlaf [784].

In 2018, de Vries reported a method for the transformation of HMF into 2-hydroxy-3-methylcyclopent-2-enone (MCP) using Ir and Ru complexes as catalysts [785]. The strategy involved the intramolecular aldol condensation of 1-hydroxyhexane-2,5-dione (HHD), as depicted in Scheme 99. The only pincer complex tested in this transformation was **Ru-MACHO-BH,** which afforded 93% of conversion of HMF with 0.5 mol% catalyst loading, 10 bar of H_2 in water at 120 °C, however with only 5% yield of 1-hydroxyhexane-2,5-dione. On the contrary, when the authors explored the hydrogenation of MCP into valuable chemicals, **Ru-MACHO-BH** afforded full conversion of MCP into 3-Methyl-1,2-cyclopentanediol, which was isolated in 96% yield as a mixture of diastereomers after 16 h (Scheme 103). Recently, de Vries has reviewed the state-of-the-art of relevant sustainable transformations of 5-hydroxymethylfurfural involving 1-hydroxyhexane-2,5-dione as a key intermediate [786].

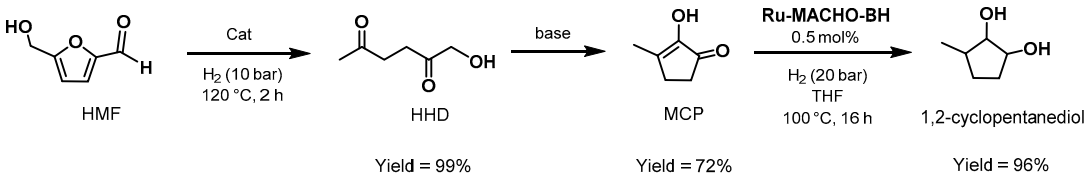

Scheme 103. Conversion of HMF to higher-value products showed by de Vries [785].

The same author also reported that the Ru-NNS complex **127** showed in Scheme 104 catalyzes the selective hydrogenation of methyl levulinate into γ-valerolactone [787]. The reaction was performed in methanol, with 0.25 mol% of **127**, 2.5 mol% of KO*t*Bu, under 50 bar of H_2 at 80 °C, affording 77% yield after 2 h (Scheme 104). In the same work, the authors explored the hydrogenation of a wide series of saturated- as well as α,β-unsaturated esters. It was possible to hydrogenate γ-valerolactone affording the ring-opened product 1,4-pentanediol in 92% yield using 0.25 mol% of catalyst **127**, 2.5 mol% of KO*t*Bu, under 60 bar of hydrogen, at 80 °C after 2 h.

In 2019, Song showed the hydrogenation of levulinic acid and methyl levulinate into γ-valerolactone catalyzed by the iron pincer complex **29** [788]. High TON and TOF up to respectively 23,000 and 1917 h^{-1} could be achieved for the hydrogenation of levulinic acid. The best results were obtained using 0.002 mol% of catalyst **29** in the presence of methanol as solvent, 1 equivalent of KOH, under 100 bar, at 100 °C for 12 h (Scheme 105). The use of H_2O as solvent was also possible and afforded TON of 22,500 and TOF of 1875 h^{-1}. When methyl levulinate was used under similar conditions, γ-valerolactone was obtained with TON up to 22,000 and TOF of 1833 h^{-1}. With higher catalyst loading (10 mol%) it was possible to afford 91% and 81% yield in GVL from levulinic acid and methyl levulinate respectively. The authors also explored the dehydration of several carbohydrates to afford LA, which was subsequently converted into GVL in high yields.

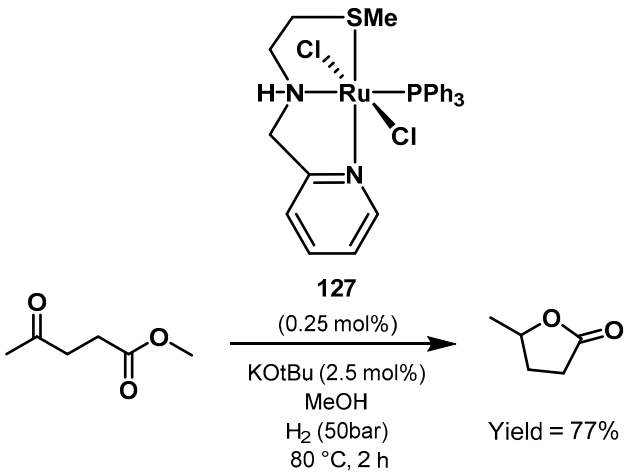

Scheme 104. Hydrogenation of methyl levulinate catalyzed by Ru-SNN catalyst **127** showed by de Vries [787].

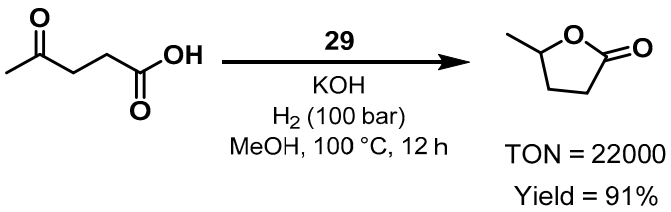

Scheme 105. Hydrogenation of levulinic acid and methyl levulinate into γ-valerolactone showed by Song [788].

Recently, our group in collaboration with Paixão have demonstrated the efficient hydrogenation of alkyl levulinates to γ-valerolactone catalyzed by either ruthenium or iridium PNP catalysts, in the presence of small amount of base additive, and at low temperature and H_2 pressure [789]. Both catalysts **Ru-MACHO** and **8** (Scheme 2) were found to be active in the conversion of both methyl as well as ethyl levulinate into γ-valerolactone, without the need of solvent and also in large scale reactions. The hydrogenation of ethyl levulinate was carried out using 0.01 mol% of catalyst at 60 °C and under 20 bar of hydrogen. Turnover numbers of 7400 and 9300 were obtained using **Ru-MACHO** and **8**, respectively (Scheme 106). In addition, a scale-up experiment was performed with a combination of mild reaction conditions and low catalyst loading; whereas **Ru-MACHO** was found to be practically inactive under the same reaction conditions, 0.050 mol% (500 ppm) of **8** led to full conversion after 72 h at 25 °C (TON = 2000) using ethanol as alcohol additive. Full conversion was also obtained for methyl levulinate under the same conditions, but with methanol as the alcoholic additive. Finally, a recycling experiments was performed using 0.5 mol% of **Ru-MACHO**; four consecutive additions of ethyl levulinate every 20 h showed full conversion in each run without detectable deactivation of the catalyst. Catalyst **8** was found to be inactive under the recycling conditions.

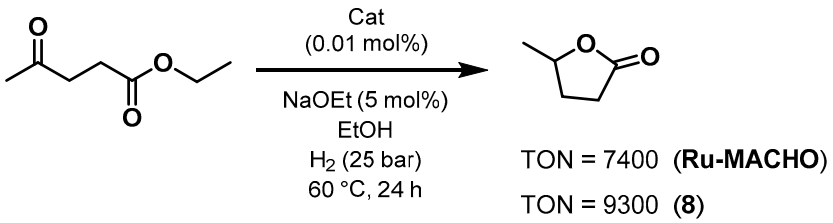

Scheme 106. Catalytic hydrogenation of ethyl levulinate to γ-valerolactone catalyzed by Ru- and Ir-PNP complexes at mild reaction conditions showed by Paixão and Nielsen [789].

3.4. Transfer Hydrogenation

Transfer hydrogenation reactions represent an elegant, sustainable strategy for the obtainment of molecules of higher complexity. The process does not require stoichiometric amount of additives and thus does not necessarily produce waste. In this transformation, hydrogen is inserted onto a molecule from an organic hydrogen source without the presence of hazardous H_2 gas. The hydrogen donors are usually easily accessible and inexpensive, such as isopropanol, methanol, formic acid, and ethanol, of which particularly the latter two are readily obtainable from renewable sources. Possibilities and applications offered by homogeneous transfer hydrogenation have been reviewed recently by Kempe [790], Corma-Sabater [791], as well as Kayaki [792], while Morris investigated the mechanism of transfer hydrogenation catalyzed by iron-group hydrides [793]. Milstein [56,64], as well as Noyori [794–797], provided fundamental milestones, dramatically expanding the scope of substrates for transfer hydrogenation and coupling reactions using homogeneous catalysis, including pincer complexes. In 2008, Grützmacher reported the first efficient transfer hydrogenation with ethanol as the hydrogen source [798]. By applying an air-sensitive rhodium complex bearing a bis(5-H-dibenzocyclohepten-5-yl)amine ligand, they could reach 98% conversion of different ketones at mild temperatures. Since then, several reports have covered the topic [799–805], using also isopropanol [806], formic acid [807], as well as glycerol [808] as the hydrogen sources. Metal pincer complexes have appeared as suitable catalysts for this type of transformations as well [116,809–813].

With regard to the past five years, Khaskin explored in 2016 the use of the Gusev SNS catalyst, known for the hydrogenation of esters [40], for an unprecedented metathesis pathway coupled with transfer hydrogenation in the presence of ethanol [814]. The authors explored the reaction of ethyl hexanoate in the presence of **Ru-MACHO**, which afforded a statistical equilibrium of products confirming the metathesis pathway. Later, the authors screened the Gusev complexes **13** and **128**, with **128** being the most efficient in producing metathesis products, with 99% selectivity after 16 h at 80 °C in toluene, using 0.02 mol% of catalyst loading and 5 mol% KO*t*Bu. The scope was extended to alkyl, aryl, and mixed alkyl-aryl esters that were all efficiently scrambled using 0.2 mol% catalyst loading. Finally, with optimized conditions, the authors explored the selective transfer hydrogenation of ethyl hexanoate using ethanol as hydrogen source; by increasing the catalyst loading to 1 mol%, in the presence of 20 equivalents of ethanol, it was possible to afford 89% yield in hexanol (Scheme 107).

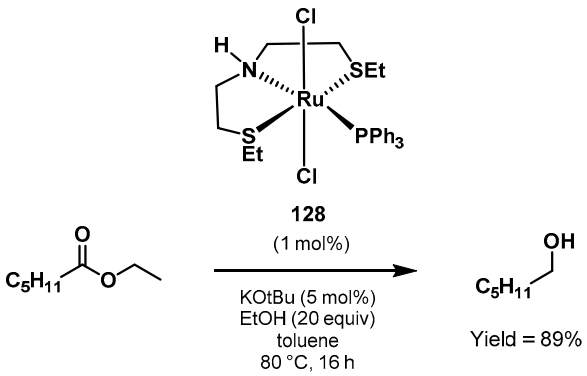

Scheme 107. Transfer hydrogenation of esters proposed by Khaskin in 2016 [814].

Thiel showed in 2018 an environmentally benign method for the hydrogenation of ketones, aldehydes and imines using ethanol as the hydrogen source, in combination with the ruthenium(II) pincer complex **129** in Figure 8 [815]. The catalyst is stable against moisture and oxygen, and allowed a wide scope of substrates; with 0.1 mol% as the catalyst loading, with 7.5 mol% KOH, in EtOH, it was possible to convert several phenyl ketones and aldehydes into the corresponding alcohols with >99% yields after 45 min, in some cases already after 15 min, at 40 °C. It was found that a rapid removal of acetic aldehyde under a constant N_2 flow is fundamental to push the equilibrium for high conversions.

However, it was not possible to hydrogenate olefins and heteroaromatic compounds with neither ethanol nor isopropanol as the hydrogen donors.

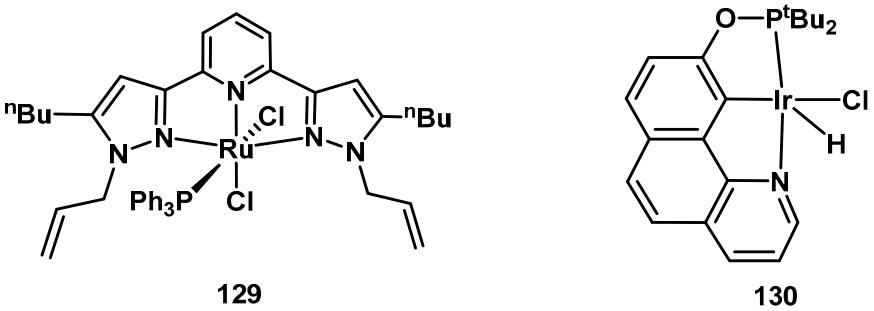

Figure 8. Ruthenium and iridium pincer catalysts reported by Thiel [815] and Huang [816] to catalyze transfer hydrogenations in the presence of ethanol.

The same year, Huang reported the transfer hydrogenation of alkenes catalyzed by the iridium-NCP pincer complex **130** containing a rigid benzoquinoline backbone in the presence of ethanol [816]. The authors explored the conversion of a wide range of substrates, from substituted alkyl alkenes and aryl alkenes, to electron-rich/deficient olefins, *O*- and *N*-heteroarenes, as well as internal alkynes. The optimization was performed using cyclooctene and 1-octene as substrates; applying 1 mol% catalyst loading, yields >99% were achieved of the hydrogenated products, with 2.2 mol% of NaO*t*Bu in ethanol, at 30 °C after 12 h. The rapid conversion of acetaldehyde, formed as the first EtOH dehydrogenation product, into ethyl acetate eliminates the possibility of catalyst poisoning by the iridium-mediated decarbonylation of the aldehyde.

In 2019, de Vries employed the iron-PNP catalyst **15** for the transfer hydrogenation of esters using ethanol as the hydrogen source [817]. The authors were able to hydrogenate more than 20 different substrates in good to excellent yields, including aromatic- and aliphatic esters and lactones. The initial screening was performed using methyl benzoate as the substrate, 5 mol% of **15** at 100 °C; after 24 h, 88% yield of benzyl alcohol was obtained. The authors also explored the use of different hydrogen sources, with isopropanol and butanol resulting in high conversion but lower selectivity in the desired product, whereas MeOH was found to poison the system. The optimized conditions were 5 mol% of catalyst, 96 equivalents of ethanol, at 100 °C for 24 h; with this protocol, the authors carried out the transfer hydrogenation of a series of relevant substrates, e.g., the bio-derived methyl oleate and α-Angelica lactone. In addition, methyl levulinate was successfully converted into 1,4-pentanediol (PDO) in a single step. Remarkably, the system is also active for the depolymerization of polyester to the diols, expanding the applicability of this protocol to the recycling of plastics as well. Notably, the same transformation for polyesters reduction was reported in 2013 by Robertson using Milstein's catalyst **4** [818].

Ethanol Upgrading

One of the most appealing processes in sustainable chemistry is the upgrading of (bio)-ethanol into useful fuels and fuel additives [819–821]. The Guerbet reaction is a process enabling the formation of C-C bonds starting from simple alcohols. In this transformation, the alcoholic substrate is dehydrogenated to form an aldehyde, which undergoes aldol condensation before the product is finally hydrogenated resulting in a higher alcohol (Scheme 108) [822]. Ethanol is currently produced from crops and used as fuel [823–825], albeit with only 70% of the energy density stored in gasoline. On the contrary, butanol presents several advantages, e.g., it has an energy density closer to that of gasoline (90%), is non-corrosive, immiscible with water and can be blended with gasoline at concentrations up to 16% [826–828]. Butanol is currently produced by bacterial fermentation of starch and sugars in the A.B.E. process [829], producing a mixture of acetone, butanol, and ethanol, while poor selectivity, separation issues, as well as low conversion and yield usually affect the Guerbet pathway [830].

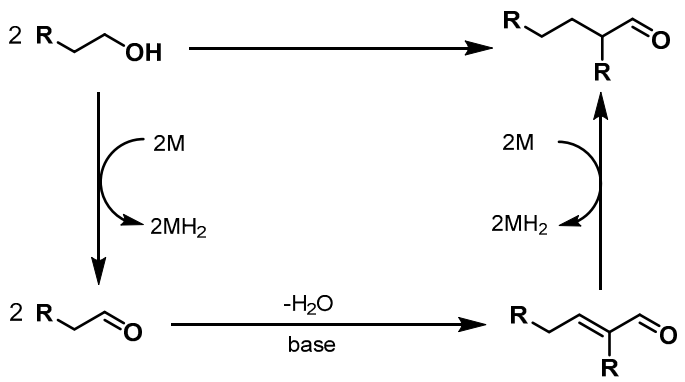

Scheme 108. Guerbet reaction.

The upgrading of ethanol results in 1-butanol and other C4/C6 products and isomers. Most of them are considered valuable bio-fuel, fuel additives, or monomers for bio-polymers. The reaction presents some drawbacks especially regarding the selectivity. *N*-butanol can undergo dehydrogenation reactions resulting in even higher alcohols and other side products. In addition, the high loading of base required, often promotes competitive reactions resulting in the formation of inactive carbonates. Research has focused on catalyst design as well as reaction conditions optimization to achieve acceptable yields and selectivity of 1-butanol.

In 2016, Milstein reported a very efficient ruthenium pincer complex catalyst for ethanol upgrading [831]. The reaction performed using 0.02 mol% of catalyst **131** in Scheme 109, EtONa (4 mol%), at 150 °C for 16 h produced the highest conversion of ethanol (66.9%) affording up to 38.4% yield in butanol. Lowering of the catalyst loading to 0.001 mol% afforded the record TON of 18,209 with 14.6% yield and 86% selectivity. Mechanistic studies and isolation of reaction intermediates led to the conclusion that the active species is the dearomatized complex **131a**, which is formed after activation by base. The major deactivation pathway is believed to occur through reaction of the formed water with ethanol and base, resulting in the formation of inactive NaOAc. In addition, the authors also explored the possibility to produce longer chain alcohols from ethanol; with a base loading of 20 mol%, it was possible to produce higher alcohols reaching a record conversion of 73.4%, with 37.6% selectivity to C6 and C8 alcohols.

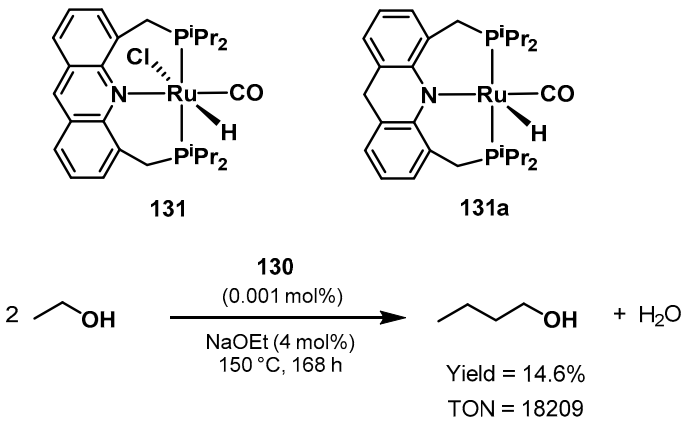

Scheme 109. Ru-PNP catalyst for ethanol upgrading developed by Milstein [831].

The same year, Szymczak proposed an air-stable Ru-NNN catalyst for the upgrading of ethanol to 1-butanol [832]. The catalyst is a modification of a previously reported catalyst (**132** in Scheme 110) found to be active in the reversible transformation between ketones and alcohols via hydrogenation and acceptorless dehydrogenation reactions [833]. The authors also carried out mechanistic studies supported by kinetic and isotopic labeling studies, proposing an inner-sphere mechanism with a β-H

elimination as the turnover-limiting step in the dehydrogenation of alcohols using catalyst **132** [834]. In this report, catalyst **133** was used for the catalytic upgrading of ethanol achieving 37% yield of 1-butanol with 78% selectivity after 2 h at 150 °C. The addition of 0.4 mol% of PPh_3 prevents phosphine dissociation, as well as the competitive EtOH decarbonylation pathway. After optimization, the catalyst **133** resulted in a TON of 530 and a TOF of 265 h^{-1} with the reaction conditions shown in Scheme 110.

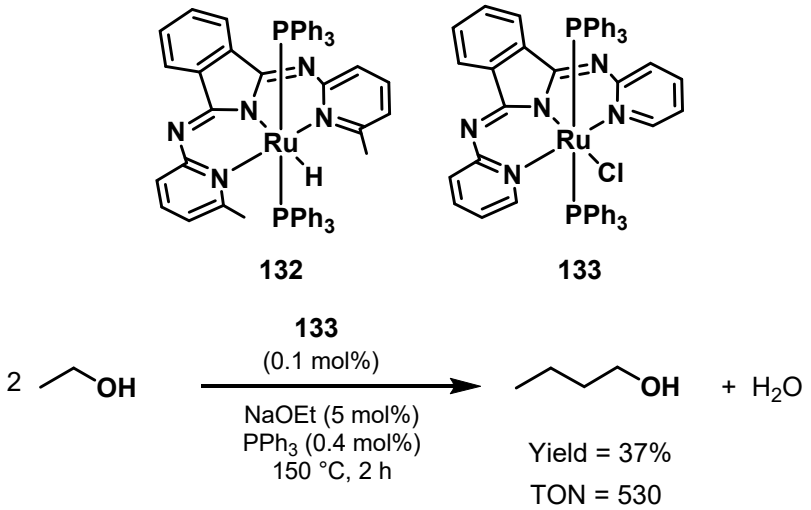

Scheme 110. Ru-NNN complexes synthetized by Szymczak and ethanol upgrading using catalyst **133** [832,833].

In 2015, Wass showed the catalytic upgrading of ethanol using different ruthenium precursors in combination with various ligands, as well as the PNP complex **Ru-MACHO** [835]. With the reaction conditions showed in Scheme 111a, **Ru-MACHO** afforded 13.3% conversion and 12.4% selectivity in 1-butanol. The best result was obtained employing $[RuCl_2(\eta 6\text{-p-cymene})]_2$ and the bidentate ligand 2-(diphenylphosphino)ethylamine, with 90% selectivity and 31% conversion.

In another work, high selectivity toward isobutanol was obtained using different combinations of ruthenium precursors and PP and PN bidentate ligands [836]. The catalyst bearing the 1,1-bis(diphenylphosphino)methane as ligand, with 200 mol% of base loading (NaOMe), 0.1 mol% of methanol, at 180 °C, afforded 75% conversion of ethanol with 99% selectivity to isobutanol and only traces of *n*-propanol and *n*-butanol.

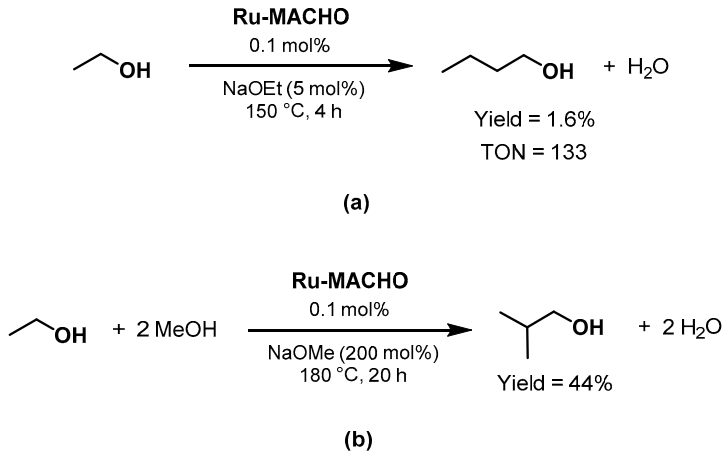

Scheme 111. Ethanol upgrading to **(a)** 1-butanol and **(b)** to isobutanol proposed by Wass [835,837].

In 2017, the same author tested the catalyst precursors *trans*-$[RuCl_2(dppm)_2]$, $[RuCl_2(dppea)_2]$, as well as **Ru-MACHO** for the upgrading of ethanol to isobutanol [837]. The pre-catalyst

trans-[$RuCl_2(dppm)_2$] was shown to be the most active in the presence of water, yielding 36% of isobutanol, at 78% selectivity from an aqueous ethanol/methanol mixture with water concentrations typical of that of a crude fermentation broth. In addition, the catalyst allows to perform the reaction using hydroxide instead of alkoxide bases. The use of H_2O/NaOH with **Ru-MACHO** led to deactivation of the catalytic system and formation of carbonate and formate salts. However, in the presence of NaOMe and without water, **Ru-MACHO** afforded 44% yield in isobutanol with 89% selectivity under the reaction conditions shown in Scheme 111b. The superior activity of *trans*-[$RuCl_2(dppm)_2$] is explained by the superior water tolerance compared to the other PN and PNP complexes tested in the work.

The same year, Liu showed the first example, and state-of-the-art, of ethanol upgrading into 1-butanol using a homogeneous non-noble-metal catalyst [838]. The manganese pincer complex **25** resulted in the extraordinary TON of 114,120 and TOF of 3078 h^{-1} with 92% selectivity and 9.8% yield of 1-butanol at 160 °C for 168 h (Scheme 112). Increasing the catalyst loading to 0.02 mol% under the same reaction conditions resulted in 14.5% yield in 1-butanol with 82% selectivity and a TON of 1031. The group also performed mechanistic studies using controlled experiments with reaction intermediates, NMR spectroscopy and single crystal X-Ray crystallography to investigate the role of the *N*-H/*N*-Me moiety of the PNP pincer ligand. The proposed catalytic cycle is depicted in Scheme 112.

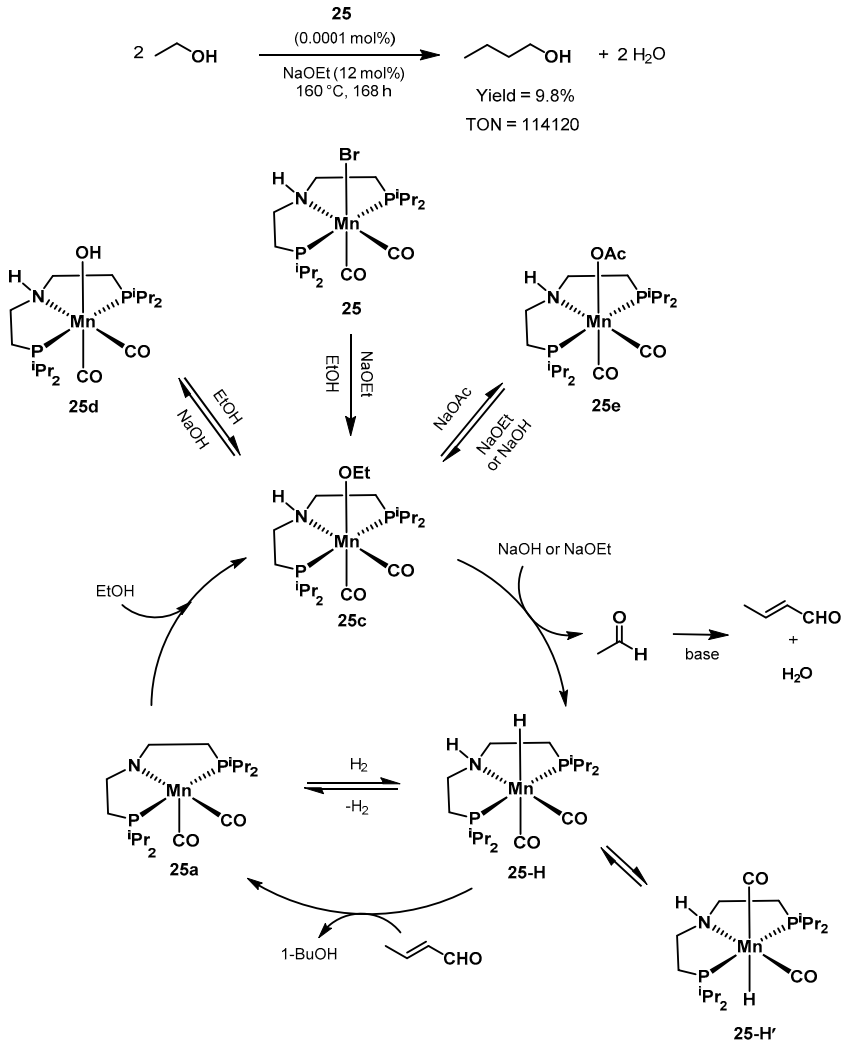

Scheme 112. Proposed catalytic cycle of complex **25** for the Guerbet reaction of ethanol to butanol proposed by Liu [838].

In 2018, Jones screened several Mn-PNP complexes of the same family as catalysts for the Guerbet reaction [839]. The chosen Mn-Br$(CO)_2$-PNP complexes bearing different substituents on the phosphorous atoms were all found to catalyze the transformation, with catalyst **25** performing best; *N*-butanol could be obtained in 31% yield using 0.5 mol% of **25**, NaOEt, at 150 °C for 48 h. High loading of the base (25 mol%) was required to maintain the catalytic activity. The water formed during the reaction promotes the major deactivation pathways.

4. Conclusions

In conclusion, we covered the main advances of the last five years in relevant sustainable chemical transformations catalyzed by pincer complexes. Dehydrogenation and hydrogenation reactions, together with valorization of biomass-derived compounds are the main processes where sustainability is predominant. In particular, efficient and continuous hydrogen release from LOHCs, as wells as CO_2 capture and hydrogenation are the main areas of interest in a hydrogen economy perspective, with methanol, formic acid, and its derivatives as the most studied alternatives. Homogeneous N_2 hydrogenation provides a clean, atom-efficient route for the synthesis of ammonia. Pincer complexes also catalyze the upgrading of ethanol into bio-fuels and the hydrogenation of biomass-derived compounds into high-value molecules.

Low catalyst loading, high selectivity, and mild reaction conditions are the main advantages of pincer-type catalysis. The applied pincer complexes show outstanding performance and promising potential for optimization. The long-term stability of the developed catalytic systems, as well as the use of expensive, rare metals are the main drawbacks that need optimization. More robust, possibly air- and moisture-stable catalysts are highly desirable to extend the lifetime and practical applicability of these otherwise promising catalysts. Remarkably, cheap and abundant first-row transition metals show very promising activity, potentially further increasing the sustainability of this versatile family of catalytic systems.

Pincer complexes have showed great reliability and flexibility for a plethora of sustainable chemical processes. Ligand design and the expanding use of first-row metals offer numerous possibilities for further optimization. Many groups are working extensively on the topic to find efficient, novel chemical and energy production routes and provide the society with sustainable solutions.

Funding: This research was funded by VILLUM FONDEN, grant number 19049, and by INDEPENDENT RESEARCH FUND DENMARK, grant number 8022-00330B.

Conflicts of Interest: The authors declare no conflict of interest.

References

1. Anastas, P.T.; Warner, J.C. *Green Chemistry: Theory and Practice 2000*; Oxford University Press: New York, NY, USA, 1998; p. 1546.
2. Grützmacher, H. Cooperating Ligands in Catalysis. *Angew. Chem. Int. Ed.* **2008**, *47*, 1814–1818. [CrossRef]
3. Askevold, B.; Roesky, H.W.; Schneider, S. Learning from the Neighbors: Improving Homogeneous Catalysts with Functional Ligands Motivated by Heterogeneous and Biocatalysis. *ChemCatChem* **2012**, *4*, 307–320. [CrossRef]
4. Lawrence, M.A.W.; Green, K.A.; Nelson, P.N.; Lorraine, S.C. Review: Pincer ligands—Tunable, versatile and applicable. *Polyhedron* **2018**, *143*, 11–27. [CrossRef]
5. Morales-Morales, D. *Pincer Compounds: Chemistry and Applications*; Elsevier: Amsterdam, The Netherlands, 2018; ISBN 9780128129326.
6. Morales-Morales, D.; Jensen, C. *The Chemistry of Pincer Compounds*; Elsevier: Amsterdam, The Netherlands, 2007; ISBN 9780444531384.
7. Moulton, B.C.J.; Shaw, B.L. *1020 J.C.S.*; Dalton: New York, NY, USA, 1975; pp. 1020–1024.
8. Liu, C.-C.; Liu, Q.-L.; Wu, Z.-Y.; Chen, Y.-C.; Xie, H.-J.; Lei, Q.-F.; Fang, W.-J. Mechanistic insights into small molecule activation induced by ligand cooperativity in PCcarbeneP nickel pincer complexes: A quantum chemistry study. *J. Mol. Model.* **2015**, *21*, 242. [CrossRef]

9. Zhao, S.; Wu, J.; Chen, W. Organometallic chemistry of bis (N-heterocyclic carbene) ligands containing a heteroarene spacer. *J. Organomet. Chem.* **2017**, *848*, 249–280. [CrossRef]
10. Pugh, D.; Danopoulos, A.A. Metal complexes with 'pincer'-type ligands incorporating N-heterocyclic carbene functionalities. *Coord. Chem. Rev.* **2007**, *251*, 610–641. [CrossRef]
11. Mejuto, C.; García-Eleno, M.A.; Guisado-Barrios, G.; Spasyuk, D.; Gusev, D.; Peris, E. Ruthenium complexes with an N-heterocyclic carbene NNC-pincer ligand: Preparation and catalytic properties. *Org. Chem. Front.* **2015**, *2*, 936–941. [CrossRef]
12. Jiang, Y.; Gendy, C.; Roesler, R. Nickel, Ruthenium, and Rhodium NCN-Pincer Complexes Featuring a Six-Membered N-Heterocyclic Carbene Central Moiety and Pyridyl Pendant Arms. *Organometallics* **2018**, *37*, 1123–1132. [CrossRef]
13. Sung, S.; Wang, Q.; Krämer, T.; Young, R.D. Synthesis and reactivity of a PCcarbeneP cobalt (i) complex: The missing link in the cobalt PXP pincer series (X = B, C, N). *Chem. Sci.* **2018**, *9*, 8234–8241. [CrossRef] [PubMed]
14. Prokopchuk, D.E.; Tsui, B.T.H.; Lough, A.J.; Morris, R.H. Intramolecular C-H/O-h bond cleavage with water and alcohol using a phosphine-free ruthenium carbene NCN Pincer Complex. *Chem. A Eur. J.* **2014**, *20*, 16960–16968. [CrossRef] [PubMed]
15. Shimoyama, Y.; Ishizuka, T.; Kotani, H.; Kojima, T. Ruthenium (II) Complexes Having a Pincer-Type Ligand with Two N-Heterocyclic Carbene Moieties. *Z. Fur. Anorg. Und. Allg. Chem.* **2018**, *644*, 611–615. [CrossRef]
16. Charra, V.; de Frémont, P.; Braunstein, P. Multidentate *N*-heterocyclic carbene complexes of the 3d metals: Synthesis, structure, reactivity and catalysis. *Coord. Chem. Rev.* **2017**, *341*, 53–176. [CrossRef]
17. Andrew, R.E.; González-Sebastián, L.; Chaplin, A.B. NHC-based pincer ligands: Carbenes with a bite. *Dalt. Trans.* **2016**, *45*, 1299–1305. [CrossRef] [PubMed]
18. Cheng, J.; Wang, L.; Wang, P.; Deng, L. High-Oxidation-State 3d Metal (Ti-Cu) Complexes with *N*-Heterocyclic Carbene Ligation. *Chem. Rev.* **2018**, *118*, 9930–9987. [CrossRef] [PubMed]
19. Liddle, S.T.; Mills, D.P.; Wooles, A.J. Early metal bis (phosphorus-stabilised) carbene chemistry. *Chem. Soc. Rev.* **2011**, *40*, 2164–2176. [CrossRef] [PubMed]
20. Zhang, D.; Zi, G. N-heterocyclic carbene (NHC) complexes of group 4 transition metals. *Chem. Soc. Rev.* **2015**, *44*, 1898–1921. [CrossRef]
21. Polukeev, A.V.; Wendt, O.F. Cyclohexane-Based Phosphinite Iridium Pincer Complexes: Synthesis, Characterization, Carbene Formation, and Catalytic Activity in Dehydrogenation Reactions. *Organometallics* **2017**, *36*, 639–649. [CrossRef]
22. Gu, S.; Chen, C.; Qiu, H.; Chen, W. Potentially Hemilabile N-Heterocyclic Carbene Palladium Complexes: Synthesis and Catalytic Applications. *Curr. Org. Chem.* **2011**, *15*, 3291–3308. [CrossRef]
23. Peris, E.; Crabtree, R.H. Recent homogeneous catalytic applications of chelate and pincer N-heterocyclic carbenes. *Coord. Chem. Rev.* **2004**, *248*, 2239–2246. [CrossRef]
24. Li, H.; Zheng, B.; Huang, K.W. A new class of PN3-pincer ligands for metal-ligand cooperative catalysis. *Coord. Chem. Rev.* **2015**, *293–294*, 116–138. [CrossRef]
25. Kisala, J.; Ruman, T. Pincer Complexes Based on Phosphinoaminopyridines: Synthesis, Structural Characterization and Catalytic Applications. *Curr. Org. Chem.* **2011**, *15*, 3486–3502. [CrossRef]
26. Benito-Garagorri, D.; Kirchner, K. Modularly designed transition metal PNP and PCP pincer complexes based on aminophosphines: Synthesis and catalytic applications. *Acc. Chem. Res.* **2008**, *41*, 201–213. [CrossRef] [PubMed]
27. Deolka, S.; Tarannam, N.; Fayzullin, R.R.; Kozuch, S.; Khaskin, E. Unusual rearrangement of modified PNP ligand based Ru complexes relevant to alcohol dehydrogenation catalysis. *Chem. Commun.* **2019**, *55*, 11350–11353. [CrossRef]
28. Henrion, M.; Roisnel, T.; Couturier, J.L.; Dubois, J.L.; Sortais, J.B.; Darcel, C.; Carpentier, J.F. Ruthenium complexes bearing amino-bis (phosphinite) or amino-bis (aminophosphine) ligands: Application in catalytic ester hydrogenation. *Mol. Catal.* **2017**, *432*, 15–22. [CrossRef]
29. Yao, C.; Chakraborty, P.; Aresu, E.; Li, H.; Guan, C.; Zhou, C.; Liang, L.C.; Huang, K.W. Monomeric nickel hydroxide stabilized by a sterically demanding phosphorus-nitrogen PN3P-pincer ligand: Synthesis, reactivity and catalysis. *Dalt. Trans.* **2018**, *47*, 16057–16065. [CrossRef]
30. Gradiski, M.V.; Tsui, B.T.H.; Lough, A.J.; Morris, R.H. PNN' & P 2 NN' ligands via reductive amination with phosphine aldehydes: Synthesis and base-metal coordination chemistry. *Dalt. Trans.* **2019**, *48*, 2150–2159.

31. Kim, Y.; Lee, J.; Son, Y.-H.; Choi, S.-U.; Alam, M.; Park, S. Novel nickel(II), palladium(II), and platinum(II) complexes having a pyrrolyl-iminophosphine (PNN) pincer: Synthesis, crystal structures, and cytotoxic activity. *J. Inorg. Biochem.* **2020**, *205*, 111015. [CrossRef]
32. Adams, G.M.; Weller, A.S. POP-type ligands: Variable coordination and hemilabile behaviour. *Coord. Chem. Rev.* **2018**, *355*, 150–172. [CrossRef]
33. Leis, W.; Mayer, H.A.; Kaska, W.C. Cycloheptatrienyl, alkyl and aryl PCP-pincer complexes: Ligand backbone effects and metal reactivity. *Coord. Chem. Rev.* **2008**, *252*, 1787–1797. [CrossRef]
34. Morales-Morales, D. Recent Applications of Phosphinite POCOP Pincer Complexes towards Organic Transformations. *Mini. Rev. Org. Chem.* **2008**, *5*, 141–152. [CrossRef]
35. Gelman, D.; Romm, R. PC(sp^3)P Transition Metal Pincer Complexes: Properties and Catalytic Applications. In *Topics in Organometallic Chemistry*; Springer: Berlin, Germany, 2013; pp. 289–317. ISBN 9783642310805.
36. Leforestier, B.; Gyton, M.R.; Chaplin, A.B. Synthesis and group 9 complexes of macrocyclic PCP and POCOP pincer ligands. *Dalt. Trans.* **2020**, *49*, 2087–2101. [CrossRef]
37. Jensen, C.M. Iridium PCP pincer complexes: Highly active and robust catalysts for novel homogeneous aliphatic dehydrogenations. *Chem. Commun.* **1999**, *3*, 2443–2449. [CrossRef]
38. Barrett, B.J.; Iluc, V.M. Coordination of a Hemilabile Pincer Ligand with an Olefinic Backbone to Mid-to-Late Transition Metals. *Inorg. Chem.* **2014**, *53*, 7248–7259. [CrossRef]
39. Schörgenhumer, J.; Zimmermann, A.; Waser, M. SNS-Ligands for Ru-Catalyzed Homogeneous Hydrogenation and Dehydrogenation Reactions. *Org. Process Res. Dev.* **2018**, *22*, 862–870. [CrossRef]
40. Spasyuk, D.; Smith, S.; Gusev, D.G. Replacing Phosphorus with Sulfur for the Efficient Hydrogenation of Esters. *Angew. Chem. Int. Ed.* **2013**, *52*, 2538–2542. [CrossRef]
41. Valdés, H.; González-Sebastián, L.; Morales-Morales, D. Aromatic para-functionalized NCN pincer compounds. *J. Organomet. Chem.* **2017**, *845*, 229–257. [CrossRef]
42. Fernández-Alvarez, F.J.; Lalrempuia, R.; Oro, L.A. Monoanionic NSiN-type ligands in transition metal coordination chemistry and catalysis. *Coord. Chem. Rev.* **2017**, *350*, 49–60. [CrossRef]
43. Garbe, S.; Krause, M.; Klimpel, A.; Neundorf, I.; Lippmann, P.; Ott, I.; Brünink, D.; Strassert, C.A.; Doltsinis, N.L.; Klein, A. Cyclometalated Pt Complexes of CNC Pincer Ligands: Luminescence and Cytotoxic Evaluation. *Organometallics* **2020**, *39*, 746–756. [CrossRef]
44. Ruan, J.; Wang, D.; Vedernikov, A.N. CH_3–X Reductive Elimination Reactivity of $Pt^{IV}Me$ Complexes Supported by a Sulfonated CNN Pincer Ligand (X = OH, CF_3CO_2, $PhNMe_2^+$). *Organometallics* **2020**, *39*, 142–152. [CrossRef]
45. Heidebrecht, J.; Gendy, C.; Gelfand, B.S.; Roesler, R. Water-soluble NNN-pincer complexes of cobalt, nickel and palladium: Solid-state structures and catalytic activity. *Polyhedron* **2018**, *143*, 138–143. [CrossRef]
46. Kozlov, V.A.; Aleksanyan, D.V.; Vasilév, A.A.; Odinets, I.L. Thiophosphoryl-, thiophosphoryloxy-, and thiophosphorylamino-benzene derivatives as novel classes of hybrid pincer ligands. *Phosphorus Sulfur Silicon Relat. Elem.* **2011**, *186*, 626–637. [CrossRef]
47. Al-Noaimi, M.; Awwadi, F.F.; Talib, W.H.; Atia, S.; Hammud, H.H. Cis and trans- palladium (II) complexes derived from SNN amidrazone pincer ligand: Synthesis, crystal structures and biological evaluation. *J. Mol. Struct.* **2019**, *1197*, 282–291. [CrossRef]
48. Okamoto, K.; Kuwabara, J.; Kanbara, T. Secondary Thioamides as Multidentate Ligands for Functional Metal Complexes. *Chem. Lett.* **2015**, *44*, 102–110. [CrossRef]
49. Simon, M.; Breher, F. Multidentate silyl ligands in transition metal chemistry. *Dalt. Trans.* **2017**, *46*, 7976–7997. [CrossRef]
50. Zhou, Y.P.; Mo, Z.; Luecke, M.P.; Driess, M. Stereoselective Transfer Semi-Hydrogenation of Alkynes to E-Olefins with N-Heterocyclic Silylene–Manganese Catalysts. *Chem. A Eur. J.* **2018**, *24*, 4780–4784. [CrossRef]
51. Kumar, A.; Rao, G.K.; Saleem, F.; Singh, A.K. Organoselenium ligands in catalysis. *Dalt. Trans.* **2012**, *41*, 11949–11977. [CrossRef]
52. Sharma, K.N.; Satrawala, N.; Srivastava, A.K.; Ali, M.; Joshi, R.K. Palladium (ii) ligated with a selenated (Se, CNHC, N-) -type pincer ligand: An efficient catalyst for Mizoroki-Heck and Suzuki-Miyaura coupling in water. *Org. Biomol. Chem.* **2019**, *17*, 8969–8976. [CrossRef]
53. Kameo, H.; Nakazawa, H. Recent developments in the coordination chemistry of multidentate ligands featuring a boron moiety. *Chem. Asian J.* **2013**, *8*, 1720–1734. [CrossRef]

54. Yamashita, M. The Organometallic Chemistry of Boron-Containing Pincer Ligands based on Diazaboroles and Carboranes. *Bull. Chem. Soc. Jpn.* **2016**, *89*, 269–281. [CrossRef]
55. Balakrishna, M.S. Unusual and rare pincer ligands: Synthesis, metallation, reactivity and catalytic studies. *Polyhedron* **2018**, *143*, 2–10. [CrossRef]
56. Van Der Boom, M.E.; Milstein, D. Cyclometalated phosphine-based pincer complexes: Mechanistic insight in catalysis, coordination, and bond activation. *Chem. Rev.* **2003**, *103*, 1759–1792. [CrossRef] [PubMed]
57. Peris, E.; Crabtree, R.H. Key factors in pincer ligand design. *Chem. Soc. Rev.* **2018**, *47*, 1959–1968. [CrossRef] [PubMed]
58. Toda, T.; Suzuki, S.; Kuwata, S. Metallo-supramolecular assembly of protic pincer-type complexes: Encapsulation of dinitrogen and carbon disulfide into a multiproton-responsive diruthenium cage. *Chem. Commun.* **2019**, *55*, 1028–1031. [CrossRef]
59. Nelson, D.J.; Nolan, S.P. Hydroxide complexes of the late transition metals: Organometallic chemistry and catalysis. *Coord. Chem. Rev.* **2017**, *353*, 278–294. [CrossRef]
60. Maser, L.; Vondung, L.; Langer, R. The ABC in pincer chemistry—From amine- to borylene- and carbon-based pincer-ligands. *Polyhedron* **2018**, *143*, 28–42. [CrossRef]
61. Gusev, D.G.; Madott, M.; Dolgushin, F.M.; Lyssenko, K.A.; Antipin, M.Y. Agostic bonding in pincer complexes of ruthenium. *Organometallics* **2000**, *19*, 1734–1739. [CrossRef]
62. Annibale, V.T.; Song, D. Multidentate actor ligands as versatile platforms for small molecule activation and catalysis. *RSC Adv.* **2013**, *3*, 11432–11449. [CrossRef]
63. Ananthnag, G.S.; Shetti, V.S. Synthesis, structure and catalysis of organometallic porphyrin-pincer hybrids: A review. *Dalt. Trans.* **2017**, *46*, 14062–14082. [CrossRef]
64. Gunanathan, C.; Milstein, D. Bond Activation and Catalysis by Ruthenium Pincer Complexes. *Chem. Rev.* **2014**, *114*, 12024–12087. [CrossRef]
65. Younus, H.A.; Ahmad, N.; Su, W.; Verpoort, F. Ruthenium pincer complexes: Ligand design and complex synthesis. *Coord. Chem. Rev.* **2014**, *276*, 112–152. [CrossRef]
66. Younus, H.A.; Su, W.; Ahmad, N.; Chen, S.; Verpoort, F. Ruthenium pincer complexes: Synthesis and catalytic applications. *Adv. Synth. Catal.* **2015**, *357*, 283–330. [CrossRef]
67. Werkmeister, S.; Junge, K.; Beller, M. Catalytic hydrogenation of carboxylic acid esters, amides, and nitriles with homogeneous catalysts. *Org. Process Res. Dev.* **2014**, *18*, 289–302. [CrossRef]
68. Gusev, D.G.; Lough, A.J. Experimental and computational study of pincer complexes of ruthenium with Py, CO, and N_2 ligands. *Organometallics* **2002**, *21*, 5091–5099. [CrossRef]
69. Gusev, D.G.; Dolgushin, F.M.; Antipin, M.Y. Hydride, borohydride, and dinitrogen pincer complexes of ruthenium. *Organometallics* **2000**, *19*, 3429–3434. [CrossRef]
70. Abbel, R.; Abdur-Rashid, K.; Faatz, M.; Hadzovic, A.; Lough, A.J.; Morris, R.H. A succession of isomers of ruthenium dihydride complexes. Which one is the ketone hydrogenation catalyst? *J. Am. Chem. Soc.* **2005**, *127*, 1870–1882. [CrossRef]
71. Bruneau, C.; Dixneuf, P.H. *Ruthenium in Catalysis*; Springer: Berlin, Germany, 2014; ISBN 9783319084817.
72. Dub, P.A.; Ikariya, T. Quantum chemical calculations with the inclusion of nonspecific and specific solvation: Asymmetric transfer hydrogenation with bifunctional ruthenium catalysts. *J. Am. Chem. Soc.* **2013**, *135*, 2604–2619. [CrossRef]
73. Bertoli, M.; Choualeb, A.; Lough, A.J.; Moore, B.; Spasyuk, D.; Gusev, D.G. Osmium and ruthenium catalysts for dehydrogenation of alcohols. *Organometallics* **2011**, *30*, 3479–3482. [CrossRef]
74. Chelucci, G.; Baldino, S.; Baratta, W. Recent advances in osmium-catalyzed hydrogenation and dehydrogenation reactions. *Acc. Chem. Res.* **2015**, *48*, 363–379. [CrossRef]
75. Bertoli, M.; Choualeb, A.; Gusev, D.G.; Lough, A.J.; Major, Q.; Moore, B. PNP pincer osmium polyhydrides for catalytic dehydrogenation of primary alcohols. *Dalt. Trans.* **2011**, *40*, 8941. [CrossRef]
76. Gusev, D.G.; Lough, A.J.; Double, C.-H. activation on osmium and ruthenium centers: Carbene vs olefin products. *Organometallics* **2002**, *21*, 2601–2603. [CrossRef]
77. Choi, J.; MacArthur, A.H.R.; Brookhart, M.; Goldman, A.S. Dehydrogenation and Related Reactions Catalyzed by Iridium Pincer Complexes. *Chem. Rev.* **2011**, *111*, 1761–1779. [CrossRef]
78. Choualeb, A.; Lough, A.J.; Gusev, D.G. Hemilabile pincer-type hydride complexes of iridium. *Organometallics* **2007**, *26*, 5224–5229. [CrossRef]

79. Clarke, Z.E.; Maragh, P.T.; Dasgupta, T.P.; Gusev, D.G.; Lough, A.J.; Abdur-Rashid, K. A family of active iridium catalysts for transfer hydrogenation of ketones. *Organometallics* **2006**, *25*, 4113–4117. [CrossRef]
80. Meiners, J.; Scheibel, M.G.; Lemée-Cailleau, M.H.; Mason, S.A.; Boeddinghaus, M.B.; Fässler, T.F.; Herdtweck, E.; Khusniyarov, M.M.; Schneider, S. Square-planar iridium (II) and iridium (III) amido complexes stabilized by a PNP pincer ligand. *Angew. Chem. Int. Ed.* **2011**, *50*, 8184–8187. [CrossRef]
81. Goldberg, J.M.; Wong, G.W.; Brastow, K.E.; Kaminsky, W.; Goldberg, K.I.; Heinekey, D.M. The Importance of Steric Factors in Iridium Pincer Complexes. *Organometallics* **2015**, *34*, 753–762. [CrossRef]
82. Scheibel, M.G.; Wu, Y.; Stückl, A.C.; Krause, L.; Carl, E.; Stalke, D.; De Bruin, B.; Schneider, S. Synthesis and reactivity of a transient, terminal nitrido complex of rhodium. *J. Am. Chem. Soc.* **2013**, *135*, 17719–17722. [CrossRef]
83. Sundermann, A.; Uzan, O.; Milstein, D.; Martin, J.M.L. Selective C-C vs C-H bond activation by rhodium (I) PCP pincer complexes. A computational study. *J. Am. Chem. Soc.* **2000**, *122*, 7095–7104. [CrossRef]
84. Urgoitia, G.; Galdón, G.; Churruca, F.; SanMartin, R.; Herrero, M.T.; Domínguez, E. Aerobic oxidation of secondary benzyl alcohols catalyzed by phosphinite-based palladium pincer complexes. *Environ. Chem. Lett.* **2018**, *16*, 1101–1108. [CrossRef]
85. Albrecht, M.; Van Koten, G. Platinum group organometallics based on "pincer" complexes: Sensors, switches, and catalysts. *Angew. Chem. Int. Ed.* **2001**, *40*, 3750–3781. [CrossRef]
86. Selander, N.; Szabó, K.J. Catalysis by palladium pincer complexes. *Chem. Rev.* **2011**, *111*, 2048–2076. [CrossRef]
87. González-Sebastián, L.; Morales-Morales, D. Cross-coupling reactions catalysed by palladium pincer complexes. A review of recent advances. *J. Organomet. Chem.* **2019**, *893*, 39–51. [CrossRef]
88. Esteruelas, M.A.; López, A.M.; Oliván, M. Polyhydrides of Platinum Group Metals: Nonclassical Interactions and σ-Bond Activation Reactions. *Chem. Rev.* **2016**, *116*, 8770–8847. [CrossRef]
89. Therrien, J.A.; Wolf, M.O.; Patrick, B.O. Synthesis and comparison of nickel, palladium, and platinum bis (*N*-heterocyclic carbene) pincer complexes for electrocatalytic CO_2 reduction. *Dalt. Trans.* **2018**, *47*, 1827–1840. [CrossRef]
90. Bauer, G.; Hu, X. Recent developments of iron pincer complexes for catalytic applications. *Inorg. Chem. Front.* **2016**, *3*, 741–765. [CrossRef]
91. Dai, H.; Guan, H. Iron Dihydride Complexes: Synthesis, Reactivity, and Catalytic Applications. *Isr. J. Chem.* **2017**, *57*, 1170–1203. [CrossRef]
92. Bhattacharya, P.; Guan, H. Synthesis and catalytic applications of iron pincer complexes. *Comments Inorg. Chem.* **2011**, *32*, 88–112. [CrossRef]
93. Balaraman, E.; Nandakumar, A.; Jaiswal, G.; Sahoo, M.K. Iron-catalyzed dehydrogenation reactions and their applications in sustainable energy and catalysis. *Catal. Sci. Technol.* **2017**, *7*, 3177–3195. [CrossRef]
94. Benito-Garagorri, D.; Puchberger, M.; Mereiter, K.; Kirchner, K. Stereospecific and reversible CO binding at iron pincer complexes. *Angew. Chem. Int. Ed.* **2008**, *47*, 9142–9145. [CrossRef]
95. Junge, K.; Schröder, K.; Beller, M. Homogeneous catalysis using iron complexes: Recent developments in selective reductions. *Chem. Commun.* **2011**, *47*, 4849. [CrossRef]
96. Bernskoetter, W.H.; Hazari, N. Hydrogenation and dehydrogenation reactions catalyzed by iron pincer compounds. In *Pincer Compounds*; Elsevier Inc.: Amsterdam, The Netherland, 2018; ISBN 9780128129326.
97. Rohit, K.R.; Radhika, S.; Saranya, S.; Anilkumar, G. Manganese-Catalysed Dehydrogenative Coupling—An Overview. *Adv. Synth. Catal.* **2020**, *362*, 1602–1650. [CrossRef]
98. Waiba, S.; Maji, B. Manganese Catalyzed Acceptorless Dehydrogenative Coupling Reactions. *ChemCatChem* **2019**, *12*, 1891–1902. [CrossRef]
99. Maji, B.; Barman, M.K. Recent Developments of Manganese Complexes for Catalytic Hydrogenation and Dehydrogenation Reactions. *Synthesis* **2017**, *49*, 3377–3393. [CrossRef]
100. Garbe, M.; Junge, K.; Beller, M. Homogeneous Catalysis by Manganese-Based Pincer Complexes. *Eur. J. Org. Chem.* **2017**, *2017*, 4344–4362. [CrossRef]
101. Eberhardt, N.A.; Guan, H. Nickel Hydride Complexes. *Chem. Rev.* **2016**, *116*, 8373–8426. [CrossRef]
102. Gafurov, Z.N.; Kagilev, A.A.; Kantyukov, A.O.; Balabaev, A.A.; Sinyashin, O.G.; Yakhvarov, D.G. Classification and synthesis of nickel pincer complexes. *Russ. Chem. Bull.* **2018**, *67*, 385–394. [CrossRef]
103. Klein, A.; Sandleben, A.; Vogt, N. Synthesis, Structure and Reactivity of Cyclometalated Nickel (II) Complexes: A Review and Perspective. *Proc. Natl. Acad. Sci. India Sect. A Phys. Sci.* **2016**, *86*, 533–549. [CrossRef]

104. Gutsulyak, D.V.; Piers, W.E.; Borau-Garcia, J.; Parvez, M. Activation of water, ammonia, and other small molecules by PC carbeneP nickel pincer complexes. *J. Am. Chem. Soc.* **2013**, *135*, 11776–11779. [CrossRef]
105. LaPierre, E.A.; Clapson, M.L.; Piers, W.E.; Maron, L.; Spasyuk, D.M.; Gendy, C. Oxygen Atom Transfer to Cationic PCPNi(II) Complexes Using Amine-N-Oxides. *Inorg. Chem.* **2018**, *57*, 495–506. [CrossRef]
106. Chapman, G.; Nicholas, K.M. Vanadium-catalyzed deoxydehydration of glycols. *Chem. Commun.* **2013**, *49*, 8199. [CrossRef]
107. Gopaladasu, T.V.; Nicholas, K.M. Carbon Monoxide (CO)- and Hydrogen-Driven, Vanadium-Catalyzed Deoxydehydration of Glycols. *ACS Catal.* **2016**, *6*, 1901–1904. [CrossRef]
108. Hanson, S.K.; Baker, R.T.; Gordon, J.C.; Scott, B.L.; Thorn, D.L. Aerobic Oxidation of Lignin Models Using a Base Metal Vanadium Catalyst. *Inorg. Chem.* **2010**, *49*, 5611–5618. [CrossRef] [PubMed]
109. Junge, K.; Papa, V.; Beller, M. Cobalt–Pincer Complexes in Catalysis. *Chem. A Eur. J.* **2019**, *25*, 122–143. [CrossRef] [PubMed]
110. Liu, W.; Sahoo, B.; Junge, K.; Beller, M. Cobalt Complexes as an Emerging Class of Catalysts for Homogeneous Hydrogenations. *Acc. Chem. Res.* **2018**, *51*, 1858–1869. [CrossRef] [PubMed]
111. Ai, W.; Zhong, R.; Liu, X.; Liu, Q. Hydride Transfer Reactions Catalyzed by Cobalt Complexes. *Chem. Rev.* **2019**, *119*, 2876–2953. [CrossRef] [PubMed]
112. Lagaditis, P.O.; Schluschaß, B.; Demeshko, S.; Würtele, C.; Schneider, S. Square-Planar Cobalt (III) Pincer Complex. *Inorg. Chem.* **2016**, *55*, 4529–4536. [CrossRef]
113. Midya, S.P.; Pitchaimani, J.; Landge, V.G.; Madhu, V.; Balaraman, E. Direct access to: N -alkylated amines and imines via acceptorless dehydrogenative coupling catalyzed by a cobalt (ii)-NNN pincer complex. *Catal. Sci. Technol.* **2018**, *8*, 3469–3473. [CrossRef]
114. Ge, H.; Jing, Y.; Yang, X. Computational Design of Cobalt Catalysts for Hydrogenation of Carbon Dioxide and Dehydrogenation of Formic Acid. *Inorg. Chem.* **2016**, *55*, 12179–12184. [CrossRef]
115. Gorgas, N.; Kirchner, K. Isoelectronic Manganese and Iron Hydrogenation/Dehydrogenation Catalysts: Similarities and Divergences. *Acc. Chem. Res.* **2018**, *51*, 1558–1569. [CrossRef]
116. Reed-Berendt, B.G.; Polidano, K.; Morrill, L.C. Recent advances in homogeneous borrowing hydrogen catalysis using earth-abundant first row transition metals. *Org. Biomol. Chem.* **2019**, *17*, 1595–1607. [CrossRef]
117. Anastas, P.T.; Zimmerman, J.B. The periodic table of the elements of green and sustainable chemistry. *Green Chem.* **2019**, 6545–6566. [CrossRef]
118. Kallmeier, F.; Kempe, R. Manganese Complexes for (De) Hydrogenation Catalysis: A Comparison to Cobalt and Iron Catalysts. *Angew. Chem. Int. Ed.* **2018**, *57*, 46–60. [CrossRef] [PubMed]
119. Nguyen, D.H.; Morin, Y.; Zhang, L.; Trivelli, X.; Capet, F.; Paul, S.; Desset, S.; Dumeignil, F.; Gauvin, R.M. Oxidative Transformations of Biosourced Alcohols Catalyzed by Earth-Abundant Transition Metals. *ChemCatChem* **2017**, *9*, 2652–2660. [CrossRef]
120. Mukherjee, A.; Milstein, D. Homogeneous Catalysis by Cobalt and Manganese Pincer Complexes. *ACS Catal.* **2018**, *8*, 11435–11469. [CrossRef]
121. Zell, T.; Langer, R. From Ruthenium to Iron and Manganese—A Mechanistic View on Challenges and Design Principles of Base-Metal Hydrogenation Catalysts. *ChemCatChem* **2018**, *10*, 1930–1940. [CrossRef]
122. Filonenko, G.A.; Van Putten, R.; Hensen, E.J.M.; Pidko, E.A. Catalytic (de) hydrogenation promoted by non-precious metals-Co, Fe and Mn: Recent advances in an emerging field. *Chem. Soc. Rev.* **2018**, *47*, 1459–1483. [CrossRef] [PubMed]
123. Alig, L.; Fritz, M.; Schneider, S. First-Row Transition Metal (De) Hydrogenation Catalysis Based on Functional Pincer Ligands. *Chem. Rev.* **2019**, *119*, 2681–2751. [CrossRef]
124. Zhang, Z.; Butt, N.A.; Zhou, M.; Liu, D.; Zhang, W. Asymmetric Transfer and Pressure Hydrogenation with Earth-Abundant Transition Metal Catalysts. *Chin. J. Chem.* **2018**, *36*, 443–454. [CrossRef]
125. Riisager, A.; Fehrmann, R.; Haumann, M.; Wasserscheid, P. Supported Ionic Liquid Phase (SILP) catalysis: An innovative concept for homogeneous catalysis in continuous fixed-bed reactors. *Eur. J. Inorg. Chem.* **2006**, 695–706. [CrossRef]
126. Selvam, T.; MacHoke, A.; Schwieger, W. Supported ionic liquids on non-porous and porous inorganic materials-A topical review. *Appl. Catal. A Gen.* **2012**, *445–446*, 92–101. [CrossRef]

127. Brünig, J.; Csendes, Z.; Weber, S.; Gorgas, N.; Bittner, R.W.; Limbeck, A.; Bica, K.; Hoffmann, H.; Kirchner, K. Chemoselective Supported Ionic-Liquid-Phase (SILP) Aldehyde Hydrogenation Catalyzed by an Fe(II) PNP Pincer Complex. *ACS Catal.* **2018**, *8*, 1048–1051. [CrossRef]
128. Castro-Amoedo, R.; Csendes, Z.; Brünig, J.; Sauer, M.; Foelske-Schmitz, A.; Yigit, N.; Rupprechter, G.; Gupta, T.; Martins, A.M.; Bica, K.; et al. Carbon-based SILP catalysis for the selective hydrogenation of aldehydes using a well-defined Fe(ii) PNP complex. *Catal. Sci. Technol.* **2018**, *8*, 4812–4820. [CrossRef]
129. Sheludko, B.; Cunningham, M.T.; Goldman, A.S.; Celik, F.E. Continuous-Flow Alkane Dehydrogenation by Supported Pincer-Ligated Iridium Catalysts at Elevated Temperatures. *ACS Catal.* **2018**, *8*, 7828–7841. [CrossRef]
130. Barman, M.K.; Waiba, S.; Maji, B. Manganese-Catalyzed Direct Olefination via an Acceptorless Dehydrogenative Coupling of Methyl Heteroarenes with Primary Alcohols. *Synlett* **2019**, *30*, 12–20.
131. Thiyagarajan, S.; Gunanathan, C. Ruthenium-Catalyzed α-Olefination of Nitriles Using Secondary Alcohols. *ACS Catal.* **2018**, *8*, 2473–2478. [CrossRef]
132. Zhang, G.; Irrgang, T.; Dietel, T.; Kallmeier, F.; Kempe, R. Manganese-Catalyzed Dehydrogenative Alkylation or α-Olefination of Alkyl-Substituted N-Heteroarenes with Alcohols. *Angew. Chem. Int. Ed.* **2018**, *57*, 9131–9135. [CrossRef] [PubMed]
133. Bauer, E.B.; Andavan, G.T.S.; Hollis, T.K.; Rubio, R.J.; Cho, J.; Kuchenbeiser, G.R.; Helgert, T.R.; Letko, C.S.; Tham, F.S. Air-and water-stable catalysts for hydroamination/cyclization. Synthesis and application of CCC-NHC pincer complexes of RH and Ir. *Org. Lett.* **2008**, *10*, 1175–1178. [CrossRef] [PubMed]
134. Cho, J.; Hollis, T.K.; Valente, E.J.; Trate, J.M. CCC-N-heterocyclic carbene pincer complexes: Synthesis, characterization and hydroamination activity of a hafnium complex. *J. Organomet. Chem.* **2011**, *696*, 373–377. [CrossRef]
135. Castonguay, A.; Spasyuk, D.M.; Madern, N.; Beauchamp, A.L.; Zargarian, D. Regioselective hydroamination of acrylonitrile catalyzed by cationic pincer complexes of nickel (II). *Organometallics* **2009**, *28*, 2134–2141. [CrossRef]
136. Takaya, J.; Iwasawa, N. Hydrocarboxylation of allenes with CO_2 catalyzed by silyl pincer-type palladium complex. *J. Am. Chem. Soc.* **2008**, *130*, 15254–15255. [CrossRef]
137. Serra, D.; Cao, P.; Cabrera, J.; Padilla, R.; Rominger, F.; Limbach, M. Development of platinum (II) and -(IV) CNC pincer complexes and their application in a hydrovinylation reaction. *Organometallics* **2011**, *30*, 1885–1895. [CrossRef]
138. Mastalir, M.; Pittenauer, E.; Allmaier, G.; Kirchner, K. Manganese-Catalyzed Aminomethylation of Aromatic Compounds with Methanol as a Sustainable C1 Building Block. *J. Am. Chem. Soc.* **2017**, *139*, 8812–8815. [CrossRef]
139. Zhang, Y.; Fang, H.; Yao, W.; Leng, X.; Huang, Z. Synthesis of Pincer Hydrido Ruthenium Olefin Complexes for Catalytic Alkane Dehydrogenation. *Organometallics* **2016**, *35*, 181–188. [CrossRef]
140. Kumar, A.; Bhatti, T.M.; Goldman, A.S. Dehydrogenation of Alkanes and Aliphatic Groups by Pincer-Ligated Metal Complexes. *Chem. Rev.* **2017**, *117*, 12357–12384. [CrossRef] [PubMed]
141. Das, K.; Kumar, A. *Alkane Dehydrogenation Reactions Catalyzed by Pincer-Metal Complexes*, 1st ed.; Elsevier Inc.: Amsterdam, The Netherlands, 2019; ISBN 9780128171172.
142. Renkema, K.B.; Kissin, Y.V.; Goldman, A.S. Mechanism of alkane transfer-dehydrogenation catalyzed by a pincer-ligated iridium complex. *J. Am. Chem. Soc.* **2003**, *125*, 7770–7771. [CrossRef] [PubMed]
143. Zhu, K.; Achord, P.D.; Zhang, X.; Krogh-Jespersen, K.; Goldman, A.S. Highly effective pincer-ligated iridium catalysts for alkane dehydrogenation. DFT calculations of relevant thermodynamic, kinetic, and spectroscopic properties. *J. Am. Chem. Soc.* **2004**, *126*, 13044–13053. [CrossRef] [PubMed]
144. Göttker-Schnetmann, I.; White, P.; Brookhart, M. Iridium Bis (phosphinite) p -XPCP Pincer Complexes: Highly Active Catalysts for the Transfer Dehydrogenation of Alkanes. *J. Am. Chem. Soc.* **2004**, *126*, 1804–1811. [CrossRef] [PubMed]
145. Nawara-Hultzsch, A.J.; Hackenberg, J.D.; Punji, B.; Supplee, C.; Emge, T.J.; Bailey, B.C.; Schrock, R.R.; Brookhart, M.; Goldman, A.S. Rational design of highly active "hybrid" phosphine-phosphinite pincer iridium catalysts for alkane metathesis. *ACS Catal.* **2013**, *3*, 2505–2514. [CrossRef]
146. Chakraborty, S.; Gellrich, U.; Diskin-Posner, Y.; Leitus, G.; Avram, L.; Milstein, D. Manganese-Catalyzed N-Formylation of Amines by Methanol Liberating H_2: A Catalytic and Mechanistic Study. *Angew. Chem.* **2017**, *129*, 4293–4297. [CrossRef]

147. Daw, P.; Chakraborty, S.; Leitus, G.; Diskin-Posner, Y.; Ben-David, Y.; Milstein, D. Selective N-Formylation of Amines with H_2 and CO_2 Catalyzed by Cobalt Pincer Complexes. *ACS Catal.* **2017**, *7*, 2500–2504. [CrossRef]
148. El-Sepelgy, O.; Matador, E.; Brzozowska, A.; Rueping, M. C-Alkylation of Secondary Alcohols by Primary Alcohols through Manganese-Catalyzed Double Hydrogen Autotransfer. *ChemSusChem* **2019**, *12*, 3099–3102. [CrossRef]
149. Freitag, F.; Irrgang, T.; Kempe, R. Cobalt-Catalyzed Alkylation of Secondary Alcohols with Primary Alcohols via Borrowing Hydrogen/Hydrogen Autotransfer. *Chem. A Eur. J.* **2017**, *23*, 12110–12113. [CrossRef] [PubMed]
150. Barman, M.K.; Jana, A.; Maji, B. Phosphine-Free NNN-Manganese Complex Catalyzed α-Alkylation of Ketones with Primary Alcohols and Friedländer Quinoline Synthesis. *Adv. Synth. Catal.* **2018**, *360*, 3233–3238. [CrossRef]
151. Peña-López, M.; Piehl, P.; Elangovan, S.; Neumann, H.; Beller, M. Manganese-Catalyzed Hydrogen-Autotransfer C–C Bond Formation: α-Alkylation of Ketones with Primary Alcohols. *Angew. Chem. Int. Ed.* **2016**, *55*, 14967–14971. [CrossRef] [PubMed]
152. Elangovan, S.; Neumann, J.; Sortais, J.B.; Junge, K.; Darcel, C.; Beller, M. Efficient and selective N-alkylation of amines with alcohols catalysed by manganese pincer complexes. *Nat. Commun.* **2016**, *7*, 1–8. [CrossRef] [PubMed]
153. Mastalir, M.; Tomsu, G.; Pittenauer, E.; Allmaier, G.; Kirchner, K. Co(II) PCP Pincer Complexes as Catalysts for the Alkylation of Aromatic Amines with Primary Alcohols. *Org. Lett.* **2016**, *18*, 3462–3465. [CrossRef] [PubMed]
154. Rösler, S.; Ertl, M.; Irrgang, T.; Kempe, R. Cobalt-Catalyzed Alkylation of Aromatic Amines by Alcohols. *Angew. Chem. Int. Ed.* **2015**, *54*, 15046–15050. [CrossRef]
155. Mastalir, M.; Stöger, B.; Pittenauer, E.; Puchberger, M.; Allmaier, G.; Kirchner, K. Air Stable Iron(II) PNP Pincer Complexes as Efficient Catalysts for the Selective Alkylation of Amines with Alcohols. *Adv. Synth. Catal.* **2016**, *358*, 3824–3831. [CrossRef]
156. Homberg, L.; Roller, A.; Hultzsch, K.C. A Highly Active PN 3 Manganese Pincer Complex Performing N-Alkylation of Amines under Mild Conditions. *Org. Lett.* **2019**, *21*, 3142–3147. [CrossRef]
157. Landge, V.G.; Mondal, A.; Kumar, V.; Nandakumar, A.; Balaraman, E. Manganese catalyzed N-alkylation of anilines with alcohols: Ligand enabled selectivity. *Org. Biomol. Chem.* **2018**, *16*, 8175–8180. [CrossRef]
158. Li, J.; Lutz, M.; Klein Gebbink, R.J.M. *N*,*N*,*O*-Coordinated tricarbonylrhenium precatalysts for the aerobic deoxydehydration of diols and polyols. *Catal. Sci. Technol.* **2020**, *10*, 3782–3788. [CrossRef]
159. Siu, T.C.; Silva, I.; Lunn, M.J.; John, A. Influence of the pendant arm in deoxydehydration catalyzed by dioxomolybdenum complexes supported by amine bisphenolate ligands. *New J. Chem.* **2020**, *44*, 9933–9941. [CrossRef]
160. Petersen, A.R.; Fristrup, P. New Motifs in Deoxydehydration: Beyond the Realms of Rhenium. *Chem. A Eur. J.* **2017**, *23*, 10235–10243. [CrossRef] [PubMed]
161. Tshibalonza, N.N.; Monbaliu, J.-C.M. The deoxydehydration (DODH) reaction: A versatile technology for accessing olefins from bio-based polyols. *Green Chem.* **2020**. [CrossRef]
162. Chen, F.; Wang, N.; Lei, H.; Guo, D.; Liu, H.; Zhang, Z.; Zhang, W.; Lai, W.; Cao, R. Electrocatalytic Water Oxidation by a Water-Soluble Copper(II) Complex with a Copper-Bound Carbonate Group Acting as a Potential Proton Shuttle. *Inorg. Chem.* **2017**, *56*, 13368–13375. [CrossRef] [PubMed]
163. Lant, H.M.C.; Michaelos, T.K.; Sharninghausen, L.S.; Mercado, B.Q.; Crabtree, R.H.; Brudvig, G.W. N,N,O Pincer Ligand with a Deprotonatable Site That Promotes Redox-Leveling, High Mn Oxidation States, and a Mn_2O_2 Dimer Competent for Catalytic Oxygen Evolution. *Eur. J. Inorg. Chem.* **2019**, *2019*, 2115–2123. [CrossRef]
164. Kohl, S.W.; Weiner, L.; Schwartsburd, L.; Konstantinovski, L.; Shimon, L.J.W.; Ben-David, Y.; Iron, M.A.; Milstein, D. Consecutive Thermal H 2 and Light-Induced O 2 Evolution from Water Promoted by a Metal Complex. *Science* **2009**, *324*, 74–77. [CrossRef]
165. Sandhya, K.S.; Suresh, C.H. Water splitting promoted by a ruthenium(II) PNN complex: An alternate pathway through a dihydrogen complex for hydrogen production. *Organometallics* **2011**, *30*, 3888–3891. [CrossRef]
166. Sandhya, K.S.; Suresh, C.H. DFT study on the mechanism of water-assisted dihydrogen elimination in group 6 octahedral metal hydride complexes. *Dalt. Trans.* **2012**, *41*, 11018–11025. [CrossRef]

167. Sandhya, K.S.; Remya, G.S.; Suresh, C.H. Pincer Ligand Modifications to Tune the Activation Barrier for H_2 Elimination in Water Splitting Milstein Catalyst. *Inorg. Chem.* **2015**, *54*, 11150–11156. [CrossRef]
168. Ma, C.; Piccinin, S.; Fabris, S. Reaction mechanisms of water splitting and H_2 evolution by a Ru(II)-pincer complex identified with Ab initio metadynamics simulations. *ACS Catal.* **2012**, *2*, 1500–1506. [CrossRef]
169. Yang, X.; Hall, M.B. Mechanism of water splitting and oxygen-oxygen bond formation by a mononuclear ruthenium complex. *J. Am. Chem. Soc.* **2010**, *132*, 120–130. [CrossRef] [PubMed]
170. Nielsen, M. Catalyst Kinetics and Stability in Homogeneous Alcohol Acceptorless Dehydrogenation. In *Advanced Chemical Kinetics*; InTech: London, UK, 2018; Chapter 6; ISBN 978-953-51-3816-7.
171. Nielsen, M. Hydrogen production by homogeneous catalysis: Alcohol acceptorless dehydrogenation. In *Hydrogen Production and Remediation of Carbon and Pollutants*; Springer: Basel, Switzerland, 2015; Chapter 1; ISBN 9783319193755.
172. Valdés, H.; García-Eleno, M.A.; Canseco-Gonzalez, D.; Morales-Morales, D. Recent Advances in Catalysis with Transition-Metal Pincer Compounds. *ChemCatChem* **2018**, *10*, 3136–3172. [CrossRef]
173. Shende, V.S.; Saptal, V.B.; Bhanage, B.M. Recent Advances Utilized in the Recycling of Homogeneous Catalysis. *Chem. Rec.* **2019**, *19*, 2022–2043. [CrossRef] [PubMed]
174. Dixneuf, P.H. *Organometallics for Green Catalysis*; Springer: Basel, Switzerland, 2019; ISBN 9783030109547.
175. Werkmeister, S.; Neumann, J.; Junge, K.; Beller, M. Pincer-Type Complexes for Catalytic (De) Hydrogenation and Transfer (De) Hydrogenation Reactions: Recent Progress. *Chem. A Eur. J.* **2015**, *21*, 12226–12250. [CrossRef]
176. Crabtree, R.H. Homogeneous Transition Metal Catalysis of Acceptorless Dehydrogenative Alcohol Oxidation: Applications in Hydrogen Storage and to Heterocycle Synthesis. *Chem. Rev.* **2017**, *117*, 9228–9246. [CrossRef]
177. Gunanathan, C.; Milstein, D. Applications of Acceptorless Dehydrogenation and Related Transformations in Chemical Synthesis. *Science* **2013**, *341*, 1229712. [CrossRef]
178. Spasyuk, D.; Smith, S.; Gusev, D.G. From esters to alcohols and back with ruthenium and osmium catalysts. *Angew. Chem. Int. Ed.* **2012**, *51*, 2772–2775. [CrossRef]
179. Spasyuk, D.; Gusev, D.G. Acceptorless dehydrogenative coupling of ethanol and hydrogenation of esters and imines. *Organometallics* **2012**, *31*, 5239–5242. [CrossRef]
180. Nielsen, M.; Junge, H.; Kammer, A.; Beller, M. Towards a green process for bulk-scale synthesis of ethyl acetate: Efficient acceptorless dehydrogenation of ethanol. *Angew. Chem. Int. Ed.* **2012**, *51*, 5711–5713. [CrossRef]
181. Sponholz, P.; Mellmann, D.; Cordes, C.; Alsabeh, P.G.; Li, B.; Li, Y.; Nielsen, M.; Junge, H.; Dixneuf, P.; Beller, M. Efficient and Selective Hydrogen Generation from Bioethanol using Ruthenium Pincer-type Complexes. *ChemSusChem* **2014**, *7*, 2419–2422. [CrossRef]
182. Li, Y.; Sponholz, P.; Nielsen, M.; Junge, H.; Beller, M. Iridium-catalyzed hydrogen production from monosaccharides, disaccharide, cellulose, and lignocellulose. *ChemSusChem* **2015**, *8*, 804–808. [CrossRef]
183. Nguyen, D.H.; Trivelli, X.; Capet, F.; Swesi, Y.; Favre-Réguillon, A.; Vanoye, L.; Dumeignil, F.; Gauvin, R.M. Deeper Mechanistic Insight into Ru Pincer-Mediated Acceptorless Dehydrogenative Coupling of Alcohols: Exchanges, Intermediates, and Deactivation Species. *ACS Catal.* **2018**, *8*, 4719–4734. [CrossRef]
184. Pandey, P.; Dutta, I.; Bera, J.K. Acceptorless Alcohol Dehydrogenation: A Mechanistic Perspective. *Proc. Natl. Acad. Sci. India Sect. A Phys. Sci.* **2016**, *86*, 561–579. [CrossRef]
185. Anaby, A.; Schelwies, M.; Schwaben, J.; Rominger, F.; Hashmi, A.S.K.; Schaub, T. Study of Precatalyst Degradation Leading to the Discovery of a New Ru0 Precatalyst for Hydrogenation and Dehydrogenation. *Organometallics* **2018**, *37*, 2193–2201. [CrossRef]
186. Dub, P.A.; Gordon, J.C. The mechanism of enantioselective ketone reduction with Noyori and Noyori-Ikariya bifunctional catalysts. *Dalt. Trans.* **2016**, *45*, 6756–6781. [CrossRef] [PubMed]
187. Remya, G.S.; Suresh, C.H. Hydrogen elimination reactivity of ruthenium pincer hydride complexes: A DFT study. *New J. Chem.* **2019**, *43*, 14634–14642. [CrossRef]
188. Handgraaf, J.-W.; Meijer, E.J. Realistic Modeling of Ruthenium-Catalyzed Transfer Hydrogenation. *J. Am. Chem. Soc.* **2007**, *129*, 3099–3103. [CrossRef]
189. Hou, C.; Zhang, Z.; Zhao, C.; Ke, Z. DFT Study of Acceptorless Alcohol Dehydrogenation Mediated by Ruthenium Pincer Complexes: Ligand Tautomerization Governing Metal Ligand Cooperation. *Inorg. Chem.* **2016**, *55*, 6539–6551. [CrossRef]

190. Awasthi, M.K.; Singh, S.K. Ruthenium Catalyzed Dehydrogenation of Alcohols and Mechanistic Study. *Inorg. Chem.* **2019**, *58*, 14912–14923. [CrossRef]
191. Chen, X.; Yang, X. Mechanistic Insights and Computational Design of Transition-Metal Catalysts for Hydrogenation and Dehydrogenation Reactions. *Chem. Rec.* **2016**, *16*, 2364–2378. [CrossRef]
192. Tao, J.; Wen, L.; Lv, X.; Qi, Y.; Yin, H. Ruthenium(II)-PNN pincer complex catalyzed dehydrogenation of benzyl alcohol to ester: A DFT study. *J. Mol. Struct.* **2016**, *1110*, 24–31. [CrossRef]
193. Ji, M.; Dong, C.; Yang, X. Density functional theory prediction of cobalt pincer complexes for catalytic dehydrogenation of ethanol. *J. Coord. Chem.* **2016**, *69*, 1380–1387. [CrossRef]
194. Dub, P.A.; Gordon, J.C. Metal-ligand bifunctional catalysis: The "Accepted" mechanism, the issue of concertedness, and the function of the ligand in catalytic cycles involving hydrogen atoms. *ACS Catal.* **2017**, *7*, 6635–6655. [CrossRef]
195. Vicent, C.; Gusev, D.G. ESI-MS Insights into Acceptorless Dehydrogenative Coupling of Alcohols. *ACS Catal.* **2016**, *6*, 3301–3309. [CrossRef]
196. Dub, P.A.; Gordon, J.C. The role of the metal-bound N–H functionality in Noyori-type molecular catalysts. *Nat. Rev. Chem.* **2018**, *2*, 396–408. [CrossRef]
197. Schneider, S.; Meiners, J.; Askevold, B. Cooperative aliphatic PNP amido pincer ligands-versatile building blocks for coordination chemistry and catalysis. *Eur. J. Inorg. Chem.* **2012**, 412–429. [CrossRef]
198. Charman, H.B. Hydride transfer reactions catalysed by metal complexes. *J. Chem. Soc. B Phys. Org.* **1967**, *36*, 629–632. [CrossRef]
199. Morton, D.; Cole-Hamilton, D.J. ChemInform Abstract: Molecular Hydrogen Complexes in Catalysis: Highly Efficient Hydrogen Production from Alcoholic Substrates Catalyzed by Ruthenium Complexes. *ChemInform* **2016**, *20*, 1154–1156. [CrossRef]
200. Morton, D.; Cole-Hamilton, D.J.; Schofield, J.A.; Pryce, R.J. Rapid thermal hydrogen production from 2,3-butanediol catalyzed by homogeneous rhodium catalysis. *Polyhedron* **1987**, *6*, 2187–2189. [CrossRef]
201. Dobscn, A.; Robinson, S.D. Catalytic dehydrogenation of primary and secondary alcohols by $Ru(OCOCF_3)_2(CO)(PPh_3)_2$. *J. Organomet. Chem.* **1975**, *87*, 52–53. [CrossRef]
202. Dobson, A.; Robinson, S.D. Complexes of the Platinum Metals. 7. Homogeneous Ruthenium and Osmium Catalysts for the Dehydrogenation of Primary and Secondary Alcohols. *Inorg. Chem.* **1977**, *16*, 137–142. [CrossRef]
203. Zhang, J.; Gandelman, M.; Shimon, L.J.W.; Rozenberg, H.; Milstein, D. Electron-rich, bulky ruthenium PNP-type complexes. Acceptorless catalytic alcohol dehydrogenation. *Organometallics* **2004**, *23*, 4026–4033. [CrossRef]
204. Zhang, J.; Leitus, G.; Ben-David, Y.; Milstein, D. Facile conversion of alcohols into esters and dihydrogen catalyzed by new ruthenium complexes. *J. Am. Chem. Soc.* **2005**, *127*, 10840–10841. [CrossRef] [PubMed]
205. Milstein, D. Discovery of environmentally benign catalytic reactions of alcohols catalyzed by pyridine-based pincer Ru complexes, based on metal-ligand cooperation. *Top. Catal.* **2010**, *53*, 915–923. [CrossRef]
206. Gunanathan, C.; Milstein, D. Metal-ligand cooperation by aromatization-dearomatization: A new paradigm in bond activation and "green" catalysis. *Acc. Chem. Res.* **2011**, *44*, 588–602. [CrossRef]
207. Milstein, D. Metal-ligand cooperation by aromatization-dearomatization as a tool in single bond activation. *Phil. Trans. R. Soc. A* **2015**, *373*, 20140189. [CrossRef]
208. Khusnutdinova, J.R.; Milstein, D. Metal-Ligand Cooperation. *Angew. Chem. Int. Ed.* **2015**, *54*, 12236–12273. [CrossRef]
209. Zell, T.; Milstein, D. Hydrogenation and Dehydrogenation Iron Pincer Catalysts Capable of Metal–Ligand Cooperation by Aromatization/Dearomatization. *Acc. Chem. Res.* **2015**, *48*, 1979–1994. [CrossRef]
210. Hale, L.V.A.; Szymczak, N.K. Hydrogen Transfer Catalysis beyond the Primary Coordination Sphere. *ACS Catal.* **2018**, *8*, 6446–6461. [CrossRef]
211. Gelman, D.; Musa, S. Coordination Versatility of sp 3-Hybridized Pincer Ligands toward Ligand–Metal Cooperative Catalysis. *ACS Catal.* **2012**, *2*, 2456–2466. [CrossRef]
212. Dub, P.A.; Ikariya, T. Catalytic Reductive Transformations of Carboxylic and Carbonic Acid Derivatives Using Molecular Hydrogen. *ACS Catal.* **2012**, *2*, 1718–1741. [CrossRef]
213. Eisenstein, O.; Crabtree, R.H. Outer sphere hydrogenation catalysis. *New J. Chem.* **2013**, *37*, 21–27. [CrossRef]
214. Yang, X. Hydrogenation of carbon dioxide catalyzed by PNP pincer iridium, iron, and cobalt complexes: A computational design of base metal catalysts. *ACS Catal.* **2011**, *1*, 849–854. [CrossRef]

215. Hasanayn, F.; Baroudi, A.; Bengali, A.A.; Goldman, A.S. Hydrogenation of dimethyl carbonate to methanol by trans-[Ru(H)$_2$(PNN)(CO)] catalysts: DFT evidence for ion-pair-mediated metathesis paths for C-OMe bond cleavage. *Organometallics* **2013**, *32*, 6969–6985. [CrossRef]
216. Li, H.; Hall, M.B. Computational mechanistic studies on reactions of transition metal complexes with noninnocent pincer ligands: Aromatization-dearomatization or not. *ACS Catal.* **2015**, *5*, 1895–1913. [CrossRef]
217. Gusev, D.G. Revised Mechanisms of the Catalytic Alcohol Dehydrogenation and Ester Reduction with the Milstein PNN Complex of Ruthenium. *Organometallics* **2020**, *39*, 258–270. [CrossRef]
218. Junge, H.; Beller, M. Ruthenium-catalyzed generation of hydrogen from iso-propanol. *Tetrahedron Lett.* **2005**, *46*, 1031–1034. [CrossRef]
219. Nielsen, M.; Kammer, A.; Cozzula, D.; Junge, H.; Gladiali, S.; Beller, M. Efficient hydrogen production from alcohols under mild reaction conditions. *Angew. Chem. Int. Ed.* **2011**, *50*, 9593–9597. [CrossRef]
220. Kuriyama, W.; Matsumoto, T.; Ogata, O.; Ino, Y.; Aoki, K.; Tanaka, S.; Ishida, K.; Kobayashi, T.; Sayo, N.; Saito, T. Catalytic hydrogenation of esters. Development of an efficient catalyst and processes for synthesising (*R*)-*1*,*2*-propanediol and *2*-(*l*-Menthoxy)ethanol. *Org. Process Res. Dev.* **2012**, *16*, 166–171. [CrossRef]
221. Gunanathan, C.; Ben-David, Y.; Milstein, D. Direct Synthesis of Amides from Alcohols and Amines with Liberation of H_2. *Science* **2007**, *317*, 790–792. [CrossRef]
222. Kumar, A.; Espinosa-Jalapa, N.A.; Leitus, G.; Diskin-Posner, Y.; Avram, L.; Milstein, D. Direct Synthesis of Amides by Dehydrogenative Coupling of Amines with either Alcohols or Esters: Manganese Pincer Complex as Catalyst. *Angew. Chem. Int. Ed.* **2017**, *56*, 14992–14996. [CrossRef] [PubMed]
223. Gusev, D.G. Rethinking the dehydrogenative amide synthesis. *ACS Catal.* **2017**, *7*, 6656–6662. [CrossRef]
224. Schley, N.D.; Dobereiner, G.E.; Crabtree, R.H. Oxidative synthesis of amides and pyrroles via dehydrogenative alcohol oxidation by ruthenium diphosphine diamine complexes. *Organometallics* **2011**, *30*, 4174–4179. [CrossRef]
225. Lane, E.M.; Uttley, K.B.; Hazari, N.; Bernskoetter, W. Iron-Catalyzed Amide Formation from the Dehydrogenative Coupling of Alcohols and Secondary Amines. *Organometallics* **2017**, *36*, 2020–2025. [CrossRef]
226. Esteruelas, M.A.; Honczek, N.; Oliván, M.; Oñate, E.; Valencia, M. Direct access to pop-type osmium(II) and osmium(IV) complexes: Osmium a promising alternative to ruthenium for the synthesis of imines from alcohols and amines. *Organometallics* **2011**, *30*, 2468–2471. [CrossRef]
227. Fertig, R.; Irrgang, T.; Freitag, F.; Zander, J.; Kempe, R. Manganese-Catalyzed and Base-Switchable Synthesis of Amines or Imines via Borrowing Hydrogen or Dehydrogenative Condensation. *ACS Catal.* **2018**, *8*, 8525–8530. [CrossRef]
228. Mastalir, M.; Glatz, M.; Gorgas, N.; Stöger, B.; Pittenauer, E.; Allmaier, G.; Veiros, L.F.; Kirchner, K. Divergent Coupling of Alcohols and Amines Catalyzed by Isoelectronic Hydride MnIand FeIIPNP Pincer Complexes. *Chem. A Eur. J.* **2016**, *22*, 12316–12320. [CrossRef]
229. Borghs, J.C.; Azofra, L.M.; Biberger, T.; Linnenberg, O.; Cavallo, L.; Rueping, M.; El-Sepelgy, O. Manganese-Catalyzed Multicomponent Synthesis of Pyrroles through Acceptorless Dehydrogenation Hydrogen Autotransfer Catalysis: Experiment and Computation. *ChemSusChem* **2019**, *12*, 3083–3088. [CrossRef]
230. Gnanaprakasam, B.; Balaraman, E.; Gunanathan, C.; Milstein, D. Synthesis of polyamides from diols and diamines with liberation of H_2. *J. Polym. Sci. Part A Polym. Chem.* **2012**, *50*, 1755–1765. [CrossRef]
231. Michlik, S.; Kempe, R. A sustainable catalytic pyrrole synthesis. *Nat. Chem.* **2013**, *5*, 140–144. [CrossRef]
232. Srimani, D.; Ben-David, Y.; Milstein, D. Direct Synthesis of Pyrroles by Dehydrogenative Coupling of β-Aminoalcohols with Secondary Alcohols Catalyzed by Ruthenium Pincer Complexes. *Angew. Chem.* **2013**, *125*, 4104–4107. [CrossRef]
233. Daw, P.; Chakraborty, S.; Garg, J.A.; Ben-David, Y.; Milstein, D. Direct Synthesis of Pyrroles by Dehydrogenative Coupling of Diols and Amines Catalyzed by Cobalt Pincer Complexes. *Angew. Chem. Int. Ed.* **2016**, *55*, 14373–14377. [CrossRef] [PubMed]
234. Midya, S.P.; Landge, V.G.; Sahoo, M.K.; Rana, J.; Balaraman, E. Cobalt-catalyzed acceptorless dehydrogenative coupling of aminoalcohols with alcohols: Direct access to pyrrole, pyridine and pyrazine derivatives. *Chem. Commun.* **2017**, *54*, 90–93. [CrossRef]

235. Borghs, J.C.; Lebedev, Y.; Rueping, M.; El-Sepelgy, O. Sustainable Manganese-Catalyzed Solvent-Free Synthesis of Pyrroles from *1,4*-Diols and Primary Amines. *Org. Lett.* **2019**, *21*, 70–74. [CrossRef] [PubMed]
236. Michlik, S.; Kempe, R. Regioselectively functionalized pyridines from sustainable resources. *Angew. Chem. Int. Ed.* **2013**, *52*, 6326–6329. [CrossRef] [PubMed]
237. Gnanaprakasam, B.; Balaraman, E.; Ben-David, Y.; Milstein, D. Synthesis of peptides and pyrazines from β-amino alcohols through extrusion of h 2 catalyzed by ruthenium pincer complexes: Ligand-controlled selectivity. *Angew. Chem. Int. Ed.* **2011**, *50*, 12240–12244. [CrossRef]
238. Daw, P.; Kumar, A.; Espinosa-Jalapa, N.A.; Diskin-Posner, Y.; Ben-David, Y.; Milstein, D. Synthesis of Pyrazines and Quinoxalines via Acceptorless Dehydrogenative Coupling Routes Catalyzed by Manganese Pincer Complexes. *ACS Catal.* **2018**, *8*, 7734–7741. [CrossRef] [PubMed]
239. Das, K.; Mondal, A.; Srimani, D. Phosphine free Mn-complex catalysed dehydrogenative C-C and C-heteroatom bond formation: A sustainable approach to synthesize quinoxaline, pyrazine, benzothiazole and quinoline derivatives. *Chem. Commun.* **2018**, *54*, 10582–10585. [CrossRef]
240. Deibl, N.; Kempe, R. Manganese-Catalyzed Multicomponent Synthesis of Pyrimidines from Alcohols and Amidines. *Angew. Chem. Int. Ed.* **2017**, *56*, 1663–1666. [CrossRef]
241. Das, U.K.; Ben-David, Y.; Diskin-Posner, Y.; Milstein, D. N-Substituted Hydrazones by Manganese-Catalyzed Coupling of Alcohols with Hydrazine: Borrowing Hydrogen and Acceptorless Dehydrogenation in One System. *Angew. Chem. Int. Ed.* **2018**, *57*, 2179–2182. [CrossRef]
242. Mastalir, M.; Glatz, M.; Pittenauer, E.; Allmaier, G.; Kirchner, K. Sustainable Synthesis of Quinolines and Pyrimidines Catalyzed by Manganese PNP Pincer Complexes. *J. Am. Chem. Soc.* **2016**, *138*, 15543–15546. [CrossRef] [PubMed]
243. Chakraborty, S.; Leitus, G.; Milstein, D. Iron-Catalyzed Mild and Selective Hydrogenative Cross-Coupling of Nitriles and Amines to Form Secondary Aldimines. *Angew. Chem.* **2017**, *129*, 2106–2110. [CrossRef]
244. Mukherjee, A.; Nerush, A.; Leitus, G.; Shimon, L.J.W.; Ben David, Y.; Espinosa Jalapa, N.A.; Milstein, D. Manganese-Catalyzed Environmentally Benign Dehydrogenative Coupling of Alcohols and Amines to Form Aldimines and H_2: A Catalytic and Mechanistic Study. *J. Am. Chem. Soc.* **2016**, *138*, 4298–4301. [CrossRef] [PubMed]
245. Dai, Z.; Luo, Q.; Meng, X.; Li, R.; Zhang, J.; Peng, T. Ru(II) complexes bearing 2,6-bis(benzimidazole-2-yl)pyridine ligands: A new class of catalysts for efficient dehydrogenation of primary alcohols to carboxylic acids and H_2 in the alcohol/CsOH system. *J. Organomet. Chem.* **2017**, *830*, 11–18. [CrossRef]
246. Zhang, L.; Nguyen, D.H.; Raffa, G.; Trivelli, X.; Capet, F.; Desset, S.; Paul, S.; Dumeignil, F.; Gauvin, R.M. Catalytic Conversion of Alcohols into Carboxylic Acid Salts in Water: Scope, Recycling, and Mechanistic Insights. *ChemSusChem* **2016**, *9*, 1413–1423. [CrossRef]
247. Luo, Q.; Dai, Z.; Luo, Q.; Jiang, H.; Li, H.; Zhang, J.; Peng, T. Ni(ii)-N′NN′ pincer complexes catalyzed dehydrogenation of primary alcohols to carboxylic acids and H_2 accompanied by alcohol etherification. *Catal. Sci. Technol.* **2017**, *7*, 2506–2511.
248. Shao, Z.; Wang, Y.; Liu, Y.; Wang, Q.; Fu, X.; Liu, Q. A general and efficient Mn-catalyzed acceptorless dehydrogenative coupling of alcohols with hydroxides into carboxylates. *Org. Chem. Front.* **2018**, *5*, 1248–1256. [CrossRef]
249. Bhatia, A.; Muthaiah, S. Well-Defined Ruthenium Complex for Acceptorless Alcohol Dehydrogenation in Aqueous Medium. *ChemistrySelect* **2018**, *3*, 3737–3741. [CrossRef]
250. Huang, F.; Liu, Z.; Yu, Z. C-alkylation of ketones and related compounds by alcohols: Transition-metal-catalyzed dehydrogenation. *Angew. Chem. Int. Ed.* **2016**. [CrossRef]
251. Wang, Z.; Pan, B.; Liu, Q.; Yue, E.; Solan, G.A.; Ma, Y.; Sun, W.H. Efficient acceptorless dehydrogenation of secondary alcohols to ketones mediated by a PNN-Ru(II) catalyst. *Catal. Sci. Technol.* **2017**, *7*, 1654–1661. [CrossRef]
252. Zhang, L.; Raffa, G.; Nguyen, D.H.; Swesi, Y.; Corbel-Demailly, L.; Capet, F.; Trivelli, X.; Desset, S.; Paul, S.; Paul, J.F.; et al. Acceptorless dehydrogenative coupling of alcohols catalysed by ruthenium PNP complexes: Influence of catalyst structure and of hydrogen mass transfer. *J. Catal.* **2016**, *340*, 331–343. [CrossRef]
253. Srimani, D.; Balaraman, E.; Gnanaprakasam, B.; Ben-David, Y.; Milstein, D. Ruthenium pincer-catalyzed cross-dehydrogenative coupling of primary alcohols with secondary alcohols under neutral conditions. *Adv. Synth. Catal.* **2012**, *354*, 2403–2406. [CrossRef]

254. De Boer, S.Y.; Korstanje, T.J.; La Rooij, S.R.; Kox, R.; Reek, J.N.H.; Van Der Vlugt, J.I. Ruthenium PNN(O) Complexes: Cooperative Reactivity and Application as Catalysts for Acceptorless Dehydrogenative Coupling Reactions. *Organometallics* **2017**, *36*, 1541–1549. [CrossRef] [PubMed]
255. Nguyen, D.H.; Trivelli, X.; Capet, F.; Paul, J.F.; Dumeignil, F.; Gauvin, R.M. Manganese Pincer Complexes for the Base-Free, Acceptorless Dehydrogenative Coupling of Alcohols to Esters: Development, Scope, and Understanding. *ACS Catal.* **2017**, *7*, 2022–2032. [CrossRef]
256. Das, U.K.; Ben-David, Y.; Leitus, G.; Diskin-Posner, Y.; Milstein, D. Dehydrogenative Cross-Coupling of Primary Alcohols to Form Cross-Esters Catalyzed by a Manganese Pincer Complex. *ACS Catal.* **2019**, *9*, 479–484. [CrossRef]
257. Gunanathan, C.; Shimon, L.J.W.; Milstein, D. Direct conversion of alcohols to acetals and H_2 catalyzed by an acridine-based ruthenium pincer complex. *J. Am. Chem. Soc.* **2009**, *131*, 3146–3147. [CrossRef]
258. Das, U.K.; Chakraborty, S.; Diskin-Posner, Y.; Milstein, D. Direct Conversion of Alcohols into Alkenes by Dehydrogenative Coupling with Hydrazine/Hydrazone Catalyzed by Manganese. *Angew. Chem.* **2018**, *130*, 13632–13636. [CrossRef]
259. Musa, S.; Shaposhnikov, I.; Cohen, S.; Gelman, D. Ligand-metal cooperation in pcppincer complexes: Rational design and catalytic activity in acceptorless dehydrogenation of alcohols. *Angew. Chem. Int. Ed.* **2011**, *50*, 3533–3537. [CrossRef]
260. Peña-López, M.; Neumann, H.; Beller, M. Iron(II) Pincer-Catalyzed Synthesis of Lactones and Lactams through a Versatile Dehydrogenative Domino Sequence. *ChemCatChem* **2015**, *7*, 865–871. [CrossRef]
261. Zhao, J.; Hartwig, J.F. Acceptorless, Neat, Ruthenium-Catalyzed Dehydrogenative Cyclization of Diols to Lactones. *Organometallics* **2005**, *24*, 2441–2446. [CrossRef]
262. Chase, P.A.; Gossage, R.A.; Van Koten, G. Modern organometallic multidentate ligand design strategies: The birth of the privileged "pincer" ligand platform. In *The Privileged Pincer-Metal Platform: Coordination Chemistry & Applications*; Springer: Basel, Switzerland, 2015; ISBN 9783319229270.
263. Van Koten, G.; Gossage, R.A. *The Privileged Pincer-Metal Platform: Coordination Chemistry & Applications*; Springer: Basel, Switzerland, 2015; ISBN 9783319229270.
264. Van Koten, G. *Organometallic Pincer Chemistry*; van Koten, G., Milstein, D., Eds.; Topics in Organometallic Chemistry; Springer: Berlin/Heidelberg, Germany, 2013; ISBN 978-3-642-31080-5.
265. Szabó, K.J.; Wendt, O.F. *Pincer and Pincer-Type Complexes: Applications in Organic Synthesis and Catalysis*; Wiley-VCH: Weinheim, Germany, 2014; ISBN 9783527681303.
266. van Koten, G. Pincer ligands as powerful tools for catalysis in organic synthesis. *J. Organomet. Chem.* **2013**, *730*, 156–164. [CrossRef]
267. Niermann, M.; Beckendorff, A.; Kaltschmitt, M.; Bonhoff, K. Liquid Organic Hydrogen Carrier (LOHC)—Assessment based on chemical and economic properties. *Int. J. Hydrog. Energy* **2019**, *44*, 6631–6654. [CrossRef]
268. Zhu, Q.-L.; Xu, Q. Liquid organic and inorganic chemical hydrides for high-capacity hydrogen storage. *Energy Environ. Sci.* **2015**, *8*, 478–512. [CrossRef]
269. Biniwale, R.B.; Rayalu, S.; Devotta, S.; Ichikawa, M. Chemical hydrides: A solution to high capacity hydrogen storage and supply. *Int. J. Hydrog. Energy* **2008**, *33*, 360–365. [CrossRef]
270. Di Profio, P.; Arca, S.; Rossi, F.; Filipponi, M. Comparison of hydrogen hydrates with existing hydrogen storage technologies: Energetic and economic evaluations. *Int. J. Hydrog. Energy* **2009**, *34*, 9173–9180. [CrossRef]
271. Sotoodeh, F.; Huber, B.J.M.; Smith, K.J. Dehydrogenation kinetics and catalysis of organic heteroaromatics for hydrogen storage. *Int. J. Hydrog. Energy* **2012**, *37*, 2715–2722. [CrossRef]
272. Züttel, A. Materials for hydrogen storage. *Mater. Today* **2003**, *6*, 24–33. [CrossRef]
273. He, T.; Pei, Q.; Chen, P. Liquid organic hydrogen carriers. *J. Energy Chem.* **2015**, *24*, 587–594. [CrossRef]
274. Preuster, P.; Papp, C.; Wasserscheid, P. Liquid organic hydrogen carriers (LOHCs): Toward a hydrogen-free hydrogen economy. *Acc. Chem. Res.* **2017**, *50*, 74–85. [CrossRef]
275. Stark, K.; Emelyanenko, V.N.; Zhabina, A.A.; Varfolomeev, M.A.; Verevkin, S.P.; Müller, K.; Arlt, W. Liquid Organic Hydrogen Carriers: Thermophysical and Thermochemical Studies of Carbazole Partly and Fully Hydrogenated Derivatives. *Ind. Eng. Chem. Res.* **2015**, *54*, 7953–7966. [CrossRef]

276. Müller, K.; Stark, K.; Emelyanenko, V.N.; Varfolomeev, M.A.; Zaitsau, D.H.; Shoifet, E.; Schick, C.; Verevkin, S.P.; Arlt, W. Liquid Organic Hydrogen Carriers: Thermophysical and Thermochemical Studies of Benzyl- and Dibenzyl-toluene Derivatives. *Ind. Eng. Chem. Res.* **2015**, *54*, 7967–7976. [CrossRef]
277. Sotoodeh, F.; Smith, K.J. An overview of the kinetics and catalysis of hydrogen storage on organic liquids. *Can. J. Chem. Eng.* **2013**, *91*, 1477–1490. [CrossRef]
278. Sotoodeh, F.; Smith, K.J. Kinetics of hydrogen uptake and release from heteroaromatic compounds for hydrogen storage. *Ind. Eng. Chem. Res.* **2010**, *49*, 1018–1026. [CrossRef]
279. Müller, K.; Aslam, R.; Fischer, A.; Stark, K.; Wasserscheid, P.; Arlt, W. Experimental assessment of the degree of hydrogen loading for the dibenzyl toluene based LOHC system. *Int. J. Hydrog. Energy* **2016**, *41*, 22097–22103. [CrossRef]
280. He, T.; Pachfule, P.; Wu, H.; Xu, Q.; Chen, P. Hydrogen carriers. *Nat. Rev. Mater.* **2016**, *1*, 16059. [CrossRef]
281. Müller, K.; Völkl, J.; Arlt, W. Thermodynamic Evaluation of Potential Organic Hydrogen Carriers. *Energy Technol.* **2013**, *1*, 20–24. [CrossRef]
282. Crabtree, R.H. Hydrogen storage in liquid organic heterocycles. *Energy Environ. Sci.* **2008**, *1*, 134. [CrossRef]
283. Markiewicz, M.; Zhang, Y.Q.; Bösmann, A.; Brückner, N.; Thöming, J.; Wasserscheid, P.; Stolte, S. Environmental and health impact assessment of Liquid Organic Hydrogen Carrier (LOHC) systems—Challenges and preliminary results. *Energy Environ. Sci.* **2015**, *8*, 1035–1045. [CrossRef]
284. Teichmann, D.; Arlt, W.; Wasserscheid, P.; Freymann, R. A future energy supply based on Liquid Organic Hydrogen Carriers (LOHC). *Energy Environ. Sci.* **2011**, *4*, 2767. [CrossRef]
285. Teichmann, D.; Stark, K.; Müller, K.; Zöttl, G.; Wasserscheid, P.; Arlt, W. Energy storage in residential and commercial buildings via Liquid Organic Hydrogen Carriers (LOHC). *Energy Environ. Sci.* **2012**, *5*, 9044. [CrossRef]
286. Teichmann, D.; Arlt, W.; Wasserscheid, P. Liquid Organic Hydrogen Carriers as an efficient vector for the transport and storage of renewable energy. *Int. J. Hydrog. Energy* **2012**, *37*, 18118–18132. [CrossRef]
287. Ahmed, A.; Al-Amin, A.Q.; Ambrose, A.F.; Saidur, R. Hydrogen fuel and transport system: A sustainable and environmental future. *Int. J. Hydrog. Energy* **2016**, *41*, 1369–1380. [CrossRef]
288. Eypasch, M.; Schimpe, M.; Kanwar, A.; Hartmann, T.; Herzog, S.; Frank, T.; Hamacher, T. Model-based techno-economic evaluation of an electricity storage system based on Liquid Organic Hydrogen Carriers. *Appl. Energy* **2017**, *185*, 320–330. [CrossRef]
289. Johnson, T.C.; Morris, D.J.; Wills, M. Hydrogen generation from formic acid and alcohols using homogeneous catalysts. *Chem. Soc. Rev.* **2010**, *39*, 81–88. [CrossRef]
290. Friedrich, A.; Schneider, S. Acceptorless dehydrogenation of alcohols: Perspectives for synthesis and H_2 storage. *ChemCatChem* **2009**, *1*, 72–73. [CrossRef]
291. Trincado, M.; Banerjee, D.; Grützmacher, H. Molecular catalysts for hydrogen production from alcohols. *Energy Environ. Sci.* **2014**, *7*, 2464–2503. [CrossRef]
292. Campos, J. Dehydrogenation of alcohols and polyols from a hydrogen production perspective. *Phys. Sci. Rev.* **2018**, *3*, 1–25.
293. Shimbayashi, T.; Fujita, K. ichi Metal-catalyzed hydrogenation and dehydrogenation reactions for efficient hydrogen storage. *Tetrahedron* **2020**, *76*, 130946. [CrossRef]
294. Onishi, N.; Laurenczy, G.; Beller, M.; Himeda, Y. Recent progress for reversible homogeneous catalytic hydrogen storage in formic acid and in methanol. *Coord. Chem. Rev.* **2018**, *373*, 317–332. [CrossRef]
295. Sordakis, K.; Tang, C.; Vogt, L.K.; Junge, H.; Dyson, P.J.; Beller, M.; Laurenczy, G. Homogeneous Catalysis for Sustainable Hydrogen Storage in Formic Acid and Alcohols. *Chem. Rev.* **2018**, *118*, 372–433. [CrossRef]
296. Trincado, M.; Grützmacher, H.; Prechtl, M.H.G. CO_2-based hydrogen storage—Hydrogen generation from formaldehyde/water. *Phys. Sci. Rev.* **2018**, *3*, 1–19.
297. Langer, R.; Thomas, Z.; Schaub, T. CO_2-based hydrogen storage: CO_2 hydrogenation to formic acid, formaldehyde and methanol. *Phys. Sci. Rev.* **2018**, *3*, 1–14.
298. Boddien, A.; Gärtner, F.; Nielsen, M.; Losse, S.; Junge, H. *Hydrogen Generation from Formic Acid and Alcohols*; Elsevier: Amsterdam, The Netherland, 2013; Volume 6, pp. 587–603. ISBN 9780080965291.
299. Enthaler, S.; von Langermann, J.; Schmidt, T. Carbon dioxide and formic acid—The couple for environmental-friendly hydrogen storage? *Energy Environ. Sci.* **2010**, *3*, 1207. [CrossRef]
300. Eppinger, J.; Huang, K.W. Formic Acid as a Hydrogen Energy Carrier. *ACS Energy Lett.* **2017**, *2*, 188–195. [CrossRef]

301. Olah, G.A.; Goeppert, A.; Prakash, G.K.S. The "Methanol Economy": General Aspects. In *Beyond Oil and Gas*; Wiley: Weinheim, Germany, 2018.
302. Olah, G.A. After oil and gas: Methanol economy. *Catal. Lett.* **2004**, *93*, 1–2. [CrossRef]
303. Stephan, D.W. A step closer to a methanol economy. *Nature* **2013**, *495*, 54–55. [CrossRef]
304. Salvi, B.L.; Subramanian, K.A.; Panwar, N.L. Alternative fuels for transportation vehicles: A technical review. *Renew. Sustain. Energy Rev.* **2013**, *25*, 404–419. [CrossRef]
305. Piola, L.; Fernández-Salas, J.A.; Nahra, F.; Poater, A.; Cavallo, L.; Nolan, S.P. Ruthenium-catalysed decomposition of formic acid: Fuel cell and catalytic applications. *Mol. Catal.* **2017**, *440*, 184–189. [CrossRef]
306. Muradov, N.; Veziroglu, T. "Green" path from fossil-based to hydrogen economy: An overview of carbon-neutral technologies. *Int. J. Hydrog. Energy* **2008**, *33*, 6804–6839. [CrossRef]
307. Olah, G.A.; Prakash, G.K.S.; Goeppert, A. Anthropogenic Chemical Carbon Cycle for a Sustainable Future. *J. Am. Chem. Soc.* **2011**, *133*, 12881–12898. [CrossRef]
308. Fu, H.C.; You, F.; Li, H.R.; He, L.N. CO_2 Capture and in situ Catalytic Transformation. *Front. Chem.* **2019**, *7*, 1–15. [CrossRef]
309. Artz, J.; Müller, T.E.; Thenert, K.; Kleinekorte, J.; Meys, R.; Sternberg, A.; Bardow, A.; Leitner, W. Sustainable Conversion of Carbon Dioxide: An Integrated Review of Catalysis and Life Cycle Assessment. *Chem. Rev.* **2018**, *118*, 434–504. [CrossRef] [PubMed]
310. Klankermayer, J.; Wesselbaum, S.; Beydoun, K.; Leitner, W. Selective Catalytic Synthesis Using the Combination of Carbon Dioxide and Hydrogen: Catalytic Chess at the Interface of Energy and Chemistry. *Angew. Chem. Int. Ed.* **2016**, *55*, 7296–7343. [CrossRef] [PubMed]
311. Langer, R.; Thomas, Z.; Suárez, A. Hydrogenation of carbonyl compounds of relevance to hydrogen storage in alcohols. *Phys. Sci. Rev.* **2018**, *3*, 1–31.
312. Song, C. Global challenges and strategies for control, conversion and utilization of CO_2 for sustainable development involving energy, catalysis, adsorption and chemical processing. *Catal. Today* **2006**, *115*, 2–32. [CrossRef]
313. Rumayor, M.; Dominguez-Ramos, A.; Irabien, A. Formic Acid manufacture: Carbon dioxide utilization alternatives. *Appl. Sci.* **2018**, *8*, 1–12. [CrossRef]
314. Obama, B. The irreversible momentum of clean energy. *Science* **2017**, *355*, 126–129. [CrossRef]
315. Li, Y.; Nielsen, M.; Li, B.; Dixneuf, P.H.; Junge, H.; Beller, M. Ruthenium-catalyzed hydrogen generation from glycerol and selective synthesis of lactic acid. *Green Chem.* **2015**, *17*, 193–198. [CrossRef]
316. Sharninghausen, L.S.; Mercado, B.Q.; Crabtree, R.H.; Hazari, N. Selective conversion of glycerol to lactic acid with iron pincer precatalysts. *Chem. Commun.* **2015**, *51*, 16201–16204. [CrossRef]
317. Chakraborty, S.; Lagaditis, P.O.; Förster, M.; Bielinski, E.A.; Hazari, N.; Holthausen, M.C.; Jones, W.D.; Schneider, S. Well-Defined Iron Catalysts for the Acceptorless Reversible Dehydrogenation-Hydrogenation of Alcohols and Ketones. *ACS Catal.* **2014**, *4*, 3994–4003. [CrossRef]
318. Lane, E.M.; Hazari, N.; Bernskoetter, W.H. Iron-catalyzed urea synthesis: Dehydrogenative coupling of methanol and amines. *Chem. Sci.* **2018**, *9*, 4003–4008. [CrossRef] [PubMed]
319. Xie, Y.; Hu, P.; Ben-David, Y.; Milstein, D. A Reversible Liquid Organic Hydrogen Carrier System Based on Methanol-Ethylenediamine and Ethylene Urea. *Angew. Chem. Int. Ed.* **2019**, *58*, 5105–5109. [CrossRef] [PubMed]
320. Alberico, E.; Nielsen, M. Towards a methanol economy based on homogeneous catalysis: Methanol to H_2 and CO_2 to methanol. *Chem. Commun.* **2015**, *51*, 6714–6725. [CrossRef] [PubMed]
321. Kothandaraman, J.; Kar, S.; Goeppert, A.; Sen, R.; Prakash, G.K.S. Advances in Homogeneous Catalysis for Low Temperature Methanol Reforming in the Context of the Methanol Economy. *Top. Catal.* **2018**, *61*, 542–559. [CrossRef]
322. Simon Araya, S.; Liso, V.; Cui, X.; Li, N.; Zhu, J.; Sahlin, S.L.; Jensen, S.H.; Nielsen, M.P.; Kær, S.K. A Review of the Methanol Economy: The Fuel Cell Route. *Energies* **2020**, *13*, 596. [CrossRef]
323. Cortright, R.D.; Davda, R.R.; Dumesic, J.A. Hydrogen from catalytic reforming of biomass-derived hydrocarbons in liquid water. In *Materials for Sustainable Energy*; Macmillan Publishers Ltd.: London, UK, 2010; pp. 289–292.
324. Shabaker, J. Aqueous-phase reforming of methanol and ethylene glycol over alumina-supported platinum catalysts. *J. Catal.* **2003**, *215*, 344–352. [CrossRef]

325. Navarro, R.M.; Peña, M.A.; Fierro, J.L.G. Hydrogen Production Reactions from Carbon Feedstocks: Fossil Fuels and Biomass. *Chem. Rev.* **2007**, *107*, 3952–3991. [CrossRef]
326. Palo, D.R.; Dagle, R.A.; Holladay, J.D. Methanol Steam Reforming for Hydrogen Production. *Chem. Rev.* **2007**, *107*, 3992–4021. [CrossRef] [PubMed]
327. Sá, S.; Silva, H.; Brandão, L.; Sousa, J.M.; Mendes, A. Catalysts for methanol steam reforming—A review. *Appl. Catal. B Environ.* **2010**, *99*, 43–57. [CrossRef]
328. Iulianelli, A.; Ribeirinha, P.; Mendes, A.; Basile, A. Methanol steam reforming for hydrogen generation via conventional and membrane reactors: A review. *Renew. Sustain. Energy Rev.* **2014**, *29*, 355–368. [CrossRef]
329. Nielsen, M.; Alberico, E.; Baumann, W.; Drexler, H.J.; Junge, H.; Gladiali, S.; Beller, M. Low-temperature aqueous-phase methanol dehydrogenation to hydrogen and carbon dioxide. *Nature* **2013**, *495*, 85–89. [CrossRef] [PubMed]
330. Rodríguez-Lugo, R.E.; Trincado, M.; Vogt, M.; Tewes, F.; Santiso-Quinones, G.; Grützmacher, H. A homogeneous transition metal complex for clean hydrogen production from methanol—Water mixtures. *Nat. Chem.* **2013**, *5*, 342–347. [CrossRef]
331. Fujita, K.; Kawahara, R.; Aikawa, T.; Yamaguchi, R. Hydrogen Production from a Methanol-Water Solution Catalyzed by an Anionic Iridium Complex Bearing a Functional Bipyridonate Ligand under Weakly Basic Conditions. *Angew. Chem. Int. Ed.* **2015**, *54*, 9057–9060. [CrossRef]
332. Alberico, E.; Sponholz, P.; Cordes, C.; Nielsen, M.; Drexler, H.J.; Baumann, W.; Junge, H.; Beller, M. Selective hydrogen production from methanol with a defined Iron pincer catalyst under mild conditions. *Angew. Chem. Int. Ed.* **2013**, *52*, 14162–14166. [CrossRef] [PubMed]
333. Hu, P.; Diskin-Posner, Y.; Ben-David, Y.; Milstein, D. Reusable homogeneous catalytic system for hydrogen production from methanol and water. *ACS Catal.* **2014**, *4*, 2649–2652. [CrossRef]
334. Monney, A.; Barsch, E.; Sponholz, P.; Junge, H.; Ludwig, R.; Beller, M. Base-free hydrogen generation from methanol using a bi-catalytic system. *Chem. Commun.* **2014**, *50*, 707–709. [CrossRef] [PubMed]
335. Agapova, A.; Junge, H.; Beller, M. Developing Bicatalytic Cascade Reactions: Ruthenium-catalyzed Hydrogen Generation from Methanol. *Chem. A Eur. J.* **2019**, *25*, 9345–9349. [CrossRef] [PubMed]
336. Bielinski, E.A.; Förster, M.; Zhang, Y.; Bernskoetter, W.H.; Hazari, N.; Holthausen, M.C. Base-Free Methanol Dehydrogenation Using a Pincer-Supported Iron Compound and Lewis Acid Co-catalyst. *ACS Catal.* **2015**, *5*, 2404–2415. [CrossRef]
337. Alberico, E.; Lennox, A.J.J.; Vogt, L.K.; Jiao, H.; Baumann, W.; Drexler, H.J.; Nielsen, M.; Spannenberg, A.; Checinski, M.P.; Junge, H.; et al. Unravelling the Mechanism of Basic Aqueous Methanol Dehydrogenation Catalyzed by Ru-PNP Pincer Complexes. *J. Am. Chem. Soc.* **2016**, *138*, 14890–14904. [CrossRef]
338. Pingen, D.; Choi, J.-H.; Allen, H.; Murray, G.; Ganji, P.; van Leeuwen, P.W.N.M.; Prechtl, M.H.G.; Vogt, D. Amide versus amine ligand paradigm in the direct amination of alcohols with Ru-PNP complexes. *Catal. Sci. Technol.* **2018**, *8*, 3969–3976. [CrossRef]
339. Dub, P.A.; Scott, B.L.; Gordon, J.C. Why does alkylation of the N-H functionality within M/NH bifunctional Noyori-type catalysts lead to turnover? *J. Am. Chem. Soc.* **2017**, *139*, 1245–1260. [CrossRef]
340. Choi, J.H.; Heim, L.E.; Ahrens, M.; Prechtl, M.H.G. Selective conversion of alcohols in water to carboxylic acids by in situ generated ruthenium trans dihydrido carbonyl PNP complexes. *Dalt. Trans.* **2014**, *43*, 17248–17254. [CrossRef]
341. Wei, Z.; De Aguirre, A.; Junge, K.; Beller, M.; Jiao, H. Exploring the mechanisms of aqueous methanol dehydrogenation catalyzed by defined PNP Mn and Re pincer complexes under base-free as well as strong base conditions. *Catal. Sci. Technol.* **2018**, *8*, 3649–3665. [CrossRef]
342. Jiang, Y.Y.; Xu, Z.Y.; Yu, H.Z.; Fu, Y. A self-catalytic role of methanol in PNP-Ru pincer complex catalysed dehydrogenation. *Sci. China Chem.* **2016**, *59*, 724–729. [CrossRef]
343. Lei, M.; Pan, Y.; Ma, X. The nature of hydrogen production from aqueous-phase methanol dehydrogenation with ruthenium pincer complexes under mild conditions. *Eur. J. Inorg. Chem.* **2015**, *2015*, 794–803. [CrossRef]
344. Yang, X. Mechanistic insights into ruthenium-catalyzed production of H_2 and CO_2 from methanol and water: A DFT study. *ACS Catal.* **2014**, *4*, 1129–1133. [CrossRef]
345. Strobel, V.; Schuster, J.J.; Braeuer, A.S.; Vogt, L.K.; Junge, H.; Haumann, M. Shining light on low-temperature methanol aqueous-phase reforming using homogeneous Ru-pincer complexes-operando Raman-GC studies. *React. Chem. Eng.* **2017**, *2*, 390–396. [CrossRef]

346. Andérez-Fernández, M.; Vogt, L.K.; Fischer, S.; Zhou, W.; Jiao, H.; Garbe, M.; Elangovan, S.; Junge, K.; Junge, H.; Ludwig, R.; et al. A Stable Manganese Pincer Catalyst for the Selective Dehydrogenation of Methanol. *Angew. Chem. Int. Ed.* **2017**, *56*, 559–562. [CrossRef] [PubMed]
347. Prichatz, C.; Alberico, E.; Baumann, W.; Junge, H.; Beller, M. Iridium–PNP Pincer Complexes for Methanol Dehydrogenation at Low Base Concentration. *ChemCatChem* **2017**, *9*, 1891–1896. [CrossRef]
348. Agapova, A.; Alberico, E.; Kammer, A.; Junge, H.; Beller, M. Catalytic Dehydrogenation of Formic Acid with Ruthenium-PNP-Pincer Complexes: Comparing N-Methylated and NH-Ligands. *ChemCatChem* **2019**, *11*, 1910–1914. [CrossRef]
349. Schwarz, C.H.; Agapova, A.; Junge, H.; Haumann, M. Immobilization of a selective Ru-pincer complex for low temperature methanol reforming–Material and process improvements. *Catal. Today* **2020**, *342*, 178–186. [CrossRef]
350. Laurenczy, G.; Dyson, P.J. Homogeneous Catalytic Dehydrogenation of Formic Acid: Progress towards a Hydrogen-Based Economy. *J. Braz. Chem. Soc.* **2014**, *25*, 2157–2163. [CrossRef]
351. Treigerman, Z.; Sasson, Y. Further Observations on the Mechanism of Formic Acid Decomposition by Homogeneous Ruthenium Catalyst. *ChemistrySelect* **2017**, *2*, 5816–5823. [CrossRef]
352. Müller, K.; Brooks, K.; Autrey, T. Hydrogen Storage in Formic Acid: A Comparison of Process Options. *Energy Fuels* **2017**, *31*, 12603–12611. [CrossRef]
353. Mellmann, D.; Sponholz, P.; Junge, H.; Beller, M. Formic acid as a hydrogen storage material-development of homogeneous catalysts for selective hydrogen release. *Chem. Soc. Rev.* **2016**, *45*, 3954–3988. [CrossRef] [PubMed]
354. Guan, C.; Pan, Y.; Zhang, T.; Ajitha, M.J.; Huang, K.W. An Update on Formic Acid Dehydrogenation by Homogeneous Catalysis. *Chem. Asian J.* **2020**, *15*, 937–946. [CrossRef] [PubMed]
355. Enthaler, S.; Loges, B. The Rise of the Iron Age in Hydrogen Evolution? *ChemCatChem* **2012**, *4*, 323–325. [CrossRef]
356. Grasemann, M.; Laurenczy, G. Formic acid as a hydrogen source—Recent developments and future trends. *Energy Environ. Sci.* **2012**, *5*, 8171. [CrossRef]
357. Fukuzumi, S.; Yamada, Y.; Suenobu, T.; Ohkubo, K.; Kotani, H. Catalytic mechanisms of hydrogen evolution with homogeneous and heterogeneous catalysts. *Energy Environ. Sci.* **2011**, *4*, 2754. [CrossRef]
358. Loges, B.; Boddien, A.; Gärtner, F.; Junge, H.; Beller, M. Catalytic Generation of Hydrogen from Formic acid and its Derivatives: Useful Hydrogen Storage Materials. *Top. Catal.* **2010**, *53*, 902–914. [CrossRef]
359. Fukuzumi, S. Bioinspired Energy Conversion Systems for Hydrogen Production and Storage. *Eur. J. Inorg. Chem.* **2008**, *2008*, 1351–1362. [CrossRef]
360. Scotti, N.; Psaro, R.; Ravasio, N.; Zaccheria, F. A new Cu-based system for formic acid dehydrogenation. *RSC Adv.* **2014**, *4*, 61514–61517. [CrossRef]
361. Enthaler, S.; Brück, A.; Kammer, A.; Junge, H.; Irran, E.; Gülak, S. Exploring the reactivity of nickel pincer complexes in the decomposition of formic acid to CO_2/H_2 and the hydrogenation of $NaHCO_3$ to HCOONa. *ChemCatChem* **2015**, *7*, 65–69. [CrossRef]
362. Jiang, K.; Xu, K.; Zou, S.; Cai, W.-B. B-Doped Pd Catalyst: Boosting Room-Temperature Hydrogen Production from Formic Acid–Formate Solutions. *J. Am. Chem. Soc.* **2014**, *136*, 4861–4864. [CrossRef] [PubMed]
363. Wang, W.-H.; Ertem, M.Z.; Xu, S.; Onishi, N.; Manaka, Y.; Suna, Y.; Kambayashi, H.; Muckerman, J.T.; Fujita, E.; Himeda, Y. Highly Robust Hydrogen Generation by Bioinspired Ir Complexes for Dehydrogenation of Formic Acid in Water: Experimental and Theoretical Mechanistic Investigations at Different pH. *ACS Catal.* **2015**, *5*, 5496–5504. [CrossRef]
364. Guerriero, A.; Bricout, H.; Sordakis, K.; Peruzzini, M.; Monflier, E.; Hapiot, F.; Laurenczy, G.; Gonsalvi, L. Hydrogen Production by Selective Dehydrogenation of HCOOH Catalyzed by Ru-Biaryl Sulfonated Phosphines in Aqueous Solution. *ACS Catal.* **2014**, *4*, 3002–3012. [CrossRef]
365. Oldenhof, S.; De Bruin, B.; Lutz, M.; Siegler, M.A.; Patureau, F.W.; Van Der Vlugt, J.I.; Reek, J.N.H. Base-free production of H_2 by dehydrogenation of formic acid using an iridium-bisMETAMORPhos complex. *Chem. A Eur. J.* **2013**, *19*, 11507–11511. [CrossRef] [PubMed]
366. Tedsree, K.; Li, T.; Jones, S.; Chan, C.W.A.; Yu, K.M.K.; Bagot, P.A.J.; Marquis, E.A.; Smith, G.D.W.; Tsang, S.C.E. Hydrogen production from formic acid decomposition at room temperature using a Ag-Pd core-shell nanocatalyst. *Nat. Nanotechnol.* **2011**, *6*, 302–307. [CrossRef] [PubMed]

367. Boddien, A.; Loges, B.; Junge, H.; Gärtner, F.; Noyes, J.R.; Beller, M. Continuous hydrogen generation from formic acid: Highly active and stable ruthenium catalysts. *Adv. Synth. Catal.* **2009**, *351*, 2517–2520. [CrossRef]
368. Fellay, C.; Dyson, P.J.; Laurenczy, G. A viable hydrogen-storage system based on selective formic acid decomposition with a ruthenium catalyst. *Angew. Chem. Int. Ed.* **2008**, *47*, 3966–3968. [CrossRef] [PubMed]
369. Loges, B.; Boddien, A.; Junge, H.; Beller, M. Controlled generation of hydrogen from formic acid amine adducts at room temperature and application in H_2/O_2 fuel cells. *Angew. Chem. Int. Ed.* **2008**, *47*, 3962–3965. [CrossRef] [PubMed]
370. Czaun, M.; Goeppert, A.; May, R.; Haiges, R.; Prakash, G.K.S.; Olah, G.A. Hydrogen Generation from Formic Acid Decomposition by Ruthenium Carbonyl Complexes. Tetraruthenium Dodecacarbonyl Tetrahydride as an Active Intermediate. *ChemSusChem* **2011**, *4*, 1241–1248. [CrossRef]
371. Fukuzumi, S.; Kobayashi, T.; Suenobu, T. Efficient Catalytic Decomposition of Formic Acid for the Selective Generation of H_2 and H/D Exchange with a Water-Soluble Rhodium Complex in Aqueous Solution. *ChemSusChem* **2008**, *1*, 827–834. [CrossRef]
372. Onishi, M. Decomposition of formic acid catalyzed by hydrido (phosphonite) cobalt (I) under photoirradiation. *J. Mol. Catal.* **1993**, *80*, 145–149. [CrossRef]
373. Zhou, X.; Huang, Y.; Xing, W.; Liu, C.; Liao, J.; Lu, T. High-quality hydrogen from the catalyzed decomposition of formic acid by Pd–Au/C and Pd–Ag/C. *Chem. Commun.* **2008**, 3540. [CrossRef] [PubMed]
374. Sponholz, P.; Mellmann, D.; Junge, H.; Beller, M. Towards a Practical Setup for Hydrogen Production from Formic Acid. *ChemSusChem* **2013**, *6*, 1172–1176. [CrossRef]
375. Loges, B.; Boddien, A.; Junge, H.; Noyes, J.R.; Baumann, W.; Beller, M. Hydrogen generation: Catalytic acceleration and control by light. *Chem. Commun.* **2009**, *28*, 4185. [CrossRef]
376. Fukuzumi, S.; Kobayashi, T.; Suenobu, T. Unusually Large Tunneling Effect on Highly Efficient Generation of Hydrogen and Hydrogen Isotopes in pH-Selective Decomposition of Formic Acid Catalyzed by a Heterodinuclear Iridium–Ruthenium Complex in Water. *J. Am. Chem. Soc.* **2010**, *132*, 1496–1497. [CrossRef] [PubMed]
377. Himeda, Y. Highly efficient hydrogen evolution by decomposition of formic acid using an iridium catalyst with *4,4′*-dihydroxy-2,2′-bipyridine. *Green Chem.* **2009**, *11*, 2018. [CrossRef]
378. Tanaka, R.; Yamashita, M.; Chung, L.W.; Morokuma, K.; Nozaki, K. Mechanistic Studies on the Reversible Hydrogenation of Carbon Dioxide Catalyzed by an Ir-PNP Complex. *Organometallics* **2011**, *30*, 6742–6750. [CrossRef]
379. Gu, X.; Lu, Z.-H.; Jiang, H.-L.; Akita, T.; Xu, Q. Synergistic Catalysis of Metal–Organic Framework-Immobilized Au–Pd Nanoparticles in Dehydrogenation of Formic Acid for Chemical Hydrogen Storage. *J. Am. Chem. Soc.* **2011**, *133*, 11822–11825. [CrossRef]
380. Bi, Q.-Y.; Du, X.-L.; Liu, Y.-M.; Cao, Y.; He, H.-Y.; Fan, K.-N. Efficient Subnanometric Gold-Catalyzed Hydrogen Generation via Formic Acid Decomposition under Ambient Conditions. *J. Am. Chem. Soc.* **2012**, *134*, 8926–8933. [CrossRef]
381. Barnard, J.H.; Wang, C.; Berry, N.G.; Xiao, J. Long-range metal–ligand bifunctional catalysis: Cyclometallated iridium catalysts for the mild and rapid dehydrogenation of formic acid. *Chem. Sci.* **2013**, *4*, 1234. [CrossRef]
382. Boddien, A.; Jackstell, R.; Junge, H.; Spannenberg, A.; Baumann, W.; Ludwig, R.; Beller, M. Ortho-metalation of iron(0) tribenzylphosphine complexes: Homogeneous catalysts for the generation of hydrogen from formic acid. *Angew. Chem. Int. Ed.* **2010**, *49*, 8993–8996. [CrossRef] [PubMed]
383. Boddien, A.; Loges, B.; Gärtner, F.; Torborg, C.; Fumino, K.; Junge, H.; Ludwig, R.; Beller, M. Iron-catalyzed hydrogen production from formic acid. *J. Am. Chem. Soc.* **2010**, *132*, 8924–8934. [CrossRef] [PubMed]
384. Boddien, A.; Mellmann, D.; Gartner, F.; Jackstell, R.; Junge, H.; Dyson, P.J.; Laurenczy, G.; Ludwig, R.; Beller, M. Efficient Dehydrogenation of Formic Acid Using an Iron Catalyst. *Science* **2011**, *333*, 1733–1736. [CrossRef] [PubMed]
385. Langer, R.; Iron, M.A.; Konstantinovski, L.; Diskin-Posner, Y.; Leitus, G.; Ben-David, Y.; Milstein, D. Iron borohydride pincer complexes for the efficient hydrogenation of ketones under mild, base-free conditions: Synthesis and mechanistic insight. *Chem. A Eur. J.* **2012**, *18*, 7196–7209. [CrossRef]
386. Zhang, J.; Leitus, G.; Ben-David, Y.; Milstein, D. Efficient homogeneous catalytic hydrogenation of esters to alcohols. *Angew. Chem. Int. Ed.* **2006**, *45*, 1113–1115. [CrossRef]

387. Langer, R.; Diskin-Posner, Y.; Leitus, G.; Shimon, L.J.W.; Ben-David, Y.; Milstein, D. Low-pressure hydrogenation of carbon dioxide catalyzed by an iron pincer complex exhibiting noble metal activity. *Angew. Chem. Int. Ed.* **2011**, *50*, 9948–9952. [CrossRef] [PubMed]
388. Zell, T.; Butschke, B.; Ben-David, Y.; Milstein, D. Efficient hydrogen liberation from formic acid catalyzed by a well-defined iron pincer complex under mild conditions. *Chem. A Eur. J.* **2013**, *19*, 8068–8072. [CrossRef]
389. Bielinski, E.A.; Lagaditis, P.O.; Zhang, Y.; Mercado, B.Q.; Würtele, C.; Bernskoetter, W.H.; Hazari, N.; Schneider, S. Lewis acid-assisted formic acid dehydrogenation using a pincer-supported iron catalyst. *J. Am. Chem. Soc.* **2014**, *136*, 10234–10237. [CrossRef] [PubMed]
390. Kothandaraman, J.; Czaun, M.; Goeppert, A.; Haiges, R.; Jones, J.P.; May, R.B.; Prakash, G.K.S.; Olah, G.A. Amine-free reversible hydrogen storage in formate salts catalyzed by ruthenium pincer complex without pH control or solvent change. *ChemSusChem* **2015**, *8*, 1442–1451. [CrossRef]
391. Mellone, I.; Gorgas, N.; Bertini, F.; Peruzzini, M.; Kirchner, K.; Gonsalvi, L. Selective Formic Acid Dehydrogenation Catalyzed by Fe-PNP Pincer Complexes Based on the 2,6-Diaminopyridine Scaffold. *Organometallics* **2016**, *35*, 3344–3349. [CrossRef]
392. Mellone, I.; Bertini, F.; Peruzzini, M.; Gonsalvi, L. An active, stable and recyclable Ru(II) tetraphosphine-based catalytic system for hydrogen production by selective formic acid dehydrogenation. *Catal. Sci. Technol.* **2016**, *6*, 6504–6512. [CrossRef]
393. Czaun, M.; Kothandaraman, J.; Goeppert, A.; Yang, B.; Greenberg, S.; May, R.B.; Olah, G.A.; Prakash, G.K.S. Iridium-Catalyzed Continuous Hydrogen Generation from Formic Acid and Its Subsequent Utilization in a Fuel Cell: Toward a Carbon Neutral Chemical Energy Storage. *ACS Catal.* **2016**, *6*, 7475–7484. [CrossRef]
394. Cohen, S.; Borin, V.; Schapiro, I.; Musa, S.; De-Botton, S.; Belkova, N.V.; Gelman, D. Ir(III)-PC(sp^3)P Bifunctional Catalysts for Production of H_2 by Dehydrogenation of Formic Acid: Experimental and Theoretical Study. *ACS Catal.* **2017**, *7*, 8139–8146. [CrossRef]
395. Musa, S.; Fronton, S.; Vaccaro, L.; Gelman, D. Bifunctional ruthenium(II) PCP pincer complexes and their catalytic activity in acceptorless dehydrogenative reactions. *Organometallics* **2013**, *32*, 3069–3073. [CrossRef]
396. Musa, S.; Ghosh, A.; Vaccaro, L.; Ackermann, L.; Gelman, D. Efficient E-Selective Transfer Semihydrogenation of Alkynes by Means of Ligand-Metal Cooperating Ruthenium Catalyst. *Adv. Synth. Catal.* **2015**, *357*, 2351–2357. [CrossRef]
397. Esteruelas, M.A.; García-Yebra, C.; Martín, J.; Oñate, E. Dehydrogenation of Formic Acid Promoted by a Trihydride-Hydroxo-Osmium(IV) Complex: Kinetics and Mechanism. *ACS Catal.* **2018**, *8*, 11314–11323. [CrossRef]
398. Pan, Y.; Pan, C.L.; Zhang, Y.; Li, H.; Min, S.; Guo, X.; Zheng, B.; Chen, H.; Anders, A.; Lai, Z.; et al. Selective hydrogen generation from formic acid with well-defined complexes of ruthenium and phosphorus-nitrogen PN3-pincer ligand. *Chem. Asian J.* **2016**, *11*, 1357–1360. [CrossRef] [PubMed]
399. He, L.-P.; Chen, T.; Gong, D.; Lai, Z.; Huang, K.-W. Enhanced Reactivities toward Amines by Introducing an Imine Arm to the Pincer Ligand: Direct Coupling of Two Amines to Form an Imine Without Oxidant. *Organometallics* **2012**, *31*, 5208–5211. [CrossRef]
400. Chen, T.; Li, H.; Qu, S.; Zheng, B.; He, L.; Lai, Z.; Wang, Z.X.; Huang, K.W. Hydrogenation of esters catalyzed by ruthenium PN3-Pincer complexes containing an aminophosphine arm. *Organometallics* **2014**, *33*, 4152–4155. [CrossRef]
401. Min, S.; Rasul, S.; Li, H.; Grills, D.C.; Takanabe, K.; Li, L.J.; Huang, K.W. Electrocatalytic Reduction of Carbon Dioxide with a Well-Defined PN3-Ru Pincer Complex. *Chempluschem* **2016**, *81*, 166–171. [CrossRef]
402. Li, H.; Gonçalves, T.P.; Hu, J.; Zhao, Q.; Gong, D.; Lai, Z.; Wang, Z.; Zheng, J.; Huang, K.W. A Pseudodearomatized PN^3P^*Ni-H Complex as a Ligand and σ-Nucleophilic Catalyst. *J. Org. Chem.* **2018**, *83*, 14969–14977. [CrossRef] [PubMed]
403. Wang, X.; Ling, E.A.P.; Guan, C.; Zhang, Q.; Wu, W.; Liu, P.; Zheng, N.; Zhang, D.; Lopatin, S.; Lai, Z.; et al. Single-Site Ruthenium Pincer Complex Knitted into Porous Organic Polymers for Dehydrogenation of Formic Acid. *ChemSusChem* **2018**, *11*, 3591–3598. [CrossRef] [PubMed]
404. Nakahara, Y.; Toda, T.; Matsunami, A.; Kayaki, Y.; Kuwata, S. Protic NNN and NCN Pincer-Type Ruthenium Complexes Featuring (Trifluoromethyl) pyrazole Arms: Synthesis and Application to Catalytic Hydrogen Evolution from Formic Acid. *Chem. Asian J.* **2018**, *13*, 73–80. [CrossRef] [PubMed]

405. Curley, J.B.; Smith, N.E.; Bernskoetter, W.H.; Hazari, N.; Mercado, B.Q. Catalytic Formic Acid Dehydrogenation and CO_2 Hydrogenation Using Iron PNRP Pincer Complexes with Isonitrile Ligands. *Organometallics* **2018**, *37*, 3846–3853. [CrossRef]
406. Smith, N.E.; Bernskoetter, W.H.; Hazari, N.; Mercado, B.Q. Synthesis and Catalytic Activity of PNP-Supported Iron Complexes with Ancillary Isonitrile Ligands. *Organometallics* **2017**, *36*, 3995–4004. [CrossRef]
407. Prichatz, C.; Trincado, M.; Tan, L.; Casas, F.; Kammer, A.; Junge, H.; Beller, M.; Grützmacher, H. Highly Efficient Base-Free Dehydrogenation of Formic Acid at Low Temperature. *ChemSusChem* **2018**, *11*, 3092–3095. [CrossRef] [PubMed]
408. Zhou, W.; Wei, Z.; Spannenberg, A.; Jiao, H.; Junge, K.; Junge, H.; Beller, M. Cobalt-Catalyzed Aqueous Dehydrogenation of Formic Acid. *Chem. A Eur. J.* **2019**, *25*, 8459–8464. [CrossRef]
409. Müller, K.; Stark, K.; Müller, B.; Arlt, W. Amine borane based hydrogen carriers: An evaluation. *Energy Fuels* **2012**, *26*, 3691–3696. [CrossRef]
410. Staubitz, A.; Robertson, A.P.M.; Manners, I. Ammonia-Borane and Related Compounds as Dihydrogen Sources. *Chem. Rev.* **2010**, *110*, 4079–4124. [CrossRef]
411. Staubitz, A.; Robertson, A.P.M.; Sloan, M.E.; Manners, I. Amine– and Phosphine–Borane Adducts: New Interest in Old Molecules. *Chem. Rev.* **2010**, *110*, 4023–4078. [CrossRef]
412. Pagano, J.K.; Stelmach, J.P.W.; Waterman, R. Cobalt-catalyzed ammonia borane dehydrocoupling and transfer hydrogenation under aerobic conditions. *Dalt. Trans.* **2015**, *44*, 12074–12077. [CrossRef] [PubMed]
413. Moury, R.; Demirci, U. Hydrazine Borane and Hydrazinidoboranes as Chemical Hydrogen Storage Materials. *Energies* **2015**, *8*, 3118–3141. [CrossRef]
414. Zhao, Q.; Li, J.; Hamilton, E.J.M.; Chen, X. The continuing story of the diammoniate of diborane. *J. Organomet. Chem.* **2015**, *798*, 24–29. [CrossRef]
415. Jepsen, L.H.; Ley, M.B.; Lee, Y.-S.; Cho, Y.W.; Dornheim, M.; Jensen, J.O.; Filinchuk, Y.; Jørgensen, J.E.; Besenbacher, F.; Jensen, T.R. Boron–nitrogen based hydrides and reactive composites for hydrogen storage. *Mater. Today* **2014**, *17*, 129–135. [CrossRef]
416. Chen, X.; Zhao, J.-C.; Shore, S.G. The Roles of Dihydrogen Bonds in Amine Borane Chemistry. *Acc. Chem. Res.* **2013**, *46*, 2666–2675. [CrossRef]
417. Stubbs, N.E.; Robertson, A.P.M.; Leitao, E.M.; Manners, I. Amine–borane dehydrogenation chemistry: Metal-free hydrogen transfer, new catalysts and mechanisms, and the synthesis of polyaminoboranes. *J. Organomet. Chem.* **2013**, *730*, 84–89. [CrossRef]
418. Peng, B.; Chen, J. Ammonia borane as an efficient and lightweight hydrogen storage medium. *Energy Environ. Sci.* **2008**. [CrossRef]
419. Davis, B.L.; Dixon, D.A.; Garner, E.B.; Gordon, J.C.; Matus, M.H.; Scott, B.; Stephens, F.H. Efficient Regeneration of Partially Spent Ammonia Borane Fuel. *Angew. Chem. Int. Ed.* **2009**, *48*, 6812–6816. [CrossRef]
420. Sutton, A.D.; Burrell, A.K.; Dixon, D.A.; Garner, E.B.; Gordon, J.C.; Nakagawa, T.; Ott, K.C.; Robinson, J.P.; Vasiliu, M. Regeneration of Ammonia Borane Spent Fuel by Direct Reaction with Hydrazine and Liquid Ammonia. *Science* **2011**, *331*, 1426–1429. [CrossRef]
421. Reller, C.; Mertens, F.O.R.L. A Self-Contained Regeneration Scheme for Spent Ammonia Borane Based on the Catalytic Hydrodechlorination of BCl 3. *Angew. Chem. Int. Ed.* **2012**, *51*, 11731–11735. [CrossRef]
422. Davis, B.L.; Rekken, B.D.; Michalczyk, R.; Garner, E.B., III; Dixon, D.A.; Kalviri, H.; Baker, R.T.; Thorn, D.L. Lewis base assisted B–H bond redistribution in borazine and polyborazylene. *Chem. Commun.* **2013**, *49*, 9095. [CrossRef] [PubMed]
423. Smythe, N.C.; Gordon, J.C. Ammonia Borane as a Hydrogen Carrier: Dehydrogenation and Regeneration. *Eur. J. Inorg. Chem.* **2010**, *2010*, 509–521. [CrossRef]
424. Keaton, R.J.; Blacquiere, J.M.; Baker, R.T. Base Metal Catalyzed Dehydrogenation of Ammonia–Borane for Chemical Hydrogen Storage. *J. Am. Chem. Soc.* **2007**, *129*, 1844–1845. [CrossRef] [PubMed]
425. Vance, J.R.; Robertson, A.P.M.; Lee, K.; Manners, I. Photoactivated, Iron-Catalyzed Dehydrocoupling of Amine-Borane Adducts: Formation of Boron-Nitrogen Oligomers and Polymers. *Chem. A Eur. J.* **2011**, *17*, 4099–4103. [CrossRef]

426. Baker, R.T.; Gordon, J.C.; Hamilton, C.W.; Henson, N.J.; Lin, P.-H.; Maguire, S.; Murugesu, M.; Scott, B.L.; Smythe, N.C. Iron Complex-Catalyzed Ammonia–Borane Dehydrogenation. A Potential Route toward B–N-Containing Polymer Motifs Using Earth-Abundant Metal Catalysts. *J. Am. Chem. Soc.* **2012**, *134*, 5598–5609. [CrossRef]
427. Duman, S.; Metin, Ö.; Özkar, S. B–N Polymer Embedded Iron(0) Nanoparticles as Highly Active and Long Lived Catalyst in the Dehydrogenation of Ammonia Borane. *J. Nanosci. Nanotechnol.* **2013**, *13*, 4954–4961. [CrossRef]
428. Lichtenberg, C.; Adelhardt, M.; Gianetti, T.L.; Meyer, K.; de Bruin, B.; Grützmacher, H. Low-Valent Iron Mono-Diazadiene Compounds: Electronic Structure and Catalytic Application. *ACS Catal.* **2015**, *5*, 6230–6240. [CrossRef]
429. Kawano, Y.; Uruichi, M.; Shimoi, M.; Taki, S.; Kawaguchi, T.; Kakizawa, T.; Ogino, H. Dehydrocoupling reactions of borane-secondary and -primary amine adducts catalyzed by group-6 carbonyl complexes: Formation of aminoboranes and borazines. *J. Am. Chem. Soc.* **2009**, *131*, 14946–14957. [CrossRef]
430. Sloan, M.E.; Staubitz, A.; Clark, T.J.; Russell, C.A.; Lloyd-Jones, G.C.; Manners, I. Homogeneous Catalytic Dehydrocoupling/Dehydrogenation of Amine–Borane Adducts by Early Transition Metal, Group 4 Metallocene Complexes. *J. Am. Chem. Soc.* **2010**, *132*, 3831–3841. [CrossRef]
431. Sonnenberg, J.F.; Morris, R.H. Evidence for Iron Nanoparticles Catalyzing the Rapid Dehydrogenation of Ammonia-Borane. *ACS Catal.* **2013**, *3*, 1092–1102. [CrossRef]
432. Chaplin, A.B.; Weller, A.S. B-H activation at a rhodium(I) center: Isolation of a bimetallic complex relevant to the transition-metal-catalyzed dehydrocoupling of amine-boranes. *Angew. Chem. Int. Ed.* **2010**, *49*, 581–584. [CrossRef] [PubMed]
433. Blaquiere, N.; Diallo-Garcia, S.; Gorelsky, S.I.; Black, D.A.; Fagnou, K. Ruthenium-catalyzed dehydrogenation of ammonia boranes. *J. Am. Chem. Soc.* **2008**, *130*, 14034–14035. [CrossRef] [PubMed]
434. Bhattacharya, P.; Krause, J.A.; Guan, H. Mechanistic Studies of Ammonia Borane Dehydrogenation Catalyzed by Iron Pincer Complexes. *J. Am. Chem. Soc.* **2014**, *136*, 11153–11161. [CrossRef] [PubMed]
435. Buss, J.A.; Edouard, G.A.; Cheng, C.; Shi, J.; Agapie, T. Molybdenum Catalyzed Ammonia Borane Dehydrogenation: Oxidation State Specific Mechanisms. *J. Am. Chem. Soc.* **2014**, *136*, 11272–11275. [CrossRef]
436. Erickson, K.A.; Stelmach, J.P.W.; Mucha, N.T.; Waterman, R. Zirconium-Catalyzed Amine Borane Dehydrocoupling and Transfer Hydrogenation. *Organometallics* **2015**, *34*, 4693–4699. [CrossRef]
437. Lin, T.-P.; Peters, J.C. Boryl-Mediated Reversible H 2 Activation at Cobalt: Catalytic Hydrogenation, Dehydrogenation, and Transfer Hydrogenation. *J. Am. Chem. Soc.* **2013**, *135*, 15310–15313. [CrossRef]
438. Lichtenberg, C.; Viciu, L.; Adelhardt, M.; Sutter, J.; Meyer, K.; de Bruin, B.; Grützmacher, H. Low-Valent Iron(I) Amido Olefin Complexes as Promotors for Dehydrogenation Reactions. *Angew. Chem. Int. Ed.* **2015**, *54*, 5766–5771. [CrossRef]
439. Conley, B.L.; Guess, D.; Williams, T.J. A Robust, Air-Stable, Reusable Ruthenium Catalyst for Dehydrogenation of Ammonia Borane. *J. Am. Chem. Soc.* **2011**, *133*, 14212–14215. [CrossRef]
440. Zhang, X.; Kam, L.; Trerise, R.; Williams, T.J. Ruthenium-Catalyzed Ammonia Borane Dehydrogenation: Mechanism and Utility. *Acc. Chem. Res.* **2017**, *50*, 86–95. [CrossRef]
441. Rossin, A.; Peruzzini, M. Ammonia-Borane and Amine-Borane Dehydrogenation Mediated by Complex Metal Hydrides. *Chem. Rev.* **2016**, *116*, 8848–8872. [CrossRef]
442. Marziale, A.N.; Friedrich, A.; Klopsch, I.; Drees, M.; Celinski, V.R.; Schmedt Auf Der Günne, J.; Schneider, S. The mechanism of borane-amine dehydrocoupling with bifunctional ruthenium catalysts. *J. Am. Chem. Soc.* **2013**, *135*, 13342–13355. [CrossRef] [PubMed]
443. Glüer, A.; Förster, M.; Celinski, V.R.; Schmedt Auf Der Günne, J.; Holthausen, M.C.; Schneider, S. Highly Active Iron Catalyst for Ammonia Borane Dehydrocoupling at Room Temperature. *ACS Catal.* **2015**, *5*, 7214–7217. [CrossRef]
444. Johnson, H.C.; Hooper, T.N.; Weller, A.S. The Catalytic Dehydrocoupling of Amine–Boranes and Phosphine–Boranes. In *Topics in Organometallic Chemistry*; Springer: Basel, Switzerland, 2015; pp. 153–220.
445. Käß, M.; Friedrich, A.; Drees, M.; Schneider, S. Ruthenium complexes with cooperative PNP ligands: Bifunctional catalysts for the dehydrogenation of ammonia-borane. *Angew. Chem. Int. Ed.* **2009**, *48*, 905–907. [CrossRef] [PubMed]

446. Friedrich, A.; Drees, M.; Schneider, S. Ruthenium-catalyzed dimethylamineborane dehydrogenation: Stepwise metal-centered dehydrocyclization. *Chem. A Eur. J.* **2009**, *15*, 10339–10342. [CrossRef]
447. Han, D.; Joksch, M.; Klahn, M.; Spannenberg, A.; Drexler, H.J.; Baumann, W.; Jiao, H.; Knitsch, R.; Hansen, M.R.; Eckert, H.; et al. Iridium(III) hydrido complexes for the catalytic dehydrogenation of hydrazine borane. *Dalt. Trans.* **2016**, *45*, 17697–17704. [CrossRef]
448. Brayton, D.F.; Jensen, C.M. Dehydrogenation of pyrrolidine based liquid organic hydrogen carriers by an iridium pincer catalyst, an isothermal kinetic study. *Int. J. Hydrog. Energy* **2015**, *40*, 16266–16270. [CrossRef]
449. Titova, E.M.; Osipova, E.S.; Pavlov, A.A.; Filippov, O.A.; Safronov, S.V.; Shubina, E.S.; Belkova, N.V. Mechanism of Dimethylamine-Borane Dehydrogenation Catalyzed by an Iridium(III) PCP-Pincer Complex. *ACS Catal.* **2017**, *7*, 2325–2333. [CrossRef]
450. Denney, M.C.; Pons, V.; Hebden, T.J.; Heinekey, D.M.; Goldberg, K.I. Efficient catalysis of ammonia borane dehydrogenation. *J. Am. Chem. Soc.* **2006**, *128*, 12048–12049. [CrossRef] [PubMed]
451. Esteruelas, M.A.; Nolis, P.; Oliván, M.; Oñate, E.; Vallribera, A.; Vélez, A. Ammonia Borane Dehydrogenation Promoted by a Pincer-Square-Planar Rhodium(I) Monohydride: A Stepwise Hydrogen Transfer from the Substrate to the Catalyst. *Inorg. Chem.* **2016**, *55*, 7176–7181. [CrossRef] [PubMed]
452. Kwan, E.H.; Ogawa, H.; Yamashita, M. A Highly Active PBP–Iridium Catalyst for the Dehydrogenation of Dimethylamine–Borane: Catalytic Performance and Mechanism. *ChemCatChem* **2017**, *9*, 2457–2462. [CrossRef]
453. Kwan, E.H.; Kawai, Y.J.; Kamakura, S.; Yamashita, M. A long-tethered (P-B-P)-pincer ligand: Synthesis, complexation, and application to catalytic dehydrogenation of alkanes. *Dalt. Trans.* **2016**, *45*, 15931–15941. [CrossRef] [PubMed]
454. Hu, P.; Ben-David, Y.; Milstein, D. Rechargeable hydrogen storage system based on the dehydrogenative coupling of ethylenediamine with ethanol. *Angew. Chem. Int. Ed.* **2016**, *55*, 1061–1064. [CrossRef] [PubMed]
455. Kothandaraman, J.; Kar, S.; Sen, R.; Goeppert, A.; Olah, G.A.; Prakash, G.K.S. Efficient Reversible Hydrogen Carrier System Based on Amine Reforming of Methanol. *J. Am. Chem. Soc.* **2017**, *139*, 2549–2552. [CrossRef] [PubMed]
456. Kim, S.H.; Hong, S.H. Ruthenium-Catalyzed Urea Synthesis Using Methanol as the C1 Source. *Org. Lett.* **2016**, *18*, 212–215. [CrossRef] [PubMed]
457. Baratta, W.; Ballico, M.; Chelucci, G.; Siega, K.; Rigo, P. Osmium(II) CNN pincer complexes as efficient catalysts for both asymmetric transfer and H_2 hydrogenation of ketones. *Angew. Chem. Int. Ed.* **2008**, *47*, 4362–4365. [CrossRef] [PubMed]
458. Abdur-Rashid, K.; Clapham, S.E.; Hadzovic, A.; Harvey, J.N.; Lough, A.J.; Morris, R.H. Mechanism of the hydrogenation of ketones catalyzed by trans-dihydrido(diamine)ruthenium(II) complexes. *J. Am. Chem. Soc.* **2002**, *124*, 15104–15118. [CrossRef]
459. Abdur-Rashid, K.; Faatz, M.; Lough, A.J.; Morris, R.H. Catalytic cycle for the asymmetric hydrogenation of prochiral ketones to chiral alcohols: Direct hydride and proton transfer from chiral catalysts trans-Ru$(H)_2$(diphosphine)(diamine) to ketones and direct addition of dihydrogen to the resulting hydridoamid. *J. Am. Chem. Soc.* **2001**, *123*, 7473–7474. [CrossRef]
460. Rautenstrauch, V.; Hoang-Cong, X.; Churlaud, R.; Abdur-Rashid, K.; Morris, R.H. Hydrogenation versus Transfer Hydrogenation of Ketones: Two Established Ruthenium Systems Catalyze Both. *Chem. A Eur. J.* **2003**, *9*, 4954–4967. [CrossRef]
461. Raja, M.U.; Ramesh, R.; Ahn, K.H. Rhodium(III) NCN pincer complexes catalyzed transfer hydrogenation of ketones. *Tetrahedron Lett.* **2009**, *50*, 7014–7017. [CrossRef]
462. Hou, C.; Li, Y.; Zhao, C.; Ke, Z. A DFT study of Co(i) and Ni(ii) pincer complex-catalyzed hydrogenation of ketones: Intriguing mechanism dichotomy by ligand field variation. *Catal. Sci. Technol.* **2019**, *9*, 125–135. [CrossRef]
463. Filonenko, G.A.; Cosimi, E.; Lefort, L.; Conley, M.P.; Copéret, C.; Lutz, M.; Hensen, E.J.M.; Pidko, E.A. Lutidine-derived Ru-CNC hydrogenation pincer catalysts with versatile coordination properties. *ACS Catal.* **2014**, *4*, 2667–2671. [CrossRef]
464. Saudan, L.A.; Saudan, C.M.; Debieux, C.; Wyss, P. Dihydrogen reduction of carboxylic esters to alcohols under the catalysis of homogeneous ruthenium complexes: High efficiency and unprecedented chemoselectivity. *Angew. Chem. Int. Ed.* **2007**, *46*, 7473–7476. [CrossRef] [PubMed]

465. Yuwen, J.; Chakraborty, S.; Brennessel, W.W.; Jones, W.D. Additive-Free Cobalt-Catalyzed Hydrogenation of Esters to Alcohols. *ACS Catal.* **2017**, *7*, 3735–3740. [CrossRef]
466. Kim, D.; Le, L.; Drance, M.J.; Jensen, K.H.; Bogdanovski, K.; Cervarich, T.N.; Barnard, M.G.; Pudalov, N.J.; Knapp, S.M.M.; Chianese, A.R. Ester Hydrogenation Catalyzed by CNN-Pincer Complexes of Ruthenium. *Organometallics* **2016**, *35*, 982–989. [CrossRef]
467. Le, L.; Liu, J.; He, T.; Malek, J.C.; Cervarich, T.N.; Buttner, J.C.; Pham, J.; Keith, J.M.; Chianese, A.R. Unexpected CNN-to-CC Ligand Rearrangement in Pincer–Ruthenium Precatalysts Leads to a Base-Free Catalyst for Ester Hydrogenation. *Organometallics* **2019**, *38*, 3311–3321. [CrossRef]
468. Filonenko, G.A.; Aguila, M.J.B.; Schulpen, E.N.; Van Putten, R.; Wiecko, J.; Müller, C.; Lefort, L.; Hensen, E.J.M.; Pidko, E.A. Bis-N-heterocyclic Carbene Aminopincer Ligands Enable High Activity in Ru-Catalyzed Ester Hydrogenation. *J. Am. Chem. Soc.* **2015**, *137*, 7620–7623. [CrossRef]
469. He, T.; Buttner, J.C.; Reynolds, E.F.; Pham, J.; Malek, J.C.; Keith, J.M.; Chianese, A.R. Dehydroalkylative Activation of CNN- A nd PNN-Pincer Ruthenium Catalysts for Ester Hydrogenation. *J. Am. Chem. Soc.* **2019**, *141*, 17404–17413. [CrossRef]
470. Acosta-Ramirez, A.; Bertoli, M.; Gusev, D.G.; Schlaf, M. Homogeneous catalytic hydrogenation of long-chain esters by an osmium pincer complex and its potential application in the direct conversion of triglycerides into fatty alcohols. *Green Chem.* **2012**, *14*, 1178. [CrossRef]
471. Chakraborty, S.; Dai, H.; Bhattacharya, P.; Fairweather, N.T.; Gibson, M.S.; Krause, J.A.; Guan, H. Iron-Based Catalysts for the Hydrogenation of Esters to Alcohols. *J. Am. Chem. Soc.* **2014**, *136*, 7869–7872. [CrossRef]
472. Werkmeister, S.; Junge, K.; Wendt, B.; Alberico, E.; Jiao, H.; Baumann, W.; Junge, H.; Gallou, F.; Beller, M. Hydrogenation of esters to alcohols with a well-defined iron complex. *Angew. Chem. Int. Ed.* **2014**, *53*, 8722–8726. [CrossRef]
473. Sun, Y.; Koehler, C.; Tan, R.; Annibale, V.T.; Song, D. Ester hydrogenation catalyzed by Ru-CNN pincer complexes. *Chem. Commun.* **2011**, *47*, 8349–8351. [CrossRef]
474. Wang, Z.; Chen, X.; Liu, B.; Liu, Q.B.; Solan, G.A.; Yang, X.; Sun, W.H. Cooperative interplay between a flexible PNN-Ru(II) complex and a NaBH4 additive in the efficient catalytic hydrogenation of esters. *Catal. Sci. Technol.* **2017**, *7*, 1297–1304. [CrossRef]
475. Yan, X.; Yang, X. Mechanistic insights into the iridium catalysed hydrogenation of ethyl acetate to ethanol: A DFT study. *Dalt. Trans.* **2018**. [CrossRef] [PubMed]
476. Spasyuk, D.; Vicent, C.; Gusev, D.G. Chemoselective hydrogenation of carbonyl compounds and acceptorless dehydrogenative coupling of alcohols. *J. Am. Chem. Soc.* **2015**, *137*, 3743–3746. [CrossRef] [PubMed]
477. Qu, S.; Dai, H.; Dang, Y.; Song, C.; Wang, Z.X.; Guan, H. Computational mechanistic study of Fe-catalyzed hydrogenation of esters to alcohols: Improving catalysis by accelerating precatalyst activation with a lewis base. *ACS Catal.* **2014**, *4*, 4377–4388. [CrossRef]
478. Wei, Z.; Jiao, H. *Bifunctional Aliphatic PNP Pincer Catalysts for Hydrogenation: Mechanisms and Scope*, 1st ed.; Elsevier: Amsterdam, The Netherland, 2019; ISBN 9780128157282.
479. Hey, D.A.; Reich, R.M.; Baratta, W.; Kühn, F.E. Current advances on ruthenium(II) N-heterocyclic carbenes in hydrogenation reactions. *Coord. Chem. Rev.* **2018**, *374*, 114–132. [CrossRef]
480. Elangovan, S.; Topf, C.; Fischer, S.; Jiao, H.; Spannenberg, A.; Baumann, W.; Ludwig, R.; Junge, K.; Beller, M. Selective Catalytic Hydrogenations of Nitriles, Ketones, and Aldehydes by Well-Defined Manganese Pincer Complexes. *J. Am. Chem. Soc.* **2016**, *138*, 8809–8814. [CrossRef]
481. Schneck, F.; Assmann, M.; Balmer, M.; Harms, K.; Langer, R. Selective Hydrogenation of Amides to Amines and Alcohols Catalyzed by Improved Iron Pincer Complexes. *Organometallics* **2016**, *35*, 1931–1943. [CrossRef]
482. Artús Suàrez, L.; Culakova, Z.; Balcells, D.; Bernskoetter, W.H.; Eisenstein, O.; Goldberg, K.I.; Hazari, N.; Tilset, M.; Nova, A. The Key Role of the Hemiaminal Intermediate in the Iron-Catalyzed Deaminative Hydrogenation of Amides. *ACS Catal.* **2018**, *8*, 8751–8762. [CrossRef]
483. Jayarathne, U.; Zhang, Y.; Hazari, N.; Bernskoetter, W.H. Selective Iron-Catalyzed Deaminative Hydrogenation of Amides. *Organometallics* **2017**, *36*, 409–416. [CrossRef]
484. Coetzee, J.; Dodds, D.L.; Klankermayer, J.; Brosinski, S.; Leitner, W.; Slawin, A.M.Z.; Cole-Hamilton, D.J. Homogeneous Catalytic Hydrogenation of Amides to Amines. *Chem. A Eur. J.* **2013**, *19*, 11039–11050. [CrossRef] [PubMed]
485. Núñez Magro, A.A.; Eastham, G.R.; Cole-Hamilton, D.J. The synthesis of amines by the homogeneous hydrogenation of secondary and primary amides. *Chem. Commun.* **2007**, *30*, 3154–3156. [CrossRef] [PubMed]

486. Hernández-Juárez, M.; Vaquero, M.; Álvarez, E.; Salazar, V.; Suárez, A. Hydrogenation of imines catalysed by ruthenium(ii) complexes based on lutidine-derived CNC pincer ligands. *Dalt. Trans.* **2013**, *42*, 351–354. [CrossRef] [PubMed]
487. Hernández-Juárez, M.; López-Serrano, J.; Lara, P.; Morales-Cerón, J.P.; Vaquero, M.; Álvarez, E.; Salazar, V.; Suárez, A. Ruthenium(II) complexes containing lutidine-derived pincer CNC ligands: Synthesis, structure, and catalytic hydrogenation of C=N bonds. *Chem. A Eur. J.* **2015**, *21*, 7540–7555. [CrossRef]
488. Perera, F. Pollution from Fossil-Fuel Combustion is the Leading Environmental Threat to Global Pediatric Health and Equity: Solutions Exist. *Int. J. Environ. Res. Public Health* **2017**, *15*, 16. [CrossRef]
489. Butler, C. Climate Change, Health and Existential Risks to Civilization: A Comprehensive Review (1989–2013). *Int. J. Environ. Res. Public Health* **2018**, *15*, 2266. [CrossRef]
490. Diffenbaugh, N.S.; Singh, D.; Mankin, J.S.; Horton, D.E.; Swain, D.L.; Touma, D.; Charland, A.; Liu, Y.; Haugen, M.; Tsiang, M.; et al. Quantifying the influence of global warming on unprecedented extreme climate events. *Proc. Natl. Acad. Sci. USA* **2017**, *114*, 4881–4886. [CrossRef]
491. Haustein, K.; Allen, M.R.; Forster, P.M.; Otto, F.E.L.; Mitchell, D.M.; Matthews, H.D.; Frame, D.J. A real-time Global Warming Index. *Sci. Rep.* **2017**, *7*, 15417. [CrossRef]
492. Aresta, M. *Carbon Dioxide as Chemical Feedstock*; John Wiley & Sons: Hoboken, NJ, USA, 2010; ISBN 9783527324750.
493. Centi, G.; Perathoner, S. Opportunities and prospects in the chemical recycling of carbon dioxide to fuels. *Catal. Today* **2009**, *148*, 191–205. [CrossRef]
494. Gibson, D.H. The organometallic chemistry of carbon dioxide. *Chem. Rev.* **1996**, *96*, 2063–2095. [CrossRef]
495. Boot-Handford, M.E.; Abanades, J.C.; Anthony, E.J.; Blunt, M.J.; Brandani, S.; Mac Dowell, N.; Fernández, J.R.; Ferrari, M.-C.; Gross, R.; Hallett, J.P.; et al. Carbon capture and storage update. *Energy Environ. Sci.* **2014**, *7*, 130–189. [CrossRef]
496. Goeppert, A.; Czaun, M.; May, R.B.; Prakash, G.K.S.; Olah, G.A.; Narayanan, S.R. Carbon Dioxide Capture from the Air Using a Polyamine Based Regenerable Solid Adsorbent. *J. Am. Chem. Soc.* **2011**, *133*, 20164–20167. [CrossRef]
497. Gibbins, J.; Chalmers, H. Carbon capture and storage. *Energy Policy* **2008**, *36*, 4317–4322. [CrossRef]
498. Leung, D.Y.C.; Caramanna, G.; Maroto-Valer, M.M. An overview of current status of carbon dioxide capture and storage technologies. *Renew. Sustain. Energy Rev.* **2014**, *39*, 426–443. [CrossRef]
499. McCulloch, S.; Keeling, S.; Malischek, R.; Stanley, T. *20 Years of Carbon Capture and Storage*; OECD: Paris, France, 2016; ISBN 9789264267800.
500. Styring, P.; Jansen, D.; de Coninck, H.; Reith, H.; Armstrong, K. *Carbon Capture and Utilisation in the Green Economy*; Centre for Low Carbon Futures: New York, NY, USA, 2011.
501. de Coninck, H.; Benson, S.M. Carbon Dioxide Capture and Storage: Issues and Prospects. *Annu. Rev. Environ. Resour.* **2014**, *39*, 243–270. [CrossRef]
502. Goeppert, A.; Czaun, M.; Surya Prakash, G.K.; Olah, G.A. Air as the renewable carbon source of the future: An overview of CO_2 capture from the atmosphere. *Energy Environ. Sci.* **2012**, *5*, 7833. [CrossRef]
503. Cuéllar-Franca, R.M.; Azapagic, A. Carbon capture, storage and utilisation technologies: A critical analysis and comparison of their life cycle environmental impacts. *J. CO_2 Util.* **2015**, *9*, 82–102. [CrossRef]
504. Takht Ravanchi, M.; Sahebdelfar, S. Carbon dioxide capture and utilization in petrochemical industry: Potentials and challenges. *Appl. Petrochem. Res.* **2014**, *4*, 63–77. [CrossRef]
505. von der Assen, N.; Jung, J.; Bardow, A. Life-cycle assessment of carbon dioxide capture and utilization: Avoiding the pitfalls. *Energy Environ. Sci.* **2013**, *6*, 2721. [CrossRef]
506. Mac Dowell, N.; Fennell, P.S.; Shah, N.; Maitland, G.C. The role of CO_2 capture and utilization in mitigating climate change. *Nat. Clim. Chang.* **2017**, *7*, 243–249. [CrossRef]
507. Arakawa, H.; Aresta, M.; Armor, J.N.; Barteau, M.A.; Beckman, E.J.; Bell, A.T.; Bercaw, J.E.; Creutz, C.; Dinjus, E.; Dixon, D.A.; et al. Catalysis Research of Relevance to Carbon Management: Progress, Challenges, and Opportunities. *Chem. Rev.* **2001**, *101*, 953–996. [CrossRef]
508. Behr, A. Carbon Dioxide as an Alternative C1 Synthetic Unit: Activation by Transition-Metal Complexes. *Angew. Chem. Int. Ed. Engl.* **1988**, *27*, 661–678. [CrossRef]
509. Qiao, J.; Liu, Y.; Hong, F.; Zhang, J. A review of catalysts for the electroreduction of carbon dioxide to produce low-carbon fuels. *Chem. Soc. Rev.* **2014**, *43*, 631–675. [CrossRef] [PubMed]

510. Yin, X.; Moss, J.R. Recent developments in the activation of carbon dioxide by metal complexes. *Coord. Chem. Rev.* **1999**, *181*, 27–59. [CrossRef]
511. Sakakura, T.; Choi, J.-C.; Yasuda, H. Transformation of Carbon Dioxide. *Chem. Rev.* **2007**, *107*, 2365–2387. [CrossRef]
512. Peters, M.; Köhler, B.; Kuckshinrichs, W.; Leitner, W.; Markewitz, P.; Müller, T.E. Chemical Technologies for Exploiting and Recycling Carbon Dioxide into the Value Chain. *ChemSusChem* **2011**, *4*, 1216–1240. [CrossRef] [PubMed]
513. Aresta, M.; Dibenedetto, A. Utilisation of CO_2 as a chemical feedstock: Opportunities and challenges. *Dalt. Trans.* **2007**, 2975. [CrossRef]
514. Asinger, F. Methanol—Chemie und Energierohstoff. In *Methanol—Chem.-und Energierohstoff*; Springer: Berlin/Heidelberg, Germany, 1986.
515. Leitner, W. Carbon Dioxide as a Raw Material: The Synthesis of Formic Acid and Its Derivatives from CO_2. *Angew. Chem. Int. Ed. Engl.* **1995**, *34*, 2207–2221. [CrossRef]
516. Leitner, W. The coordination chemistry of carbon dioxide and its relevance for catalysis: A critical survey. *Coord. Chem. Rev.* **1996**, *153*, 257–284. [CrossRef]
517. Jessop, P.G.; Ikariya, T.; Noyori, R. Homogeneous Hydrogenation of Carbon Dioxide. *Chem. Rev.* **1995**, *95*, 259–272. [CrossRef]
518. Olah, G.A.; Goeppert, A.; Prakash, G.K.S. Methanol-Based Chemicals, Synthetic Hydrocarbons and Materials. In *Beyond Oil and Gas: The Methanol Economy*; Wiley: Weinheim, Germany, 2009; pp. 375–386.
519. Goeppert, A.; Czaun, M.; Jones, J.-P.; Surya Prakash, G.K.; Olah, G.A. Recycling of carbon dioxide to methanol and derived products—Closing the loop. *Chem. Soc. Rev.* **2014**, *43*, 7995–8048. [CrossRef] [PubMed]
520. Olah, G.A. Towards Oil Independence Through Renewable Methanol Chemistry. *Angew. Chem. Int. Ed.* **2013**, *52*, 104–107. [CrossRef]
521. Malik, K.; Singh, S.; Basu, S.; Verma, A. Electrochemical reduction of CO_2 for synthesis of green fuel. *Wiley Interdiscip. Rev. Energy Environ.* **2017**, *6*, e244. [CrossRef]
522. Álvarez, A.; Bansode, A.; Urakawa, A.; Bavykina, A.V.; Wezendonk, T.A.; Makkee, M.; Gascon, J.; Kapteijn, F. Challenges in the Greener Production of Formates/Formic Acid, Methanol, and DME by Heterogeneously Catalyzed CO_2 Hydrogenation Processes. *Chem. Rev.* **2017**, *117*, 9804–9838. [CrossRef]
523. Behrens, M. Heterogeneous Catalysis of CO_2 Conversion to Methanol on Copper Surfaces. *Angew. Chem. Int. Ed.* **2014**, *53*, 12022–12024. [CrossRef]
524. Dang, S.; Yang, H.; Gao, P.; Wang, H.; Li, X.; Wei, W.; Sun, Y. A review of research progress on heterogeneous catalysts for methanol synthesis from carbon dioxide hydrogenation. *Catal. Today* **2019**, *330*, 61–75. [CrossRef]
525. Jessop, P.G. Homogeneous Hydrogenation of Carbon Dioxide. In *The Handbook of Homogeneous Hydrogenation*; WILEY-VCH: Weinheim, Germany, 2007; ISBN 9783527311613.
526. Wang, W.; Wang, S.; Ma, X.; Gong, J. Recent advances in catalytic hydrogenation of carbon dioxide. *Chem. Soc. Rev.* **2011**, *40*, 3703. [CrossRef] [PubMed]
527. Benson, E.E.; Kubiak, C.P.; Sathrum, A.J.; Smieja, J.M. Electrocatalytic and homogeneous approaches to conversion of CO_2 to liquid fuels. *Chem. Soc. Rev.* **2009**, *38*, 89–99. [CrossRef] [PubMed]
528. Sanz, S.; Azua, A.; Peris, E. '(η6-arene)Ru(bis-NHC)' complexes for the reduction of CO_2 to formate with hydrogen and by transfer hydrogenation with iPrOH. *Dalt. Trans.* **2010**, *39*, 6339. [CrossRef] [PubMed]
529. Li, X.; He, X.; Liu, X.; He, L.N. Ruthenium-promoted reductive transformation of CO_2. *Sci. China Chem.* **2017**, *60*, 841–852. [CrossRef]
530. Wiedner, E.S.; Linehan, J.C. Making a Splash in Homogeneous CO_2 Hydrogenation: Elucidating the Impact of Solvent on Catalytic Mechanisms. *Chem. A Eur. J.* **2018**, *24*, 16964–16971. [CrossRef]
531. Janes, T.; Yang, Y.; Song, D. Chemical reduction of CO_2 facilitated by C-nucleophiles. *Chem. Commun.* **2017**, *53*, 11390–11398. [CrossRef] [PubMed]
532. Jiang, C.; Nichols, A.W.; Machan, C.W. A look at periodic trends in d-block molecular electrocatalysts for CO_2 reduction. *Dalt. Trans.* **2019**, *48*, 9454–9468. [CrossRef]
533. Fernández-Alvarez, F.J.; Iglesias, M.; Oro, L.A.; Polo, V. CO_2 activation and catalysis driven by iridium complexes. *ChemCatChem* **2013**, *5*, 3481–3494. [CrossRef]
534. Kang, P.; Chen, Z.; Brookhart, M.; Meyer, T.J. Electrocatalytic Reduction of Carbon Dioxide: Let the Molecules Do the Work. *Top. Catal.* **2015**, *58*, 30–45. [CrossRef]

535. Jessop, P.G.; Joó, F.; Tai, C.-C. Recent advances in the homogeneous hydrogenation of carbon dioxide. *Coord. Chem. Rev.* **2004**, *248*, 2425–2442. [CrossRef]
536. Badiei, Y.M.; Wang, W.-H.; Hull, J.F.; Szalda, D.J.; Muckerman, J.T.; Himeda, Y.; Fujita, E. Cp*Co(III) Catalysts with Proton-Responsive Ligands for Carbon Dioxide Hydrogenation in Aqueous Media. *Inorg. Chem.* **2013**, *52*, 12576–12586. [CrossRef] [PubMed]
537. Jeletic, M.S.; Mock, M.T.; Appel, A.M.; Linehan, J.C. A Cobalt-Based Catalyst for the Hydrogenation of CO_2 under Ambient Conditions. *J. Am. Chem. Soc.* **2013**, *135*, 11533–11536. [CrossRef] [PubMed]
538. Zhang, G.; Vasudevan, K.V.; Scott, B.L.; Hanson, S.K. Understanding the Mechanisms of Cobalt-Catalyzed Hydrogenation and Dehydrogenation Reactions. *J. Am. Chem. Soc.* **2013**, *135*, 8668–8681. [CrossRef] [PubMed]
539. Glüer, A.; Schneider, S. Iron catalyzed hydrogenation and electrochemical reduction of CO_2: The role of functional ligands. *J. Organomet. Chem.* **2018**, *861*, 159–173. [CrossRef]
540. Jeletic, M.S.; Helm, M.L.; Hulley, E.B.; Mock, M.T.; Appel, A.M.; Linehan, J.C. A Cobalt Hydride Catalyst for the Hydrogenation of CO_2: Pathways for Catalysis and Deactivation. *ACS Catal.* **2014**, *4*, 3755–3762. [CrossRef]
541. Jeletic, M.S.; Hulley, E.B.; Helm, M.L.; Mock, M.T.; Appel, A.M.; Wiedner, E.S.; Linehan, J.C. Understanding the Relationship Between Kinetics and Thermodynamics in CO_2 Hydrogenation Catalysis. *ACS Catal.* **2017**, *7*, 6008–6017. [CrossRef]
542. Shaffer, D.W.; Johnson, S.I.; Rheingold, A.L.; Ziller, J.W.; Goddard, W.A.; Nielsen, R.J.; Yang, J.Y. Reactivity of a Series of Isostructural Cobalt Pincer Complexes with CO_2, CO, and H^+. *Inorg. Chem.* **2014**, *53*, 13031–13041. [CrossRef] [PubMed]
543. Hojilla Atienza, C.C.; Milsmann, C.; Semproni, S.P.; Turner, Z.R.; Chirik, P.J. Reversible Carbon–Carbon Bond Formation Induced by Oxidation and Reduction at a Redox-Active Cobalt Complex. *Inorg. Chem.* **2013**, *52*, 5403–5417. [CrossRef] [PubMed]
544. Dubey, A.; Nencini, L.; Fayzullin, R.R.; Nervi, C.; Khusnutdinova, J.R. Bio-Inspired Mn(I) Complexes for the Hydrogenation of CO_2 to Formate and Formamide. *ACS Catal.* **2017**, *7*, 3864–3868. [CrossRef]
545. Jewess, M.; Crabtree, R.H. Electrocatalytic Nitrogen Fixation for Distributed Fertilizer Production? *ACS Sustain. Chem. Eng.* **2016**, *4*, 5855–5858. [CrossRef]
546. Liu, H. *Ammonia Synthesis Catalysts: Innovation and Practice*; World Scientific: Beijing, China, 2013; ISBN 9789814355780.
547. Jacobsen, C.J.H.; Dahl, S.; Clausen, B.S.; Bahn, S.; Logadottir, A.; Nørskov, J.K. Catalyst Design by Interpolation in the Periodic Table: Bimetallic Ammonia Synthesis Catalysts. *J. Am. Chem. Soc.* **2001**, *123*, 8404–8405. [CrossRef]
548. Liu, H. Ammonia synthesis catalyst 100 years: Practice, enlightenment and challenge. *Chinese J. Catal.* **2014**, *35*, 1619–1640. [CrossRef]
549. Levi, P.G.; Cullen, J.M. Mapping Global Flows of Chemicals: From Fossil Fuel Feedstocks to Chemical Products. *Environ. Sci. Technol.* **2018**, *52*, 1725–1734. [CrossRef]
550. Canfield, D.E.; Glazer, A.N.; Falkowski, P.G. The Evolution and Future of Earth's Nitrogen Cycle. *Science* **2010**, *330*, 192–196. [CrossRef]
551. Galloway, J.N.; Townsend, A.R.; Erisman, J.W.; Bekunda, M.; Cai, Z.; Freney, J.R.; Martinelli, L.A.; Seitzinger, S.P.; Sutton, M.A. Transformation of the Nitrogen Cycle: Recent Trends, Questions, and Potential Solutions. *Science* **2008**, *320*, 889–892. [CrossRef]
552. Gruber, N.; Galloway, J.N. An Earth-system perspective of the global nitrogen cycle. *Nature* **2008**, *451*, 293–296. [CrossRef]
553. U.S. Geological Survay. *Mineral Commodity Summaries*; U.S. Geological Survay: Reston, VA, USA, 2020; ISBN 9781411343627.
554. Lipman, T.; Shah, N. Ammonia as an Alternative Energy Storage Medium for Hydrogen Fuel Cells: Scientific and Technical Review for Near-Term Stationary Power Demonstration Projects, Final Report. *Inst. Transp. Stud. Res. Rep. Work. Pap. Proc.* 2007. Available online: https://escholarship.org/uc/item/7z69v4wp (accessed on 9 July 2020).
555. Lan, R.; Irvine, J.T.S.; Tao, S. Ammonia and related chemicals as potential indirect hydrogen storage materials. *Int. J. Hydrog. Energy* **2012**, *37*, 1482–1494. [CrossRef]
556. Lan, R.; Tao, S. Ammonia as a Suitable Fuel for Fuel Cells. *Front. Energy Res.* **2014**, *2*, 1–4. [CrossRef]

557. Federsel, C.; Jackstell, R.; Beller, M. State-of-the-art catalysts for hydrogenation of carbon dioxide. *Angew. Chem. Int. Ed.* **2010**, *49*, 6254–6257. [CrossRef] [PubMed]
558. Kar, S.; Goeppert, A.; Prakash, G.K.S. Integrated CO_2 Capture and Conversion to Formate and Methanol: Connecting Two Threads. *Acc. Chem. Res.* **2019**, *52*, 2892–2903. [CrossRef]
559. Kar, S.; Kothandaraman, J.; Goeppert, A.; Prakash, G.K.S. Advances in catalytic homogeneous hydrogenation of carbon dioxide to methanol. *J. CO_2 Util.* **2018**, *23*, 212–218. [CrossRef]
560. Munshi, P.; Main, A.D.; Linehan, J.C.; Tai, C.C.; Jessop, P.G. Hydrogenation of carbon dioxide catalyzed by ruthenium trimethylphosphine complexes: The accelerating effect of certain alcohols and amines. *J. Am. Chem. Soc.* **2002**, *124*, 7963–7971. [CrossRef]
561. Urakawa, A.; Jutz, F.; Laurenczy, G.; Baiker, A. Carbon dioxide hydrogenation catalyzed by a ruthenium dihydride: A DFT and high-pressure spectroscopic investigation. *Chem. A Eur. J.* **2007**, *13*, 3886–3899. [CrossRef]
562. Jessop, P.G.; Hsiao, Y.; Ikariya, T.; Noyori, R. Homogeneous Catalysis in Supercritical Fluids: Hydrogenation of Supercritical Carbon Dioxide to Formic Acid, Alkyl Formates, and Formamides. *J. Am. Chem. Soc.* **1996**, *118*, 344–355. [CrossRef]
563. Jessop, P.G.; Ikariya, T.; Noyori, R. Homogeneous catalytic hydrogenation of supercritical carbon dioxide. *Nature* **1994**, *368*, 231–233. [CrossRef]
564. Graf, E.; Leitner, W. Direct formation of formic acid from carbon dioxide and dihydrogen using the $[\{Rh(cod)Cl\}_2]$–$Ph_2P(CH_2)_4PPh_2$ catalyst system. *J. Chem. Soc., Chem. Commun.* **1992**, 623–624. [CrossRef]
565. Gassner, F.; Leitner, W. Hydrogenation of carbon dioxide to formic acid using water-soluble rhodium catalyststs. *J. Chem. Soc. Chem. Commun.* **1993**, 1465. [CrossRef]
566. Angermund, K.; Baumann, W.; Dinjus, E.; Fornika, R.; Görls, H.; Kessler, M.; Krüger, C.; Leitner, W.; Lutz, F. Complexes [(P2)Rh(hfacac)] as Model Compounds for the Fragment [(P2)Rh] and as Highly Active Catalysts for CO_2 Hydrogenation: The Accessible Molecular Surface (AMS) Model as an Approach to Quantifying the Intrinsic Steric Properties of Chelating Ligands i. *Chem. A Eur. J.* **1997**, *3*, 755–764. [CrossRef]
567. Himeda, Y.; Onozawa-Komatsuzaki, N.; Sugihara, H.; Kasuga, K. Simultaneous tuning of activity and water solubility of complex catalysts by acid-base equilibrium of ligands for conversion of carbon dioxide. *Organometallics* **2007**, *26*, 702–712. [CrossRef]
568. Tanaka, R.; Yamashita, M.; Nozaki, K. Catalytic Hydrogenation of Carbon Dioxide Using Ir(III)-Pincer Complexes RID E-4607-2010 RID E-8779-2010. *J. Am. Chem. Soc.* **2009**, *131*, 14168–14169. [CrossRef] [PubMed]
569. Schmeier, T.J.; Dobereiner, G.E.; Crabtree, R.H.; Hazari, N. Secondary coordination sphere interactions facilitate the insertion step in an iridium(III) CO_2 reduction catalyst. *J. Am. Chem. Soc.* **2011**, *133*, 9274–9277. [CrossRef]
570. Federsel, C.; Boddien, A.; Jackstell, R.; Jennerjahn, R.; Dyson, P.J.; Scopelliti, R.; Laurenczy, G.; Beller, M. A well-defined iron catalyst for the reduction of bicarbonates and carbon dioxide to formates, alkyl formates, and formamides. *Angew. Chem. Int. Ed.* **2010**, *49*, 9777–9780. [CrossRef]
571. Balaraman, E.; Gunanathan, C.; Zhang, J.; Shimon, L.J.W.; Milstein, D. Efficient hydrogenation of organic carbonates, carbamates and formates indicates alternative routes to methanol based on CO_2 and CO. *Nat. Chem.* **2011**, *3*, 609–614. [CrossRef] [PubMed]
572. Huff, C.A.; Sanford, M.S. Cascade catalysis for the homogeneous hydrogenation of CO_2 to methanol. *J. Am. Chem. Soc.* **2011**, *133*, 18122–18125. [CrossRef]
573. Balaraman, E.; Ben-David, Y.; Milstein, D. Unprecedented catalytic hydrogenation of urea derivatives to amines and methanol. *Angew. Chem. Int. Ed.* **2011**, *50*, 11702–11705. [CrossRef] [PubMed]
574. Ostapowicz, T.G.; Hölscher, M.; Leitner, W. CO_2 insertion into metal-carbon bonds: A computational study of RhI pincer complexes. *Chem. A Eur. J.* **2011**, *17*, 10329–10338. [CrossRef]
575. Ostapowicz, T.G.; Schmitz, M.; Krystof, M.; Klankermayer, J.; Leitner, W. Carbon dioxide as a C1 building block for the formation of carboxylic acids by formal catalytic hydrocarboxylation. *Angew. Chem. Int. Ed.* **2013**, *52*, 12119–12123. [CrossRef]
576. Wesselbaum, S.; Vom Stein, T.; Klankermayer, J.; Leitner, W. Hydrogenation of carbon dioxide to methanol by using a homogeneous ruthenium-phosphine catalyst. *Angew. Chem. Int. Ed.* **2012**, *51*, 7499–7502. [CrossRef] [PubMed]

577. Geilen, F.M.A.; Engendahl, B.; Hölscher, M.; Klankermayer, J.; Leitner, W. Selective Homogeneous Hydrogenation of Biogenic Carboxylic Acids with [Ru(TriPhos)H] +: A Mechanistic Study. *J. Am. Chem. Soc.* **2011**, *133*, 14349–14358. [CrossRef] [PubMed]
578. Wesselbaum, S.; Moha, V.; Meuresch, M.; Brosinski, S.; Thenert, K.M.; Kothe, J.; vom Stein, T.; Englert, U.; Hölscher, M.; Klankermayer, J.; et al. Hydrogenation of carbon dioxide to methanol using a homogeneous ruthenium-Triphos catalyst: From mechanistic investigations to multiphase catalysis. *Chem. Sci.* **2015**, *6*, 693–704. [CrossRef]
579. Beydoun, K.; Vom Stein, T.; Klankermayer, J.; Leitner, W. Ruthenium-catalyzed direct methylation of primary and secondary aromatic amines using carbon dioxide and molecular hydrogen. *Angew. Chem. Int. Ed.* **2013**, *52*, 9554–9557. [CrossRef]
580. Kang, P.; Cheng, C.; Chen, Z.; Schauer, C.K.; Meyer, T.J.; Brookhart, M. Selective electrocatalytic reduction of CO_2 to formate by water-stable iridium dihydride pincer complexes. *J. Am. Chem. Soc.* **2012**, *134*, 5500–5503. [CrossRef]
581. Osadchuk, I.; Tamm, T.; Ahlquist, M.S.G. Reduced State of Iridium PCP Pincer Complexes in Electrochemical CO_2 Hydrogenation. *ACS Catal.* **2016**, *6*, 3834–3839. [CrossRef]
582. Elmas, S.; Subhani, M.A.; Vogt, H.; Leitner, W.; Müller, T.E. Facile insertion of CO_2 into metal-phenoxide bonds. *Green Chem.* **2013**, *15*, 1356–1360. [CrossRef]
583. Vogt, M.; Rivada-Wheelaghan, O.; Iron, M.A.; Leitus, G.; Diskin-Posner, Y.; Shimon, L.J.W.; Ben-David, Y.; Milstein, D. Anionic nickel(II) complexes with doubly deprotonated PNP pincer-type ligands and their reactivity toward CO_2. *Organometallics* **2013**, *32*, 300–308. [CrossRef]
584. Hull, J.F.; Himeda, Y.; Wang, W.-H.; Hashiguchi, B.; Periana, R.; Szalda, D.J.; Muckerman, J.T.; Fujita, E. Reversible hydrogen storage using CO_2 and a proton-switchable iridium catalyst in aqueous media under mild temperatures and pressures. *Nat. Chem.* **2012**, *4*, 383–388. [CrossRef] [PubMed]
585. Sordakis, K.; Tsurusaki, A.; Iguchi, M.; Kawanami, H.; Himeda, Y.; Laurenczy, G. Carbon Dioxide to Methanol: The Aqueous Catalytic Way at Room Temperature. *Chem. A Eur. J.* **2016**, *22*, 15605–15608. [CrossRef] [PubMed]
586. Rezayee, N.M.; Huff, C.A.; Sanford, M.S. Tandem amine and ruthenium-catalyzed hydrogenation of CO_2 to methanol. *J. Am. Chem. Soc.* **2015**, *137*, 1028–1031. [CrossRef] [PubMed]
587. Khusnutdinova, J.R.; Garg, J.A.; Milstein, D. Combining Low-Pressure CO_2 Capture and Hydrogenation to Form Methanol. *ACS Catal.* **2015**, *5*, 2416–2422. [CrossRef]
588. Shao, R.; Stangeland, A. Amines Used in CO_2 Capture-Health and Environmental Impacts. Bellona Found. Norway, Oslo. 2009. Available online: https://network.bellona.org/content/uploads/sites/3/fil_Bellona_report_September_2009_-_Amines_used_in_CO2_capture.pdf (accessed on 9 July 2020).
589. Kothandaraman, J.; Goeppert, A.; Czaun, M.; Olah, G.A.; Prakash, G.K.S. Conversion of CO_2 from Air into Methanol Using a Polyamine and a Homogeneous Ruthenium Catalyst. *J. Am. Chem. Soc.* **2016**, *138*, 778–781. [CrossRef]
590. Kar, S.; Sen, R.; Goeppert, A.; Prakash, G.K.S. Integrative CO_2 Capture and hydrogenation to methanol with reusable catalyst and amine: Toward a carbon neutral methanol economy. *J. Am. Chem. Soc.* **2018**, *140*, 1580–1583. [CrossRef]
591. Kar, S.; Goeppert, A.; Prakash, G.K.S. Combined CO_2 Capture and Hydrogenation to Methanol: Amine Immobilization Enables Easy Recycling of Active Elements. *ChemSusChem* **2019**, *12*, 3172–3177. [CrossRef]
592. Kar, S.; Sen, R.; Kothandaraman, J.; Goeppert, A.; Chowdhury, R.; Munoz, S.B.; Haiges, R.; Prakash, G.K.S. Mechanistic Insights into Ruthenium-Pincer-Catalyzed Amine-Assisted Homogeneous Hydrogenation of CO_2 to Methanol. *J. Am. Chem. Soc.* **2019**, *141*, 3160–3170. [CrossRef]
593. Rawat, K.S.; Pathak, B. Aliphatic Mn-PNP complexes for the CO_2 hydrogenation reaction: A base free mechanism. *Catal. Sci. Technol.* **2017**, *7*, 3234–3242. [CrossRef]
594. Mandal, S.C.; Rawat, K.S.; Nandi, S.; Pathak, B. Theoretical insights into CO_2 hydrogenation to methanol by a Mn-PNP complex. *Catal. Sci. Technol.* **2019**, *9*, 1867–1878. [CrossRef]
595. Kar, S.; Goeppert, A.; Kothandaraman, J.; Prakash, G.K.S. Manganese-Catalyzed Sequential Hydrogenation of CO_2 to Methanol via Formamide. *ACS Catal.* **2017**, *7*, 6347–6351. [CrossRef]
596. Sen, R.; Goeppert, A.; Kar, S.; Prakash, G.K.S. Hydroxide Based Integrated CO_2 Capture from Air and Conversion to Methanol. *J. Am. Chem. Soc.* **2020**, *142*, 4544–4549. [CrossRef] [PubMed]

597. Schneidewind, J.; Adam, R.; Baumann, W.; Jackstell, R.; Beller, M. Low-Temperature Hydrogenation of Carbon Dioxide to Methanol with a Homogeneous Cobalt Catalyst. *Angew. Chem. Int. Ed.* **2017**, *56*, 1890–1893. [CrossRef] [PubMed]
598. Korstanje, T.J.; Ivar van der Vlugt, J.; Elsevier, C.J.; de Bruin, B. Hydrogenation of carboxylic acids with a homogeneous cobalt catalyst. *Science* **2015**, *350*, 298–302. [CrossRef]
599. Scharnagl, F.K.; Hertrich, M.F.; Neitzel, G.; Jackstell, R.; Beller, M. Homogeneous Catalytic Hydrogenation of CO_2 to Methanol—Improvements with Tailored Ligands. *Adv. Synth. Catal.* **2019**, *361*, 374–379.
600. Schieweck, B.G.; Klankermayer, J. Tailor-made Molecular Cobalt Catalyst System for the Selective Transformation of Carbon Dioxide to Dialkoxymethane Ethers. *Angew. Chem. Int. Ed.* **2017**, *56*, 10854–10857. [CrossRef]
601. Kumar, A.; Janes, T.; Espinosa-Jalapa, N.A.; Milstein, D. Manganese Catalyzed Hydrogenation of Organic Carbonates to Methanol and Alcohols. *Angew. Chem. Int. Ed.* **2018**, *57*, 12076–12080. [CrossRef] [PubMed]
602. Zubar, V.; Lebedev, Y.; Azofra, L.M.; Cavallo, L.; El-Sepelgy, O.; Rueping, M. Hydrogenation of CO_2-Derived Carbonates and Polycarbonates to Methanol and Diols by Metal–Ligand Cooperative Manganese Catalysis. *Angew. Chem. Int. Ed.* **2018**, *57*, 13439–13443. [CrossRef] [PubMed]
603. Ma, Q.Q.; Liu, T.; Li, S.; Zhang, J.; Chen, X.; Guan, H. Highly efficient reduction of carbon dioxide with a borane catalyzed by bis(phosphinite) pincer ligated palladium thiolate complexes. *Chem. Commun.* **2016**, *52*, 14262–14265. [CrossRef]
604. Erken, C.; Kaithal, A.; Sen, S.; Weyhermüller, T.; Hölscher, M.; Werlé, C.; Leitner, W. Manganese-catalyzed hydroboration of carbon dioxide and other challenging carbonyl groups. *Nat. Commun.* **2018**, *9*, 1–9. [CrossRef]
605. Motokura, K.; Kashiwame, D.; Takahashi, N.; Miyaji, A.; Baba, T. Highly Active and Selective Catalysis of Copper Diphosphine Complexes for the Transformation of Carbon Dioxide into Silyl Formate. *Chem. A Eur. J.* **2013**, *19*, 10030–10037. [CrossRef]
606. Rit, A.; Zanardi, A.; Spaniol, T.P.; Maron, L.; Okuda, J. A Cationic Zinc Hydride Cluster Stabilized by an N-Heterocyclic Carbene: Synthesis, Reactivity, and Hydrosilylation Catalysis. *Angew. Chem. Int. Ed.* **2014**, *53*, 13273–13277. [CrossRef]
607. Tüchler, M.; Gärtner, L.; Fischer, S.; Boese, A.D.; Belaj, F.; Mösch-Zanetti, N.C. Efficient CO_2 Insertion and Reduction Catalyzed by a Terminal Zinc Hydride Complex. *Angew. Chem. Int. Ed.* **2018**, *57*, 6906–6909. [CrossRef]
608. Eisenschmid, T.C.; Eisenberg, R. The iridium complex catalyzed reduction of carbon dioxide to methoxide by alkylsilanes. *Organometallics* **1989**, *8*, 1822–1824. [CrossRef]
609. Riduan, S.N.; Zhang, Y.; Ying, J.Y. Conversion of Carbon Dioxide into Methanol with Silanes over N-Heterocyclic Carbene Catalysts. *Angew. Chem. Int. Ed.* **2009**, *48*, 3322–3325. [CrossRef]
610. Metsänen, T.T.; Oestreich, M. Temperature-Dependent Chemoselective Hydrosilylation of Carbon Dioxide to Formaldehyde or Methanol Oxidation State. *Organometallics* **2015**, *34*, 543–546. [CrossRef]
611. Scheuermann, M.L.; Semproni, S.P.; Pappas, I.; Chirik, P.J. Carbon dioxide hydrosilylation promoted by cobalt pincer complexes. *Inorg. Chem.* **2014**, *53*, 9463–9465. [CrossRef] [PubMed]
612. Huang, F.; Zhang, C.; Jiang, J.; Wang, Z.-X.; Guan, H. How Does the Nickel Pincer Complex Catalyze the Conversion of CO_2 to a Methanol Derivative? A Computational Mechanistic Study. *Inorg. Chem.* **2011**, *50*, 3816–3825. [CrossRef] [PubMed]
613. Bertini, F.; Glatz, M.; Stöger, B.; Peruzzini, M.; Veiros, L.F.; Kirchner, K.; Gonsalvi, L. Carbon Dioxide Reduction to Methanol Catalyzed by Mn(I) PNP Pincer Complexes under Mild Reaction Conditions. *ACS Catal.* **2019**, *9*, 632–639. [CrossRef]
614. Mazzotta, M.G.; Xiong, M.; Abu-Omar, M.M. Carbon Dioxide Reduction to Silyl-Protected Methanol Catalyzed by an Oxorhenium Pincer PNN Complex. *Organometallics* **2017**, *36*, 1688–1691. [CrossRef]
615. Ryabchuk, P.; Stier, K.; Junge, K.; Checinski, M.P.; Beller, M. Molecularly Defined Manganese Catalyst for Low-Temperature Hydrogenation of Carbon Monoxide to Methanol. *J. Am. Chem. Soc.* **2019**, *141*, 16923–16929. [CrossRef]
616. Kar, S.; Goeppert, A.; Prakash, G.K.S. Catalytic Homogeneous Hydrogenation of CO to Methanol via Formamide. *J. Am. Chem. Soc.* **2019**, *141*, 12518–12521. [CrossRef]

617. Schneck, F.; Schendzielorz, F.; Hatami, N.; Finger, M.; Würtele, C.; Schneider, S. Photochemically Driven Reverse Water-Gas Shift at Ambient Conditions mediated by a Nickel Pincer Complex. *Angew. Chem. Int. Ed.* **2018**, *57*, 14482–14487. [CrossRef]
618. Schneck, F.; Ahrens, J.; Finger, M.; Stückl, A.C.; Würtele, C.; Schwarzer, D.; Schneider, S. The elusive abnormal CO_2 insertion enabled by metal-ligand cooperative photochemical selectivity inversion. *Nat. Commun.* **2018**, *9*, 1–8. [CrossRef]
619. Feller, M.; Ben-Ari, E.; Diskin-Posner, Y.; Milstein, D. CO_2 activation by metal–ligand-cooperation mediated by iridium pincer complexes. *J. Coord. Chem.* **2018**, *71*, 1679–1689. [CrossRef]
620. Feller, M.; Gellrich, U.; Anaby, A.; Diskin-Posner, Y.; Milstein, D. Reductive Cleavage of CO_2 by Metal-Ligand-Cooperation Mediated by an Iridium Pincer Complex. *J. Am. Chem. Soc.* **2016**, *138*, 6445–6454. [CrossRef] [PubMed]
621. Anaby, A.; Feller, M.; Ben-David, Y.; Leitus, G.; Diskin-Posner, Y.; Shimon, L.J.W.; Milstein, D. Bottom-Up Construction of a CO_2-Based Cycle for the Photocarbonylation of Benzene, Promoted by a Rhodium(I) Pincer Complex. *J. Am. Chem. Soc.* **2016**, *138*, 9941–9950. [CrossRef]
622. Krishnan, V.M.; Arman, H.D.; Tonzetich, Z.J. Preparation and reactivity of a square-planar PNP cobalt(II)-hydrido complex: Isolation of the first {Co-NO} 8 -hydride. *Dalt. Trans.* **2018**, *47*, 1435–1441. [CrossRef] [PubMed]
623. Muller, K.; Sun, Y.; Heimermann, A.; Menges, F.; Niedner-Schatteburg, G.; van Wüllen, C.; Thiel, W.R. Structure-Reactivity Relationships in the Hydrogenation of Carbon Dioxide with Ruthenium Complexes Bearing Pyridinylazolato Ligands. *Chem. A Eur. J.* **2013**, *19*, 7825–7834. [CrossRef]
624. Thai, T.-T.; Therrien, B.; Süss-Fink, G. Arene ruthenium oxinato complexes: Synthesis, molecular structure and catalytic activity for the hydrogenation of carbon dioxide in aqueous solution. *J. Organomet. Chem.* **2009**, *694*, 3973–3981. [CrossRef]
625. Gao, Y.; Kuncheria, J.K.; Jenkins, H.A.; Puddephatt, R.J.; Yap, G.P.A. The interconversion of formic acid and hydrogen/carbon dioxide using a binuclear ruthenium complex catalyst. *J. Chem. Soc. Dalt. Trans.* **2000**, 3212–3217. [CrossRef]
626. Zhang, J.Z.; Li, Z.; Wang, H.; Wang, C.Y. Homogeneous catalytic synthesis of formic acid (salts) by hydrogenation of CO_2 with H_2 in the presence of ruthenium species. *J. Mol. Catal. A Chem.* **1996**, *112*, 9–14. [CrossRef]
627. Wesselbaum, S.; Hintermair, U.; Leitner, W. Continuous-Flow Hydrogenation of Carbon Dioxide to Pure Formic Acid using an Integrated $scCO_2$ Process with Immobilized Catalyst and Base. *Angew. Chem. Int. Ed.* **2012**, *51*, 8585–8588. [CrossRef]
628. Boddien, A.; Federsel, C.; Sponholz, P.; Mellmann, D.; Jackstell, R.; Junge, H.; Laurenczy, G.; Beller, M. Towards the development of a hydrogen battery. *Energy Environ. Sci.* **2012**, *5*, 8907. [CrossRef]
629. Elek, J.; Nádasdi, L.; Papp, G.; Laurenczy, G.; Joó, F. Homogeneous hydrogenation of carbon dioxide and bicarbonate in aqueous solution catalyzed by water-soluble ruthenium(II) phosphine complexes. *Appl. Catal. A Gen.* **2003**, *255*, 59–67. [CrossRef]
630. Jantke, D.; Pardatscher, L.; Drees, M.; Cokoja, M.; Herrmann, W.A.; Kühn, F.E. Hydrogen Production and Storage on a Formic Acid/Bicarbonate Platform using Water-Soluble N -Heterocyclic Carbene Complexes of Late Transition Metals. *ChemSusChem* **2016**, *9*, 2849–2854. [CrossRef]
631. Chatterjee, D.; Sarkar, P. Ru III (edta) catalyzed hydrogenation of bicarbonate to formate. *J. Coord. Chem.* **2016**, *69*, 650–655. [CrossRef]
632. Boddien, A.; Gärtner, F.; Federsel, C.; Sponholz, P.; Mellmann, D.; Jackstell, R.; Junge, H.; Beller, M. CO_2-"Neutral" Hydrogen Storage Based on Bicarbonates and Formates. *Angew. Chem. Int. Ed.* **2011**, *50*, 6411–6414. [CrossRef] [PubMed]
633. Federsel, C.; Jackstell, R.; Boddien, A.; Laurenczy, G.; Beller, M. Ruthenium-Catalyzed Hydrogenation of Bicarbonate in Water. *ChemSusChem* **2010**, *3*, 1048–1050. [CrossRef] [PubMed]
634. Ziebart, C.; Federsel, C.; Anbarasan, P.; Jackstell, R.; Baumann, W.; Spannenberg, A.; Beller, M. Well-defined iron catalyst for improved hydrogenation of carbon dioxide and bicarbonate. *J. Am. Chem. Soc.* **2012**, *134*, 20701–20704. [CrossRef]
635. Federsel, C.; Ziebart, C.; Jackstell, R.; Baumann, W.; Beller, M. Catalytic hydrogenation of carbon dioxide and bicarbonates with a well-defined cobalt dihydrogen complex. *Chem. A Eur. J.* **2012**, *18*, 72–75. [CrossRef]

636. Liu, Q.; Wu, L.; Gülak, S.; Rockstroh, N.; Jackstell, R.; Beller, M. Towards a sustainable synthesis of formate salts: Combined catalytic methanol dehydrogenation and bicarbonate hydrogenation. *Angew. Chem. Int. Ed.* **2014**, *53*, 7085–7088. [CrossRef] [PubMed]
637. Huff, C.A.; Sanford, M.S. Catalytic CO_2 hydrogenation to formate by a ruthenium pincer complex. *ACS Catal.* **2013**. [CrossRef]
638. Filonenko, G.A.; van Putten, R.; Schulpen, E.N.; Hensen, E.J.M.; Pidko, E.A. Highly Efficient Reversible Hydrogenation of Carbon Dioxide to Formates Using a Ruthenium PNP-Pincer Catalyst. *ChemCatChem* **2014**, *6*, 1526–1530. [CrossRef]
639. Zhang, Y.; MacIntosh, A.D.; Wong, J.L.; Bielinski, E.A.; Williard, P.G.; Mercado, B.Q.; Hazari, N.; Bernskoetter, W.H. Iron catalyzed CO_2 hydrogenation to formate enhanced by Lewis acid co-catalysts. *Chem. Sci.* **2015**, *6*, 4291–4299. [CrossRef]
640. Bernskoetter, W.H.; Hazari, N. Reversible Hydrogenation of Carbon Dioxide to Formic Acid and Methanol: Lewis Acid Enhancement of Base Metal Catalysts. *Acc. Chem. Res.* **2017**, *50*, 1049–1058. [CrossRef] [PubMed]
641. Spentzos, A.Z.; Barnes, C.L.; Bernskoetter, W.H. Effective Pincer Cobalt Precatalysts for Lewis Acid Assisted CO_2 Hydrogenation. *Inorg. Chem.* **2016**, *55*, 8225–8233. [CrossRef]
642. Mills, M.R.; Barnes, C.L.; Bernskoetter, W.H. Influences of Bifunctional PNP-Pincer Ligands on Low Valent Cobalt Complexes Relevant to CO_2 Hydrogenation. *Inorg. Chem.* **2018**, *57*, 1590–1597. [CrossRef]
643. Rivada-Wheelaghan, O.; Dauth, A.; Leitus, G.; Diskin-Posner, Y.; Milstein, D. Synthesis and reactivity of iron complexes with a new pyrazine-based pincer ligand, and application in catalytic low-pressure hydrogenation of carbon dioxide. *Inorg. Chem.* **2015**, *54*, 4526–4538. [CrossRef]
644. Bertini, F.; Gorgas, N.; Stöger, B.; Peruzzini, M.; Veiros, L.F.; Kirchner, K.; Gonsalvi, L. Efficient and Mild Carbon Dioxide Hydrogenation to Formate Catalyzed by Fe(II) Hydrido Carbonyl Complexes Bearing 2,6-(Diaminopyridyl)diphosphine Pincer Ligands. *ACS Catal.* **2016**, *6*, 2889–2893. [CrossRef]
645. Kothandaraman, J.; Goeppert, A.; Czaun, M.; Olah, G.A.; Surya Prakash, G.K. CO_2 capture by amines in aqueous media and its subsequent conversion to formate with reusable ruthenium and iron catalysts. *Green Chem.* **2016**, *18*, 5831–5838. [CrossRef]
646. Kar, S.; Goeppert, A.; Galvan, V.; Chowdhury, R.; Olah, J.; Prakash, G.K.S. A Carbon-Neutral CO_2 Capture, Conversion, and Utilization Cycle with Low-Temperature Regeneration of Sodium Hydroxide. *J. Am. Chem. Soc.* **2018**, *140*, 16873–16876. [CrossRef] [PubMed]
647. Treigerman, Z.; Sasson, Y. Generation and Quantification of Formate Ion Produced from Aqueous Sodium Bicarbonate in the Presence of Homogeneous Ruthenium Catalyst. *ACS Omega* **2018**, *3*, 12797–12801. [CrossRef]
648. Dai, Z.; Luo, Q.; Cong, H.; Zhang, J.; Peng, T. New Ru(ii) N′NN′-type pincer complexes: Synthesis, characterization and the catalytic hydrogenation of CO_2 or bicarbonates to formate salts. *New J. Chem.* **2017**, *41*, 3055–3060. [CrossRef]
649. Bertini, F.; Glatz, M.; Gorgas, N.; Stöger, B.; Peruzzini, M.; Veiros, L.F.; Kirchner, K.; Gonsalvi, L. Carbon dioxide hydrogenation catalysed by well-defined Mn(i) PNP pincer hydride complexes. *Chem. Sci.* **2017**, *8*, 5024–5029. [CrossRef]
650. Ramaraj, A.; Nethaji, M.; Jagirdar, B.R. Hydrogenation of CO_2, carbonyl and imine substrates catalyzed by $[IrH_3(^{Ph}PN^{H}P)]$ complex. *J. Organomet. Chem.* **2019**, *883*, 25–34. [CrossRef]
651. Lo, H.K.; Copéret, C. CO_2 Hydrogenation to Formate with Immobilized Ru-Catalysts Based on Hybrid Organo-Silica Mesostructured Materials. *ChemCatChem* **2019**, *11*, 430–434. [CrossRef]
652. Foster, S.L.; Bakovic, S.I.P.; Duda, R.D.; Maheshwari, S.; Milton, R.D.; Minteer, S.D.; Janik, M.J.; Renner, J.N.; Greenlee, L.F. Catalysts for nitrogen reduction to ammonia. *Nat. Catal.* **2018**, *1*, 490–500. [CrossRef]
653. Hölscher, M.; Prechtl, M.H.G.; Leitner, W. Can $[M(H)_2(H_2)(PXP)]$ pincer complexes (M = Fe, Ru, Os; X = N, O, S) serve as catalyst lead structures for NH_3 synthesis from N_2 and H_2? *Chem. A Eur. J.* **2007**, *13*, 6636–6643. [CrossRef]
654. Stucke, N.; Flöser, B.M.; Weyrich, T.; Tuczek, F. Nitrogen Fixation Catalyzed by Transition Metal Complexes: Recent Developments. *Eur. J. Inorg. Chem.* **2018**, *2018*, 1337–1355. [CrossRef]
655. Nishibayashi, Y. Development of catalytic nitrogen fixation using transition metal-dinitrogen complexes under mild reaction conditions. *Dalt. Trans.* **2018**, *47*, 11290–11297. [CrossRef]
656. Nishibayashi, Y. Recent Progress in Transition-Metal-Catalyzed Reduction of Molecular Dinitrogen under Ambient Reaction Conditions. *Inorg. Chem.* **2015**, *54*, 9234–9247. [CrossRef]

657. Tanabe, Y.; Nishibayashi, Y. Catalytic Dinitrogen Fixation to Form Ammonia at Ambient Reaction Conditions Using Transition Metal-Dinitrogen Complexes. *Chem. Rec.* **2016**, *16*, 1549–1577. [CrossRef]
658. Nishibayashi, Y. Molybdenum-catalyzed reduction of molecular dinitrogen into ammonia under ambient reaction conditions. *Comptes Rendus Chim.* **2015**, *18*, 776–784. [CrossRef]
659. Burford, R.J.; Fryzuk, M.D. Examining the relationship between coordination mode and reactivity of dinitrogen. *Nat. Rev. Chem.* **2017**, *1*, 0026. [CrossRef]
660. Shipman, M.A.; Symes, M.D. Recent progress towards the electrosynthesis of ammonia from sustainable resources. *Catal. Today* **2017**, *286*, 57–68. [CrossRef]
661. Cherkasov, N.; Ibhadon, A.O.; Fitzpatrick, P. A review of the existing and alternative methods for greener nitrogen fixation. *Chem. Eng. Process Process Intensif.* **2015**, *90*, 24–33. [CrossRef]
662. Giddey, S.; Badwal, S.P.S.; Kulkarni, A. Review of electrochemical ammonia production technologies and materials. *Int. J. Hydrog. Energy* **2013**, *38*, 14576–14594. [CrossRef]
663. Cui, X.; Tang, C.; Zhang, Q. A Review of Electrocatalytic Reduction of Dinitrogen to Ammonia under Ambient Conditions. *Adv. Energy Mater.* **2018**, *8*, 1800369. [CrossRef]
664. Roux, Y.; Duboc, C.; Gennari, M. Molecular Catalysts for N_2 Reduction: State of the Art, Mechanism, and Challenges. *ChemPhysChem* **2017**, *18*, 2606–2617. [CrossRef] [PubMed]
665. Tanaka, H.; Nishibayashi, Y.; Yoshizawa, K. Interplay between Theory and Experiment for Ammonia Synthesis Catalyzed by Transition Metal Complexes. *Acc. Chem. Res.* **2016**, *49*, 987–995. [CrossRef] [PubMed]
666. van der Ham, C.J.M.; Koper, M.T.M.; Hetterscheid, D.G.H. Challenges in reduction of dinitrogen by proton and electron transfer. *Chem. Soc. Rev.* **2014**, *43*, 5183–5191. [CrossRef] [PubMed]
667. Renner, J.N.; Greenlee, L.F.; Ayres, K.E.; Herring, A.M. Electrochemical Synthesis of Ammonia: A Low Pressure, Low Temperature Approach. *Interface Mag.* **2015**, *24*, 51–57. [CrossRef]
668. Allen, A.D.; Senoff, C.V. Nitrogenopentammineruthenium(II) complexes. *Chem. Commun.* **1965**, *24*, 621–622. [CrossRef]
669. Benedek, Z.; Papp, M.; Oláh, J.; Szilvási, T. Identifying the Rate-Limiting Elementary Steps of Nitrogen Fixation with Single-Site Fe Model Complexes. *Inorg. Chem.* **2018**, *57*, 8499–8508. [CrossRef] [PubMed]
670. Tanabe, Y.; Nishibayashi, Y. Recent advances in nitrogen fixation upon vanadium complexes. *Coord. Chem. Rev.* **2019**, *381*, 135–150. [CrossRef]
671. Clentsmith, G.K.B.; Bates, V.M.E.; Hitchcock, P.B.; Cloke, F.G.N. Reductive Cleavage of Dinitrogen by a Vanadium Diamidoamine Complex: The Molecular Structures of $[V(Me_3SiN\{CH_2CH_2NSiMe_3\}_2)(\mu\text{-}N)]_2$ and $K[V(Me_3SiN\{CH_2CH_2NSiMe_3\}_2)(\mu\text{-}N)]_2$. *J. Am. Chem. Soc.* **1999**, *121*, 10444–10445. [CrossRef]
672. Gradert, C.; Stucke, N.; Krahmer, J.; Näther, C.; Tuczek, F. Molybdenum complexes supported by mixed NHC/phosphine ligands: Activation of N_2 and reaction with $P(OMe)_3$ to the first meta-phosphite complex. *Chem. A Eur. J.* **2015**, *21*, 1130–1137. [CrossRef]
673. Husch, T.; Reiher, M. Mechanistic Consequences of Chelate Ligand Stabilization on Nitrogen Fixation by Yandulov-Schrock-Type Complexes. *ACS Sustain. Chem. Eng.* **2017**, *5*, 10527–10537. [CrossRef]
674. Hidai, M.; Tominari, K.; Uchida, Y. Preparation and properties of dinitrogen-molybdenum complexes. *J. Am. Chem. Soc.* **1972**, *94*, 110–114. [CrossRef]
675. Hidai, M.; Mizobe, Y. Research inspired by the chemistry of nitrogenase Novel metal complexes and their reactivity toward dinitrogen, nitriles, and alkynes. *Can. J. Chem.* **2005**, *83*, 358–374. [CrossRef]
676. Studt, F.; Lehnert, N.; Wiesler, B.E.; Scherer, A.; Beckhaus, R.; Tuczek, F. Spectroscopic Comparison of Dinuclear Ti^+ and Ti^{2+} $\mu\text{-}\eta^1{:}\eta^1$ Dinitrogen Complexes with Cp*/Pentafulvene and Amine/Amide Ligation: Moderate versus Strong Activation of N_2. *Eur. J. Inorg. Chem.* **2006**, *2006*, 291–297. [CrossRef]
677. Fryzuk, M.D. Transformation of Coordinated Dinitrogen by Reaction with Dihydrogen and Primary Silanes. *Science* **1997**, *275*, 1445–1447. [CrossRef]
678. Bobadova-Parvanova, P.; Wang, Q.; Quinonero-Santiago, D.; Morokuma, K.; Musaev, D.G. Does Dinitrogen Hydrogenation Follow Different Mechanisms for $[(\eta^5\text{-}C_5Me_4H)_2Zr]_2(\mu_2,\eta^2,\eta^2\text{-}N_2)$ and $\{[PhP(CH_2SiMe_2NSiMe_2CH_2)PPh]Zr\}_2(\mu_2,\eta^2,\eta^2\text{-}N_2)$ Complexes? A Computational Study. *J. Am. Chem. Soc.* **2006**, *128*, 11391–11403. [CrossRef]
679. Hoffman, B.M.; Lukoyanov, D.; Yang, Z.-Y.; Dean, D.R.; Seefeldt, L.C. Mechanism of Nitrogen Fixation by Nitrogenase: The Next Stage. *Chem. Rev.* **2014**, *114*, 4041–4062. [CrossRef]
680. Hu, Y.; Ribbe, M.W. Nitrogenases-A Tale of Carbon Atom(s). *Angew. Chem. Int. Ed.* **2016**, *55*, 8216–8226. [CrossRef] [PubMed]

681. Solari, E.; Da Silva, C.; Iacono, B.; Hesschenbrouck, J.; Rizzoli, C.; Scopelliti, R.; Floriani, C. Photochemical activation of the N≡N bond in a dimolybdenum-dinitrogen complex: Formation of a molybdenum nitride. *Angew. Chem. Int. Ed.* **2001**, *40*, 3907–3909. [CrossRef]
682. Reiher, M.; Kirchner, B.; Hutter, J.; Sellmann, D.; Hess, B.A. A Photochemical Activation Scheme of Inert Dinitrogen by Dinuclear RuII and FeII Complexes. *Chem. A Eur. J.* **2004**, *10*, 4443–4453. [CrossRef] [PubMed]
683. Kunkely, H.; Vogler, A. Photolysis of Aqueous $[(NH_3)_5Os(\mu\text{-}N_2)Os(NH_3)_5]^{5+}$: Cleavage of Dinitrogen by an Intramolecular Photoredox Reaction. *Angew. Chem. Int. Ed.* **2010**, *49*, 1591–1593. [CrossRef] [PubMed]
684. Huss, A.S.; Curley, J.J.; Cummins, C.C.; Blank, D.A. Relaxation and Dissociation Following Photoexcitation of the $(\mu\text{-}N_2)[Mo(N[t\text{-}Bu]Ar)_3]_2$ Dinitrogen Cleavage Intermediate. *J. Phys. Chem. B* **2013**, *117*, 1429–1436. [CrossRef] [PubMed]
685. Fieser, M.E.; Bates, J.E.; Ziller, J.W.; Furche, F.; Evans, W.J. Dinitrogen Reduction via Photochemical Activation of Heteroleptic Tris(cyclopentadienyl) Rare-Earth Complexes. *J. Am. Chem. Soc.* **2013**, *135*, 3804–3807. [CrossRef] [PubMed]
686. Fieser, M.E.; Johnson, C.W.; Bates, J.E.; Ziller, J.W.; Furche, F.; Evans, W.J. Dinitrogen Reduction, Sulfur Reduction, and Isoprene Polymerization via Photochemical Activation of Trivalent Bis(cyclopentadienyl) Rare-Earth-Metal Allyl Complexes. *Organometallics* **2015**, *34*, 4387–4393. [CrossRef]
687. Miyazaki, T.; Tanaka, H.; Tanabe, Y.; Yuki, M.; Nakajima, K.; Yoshizawa, K.; Nishibayashi, Y. Cleavage and Formation of Molecular Dinitrogen in a Single System Assisted by Molybdenum Complexes Bearing Ferrocenyldiphosphine. *Angew. Chem. Int. Ed.* **2014**, *53*, 11488–11492. [CrossRef]
688. Rebreyend, C.; de Bruin, B. Photolytic N_2 Splitting: A Road to Sustainable NH_3 Production? *Angew. Chem. Int. Ed.* **2015**, *54*, 42–44. [CrossRef]
689. Schrock, R.R. Catalytic reduction of dinitrogen to ammonia by molybdenum: Theory versus experiment. *Angew. Chem. Int. Ed.* **2008**, *47*, 5512–5522. [CrossRef]
690. Yandulov, D.V.; Schrock, R. Catalytic Reduction of Dinitrogen to Ammonia at a Single Molybdenum Center. *Science* **2003**, *301*, 76–78. [CrossRef] [PubMed]
691. Arashiba, K.; Miyake, Y.; Nishibayashi, Y. A molybdenum complex bearing PNP-type pincer ligands leads to the catalytic reduction of dinitrogen into ammonia. *Nat. Chem.* **2011**, *3*, 120–125. [CrossRef] [PubMed]
692. Tanaka, H.; Arashiba, K.; Kuriyama, S.; Sasada, A.; Nakajima, K.; Yoshizawa, K.; Nishibayashi, Y. Unique behaviour of dinitrogen-bridged dimolybdenum complexes bearing pincer ligand towards catalytic formation of ammonia. *Nat. Commun.* **2014**, *5*, 3737. [CrossRef] [PubMed]
693. Kuriyama, S.; Arashiba, K.; Nakajima, K.; Tanaka, H.; Kamaru, N.; Yoshizawa, K.; Nishibayashi, Y. Catalytic Formation of Ammonia from Molecular Dinitrogen by Use of Dinitrogen-Bridged Dimolybdenum–Dinitrogen Complexes Bearing PNP-Pincer Ligands: Remarkable Effect of Substituent at PNP-Pincer Ligand. *J. Am. Chem. Soc.* **2014**, *136*, 9719–9731. [CrossRef]
694. Kuriyama, S.; Arashiba, K.; Nakajima, K.; Tanaka, H.; Yoshizawa, K.; Nishibayashi, Y. Nitrogen fixation catalyzed by ferrocene-substituted dinitrogen-bridged dimolybdenum-dinitrogen complexes: Unique behavior of ferrocene moiety as redox active site. *Chem. Sci.* **2015**, *6*, 3940–3951. [CrossRef]
695. Kuriyama, S.; Arashiba, K.; Nakajima, K.; Tanaka, H.; Yoshizawa, K.; Nishibayashi, Y. Azaferrocene-Based PNP-Type Pincer Ligand: Synthesis of Molybdenum, Chromium, and Iron Complexes and Reactivity toward Nitrogen Fixation. *Eur. J. Inorg. Chem.* **2016**, *2016*, 4856–4861. [CrossRef]
696. Klopsch, I.; Yuzik-Klimova, E.Y.; Schneider, S. Functionalization of N_2 by Mid to Late Transition Metals via N–N Bond Cleavage. In *Topics in Organometallic Chemistry*; Springer: Basel, Switzerland, 2017; pp. 71–112.
697. Silantyev, G.A.; Förster, M.; Schluschaß, B.; Abbenseth, J.; Würtele, C.; Volkmann, C.; Holthausen, M.C.; Schneider, S. Dinitrogen Splitting Coupled to Protonation. *Angew. Chem. Int. Ed.* **2017**, *56*, 5872–5876. [CrossRef]
698. Klopsch, I.; Finger, M.; Würtele, C.; Milde, B.; Werz, D.B.; Schneider, S. Dinitrogen Splitting and Functionalization in the Coordination Sphere of Rhenium. *J. Am. Chem. Soc.* **2014**, *136*, 6881–6883. [CrossRef]
699. Lindley, B.M.; Van Alten, R.S.; Finger, M.; Schendzielorz, F.; Würtele, C.; Miller, A.J.M.; Siewert, I.; Schneider, S. Mechanism of Chemical and Electrochemical N_2 Splitting by a Rhenium Pincer Complex. *J. Am. Chem. Soc.* **2018**, *140*, 7922–7935. [CrossRef]
700. Klopsch, I.; Kinauer, M.; Finger, M.; Würtele, C.; Schneider, S. Conversion of Dinitrogen into Acetonitrile under Ambient Conditions. *Angew. Chem. Int. Ed.* **2016**, *55*, 4786–4789. [CrossRef]

701. Arashiba, K.; Kinoshita, E.; Kuriyama, S.; Eizawa, A.; Nakajima, K.; Tanaka, H.; Yoshizawa, K.; Nishibayashi, Y. Catalytic Reduction of Dinitrogen to Ammonia by Use of Molybdenum–Nitride Complexes Bearing a Tridentate Triphosphine as Catalysts. *J. Am. Chem. Soc.* **2015**, *137*, 5666–5669. [CrossRef] [PubMed]
702. Eizawa, A.; Arashiba, K.; Tanaka, H.; Kuriyama, S.; Matsuo, Y.; Nakajima, K.; Yoshizawa, K.; Nishibayashi, Y. Remarkable catalytic activity of dinitrogen-bridged dimolybdenum complexes bearing NHC-based PCP-pincer ligands toward nitrogen fixation. *Nat. Commun.* **2017**, *8*, 14874. [CrossRef] [PubMed]
703. Matoba, K.; Eizawa, A.; Nishimura, S.; Arashiba, K.; Nakajima, K.; Nishibayashi, Y. Practical Synthesis of a PCP-Type Pincer Ligand and Its Metal Complexes. *Synthesis* **2018**, *50*, 1015–1019. [CrossRef]
704. Kinoshita, E.; Arashiba, K.; Kuriyama, S.; Eizawa, A.; Nakajima, K.; Nishibayashi, Y. Synthesis and Catalytic Activity of Molybdenum-Nitride Complexes Bearing Pincer Ligands. *Eur. J. Inorg. Chem.* **2015**, *2015*, 1789–1794. [CrossRef]
705. Sheng, X.L.; Batista, E.R.; Duan, Y.X.; Tian, Y.H. Dimension and bridging ligand effects on Mo-mediated catalytic transformation of dinitrogen to ammonia: Chain-like extended models of Nishibayashi's catalyst. *Comput. Theor. Chem.* **2016**, *1095*, 134–141. [CrossRef]
706. Anderson, J.S.; Rittle, J.; Peters, J.C. Catalytic conversion of nitrogen to ammonia by an iron model complex. *Nature* **2013**, *501*, 84–87. [CrossRef]
707. Chalkley, M.J.; Del Castillo, T.J.; Matson, B.D.; Roddy, J.P.; Peters, J.C. Catalytic N_2-to-NH_3 Conversion by Fe at Lower Driving Force: A Proposed Role for Metallocene-Mediated PCET. *ACS Cent. Sci.* **2017**, *3*, 217–223. [CrossRef]
708. Chalkley, M.J.; Del Castillo, T.J.; Matson, B.D.; Peters, J.C. Fe-Mediated Nitrogen Fixation with a Metallocene Mediator: Exploring pK_a Effects and Demonstrating Electrocatalysis. *J. Am. Chem. Soc.* **2018**, *140*, 6122–6129. [CrossRef]
709. Arashiba, K.; Eizawa, A.; Tanaka, H.; Nakajima, K.; Yoshizawa, K.; Nishibayashi, Y. Catalytic nitrogen fixation via direct cleavage of nitrogen-nitrogen triple bond of molecular dinitrogen under ambient reaction conditions. *Bull. Chem. Soc. Jpn.* **2017**, *90*, 1111–1118. [CrossRef]
710. Itabashi, T.; Mori, I.; Arashiba, K.; Eizawa, A.; Nakajima, K.; Nishibayashi, Y. Effect of substituents on molybdenum triiodide complexes bearing PNP-type pincer ligands toward catalytic nitrogen fixation. *Dalt. Trans.* **2019**, *48*, 3182–3186. [CrossRef]
711. Fajardo, J.; Peters, J.C. Catalytic Nitrogen-to-Ammonia Conversion by Osmium and Ruthenium Complexes. *J. Am. Chem. Soc.* **2017**, *139*, 16105–16108. [CrossRef] [PubMed]
712. Del Castillo, T.J.; Thompson, N.B.; Suess, D.L.M.; Ung, G.; Peters, J.C. Evaluating Molecular Cobalt Complexes for the Conversion of N_2 to NH_3. *Inorg. Chem.* **2015**, *54*, 9256–9262. [CrossRef] [PubMed]
713. Kuriyama, S.; Arashiba, K.; Nakajima, K.; Matsuo, Y.; Tanaka, H.; Ishii, K.; Yoshizawa, K.; Nishibayashi, Y. Catalytic transformation of dinitrogen into ammonia and hydrazine by iron-dinitrogen complexes bearing pincer ligand. *Nat. Commun.* **2016**, *7*, 1–9. [CrossRef] [PubMed]
714. Sekiguchi, Y.; Kuriyama, S.; Eizawa, A.; Arashiba, K.; Nakajima, K.; Nishibayashi, Y. Synthesis and reactivity of iron-dinitrogen complexes bearing anionic methyl- and phenyl-substituted pyrrole-based PNP-type pincer ligands toward catalytic nitrogen fixation. *Chem. Commun.* **2017**, *53*, 12040–12043. [CrossRef] [PubMed]
715. Kuriyama, S.; Arashiba, K.; Tanaka, H.; Matsuo, Y.; Nakajima, K.; Yoshizawa, K.; Nishibayashi, Y. Direct Transformation of Molecular Dinitrogen into Ammonia Catalyzed by Cobalt Dinitrogen Complexes Bearing Anionic PNP Pincer Ligands. *Angew. Chem. Int. Ed.* **2016**, *55*, 14291–14295. [CrossRef]
716. Sekiguchi, Y.; Arashiba, K.; Tanaka, H.; Eizawa, A.; Nakajima, K.; Yoshizawa, K.; Nishibayashi, Y. Catalytic Reduction of Molecular Dinitrogen to Ammonia and Hydrazine Using Vanadium Complexes. *Angew. Chem. Int. Ed.* **2018**, *57*, 9064–9068. [CrossRef]
717. Sekiguchi, Y.; Meng, F.; Tanaka, H.; Eizawa, A.; Arashiba, K.; Nakajima, K.; Yoshizawa, K.; Nishibayashi, Y. Synthesis and reactivity of titanium- and zirconium-dinitrogen complexes bearing anionic pyrrole-based PNP-type pincer ligands. *Dalt. Trans.* **2018**, *47*, 11322–11326. [CrossRef]
718. Doyle, L.R.; Wooles, A.J.; Jenkins, L.C.; Tuna, F.; McInnes, E.J.L.; Liddle, S.T. Catalytic Dinitrogen Reduction to Ammonia at a Triamidoamine-Titanium Complex. *Angew. Chem. Int. Ed.* **2018**, *57*, 6314–6318. [CrossRef]
719. Tanabe, Y.; Arashiba, K.; Nakajima, K.; Nishibayashi, Y. Catalytic Conversion of Dinitrogen into Ammonia under Ambient Reaction Conditions by Using Proton Source from Water. *Chem. An Asian J.* **2017**, *12*, 2544–2548. [CrossRef]

720. Higuchi, J.; Kuriyama, S.; Eizawa, A.; Arashiba, K.; Nakajima, K.; Nishibayashi, Y. Preparation and reactivity of iron complexes bearing anionic carbazole-based PNP-type pincer ligands toward catalytic nitrogen fixation. *Dalt. Trans.* **2018**, *47*, 1117–1121. [CrossRef]
721. Wickramasinghe, L.A.; Ogawa, T.; Schrock, R.R.; Müller, P. Reduction of Dinitrogen to Ammonia Catalyzed by Molybdenum Diamido Complexes. *J. Am. Chem. Soc.* **2017**, *139*, 9132–9135. [CrossRef] [PubMed]
722. Kiernicki, J.J.; Zeller, M.; Szymczak, N.K. Hydrazine Capture and N-N Bond Cleavage at Iron Enabled by Flexible Appended Lewis Acids. *J. Am. Chem. Soc.* **2017**, *139*, 18194–18197. [CrossRef] [PubMed]
723. Connor, G.P.; Lease, N.; Casuras, A.; Goldman, A.S.; Holland, P.L.; Mayer, J.M. Protonation and electrochemical reduction of rhodium- and iridium-dinitrogen complexes in organic solution. *Dalt. Trans.* **2017**, *46*, 14325–14330. [CrossRef]
724. Stucke, N.; Krahmer, J.; Näther, C.; Tuczek, F. Molybdenum Complexes Supported by PN3P Pincer Ligands: Synthesis, Characterization, and Application to Synthetic Nitrogen Fixation. *Eur. J. Inorg. Chem.* **2018**, *2018*, 5108–5116. [CrossRef]
725. Shiina, K. Reductive silylation of molecular nitrogen via fixation to tris (trialkylsilyl) amine. *J. Am. Chem. Soc.* **1972**, *94*, 9266–9267. [CrossRef]
726. Komori, K.; Oshita, H.; Mizobe, Y.; Hidai, M. Preparation and properties of molybdenum and tungsten dinitrogen complexes. 25. Catalytic conversion of molecular nitrogen into silylamines using molybdenum and tungsten dinitrogen complexes. *J. Am. Chem. Soc.* **1989**, *111*, 1939–1940. [CrossRef]
727. Tanaka, H.; Sasada, A.; Kouno, T.; Yuki, M.; Miyake, Y.; Nakanishi, H.; Nishibayashi, Y.; Yoshizawa, K. Molybdenum-Catalyzed Transformation of Molecular Dinitrogen into Silylamine: Experimental and DFT Study on the Remarkable Role of Ferrocenyldiphosphine Ligands. *J. Am. Chem. Soc.* **2011**, *133*, 3498–3506. [CrossRef] [PubMed]
728. Yuki, M.; Tanaka, H.; Sasaki, K.; Miyake, Y.; Yoshizawa, K.; Nishibayashi, Y. Iron-catalysed transformation of molecular dinitrogen into silylamine under ambient conditions. *Nat. Commun.* **2012**, *3*, 1254. [CrossRef]
729. Araake, R.; Sakadani, K.; Tada, M.; Sakai, Y.; Ohki, Y. [Fe_4] and [Fe_6] Hydride Clusters Supported by Phosphines: Synthesis, Characterization, and Application in N_2 Reduction. *J. Am. Chem. Soc.* **2017**, *139*, 5596–5606. [CrossRef]
730. Imayoshi, R.; Nakajima, K.; Nishibayashi, Y. Vanadium-catalyzed Reduction of Molecular Dinitrogen into Silylamine under Ambient Reaction Conditions. *Chem. Lett.* **2017**, *46*, 466–468. [CrossRef]
731. Kawaguchi, M.; Shin-ichi, H.; Mori, M. Incorporation of molecular nitrogen into organic compounds. Titanium catalyzed nitrogenation. *Tetrahedron Lett.* **1993**, *34*, 6907–6910. [CrossRef]
732. Ghana, P.; van Krüchten, F.D.; Spaniol, T.P.; van Leusen, J.; Kögerler, P.; Okuda, J. Conversion of dinitrogen to tris(trimethylsilyl)amine catalyzed by titanium triamido-amine complexes. *Chem. Commun.* **2019**, *55*, 3231–3234. [CrossRef] [PubMed]
733. Siedschlag, R.B.; Bernales, V.; Vogiatzis, K.D.; Planas, N.; Clouston, L.J.; Bill, E.; Gagliardi, L.; Lu, C.C. Catalytic Silylation of Dinitrogen with a Dicobalt Complex. *J. Am. Chem. Soc.* **2015**, *137*, 4638–4641. [CrossRef] [PubMed]
734. Imayoshi, R.; Tanaka, H.; Matsuo, Y.; Yuki, M.; Nakajima, K.; Yoshizawa, K.; Nishibayashi, Y. Cobalt-Catalyzed Transformation of Molecular Dinitrogen into Silylamine under Ambient Reaction Conditions. *Chem. A Eur. J.* **2015**, *21*, 8905–8909. [CrossRef] [PubMed]
735. Dzik, W. Silylation of Dinitrogen Catalyzed by Hydridodinitrogentris(Triphenylphosphine)Cobalt(I). *Inorganics* **2016**, *4*, 21. [CrossRef]
736. Gao, Y.; Li, G.; Deng, L. Bis(dinitrogen)cobalt(−1) Complexes with NHC Ligation: Synthesis, Characterization, and Their Dinitrogen Functionalization Reactions Affording Side-on Bound Diazene Complexes. *J. Am. Chem. Soc.* **2018**, *140*, 2239–2250. [CrossRef]
737. Suzuki, T.; Fujimoto, K.; Takemoto, Y.; Wasada-Tsutsui, Y.; Ozawa, T.; Inomata, T.; Fryzuk, M.D.; Masuda, H. Efficient Catalytic Conversion of Dinitrogen to $N(SiMe_3)_3$ Using a Homogeneous Mononuclear Cobalt Complex. *ACS Catal.* **2018**, *8*, 3011–3015. [CrossRef]
738. Tanabe, Y.; Nishibayashi, Y. Recent advances in catalytic silylation of dinitrogen using transition metal complexes. *Coord. Chem. Rev.* **2019**, *389*, 73–93. [CrossRef]
739. Liao, Q.; Cavaillé, A.; Saffon-Merceron, N.; Mézailles, N. Direct Synthesis of Silylamine from N_2 and a Silane: Mediated by a Tridentate Phosphine Molybdenum Fragment. *Angew. Chem. Int. Ed.* **2016**, *128*, 11378–11382. [CrossRef]

740. Imayoshi, R.; Nakajima, K.; Takaya, J.; Iwasawa, N.; Nishibayashi, Y. Synthesis and Reactivity of Iron– and Cobalt–Dinitrogen Complexes Bearing PSiP-Type Pincer Ligands toward Nitrogen Fixation. *Eur. J. Inorg. Chem.* **2017**, *2017*, 3768. [CrossRef]
741. Huber, G.W.; Iborra, S.; Corma, A. Synthesis of Transportation Fuels from Biomass: Chemistry, Catalysts, and Engineering. *Chem. Rev.* **2006**, *106*, 4044–4098. [CrossRef] [PubMed]
742. Chheda, J.N.; Huber, G.W.; Dumesic, J.A. Liquid-Phase Catalytic Processing of Biomass-Derived Oxygenated Hydrocarbons to Fuels and Chemicals. *Angew. Chem. Int. Ed.* **2007**, *46*, 7164–7183. [CrossRef] [PubMed]
743. Corma, A.; Iborra, S.; Velty, A. Chemical Routes for the Transformation of Biomass into Chemicals. *Chem. Rev.* **2007**, *107*, 2411–2502. [CrossRef] [PubMed]
744. Marshall, A.-L.; Alaimo, P.J. Useful Products from Complex Starting Materials: Common Chemicals from Biomass Feedstocks. *Chem. A Eur. J.* **2010**, *16*, 4970–4980. [CrossRef] [PubMed]
745. Werpy, T.A.; Holladay, J.E.; White, J.F. *Top Value Added Chemicals from Biomass: I. Results of Screening for Potential Candidates from Sugars and Synthesis Gas*; Pacific Northwest National Lab.: Richland, WA, USA, 2004.
746. Takagaki, A.; Nishimura, S.; Ebitani, K. Catalytic Transformations of Biomass-Derived Materials into Value-Added Chemicals. *Catal. Surv. Asia* **2012**, *16*, 164–182. [CrossRef]
747. Zhou, C.-H.; Xia, X.; Lin, C.-X.; Tong, D.-S.; Beltramini, J. Catalytic conversion of lignocellulosic biomass to fine chemicals and fuels. *Chem. Soc. Rev.* **2011**, *40*, 5588. [CrossRef]
748. Zakzeski, J.; Bruijnincx, P.C.A.; Jongerius, A.L.; Weckhuysen, B.M. The Catalytic Valorization of Lignin for the Production of Renewable Chemicals. *Chem. Rev.* **2010**, *110*, 3552–3599. [CrossRef] [PubMed]
749. Cao, L.; Yu, I.K.M.; Liu, Y.; Ruan, X.; Tsang, D.C.W.; Hunt, A.J.; Ok, Y.S.; Song, H.; Zhang, S. Lignin valorization for the production of renewable chemicals: State-of-the-art review and future prospects. *Bioresour. Technol.* **2018**, *269*, 465–475. [CrossRef]
750. Azadi, P.; Inderwildi, O.R.; Farnood, R.; King, D.A. Liquid fuels, hydrogen and chemicals from lignin: A critical review. *Renew. Sustain. Energy Rev.* **2013**, *21*, 506–523. [CrossRef]
751. van Putten, R.-J.; van der Waal, J.C.; de Jong, E.; Rasrendra, C.B.; Heeres, H.J.; de Vries, J.G. Hydroxymethylfurfural, A Versatile Platform Chemical Made from Renewable Resources. *Chem. Rev.* **2013**, *113*, 1499–1597. [CrossRef]
752. Rosatella, A.A.; Simeonov, S.P.; Frade, R.F.M.; Afonso, C.A.M. 5-Hydroxymethylfurfural (HMF) as a building block platform: Biological properties, synthesis and synthetic applications. *Green Chem.* **2011**, *13*, 754. [CrossRef]
753. Wright, W.R.H.; Palkovits, R. Development of Heterogeneous Catalysts for the Conversion of Levulinic Acid to γ-Valerolactone. *ChemSusChem* **2012**, *5*, 1657–1667. [CrossRef] [PubMed]
754. Liguori, F.; Moreno-Marrodan, C.; Barbaro, P. Environmentally Friendly Synthesis of γ-Valerolactone by Direct Catalytic Conversion of Renewable Sources. *ACS Catal.* **2015**, *5*, 1882–1894. [CrossRef]
755. Démolis, A.; Essayem, N.; Rataboul, F. Synthesis and Applications of Alkyl Levulinates. *ACS Sustain. Chem. Eng.* **2014**, *2*, 1338–1352. [CrossRef]
756. Raspolli Galletti, A.M.; Antonetti, C.; Ribechini, E.; Colombini, M.P.; Nassi o Di Nasso, N.; Bonari, E. From giant reed to levulinic acid and gamma-valerolactone: A high yield catalytic route to valeric biofuels. *Appl. Energy* **2013**, *102*, 157–162. [CrossRef]
757. Bond, J.Q.; Alonso, D.M.; Wang, D.; West, R.M.; Dumesic, J.A. Integrated Catalytic Conversion of -Valerolactone to Liquid Alkenes for Transportation Fuels. *Science* **2010**, *327*, 1110–1114. [CrossRef]
758. Yan, K.; Yang, Y.; Chai, J.; Lu, Y. Catalytic reactions of gamma-valerolactone: A platform to fuels and value-added chemicals. *Appl. Catal. B Environ.* **2015**, *179*, 292–304. [CrossRef]
759. Mika, L.T.; Cséfalvay, E.; Horváth, I.T. The role of water in catalytic biomass-based technologies to produce chemicals and fuels. *Catal. Today* **2015**, *247*, 33–46. [CrossRef]
760. Horváth, I.T. Solvents from nature. *Green Chem.* **2008**, *10*, 1024. [CrossRef]
761. Portillo Perez, G.; Mukherjee, A.; Dumont, M.J. Insights into HMF catalysis. *J. Ind. Eng. Chem.* **2019**, *70*, 1–34. [CrossRef]
762. Omoruyi, U.; Page, S.; Hallett, J.; Miller, P.W. Homogeneous catalyzed reactions of levulinic acid: To Γ-valerolactone and beyond. *ChemSusChem* **2016**, *9*, 2037–2047. [CrossRef] [PubMed]
763. Deng, L.; Li, J.; Lai, D.-M.; Fu, Y.; Guo, Q.-X. Catalytic Conversion of Biomass-Derived Carbohydrates into γ-Valerolactone without Using an External H 2 Supply. *Angew. Chem. Int. Ed.* **2009**, *48*, 6529–6532. [CrossRef] [PubMed]

764. Qi, L.; Horváth, I.T. Catalytic Conversion of Fructose to γ-Valerolactone in γ-Valerolactone. *ACS Catal.* **2012**, *2*, 2247–2249. [CrossRef]
765. Tukacs, J.M.; Király, D.; Strádi, A.; Novodarszki, G.; Eke, Z.; Dibó, G.; Kégl, T.; Mika, L.T. Efficient catalytic hydrogenation of levulinic acid: A key step in biomass conversion. *Green Chem.* **2012**, *14*, 2057. [CrossRef]
766. Tukacs, J.M.; Novák, M.; Dibó, G.; Mika, L.T. An improved catalytic system for the reduction of levulinic acid to γ-valerolactone. *Catal. Sci. Technol.* **2014**, *4*, 2908–2912. [CrossRef]
767. Fábos, V.; Mika, L.T.; Horváth, I.T. Selective Conversion of Levulinic and Formic Acids to γ-Valerolactone with the Shvo Catalyst. *Organometallics* **2014**, *33*, 181–187. [CrossRef]
768. Geilen, F.M.A.; Engendahl, B.; Harwardt, A.; Marquardt, W.; Klankermayer, J.; Leitner, W. Selective and Flexible Transformation of Biomass-Derived Platform Chemicals by a Multifunctional Catalytic System. *Angew. Chem. Int. Ed.* **2010**, *49*, 5510–5514. [CrossRef]
769. vom Stein, T.; Meuresch, M.; Limper, D.; Schmitz, M.; Hölscher, M.; Coetzee, J.; Cole-Hamilton, D.J.; Klankermayer, J.; Leitner, W. Highly Versatile Catalytic Hydrogenation of Carboxylic and Carbonic Acid Derivatives using a Ru-Triphos Complex: Molecular Control over Selectivity and Substrate Scope. *J. Am. Chem. Soc.* **2014**, *136*, 13217–13225. [CrossRef]
770. Meuresch, M.; Westhues, S.; Leitner, W.; Klankermayer, J. Tailor-Made Ruthenium-Triphos Catalysts for the Selective Homogeneous Hydrogenation of Lactams. *Angew. Chem. Int. Ed.* **2016**, *55*, 1392–1395. [CrossRef]
771. vom Stein, T.; Weigand, T.; Merkens, C.; Klankermayer, J.; Leitner, W. Trimethylenemethane-Ruthenium(II)-Triphos Complexes as Highly Active Catalysts for Catalytic C–O Bond Cleavage Reactions of Lignin Model Compounds. *ChemCatChem* **2013**, *5*, 439–441. [CrossRef]
772. Cui, X.; Li, Y.; Topf, C.; Junge, K.; Beller, M. Direct Ruthenium-Catalyzed Hydrogenation of Carboxylic Acids to Alcohols. *Angew. Chem. Int. Ed.* **2015**, *54*, 10596–10599. [CrossRef] [PubMed]
773. Li, Y.; Topf, C.; Cui, X.; Junge, K.; Beller, M. Lewis Acid Promoted Ruthenium(II)-Catalyzed Etherifications by Selective Hydrogenation of Carboxylic Acids/Esters. *Angew. Chem. Int. Ed.* **2015**, *54*, 5196–5200. [CrossRef]
774. Dutta Chowdhury, A.; Jackstell, R.; Beller, M. Towards the Efficient Development of Homogeneous Catalytic Transformation to γ-Valerolactone from Biomass-Derived Platform Chemicals. *ChemCatChem* **2014**, *6*, 3360–3365. [CrossRef]
775. Balaraman, E.; Fogler, E.; Milstein, D. Efficient hydrogenation of biomass-derived cyclic di-esters to *1*,*2*-diols. *Chem. Commun.* **2012**, *48*, 1111–1113. [CrossRef] [PubMed]
776. Deng, J.; Wang, Y.; Pan, T.; Xu, Q.; Guo, Q.-X.; Fu, Y. Conversion of Carbohydrate Biomass to γ-Valerolactone by using Water-Soluble and Reusable Iridium Complexes in Acidic Aqueous Media. *ChemSusChem* **2013**, *6*, 1163–1167. [CrossRef]
777. Wang, S.; Huang, H.; Dorcet, V.; Roisnel, T.; Bruneau, C.; Fischmeister, C. Efficient Iridium Catalysts for Base-Free Hydrogenation of Levulinic Acid. *Organometallics* **2017**, *36*, 3152–3162. [CrossRef]
778. Ortiz-Cervantes, C.; Flores-Alamo, M.; García, J.J. Hydrogenation of Biomass-Derived Levulinic Acid into γ-Valerolactone Catalyzed by Palladium Complexes. *ACS Catal.* **2015**, *5*, 1424–1431. [CrossRef]
779. Dwivedi, A.D.; Gupta, K.; Tyagi, D.; Rai, R.K.; Mobin, S.M.; Singh, S.K. Ruthenium and Formic Acid Based Tandem Catalytic Transformation of Bioderived Furans to Levulinic Acid and Diketones in Water. *ChemCatChem* **2015**, *7*, 4050–4058. [CrossRef]
780. Li, W.; Xie, J.-H.; Lin, H.; Zhou, Q.-L. Highly efficient hydrogenation of biomass-derived levulinic acid to γ-valerolactone catalyzed by iridium pincer complexes. *Green Chem.* **2012**, *14*, 2388. [CrossRef]
781. Gao, H.; Chen, J. Hydrogenation of biomass-derived levulinic acid to γ-valerolactone catalyzed by PNP-Ir pincer complexes: A computational study. *J. Organomet. Chem.* **2015**, *797*, 165–170. [CrossRef]
782. Phanopoulos, A.; White, A.J.P.; Long, N.J.; Miller, P.W. Catalytic Transformation of Levulinic Acid to 2-Methyltetrahydrofuran Using Ruthenium-N-Triphos Complexes. *ACS Catal.* **2015**, *5*, 2500–2512. [CrossRef]
783. Deng, L.; Kang, B.; Englert, U.; Klankermayer, J.; Palkovits, R. Direct hydrogenation of biobased carboxylic acids mediated by a nitrogen-centered tridentate phosphine ligand. *ChemSusChem* **2016**, *9*, 177–180. [CrossRef] [PubMed]
784. Sullivan, R.J.; Kim, J.; Hoyt, C.; Silks, L.A.; Schlaf, M. Ruthenium-8-quinolinethiolate-phenylterpyridine versus ruthenium-bipyridine-phenyl-terpyridine complexes as homogeneous water and high temperature stable hydrogenation catalysts for biomass-derived substrates. *Polyhedron* **2016**, *108*, 104–114. [CrossRef]

785. Wozniak, B.; Spannenberg, A.; Li, Y.; Hinze, S.; de Vries, J.G. Cyclopentanone Derivatives from 5-Hydroxymethylfurfural via 1-Hydroxyhexane-2,5-dione as Intermediate. *ChemSusChem* **2018**, *11*, 356–359. [CrossRef] [PubMed]
786. Wozniak, B.; Tin, S.; de Vries, J.G. Bio-based building blocks from 5-hydroxymethylfurfural via 1-hydroxyhexane-2,5-dione as intermediate. *Chem. Sci.* **2019**, *10*, 6024–6034. [CrossRef] [PubMed]
787. Stadler, B.M.; Puylaert, P.; Diekamp, J.; van Heck, R.; Fan, Y.; Spannenberg, A.; Hinze, S.; de Vries, J.G. Inexpensive Ruthenium NNS-Complexes as Efficient Ester Hydrogenation Catalysts with High C=O vs. C=C Selectivities. *Adv. Synth. Catal.* **2018**, *360*, 1151–1158. [CrossRef]
788. Yi, Y.; Liu, H.; Xiao, L.P.; Wang, B.; Song, G. Highly Efficient Hydrogenation of Levulinic Acid into γ-Valerolactone using an Iron Pincer Complex. *ChemSusChem* **2018**, *11*, 1474–1478. [CrossRef]
789. Padilla, R.; Jørgensen, M.S.B.; Paixão, M.W.; Nielsen, M. Efficient catalytic hydrogenation of alkyl levulinates to γ-valerolactone. *Green Chem.* **2019**, *21*, 5195–5200. [CrossRef]
790. Irrgang, T.; Kempe, R. 3d-Metal Catalyzed N- and C-Alkylation Reactions via Borrowing Hydrogen or Hydrogen Autotransfer. *Chem. Rev.* **2019**, *119*, 2524–2549. [CrossRef]
791. Corma, A.; Navas, J.; Sabater, M.J. Advances in One-Pot Synthesis through Borrowing Hydrogen Catalysis. *Chem. Rev.* **2018**, *118*, 1410–1459. [CrossRef]
792. Matsunami, A.; Kayaki, Y. Upgrading and expanding the scope of homogeneous transfer hydrogenation. *Tetrahedron Lett.* **2018**, *59*, 504–513. [CrossRef]
793. Morris, R.H. Mechanisms of the H_2- and transfer hydrogenation of polar bonds catalyzed by iron group hydrides. *Dalt. Trans.* **2018**, *47*, 10809–10826. [CrossRef] [PubMed]
794. Hashiguchi, S.; Fujii, A.; Takehara, J.; Ikariya, T.; Noyori, R. Asymmetric Transfer Hydrogenation of Aromatic Ketones Catalyzed by Chiral Ruthenium(II) Complexes. *J. Am. Chem. Soc.* **1995**, *117*, 7562–7563. [CrossRef]
795. Noyori, R.; Hashiguchi, S. Asymmetric Transfer Hydrogenation Catalyzed by Chiral Ruthenium Complexes. *Acc. Chem. Res.* **1997**, *30*, 97–102. [CrossRef]
796. Ikariya, T. Bifunctional Transition Metal-Based Molecular Catalysts for Asymmetric Syntheses. In *Topics in Organometallic Chemistry*; Springer: Berlin/Heidelberg, Germany, 2011; pp. 31–53. ISBN 9783642207303.
797. Haack, K.-J.; Hashiguchi, S.; Fujii, A.; Ikariya, T.; Noyori, R. The Catalyst Precursor, Catalyst, and Intermediate in the RuII-Promoted Asymmetric Hydrogen Transfer between Alcohols and Ketones. *Angew. Chem. Int. Ed. Engl.* **1997**, *36*, 285–288. [CrossRef]
798. Zweifel, T.; Naubron, J.-V.; Büttner, T.; Ott, T.; Grützmacher, H. Ethanol as Hydrogen Donor: Highly Efficient Transfer Hydrogenations with Rhodium(I) Amides. *Angew. Chem. Int. Ed.* **2008**, *47*, 3245–3249. [CrossRef]
799. Samec, J.S.M.; Bäckvall, J.-E.; Andersson, P.G.; Brandt, P. Mechanistic aspects of transition metal-catalyzed hydrogen transfer reactions. *Chem. Soc. Rev.* **2006**, *35*, 237. [CrossRef]
800. Foubelo, F.; Nájera, C.; Yus, M. Catalytic asymmetric transfer hydrogenation of ketones: Recent advances. *Tetrahedron Asymmetry* **2015**, *26*, 769–790. [CrossRef]
801. Mai, V.H.; Lee, S.-H.; Nikonov, G.I. Transfer Hydrogenation of Unsaturated Substrates by Half-sandwich Ruthenium Catalysts using Ammonium Formate as Reducing Reagent. *ChemistrySelect* **2017**, *2*, 7751–7757. [CrossRef]
802. Kayan, C.; Meriç, N.; Aydemir, M.; Ocak, Y.S.; Baysal, A.; Temel, H. Novel cyclohexyl-based aminophosphine ligands and use of their Ru(II) complexes in transfer hydrogenation of ketones. *Appl. Organomet. Chem.* **2014**, *28*, 127–133. [CrossRef]
803. Ikariya, T.; Blacker, A.J. Asymmetric Transfer Hydrogenation of Ketones with Bifunctional Transition Metal-Based Molecular Catalysts. *Acc. Chem. Res.* **2007**, *40*, 1300–1308. [CrossRef] [PubMed]
804. Lundberg, H.; Adolfsson, H. Ruthenium-catalyzed asymmetric transfer hydrogenation of ketones in ethanol. *Tetrahedron Lett.* **2011**, *52*, 2754–2758. [CrossRef]
805. Castellanos-Blanco, N.; Arévalo, A.; García, J.J. Nickel-catalyzed transfer hydrogenation of ketones using ethanol as a solvent and a hydrogen donor. *Dalt. Trans.* **2016**, *45*, 13604–13614. [CrossRef] [PubMed]
806. Sanz, S.; Benítez, M.; Peris, E. A New Approach to the Reduction of Carbon Dioxide: CO_2 Reduction to Formate by Transfer Hydrogenation in i PrOH. *Organometallics* **2010**, *29*, 275–277. [CrossRef]
807. Wei, Y.; Wang, C.; Jiang, X.; Xue, D.; Li, J.; Xiao, J. Highly efficient transformation of levulinic acid into pyrrolidinones by iridium catalysed transfer hydrogenation. *Chem. Commun.* **2013**, *49*, 5408. [CrossRef]
808. Crabtree, R.H. Transfer Hydrogenation with Glycerol as H-Donor: Catalyst Activation, Deactivation and Homogeneity. *ACS Sustain. Chem. Eng.* **2019**, *7*, 15845–15853. [CrossRef]

809. Chen, T.; He, L.-P.; Gong, D.; Yang, L.; Miao, X.; Eppinger, J.; Huang, K.-W. Ruthenium(II) pincer complexes with oxazoline arms for efficient transfer hydrogenation reactions. *Tetrahedron Lett.* **2012**, *53*, 4409–4412. [CrossRef]
810. He, L.-P.; Chen, T.; Xue, D.-X.; Eddaoudi, M.; Huang, K.-W. Efficient transfer hydrogenation reaction Catalyzed by a dearomatized PN3P ruthenium pincer complex under base-free Conditions. *J. Organomet. Chem.* **2012**, *700*, 202–206. [CrossRef]
811. Gladiali, S.; Alberico, E. Asymmetric transfer hydrogenation: Chiral ligands and applications. *Chem. Soc. Rev.* **2006**, *35*, 226–236. [CrossRef]
812. Baldino, S.; Facchetti, S.; Zanotti-Gerosa, A.; Nedden, H.G.; Baratta, W. Transfer Hydrogenation and Hydrogenation of Commercial-Grade Aldehydes to Primary Alcohols Catalyzed by 2-(Aminomethyl)pyridine and Pincer Benzo[*h*]quinoline Ruthenium Complexes. *ChemCatChem* **2016**, *8*, 2279–2288. [CrossRef]
813. Liu, W.-P.; Yuan, M.-L.; Yang, X.-H.; Li, K.; Xie, J.-H.; Zhou, Q.-L. Efficient asymmetric transfer hydrogenation of ketones in ethanol with chiral iridium complexes of spiroPAP ligands as catalysts. *Chem. Commun.* **2015**, *51*, 6123–6125. [CrossRef] [PubMed]
814. Dubey, A.; Khaskin, E. Catalytic Ester Metathesis Reaction and Its Application to Transfer Hydrogenation of Esters. *ACS Catal.* **2016**, *6*, 3998–4002. [CrossRef]
815. Weingart, P.; Thiel, W.R. Applying Le Chatelier's Principle for a Highly Efficient Catalytic Transfer Hydrogenation with Ethanol as the Hydrogen Source. *ChemCatChem* **2018**, *10*, 4858–4862. [CrossRef]
816. Wang, Y.; Huang, Z.; Leng, X.; Zhu, H.; Liu, G.; Huang, Z. Transfer Hydrogenation of Alkenes Using Ethanol Catalyzed by a NCP Pincer Iridium Complex: Scope and Mechanism. *J. Am. Chem. Soc.* **2018**, *140*, 4417–4429. [CrossRef] [PubMed]
817. Farrar-Tobar, R.A.; Wozniak, B.; Savini, A.; Hinze, S.; Tin, S.; de Vries, J.G. Base-Free Iron Catalyzed Transfer Hydrogenation of Esters Using EtOH as Hydrogen Source. *Angew. Chem. Int. Ed.* **2019**, *58*, 1129–1133. [CrossRef]
818. Krall, E.M.; Klein, T.W.; Andersen, R.J.; Nett, A.J.; Glasgow, R.W.; Reader, D.S.; Dauphinais, B.C.; Mc Ilrath, S.P.; Fischer, A.A.; Carney, M.J.; et al. Controlled hydrogenative depolymerization of polyesters and polycarbonates catalyzed by ruthenium(ii) PNN pincer complexes. *Chem. Commun.* **2014**, *50*, 4884. [CrossRef]
819. Sun, J.; Wang, Y. Recent advances in catalytic conversion of ethanol to chemicals. *ACS Catal.* **2014**, *4*, 1078–1090. [CrossRef]
820. Ndou, A.S.; Plint, N.; Coville, N.J. Dimerisation of ethanol to butanol over solid-base catalysts. *Appl. Catal. A Gen.* **2003**, *251*, 337–345. [CrossRef]
821. Chakraborty, S.; Piszel, P.E.; Hayes, C.E.; Baker, R.T.; Jones, W.D. Highly Selective Formation of n-Butanol from Ethanol through the Guerbet Process: A Tandem Catalytic Approach. *J. Am. Chem. Soc.* **2015**, *137*, 14264–14267. [CrossRef]
822. Aitchison, H.; Wingad, R.L.; Wass, D.F. Homogeneous Ethanol to Butanol Catalysi-Guerbet Renewed. *ACS Catal.* **2016**, *6*, 7125–7132. [CrossRef]
823. Sheehan, J.; Aden, A.; Paustian, K.; Killian, K.; Brenner, J.; Walsh, M.; Nelson, R. Energy and Environmental Aspects of Using Corn Stover for Fuel Ethanol. *J. Ind. Ecol.* **2003**, *7*, 117–146. [CrossRef]
824. Kim, S.; Dale, B.E. Life cycle assessment of various cropping systems utilized for producing biofuels: Bioethanol and biodiesel. *Biomass Bioenergy* **2005**, *29*, 426–439. [CrossRef]
825. Wu, M.; Wang, M.; Huo, H. Fuel-Cycle Assessment of Selected Bioethanol Production Pathways in the United States. *Renew. Energy* **2006**, *120*.
826. Atsumi, S.; Cann, A.F.; Connor, M.R.; Shen, C.R.; Smith, K.M.; Brynildsen, M.P.; Chou, K.J.Y.; Hanai, T.; Liao, J.C. Metabolic engineering of Escherichia coli for 1-butanol production. *Metab. Eng.* **2008**, *10*, 305–311. [CrossRef] [PubMed]
827. Xue, C.; Zhao, X.-Q.; Liu, C.-G.; Chen, L.-J.; Bai, F.-W. Prospective and development of butanol as an advanced biofuel. *Biotechnol. Adv.* **2013**, *31*, 1575–1584. [CrossRef] [PubMed]
828. Dürre, P. Biobutanol: An attractive biofuel. *Biotechnol. J.* **2007**, *2*, 1525–1534. [CrossRef] [PubMed]
829. Jin, C.; Yao, M.; Liu, H.; Lee, C.F.; Ji, J. Progress in the production and application of n-butanol as a biofuel. *Renew. Sustain. Energy Rev.* **2011**, *15*, 4080–4106. [CrossRef]
830. Veibel, S.; Nielsen, J.I. On the mechanism of the Guerbet reaction. *Tetrahedron* **1967**, *23*, 1723–1733. [CrossRef]

831. Xie, Y.; Ben-David, Y.; Shimon, L.J.W.; Milstein, D. Highly Efficient Process for Production of Biofuel from Ethanol Catalyzed by Ruthenium Pincer Complexes. *J. Am. Chem. Soc.* **2016**, *138*, 9077–9080. [CrossRef]
832. Tseng, K.N.T.; Lin, S.; Kampf, J.W.; Szymczak, N.K. Upgrading ethanol to 1-butanol with a homogeneous air-stable ruthenium catalyst. *Chem. Commun.* **2016**, *52*, 2901–2904. [CrossRef]
833. Tseng, K.N.T.; Kampf, J.W.; Szymczak, N.K. Base-free, acceptorless, and chemoselective alcohol dehydrogenation catalyzed by an amide-derived NNN-ruthenium(II) hydride complex. *Organometallics* **2013**, *32*, 2046–2049. [CrossRef]
834. Tseng, K.N.T.; Kampf, J.W.; Szymczak, N.K. Mechanism of *N*,*N*,*N*-Amide Ruthenium(II) Hydride Mediated Acceptorless Alcohol Dehydrogenation: Inner-Sphere β-H Elimination versus Outer-Sphere Bifunctional Metal-Ligand Cooperativity. *ACS Catal.* **2015**, *5*, 5468–5485. [CrossRef]
835. Wingad, R.L.; Gates, P.J.; Street, S.T.G.; Wass, D.F. Catalytic Conversion of Ethanol to n-Butanol Using Ruthenium P-N Ligand Complexes. *ACS Catal.* **2015**, *5*, 5822–5826. [CrossRef]
836. Everett, M.; Pellow, K.J.; Wass, D.F. Catalytic conversion of methanol/ethanol to isobutanol—A highly selective route to an advanced biofuel. *Chem. Commun.* **2016**, *52*, 5202–5204.
837. Pellow, K.J.; Wingad, R.L.; Wass, D.F. Towards the upgrading of fermentation broths to advanced biofuels: A water tolerant catalyst for the conversion of ethanol to isobutanol. *Catal. Sci. Technol.* **2017**, *7*, 5128–5134. [CrossRef]
838. Fu, S.; Shao, Z.; Wang, Y.; Liu, Q. Manganese-Catalyzed Upgrading of Ethanol into 1-Butanol. *J. Am. Chem. Soc.* **2017**, *139*, 11941–11948. [CrossRef]
839. Kulkarni, N.V.; Brennessel, W.W.; Jones, W.D. Catalytic Upgrading of Ethanol to n-Butanol via Manganese-Mediated Guerbet Reaction. *ACS Catal.* **2018**, *8*, 997–1002. [CrossRef]

Appendix F – Paper II

This work will disclose the use of pincer complexes and ionic liquid for the reversible hydrogenation of CO_2 and the dehydrogenation of FA at mild conditions. In detail, in this paper I will show the best results presented in this thesis for both CO_2 hydrogenation (Chapter 4) as well as FA dehydrogenation (Chapter 5). In addition, the possibility to apply such systems for the reversible storage of energy (Chapter 6) will be highlighted as well. The work presented in this paper was conducted at DTU Chemistry in collaboration with PhD student Brenda Rabell, postdoc Rosa Padilla, and Assoc Prof Martin Nielsen.

Paper in preparation.

Efficient additive-free reversible catalytic hydrogenation of CO_2 and formic acid dehydrogenation under mild conditions

*L.Piccirilli, B. Rabell, R. Padilla, A. Riisager, M. Nielsen**

Department of Chemistry, Technical University of Denmark, DK-2800 Kgs. Lyngby, Denmark;
** Correspondence: marnie@kemi.dtu.dk; Tel.: +45-24651045*

Abstract

Hydrogen is considered an ideal energy carrier that can help to tackle climate change and substitute fossil fuels for the future energy demand. Green hydrogen from renewable energy will promote CO_2 capturing and utilization (CCU) processes connecting both the chemical and the energy sectors. Here, we demonstrate high catalytic activity of Ru-PNP catalysts in ionic liquid (IL) for the hydrogenation of CO_2 to formic acid (FA) and the reverse dehydrogenation of FA under very mild conditions without the use of additives. The hydrogenation of CO_2 proceeds already at 25 ºC under a flow of CO_2/H_2 at 1 bar leading to 14 mol% FA/IL. Simply increasing the pressure to 40 bar of 1:1 CO_2/H_2 provides up to 1.26 equivalents of FA to IL. Thermally induced FA dehydrogenation occurs at <100 ºC in otherwise identical reaction conditions as for the CO_2 hydrogenation resulting in turnover frequencies (TOF) up to approximately 12.000 h^{-1}.

Applying a continuous feed of FA to 4 mL of the IL 1-butyl-3-methylimidazolium acetate (BMIM Ac) containing 0.021 mmol of Ru-MACHO-BH at 95 ºC leads to a highly stable production of pure CO_2 and H_2 with no observable CO (100 ppm detection limit). Thus, the reaction afforded an overall turnover number (TON) of 18 million after 4 months under heat-integrated conditions for fuel cells application. Finally, it was possible to perform at least 12 cycles of hydrogenation/dehydrogenation with retention of the catalytic activity by simply changing pressure and/or temperature. Overall, we demonstrate a novel and remarkably efficient approach for a CO_2/FA-based energy system with high practicality and flexibility as well as stability over prolonged times.

Introduction

Society needs new and green energy solutions to satisfy the growing energy demands. Hydrogen economy and Power-to-X technologies will likely be main players in this green transition. Carbon capture and utilization (CCU) can reduce our dependence on petrochemicals providing a useful building block for the synthesis of a wide range of industrially relevant chemicals [45,46] and fuels [47], such as energy carriers as described by Leitner [67] and Olah [68,69]. Formic acid (FA) is the first product of CO_2 hydrogenation and a candidate as a Liquid Organic Hydrogen Carrier (LOHC) for the long-term, safe and practical energy storage (4,4 wt% H_2) [329,330]. It decomposes to a 1:1 mixture of H_2 and CO_2 where hydrogen is converted into electricity, while the released CO_2 is captured and converted back to FA, closing an ideal carbon-free energy cycle [36,309,331–333].

Homogeneous organometallic hydrogenation and dehydrogenation are two of the main approaches to the reversible interconversion between CO_2 and FA [331,334]. Recently, we reviewed the main advances in the use of homogeneous pincer complexes for these type of relevant sustainable transformations [88]. In the effort of developing efficient and stable systems, researchers have proposed different strategies for both CO_2 valorization to FA [65,200,202,249,250,335,336], as well as FA dehydrogenation [166,245,255,322,326]. Conventionally, all the reported systems require sacrificial additives (e.g. inorganic bases and solvents) to achieve satisfactory activity and stability, at the same time lowering the overall atom efficiency and volumetric/gravimetric energy storage potential.

There are only few examples of reversible systems reported in the literature [248,254]. For instance, Pidko reported the reversible hydrogenation of CO_2 to formate employing a Milstein Ru-PNP catalyst in DMF/DBU mixtures, demonstrating 10 cycles of H_2 storage-release by only switching the temperature between 65 ºC and 90 ºC as well as the pressure between 5-40 bar and 1 bar [248]. Hull, Himeda and Fujita employed a dinuclear iridium catalyst and sacrificial $KHCO_3$ and H_2SO_4 to switch between CO_2 hydrogenation and FA dehydrogenation [254]. The hydrogenation proceeded at 30 ºC under 1:1 CO_2/H_2 at 1 bar, and the dehydrogenation at 50 ºC. Likewise, Himeda showed that a pyridyl-pyrazole Cp^*-Ir catalyst hydrogenates CO_2 in presence of 1.0 M $NaHCO_3$ (aq) under 10 bar of 1:1 CO_2/H_2 at 50 ºC, giving TON = 7850 and TOF = 164 h^{-1} after 48 h [255]. Changing the

reaction conditions to 4 M of FA (aq) and 70 ºC, the same catalyst dehydrogenates a continuous flow of 20 M FA (aq) affording TON = 10 million after 35 days. However, it is unclear whether the source of formic acid is CO_2 or the bicarbonate, and the authors did not demonstrate cycles of reversible transformation.

Ionic liquids are a wide family of compounds existing purely in the ionic form. Their non-volatility, structure-tunability, and high CO_2 uptake capacity render ionic liquids (ILs) an useful media for carbon dioxide capture [192–194,258]. In 2011, Rogers showed the chemisorption of carbon dioxide using 1,3-dialkylimidazolium acetate ionic liquids, opposed to the physisorption usually involved with ionic liquid-mediated CO_2 capture [279]. Supported by single-crystal X-ray analysis, the authors demonstrated the presence of carbene species able to bind CO_2 selectively and reversibly. However, besides the use of ILs as reaction additives [200–202], organometallic catalysts operating exclusively in ionic liquid media are scarcely reported.

An energy system based on CO_2/FA requires a clean flow of hydrogen gas released, without the presence of any vaporized solvents and volatile additives that would decrease the H_2 storage capacity and potentially damage the fuel cell. The negligible vapor pressure and high chemical and thermal stability of ILs allow the obtainment of a clean flow of hydrogen without any organic contaminants that could damage a fuel cell. Another important aspect for a viable energy system is the ability to operate reversibly under a wide range of pressures and temperatures. As described before, there are only few examples of catalytic systems that fulfill all of these features and are able to perform both steps of energy storage and release without the use of additional additives and by only changing one reaction parameter.

In this study, we investigate the reactivity of ruthenium-PNP pincer complexes in ionic liquid media for the hydrogenation of CO_2 into formic acid and the reverse formic acid dehydrogenation reaction for hydrogen release under mild reaction conditions (Scheme 1). We sought to develop a catalytic additive free reaction employing only the ionic liquid as solvent. We hypothesized that the ionic liquid anion can perform the pre-catalyst activation step usually required for the activation of Ru-PNP pincer pre-catalysts. Indeed, we demonstrate the unprecedented activation of Ru-PNP complexes promoted by the IL anion, as well as the efficiently catalyzed formic acid dehydrogenation without the use of bases. Furthermore, carbene species on imidazolium cation of the ionic liquid functions could act as a CO_2 capturing agent avoiding the use of other CO_2-trapping agents. Indeed, the hydrogenation of CO_2 proceeds already at room temperature, and release of hydrogen from formic acid is possible at temperatures compatible with PEM fuel cell application. By simply changing either temperature or pressure, the same system catalyzes up to 12 cycles of hydrogenation/dehydrogenation without any observable loss in activity under ambient conditions. The combination of Ru-PNP and IL is robust, flexible and stable under a wide range of temperatures, pressures, and catalyst concentration in the ionic liquid. The extreme simplicity and stability of this formate-based hydrogen storage system demonstrate its viable implementation within hydrogen energy technologies.

CO_2 hydrogenation

In agreement with Rogers´s findings [279], EMIM Ac readily traps CO_2 by simple bubbling through the IL solution at room temperature, while faster and more efficient CO_2 trapping is performed under pressure and in shorter times (Figure S2). Initially, we explored the reactivity of a series of ruthenium catalysts for the hydrogenation of CO_2 at mild conditions using 1-ethyl-2-methylimidazolium acetate (EMIM Ac) as the only reaction medium (Table S1).

To our delight, the catalyst **Ru-1** (0.02 mmol) afforded 99% conversion of CO_2 and a TON of 198 at 25 ºC after 18 hours (Table S1, Entry 11). The –Cl and –OAc analogues **Ru-2** and **Ru-3** showed comparable results, affording a TON of 70 and 61 respectively (Entries 9-10, Table S1). On the contrary, the $^{pCy-}$, $^{tBu-}$ and $^{Ph-}$PNP congeners showed poorer or absent productivity in comparison with the $^{iPr-}$PNP analogues under the same reaction conditions. The higher solubility of the ^{iPr}-PNP ligands in EMIM Ac at room temperature could explain the observed catalytic activity. In light of their catalytic activity, other viable catalysts including the ruthenium triphenylphosphine precursor **Ru-6**, the Milstein´s catalyst **Ru-7** and the Triphos complex **Ru-8** where evaluated. However, none of them promoted visible formation of FA. The iridium catalyst **Ir-1** also showed moderate catalytic activity affording a TON = 81. In order to demostrate that EMIM Ac effectively activates the pre-catalysts by interaction of the acetate anion with the metal center, we followed the reaction by ^{1}H-NMR. Thus, the ^{1}H NMR spectrum showed the hydride peak associated with the acetate complex at -17.93 ppm, likely the main resting state in the presence of EMIM Ac (Figures S3-S5). After the reaction is complete, ^{1}NMR analysis showed the presence of the acetate specie as the main resting state (Figure S6-S9). In the initial screening in Table S1, **Ru-2** and **Ru-3** afforded similar results, comparable with **Ru-1**; indeed, once **Ru-2** is activated by

EMIM Ac, it results in the formation of the same acetate complex **Ru-3** (Figure S10), explaining the similar catalytic behavior of the three ^{iPr}-PNP catalysts.

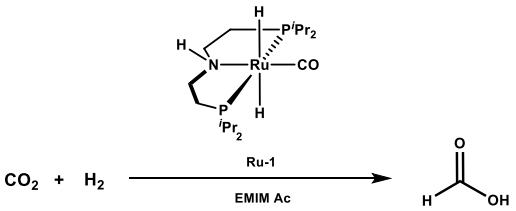

Entry	Cat. Loading (mmol)	Conc (M)	CO_2/H_2 (bar)	T [ºC]	Time [h]	TON	TOF [h^{-1}]	Formate/IL[a] (%)
1	0.02	0.02	5:5	rt	18	16	-	5
2	0.02	0.02	5:10	rt	18	26	-	8
3	0.02	0.02	10:10	rt	18	71	4	22
4	0.02	0.02	10:20	rt	18	198	10	75
5	0.02	0.02	15:15	rt	18	184	10	70
6	0.02	0.02	20:20	rt	54	113 (18 h) 358 (36 h) 405 (54 h)	7	35 111 126
7	0.04	0.04	10:20	rt	18	141	8	92
8	0.002	0.004	15:15	rt	18	280	15	2
9	0.02	0.02	10:20	rt	6	92	15	30
10	0.004	0.002	15:15	50	18	1515	84	47
11	0.004	0.004	15:15	80	1	258	258	16
12	0.004	0.004	15:15	80	6	1052	175	65
13	0.004	0.002	15:15	80	18	1935	107	60
14	0.002	0.0004	15:15	80	18	3085	171	22
15	0.002	0,0001	30:30	80	36	32411	1000 (18 h) 900 (36 h)	67

[a] Reactions reproducible within a 10% error.

Table 1: Screening of reaction conditions for the hydrogenation of CO_2 at mild conditions using **Ru-1** and EMIM Ac.

The optimization of reaction conditions using Ru-1 and EMIM Ac is described in the Table 1. CO_2 and H_2 relative pressures play a major role if the reaction is carried out at room temperature (Entries 1-6). It is beneficial to use hydrogen gas in excess to facilitate its diffusion within the viscous IL phase, which solidifies when high amount of CO_2 are trapped at room temperature. The stirring rate is also important to avoid formation of the solid product after CO_2 chemisorption (EMIM-CO_2, Figure S2). Loading the autoclave with 10:20 or 15:15 lead to similar results (entries 4,5). Further increasing the pressure to 20:20 bar of CO_2:H_2 resulted in only 35% FA/IL, with visible formation of EMIM-CO_2 (Entry 6). Nevertheless, of great importance for an energy storage device, it is possible to reload the system by simply applying additional CO_2:H_2 pressure resulting in an over-stoichiometric amount of FA/IL = 1.26. Increasing the catalyst loading to 0.04 mmol led to a 1:1 mixture FA/IL (Entry 7), whereas lowering it to 4 μmol resulted in only 2% FA/IL and a TON = 280 (5 mL EMIM Ac, Entry 8). As expected, shorter times lead to lower formate production (Entry 9). To identify the optimal reaction conditions, we examined the activity of the catalysts **Ru-1** at different temperatures. For example, increasing the temperature to 50ºC and 80ºC led to an improvement of the catalytic activity with possibility to decrease the catalyst loading, the reaction time, and use 1:1 CO_2:H_2 pressures (Entries 10-14). This is likely explained by the easiest gas diffusion of CO_2/H_2 within the IL phase, together with higher catalyst solubility at higher temperatures. In addition, under these conditions, the formation of the solid product due to CO_2 chemisorption from EMIM-CO_2 is prevented. Later, we scaled-up the reaction using 15 mL of EMIM Ac and 60 bar of CO_2:H_2 to facilitate gas-diffusion and mass transport within the IL phase. Applying 0.002 mmol of **Ru-1** results in a TON of 18886, which raises up to 32411 when additional 60 bar of CO_2:H_2 are applied after 18h at 80 ºC (Entry 15). Loading the autoclave a third time resulted in only a small increase in the formate/IL ratio (67% to 71%), probably explained by the competing formic acid dehydrogenation at 80 ºC in the presence of high concentrations of formic acid

in the IL. Importantly, all manipulations were performed at ambient conditions, indicating the high stability and robustness of the Ru-PNP complexes in ionic liquid system. Applying 25 bar of CO_2 in an autoclave in the presence of EMIM Ac resulted in 34 mol% of CO_2 trapped to the IL after 45 minutes. Later, the gas was released down to 5 bar, and 0.02 mmol of **Ru-2** and 25 bar of hydrogen were added, affording a TON = 359 after 18h at 50ºC (to liquefy the trapped CO_2) (Scheme 2a). In a similar fashion, bubbling of CO_2 in EMIM Ac for 48h at ambient conditions, followed by addition of 0.02 mmol of **Ru-2** and hydrogen pressure in autoclave (25 bar), resulted in a TON of 156 and a Formate/IL = 38% at 50 ºC (Scheme 2b). Direct bubbling of CO_2 in 1.5 mL of EMIM Ac at room temperature resulted in 10 mol% of CO_2 trapped after 24 h. Addition of **Ru-1** (0.02 mmol) and switching the atmosphere to hydrogen with a balloon at ambient conditions resulted in 12 mol% of FA/IL (TON = 60) after 96 h (Scheme 2c). Finally, we show the possibility of bubbling directly a mixture of CO_2:H_2 at ambient conditions in a solution of EMIM Ac containing 0.07 mmol of **Ru-1**: using a 1:5 flow of CO_2:H_2 it was possible to achieve 14 mol% of FA/IL (TON = 15) after 96 h.

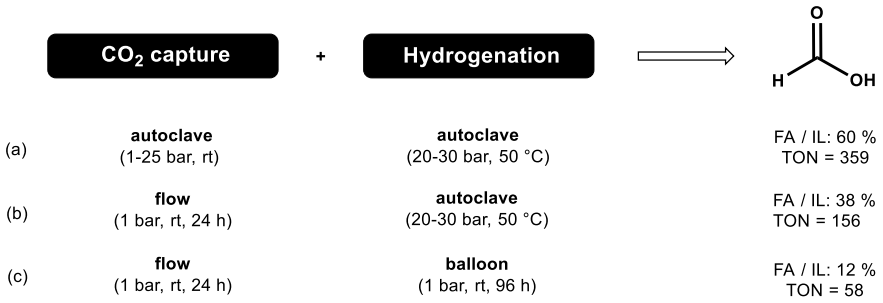

Scheme 2: Alternatives for CO_2 capture and hydrogenation under different reaction conditions.

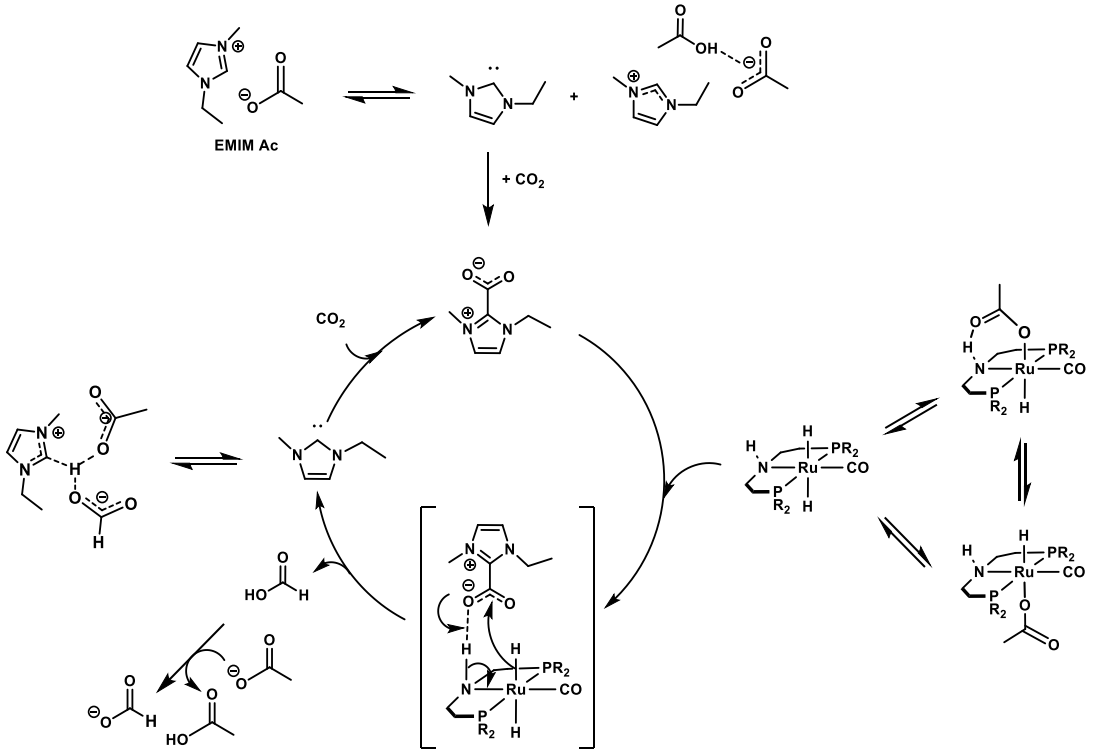

Scheme 3: Suggested mechanism for CO_2 activation via carbene specie followed by Ru-PNP catalyzed hydrogenation to formic acid.

We investigated the mechanism of the reaction performing labeling experiments with both ^{2}H and ^{13}C NMR in the presence of EMIM Ac and **Ru-2** (Figures S11 and S12). NMR analysis confirms the proposed mechanism for CO_2 activation via carbene, and subsequent hydride transfer from the catalyst to the trapped CO_2 resulting in a mixture of formic acid/formate (Scheme 3). As shown in the ^{2}H-NMR spectrum in Figure S2, a formate peak is present at 8.60 ppm, together with another deuterium atom (9.55 ppm) that is exchanged at the C2 position of the imidazole ring. Hence, we propose the catalytic cycle in Scheme 3, with CO_2 activation promoted by the IL, and following hydrogenation performed by the catalyst with consequent formation of formic acid and restoring of the carbene specie.

Formic Acid dehydrogenation

After the catalytic studies for CO_2 hydrogenation, we decided to explore the reverse formic acid dehydrogenation at temperatures below 100 ºC. Based on the findings from CO_2 hydrogenation, we decided to use BMIM Ac as the ionic liquid of choice to avoid high content of CO_2 trapped that could affect the hydrogen release from the reaction mixture. We performed a screening of Ru-PNP catalysts at 80ºC in batch conditions, measuring the gas evolution via a mass flow meter and analyzing the gas composition with a MicroGC (Table 2).

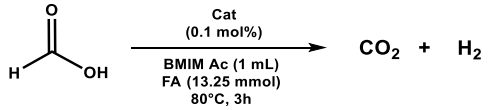

Entry	Catalyst	TON	TOF (h^{-1})	Conversion (%)
1	Ru-MACHO	1000	500	>99
2	Ru-2	1000	500	>99
3	Ru-3	1000	500	>99
4	Ru-1	1000	500	>99
5	Ru-MACHO-BH	1000	500	>99
6[a]	Ru-MACHO-BH	1000	500	>99
7[b]	Ru-MACHO-BH	3780	1260	>99
8[c]	Ru-MACHO-BH	-	-	-
9[d]	Ru-MACHO-BH	12050	502	90
10[e]	Ru-MACHO-BH	16750	930	95

[a] EMIM AC.
[b] Ru-MACHO-BH (0.025 mol%).
[c] Ru-MACHO-BH (0.006 mol%), FA (53 mmol).
[d] Ru-MACHO-BH (3 µmol), BMIM Ac (3 mL), FA (39.8 mmol), 95 ºC, 18h.
[e] Ru-MACHO-BH (3 µmol), BMIM Ac (3 mL), FA (26.5x2 mmol), 95 ºC, 18h (second addition of FA after 5h).

Table 2: Optimization of FA dehydrogenation in batch conditions.

In the presence of BMIM Ac, all the screened catalysts reached full conversion within 2 hours (Entries 1-5). No clear difference was observed between BMIM Ac and EMIM Ac (Entry 6). As depicted in Figure S13, after completeness of the reaction, it is possible to notice the presence of CO_2 being trapped in the IL mixture, as well as the **Ru-1-CHOO** specie (*vide supra*). Lowering the catalyst loading to 0.025 mol% led to higher turnover number (3780, Entry 7), whereas increasing the initial loading of formic acid results in deactivation of the catalyst (Entry 8). This shows that higher FA loadings need to be balanced with increased IL volume in order to balance the increased acidity of the mixture. In fact, a TON of 12050 was obtained at 95ºC after 18 hours with 0.008 mol% of **Ru-MACHO-BH** in 3 mL of BMIM Ac (Entry 9). In a similar experiment, two aliquots of FA were added at different times resulting in an overall TON of 16750 (Entry 10). No CO was detected by Micro-GC under the reaction conditions used (Figure S18).

As shown in Figure 1, the gas evolution profile of a typical batch experiment appears very rapid as soon as the formic acid is added to the mixture of ionic liquid and catalyst, and slowly decreases until all formic acid is consumed. In addition, it is possible to add

more formic acid with the gas evolution showing the same behavior (Figure 1, final TON = 2548). This clearly shows that the reaction is highly dependent on the rate at which formic acid is added, indicating that high turnover numbers and frequencies are possible keeping the IL/FA ratio at an optimal level, while deactivation of the catalyst occurs at high FA concentrations. In addition, we gladly observed that a mixture containing **Ru-MACHO** and BMIM Ac was active after 4 weeks of simple storage at ambient conditions and retained the same catalytic activity when more formic acid was added after heating at 80ºC. These findings inspired us to evaluate the robustness and stability of our catalytic systems for continuous formic acid feed, simulating an application such as automotive fuel cell technologies (see *Formic Acid dehydrogenation – Continuous flow*).

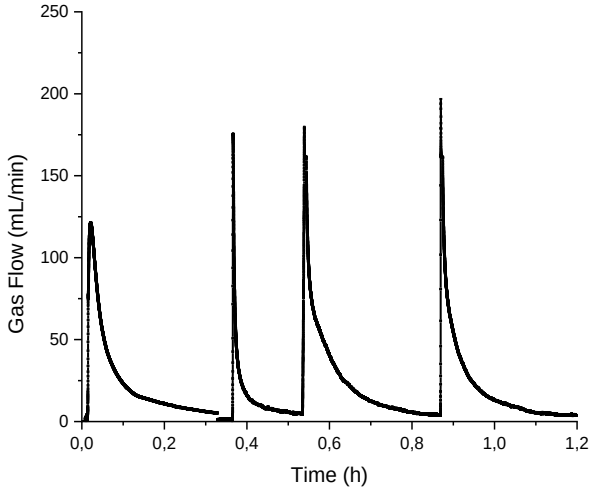

Figure 1: Gas evolution for formic acid dehydrogenation in batch. Reaction conditions: 0.013 mmol Ru-MACHO-BH (0.1 mol%), BMIM Ac (1 mL), FA (13.25 mmol), 80 ºC. Three more addition of FA of 0.25 mL each.

CO_2 hydrogenation / FA dehydrogenation cycles

During our studies CO_2 hydrogenation, we observed the reversibility of the process: by simply applying heat (>60ºC), it was possible to release a 1:1 mixture of H_2:CO_2 restoring the system that could undergo another cycle of hydrogenation. In addition, we showed that formic acid dehydrogenation is favored at T > 50 ºC in the presence of the same catalyst performing CO_2 hydrogenation at low temperature (**Ru-1** and **Ru-2**).

Based on these findings, we tested the stability of our system performing cycles of hydrogenation/dehydrogenation using **Ru-1** (See Figure S15 for **Ru-2**). In a straightforward way, by a simple pressure switch, it is possible to load the system (*hypothetic energy device)* applying CO_2:H_2 pressure, and readily release hydrogen by keeping the reaction vessel at 80 ºC (Figure S14). At a low catalyst loading of 0.004 mmol, **Ru-1** resulted in an overall TON of 51761 after 10 cycles with no indication of catalyst deactivation (Figure 2, right). By controlling either pressure, temperature or catalyst loading, it is possible to shift the equilibrium towards either the hydrogenation or the dehydrogenation, confirming the remarkable flexibility and stability of the system in operating at different reaction conditions.

In a similar fashion, it is possible to perform the hydrogenation step at room temperature under 30 bar of 1:2 CO_2:H_2, with hydrogen release favored by heating at T>80 ºC (Figure 2). Catalyst loading can be adjusted accordingly to the temperature chosen for the hydrogenation step (higher at low T). Both **Ru-1** and **Ru-2** catalyzed up to 12 cycles of HD/DH without observable loss of catalytic activity. **Ru-2** performed better than **Ru-1** under these conditions and with lower catalyst loading, as shown in Figure S14. Importantly from a practical point of view, it is possible to perform the hydrogen release step by keeping the system closed, resulting in the production of pressurized hydrogen (up to 10 bar in a single dehydrogenation step).

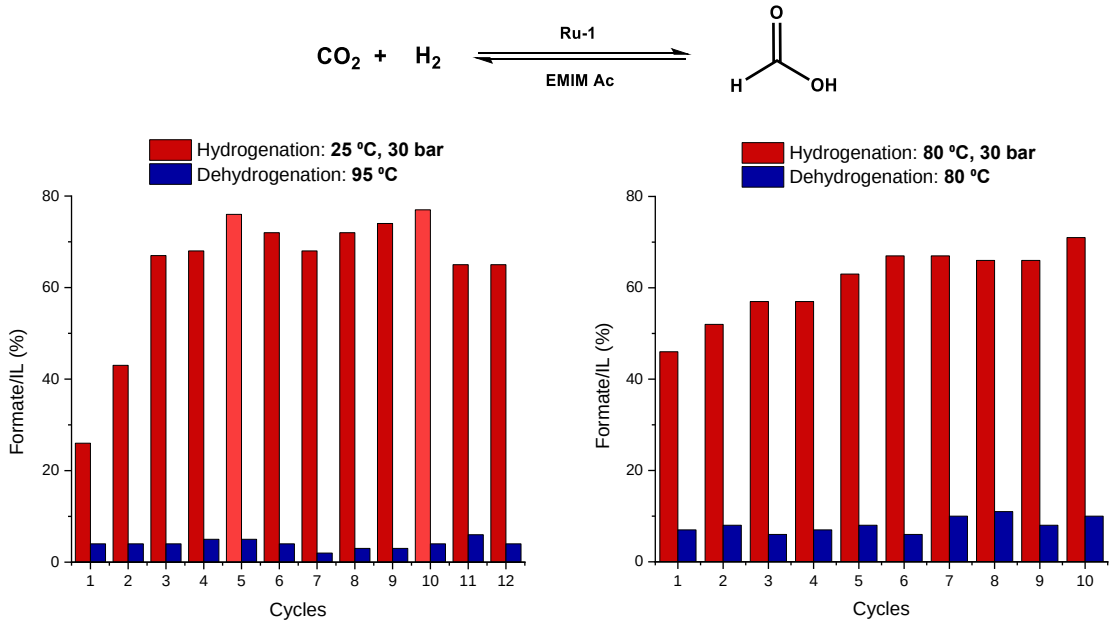

Figure 2: Cycles experiment of CO_2 hydrogenation followed by hydrogen release. Left: Ru-1 (0.07 mmol), EMIM Ac (2 mL), 10:20 bar CO_2:H_2, 18 h for the hydrogenation (72 h in lighter bars), open autoclave (4 h) for the dehydrogenation. Right: Ru-1 (0.004 mmol), EMIM Ac (3 mL), 10:20 bar CO_2:H_2, 18 h for the hydrogenation, open autoclave (18 h) for the dehydrogenation.

Formic Acid dehydrogenation – Continuous flow

We optimized our system for FA dehydrogenation by feeding FA continuously using a syringe pump, as depicted in Figure S1. Increasing the temperature from 80 ºC to 95 ºC allows the use of higher FA rates, still being within the temperature range of a PEMFC off-heat (Entry 1, Table S2). The $^{i\text{-}Pr}$-PNP catalysts showed inferior stability towards high formic acid concentrations. Under the same reaction conditions, **Ru-1** and **Ru-2** reached a maximum TOF of 7288 h^{-1} before visible accumulation of FA in the mixture (Entries 2,3, Table S2). **Ru-MACHO** and **Ru-MACHO-BH** could bear a formic acid flow up to 10 mL/h, corresponding to a maximum turnover frequency of 10600 h^{-1} (Entries 4-5, Table S2). Lowering the catalyst concentration from 0.01 to 0.005 M, resulted in higher stability with retention of the catalytic activity of the catalyst, prof of the stabilizing effect of the ionic liquid towards the acidity of formic acid for prolonged times (Table S3). As shown in Figure 3, the gas evolution profile follows the changes in formic acid rate, confirming our hypothesis.

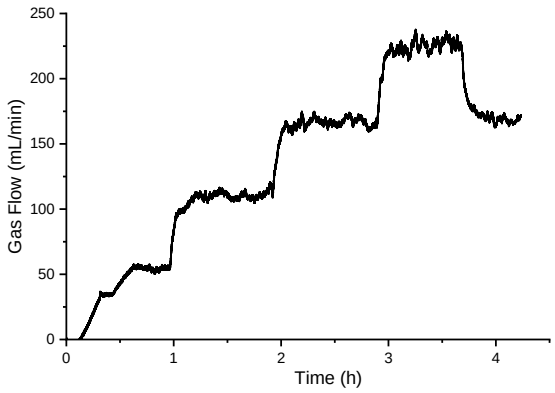

Figure 3: Gas evolution profile of continuous flow formic acid dehydrogenation. Reaction conditions: Ru-MACHO-BH (0.02 mmol), BMIM Ac (3 mL), 95 ºC; final TON = 2.171.653.

To demonstrate the longevity of our catalytic system, the reaction was extended for several days. Therefore, applying 0.02 mmol of **Ru-MACHO-BH** in BMIM Ac at 95 ºC, it was possible to dehydrogenate up to 14.5 liters of formic acid (FA/IL > 3600) at an average rate of 8000 h^{-1}, resulting in a turnover number of 18.1 million after 112 days (Figure 4, S16). After 79 days, we noticed accumulation of formic acid in the reaction flask with consequent decrease in the gas flow (first gray bar in the graph). We removed the excess of formic acid and restarted the reaction. It was not possible to achieve the same rate in activity, but only its 80% (see Figure S16e). Afterwards, the system remained stable at an average rate of 7950 h^{-1} (FA rate of 6 mL/h – 160 mL/min gas flow) until day 112 when the reaction was stopped (Figure S16). It was possible to stop the system, which was cooled at room temperature for 4 days before heating up again to 95 ºC and restoring the formic acid feed (second gray bar in the graph). ^{1}H-NMR analysis revealed that the acetate anion was completely replaced by formate over the 3 months of reaction, resulting in the formation of the corresponding BMIM CHOO IL (Figure S17). Similarly to batch conditions, no CO was detected by various measurements over the 108 days (Figure S19).

Overall, this result exceeds previously reported catalytic systems in terms of both activity and stability over time. Importantly, as opposed to classical batch set-ups where formic acid is added initially, here we demonstrated a practical and small unit that simulates the conditions of for example a hydrogen vehicle. Also important on a practical perspective, all the manipulations were performed with no precautions under ambient conditions, using commercial grade FA without prior purification. The possibility of using neat formic acid allows the maximum gravimetric H_2 content of the system, maximizing its energetic and volumetric properties in a reduced scale.

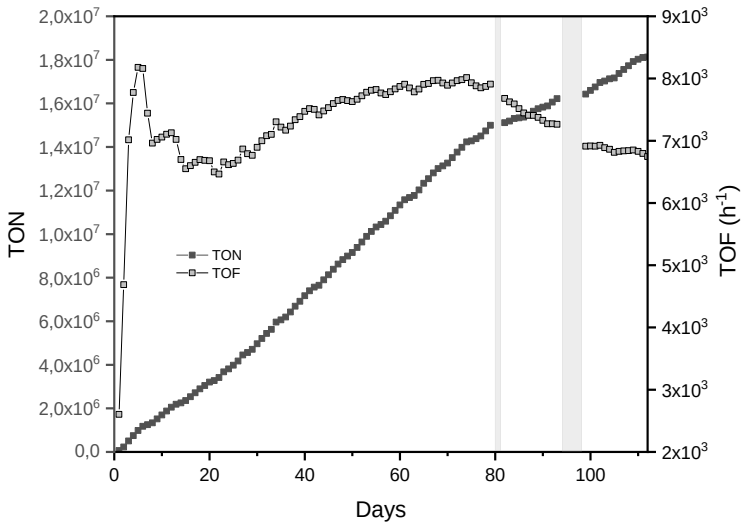

Figure 4: Gas evolution profile of long-term continuous flow formic acid dehydrogenation.
Reaction conditions: Ru-MACHO-BH (0.02 mmol), BMIM Ac (4 mL), 95 ºC.

Conclusions

In this work, we demonstrated a new approach for a CO_2-neutral energy system based on Ru-PNP pincer organometallic complexes in ionic liquid as the only reaction media. The system shows high activity and stability towards the hydrogenation of CO_2 already at ambient conditions (25 ºC, 1 bar). The dehydrogenation of formic acid proceeds at temperatures compatible with PEM fuel cell application (T = 80-95 ºC) with turnover frequencies up to 10^4. The optimized system remained stable for up to 4 months, achieving an overall TON of 18 million, the best result published to date in terms of both catalyst activity and stability over extended reaction times. Hydrogen is released with no contamination of vaporized solvents or bases, and no detectable CO in the gas stream. The system catalyzes up to 10 cycles of hydrogenation/dehydrogenation with retention of the catalytic activity and stability over time. Switching between the cycles is favored by simply changing either pressure or temperature conditions.

The system show extreme flexibility, stability and reversibility under a wide range of temperatures, pressures, times and catalyst loading. All of these features make the system a promising candidate for energy storage technologies based on H_2-formic acid. The system presents several practical advantages such as storage and manipulations performed under ambient conditions, as well as the possibility to dehydrogenate neat formic acid maximizing the atom efficiency and hydrogen gravimetric content of the system. It is possible to pause and stop the system, which could potentially be positioned in a small compartment with formic acid that is added continuously from a separate container: this represent the ideal condition for practical implementation of the technology for low-temperature hydrogen release compatible with fuel cell technologies within the automotive sector.

Supplementary Information

Efficient additive-free reversible catalytic hydrogenation of CO_2 and formic acid dehydrogenation under mild conditions

*L.Piccirilli, B. Rabell, R. Padilla, A. Riisager, M. Nielsen**

Department of Chemistry, Technical University of Denmark, DK-2800 Kgs. Lyngby, Denmark;
** Correspondence: marnie@kemi.dtu.dk; Tel.: +45-24651045*

Table of Contents

1. General Information

The ionic liquids were purchased from Iolitec. Ru-MACHO, Ru-MACHO-BH, Ru-2, Ru-4 and Ru-5 were purchased from StremChemicals and stored in a glove box. Ru-1 [236] and Ru-3 [106] were synthetized modifying reported procedures starting from the precursor Ru-2. Formic acid (89%, 96% and 98-100%) was obtained from Merck. Deuterated acetonitrile for NMR analysis from Fluorochem. The NMR spectra were recorded on a Bruker Avance III 400 or 600 MHz spectrometer and were referenced on the solvent peak.

2. Procedure for the hydrogenation of CO_2

In a typical experiment, the autoclave vessel was loaded with the desired volume of the ionic liquid and the catalyst. The autoclave was flushed with CO_2 three times to remove air before applying the desired pressure of CO_2/H_2 and the desired temperature under stirring at 800 rpm. The reaction was then cooled (when above room temperature), the remaining pressure released, and the reaction mixture was analyzed by 1H-NMR using the ionic liquid as the reference.

3. Procedure for the cycle experiments

The first hydrogenation step was performed as described in the previous section for CO_2 hydrogenation. The reaction was then cooled to room temperature and the gas released carefully. A sample for ^{1}H-NMR was taken before loading the autoclave again at 80ºC for the dehydrogenation step. Similarly, after the dehydrogenation the autoclave was cooled to room temperature in order to take a sample for NMR analysis.

4. Procedure for the dehydrogenation of formic acid (batch)

In a typical experiment, the catalyst was scaled in a two-necks flask inside the glove box. Later, the desired volume of ionic liquid is added. The mixture was stirred at the chosen temperature until complete dissolution of the catalyst and formic acid is added with a gentle flow of argon to facilitate hydrogen release. One sample for NMR analysis was taken after 2h. After 3h, the reaction mixture was cooled to room temperature and analyzed by ^{1}H-NMR using 1,4-dioxane as internal standard.

5. Procedure for the dehydrogenation of formic acid (flow)

In a typical experiment, the catalyst was weighted in a three-neck flask inside the glovebox. Later, the desired volume of ionic liquid is added. The mixture was stirred at the chosen temperature until complete dissolution of the catalyst. The syringe pump was loaded with a 60 mL PP syringe. The rate was slowly increased to assess the maximum TOF until visible formic acid accumulation was observed, determining the end of the reaction. The gas flow evolution was measured by means of a MFM and the gas composition analyzed via MicroGC analysis.

In the final long-term experiment, the reaction was prepared as described before, at 95ºC with 320 rpm stirring velocity. The flow was changed accordingly to the time available (for example slower during the weekends). The maximum rate of formic acid was 8.4 mL/h, corresponding to a TOF = 10.050 h^{-1} and a gas evolution fluctuating between 230-250 mL/min.

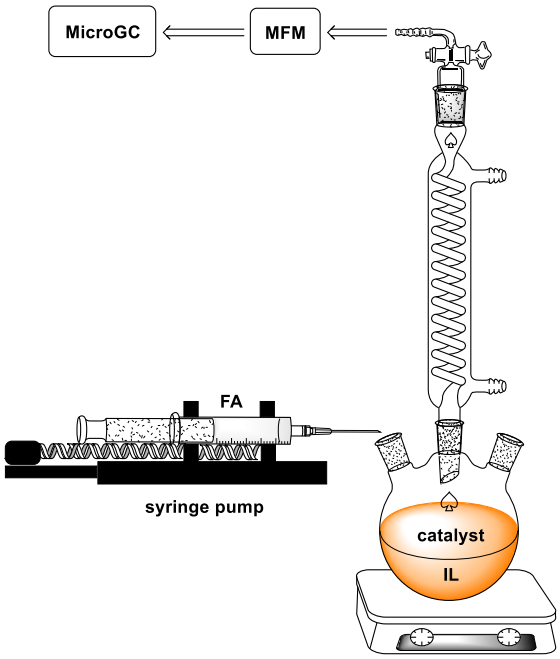

Figure S1: Schematic representation of the reaction set-up for continuous flow formic acid dehydrogenation**.**

Complete screening of catalysts for the hydrogenation of CO_2 to formic acid

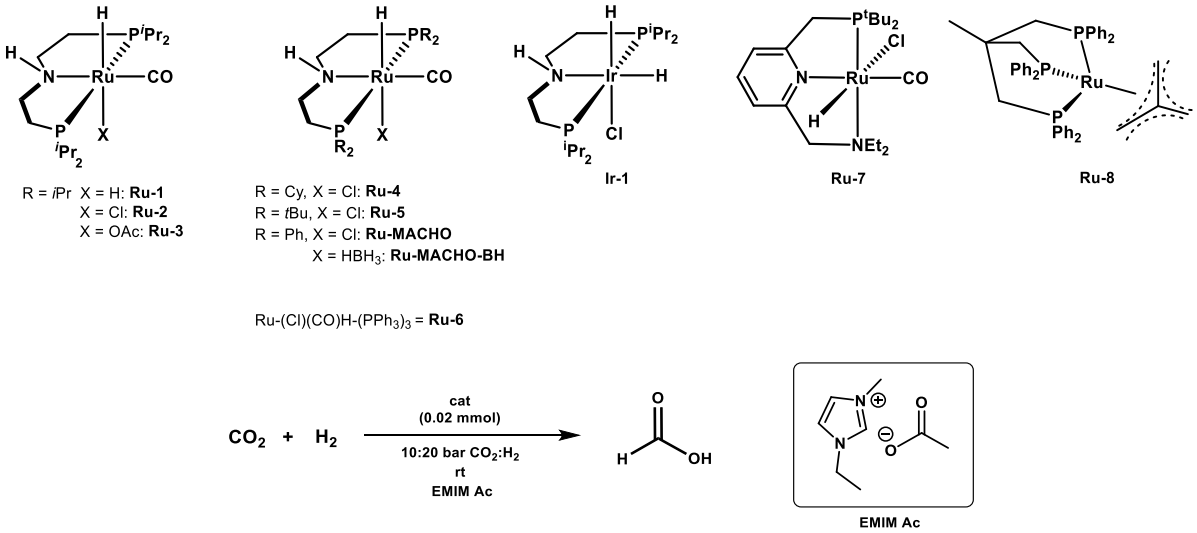

Entry	Catalyst	TON	TOF (h^{-1})	Formate Yield (a) (%)	Formate/IL (%)
1 LP247	Ru-6	-	-	-	<5
2	Ru-7	-	-	-	<5
3	Ru-8	-	-	-	<5
4 LP212	Ru-MACHO	-	-	-	<5
5 LP213	Ru-MACHO-BH	-	-	-	<5
6 LP153	Ru-4	22	2	11	7
7 LP152	Ru-5	66	4	36	22
8 LP040-B (b)	Ir-1	81	4	36	28
9 LP066	Ru-3	109	6	61	36
10 LP036-B	Ru-2	106	8	70	35
11 LP062	Ru-1	198	10	>99	65

Table S1: Screening of catalysts for the hydrogenation of CO_2 to FA.

Reactivity of EMIM Ac with CO_2

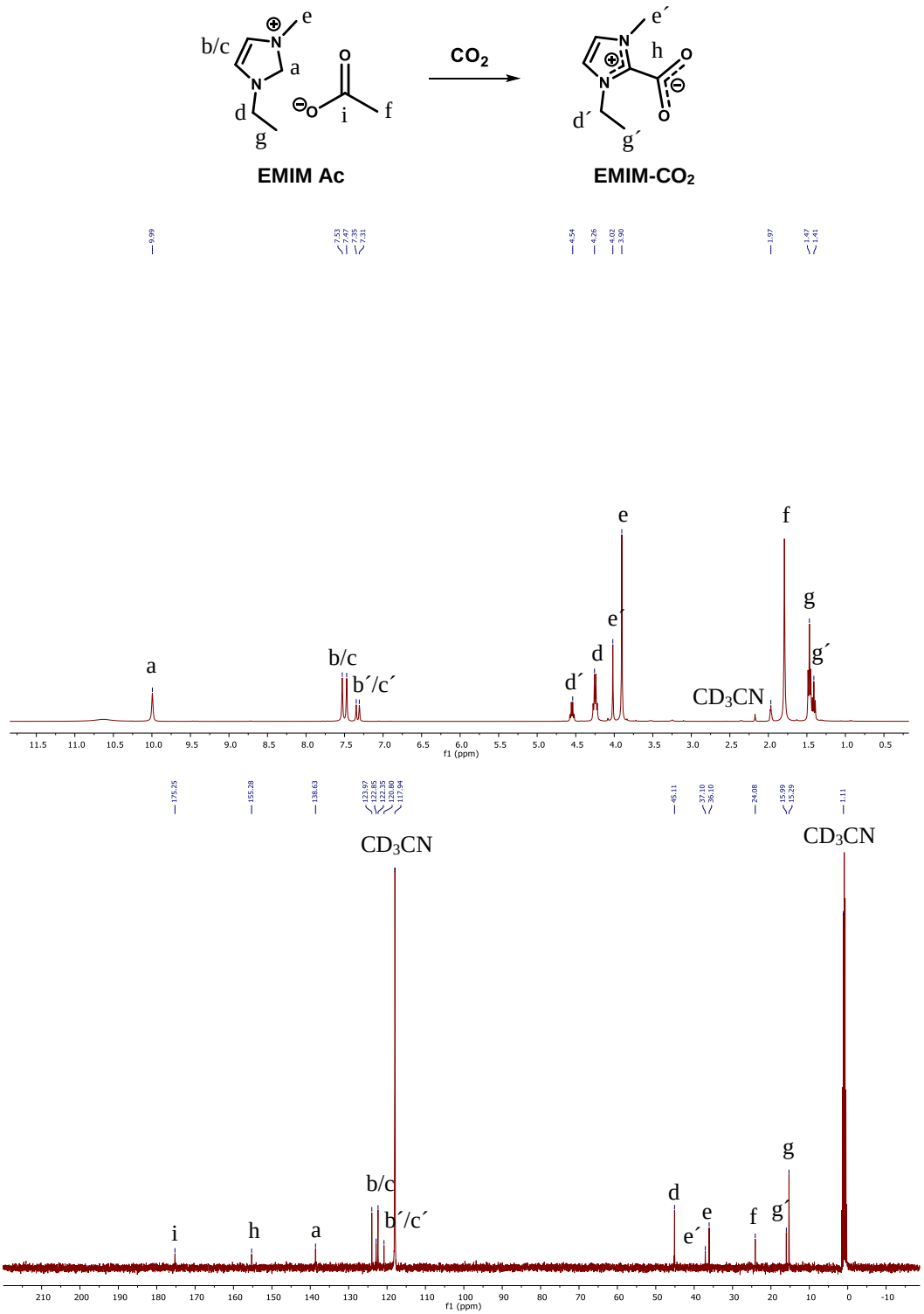

Figure S2: ^{1}H-NMR (up) and ^{13}C-NMR (down) spectra of EMIM Ac in the presence of CO_2 (CD_3CN, 25 ^{o}C, 400 MHz).

Reactivity of Ru-1 with EMIM Ac

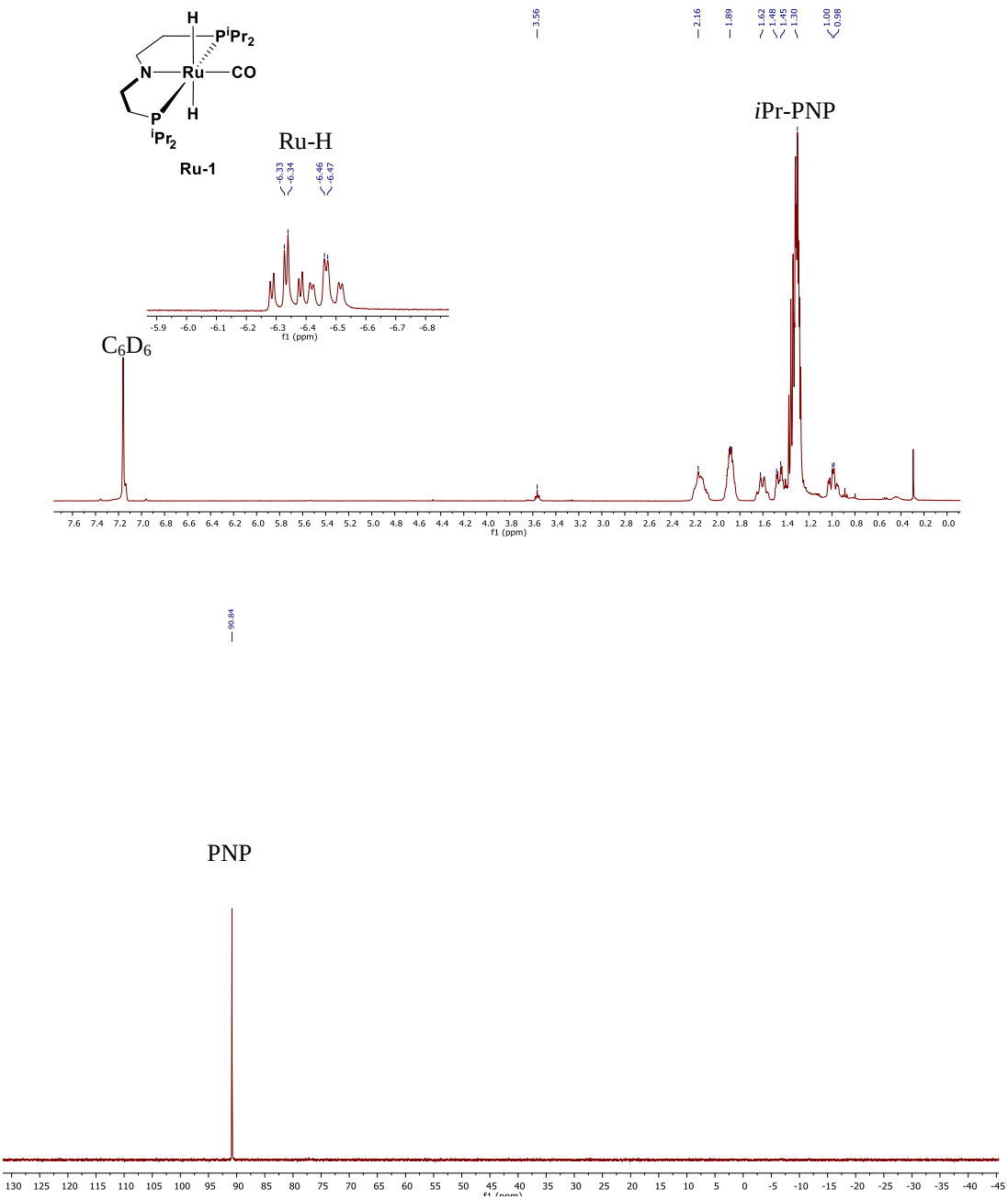

Figure S3: ^{1}H (up) and ^{31}P (down) NMR spectra of Ru-1 (C_6D_6, 25 ºC, 400 MHz).

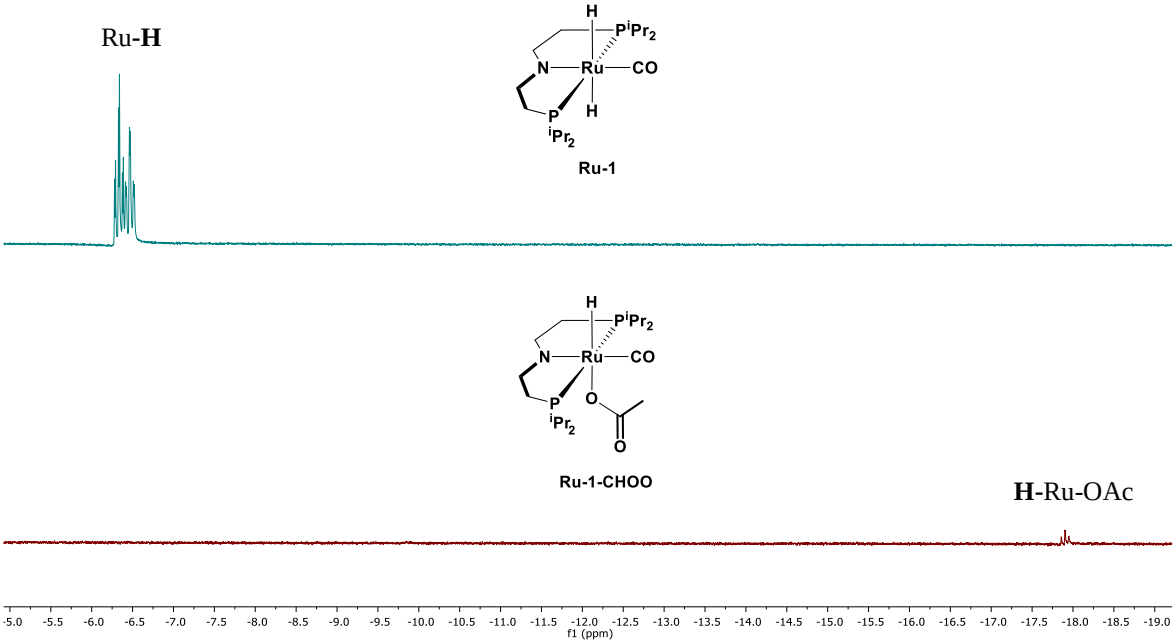

Figure S4: ^{1}H-NMR spectrum of Ru-1 (down) and Ru-1 in the presence of EMIM Ac (up) (C_6D_6, 25 ºC, 400 MHz).

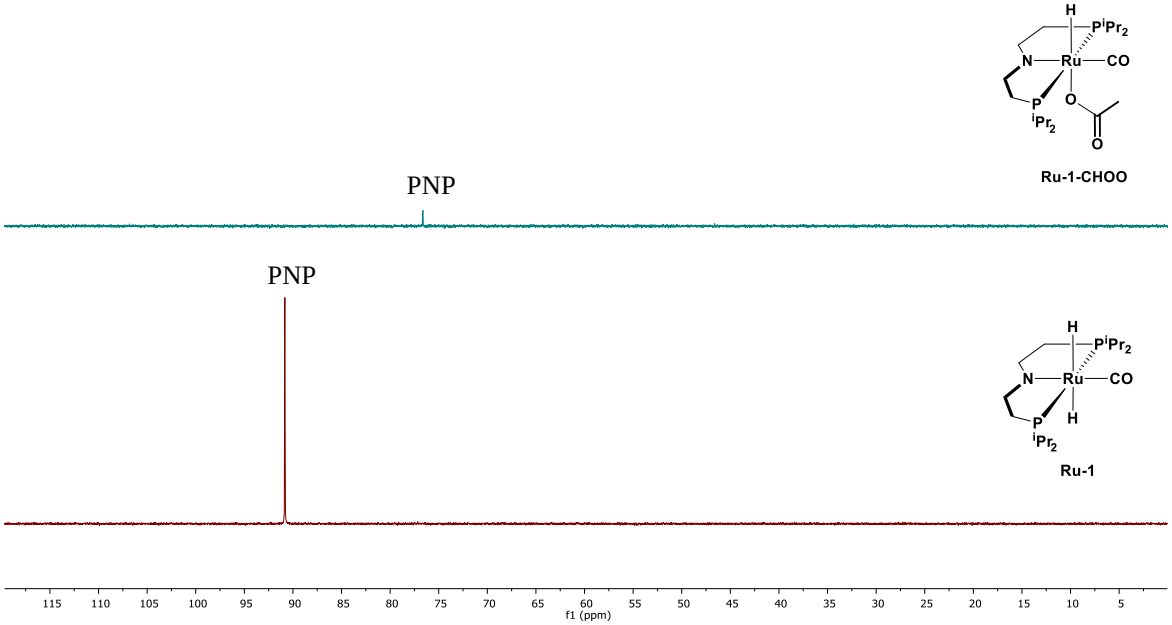

Figure S5: ^{31}P spectrum of Ru-1 (down) and Ru-1 in the presence of EMIM Ac (up) (C_6D_6, 25 ºC, 400 MHz).

Reaction mixture after completeness of the hydrogenation reaction

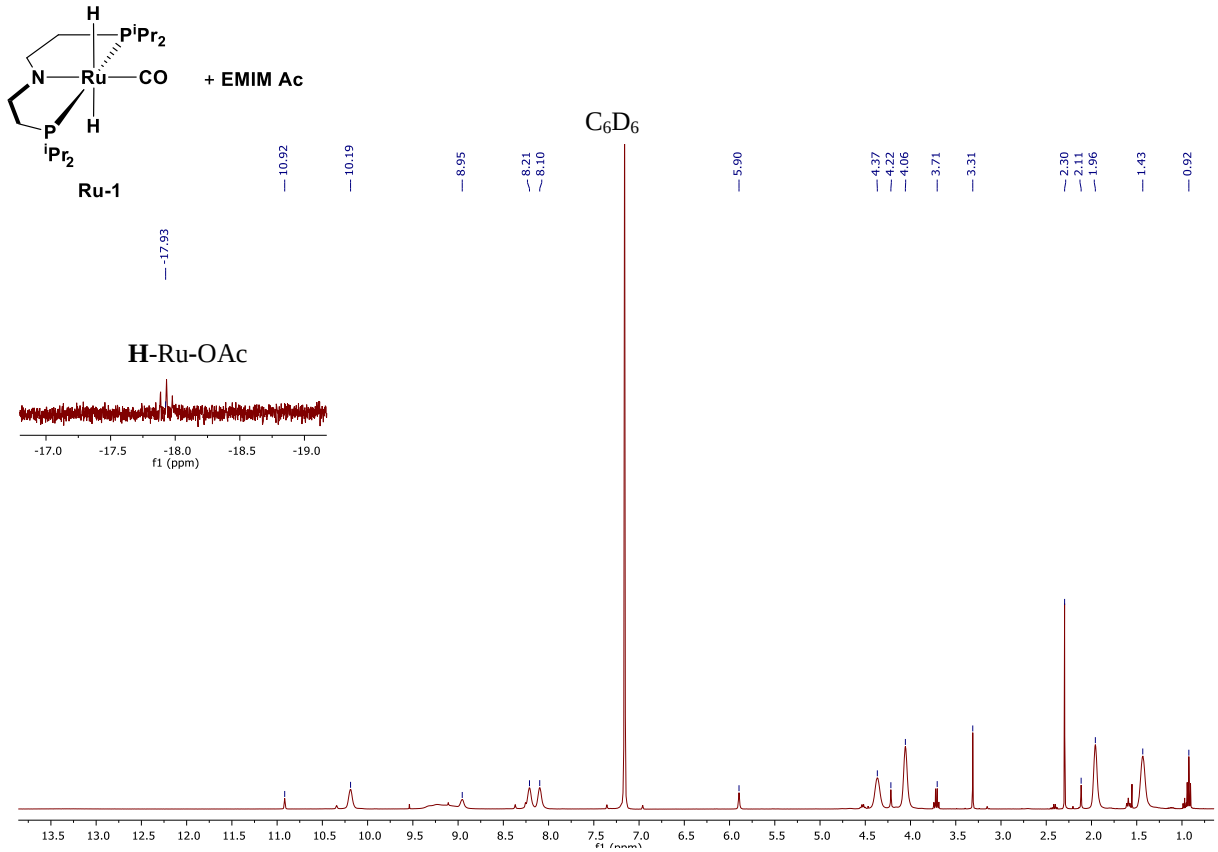

Figure S6: ^{1}H spectrum of Ru-1 in EMIM Ac after catalytic CO_2 hydrogenation (C_6D_6, 25 ºC, 400 MHz).

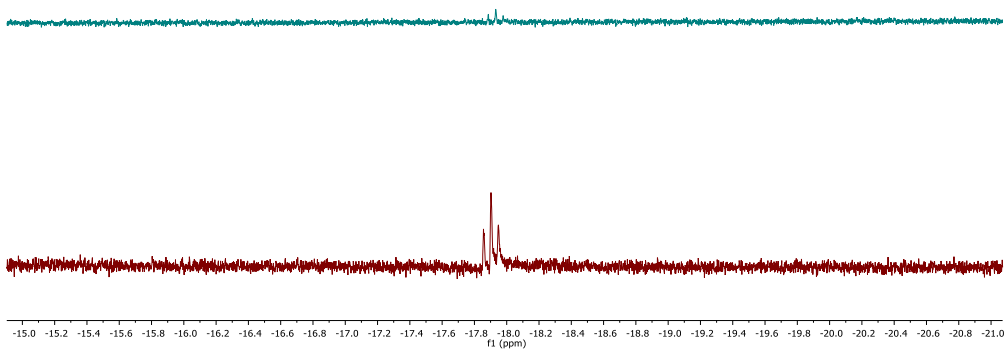

Figure S7: ^{1}H spectrum of Ru-1 in EMIM Ac (down) and Ru-1 after catalytic CO_2 hydrogenation in EMIM Ac (up) (C_6D_6, 25 ºC, 400 MHz).

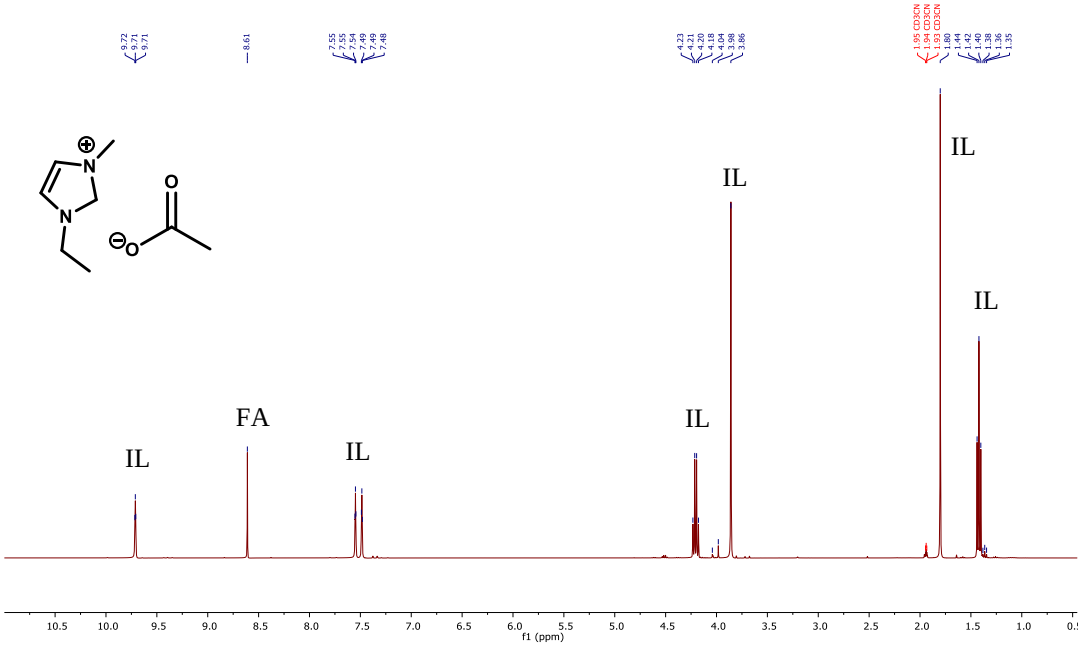

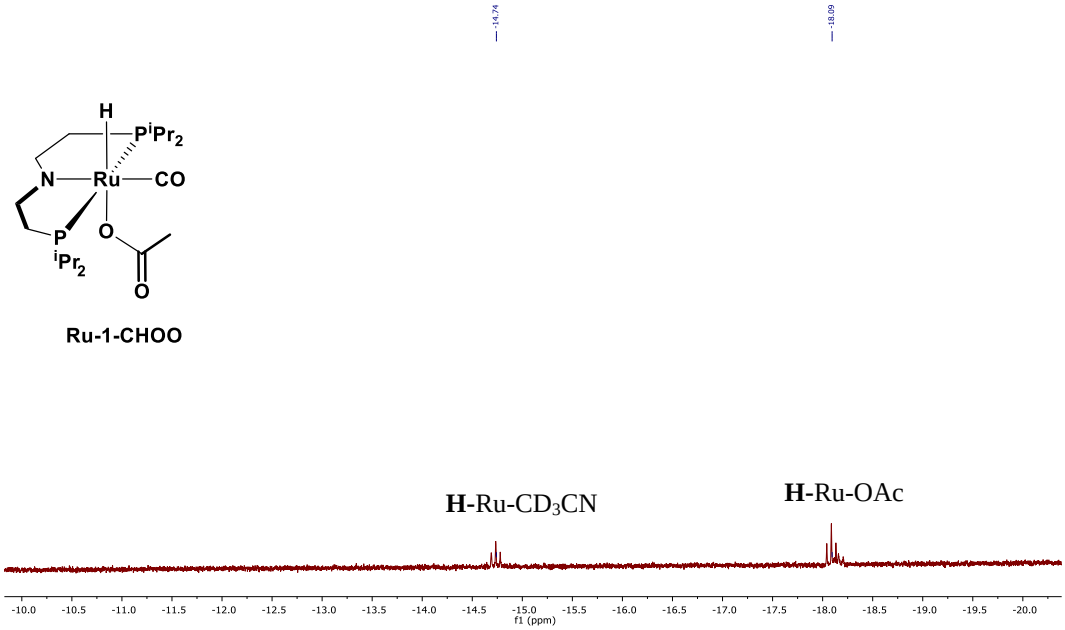

Figure S8: ^{1}NMR of the reaction mixture after catalytic CO_2 hydrogenation to FA. Reaction conditions: Ru-1 (0.02 mmol), EMIM Ac (1 mL), CO_2 (20bar), H_2 (20 bar), rt, 18h (CD_3CN, 25 ^{o}C, 400 MHz). (See Figure S2 for IL assignment).

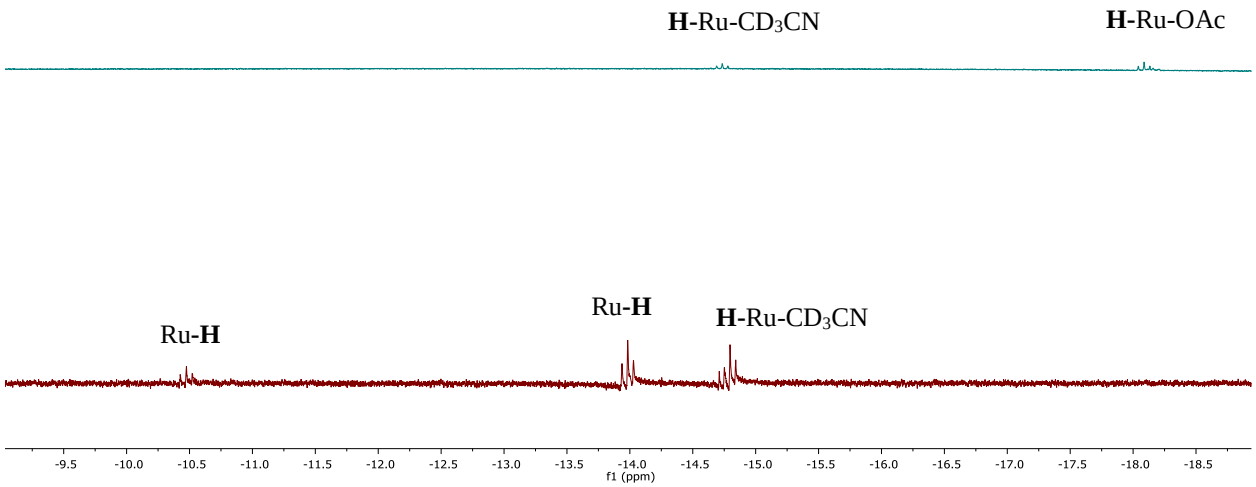

Figure S9: ^{1}H spectrum of Ru-1 in CD_3CN (down) and Ru-1 after catalytic CO_2 hydrogenation in EMIM Ac (up) in CD_3CN (25 ºC, 400 MHz).

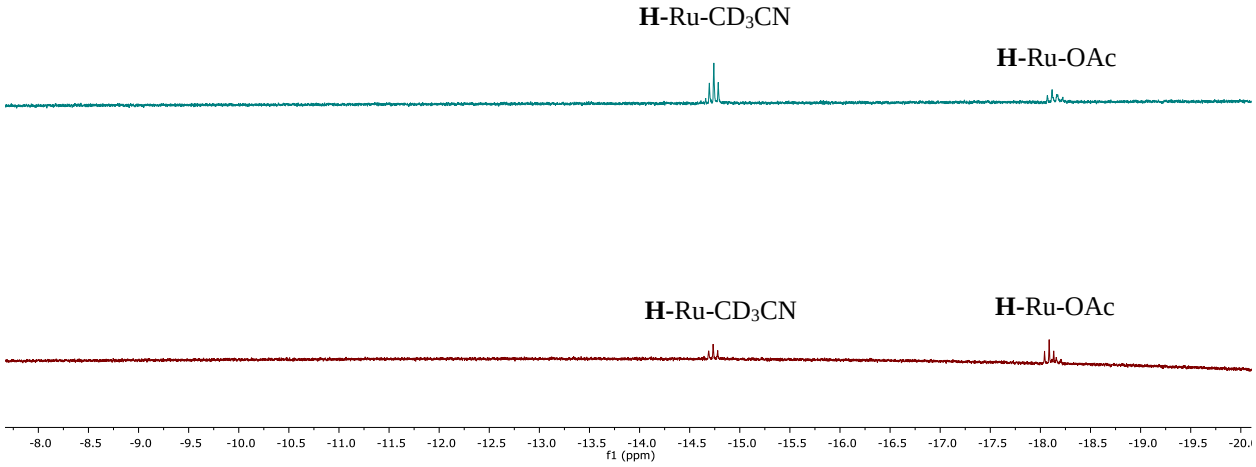

Figure S10: ^{1}H spectrum of Ru-1 (down) and Ru-2 (up) after catalytic CO_2 hydrogenation in EMIM Ac (CD_3CN, 25 ºC, 400 MHz).

Labeling experiment with D_2

^2H

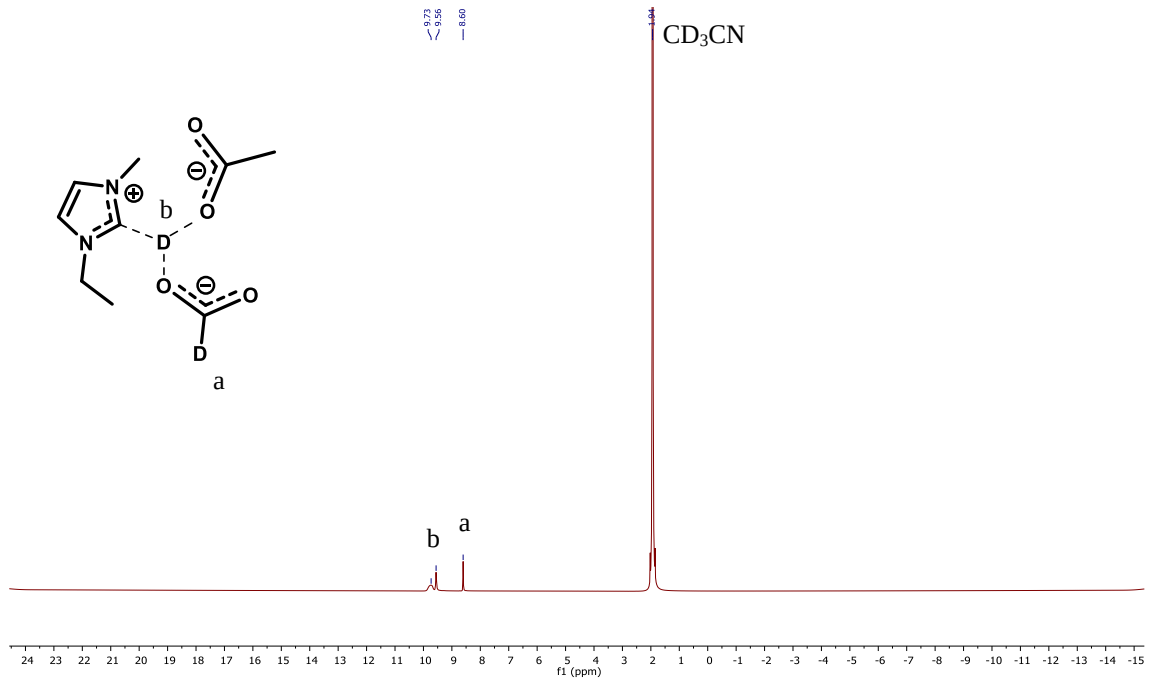

Figure S11: Labeling experiment with deuterium (CD_3CN, 25 ºC, 400 MHz). Reaction conditions: Ru-2 (0.02 mmol), EMIM Ac (1 mL), CO_2 (5 bar), D_2 (15 bar), 50ºC, 18h.

Labeling experiment with $^{13}CO_2$

^{1}H

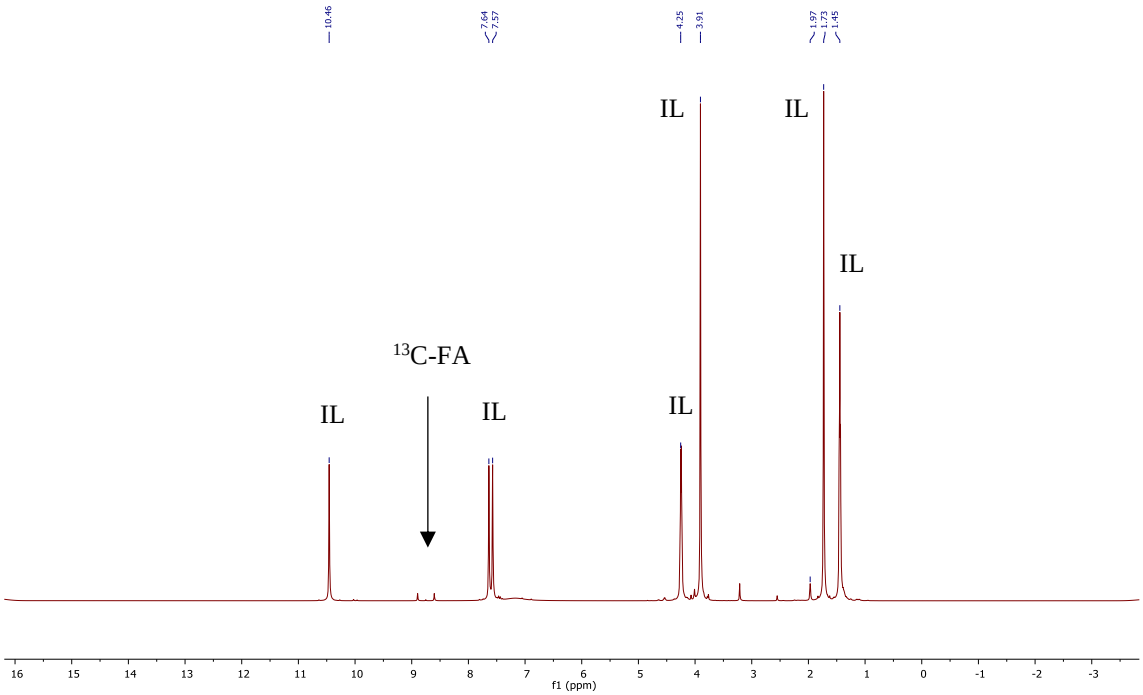

^{1}H w. ^{13}C decoupling

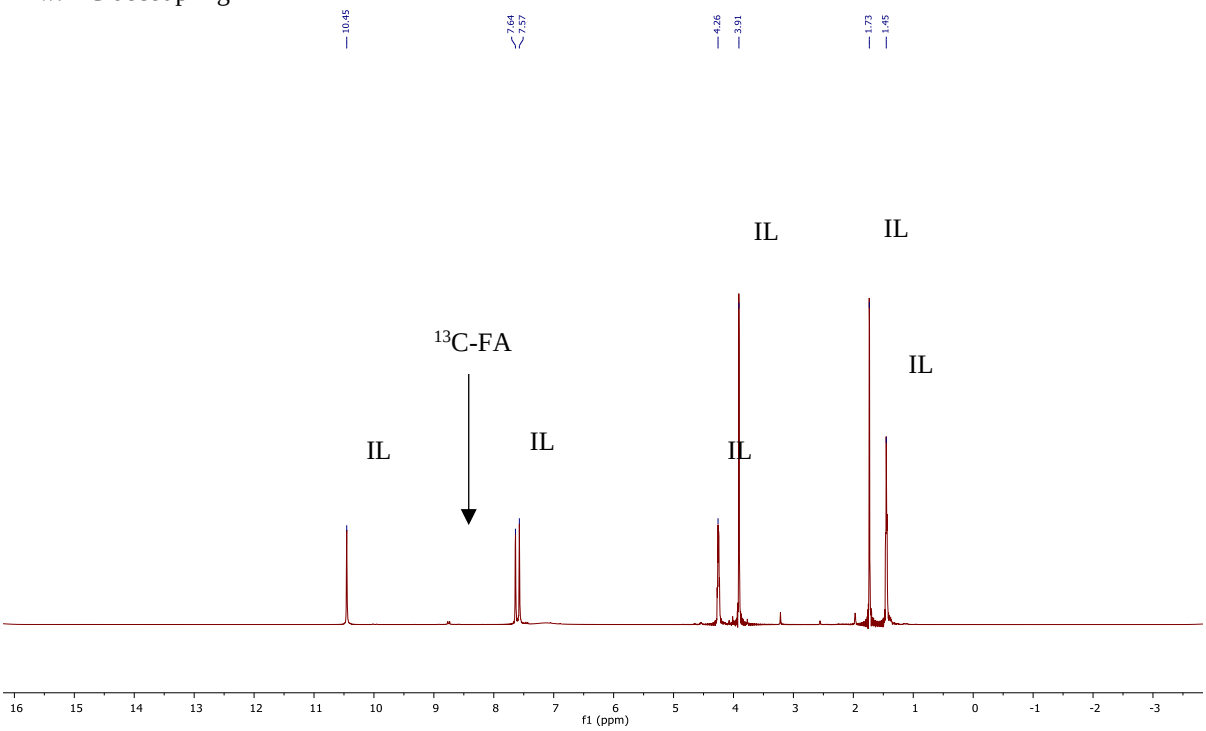

13C w. 1H decoupling

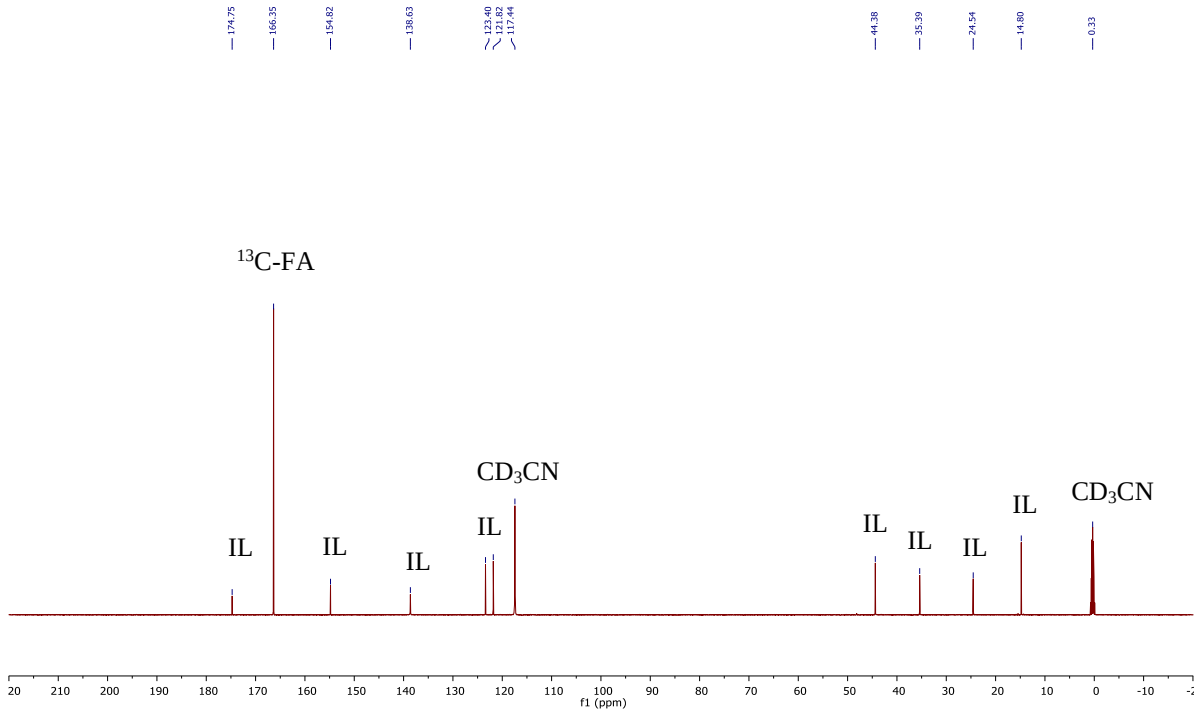

^{13}C without ^{1}H decoupling.

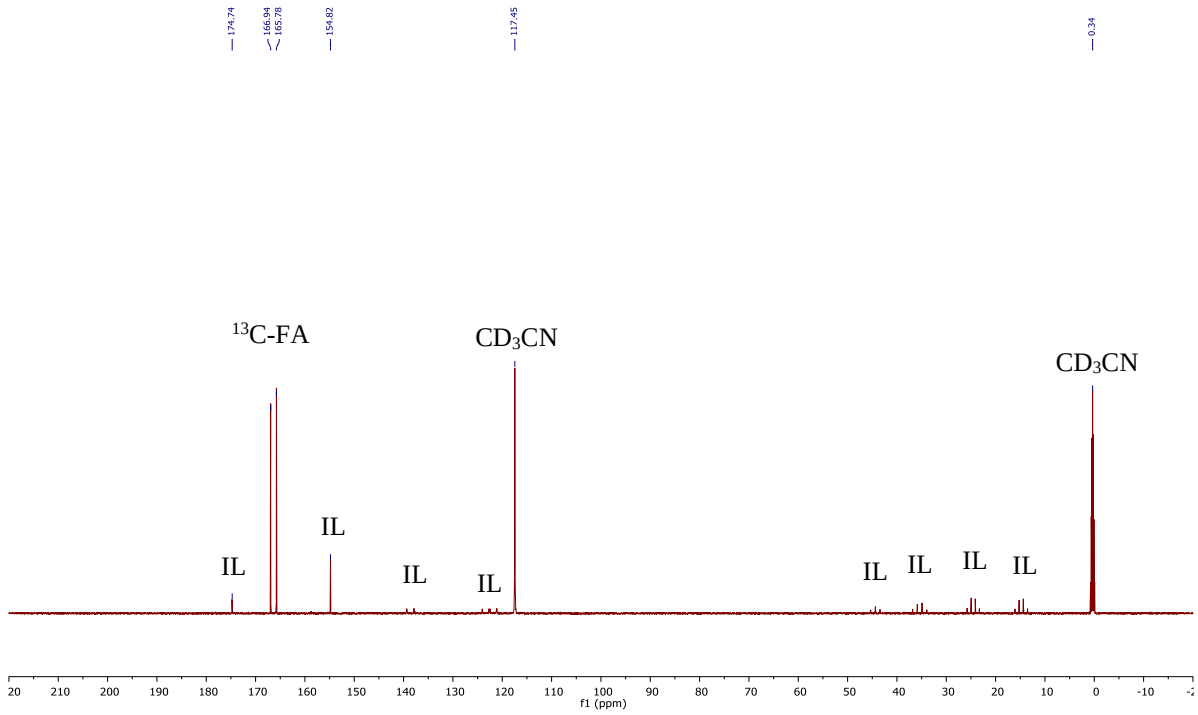

Figure S12: Labeling experiment with $^{13}CO_2$ (CD_3CN, 25 ºC, 400 MHz). Reaction conditions: Ru-2 (0.02 mmol), EMIM Ac (1 mL), $^{13}CO_2$ (1 bar), H_2 (15 bar), 50ºC, 24h. (See Figure S2 for IL assignment).

Reaction mixture after completeness of the dehydrogenation reaction (batch)

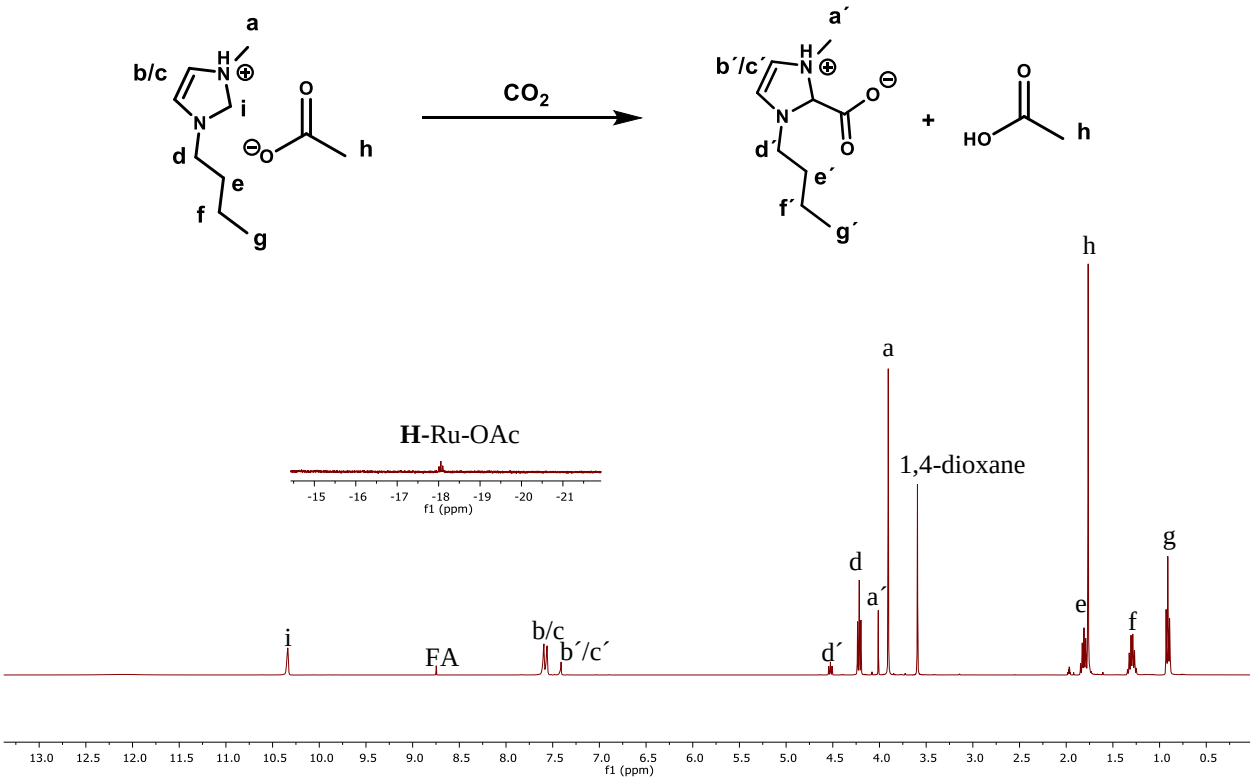

Figure S13: ^{1}NMR of the reaction mixture after catalytic dehydrogenation of FA (CD_3CN, 25 ºC, 400 MHz). Reaction conditions in entry 4, Table 2. It is possible to notice the presence of CO_2 trapped.

^{1}NMR analysis of cycle experiments

Dehydrogenation

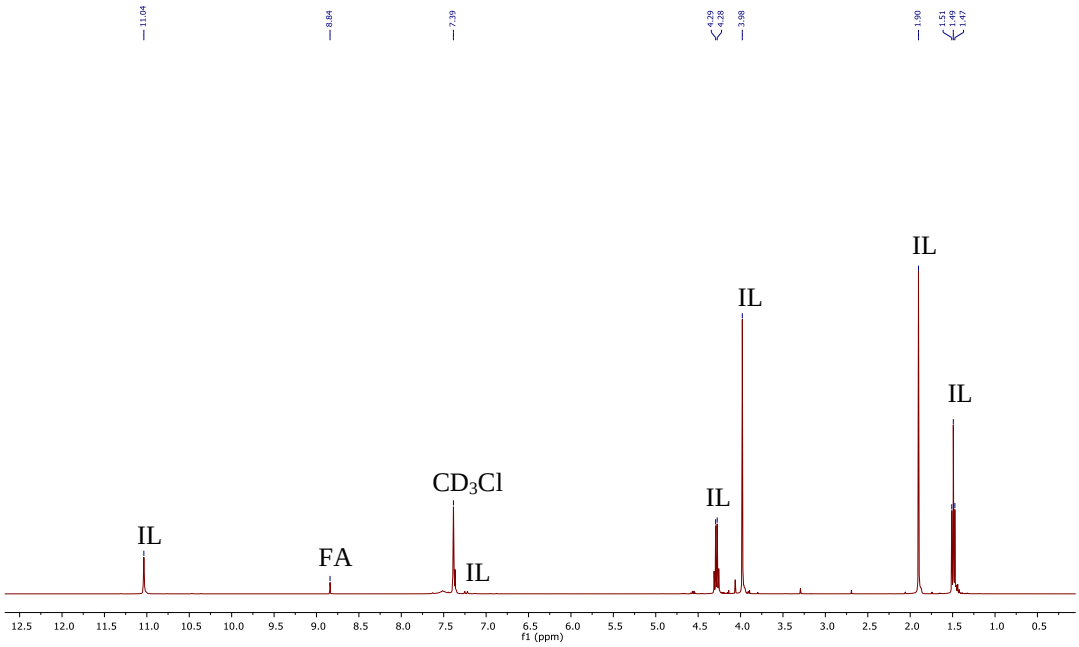

Hydrogenation

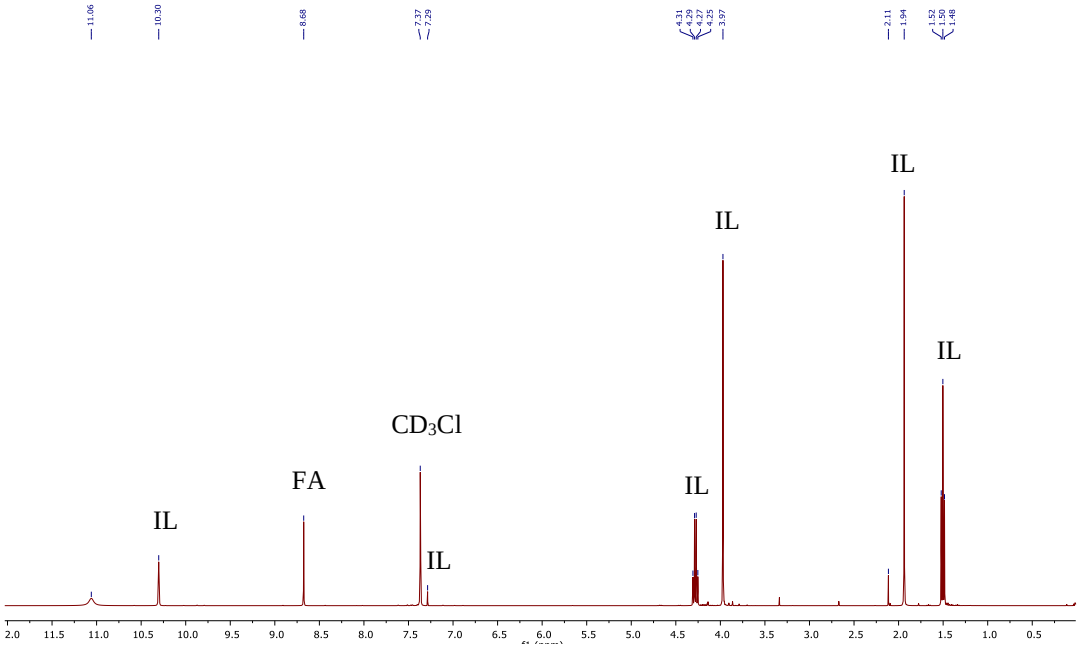

Figure S14: Reaction conditions: Ru-1 (0.004 mmol), EMIM Ac (3 mL), 80ºC, 18h. CO_2 (10 bar), H_2 (20 bar) for the hydrogenation. See Figure S2 for IL assignment. (CD_3Cl, 25 ºC, 400 MHz).

Cycles experiments with Ru-2

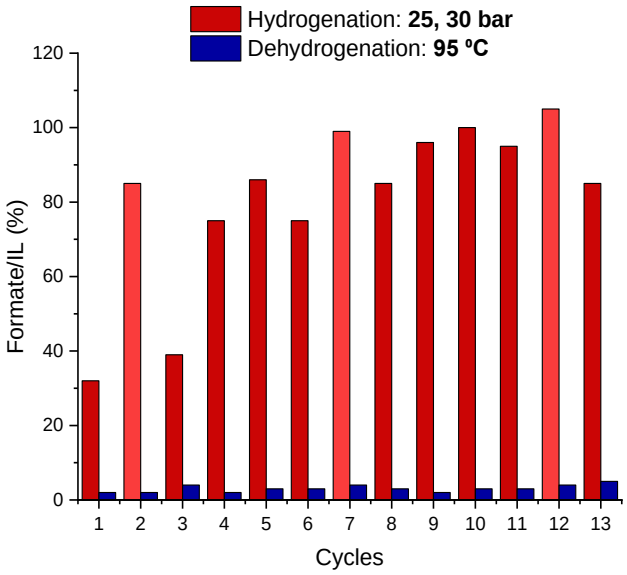

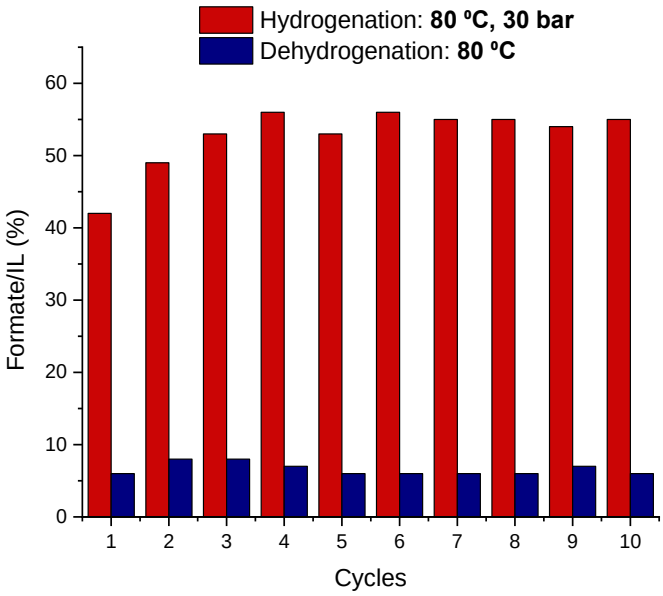

Figure S15: Cycles experiment of CO_2 hydrogenation followed by hydrogen release. Up: Ru-2 (0.05 mmol), EMIM Ac (2 mL), 10:20 bar CO_2:H_2, 18 h for the hydrogenation (72 h in the lighter bars), open autoclave (4 h) for the dehydrogenation. Down: Ru-2 (0.02 mmol), EMIM Ac (3 mL), 10:20 bar CO_2:H_2, 18 h for the hydrogenation, open autoclave (18 h) for the dehydrogenation.

Continuous-flow formic acid dehydrogenation: screening of catalysts

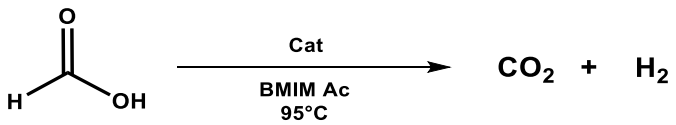

Entry	Catalyst	Cat load (mmol)	TOF max (h^{-1})
1 FAD44	Ru-MACHO-BH	0.027	4908
2 FAD52	Ru-1	0.020	7288
3 FAD57	Ru-2	0.020	7288
4 FAD55	Ru-MACHO	0.020	10800
5 FAD68	Ru-MACHO-BH	0.025	10600

* FAD 44: 80ºC

Table S2: Screening of catalysts for the dehydrogenation of formic acid under continuous flow.

Continuous-flow formic acid dehydrogenation: long-term experiments

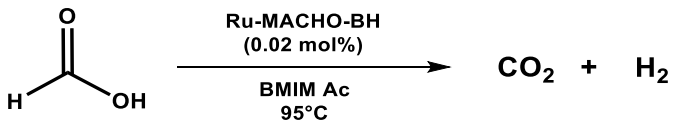

Entry	BMIM Ac (mL)	Concentration (M)	TON	TOF_{med} (h^{-1})
FAD75	2	0.01	980.000 (9 days)	4.500
FAD84	3	0.007	2.171.653 (15 days)	6.030
FAD86	4	0.005	15.143.315 (79 days)	7.986

Table S3: Optimization of FA dehydrogenation under flow conditions.

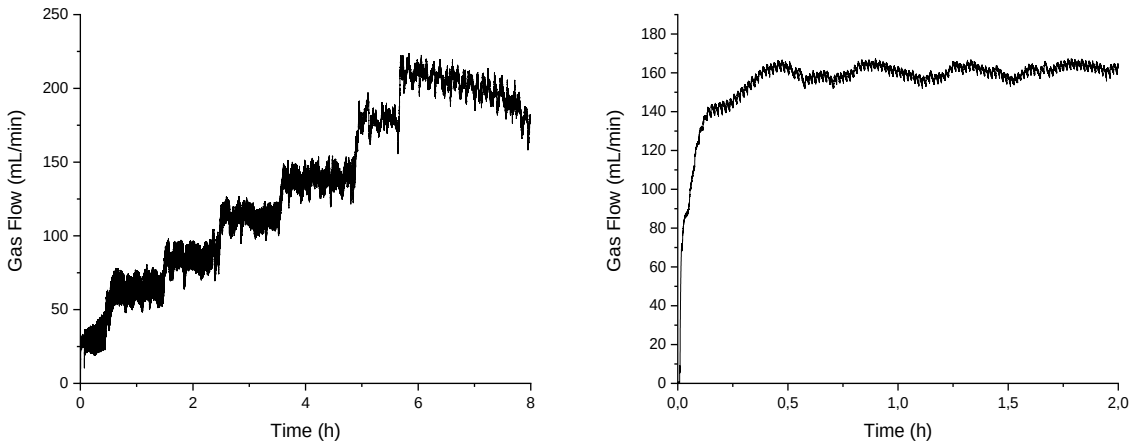

Figure S16: Gas flow evolution measured over the long-term experiment showed in Figure 4. The red numbers in Figures e and f indicate the turnover frequency (h^{-1}).

^{1}NMR analysis of long-term continuous flow formic acid dehydrogenation

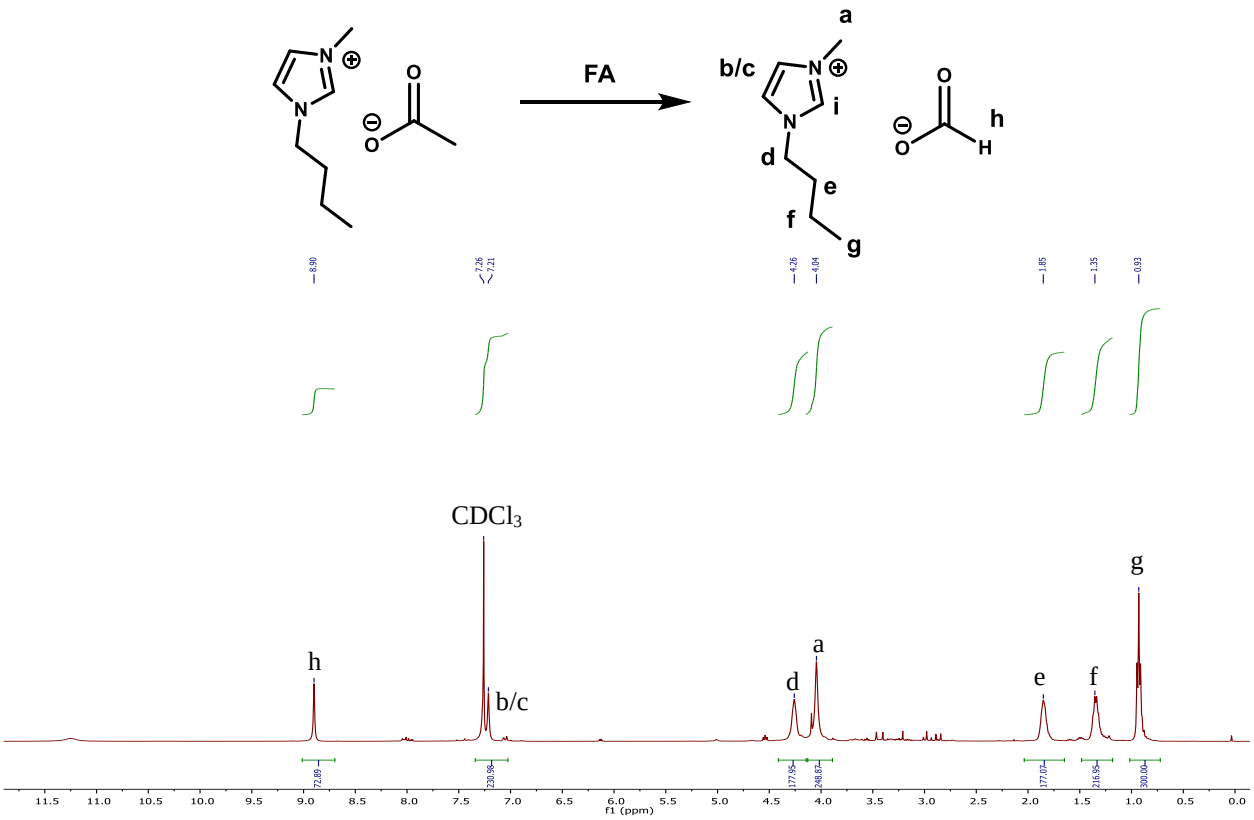

Figure S17: ^{1}H NMR of the reaction mixture of the long-term experiment in Figure 4 (day 105). (CD_3Cl, 25 ºC, 400 MHz).

GC report of FA dehydrogenation under batch conditions

External Standard Report

Page 1 of 2

Method Name: C:\Users\Administrator\Agilent\Method\20190717_Luca_Final.met
Data: C:\Users\Administrator\Agilent\Result\161_FAD27-MACHOBH-BATCH_2021-10-20 09-59-48 (GMT +02-00).dat.rslt\161_FAD27-MACHOBH-BATCH_2021-10-20 10-41-35 (GMT +02-00)-Rep6.dat
User: SYSTEM (SYSTEM)
Acquired: 10/20/2021 10:42:22 AM (GMT +02:00)
Printed: 10/28/2021 1:49:58 PM (GMT +02:00)

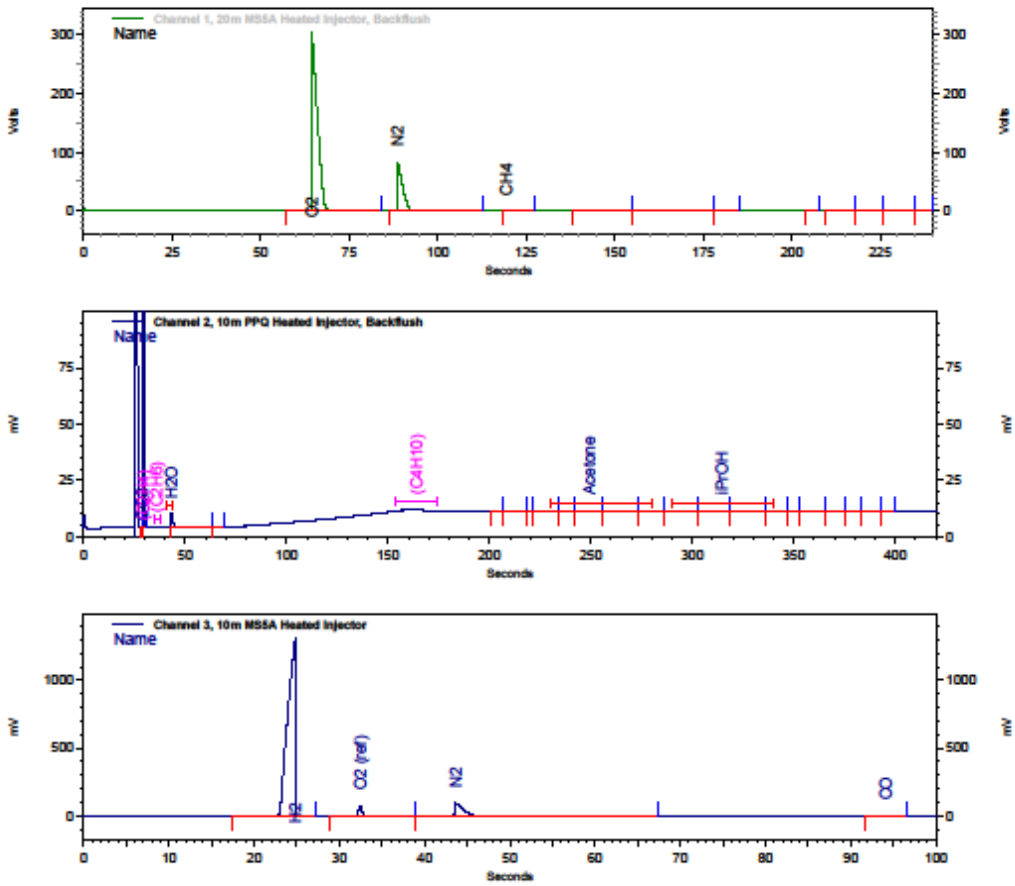

Channel 1, 20m MS5A Heated Injector, Backflush Results

Pk #	Name	Retention Time	Area	Concentration
1	O2	64.5	55408347	**51.5**
2	N2	88.7	14691423	**13.3**
3	CH4	119.4	402	**0.0**
	CO			**0.0 BDL**

External Standard Report

Method Name: C:\Users\Administrator\Agilent\Method\20190717_Luca_Final.met
Data: C:\Users\Administrator\Agilent\Result\161_FAD27-MACHOBH-BATCH_2021-10-20 09-59-48 (GMT +02-00).dat.rslt\161_FAD27-MACHOBH-BATCH_2021-10-20 10-41-35 (GMT +02-00)-Rep6.dat
User: SYSTEM (SYSTEM)
Acquired: 10/20/2021 10:42:22 AM (GMT +02:00)
Printed: 10/28/2021 1:49:58 PM (GMT +02:00)

Totals		70100172	**64.8**

Channel 2, 10m PPQ Heated Injector, Backflush Results

Pk #	*Name*	*Retention Time*	*Area*	*Concentration*
2	CO2	29.0	31956999	**15.6**
	C2H4			**0.0 BDL**
	C2H6			**0.0 BDL**
3	H2O	43.3	727980	**10.7**
	C4H10			**0.0 BDL**
10	Acetone	249.1	2754	**0.0**
14	iPrOH	314.4	3274	**0.0**
Totals			32691007	**26.3**

Channel 3, 10m MS5A Heated Injector Results

Pk #	*Name*	*Retention Time*	*Area*	*Concentration*
1	H2	24.9	139563171	**18.4**
2	O2 (ref)	32.4	3512694	**3.7**
3	N2	43.6	10596593	**14.7**
4	CO	94.1	637	**0.0**
Totals			153673095	**36.7**

Figure S18: Micro-GC report of FA dehydrogenation under batch conditions (Entry 5, Table 2 in the main text).

GCreport of continuous flow FA dehydrogenation (day 58)

External Standard Report

Page 1 of 2

Method Name: C:\Users\Administrator\Agilent\Method\20190717_Luca_Final.met
Data: C:\Users\Administrator\Agilent\Result\FA syringe pump\159_FAD86_day58_ArFirst_2021-09-28 10-11-15 (GMT +02-00).dat.rslt\159_FAD86_day58_ArFirst_2021-09-28 13-32-49 (GMT +02-00)-Rep25.dat
User: SYSTEM (SYSTEM)
Acquired: 9/28/2021 1:33:42 PM (GMT +02:00)
Printed: 10/28/2021 1:56:57 PM (GMT +02:00)

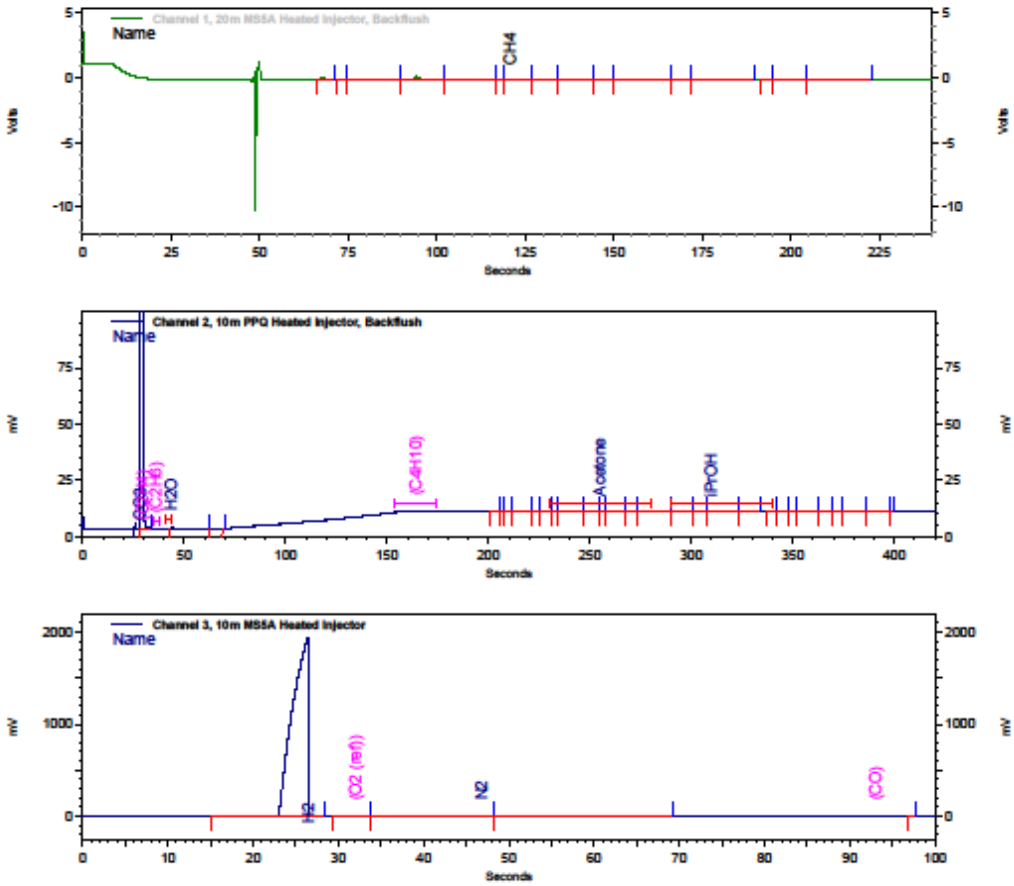

Channel 1, 20m MS5A Heated Injector, Backflush Results

Pk #	Name	Retention Time	Area	Concentration
	O2			0.0 BDL
	N2			0.0 BDL
7	CH4	120.6	3447	0.0
	CO			0.0 BDL

External Standard Report

Method Name: C:\Users\Administrator\Agilent\Method\20190717_Luca_Final.met
Data: C:\Users\Administrator\Agilent\Result\FA syringe pump\159_FAD86_day58_ArFirst_2021-09-28 10-11-15 (GMT +02-00).dat.rslt\159_FAD86_day58_ArFirst_2021-09-28 13-32-49 (GMT +02-00)-Rep25.dat
User: SYSTEM (SYSTEM)
Acquired: 9/28/2021 1:33:42 PM (GMT +02:00)
Printed: 10/28/2021 1:56:57 PM (GMT +02:00)

Totals		3447	0.0

Channel 2, 10m PPQ Heated Injector, Backflush Results

Pk #	*Name*	*Retention Time*	*Area*	*Concentration*
1	CO2	28.0	115218056	56.3
	C2H4			0.0 BDL
	C2H6			0.0 BDL
2	H2O	43.7	90414017	1325.5
	C4H10			0.0 BDL
13	Acetone	254.6	2659	0.0
19	iPrOH	309.6	21079	0.0
Totals			205655811	1381.8

Channel 3, 10m MS5A Heated Injector Results

Pk #	*Name*	*Retention Time*	*Area*	*Concentration*
1	H2	26.4	402568512	53.0
	O2 (ref)			0.0 BDL
3	N2	46.8	147920	0.2
	CO			0.0 BDL
Totals			402716432	53.2

Figure S19: Micro-GC report of FA dehydrogenation under continuous flow (experiment in Figure 4 in the main text).

.

Appendix G – Paper III

Based on the findings showed in Chapter 5, this work will discuss the reactivity of Ru-PNP catalysts in ILs different from imidazolium acetate species (discussed in Paper II). The remarkably promising results obtained with both EMIM CHOO and EMIM Et_2PO_4, together with the optimization of H_2 prduction under pressure will represent the highlights of this paper, representing a perfect follow-up of Paper II. The experimental and intellectual work was conducted at DTU Chemistry in collaboration with PhD student Brenda Rabell, postdoc Rosa Padilla, and Assoc Prof Martin Nielsen.

Paper in preparation.

Flexible and robust formic acid dehydrogenation using Ru-PNP complexes and ionic liquids

*L.Piccirilli, B. Rabell, R. Padilla, A. Riisager, M. Nielsen**

Department of Chemistry, Technical University of Denmark, DK-2800 Kgs. Lyngby, Denmark;
** Correspondence: marnie@kemi.dtu.dk; Tel.: +45-24651045*

Abstract

The use of a Liquid Organic Hydrogen Carrier (LOHC) allows moving of renewable high-density energy across long distances. Formic acid (FA) is considered a viable LOHC candidate with 4.4 wt% of hydrogen storage capacity. We recently reported on the reversible CO_2 hydrogenation/FA dehydrogenation under mild conditions. Herein, we investigate more in detail the dehydrogenation of FA for continuous hydrogen release at temperatures compatible with proton exchange membrane fuel cell technologies. The combination of a Ru-PNP catalyst and an ionic liquid perform FA dehydrogenation at T<100 ºC without the presence of an additive. In addition, we demonstrate the possibility of producing high-pressure hydrogen up to 100 bar. This feature is scarcely reported in literature, but represent a main aspect towards a possible implementation of FA within the hydrogen economy.

Introduction

The urgency of the climate change problem calls for a rapid transition of our current energy systems to a sustainable and climate-neutral one [3]. The green transition should provide sustainable economic development and viable solutions. Hence it is appropriate, when possible, to use existing infrastructures and facilities. Hydrogen-based fuels are potentially a group of main green solutions of the future [8]. Green H_2 can be obtained from water electrolysis, and is characterized by an exceptionally high gravimetric energy density (33.3 kWh/kg). Established technologies for compressed and cryogenic hydrogen apply drastic conditions (up to 700 bar and -253°C, respectively) to increase the volumetric storage density of hydrogen, requiring technically demanding and costly infrastructures. Hence, storage and transportation, together with the high production cost of green hydrogen are hindering the fast development of hydrogen technologies [14].

LOHC fuels are a viable solution for the storage and transportation of renewable energy [23,24,359]. While hydrogen handling in form of liquids allows for using the existing fuel infrastructure, it also builds on the public confidence in dealing with liquid energy carriers. LOHCs offer the possibility to store energy by chemically binding hydrogen onto a liquid molecule, avoiding energetic costs associated with hydrogen compression and/or liquefaction. This possibility of storing energy in formic acid is of great importance considering the discontinuous nature of renewable sources such as solar and wind energy.

Among the future potential and technical applications of LOHC-bound hydrogen, the on-board hydrogen generation for a fuel cell vehicle is a particularly promising concept to enable future zero-emission mobility technologies. Such systems work most effectively if the loss heat of the fuel cell (FC) is directly used to drive the endothermal hydrogen release from the LOHC, a concept that requires the FC temperature to exceed the dehydrogenation temperature.

Formic acid (FA) has been widely proposed as a viable Liquid Organic Hydrogen Carrier (LOHC) [309]. Currently, it is produced from CO and methanol derived from fossil feedstock. The possibility to use green hydrogen for the direct CO_2 capture from air and conversion to FA by means of a catalyzed hydrogenation reaction, represents an ideal CO_2-free energy cycle [360]. FA production from biomass has also been demonstrated [74,76], together with its further transformation into syn-gas followed by Fischer-Tropsch synthesis of hydrocarbons [77]. FA is liquid and safe to handle at ambient conditions, avoiding energetic costs and safety issues associated with hydrogen compression. It has a hydrogen capacity of 4.4 wt%, but due to its high density of 1.22 g/cm^3, it possesses a volumetric capacity of 53 g H_2/L. This corresponds to an energy density of 1.77 kW·h/L, higher than commercial 70 MPa hydrogen tanks (1.4 kW·h/L) [310], indicating that FA may be suitable for automotive and mobile applications.

When considering the state-of-the-art technology for proton-exchange membrane fuel cell (PEM-FC), it is essential that hydrogen is released from the LOHC at temperatures <100 ºC to ensure full heat-integration [12]. In addition, the flow of hydrogen gas should be free of contaminants such as volatile solvents and carbon monoxide that could hamper the functionality of the fuel cell.

The literature is rich with examples of homogeneously catalyzed FA decomposition [312–316]. Some studies reported the use of first-row transition metals [317][160][161][318][319]; however, these complexes usually exhibit lower activity and stability when compared to more established catalysts based on ruthenium and iridium. Many of the reported results employ bases (amines, formates, DBU) to control the pH of the reaction and avoid catalyst degradation. The use of volatile organic solvents is also widely reported (THF, dioxane, DMF). Himeda showed an iridium Cp^* complex (**Ir-2**) that afforded a TON = 10 million for the continuous flow dehydrogenation of 20 M of FA (aq) at 70 ºC [255]. Milstein recently reported a Ru-acridine pincer complex (**Ru-5**) that dehydrogenates neat formic acid affording a TON = 1.7 million [322]. The same work also addressed the possibility to produce hydrogen under pressure. **Ru-5** afforded up to 100 bar in less than 1 h. The best reported system for hydrogen evolution under pressurized conditions was reported by Kawanami in 2016 using **Ir-3** [323]. The system produced up to 115 MPa, corresponding to >120 L of hydrogen released. Later, the same author further investigated the process exploring the influence of both solvents [324] and ligands [325].

The possibility to release hydrogen from FA without the use of reaction additives allow full energy storage potential and the production of a clean H_2 flow without the contamination of organic molecules vapors. Other studies reported the dehydrogenation of variously diluted aqueous FA mixtures; this aspect lowers the overall energy storage potential, and can lead to the presence of vapor in the hydrogen gas stream. Hence, the possibility to dehydrogenate neat formic acid is of great industrial interest. At the same time, small amounts of water and other impurities should be tolerated by a candidate catalytic system for every-day applications. In addition, the possibility to produce pressurized hydrogen is a useful feature for industrial implementation due to the possibility of storing hydrogen when is not needed.

Herein, we demonstrate a continuous, selective hydrogen release from the LOHC candidate FA at temperatures below 100 °C and thus under conditions that enable a heat transfer of waste heat from a PEM-FC to the hydrogen release unit. The reaction is catalyzed by organometallic ruthenium-PNP complexes in ionic liquid. The ionic liquid allows the obtainment of a clean flow of hydrogen gas without the presence of volatile contaminants. In addition, we demonstrate the possibility of producing high-pressure hydrogen in a closed system, an important feature for practical implementation of the technology.

Results and Discussion

Batch

We started our investigation by screening ionic liquids bearing different anions with basic and coordinating properties in the presence of the pre-catalyst **Ru-MACHO**. We demonstrated that suitable ILs can activate the pre-catalyst with in-situ formation of the catalytic active species without the addition of any basic additives (Table S2). Moreover, the anion is the key component for the chemical properties of the ionic liquid [185], i.e. contemporarily acting as a ligand for the catalyst as well as a buffer to balance the acidity of formic acid. Poor or absent gas evolution was observed at room temperature, together with scarce solubility of the catalysts. Clear hydrogen evolution was observed at temperatures >50 ºC in the presence of BMIM Ac, EMIM Ac, EMIM Et_2PO_4, Choline Ac and BMMIM NTf_2, as well as the ammonium formate ILs DAF and DAF(H) that afforded full conversion of FA (Table S2). The hydroxi-ammonium ILs DAF and Choline Ac were found to be very active with visible hydrogen evolution observed already at T<50 ºC. However, the solution of catalyst and ILs appears turbid, with formation of a thick layer of foam. In the case of DAF and DAF(H), increasing the temperature to >80 ºC leads to visible degradation of the IL resulting in sub-stoichiometric amount of formate compared to the ammonium cation. Increasing the reaction time resulted in the complete disappearance of the formate anion after 72 h. Hence, we excluded this family of ILs from further screening due to their instability.

Table 1 shows the screening of catalysts and reaction conditions with selected ionic liquids. For instance, **Ru-1** resulted in TOF = 333 h^{-1} after 3 hours, while **Ru-3** afforded full conversion within 2h (TOF = 500 h^{-1}), in presence of the bis(fluorosulfonyl)imide IL (BMMIM NTf_2) at 80 ºC. Our observations indicated that –H and –OAc catalysts are active species for FA dehydrogenation and are stabilized by the presence of a non-coordinating ionic liquid at low formic acid concentration (Table 1, Entries 1 and 2).

Likewise, EMIM Et_2PO_4 also proved to be a suitable solvent for this transformation, affording 99% conversion after 2h using Ru-MACHO-BH as catalyst under the same reaction conditions (Entry 3). Increasing by two times the amount of the FA with catalyst loading of 0.16 mol% achieved complete FA consumption in only 1 hour (Table 1, Entry 4). Importantly, the mixture containing **Ru-MACHO-BH** and EMIM Et_2PO_4 was still active after X days storaged at ambient conditions, confirming the remarkable stability of Ru-PNP catalysts in ILs.

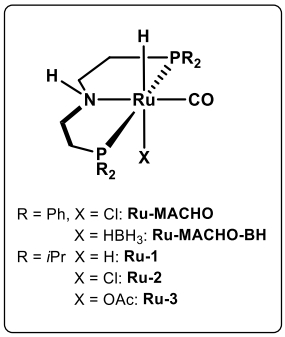

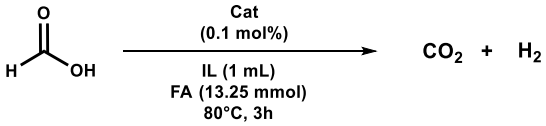

Entry	Catalyst	IL	TON	TOF (h^{-1})	Conversion (%)
1 FAD 38	Ru-3	BMMIM NTf_2	1000	500	>99
2 FAD 39	Ru-1	BMMIM NTf_2	1000	333	>99
3 FAD32	Ru-MACHO-BH	EMIM Et_2PO_4	1000	500	>99
4[a] FAD41	Ru-MACHO-BH	EMIM Et_2PO_4	615	615	>99
5 FAD37	Ru-MACHO-BH	EMIM CHOO	1000	500	>99
6[b] FAD 98	Ru-MACHO-BH	EMIM CHOO	2000	110	>99
7[c] FAD 98 hT	Ru-MACHO-BH	EMIM CHOO	4000	166	>99

[a] Cat load 0.16 mol%, FA 26.5 mmol.
[b] Cat load 0.05 mol%, FA 26.5 mmol, 18h.
[c] Cat load 0.05 mol%, FA (26.5x2 mmol), 95 ºC, 24h.

Table 1: Screening of catalysts and ionic liquids for FA dehydrogenation in batch conditions.

In addition, EMIM CHOO afforded full conversion of FA after 2 h in the presence of 0.1 mol% of **Ru-MACHO-BH** (Table 1, Entry 5). Subsequent investigations were focused on the effect of the concentration of FA. As for the other ILs, doubling the initial loading of FA (26.5 mmol) resulted in slower rate of reaction with a TOF= 100 h^{-1} after 18h (Table 1, Entry 6) at 80 ºC. Thus, it appears that applying higher temperature leads to improvement in the catalytic activity and better results were obtained at 95 ºC. Full FA conversion (99%) was achieved after 5 hours, followed by the addition of a second aliquot of FA, resulting in an overall turnover number of 4000 (Entry 7).

Interestingly, the ^1H NMR analysis of the reaction mixture after FA dehydrogenation showed the presence of CO_2 trapped in the IL when using EMIM CHOO. The presence of hydride signals indicates the presence of catalytically active species, with the hydride peak at -17.2 associated with the Ru-formate complex formed by coordination of the IL anion (Figure S1). EMIM Et_2PO_4 does not show any evidence of chemisorbed CO_2, confirming our previous findings showing that this IL is inactive towards CO_2 hydrogenation to FA. Also in this case, the presence of hydride signals corroborates the stability of Ru-species in IL (Figure S2).

Continuous Flow

In our previous work, we demonstrated that BMIM Ac is a suitable reaction medium for continuous flow FA dehydrogenation in the presence of **Ru-MACHO-BH**, with a turnover number exceeding 15 million and a catalyst stability of over 4 months. In a long-term experiment with BMIM Ac, the acetate anion was quantitatively replaced by formate with consequent formation of the corresponding imidazolium formate IL. Hence, we further investigated the use of EMIM CHOO, as well as EMIM Et_2PO_4, for the continuous flow dehydrogenation of FA using **Ru-MACHO-BH** (Table S3).

^{1}H NMR analysis showed that the FA amount in solution remains constant going from 8 to 9.5 mL/h of FA feeding rate, indicating quantitative consumption of the FA that is added to the reaction flask (Figure S3). The maximum turnover frequency observed was 11990 h^{-1}, corresponding to a FA rate of 9.5 mL/h at 95 ºC (Entry 3, Table S3). Increasing the flow of FA from 8 mL/h to 10 mL/h led to no visible gas evolution and accumulation of unconverted FA, resulting in the deactivation of the catalytic system. The same behavior is observed if the FA flow is set directly at 8 mL/h since the beginning (Entry 4, Table S3). Presumably, a gradual ramp is required to reach the optimal conversion rate (e.g., 1 mL/h increase every 15/20 min approx.).

Doubling the IL loading to 0.026 mol (4 g) did not lead to improved catalytic activity (Entry 5, Table S3). When the system is left overnight at 95 ºC without any formic acid being added, it results in the formation of a carboxylate ionic liquid, where CO_2 is trapped up to 60 mol% (Figure S4). If the reaction mixture is cooled to room temperature, off-white crystals precipitate in the reaction flask. Single-crystal X-ray diffraction shows the formation of a carboxylate specie observed by Rogers in a previous report [287], indicating high concentrations of CO_2 captured (See Appendix B). Importantly, it is possible to restart the reaction by simply restoring the FA feed with proper ramp, both if the system is kept at 95 ºC or cooled to room temperature and heated again. The long-term stability of EMIM CHOO as the reaction solvent for continuous flow FA dehydrogenation was demonstrated in our previous work.

Later, we investigated the use of EMIM Et_2PO_4. Similarly, starting the reaction with a high FA feed (5.5 mL/h) resulted in rapid deactivation of the system (Entry 6, Table S3). Hence, we increased the volume of IL and started another experiment with gradual ramp from 2 to 10 mL/h. Applying 0.02 mmol of **Ru-MACHO-BH** in 3 mL of EMIM Et_2PO_4, the system afforded a TON of 684.000 after 5 days, with a maximum turnover frequency of 12620 h^{-1} at 95 ºC (Entry 7, Table S3). At this point, we tried to further increase the FA rate (from 10 to 12 mL/h) but it resulted in rapid accumulation of FA. ^{1}H NMR analysis of the reaction mixture after accumulation of FA shows retained stability of the anion liquid, with stoichiometric amount of cation/anion after 5 days at 95 ºC (Figure S5). Importantly, once the maximum flow that the system can tolerate is demonstrated, it is possible to change the FA feed between the allowed values as the user wants, hence controlling the amount of hydrogen that is released by the system (Figure S6). This can be also done by simply adjusting the catalyst concentration in the IL and the scale of the "catalytic bed". This feature is of extreme importance for practical application of the technology, i.e. in the automotive sector.

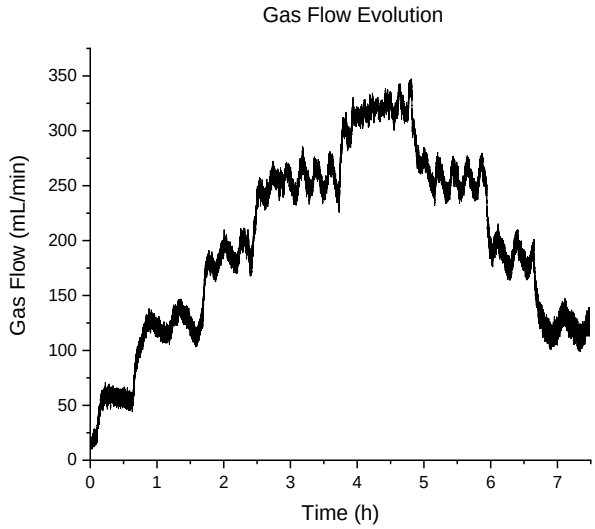

Figure 1: Gas flow evolution of continuous flow FA dehydrogenation (Entry 8, Table S3).

Dehydrogenation in a closed system

We investigated the possibility to produce hydrogen pressure under closed conditions using a sealed autoclave to monitor the gas evolution. To our delight, applying 0.02 mmol (0.08 mol%) of Ru-MACHO-BH in the presence of EMIM CHOO at 80 ºC resulted in full conversion of FA and 35 bar of pressure produced after 2 hours (Entry 1, Table 2). Similar to continuous flow conditions, the reaction mixture solidified after cooling to room temperature, with 14 mol% of CO_2 trapped as a carboxylate (Figure S7) that can be removed by simply heating the IL/cat mixture. ^{1}H NMR analysis shows the presence of hydride signals, indicating the presence of catalytically active species and possibility to repeat the operation.

Decreasing the catalyst loading to 0.05 mol% and 0.02 mol% and increasing the size of the autoclave (22 mL reaction vessel) resulted in 35 and 20 bar of pressure produced after 18h respectively (Entry 2,3). We demonstrated that **Ru-2** is an active catalyst for CO_2 hydrogenation to FA (Chapter 3). Hence, we tried to mix **Ru-MACHO-BH** and **Ru-2** in a 1:1 molar ratio (Entry 4). The addition of **Ru-2** did not change the FA conversion nor the pressure produced, showing that at high temperatures the hydrogenation of CO_2 does not compete with FA dehydrogenation. We scaled up the reaction in order to produce higher hydrogen pressures. Entries 5 and 6 show that if one want to obtain high pressures, the increase in formic acid loading should be followed by an increase in the ionic liquid content to balance the increasing acidity of the mixture. In addition, longer times allow the obtainment of higher H_2 pressures. This corroborates our findings from the batch reactions, where high concentrations of FA results in formic acid deactivation. The maximum pressure produced using EMIM CHOO was 125 bar at 90 ºC after 72 h (Entry 7).

Later, we investigated the use of BMIM Ac and EMIM Ac (Entries 8-12). Similarly to EMIM CHOO, the volume ratio of IL and FA should be similar in order to stabilize the catalyst and prevent deactivation. After optimization, it was possible to obtain up to 105 bar of H_2/CO_2 after 72 h (Entry 12).

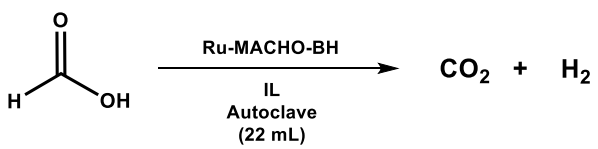

Entry	Cat Load (mol%)	IL	IL (mol)	FA (mmol)	T (°C)	Time (h)	Pressure produced
1[a]- FAD 64	0.08	EMIM CHOO	0.01	26.5	80	2	35
2- FAD76	0.05	EMIM CHOO	0.01	39.7	80	18	35
3 -FAD78	0.02	EMIM CHOO	0.01	79.5	80	18	20
4[b]- FAD77	0.05	EMIM CHOO	0.01	39.7	80	18	35
5- FAD85	0.01	EMIM CHOO	0.025	119.3	90	18	15
6-FAD91	0.01	EMIM CHOO	0.07	159	90	72	65
7- FAD97	0.02	EMIM CHOO	0.05	212	90	72	125
8- FAD87	0.02	BMIM Ac	0.03	79.5	80	18	50
9- FAD88	0.01	BMIM Ac	0.03	132.5	80	18	10
10- FAD96	0.01	EMIM Ac	0.06	159	90	72	90
11- FAD90	0.01	BMIM Ac	0.07	212	90	60	15 (24h) 15 (60h)
12- FAD89	0.01	BMIM Ac	0.06	159	90	72	35 (24 h) 75 (48h) 105[c] (72h)

[a] 12 mL reaction vessel
[b] Ru-MACHO-BH + Ru-2
[c] 85 bar when cooled to rt

Table 2: Optimization for the dehydrogenation of formic acid under pressure.

MicroGC analysis revealed that long reaction times and high pressures lead to CO production (>100 ppm), indicating that water gas-shift reaction might occur under these conditions (Figure S12). This occurs in the presence of both BMIM Ac and EMIM CHOO. Nevertheless, based on our findings from continuous-flow FA dehydrogenation, it is possible to envision a system where FA is added at a rate that produces the desired pressure. Importantly, reactions carried out at lower temperature and pressure (Entries 1-5) show no visible CO formation (Figure S11), indicating the possibility of obtaining clean pressurized hydrogen without the contamination of CO under optimized conditions.

Conclusions

In conclusion, we demonstrated that the combination of Ru-PNP and ionic liquids is an effective system for continuous hydrogen release from formic acid. The system presented in this work presents several advantages: (a) the Ru-PNP/IL couple shows great flexibility under a wide range of reaction conditions, catalyst loading, temperature and pressure. (b) There is the possibility to feed formic acid continuously from a separate compartment, as opposed to other methods were the catalyst is dispersed in large amounts of FA. (c) The system is stable under ambient conditions, does not require inert atmosphere, and it can tolerate the addition of commercial grade formic acid without prior purification. (d) It is possible to produce pressurized hydrogen without the contamination of CO (< 100 ppm) if the total pressure does not exceed 50 bar. Indeed, all these characteristics are valuable for fuel cell technology using FA as LOHC.

Supplementary Information

Continuous flow formic acid dehydrogenation using Ru-PNP complexes and ionic liquids

L.Piccirilli, M. Padilla, B. Rabell, M. Nielsen.

Department of Chemistry, Technical University of Denmark, DK-2800 Kgs. Lyngby, Denmark;
** Correspondence: marnie@kemi.dtu.dk; Tel.: +45-24651045*

Table of Contents

Supplementary methods

Supplementary data

1. General Information

The ionic liquids tested in this work were purchased from Iolitec. Ru-MACHO, Ru-MACHO-BH and Ru-2 were purchased from StremChemicals and stored in a glove box. Ru-1 and Ru-3 were synthetized following reported procedures [106,125]. Formic acid (89%, 96% and 98-100%) and NMR solvents were purchased from known vendors (Merck, Supelco, Fluorochem). The ^{1}H, ^{31}P, and ^{13}C NMR spectra were recorded on a Bruker Avance III 400 or 600 MHz spectrometer and were referenced on the solvent peak.

2. Synthesis of EMIM CHOO

In a typical experiment, 100 g of EMIM $MeOCO_2$ (30% wt in MeOH) was stirred vigorously in a round-bottom flask under ambient conditions and formic acid was added in stoichiometric amount dropwise. After the evolution of CO_2 gas has ceased, the mixture was dried in a rotary evaporator to remove the excess of MeOH. Later, the ionic liquid was further dried under high vacuum at 50 ºC overnight until precipitation of white crystals of EMIM $CHOO^-$.

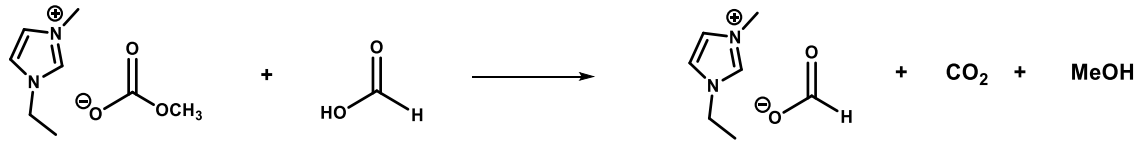

Scheme S1: Reaction scheme for the synthesis of EMIM CHOO.

3. Procedure for the dehydrogenation of formic acid (batch)

In a typical experiment, the catalyst was scaled in a two-necks flask inside the glove box. Later, the desired volume of ionic liquid is added. The mixture was stirred at the chosen temperature until complete dissolution of the catalyst and formic acid is added with a gentle flow of argon to facilitate hydrogen release. One sample for NMR analysis was taken after 2h. After 3h, the reaction mixture was cooled to room temperature and analyzed by ^{1}H-NMR using 1,4-dioxane as internal standard.

4. Procedure for the dehydrogenation of formic acid (flow)

In a typical experiment, the catalyst was weighted in a three-neck flask inside the glovebox. Later, the desired volume of ionic liquid is added. The mixture was stirred at the chosen temperature until complete dissolution of the catalyst. The syringe pump was loaded with a 60 mL PP syringe. The rate was slowly increased to assess the maximum TOF until visible formic acid accumulation was observed, determining the end of the reaction.

Preliminary screening in high-pressure vials for formic acid dehydrogenation

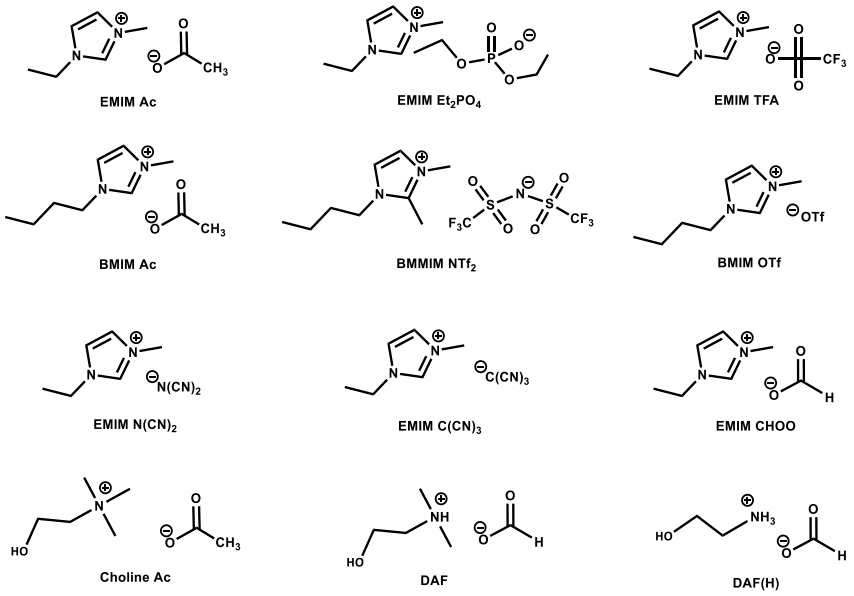

Entry	Catalyst	IL	Conversion (%)
1	Ru-MACHO	EMIM Ac	Full conversion
2		BMIM Ac	Full conversion
3		BMMIM NTf_2	<10%
4		BMIM OTf	<10%
5		EMIM TFA	<10%
6		Choline Ac	Full conversion
7		EMIM Et_2PO_4	Full conversion
8		BMIM $C(CN)_3$	<10%
9[b]		EMIM $N(CN)_2$	<10%
10[b]		EMIM $EtSO_4$	<10%
11	Ru-MACHO-BH	BMIM Ac	Full conversion
12	Ru-3	BMIM Ac	Full conversion
13	Ru-2	BMIM Ac	Full conversion
14[a]	Ru-MACHO	BMIM Ac	<10%
15[a]	Ru-MACHO-BH	BMIM Ac	<10%
16[a]	Ru-2	BMIM Ac	<10%
17	Ru-3	BMMIM NTf_2	Full conversion
18	Ru-1	BMMIM NTf_2	Full conversion
19[c]	Ru-MACHO-BH	DAF	Full conversion
20[d]	Ru-MACHO	DAF(H)	Full conversion

Reaction conditions when not specified: Cat loading (0.1 mol%), IL (0.5 mL), FA (6.6 mmol), 80ºC, 3h.
[a] Cat loading (0.05 mol%), FA (13.25 mmol).
[b] IL (1 mL), FA (13.25 mmol).
[c] Cat loading (0.2 mol%), IL (2 mL), FA (23.25 mmol), ramp 25-80 ºC, 72h.
[d] IL (1 mL), FA (26.5 mmol), 60 ºC, 24h.

Table S2: Preliminary screening of catalysts (see main text for structures) and ionic liquids for FA dehydrogenation in high pressure vials.

^{1}H NMR analysis of the reaction mixture after FA dehydrogenation under batch conditions (EMIM CHOO)

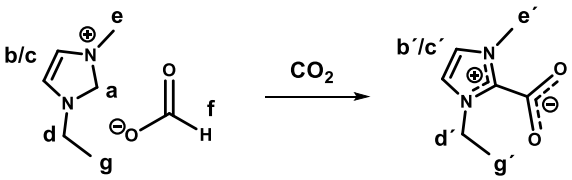

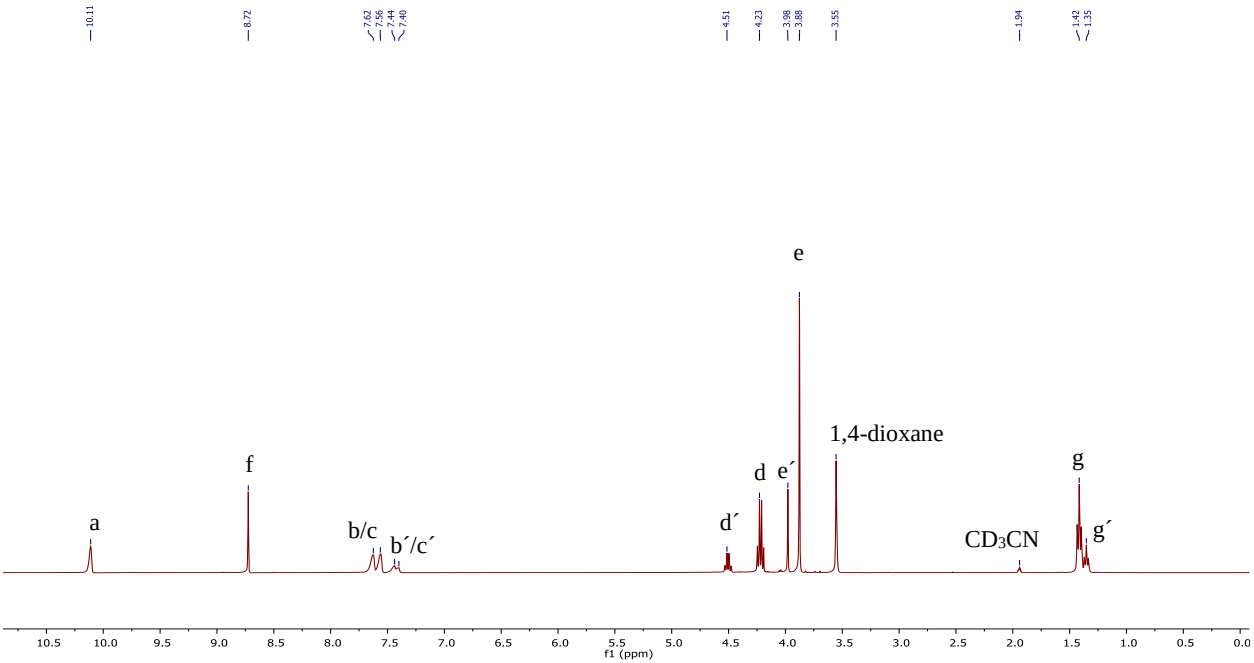

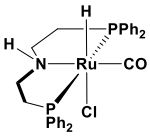

Ru-MACHO-BH

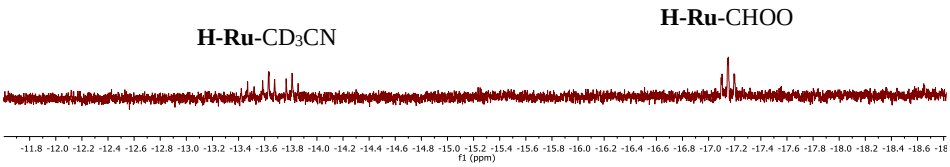

Figure S1: ^{1}H NMR spectrum of the reaction mixture and M-hydride region after FA dehydrogenation (Entry 4, Table 1).

^{1}H NMR analysis of the reaction mixture after FA dehydrogenation under batch conditions (EMIM Et_2PO_4)

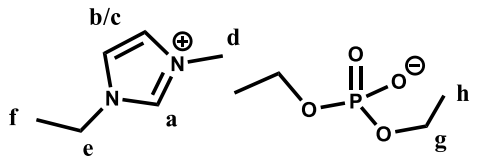

EMIM Et_2PO_4

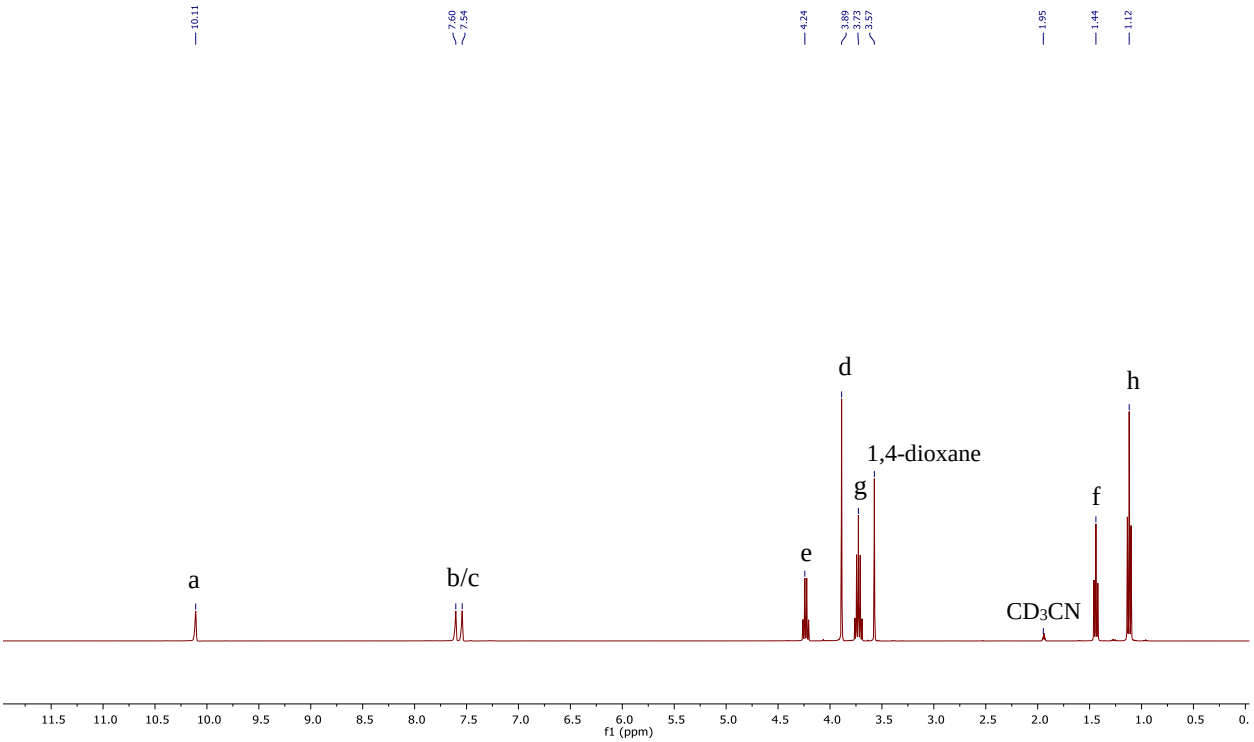

H-Ru-CD_3CN

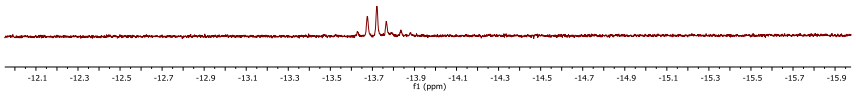

Figure S2: ^{1}H NMR spectrum of the reaction mixture and M-hydride region after FA dehydrogenation (Entry 3, Table 1).

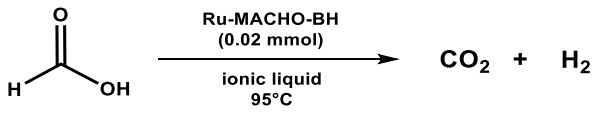

Entry	Ionic Liquid	Ionic Liquid (mol)	TOF max [a] (h^{-1})
1	EMIM CHOO	0.013	11990
2	EMIM CHOO	0.013	-
3	EMIM CHOO	0.026	10720
4	EMIM Et_2PO_4	0.009	-
5	EMIM Et_2PO_4	0.013	12620
6 (on going)	EMIM Et_2PO_4	0.017	12620

[a] measured at the last FA flow before visible accumulation.

Table S3: Optimization for the dehydrogenation of formic acid under continuous flow.

^{1}H NMR analysis of the reaction mixture during continuous flow FA dehydrogenation

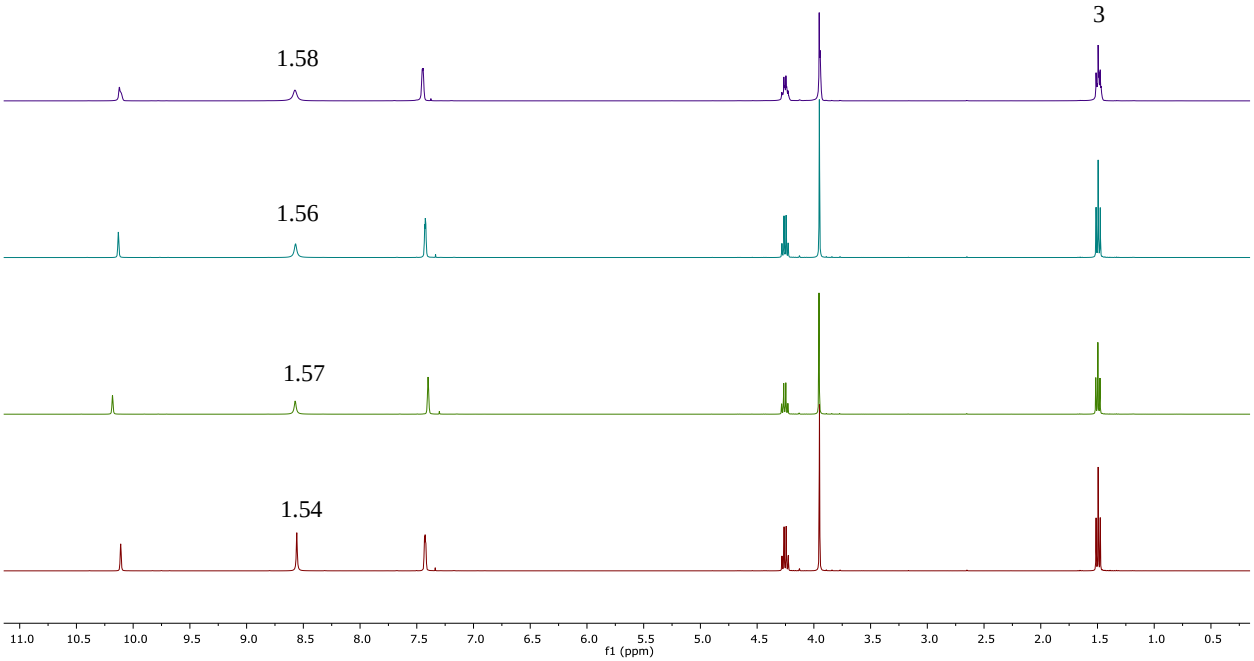

Figure S3: ^{1}H NMR spectrum of the reaction mixture at different FA addition rates (entry 1, Table 2 in the main text). The numbers indicate the relative amounts based on NMR integration. See Figure S1 for EMIM CHOO assignment.

^{1}H NMR analysis of the reaction mixture after continuous flow FA dehydrogenation (EMIM CHOO)

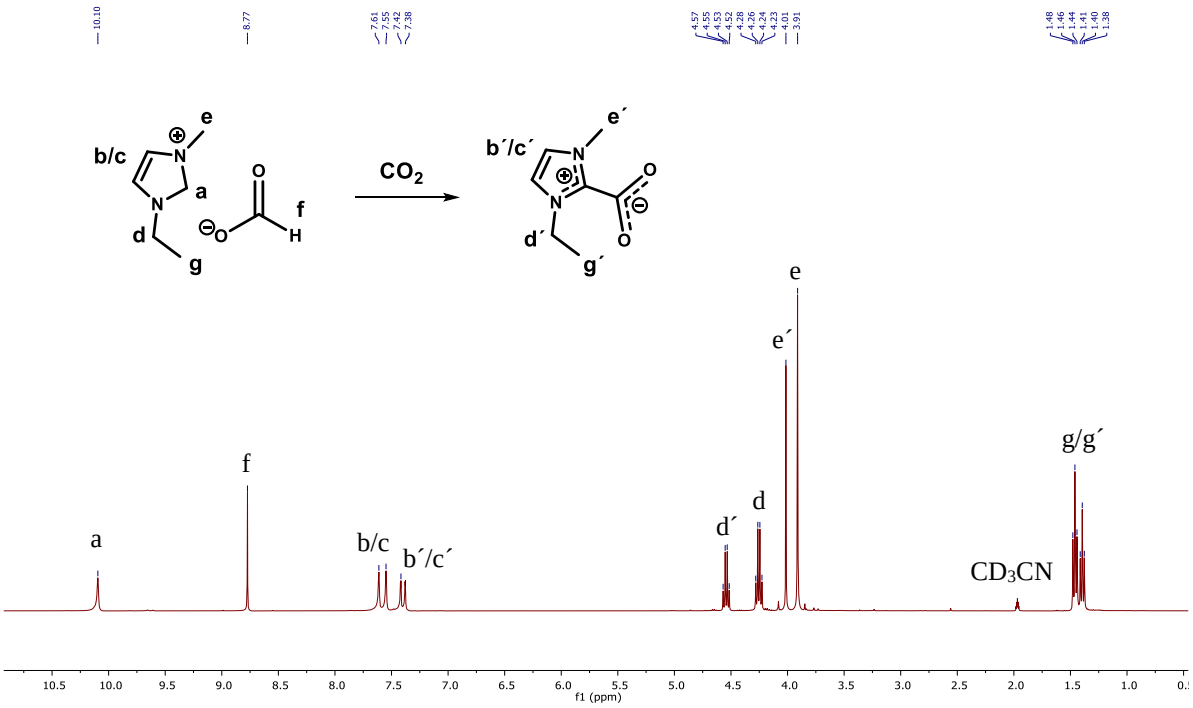

Figure S4: ^{1}H NMR spectrum of the reaction mixture left at 95 ºC overnight (entry 3, Table S3 in the main text).

^{1}H NMR analysis of the reaction mixture after continuous flow FA dehydrogenation (EMIM Et_2PO_4)

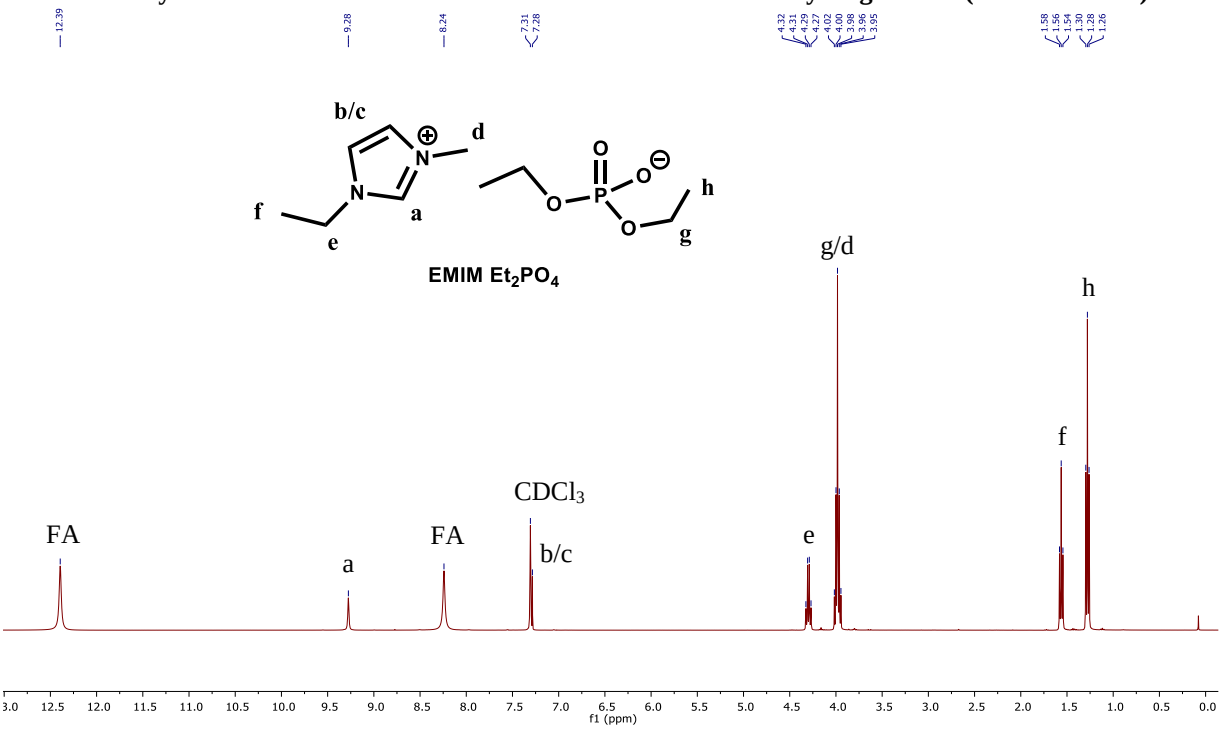

Figure S5: ^{1}H NMR spctrum of the reaction mixture after completeness of FA dehydrogenation (entry 7, Table S3).

Gas evolution of FA dehydrogenation under continuous flow

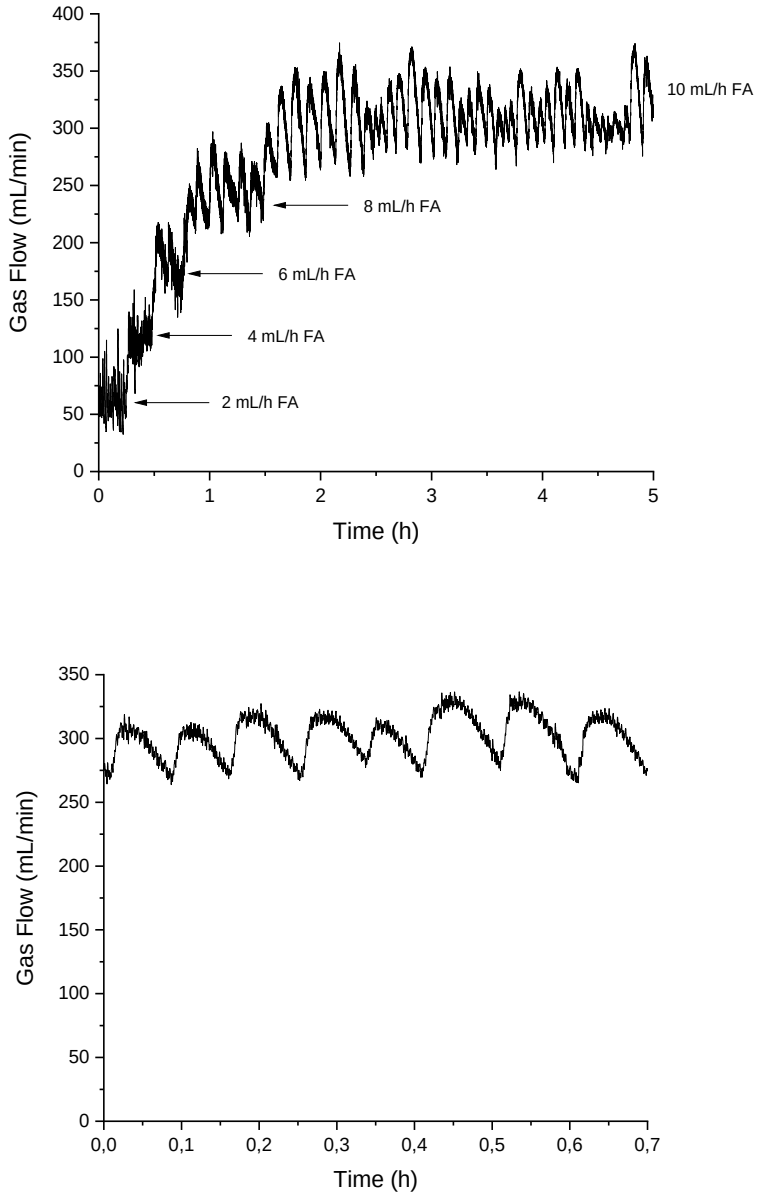

Figure S6: Gas flow evolution of continuous flow FA dehydrogenation. Reaction conditions: Ru-MACHO-BH (0.02 mmol), EMIM Et_2PO_4 (3 mL), 95 ºC (Entry 7, Table S3). Note: the fluctuations are due to the inconstant dropping from the syringes, and passing of the flow through pipes of different sizes that can create local overpressures.

^{1}H NMR analysis of FA dehydrogenation in a closed system

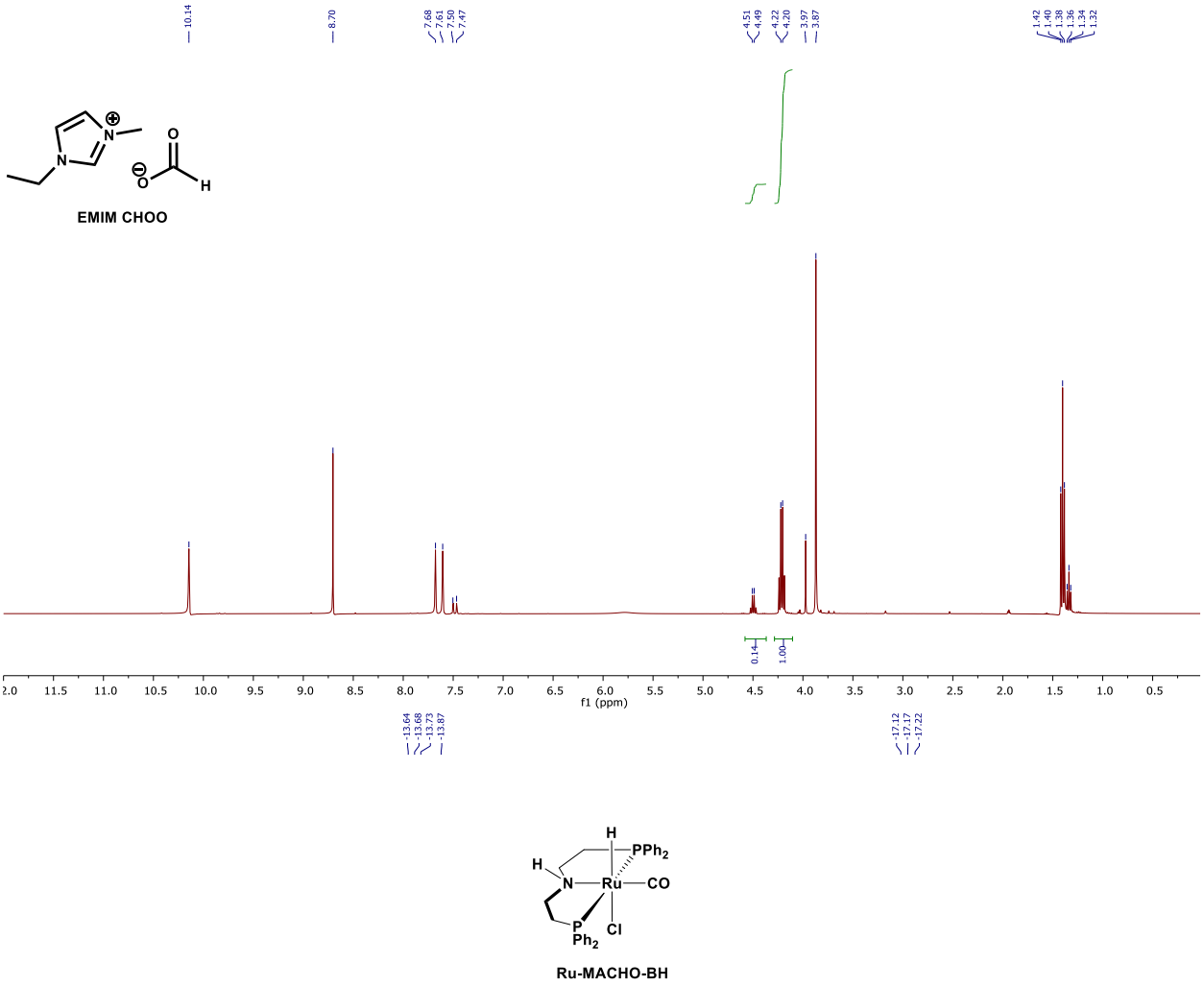

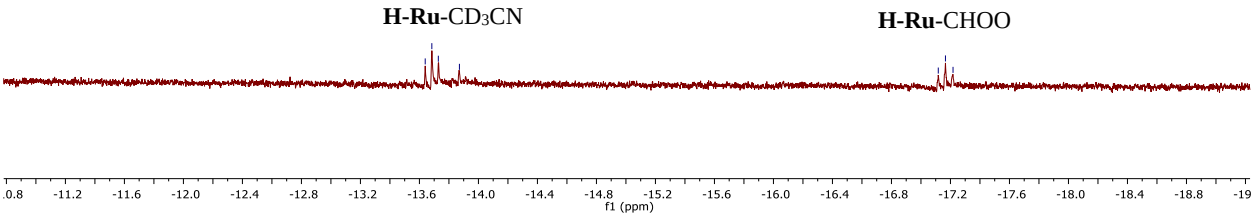

Figure S7: ^{1}H NMR spectrum of the reaction mixture and M-hydride region after hydrogen evolution under pressure (Entry 1, Table 2 in the main text). See Figure S1 for the assignment of EMIM CHOO.

GC report of FA dehydrogenation under continuous flow

External Standard Report

Page 1 of 2

Method Name: C:\Users\Administrator\Agilent\Method\20190717_Luca_Final.met
Data: C:\Users\Administrator\Agilent\Result\FAD100_2022-02-09 15-01-44 (GMT +01-00).dat.rslt\FAD99_2022-02-09 15-18-12 (GMT +01-00)-Rep3.dat
User: SYSTEM (SYSTEM)
Acquired: 2/9/2022 3:19:00 PM (GMT +01:00)
Printed: 2/14/2022 1:06:21 PM (GMT +01:00)

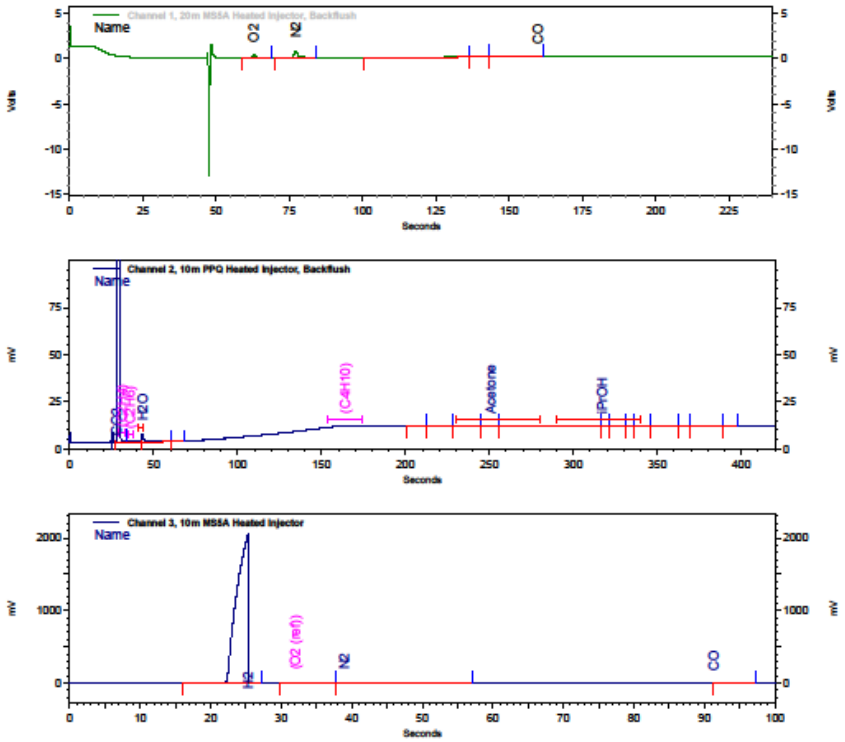

Channel 1, 20m MS5A Heated Injector, Backflush Results

Pk #	Name	Retention Time	Area	Concentration
1	O2	62.8	29388	0.0
2	N2	77.2	103322	0.1
	CH4			0.0 BDL
5	CO	159.8	2547	0.0

External Standard Report

Method Name: C:\Users\Administrator\Agilent\Method\20190717_Luca_Final.met
Data: C:\Users\Administrator\Agilent\Result\FAD100_2022-02-09 15-01-44 (GMT +01-00).dat.rslt\FAD99_2022-02-09 15-18-12 (GMT +01-00)-Rep3.dat
User: SYSTEM (SYSTEM)
Acquired: 2/9/2022 3:19:00 PM (GMT +01:00)
Printed: 2/14/2022 1:06:21 PM (GMT +01:00)

Totals		135257	0.1

Channel 2, 10m PPQ Heated Injector, Backflush Results

Pk #	Name	Retention Time	Area	Concentration
1	CO2	27.9	118236927	57.7
	C2H4			0.0 BDL
	C2H6			0.0 BDL
2	H2O	43.4	525658	7.7
	C4H10			0.0 BDL
7	Acetone	250.7	2631	0.0
9	iPrOH	317.0	7663	0.0
Totals			118772879	65.5

Channel 3, 10m MS5A Heated Injector Results

Pk #	Name	Retention Time	Area	Concentration
1	H2	25.3	383434795	50.5
	O2 (ref)			0.0 BDL
3	N2	38.9	116368	0.2
4	CO	91.4	11837	0.0
Totals			383563000	50.6

Figure S8: GC report of FA dehydrogenation under continuous flow (Entry 7, Table S3). Note: the given value of water concentration by the instrument is due to no calibration.

External Standard Report

Page 1 of 2

Method Name: C:\Users\Administrator\Agilent\Method\20190717_Luca_Final_short.met
Data: C:\Users\Administrator\Agilent\Result\FAD106-EMIMForm_2022-02-22 14-19-10 (GMT +01-00).dat.rslt\FAD106-EMIMForm_2022-02-22 14-19-13 (GMT +01-00)-Rep1.dat
User: SYSTEM (SYSTEM)
Acquired: 2/22/2022 2:19:39 PM (GMT +01:00)
Printed: 2/23/2022 11:52:22 AM (GMT +01:00)

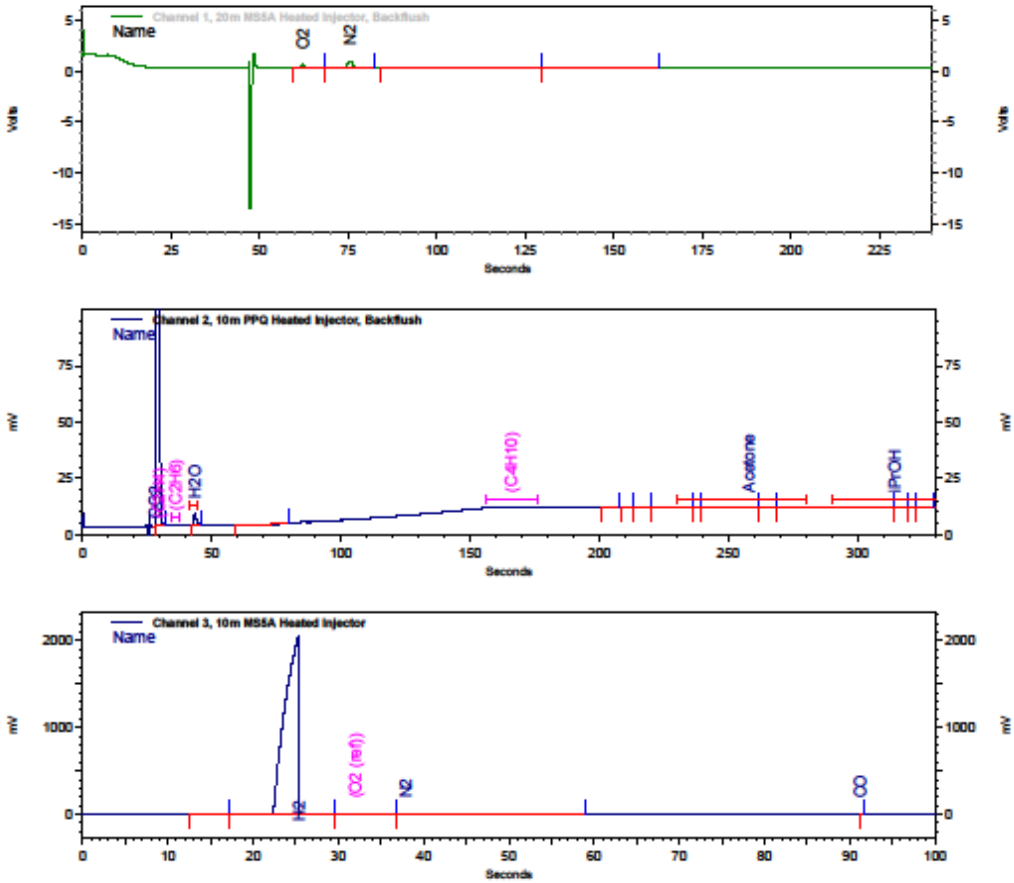

Channel 1, 20m MS5A Heated Injector, Backflush Results

Pk #	*Name*	*Retention Time*	*Area*	*Concentration*
1	O2	62.2	33549	**0.0**
2	N2	75.5	110429	**0.1**
	CH4			**0.0 BDL**
	CO			**0.0 BDL**

External Standard Report

Method Name: C:\Users\Administrator\Agilent\Method\20190717_Luca_Final_short.met
Data: C:\Users\Administrator\Agilent\Result\FAD106-EMIMForm_2022-02-22 14-19-10 (GMT +01-00).dat.rslt\FAD106-EMIMForm_2022-02-22 14-19-13 (GMT +01-00)-Rep1.dat
User: SYSTEM (SYSTEM)
Acquired: 2/22/2022 2:19:39 PM (GMT +01:00)
Printed: 2/23/2022 11:52:22 AM (GMT +01:00)

Totals		143978	0.1

Channel 2, 10m PPQ Heated Injector, Backflush Results

Pk #	*Name*	*Retention Time*	*Area*	*Concentration*
1	CO2	28.0	115252846	56.3
	C2H4			0.0 BDL
	C2H6			0.0 BDL
2	H2O	43.4	538689	7.9
	C4H10			0.0 BDL
9	Acetone	257.9	5991	0.0
12	iPrOH	314.3	3437	0.0
Totals			115800963	64.2

Channel 3, 10m MS5A Heated Injector Results

Pk #	*Name*	*Retention Time*	*Area*	*Concentration*
2	H2	25.4	381086505	50.2
	O2 (ref)			0.0 BDL
4	N2	37.9	129896	0.2
5	CO	91.2	185	0.0
Totals			381216586	50.3

Figure S9: GC report of FA dehydrogenation under continuous flow (Entry 5, Table S3). Note: the given value of water concentration by the instrument is due to no calibration.

GC report of FA dehydrogenation in a closed system

External Standard Report

Page 1 of 2

Method Name: C:\Users\Administrator\Agilent\Method\20190717_Luca_Final.met
Data: C:\Users\Administrator\Agilent\Result\FA autoclave\112LPFAD64_autoclave_2021-05-07 09-45-34 (GMT +02-00).dat.rslt\112LPFAD64_autoclave_2021-05-07 11-01-00 (GMT +02-00)-Rep10.dat
User: SYSTEM (SYSTEM)
Acquired: 5/7/2021 11:01:52 AM (GMT +02:00)
Printed: 10/28/2021 1:49:02 PM (GMT +02:00)

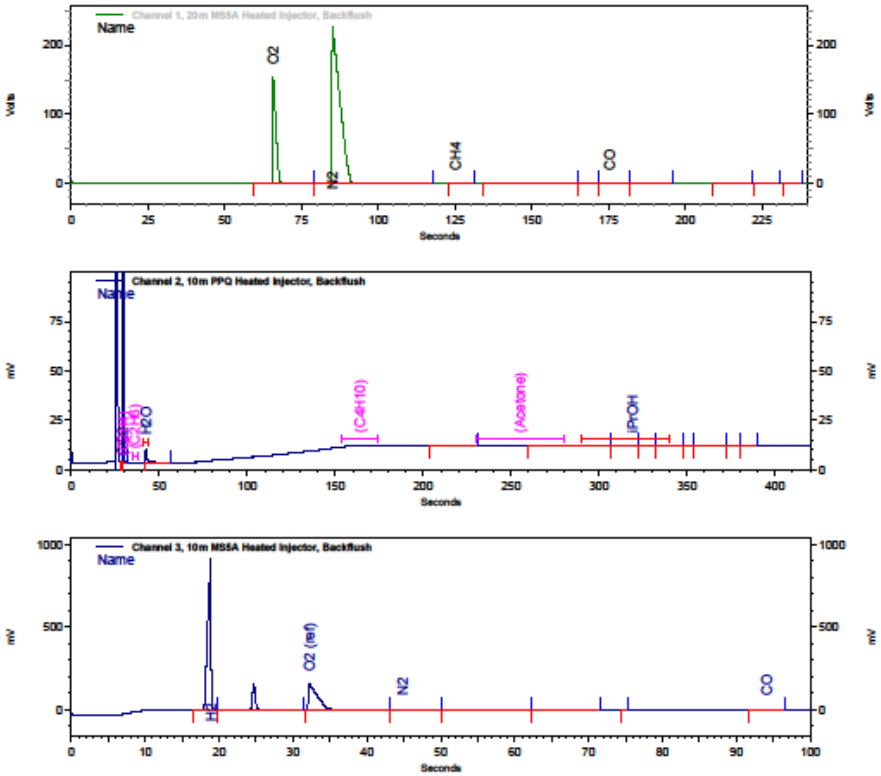

Channel 1, 20m MS5A Heated Injector, Backflush Results

Pk #	Name	Retention Time	Area	Concentration
1	O2	65.8	17875842	**16.6**
2	N2	85.1	66579868	**60.5**
3	CH4	125.1	335	**0.0**
6	CO	175.4	1418	**0.0**

External Standard Report

Method Name: C:\Users\Administrator\Agilent\Method\20190717_Luca_Final.met
Data: C:\Users\Administrator\Agilent\Result\FA autoclave\112LPFAD64_autoclave_2021-05-07 09-45-34 (GMT +02-00).dat.rslt\112LPFAD64_autoclave_2021-05-07 11-01-00 (GMT +02-00)-Rep10.dat
User: SYSTEM (SYSTEM)
Acquired: 5/7/2021 11:01:52 AM (GMT +02:00)
Printed: 10/28/2021 1:49:02 PM (GMT +02:00)

Totals		84457463	77.1

Channel 2, 10m PPQ Heated Injector, Backflush Results

Pk #	*Name*	*Retention Time*	*Area*	*Concentration*
2	CO2	29.2	17977361	8.8
	C2H4			0.0 BDL
	C2H6			0.0 BDL
3	H2O	42.4	709319	10.4
	C4H10			0.0 BDL
	Acetone			0.0 BDL
6	iPrOH	319.1	5670	0.0
Totals			18692350	19.2

Channel 3, 10m MS5A Heated Injector, Backflush Results

Pk #	*Name*	*Retention Time*	*Area*	*Concentration*
1	H2	18.9	46911086	6.2
3	O2 (ref)	32.2	20933122	21.9
4	N2	44.8	68118	0.1
8	CO	94.1	2884	0.0
Totals			67915210	28.2

Figure S10: GC report of FA dehydrogenation in a closed system without CO detected (Entry 1, Table 3 in the main text – with EMIM CHOO). Note: the given value of water concentration by the instrument is due to no calibration.

External Standard Report

Page 1 of 2

Method Name: C:\Users\Administrator\Agilent\Method\20190717_Luca_Final.met
Data: C:\Users\Administrator\Agilent\Result\FA autoclave\153_FAD97_2021-10-11 11-18-05 (GMT +02-00).dat.rslt\153_FAD97_2021-10-11 11-18-07 (GMT +02-00)-Rep1.dat
User: SYSTEM (SYSTEM)
Acquired: 10/11/2021 11:18:34 AM (GMT +02:00)
Printed: 10/28/2021 1:45:54 PM (GMT +02:00)

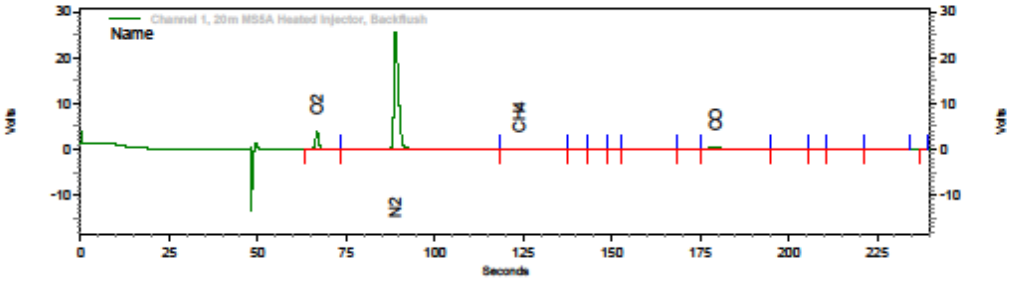

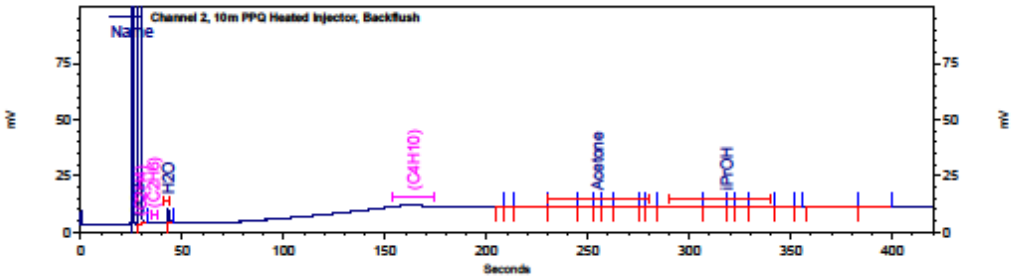

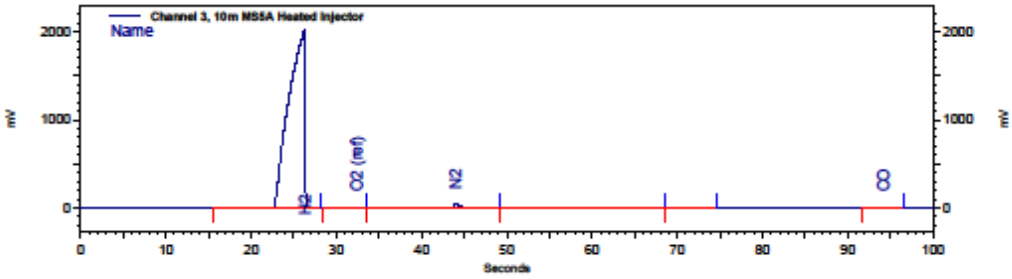

Channel 1, 20m MS5A Heated Injector, Backflush Results

Pk #	*Name*	*Retention Time*	*Area*	*Concentration*
1	O2	66.8	355083	**0.3**
2	N2	88.9	3711443	**3.4**
3	CH4	123.8	1384	**0.0**
9	CO	179.3	88208	**0.1**

External Standard Report

Method Name: C:\Users\Administrator\Agilent\Method\20190717_Luca_Final.met
Data: C:\Users\Administrator\Agilent\Result\FA autoclave\153_FAD97_2021-10-11 11-18-05 (GMT +02-00).dat.rslt\153_FAD97_2021-10-11 11-18-07 (GMT +02-00)-Rep1.dat
User: SYSTEM (SYSTEM)
Acquired: 10/11/2021 11:18:34 AM (GMT +02:00)
Printed: 10/28/2021 1:45:54 PM (GMT +02:00)

Totals		4156118	3.8

Channel 2, 10m PPQ Heated Injector, Backflush Results

Pk #	*Name*	*Retention Time*	*Area*	*Concentration*
1	CO2	28.1	91442313	44.7
	C2H4			0.0 BDL
	C2H6			0.0 BDL
2	H2O	43.1	609539	8.9
	C4H10			0.0 BDL
8	Acetone	254.6	508	0.0
15	iPrOH	318.3	680	0.0
Totals			92053040	53.6

Channel 3, 10m MS5A Heated Injector Results

Pk #	*Name*	*Retention Time*	*Area*	*Concentration*
1	H2	26.3	439299225	57.8
2	O2 (ref)	32.4	356804	0.4
3	N2	44.0	3097630	4.3
6	CO	94.1	62770	0.1
Totals			442816429	62.6

Figure S11: GC report of FA dehydrogenation in a closed system with CO detected (Entry 7, Table 3 in the main text – with EMIM CHOO). Note: the given value of water concentration by the instrument is due to no calibration.

Appendix H – Paper IV

This work was conducted in collaboration with our partners at Friedrich-Alexander-Universität (FAU) Erlangen-Nürnberg where I spent my period of external stay in September 2020. Most of the experimental work was performed at DTU Chemistry in collaboration with postdoc Rosa Padilla and Assoc Prof Martin Nielsen. This included the preliminary batch experiments and demonstration of the principles, the characterization of SILP materials using NMR, BET, and TGA techniquesn and writing of the draft here proposed. During my stay at FAU, under the supervision of Doc. Marco Haumann, I was able to evaluate the catalytic activity of my SILP catalysts using the pilot-plant reactor available at FAU, of which PhD student Melanie Eßl was responsible. Melanie contributed greatly with daily help in the use of the reactor, as well as with data processing and analysis, hence providing the plots showed in the papers regarding gas-flow reactions.

Paper in preparation.

Low-temperature continuous flow isopropanol dehydrogenation using a Ru-SILP catalyst

*L.Piccirilli, M. Eßl, R. Padilla, M. Haumann, A. Riisager, M. Nielsen**

Department of Chemistry, Technical University of Denmark, DK-2800 Kgs. Lyngby, Denmark;
** Correspondence: marnie@kemi.dtu.dk; Tel.: +45-24651045*

Abstract

The development of efficient catalytic systems for low temperature dehydrogenation reactions will play an important role in the implementation of the hydrogen economy on a large scale. Herein, we disclose the reactivity of Ru-PNP catalysts in ionic liquid for the dehydrogenation of the hydrogen carrier isopropanol (*i*PrOH) under mild conditions without the use of external additives. We also show the immobilization of a Ru-PNP catalyst using the supported ionic liquid phase (SILP) technology, and demonstrate its catalytic activity for the dehydrogenation of *i*PrOH under gas-phase continuous flow conditions in a fixed-bed reactor. The system is highly stable for up to 100 hours and approaches thermodynamic equilibrium below 120 ºC.

Introduction

The large-scale production of green hydrogen is developing rapidly in terms of both size and capacity [7]. For instance, the European Union has issued a hydrogen strategy to build a new pipeline system for efficiently transporting the hydrogen in long distances [15,16]. The requirements for the infrastructure are similar to those required for transporting natural gas. In fact, the blending of H_2 with CH_4 in existing gas pipelines has demonstrated [17]. However, hydrogen storage and transportation, as well as its utilization as an energy carrier still represent a challenge. To overcome this issue, the use of a liquid organic hydrogen carrier (LOHC) represents a promising solution for the storage and local distribution of hydrogen in a safe manner, avoiding safety issues and energetic costs associated with hydrogen compression and liquefaction, providing a fuel with high energy density [8,24,30–32]. Then, hydrogen is released from the LOHC on the site of application using a catalytic dehydrogenation catalyst (e.g. a PEM fuel cell driven vehicle fed by H_2-lean LOHC and reloaded at the local recharging green hydrogen plant). Several studies describes the potential of LOHC as suitable hydrogen carriers from an economical and practical point of view [42,43]. Many types of LOHC candidates have been proposed, ranging from small molecules such as methanol [34], formic acid [36], ammonia [37], ammonia/amine-boranes [38], as well as aromatic compounds such as N-ethylcarbazole [39] or dibenzyltoluene [40].

The high temperatures required for the hydrogen release step still represents a big challenge towards the implementation of the LOHC technology on a large scale [361]. In the automotive sector, hydrogen release from the LOHC has to be performed at temperatures 80 ºC≤T≤120 ºC to ensure heat-integration with proton-exchange membrane fuel cells (PEMFC) [44]. Higher temperatures are possible for stationary applications, where heavier and bigger types of fuel cells can operate at higher temperatures providing high-energy outputs (solid oxide fuel cells) [11,13].

The couple *i*PrOH /acetone has been proposed as a viable LOHC system though transfer hydrogenation [341]. In fact, *i*PrOH offers a hydrogen capacity of 3.3 mass% and an energy storage density of 1,11 kWh/kg (or 0.87 kWh/L). Conventionally, this secondary alcohol can be obtained from acetone by catalytic hydrogenation step using both homogeneous and heterogeneous catalytic systems [338,339], or directly by electrochemical water splitting [340]. Direct isopropanol fuel cells represent a solution that does not require prior hydrogen release from the LOHC emitting no CO_2 in the oxidation process [342]. Likewise, *i*PrOH dehydrogenation to afford hydrogen and simultaneous acetone formation serves as another viable option, since only pure hydrogen is admitted to the fuel cell. However, state-of-the-art catalysts for this transformation operates at temperature that are too high for PEMFC utilization. In addition, the transfer hydrogenation of acetone has been proposed as a strategy to reduce the temperature required for the dehydrogenation of bigger LOHC molecules such as dibenzyltoluene [343].

Organometallic transition metal complexes have been widely reported for the dehydrogenation of several LOHCs candidates at very mild conditions [313]. In particular, ruthenium PNP pincer catalysts are a class of very stable, active and selective catalysts for a wide range of (de)hydrogenation reactions [88,345]. Beller reported the state-of-the-art system for homogeneously catalyzed dehydrogenation of *i*PrOH using the ruthenium organometallic complex **Ru-1** (Figure 2) affording a TOF = 2048 h^{-1} after 2 hours

at 90 ºC [236]. Significant examples of Ru-PNP complexes have been well recognized for the acceptorless dehydrogenation of a plethora of LOHC candidates such as methanol [125,165], formic acid [36,166,326], and alcohols [89,123,126,344].

Toward the design of sustainable chemicals for energy applications, ionic liquids (ILs) are proposed to replace organic solvents as alternative reaction medium for homogeneous catalysis, hence avoiding the presence of volatile species in the produced hydrogen flow. By definition these materials are salts and stable liquids at temperatures <100 ºC [171]. Along with their extraordinary properties ILs have been reported as active co-catalysts, offering a wide spectrum of possible applications [175,204]. For example, the supported ionic liquid phase (SILP) technology is a solution to merge the advantages of both homogeneous and heterogeneous catalysis, i.e. high selectivity and mild reaction conditions together with increased stability given by the support material (Figure 1). Importantly, from a sustainable point of view the amount of both catalyst and IL is minimized by the high dispersion within the mesoporous support. The SILP catalyst allows continuous product separation from the catalytic active phase, usually a challenge in traditional homogeneous catalysis, enabling the use of fixed-bed reactors [359].

SILP materials have been successfully applied to a series of transformations such as hydroformylation [212–214], water-gas shift [228,230], alkylations [226], hydrosilylation [222], NH_3 adsorption [232]. Kirchner and Hoffmann reported Fe-PNP complexes supported on a silica material using the SILP technology for the selective hydrogenation of aldehydes to alcohols [216,347]. Recently, Haumann explored the immobilization of a Ru-PNP catalyst on an alumina support material for methanol reforming [234], later improved by the addition of a co-catalyst of the same Ru-PNP family compounds [235].

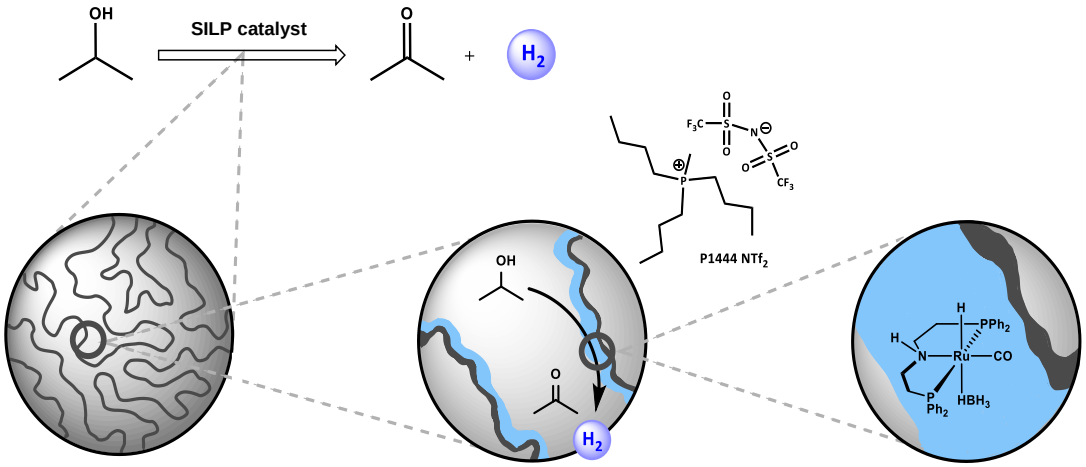

Figure 1: Schematic representation of the supported ionic liquid phase (SILP) technology with the catalyst and ionic liquid (IL) used in this study.

Herein, we explore the reactivity of Ru-PNP catalysts in ILs applied to the dehydrogenation of the LOHC *i*PrOH under mild conditions. We show that the IL activates the pre-catalyst without the need of a base and stabilize catalytic after species in solution. Hydrogen release is possible from Ru-PNP/IL mixtures under batch conditions at temperatures <100 ºC. Hence, we show the first example of gas-phase *i*PrOH dehydrogenation using an organometallic ruthenium catalyst supported on a silica support material. The system shows stable hydrogen evolution with acetone as the only by-product, and remains active for reaction times up to 100 hours. Following up on previous studies by Haumann, we demonstrate that Ru-PNP complexes can be effectively supported and immobilized using the SILP technology, affording a macroscopic heterogeneous catalyst retaining its homogeneous features.

Results and discussion

Preliminary screening

We commenced our studies with a preliminary screening of catalysts under batch conditions to find the most promising catalytic systems before implementing it to the the SILP technology. In order to do so, imidazolium ion based ILS containing various anions were tested as reaction media. We hypothesized that the anion of the IL plays a major role in the activation of the pre-catalyst **Ru-MACHO** (Figure 2) forming the activated species normally produced by an (in)organic base in the presence of a solvent via elimination of the [Ru-PNP] amino proton or abstraction of [RuCl] chlorido ligand. The resulting amido monohydride complexes (such as **Ru-4** in Figure 2) are commonly proposed as the active species for dehydrogenation of alcohols. We speculated that a suitable IL containing a sufficiently basic anion could perform this step, whereby the IL acts both as solvent and as catalyst activator. Indeed, conversion of *i*PrOH to acetone were observed in the preliminary experiments with Pyrr OTf, BMIM OTf, EMIM OTf, BMMIM NTf_2, EMIM $MeSO_4$ in the presence of **Ru-MACHO** at 120 ºC.

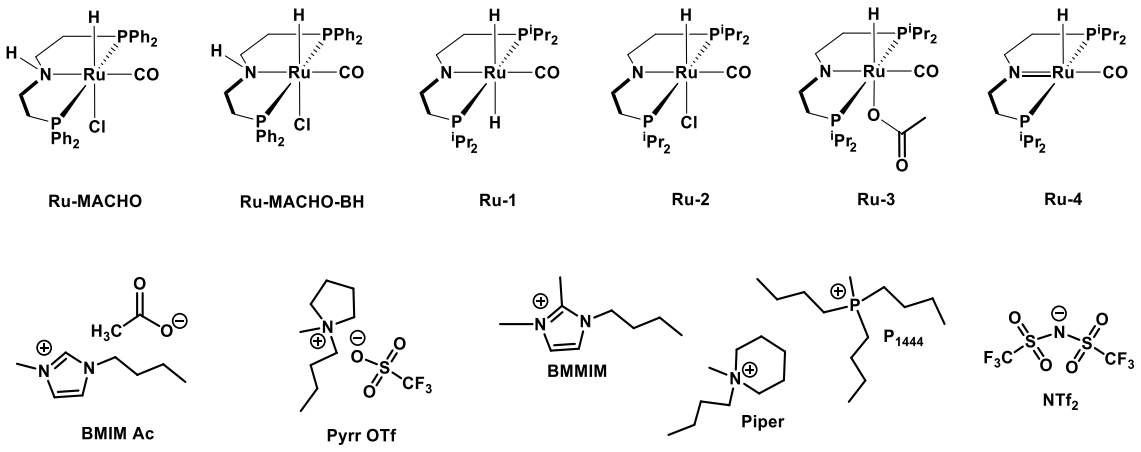

Figure 2: Overview of the Ru-PNP catalysts and ionic liquids used in this study.

In order to confirm our hypothesis on the role of the IL, we carried ^{1}H NMR studies of the generated Ru-H species in presence of the corresponding IL. For this purpose, we monitored the composition of the reaction mixture of Ru MACHO in presence of BMIM Ac. The IL promoted the fast activation step on the precatalyst, forming the acetate complex as suggested for the Ru-H peak observed at -18 ppm in the hydride region (Figures S1-S6). On the other hand, in presence of triflate (OTf) and bistriflimide (NTf_2) anions, no hydride peaks were observed. To comprehend the nature of the main resting species of the organometallic complex in solution, we synthetized the acetate complex **Ru-3** (Figure 2) and mixed it with *i*PrOH and ionic liquid (BMIM Ac, BMMIM NTf_2 or Pyrr OTf). The hydride peaks associated with **Ru-3** did not change in the presence of either *i*PrOH or the three different ionic liquids (Figures S7-S8). When using BMIM Ac, the intensity of the peak at -18 ppm increased compared to those at -14 ppm (associated with CD_3CN coordinated to Ru) indicating a major amount of Ru-acetate species in solution (Figure S8). With BMMIM NTf_2 and Pyrr OTf, the addition of *i*PrOH to the solution of catalyst/IL results in the disappearance of the acetate hydride peak, with an increase of the other peaks at -14.7 ppm (Figure S9, S10). This indicates that reactivity is possible using these anions, whereas an excess of acetate seems to block further reactivity towards *i*PrOH due to formation of stable Ru-acetate resting species.

We performed qualitative stability studies of selected ILs by keeping the temperature stable at 120 ºC for 3 days. A change of color toward darker shades was observed for all the samples except for BMMIM NTf_2 and less harsh for Pyrr OTf. On the contrary, imidazolium ionic liquids turned dark orange or brown. The cause for the change of color can be attributed to the presence of free carbene species formed by deprotonation of the imidazole ring performed by the IL anion. Moreover, it is known that carbene functionalities can coordinate transition metal complexes with consequent formation of inactive species.

Isopropanol dehydrogenation – Batch reactions

A benchmark experiment with **Ru-MACHO** (0.1 mmol) and BMIM Ac (4 mL) dehydrogenated *i*PrOH (9 mmol) at 120 ºC after 2 hours. The subsequent distillation of the liquid mixture showed traces of acetone at X ppm observed by ^{1}H NMR ($CDCl_3$ and D_2O), albeit with very low conversion of *i*PrOH (< 1%) (Figure S11, S12). Further screening with BMIM Ac and **Ru-MACHO** in presence of additives (e.g, Li^+ salts, NaOH, Et_3N, F_3COOH, CH_3COOH) did not have a beneficial effect on the catalytic activity. Later, we explored the catalytic activity of different Ru-PNP catalysts (Figure 2), including the state-of-the-art complex **Ru-1** for *i*PrOH dehydrogenation using BMMIM NTf_2 as the ionic liquid of choice.

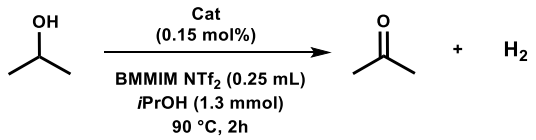

Entry	Catalyst (mol%[a])	TON	TOF [h^{-1}]	Conversion[b] [%]
1	**Ru-MACHO**	-	-	<5
2	**Ru-MACHO-BH**	65	33	10
3	**Ru-1**	110	55	15
4	**Ru-2**	-	-	<5
5	**Ru-3**	-	-	<5
6	**Ru-4**	84	42	13

Table 1: Screening of Ru-PNP complexes for *i*PrOH dehydrogenation. Reactions reproducible within a 10% error. [a] Mol% with respect to *i*PrOH. [b] Determined by ^{1}NMR.

Treatment of Ru-MACHO with the ionic liquid under suitable reaction conditions did not result in any observable catalytic activity. Interestingly, **Ru-MACHO-BH** showed 10% conversion and a TOF = 33. As opposed to the chlorido ligand in Ru- MACHO, the HBH_3 group can be removed by simple heating with no induction period observed explaining this result. When comparing the influence of the phosphorus substituent, we observed that low catalyst loading of **Ru-1** (2 μmol) in 0.25 mL of BMMIM NTf_2 afforded 15% conversion of *i*PrOH and a TON of 110 after 2 hours at 90 ºC under refluxing conditions (Table 1, Entry 3). Notably, the congener catalyst **Ru-2** was found to be completely inactive under similar reaction conditions (Table1, Entries 1,4). **Ru-3** did not produce any observable evolution of hydrogen with BMMIM NTf_2 (Entry 5), confirming the detrimental effect of the acetate anion already at catalytic amounts. Using the pre-activated catalyst **Ru-4** resulted in 13% conversion and TON = 84 (Entry 6). Two overlapping hydride signals at –9 ppm show the presence of catalytically active species after the reaction is completed for both **Ru-1** and **Ru-6** (Figures S13, S14).

For the next step of the study, we screened different ionic liquids and reaction conditions. The results are summarized in Table S1. In the presence of BMIM Ac, **Ru-1** becomes completely inactive showing no detectable conversion (Entry 1, Table S1), and resulting in the presence of the same acetato species previously discussed (*vide supra*). We noticed that the hydrido chloride system **Ru-2** combined with a base (NaOEt) lead to the active species otherwise not formed in presence of the IL (Entry 2, Table S1). Longer reaction times does not lead to increased conversion, indicating that the reversible hydrogenation of acetone occurs at the same rate under this reaction conditions once an equilibrium is reached (Entry 3, Table S1). In a separate experiment with higher catalyst loading, the same conversion (8%) was measured after 5, 10 and 20 minutes (Entry 4, Table S1). Scaling up of the reaction resulted in 10% conversion and a TON of 105 (Entry 5, Table S1). **Ru-4 (**0.05 mol%) afforded a TON = 150 (Entry 6, Table S1). Comparable values of conversions as the one showed in Table 1 were obtained for both **Ru-1** and **Ru-4** in a closed system (pressure vials) under the same reaction conditions.

Based on these results, we optimized the system using **Ru-1**. As showed in Table 2, varying the volumetric ratio of IL/*i*PrOH resulted in the same conversion of 10% (Entries 1-3) indicating that the reaction reaches a thermodynamic plateau. Hence, we continued the optimization using a IL/iPrOH ration of 0.5 which allows for higher turnover numbers. Increasing the temperature

to 120 ºC led to higher conversion (15%) and a TON = 85 (Entry 4). The ionic liquid cation seems to have an influence on the catalytic activities; the saturated pyrrolidinium and piperidinium gave superior results compared to the imidazolium IL (Entries 2, 5, 6), in the order PIPER > Pyrr > BMMIM. As observed in the initial screening, increasing the reaction time to 18 hours did not produce better results (Entry 7). Finally, decreasing the catalyst loading to 0.05 mol% provided the best TON = 380 (TOF = 190 h^{-1}) at 100 ºC after 2 hours using PIPER NTf_2 (Entry 8). **Ru-MACHO-BH** was also active in the presence of Pyrr NTf_2 and P_{1444} NTf_2, affording a TON of 70 and 68, respectively, after 2 hours (Entries 9 and 10).

Entry	Catalyst (mol%[a])	Ionic liquid (mL)	IL/*i*PrOH (v/v)	Time [h]	T [ºC]	TON	Conversion[b] [%]
1[d]	**Ru-1** (0.20)	BMMIM NTf_2	1	1.5	90	60	10
2	**Ru-1** (0.10)	BMMIM NTf_2	0.5	1.5	90	114	11
3[cd]	**Ru-1** (0.35)	BMMIM NTf_2	2	1	90	25	10
4[d]	**Ru-1** (0.20)	BMMIM NTf_2	1	2	120	85	15
5	**Ru-1** (0.15)	Pyrr NTf_2	0.5	2	100	160	23
6	**Ru-1** (0.12)	PIPER NTf_2	0.5	1	100	180	21
7	**Ru-1** (0.14)	PIPER NTf_2	0.5	18	100	170	23
8	**Ru-1** (0.05)	PIPER NTf_2	0.5	2	100	380	19
9	**Ru-MACHO-BH** (0.15)	Pyrr NTf_2	0.5	2	100	70	10
10	**Ru-MACHO-BH** (0.20)	P_{1444} NTf_2	0.5	2	110	68	13

Table 2: Optimization of *i*PrOH dehydrogenation in batch conditions using **Ru-1** and **Ru-MACHO-BH**. Reactions reproducible within a 10% error. [a] Mol% with respect to *i*PrOH. [b] Determined by ^{1}NMR. [c] 2 mL IL. [d] 13 mmol *i*PrOH.

In summary, batch experiments demonstrated that the system Ru-PNP/IL is active for *i*PrOH dehydrogenation under mild conditions, reaching equilibrium plateaus at reaction temperatures compatible with PEMFC technologies. We therefore next used homogeneously dissolved transition metal complex (Ru-PNP/IL) using the SILP technology for *i*PrOH dehydrogenation under continuous flow conditions.

Isopropanol dehydrogenation - Continuous flow

Based on the findings from the batch experiments, we started our investigation by preparing a number of SILP materials using **Ru-1** or **Ru-MACHO-BH** as catalyst and PIPER NTf_2 as IL. We screened different Ru/SiO_2 wt% ratios and the mesoporous silica 100 and silica 60, differing for pore size and volume (measured by BET analysis). We chose the percentage of volumetric pore filling (α) to be consistently 20% for all the samples to avoid overfilling and saturation of the pores.

The catalytic tests were carried out in a fixed-bed reactor equipped with a MicroGC for the analysis of the gaseous products (Scheme 1). Opposed to the findings in batch conditions, **Ru-1** was inactive when exposed to a gaseous *i*PrOH feed (Table S2). Apparently, it seems that the complex deactivates during the manipulations before reaction start. On the contrary, the SILP materials containing **Ru-MACHO-BH** in Ru/SiO_2 > 0.5 wt% produced a stable flow of hydrogen, with the conversion of *i*PrOH that follows the temperature profile in the reactor, very close to the calculated equilibrium conversion during the initial times of reaction (Figure S15). Both silica supports were suitable for this transformation; we decided to continue the screening using silica 100 that possesses bigger pore size and volume, which should allow easier gas diffusion and lower degree of condensation and accumulation of *i*PrOH and/or impurities in the catalytic bed.

Figure 3 shows the conversion profile of a SILP catalyst containing 1% Ru/SiO_2 of **Ru-MACHO-BH**, PIPER NTf_2 and silica 100 as the support material. The *i*PrOH feed was set at 30 g/h without dilution with inert gas. The conversion varies from 3-15% according to the changes in temperature, with a selectivity >95 % towards hydrogen and acetone. However, when the temperature was increased again, the conversion does not reach the initial values indicating some degree of deactivation of the SILP catalyst. The same SILP material was reused in a second experiment and exhibited a substantial loss of activity, as shown in Figure 3c.

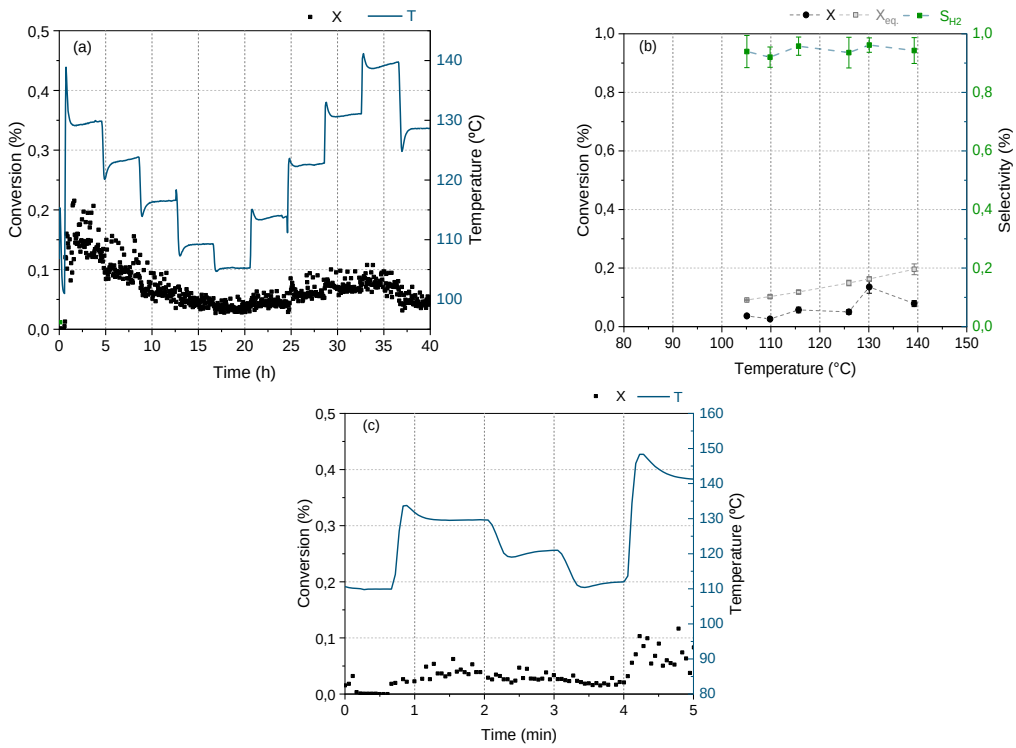

Figure 3: SILP catalyst: Ru/SiO_2 (1 wt%), α=20% of PIPER NTf_2 and silica 100.

A similar deactivation pattern was observed using a SILP catalyst with Ru/SiO_2 = 0.5% with otherwise identical composition (Figure S16). Keeping the temperature stable at 110 ºC leads to a similar deactivation profile as the one observed in the temperature ramp experiments, in the presence of both silica 60 and silica 100 (Figure S17).

We also screened different bistriflimide ionic liquids varying the cation, possibly influencing parameters such as wettability and viscosity. We tested imidazolium-, pyrrolidinium-, and phosphonium-based ionic liquids; however, no clear influence of the cation on the catalytic activity was observed under experimental conditions (Figure S18).

We tried to assess the robustness of the system by feeding 30 g/h of a mixture of 25 vol% acetone in *i*PrOH with the purpose of simulating operative conditions where unconverted *i*PrOH is recycled with the presence of acetone in the feed. The SILP catalyst with Ru/SiO_2 = 1 wt% and P_{1444} NTf_2 resulted in poorer activity compared to a pure *i*PrOH feed; however, the system was still able to release hydrogen from *i*PrOH, with a stable conversion of 5-7% at 110-130 ºC over 18 hours of experiment (Figure S19).

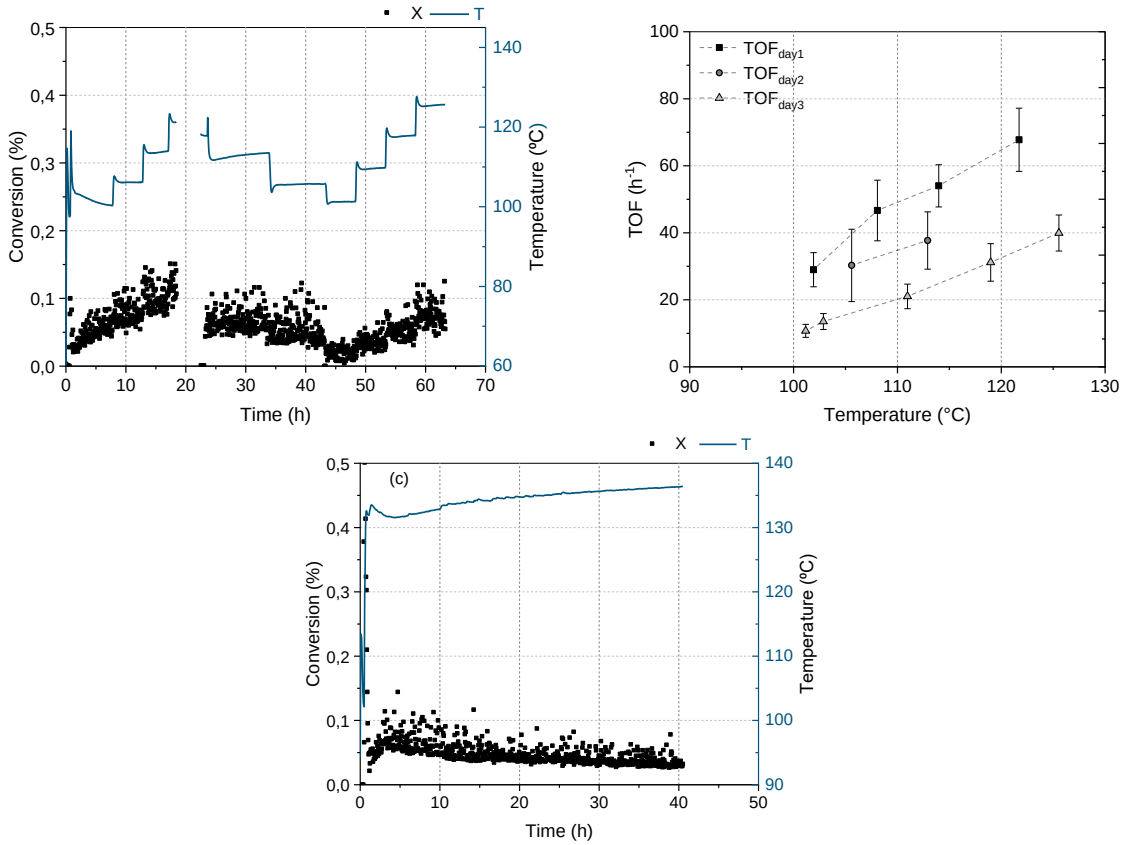

Figure 4: a) in the missing space the catalyst was exposed to 25% acetone in IPA. b) TOF. c) experiment after 4 months of storage.

In a following experiment, 4g of the SILP catalyst (Ru/SiO_2 = 0.9 wt%, P_{1444} NTf_2, silica 100) was diluted with 1g of calcined silica 100 to ensure maximum dispersion of the catalytic active phase. The SILP was exposed to changes in temperature and reaction conditions and the reactor stopped overnight for two times over 3 days (Figure 4). As shown in Figure 4b, it is possible to observe a consistent decrease in the turnover frequencies achieved by the catalyst over the 3 days, with a deactivation profile that seems to be independent from the different temperatures and reaction conditions used. Nevertheless, in the first 20 h of reaction, the system shows high selectivity and conversion values that are very close to the calculated equilibrium (Figure S20), affording a maximum turnover frequency of 70 h^{-1} at 120 ºC (Figure 4b) from 30 g/h of undiluted IPA. In Figure 4c, the same SILP catalyst was reused in a second experiment after 4 months of simple storage at ambient conditions. The system was stable for up to 40 h at 130 ºC, showing that catalytic activity is not fully lost.

In a final long-term experiment, a SILP catalyst containing **Ru-MACHO-BH** (Ru/SiO_2 = 1%), P_{1444} NTf_2 and silica 100 was exposed to changes in temperature, different dilutions of *i*PrOH in N_2, as well as to a 25 vol% acetone/ *i*PrOH mixture as the feed (Figure 5, Figure S21). The *i*PrOH feed was diluted with N_2 (80 vol% of *i*PrOH in N_2, 30 g/h *i*PrOH - 46 ml/min N_2) to prevent

condensation and accumulation of *i*PrOH in the catalytic bed, a potential cause of the decreased activity. The deactivation profile (red line in Figure 5) seems to be independent of the different reaction conditions. Dilution of *i*PrOH with N_2 did not lead to any observable effect on the catalytic activity and stability (Figure S22). In fact, when comparing two experiments using the same catalyst but different dilutions (40 and 80 vol% of *i*PrOH in N_2), similar deactivation profiles occur. The same behavior was observed during the acetone dilution and the temperature variations, with a consistent decrease in activity that is largely independent of the reaction conditions (Figure S23 and S24). The reaction follows a first order kinetic profile, as shown in Figure S25. The calculated activation energy was 53.45 KJ/mol.

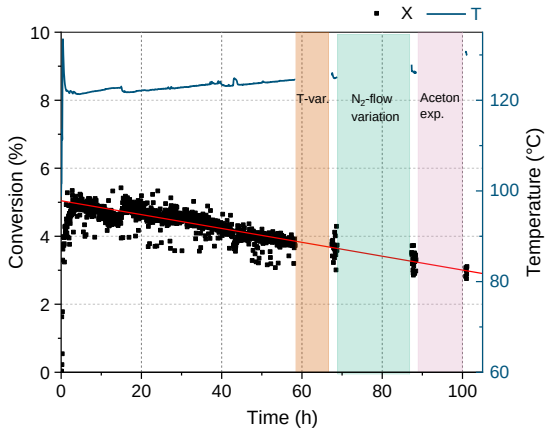

Figure 5: a) Long time experiment; Ru/SiO_2 = 1 wt%, P_{1444} NTf_2, silica 100.

All of the tested SILP materials (initially white) turned brown after catalytic tests in the reactor tube or if exposed in air for long times, indicating degradation of the IL and/or the catalyst. After extraction of the catalyst/IL phase from the exhaust SILP catalysts with DCM, ^{1}NMR analysis shows the presence of *i*PrOH, acetone and water. These substances may well clog the pores of the porous support, resulting in decreased activity over time, even with possible formation of inactive ruthenium species (Figure S26, S27).

We performed NMR studies in solution to elucidate the stability and possible deactivation explanations of the mixture **Ru-MACHO-BH** and P_{1444} NTf_2. As shown in Figure S28-30, the corresponding signals of **Ru-MACHO-BH** are still detectable after addition of both P_{1444} NTf_2 and *i*PrOH. However, bubbling argon through a solution of **Ru-MACHO-BH** in P_{1444} NTf_2 resulted in the disappearance of the hydride signals and a visible degradation of the aromatic part of the catalyst (Figure S31). We conducted more NMR analysis after extracting the catalytic active phase from a freshly prepared SILP with dry DCM. Figure S32 shows the ^{1}NMR of **Ru-MACHO-BH** staggered with a solution of the extracted, freshly prepared, SILP catalyst containing **Ru-MACHO-BH** and P_{1444} NTf_2. Again, the main peaks identifying the catalyst were conserved. Finally, Figure S33 shows the extracted solution from a SILP material tested in the fixed bad reactor. It is possible to notice some degree of degradation in the aromatic region but the presence of hydride signals indicates the presence of catalytically active Ru species.

It has to be noted that commercial grade *i*PrOH without prior purification was used as a feed, which can lead to accumulation of impurities as well as water over extended reaction times. In addition to mechanical stress causing movement of the ionic liquid at high gas flows, probably not all the Ru-PNP catalyst is fully dispersed and homogenized in the IL phase. Indeed, the catalytic activity is not fully lost after 100 hours on stream, indicating that part of the homogeneous system is still active, as corroborated by the extracted liquid phase containing metal-hydride signals.

Conclusions

In summary, we demonstrated the first example of gas-phase *i*PrOH dehydrogenation using a homogeneous organometallic complex. Differences between the batch and continuous flow conditions show a synergistic effect of Ru-PNP, IL and support material on the final catalytic performance and stability. This preliminary study open up for further optimization in every single aspect concerning the optimization of a SILP material for dehydrogenation reactions at mild conditions. Changing support, pore´s filling percentage, anchoring the ionic liquid to the support covalently, optimization of the Ru-PNP catalyst. Longer time experiments can assess if the catalyst completely deactivates.

Experimental

Catalyst preparation

Ru-MACHO-BH, **Ru-MACHO**, and **Ru-2** were purchased from StremChemicals and stored in a glove box. **Ru-1**, **Ru-3**, and **Ru-6** were synthetized according to reported procedures [125].

Procedure for batch isopropanol dehydrogenation

In a typical experiment, the desired amount of catalyst was scaled in a glove box and transferred in a dry flask. Later, the ionic liquid was added and the resulting mixture stirred while heating to the desired temperature until full catalyst solubility. Finally, anhydrous *i*PrOH was added by means of a syringe in the reaction flask that was set under refluxing conditions with a gentle argon flow to facilitate hydrogen release from the solution. After the reaction was completed, the solution was cooled to room temperature and a sample was taken for NMR analysis for the quantification of the acetone produced.

Preparation of SILP catalysts

All manipulations were performed under Schlenk conditions. The silica precursor was calcined at 600ºC overnight and stored in a glove box. The SILP catalysts were prepared by dissolving the desired amounts of catalyst (Ru/SiO_2) in dry dichloromethane. Later, the ionic liquid was added and the mixture stirred for 10 minutes to allow full catalyst solubility. The support material is then added to the mixture under vigorous stirring for not more than 20 minutes, in order to avoid mechanical stress on the support material. Finally, the solvent is evaporated under vacuum and the SILP material is stored in a glove box until catalytic use. The percentage of pore filling was measured as follows:

$$\alpha = \frac{m_{IL}/\rho_{IL}}{m_{Support} * Pore\ Vol_{Support}}$$

Continuous gas-phase reactor setup

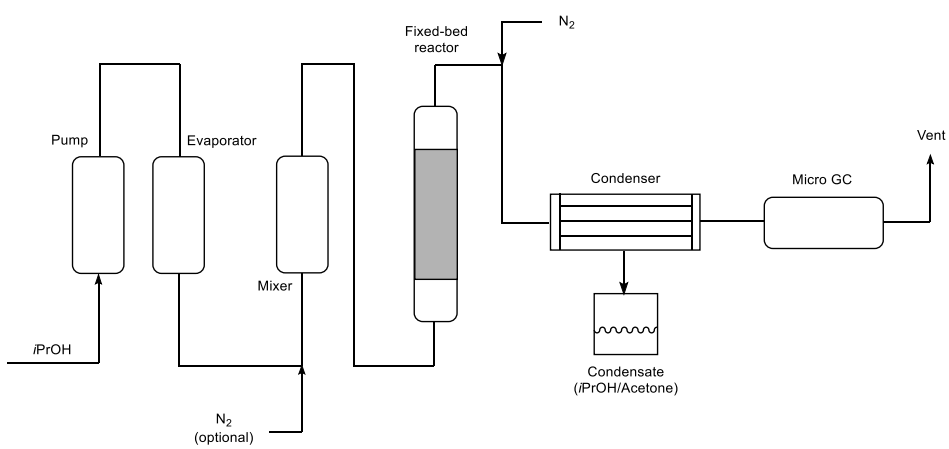

Scheme 1: Schematic representation of the fixed-bed reactor used in this study for continuous flow dehydrogenation of *i*PrOH using Ru-SILP catalysts.

Supplementary Information

Low-temperature continuous flow isopropanol dehydrogenation using a Ru-SILP catalyst

*L.Piccirilli, M. Eßl, R. Padilla, M. Haumann, A. Riisager, M. Nielsen**

Department of Chemistry, Technical University of Denmark, DK-2800 Kgs. Lyngby, Denmark;
** Correspondence: marnie@kemi.dtu.dk; Tel.: +45-24651045*

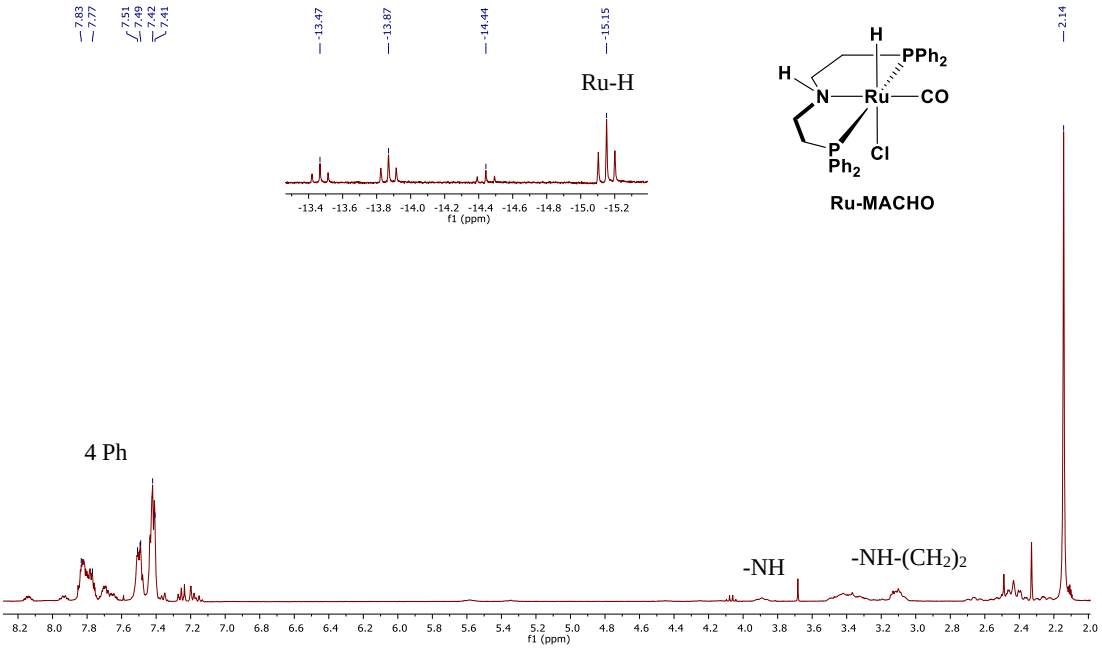

Figure S1. ^{1}H NMR spectrum of Ru-MACHO (CD_3CN, 25 ºC 400 MHz).

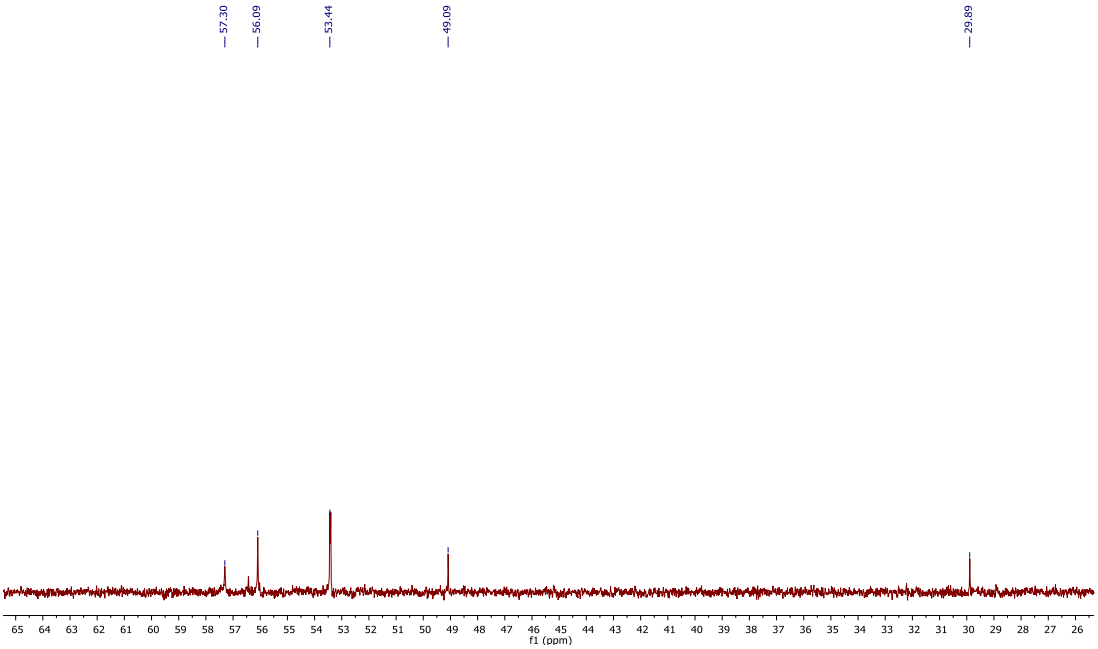

Figure S2. ^{31}P NMR spectrum of Ru-MACHO (CD_3CN, 25 ºC, 400 MHz).

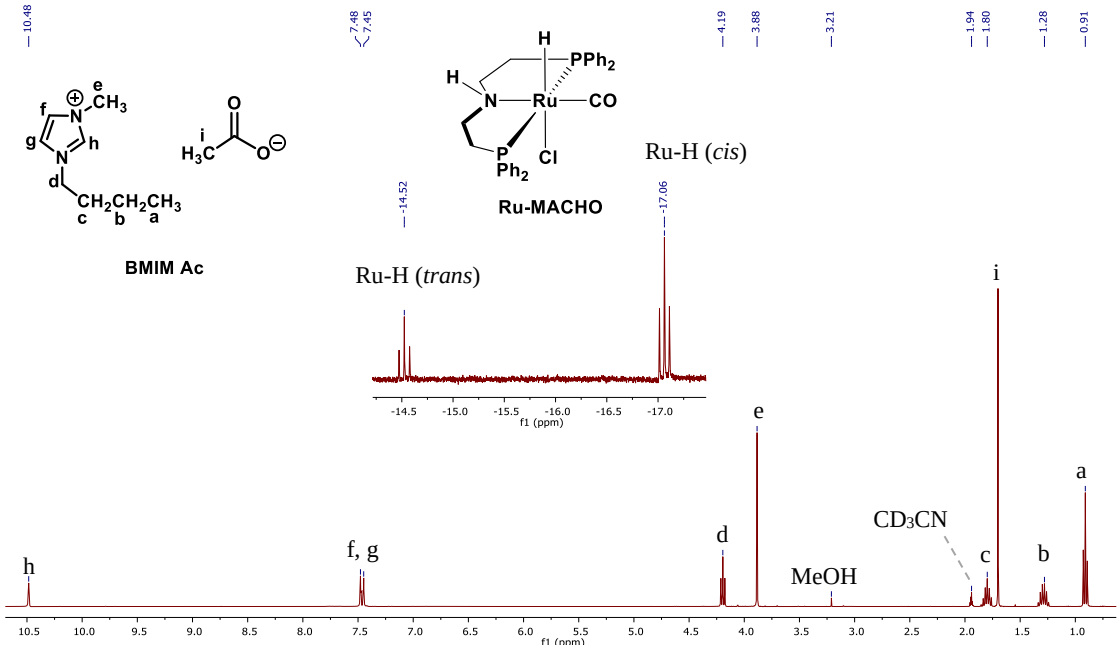

Figure S3. ^{1}H NMR spectrum of Ru-MACHO in BMIM Ac (CD_3CN, 25 ºC 400 MHz). Note: MeOH is present as an impurity in the IL (from synthesis procedure).

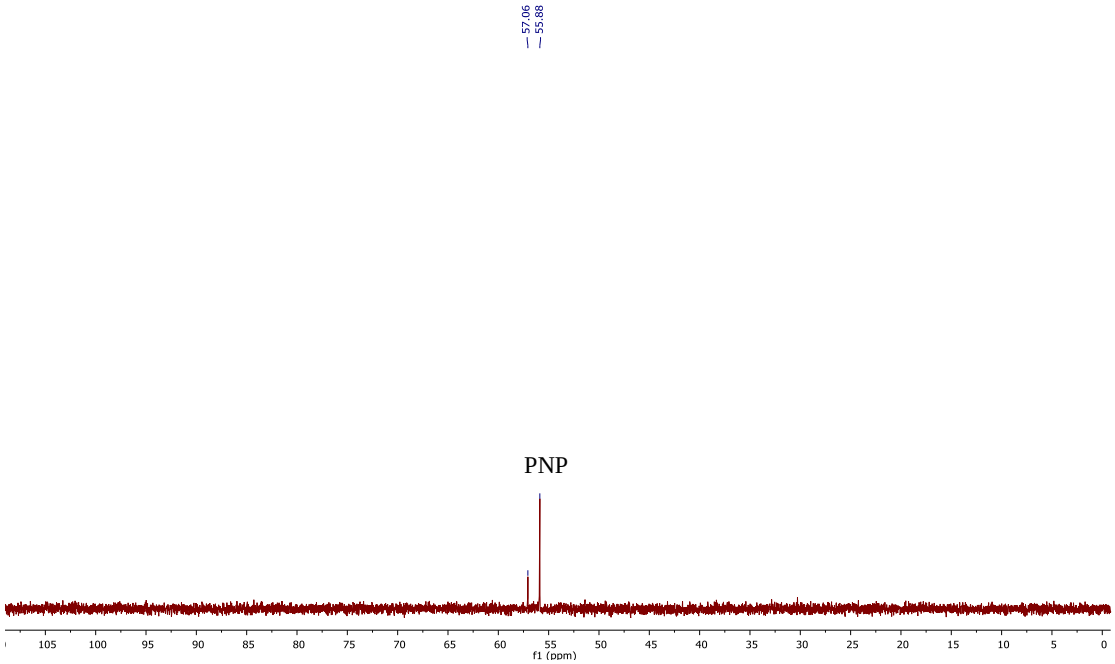

Figure S4. ^{31}P NMR spectrum of Ru-MACHO in BMIM Ac (CD_3CN, 25 ºC 400 MHz).

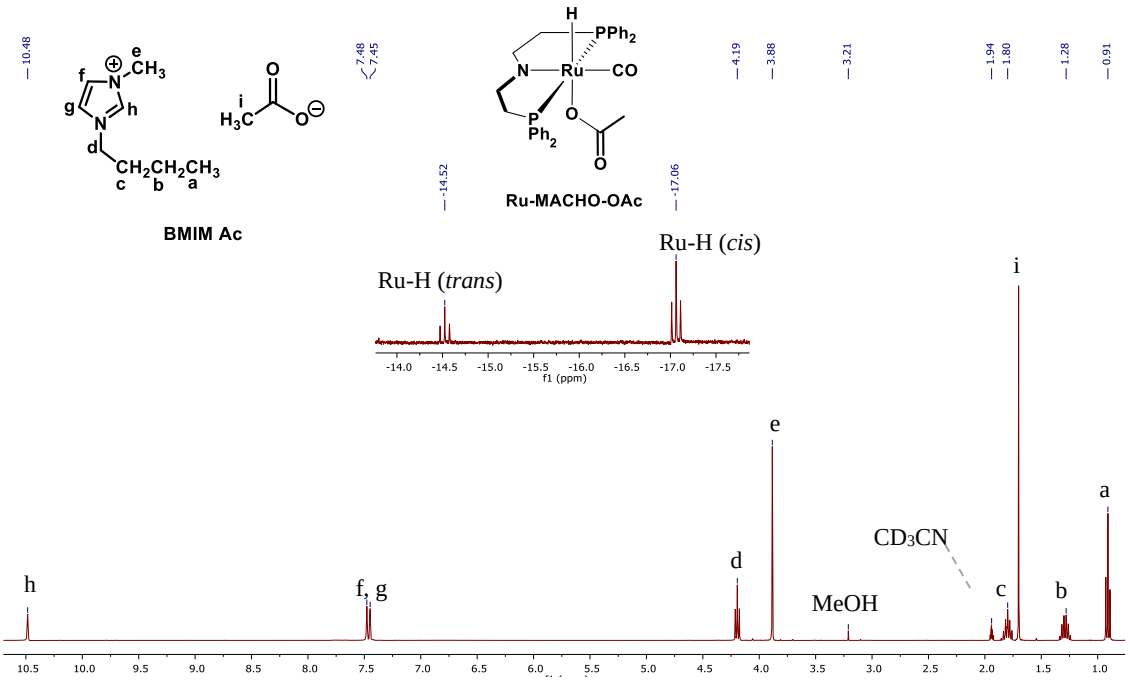

Figure S5. ^{1}H NMR spectrum of Ru-MACHO-OAc species generated in presence of BMIM Ac (CD_3CN, 25 ºC 400 MHz). Note: MeOH is present as an impurity in the IL (from synthesis procedure).

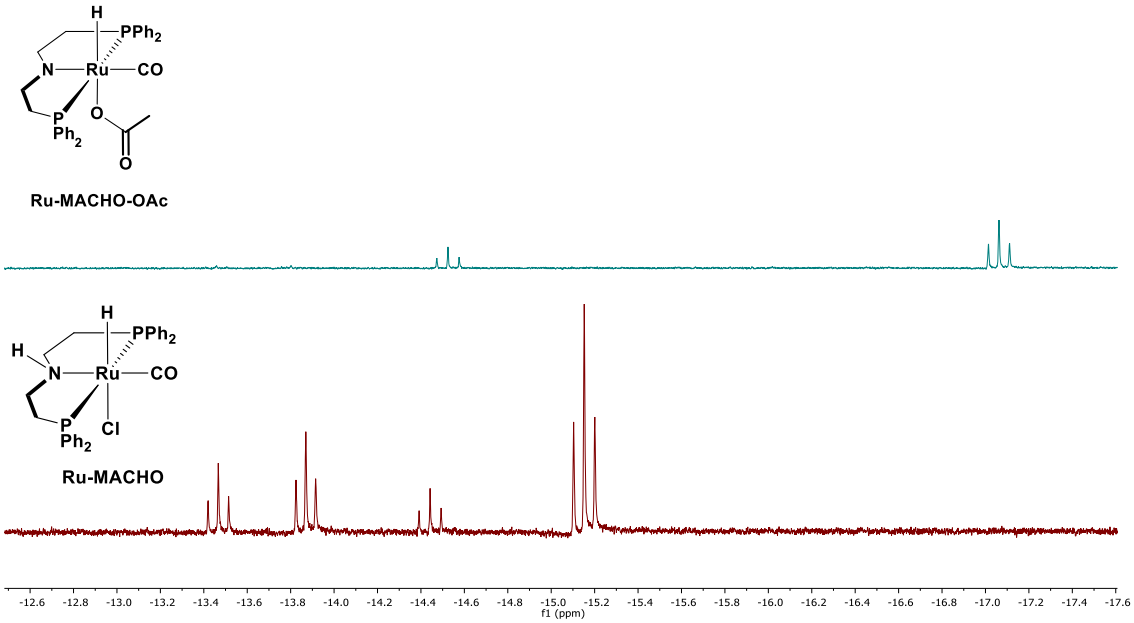

Figure S6. ^{1}H NMR spectrum of M-hydride region for **Ru-MACHO** (down) and Ru-MACHO in BMIM Ac (up) (CD_3CN, 25 ºC 400 MHz).

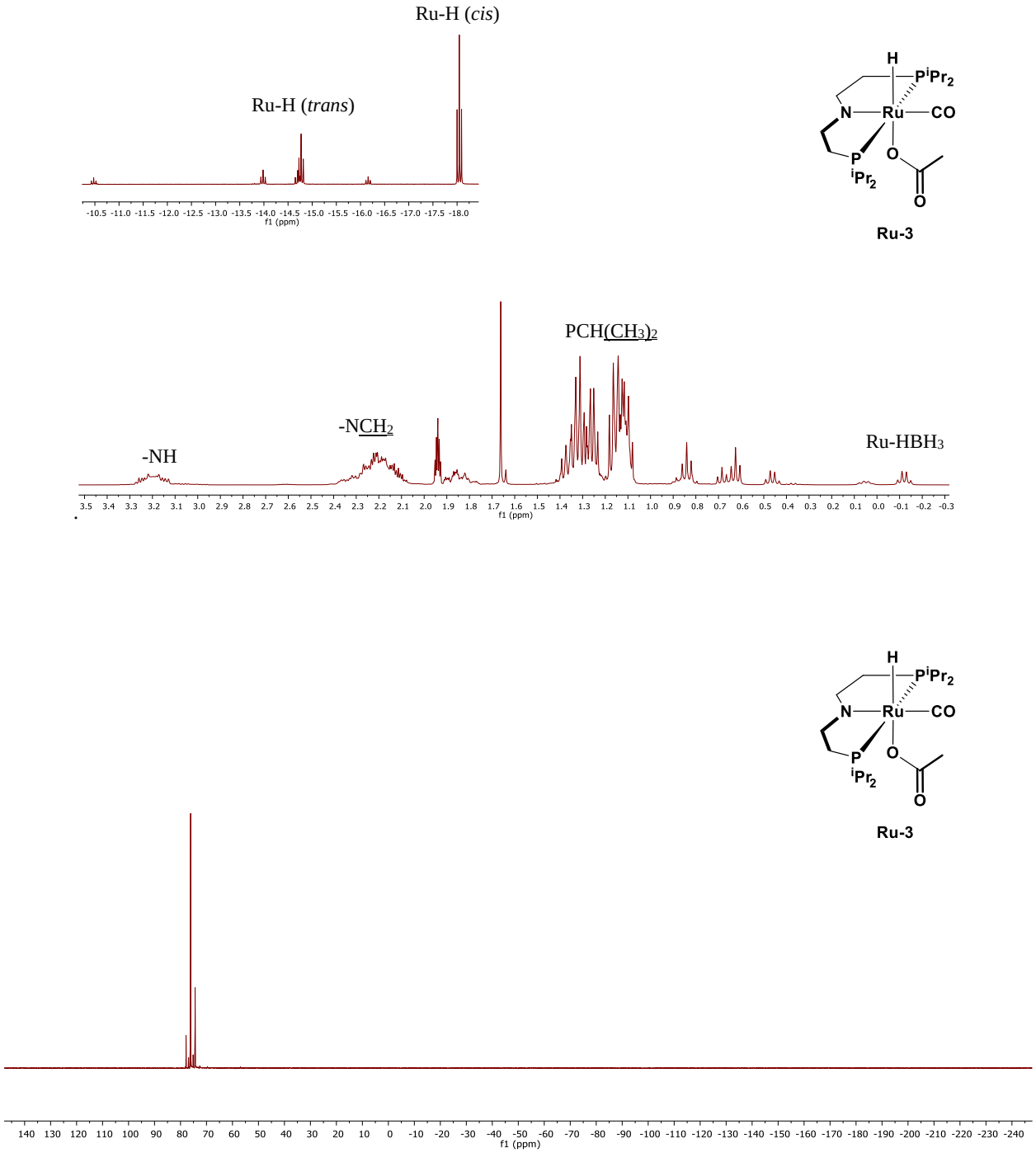

Figure S7. ^{1}H NMR (up) and ^{31}P NMR (down) spectra of **Ru-3** (CD_3CN, 25 ºC 400 MHz).

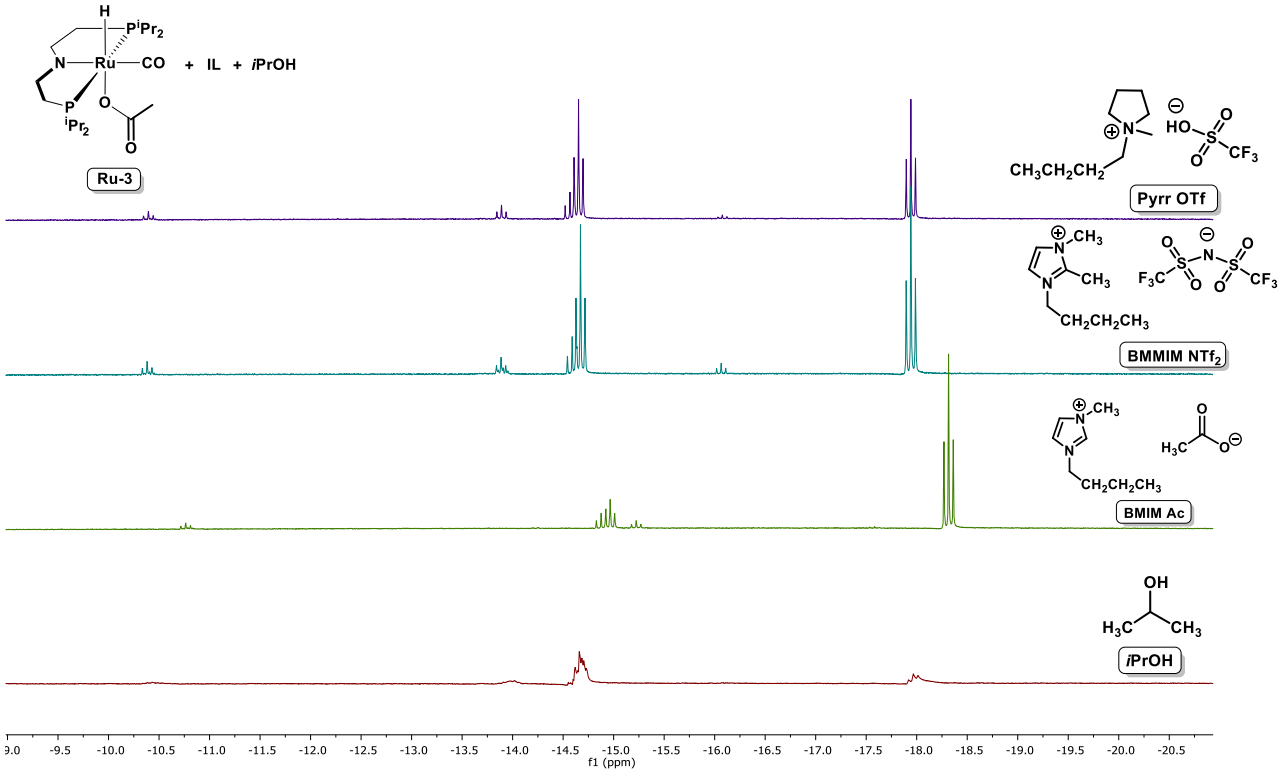

Figure S8. ^{1}H NMR spectra of **Ru-3** in different media: *i*PrOH, BMIM Ac, BMMIM NTf_2 and Pyrr OTf (CD_3CN, 25 ºC 400 MHz).

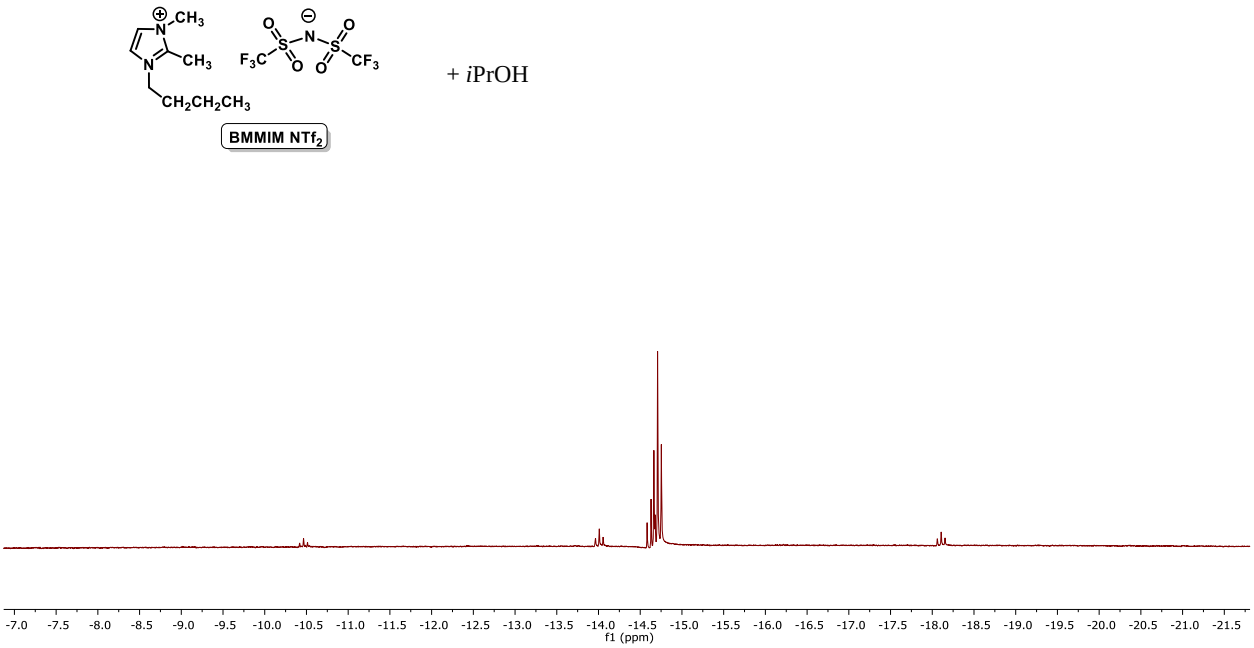

Figure S9: ^{1}H NMR spectrum of Ru-3 in BMMIM NTf_2 and *i*PrOH (CD_3CN).

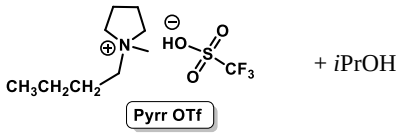

+ *i*PrOH

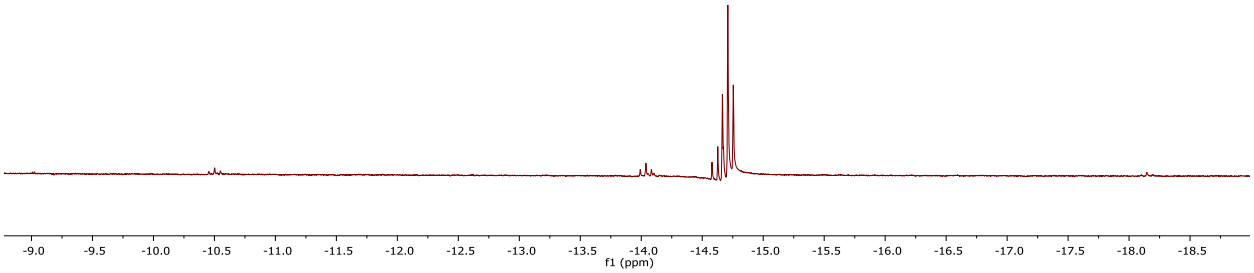

Figure S10: ^{1}H NMR spectrum of Ru-3 in Pyrr OTf and *i*PrOH (CD_3CN).

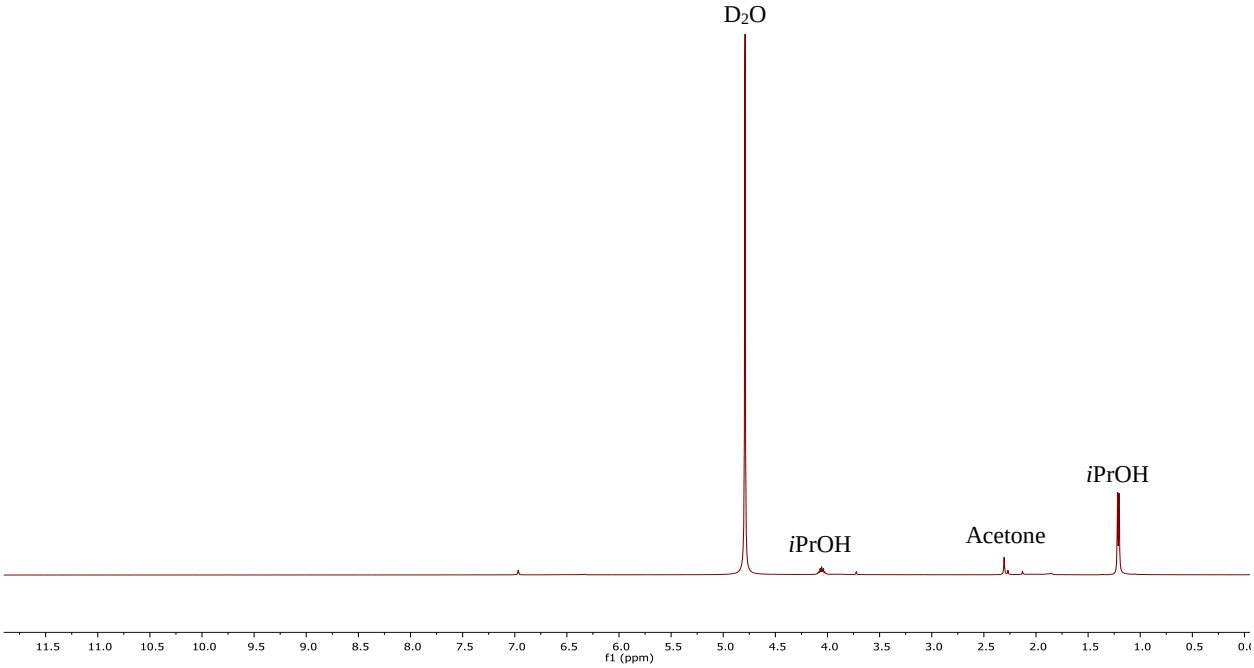

Figure S11: ^{1}H-NMR spectrum of the distillate from *i*PrOH dehydrogenation (D_2O).

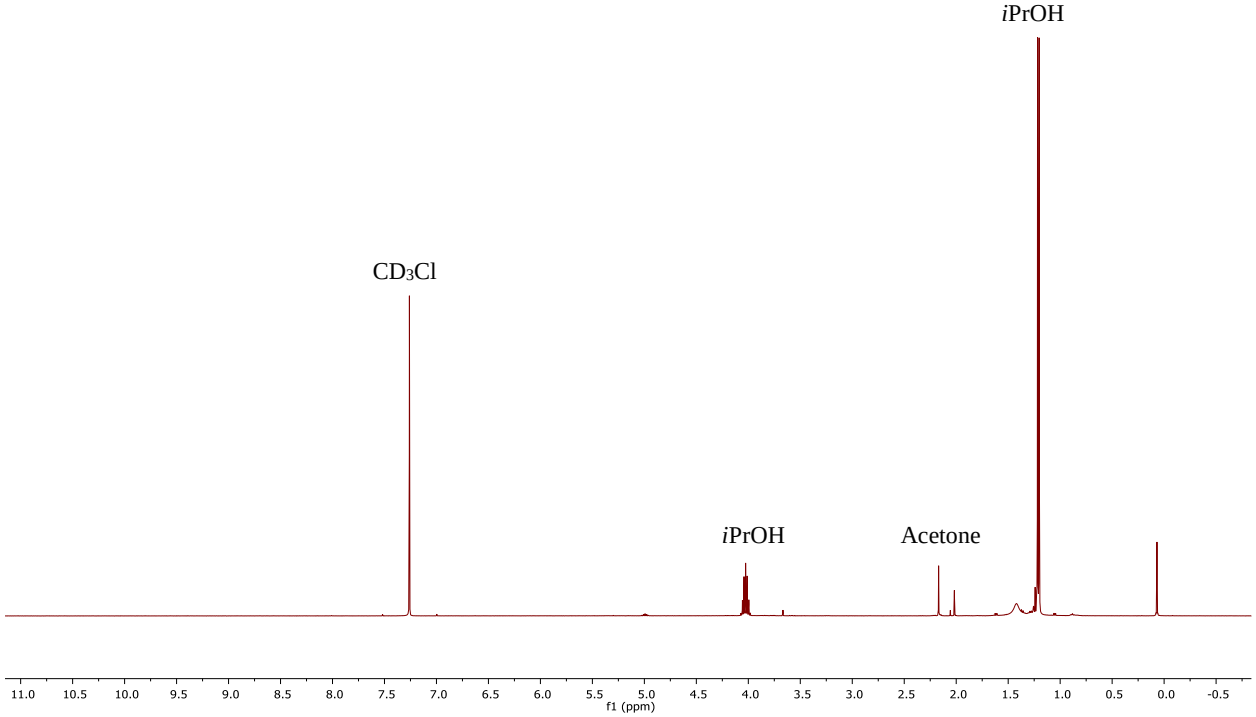

Figure S12: ^{1}H-NMR spectrum of the distillate from *i*PrOH dehydrogenation (CD_3Cl).

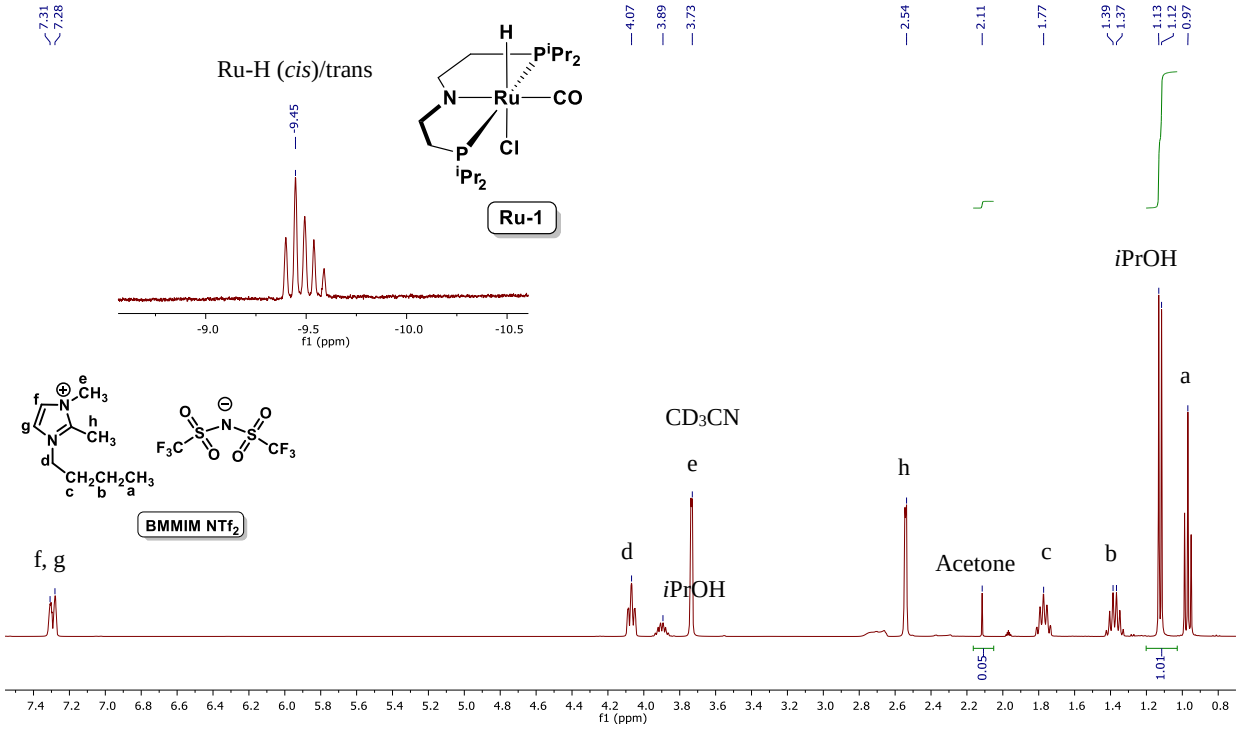

Figure S13. ^{1}H NMR spectrum of **Ru-1** in BMMIM NTf_2 after *i*PrOH dehydrogenation (Table S1, entry 3) (CD_3CN, 25 °C 400 MHz).

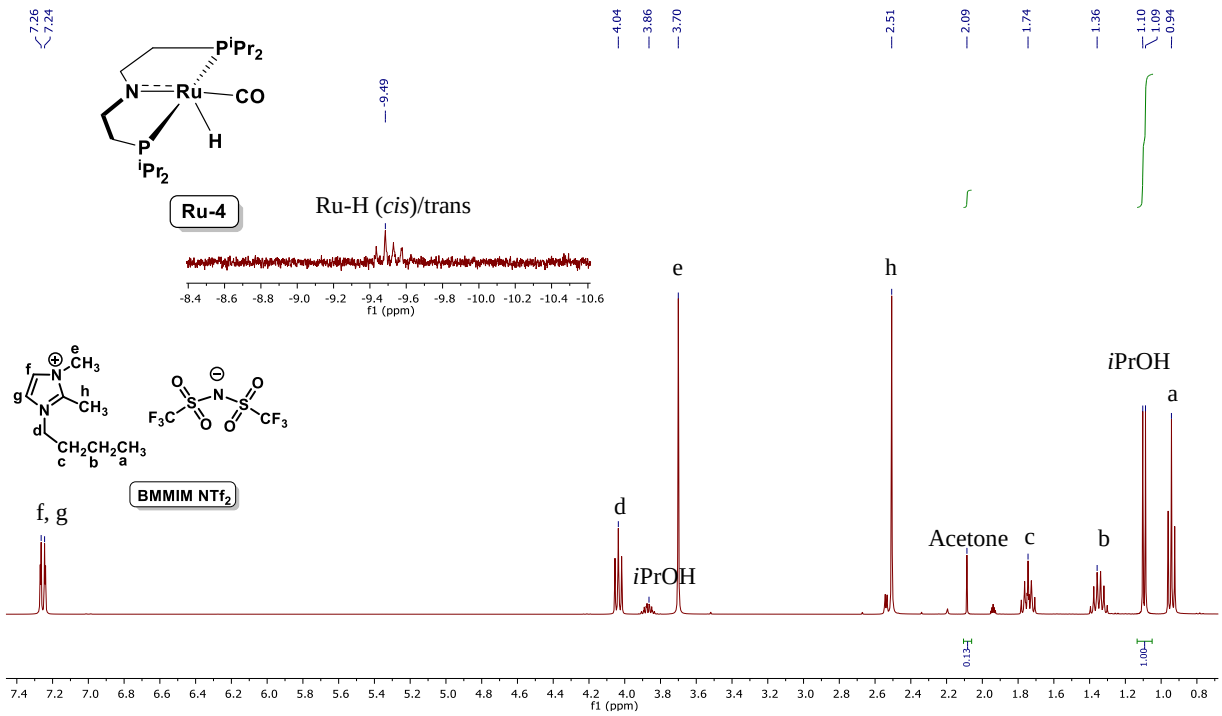

Figure S14. ^{1}H NMR spectrum of Ru-4 in BMMIM NTf_2 after *i*PrOH dehydrogenation (Table S1, entry 6) (CD_3CN, 25 ºC 400 MHz).

Entry	Catalyst (mol%[a])	Ionic liquid (mL)	*i*PrOH [mmol]	Time [h]	T [ºC]	TON	Conversion[b] [%]
1	**Ru-1** (0.20)	BMIM Ac (1)	5.2	2	90	/	<5
2[c]	**Ru-2** (0.15)	Pyrr NTf_2 (1)	26	1	100	90	14
3	**Ru-1** (0.15)	BMMIM NTf_2 (1)	6.5	18	90	60	8
4	**Ru-1** (1.20)	BMMIM NTf_2 (0.5)	1.3	0.3	90	6	8
5	**Ru-1** (0.10)	BMMIM NTf_2 (1)	5.2	1.5	90	105	10
6	**Ru-4** (0.05)	PIPER NTf_2 (1)	26	1.5	100	150	7

Reactions reproducible within a 10% error. [a] Mol% with respect to *i*PrOH. [b] Determined by ^{1}NMR. [c] With NaOEt (2 eq with respect to Ru-2).

Table S1. Screening of reaction conditions for *i*PrOH dehydrogenation.

Catalyst	Silica 100 Ru/SiO_2 wt%	Silica 60 Ru/SiO_2 wt%
	0,5	0,35
Ru-H	1	0,1
	0,1	0,91
	0,5	0,1
Ru-MACHO-BH	**1**	**0,87**
	0,1	-

Table S2. Screening of SILP materials for initial tests in fixed-bed reactor. In bold the SILP catalysts that showed activity under continuous flow fixed-bed conditions.

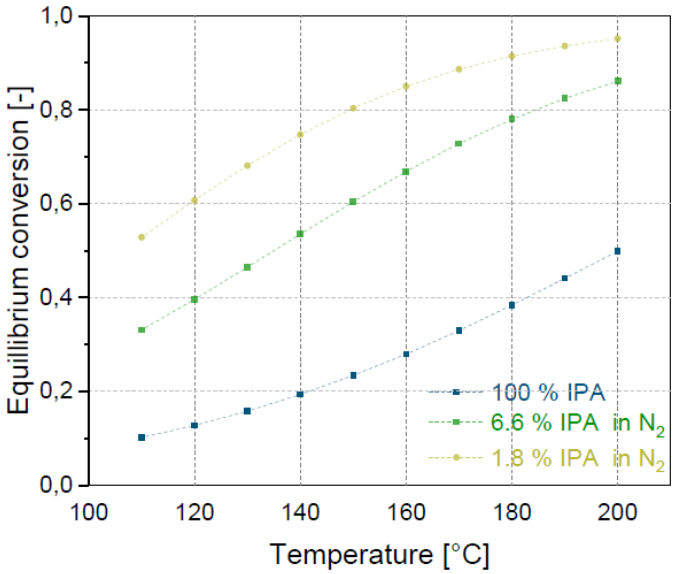

Figure S15. Thermodynamic equilibrium conversion vs temperature at different isopropanol dilution in nitrogen.

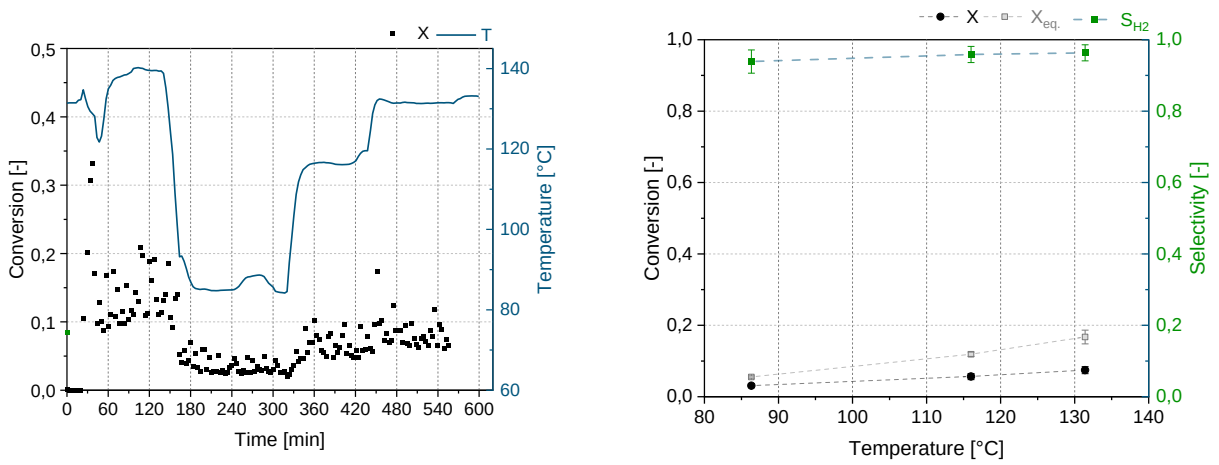

Figure S16. 0.5 wt% Ru/SiO_2, PIPER NTf_2, silica 100, α = 20%

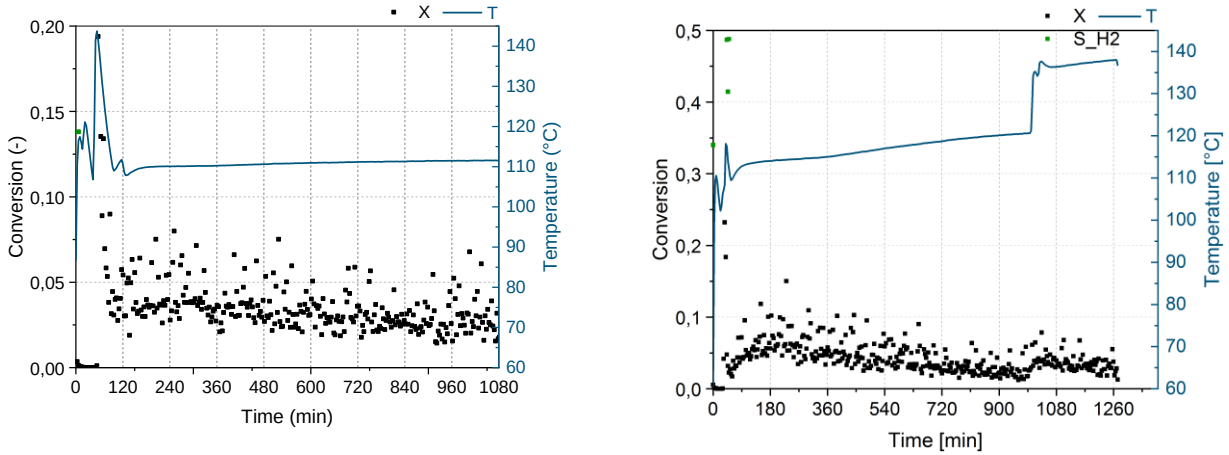

Figure S17. (a) Ru/SiO_2 = 0.87 wt%, PIPER NTf_2, silica 60, α = 20%; (b) Ru/SiO_2 = 0.87 wt%, Pyrr NTf_2, silica 100, α = 20%; undiluted IPA for both.

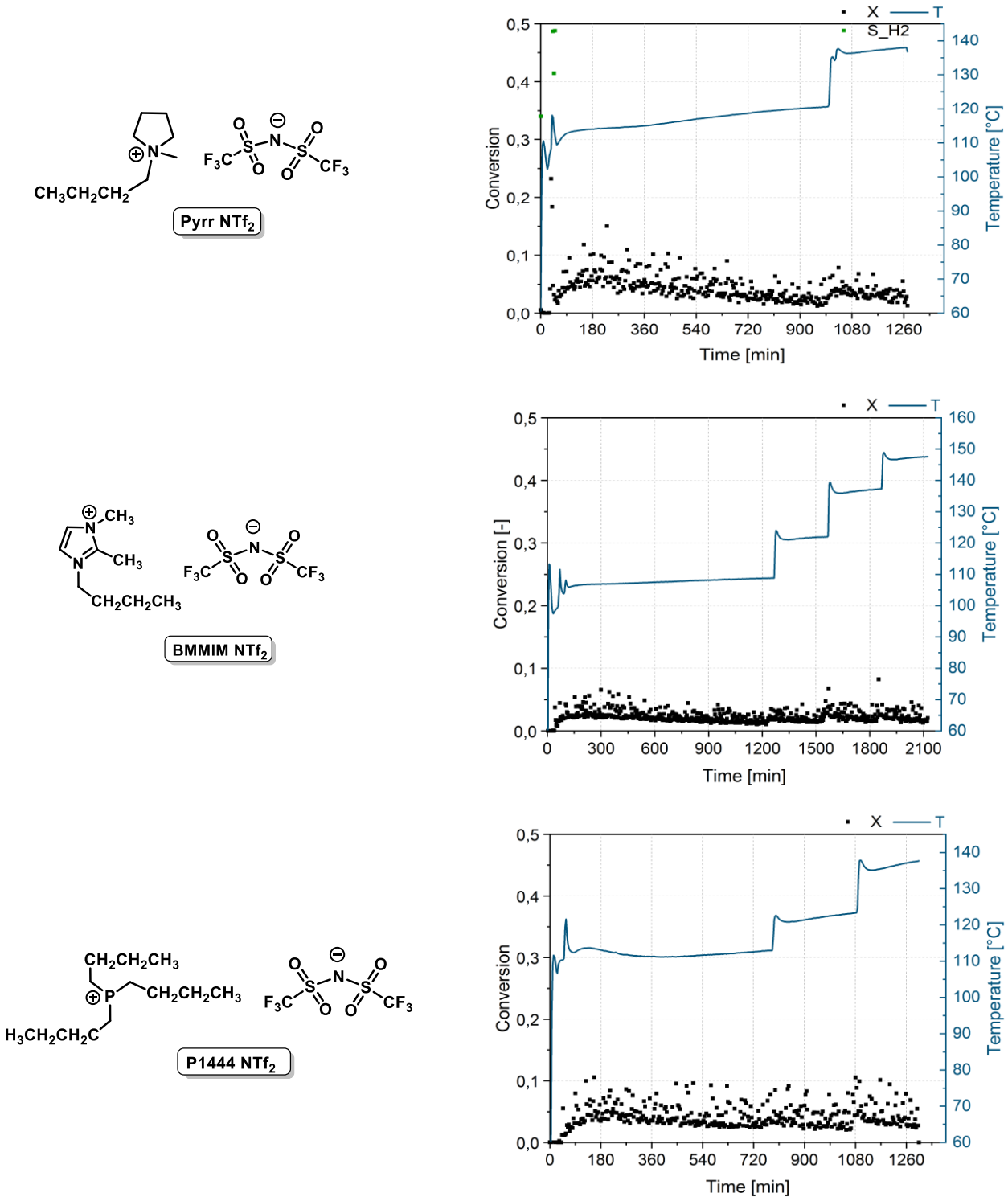

Figure S18. Screening of different cations. Ru/SiO_2 = 0.6 wt%, α = 20%, Silica 100, undiluted IPA.

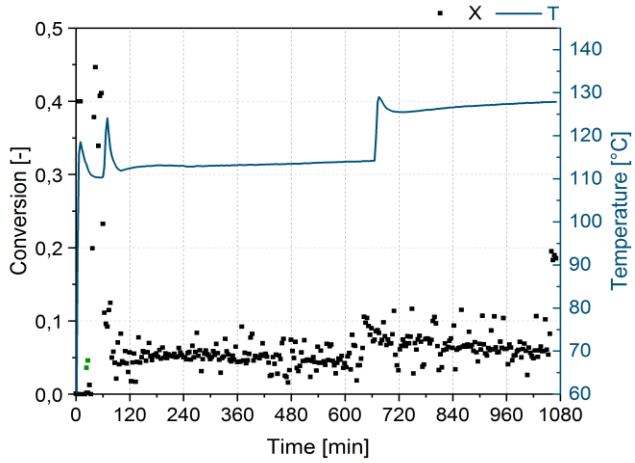

Figure S19. Acetone - isopropanol 25-75 vol%. Ru/SiO_2 = 1 wt%, P_{1444} NTf_2, silica 100, α = 20%.

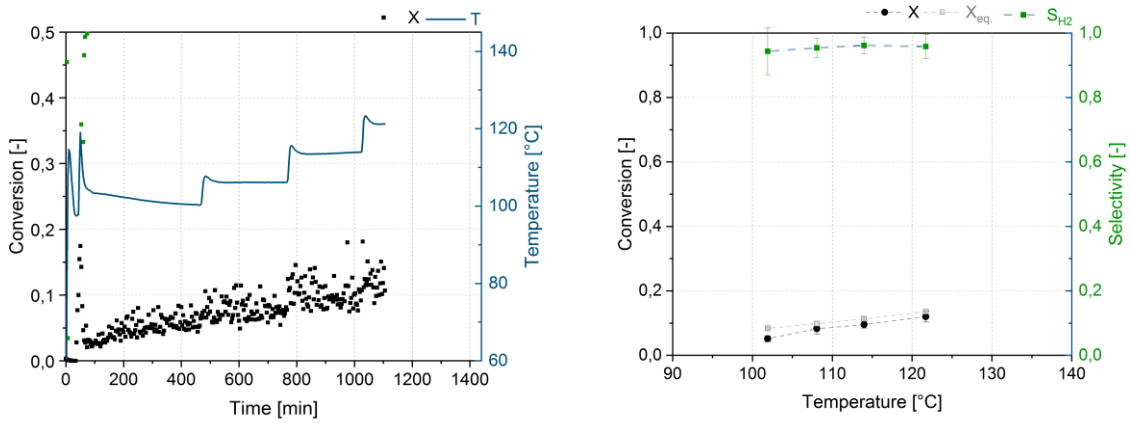

Figure S20. Ru/SiO_2 = 0.9 wt%, P_{1444} NTf_2, Silica 100, α = 20%, undiluted IPA.

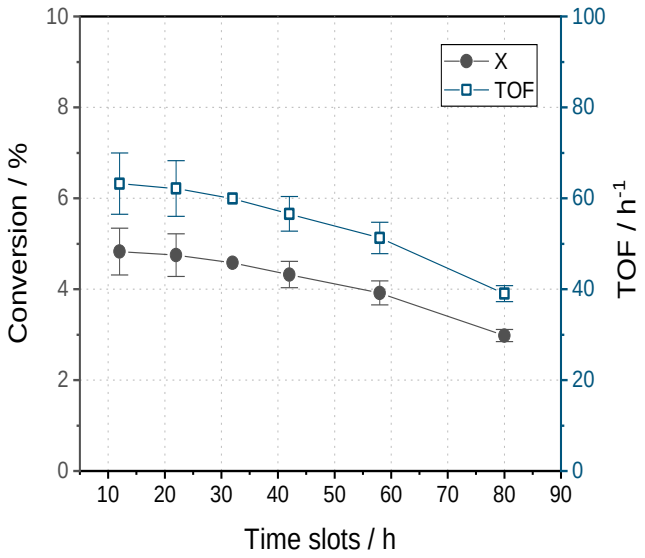

Figure S21. Long-term experiment, nitrogen flow dilution. Ru/SiO_2 = 1 wt%, P_{1444} NTf_2, silica 100, α = 20%.

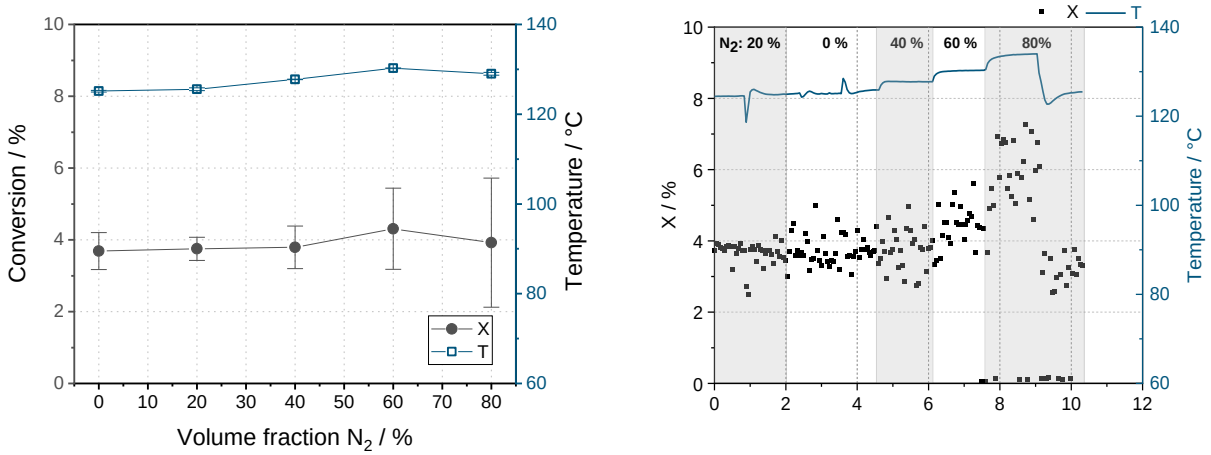

Figure S22. Long-term experiment, nitrogen flow dilution. Ru/SiO_2 = 1 wt%, P_{1444} NTf_2, silica 100, α = 20%.

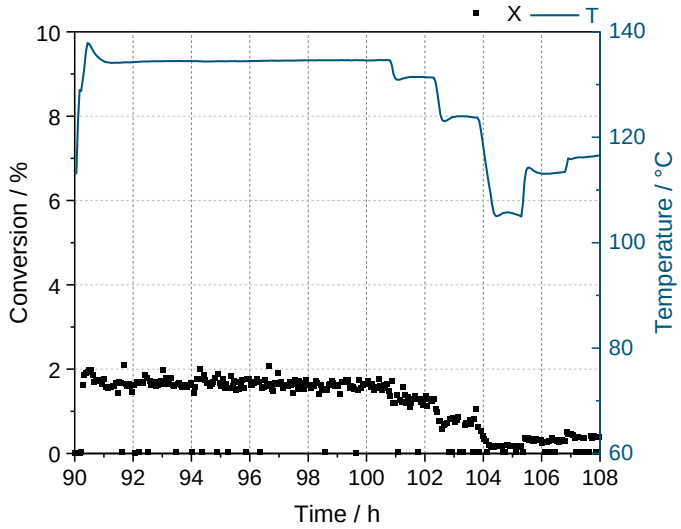

Figure S23. Long-term experiment: acetone dilution. Ru/SiO_2 = 1 wt%, P_{1444} NTf_2, silica 100, α = 20%.

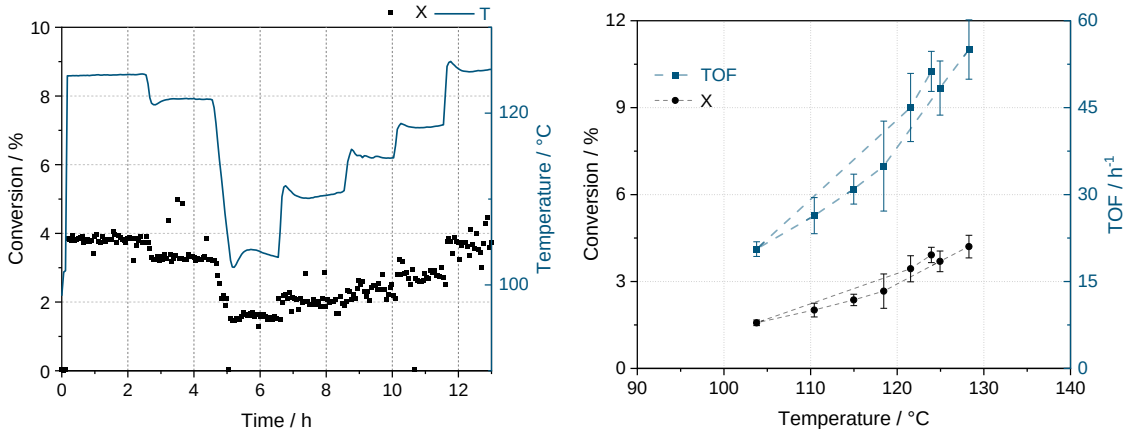

Figure S24. Long-term experiment: temperature variations. Ru/SiO_2 = 1 wt%, P_{1444} NTf_2, silica 100, α = 20%.

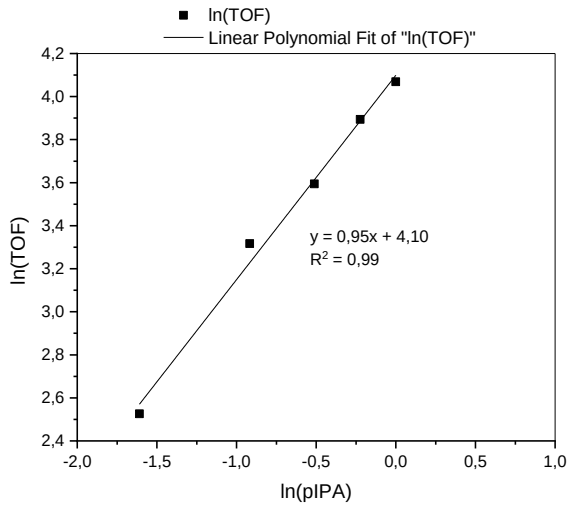

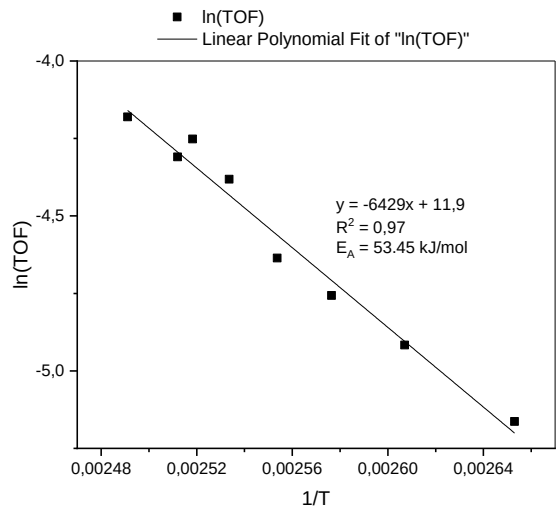

$$\ln(TOF) = \ln(C) + n * \ln(p_{IPA})^2$$

$$\ln(TOF) = \ln(C) - \frac{E_a}{RT}$$

Figure S25: Kinetic calculations.

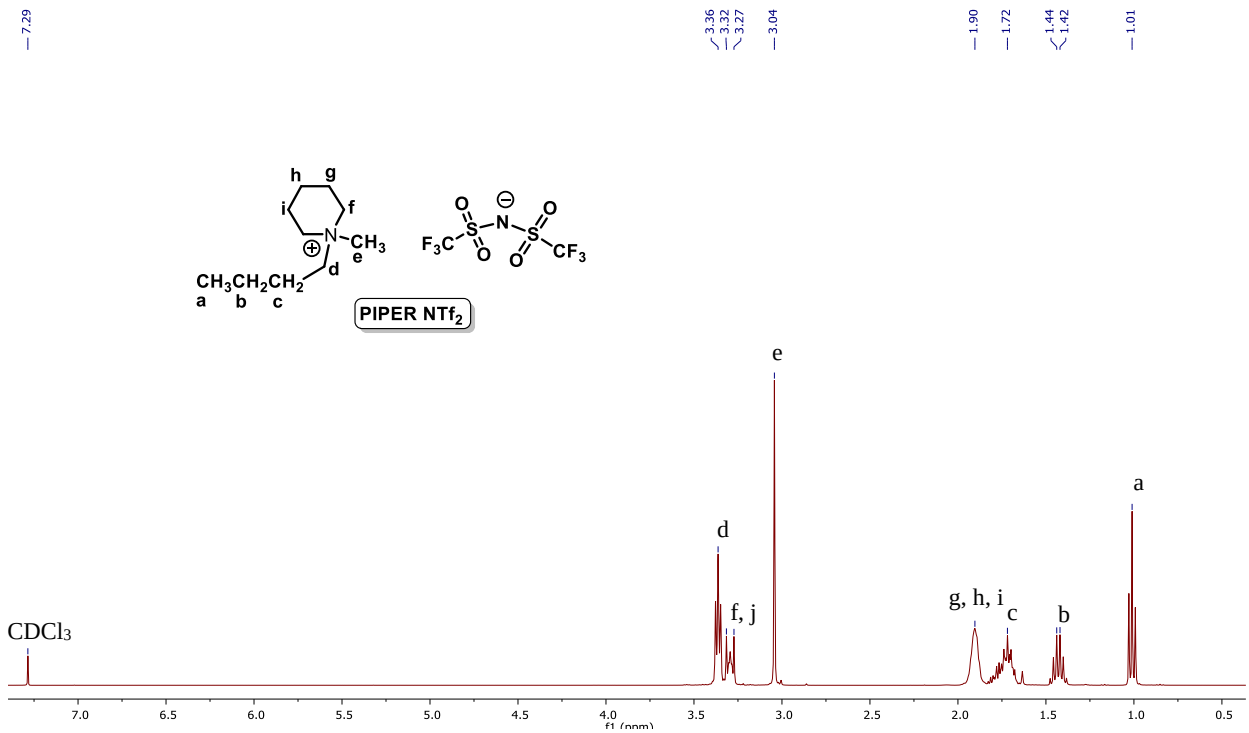

Figure S26. ^{1}H NMR spectrum of PIPER NTf_2 ($CDCl_3$, 25 ºC 400 MHz).

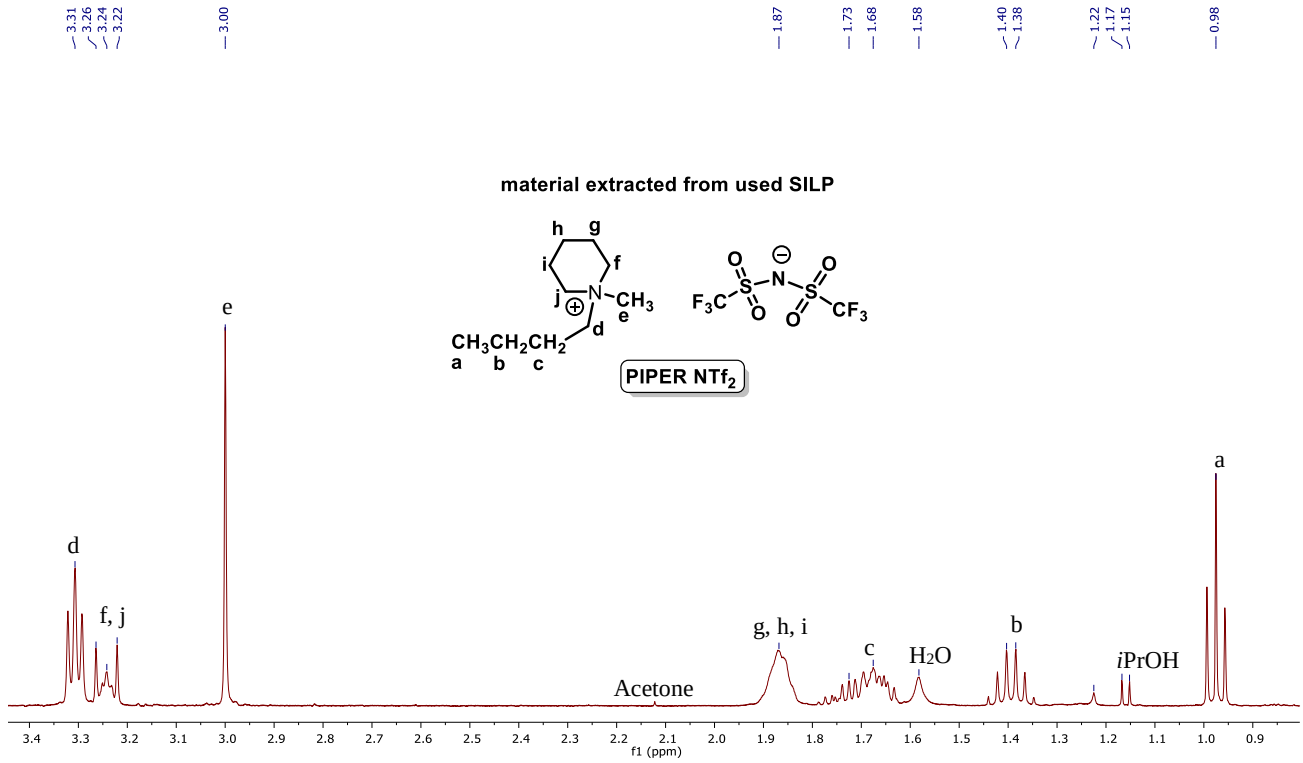

Figure S27. ^{1}H-NMR spectrum of extracted SILP after reaction in the fixed-bed reactor ($CDCl_3$, 25 ºC 400 MHz).

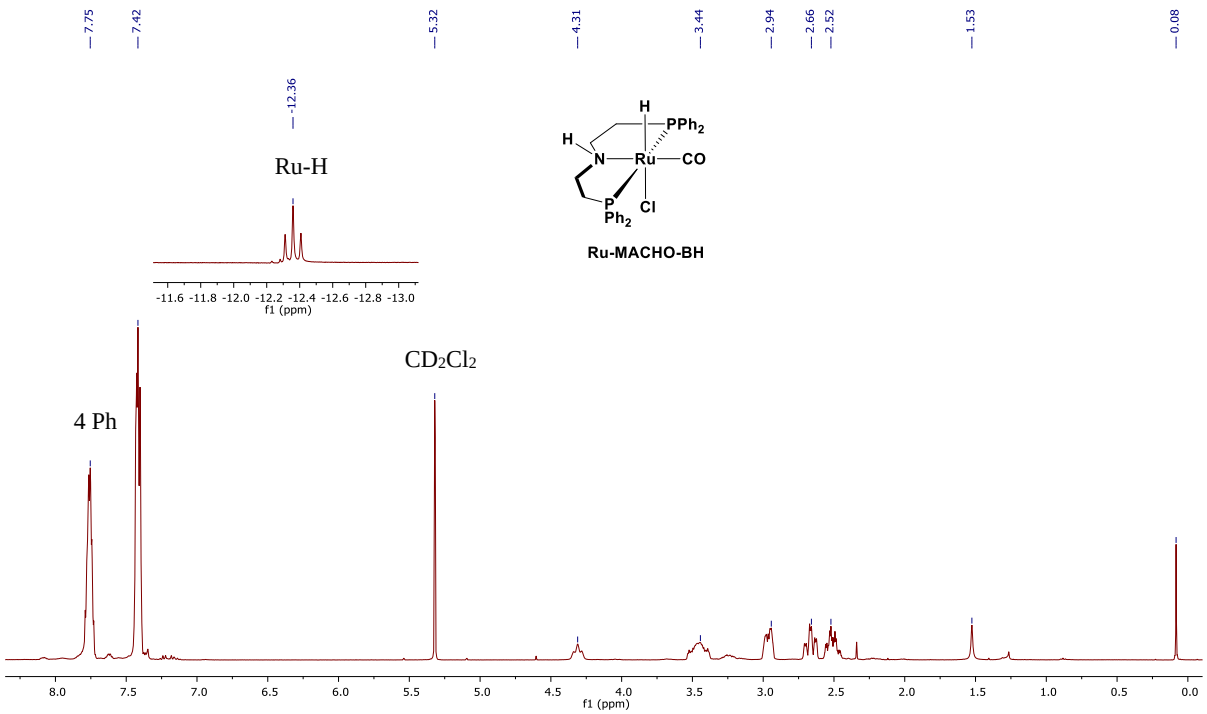

Figure S28. ^{1}H-NMR spectrum of Ru-MACHO-BH (CD_2Cl_2, 25 ºC 400 MHz).

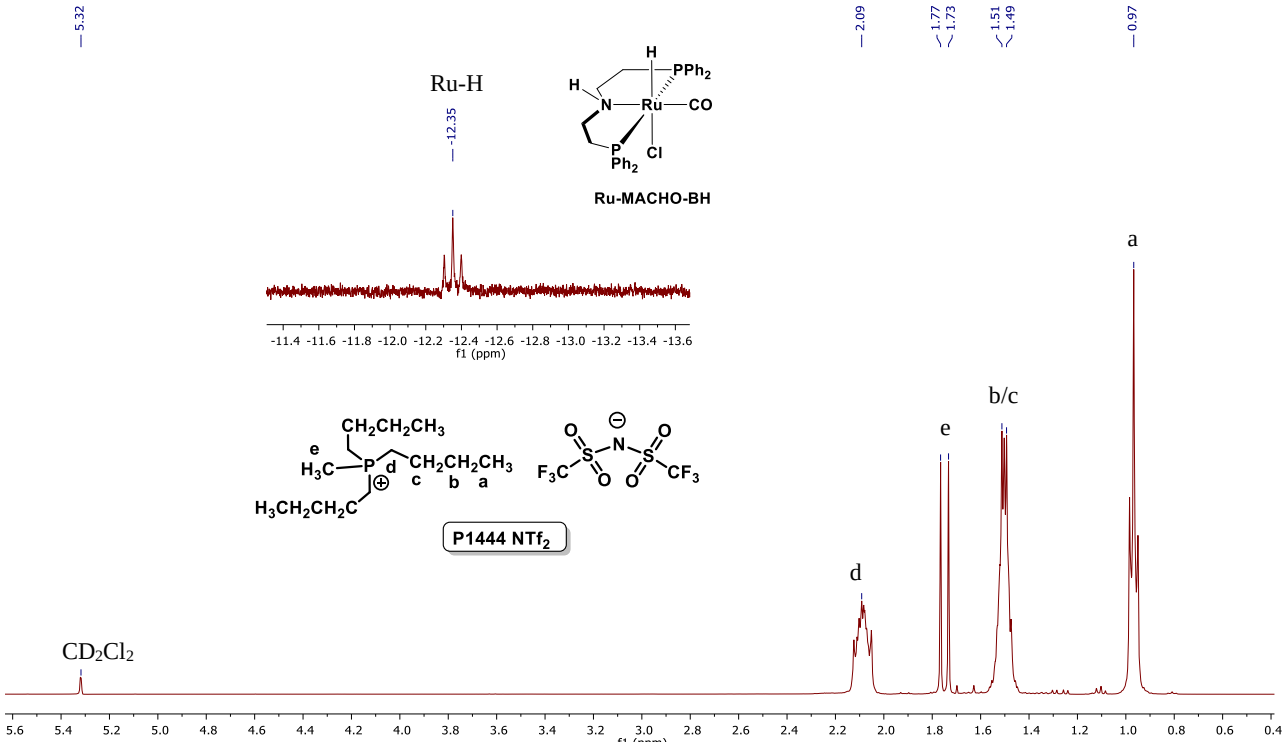

Figure S29. ^{1}H NMR spectrum of Ru-MACHO-BH with P_{1444} NTf_2 (CD_2Cl_2, 25 ºC 400 MHz).

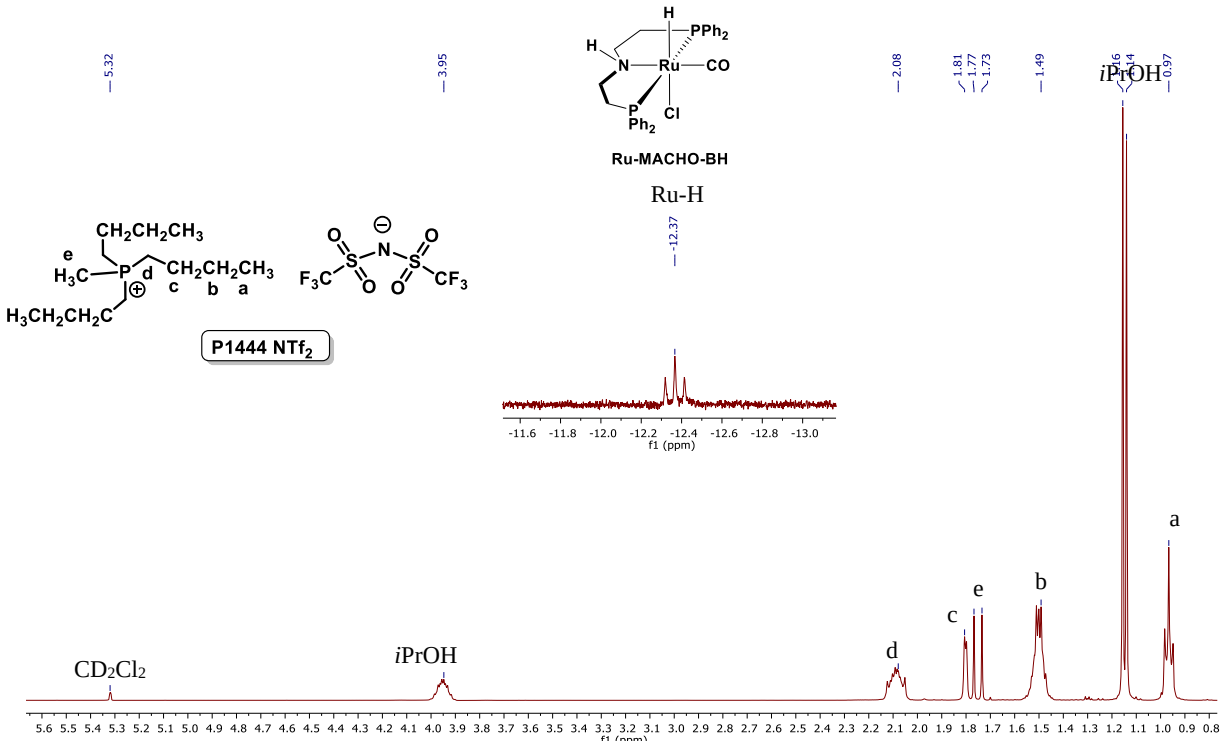

Figure S30: ^{1}H NMR spectrum of Ru-MACHO-BH in P_{1444} NTf_2 and *i*PrOH (*d*-DCM).

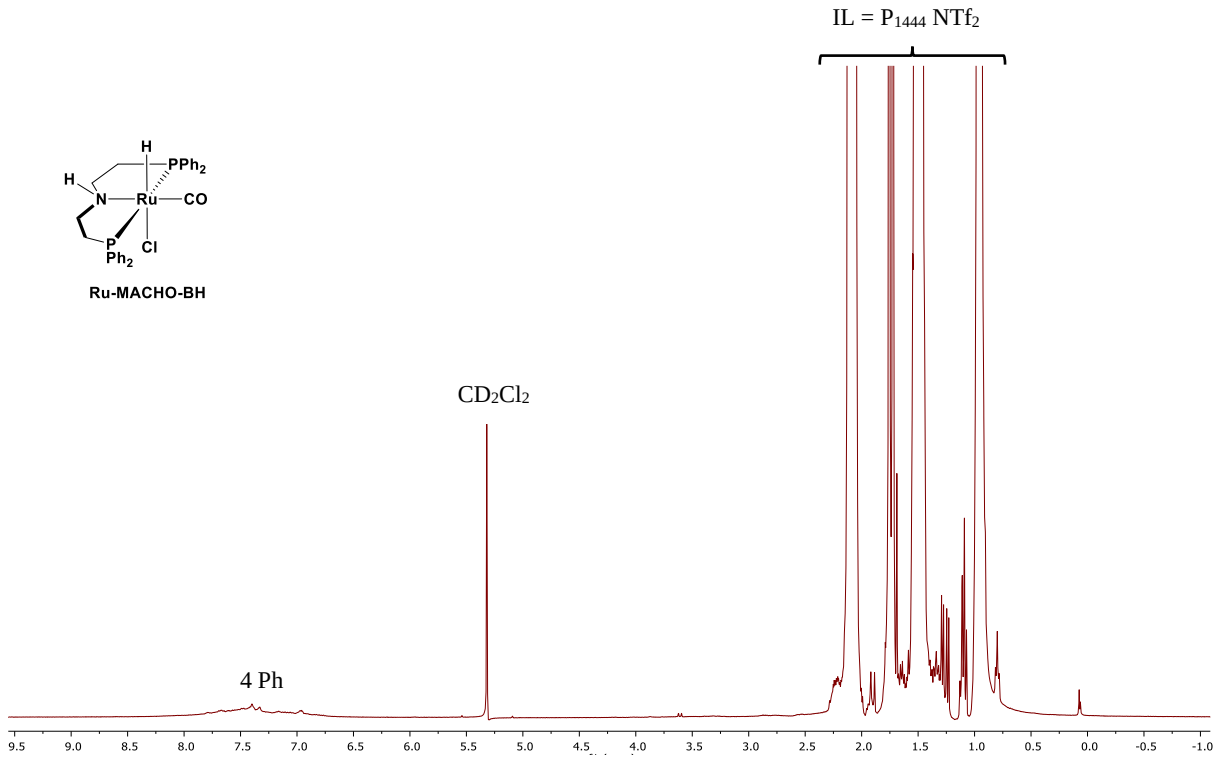

Figure S31. ^{1}H NMR spectrum of Ru-MACHO-BH in P_{1444} NTf_2 after bubbling of argon for 72h (CD_2Cl_2, 25 ºC 400 MHz).

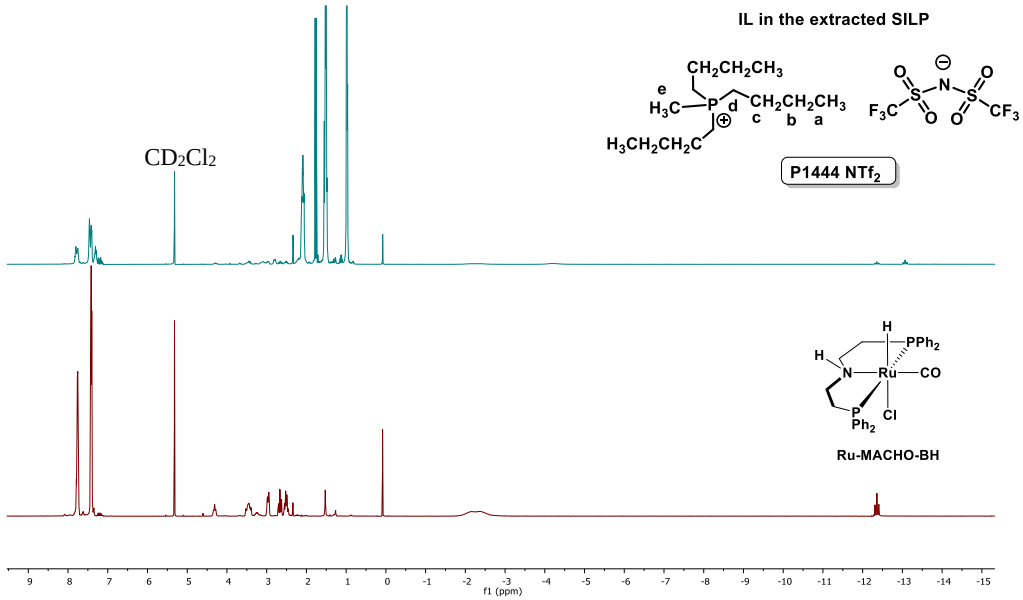

Figure S32. ^{1}H NMR plot of Ru-MACHO-BH (down) staggered with a solution of the extracted/prepared SILP catalyst, containing Ru-MACHO-BH and P_{1444} NTf_2 (up). Extracted SILP: Ru/SiO_2 = 1 wt%, P_{1444} NTf_2, silica 100, α = 20%.

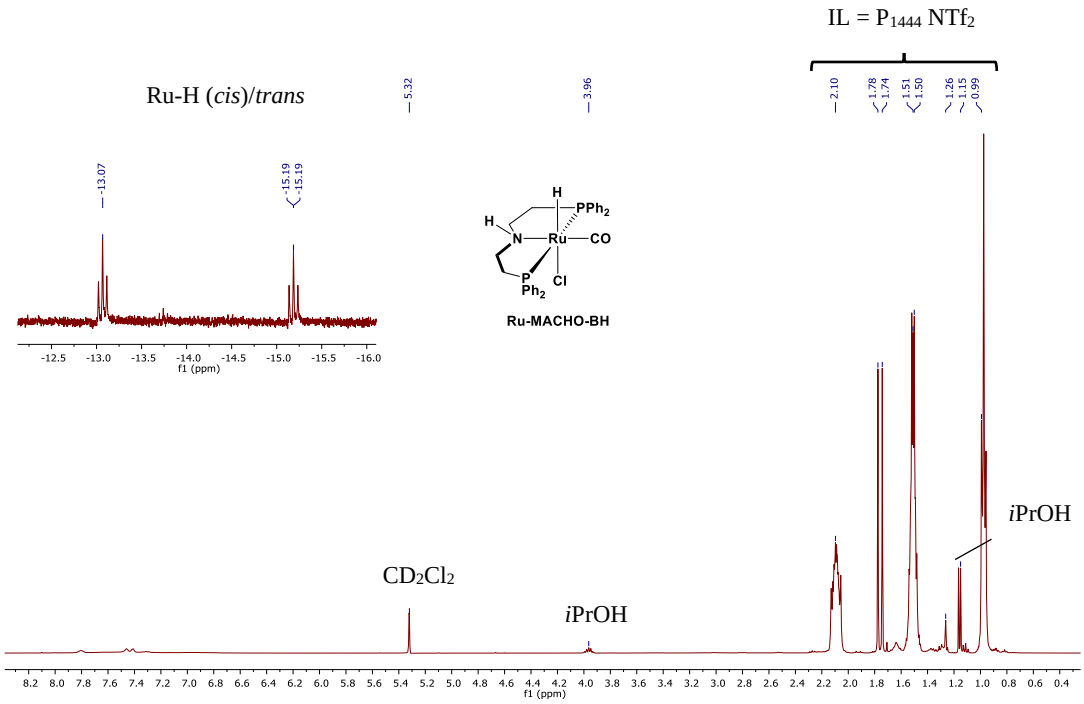

Figure S33. ^{1}H NMR analysis of the extract solution from a SILP sample used in the fixed-bed reactor. Ru/SiO_2 = 1 %, P_{1444} NTf_2, silica 100, α = 20%.

Appendix I – Paper V

This work represents a follow-up paper that will follow publication of Paper II. While the main results showed in this thesis for CO_2 hydrogenation will be discussed in the former, this publication will cover most of the optimization methods and complete screening of catalysts, ILs and reaction conditions showed in Chapter 4. In addition, this work can potentially be expanded with addition of more experimental results. For example, more investigations can lead to fast optimization in the use of biogas as a CO_2 source, further expanding the applicability of the Ru-PNP/IL system. In addition, PhD student Brenda Rabell is currently carrying out studies on synthesis of functionalized ILs, as well as the possibility to promote FA formation and separation in the presence of amine additives. As such, I am not providing the draft since the status of this article is the most developing among the planned publications; only an example of abstract is showed.

Paper in preparation.

Reactivity of Ru-PNP complexes in ionic liquids for the hydrogenation of carbon dioxide to formic acid

*L.Piccirilli, B. Rabell, R. Padilla, A. Riisager, M. Nielsen**

Department of Chemistry, Technical University of Denmark, DK-2800 Kgs. Lyngby, Denmark;
** Correspondence: marnie@kemi.dtu.dk; Tel.: +45-24651045*

Abstract

Carbon dioxide is expected to replace common fossil fuels for the bulk synthesis of chemicals and fuels. Among the possible hydrogenation products, formic acid is a particularly desirable target compound thanks to its hydrogen storing properties. Herein, we explore the reactivity of active ruthenium catalysts for the hydrogenation of CO_2 to formic acid in ionic liquids. The ionic liquid captures CO_2 already at room temperature, while a Ru-PNP complex performs efficient hydride transfer to the trapped carboxylate resulting in the formation of formic acid. The addition of a co-ionic liquid (BMMIM NTf_2) leads to higher reactivity and avoids the formation of solid products due to CO_2 chemisorption. The use of amine additives increases the rate of formic acid production and facilitates gas diffusion within the ionic liquid phase. Remarkably, the system is highly active towards the hydrogenation of CO_2 using biogas as the carbon source.

9. References

1. Humphries, R. The challenge of climate change. *Rev. Environ. Sci. Biotechnol.* **2010**, *9*, 95–98.

2. Palmer, T.; Stevens, B. The scientific challenge of understanding and estimating climate change. *Proc. Natl. Acad. Sci.* **2019**, *116*, 24390–24395.

3. Midilli, A.; Dincer, I.; Ay, M. Green energy strategies for sustainable development. *Energy Policy* **2006**, *34*, 3623–3633.

4. UNEP *The emissions gap report 2019 (full report)*; 2019; ISBN 9789280737660.

5. Fawzy, S.; Osman, A.I.; Doran, J.; Rooney, D.W. Strategies for mitigation of climate change: a review. *Environ. Chem. Lett.* **2020**, *18*, 2069–2094.

6. Bockris, J.O.M. The hydrogen economy: Its history. *Int. J. Hydrogen Energy* **2013**, *38*, 2579–2588.

7. Anon The Future of Hydrogen - Seizing today's opportunities - Report prepared for the G20, Japan. *Int. Energy Agency* **2019**.

8. Preuster, P.; Alekseev, A.; Wasserscheid, P. Hydrogen Storage Technologies for Future Energy Systems. *Annu. Rev. Chem. Biomol. Eng.* **2017**, *8*, 445–471.

9. Pursiheimo, E.; Holttinen, H.; Koljonen, T. Inter-sectoral effects of high renewable energy share in global energy system. *Renew. Energy* **2019**, *136*, 1119–1129.

10. Preuster, P.; Alekseev, A.; Wasserscheid, P. Hydrogen storage technologies for future energy systems. *Annu. Rev. Chem. Biomol. Eng.* **2017**, *8*, 445–471.

11. Dodds, P.E.; Staffell, I.; Hawkes, A.D.; Li, F.; Grünewald, P.; McDowall, W.; Ekins, P. Hydrogen and fuel cell technologies for heating: A review. *Int. J. Hydrogen Energy* **2015**, *40*, 2065–2083.

12. Olabi, A.G.; Wilberforce, T.; Abdelkareem, M.A. Fuel cell application in the automotive industry and future perspective. *Energy* **2021**, *214*, 118955.

13. Kirubakaran, A.; Jain, S.; Nema, R.K. A review on fuel cell technologies and power electronic interface. *Renew. Sustain. Energy Rev.* **2009**, *13*, 2430–2440.

14. Armaroli, N.; Balzani, V. The Hydrogen Issue. *ChemSusChem* **2011**, *4*, 21–36.

15. Wang, A.; Van der Leun, K.; Peters, D.; Buseman, M. European Hydrogen Backbone. **2020**, 24.

16. Penev, M.; Zuboy, J.; Hunter, C. Economic analysis of a high-pressure urban pipeline concept (HyLine) for delivering hydrogen to retail fueling stations. *Transp. Res. Part D Transp. Environ.* **2019**, *77*, 92–105.

17. Chae, M.J.; Kim, J.H.; Moon, B.; Park, S.; Lee, Y.S. The present condition and outlook for hydrogen-natural gas blending technology. *Korean J. Chem. Eng.* **2022**, *39*, 251–262.

18. Guerra, K.; Haro, P.; Gutiérrez, R.E.; Gómez-Barea, A. Facing the high share of variable renewable energy in the power system: Flexibility and stability requirements. *Appl. Energy* **2022**, *310*, 118561.

19. Sun, Y.; Delucchi, M.; Ogden, J. The impact of widespread deployment of fuel cell vehicles on platinum demand and price. *Int. J. Hydrogen Energy* **2011**, *36*, 11116–11127.

20. Ren, X.; Lv, Q.; Liu, L.; Liu, B.; Wang, Y.; Liu, A.; Wu, G. Current progress of Pt and Pt-based electrocatalysts used for fuel cells. *Sustain. Energy Fuels* **2019**, *4*, 15–30.

21. Asset, T.; Atanassov, P. Iron-Nitrogen-Carbon Catalysts for Proton Exchange Membrane Fuel Cells. *Joule* **2020**, *4*, 33–44.

22. Iqbal, M.Z.; Rehman, A.U.; Siddique, S. Prospects and challenges of graphene based fuel cells. *J. Energy Chem.* **2019**, *39*, 217–234.

23. Preuster, P.; Papp, C.; Wasserscheid, P. Liquid organic hydrogen carriers (LOHCs): Toward a hydrogen-free hydrogen economy. *Acc. Chem. Res.* **2017**, *50*, 74–85.

24. Aakko-Saksa, P.T.; Cook, C.; Kiviaho, J.; Repo, T. Liquid organic hydrogen carriers for transportation and storing of renewable energy – Review and discussion. *J. Power Sources* **2018**, *396*, 803–823.

25. He, T.; Pei, Q.; Chen, P. Liquid organic hydrogen carriers. *J. Energy Chem.* **2015**, *24*, 587–594.

26. Sakintuna, B.; Lamari-Darkrim, F.; Hirscher, M. Metal hydride materials for solid hydrogen storage: A review. *Int. J. Hydrogen Energy* **2007**, *32*, 1121–1140.

27. Suh, M.P.; Park, H.J.; Prasad, T.K.; Lim, D.-W. Hydrogen Storage in Metal–Organic Frameworks. *Chem. Rev.* **2012**, *112*, 782–835.

28. Yürüm, Y.; Taralp, A.; Veziroglu, T.N. Storage of hydrogen in nanostructured carbon materials. *Int. J. Hydrogen Energy* **2009**, *34*, 3784–3798.

29. Biniwale, R.B.; Rayalu, S.; Devotta, S.; Ichikawa, M. Chemical hydrides: A solution to high capacity hydrogen storage and supply. *Int. J. Hydrogen Energy* **2008**, *33*, 360–365.

30. Preuster, P.; Papp, C.; Wasserscheid, P. Liquid Organic Hydrogen Carriers (LOHCs): Toward a Hydrogen-free Hydrogen Economy. *Acc. Chem. Res.* **2017**, *50*, 74–85.

31. Teichmann, D.; Arlt, W.; Wasserscheid, P. Liquid Organic Hydrogen Carriers as an efficient vector for the transport and storage of renewable energy. *Int. J. Hydrogen Energy* **2012**, *37*, 18118–18132.

32. Modisha, P.M.; Ouma, C.N.M.; Garidzirai, R.; Wasserscheid, P.; Bessarabov, D. The Prospect of Hydrogen Storage Using Liquid Organic Hydrogen Carriers. *Energy & Fuels* **2019**, *33*, 2778–2796.

33. Ahmed, A.; Al-Amin, A.Q.; Ambrose, A.F.; Saidur, R. Hydrogen fuel and transport system: A sustainable and environmental future. *Int. J. Hydrogen Energy* **2016**, *41*, 1369–1380.

34. Alberico, E.; Nielsen, M. Towards a methanol economy based on homogeneous catalysis: Methanol to H2 and CO2 to methanol. *Chem. Commun.* **2015**, *51*, 6714–6725.

35. Simon Araya, S.; Liso, V.; Cui, X.; Li, N.; Zhu, J.; Sahlin, S.L.; Jensen, S.H.; Nielsen, M.P.; Kær, S.K. A Review of The Methanol Economy: The Fuel Cell Route. *Energies* **2020**, *13*, 596.

36. Mellmann, D.; Sponholz, P.; Junge, H.; Beller, M. Formic acid as a hydrogen storage material-development of homogeneous catalysts for selective hydrogen release. *Chem. Soc. Rev.* **2016**, *45*, 3954–3988.

37. Klerke, A.; Christensen, C.H.; Nørskov, J.K.; Vegge, T. Ammonia for hydrogen storage: challenges and opportunities. *J. Mater. Chem.* **2008**, *18*, 2304.

38. Rossin, A.; Peruzzini, M. Ammonia-Borane and Amine-Borane Dehydrogenation Mediated by Complex Metal Hydrides. *Chem. Rev.* **2016**, *116*, 8848–8872.

39. Sotoodeh, F.; Huber, B.J.M.; Smith, K.J. Dehydrogenation kinetics and catalysis of organic heteroaromatics for hydrogen storage. *Int. J. Hydrogen Energy* **2012**, *37*, 2715–2722.

40. Müller, K.; Aslam, R.; Fischer, A.; Stark, K.; Wasserscheid, P.; Arlt, W. Experimental assessment of the degree of

hydrogen loading for the dibenzyl toluene based LOHC system. *Int. J. Hydrogen Energy* **2016**, *41*, 22097–22103.

41. Jorschick, H.; Bulgarin, A.; Alletsee, L.; Preuster, P.; Bösmann, A.; Wasserscheid, P. Charging a Liquid Organic Hydrogen Carrier with Wet Hydrogen from Electrolysis. *ACS Sustain. Chem. Eng.* **2019**, *7*, 4186–4194.

42. Eypasch, M.; Schimpe, M.; Kanwar, A.; Hartmann, T.; Herzog, S.; Frank, T.; Hamacher, T. Model-based techno-economic evaluation of an electricity storage system based on Liquid Organic Hydrogen Carriers. *Appl. Energy* **2017**, *185*, 320–330.

43. Niermann, M.; Beckendorff, A.; Kaltschmitt, M.; Bonhoff, K. Liquid Organic Hydrogen Carrier (LOHC) – Assessment based on chemical and economic properties. *Int. J. Hydrogen Energy* **2019**, *44*, 6631–6654.

44. Müller, K.; Skeledzic, T.; Wasserscheid, P. Strategies for Low-Temperature Liquid Organic Hydrogen Carrier Dehydrogenation. *Energy & Fuels* **2021**, *35*, 10929–10936.

45. Zhang, Z.; Pan, S.-Y.; Li, H.; Cai, J.; Olabi, A.G.; Anthony, E.J.; Manovic, V. Recent advances in carbon dioxide utilization. *Renew. Sustain. Energy Rev.* **2020**, *125*, 109799.

46. Dabral, S.; Schaub, T. The Use of Carbon Dioxide (CO 2) as a Building Block in Organic Synthesis from an Industrial Perspective. *Adv. Synth. Catal.* **2019**, *361*, 223–246.

47. Centi, G.; Perathoner, S. Opportunities and prospects in the chemical recycling of carbon dioxide to fuels. *Catal. Today* **2009**, *148*, 191–205.

48. Peters, M.; Köhler, B.; Kuckshinrichs, W.; Leitner, W.; Markewitz, P.; Müller, T.E. Chemical Technologies for Exploiting and Recycling Carbon Dioxide into the Value Chain. *ChemSusChem* **2011**, *4*, 1216–1240.

49. Al-Mamoori, A.; Krishnamurthy, A.; Rownaghi, A.A.; Rezaei, F. Carbon Capture and Utilization Update. *Energy Technol.* **2017**, *5*, 834–849.

50. Sancho-Sanz, I.; Korili, S.A.; Gil, A. Catalytic valorization of CO 2 by hydrogenation: current status and future trends . *Catal. Rev.* **2021**, *00*, 1–75.

51. Bocchini, S.; Castro, C.; Cocuzza, M.; Ferrero, S.; Latini, G.; Martis, A.; Pirri, F.; Scaltrito, L.; Rocca, V.; Verga, F.; et al. The virtuous CO2 circle or the three cs: Capture, cache, and convert. *J. Nanomater.* **2017**, *2017*.

52. Wei, J.; Yao, R.; Han, Y.; Ge, Q.; Sun, J. Towards the development of the emerging process of CO 2 heterogenous hydrogenation into high-value unsaturated heavy hydrocarbons. *Chem. Soc. Rev.* **2021**, *50*, 10764–10805.

53. Wang, M.; Lawal, A.; Stephenson, P.; Sidders, J.; Ramshaw, C. Post-combustion CO2 capture with chemical absorption: A state-of-the-art review. *Chem. Eng. Res. Des.* **2011**, *89*, 1609–1624.

54. Perathoner, S.; Van Geem, K.M.; Marin, G.B.; Centi, G. Reuse of CO 2 in energy intensive process industries. *Chem. Commun.* **2021**, *57*, 10967–10982.

55. de Coninck, H.; Benson, S.M. Carbon Dioxide Capture and Storage: Issues and Prospects. *Annu. Rev. Environ. Resour.* **2014**, *39*, 243–270.

56. Zahasky, C.; Krevor, S. Global geologic carbon storage requirements of climate change mitigation scenarios. *Energy Environ. Sci.* **2020**, *13*, 1561–1567.

57. Jakobsen, J.B.; Rønne, M.H.; Daasbjerg, K.; Skrydstrup, T. Are Amines the Holy Grail for Facilitating CO2 Reduction? *Angew. Chemie - Int. Ed.* **2021**, *60*, 9174–9179.

58. Klankermayer, J.; Wesselbaum, S.; Beydoun, K.; Leitner, W. Selective Catalytic Synthesis Using the Combination of Carbon Dioxide and Hydrogen: Catalytic Chess at the Interface of Energy and Chemistry. *Angew. Chemie - Int. Ed.* **2016**, *55*, 7296–7343.

59. Wagner, A.; Sahm, C.D.; Reisner, E. Towards molecular understanding of local chemical environment effects in electro- and photocatalytic CO2 reduction. *Nat. Catal.* **2020**, *3*, 775–786.

60. Jones, J.-P.; Prakash, G.K.S.; Olah, G.A. Electrochemical CO 2 Reduction: Recent Advances and Current Trends. *Isr. J. Chem.* **2014**, *54*, 1451–1466.

61. Kumar, B.; Brian, J.P.; Atla, V.; Kumari, S.; Bertram, K.A.; White, R.T.; Spurgeon, J.M. New trends in the development of heterogeneous catalysts for electrochemical CO 2 reduction. *Catal. Today* **2016**, *270*, 19–30.

62. Ra, E.C.; Kim, K.Y.; Kim, E.H.; Lee, H.; An, K.; Lee, J.S. Recycling Carbon Dioxide through Catalytic Hydrogenation: Recent Key Developments and Perspectives. *ACS Catal.* **2020**, *10*, 11318–11345.

63. Xie, S.; Zhang, W.; Lan, X.; Lin, H. CO2 Reduction to Methanol in the Liquid Phase: A Review. *ChemSusChem* **2020**, *13*, 6141–6159.

64. Gunasekar, G.H.; Park, K.; Jung, K.D.; Yoon, S. Recent developments in the catalytic hydrogenation of CO2 to formic acid/formate using heterogeneous catalysts. *Inorg. Chem. Front.* **2016**, *3*, 882–895.

65. Wang, W.H.; Himeda, Y.; Muckerman, J.T.; Manbeck, G.F.; Fujita, E. CO2 Hydrogenation to Formate and Methanol as an Alternative to Photo- and Electrochemical CO2 Reduction. *Chem. Rev.* **2015**, *115*, 12936–12973.

66. Schwab, E.; Milanov, A.; Schunk, S.A.; Behrens, A.; Schödel, N. Dry Reforming and Reverse Water Gas Shift: Alternatives for Syngas Production? *Chemie Ing. Tech.* **2015**, *87*, 347–353.

67. Leitner, W. Carbon Dioxide as a Raw Material: The Synthesis of Formic Acid and Its Derivatives from CO2. *Angew. Chemie Int. Ed. English* 1995.

68. Olah, G.A. Beyond Oil and Gas: The Methanol Economy. *Angew. Chemie Int. Ed.* **2005**, *44*, 2636–2639.

69. Olah, G.A.; Goeppert, A.; Prakash, G.K.S. The "Methanol Economy": General Aspects. In *Beyond Oil and Gas*; 2018.

70. Kar, S.; Kothandaraman, J.; Goeppert, A.; Prakash, G.K.S. Advances in catalytic homogeneous hydrogenation of carbon dioxide to methanol. *J. CO2 Util.* 2018.

71. Bai, S.T.; De Smet, G.; Liao, Y.; Sun, R.; Zhou, C.; Beller, M.; Maes, B.U.W.; Sels, B.F. Homogeneous and heterogeneous catalysts for hydrogenation of CO2to methanol under mild conditions. *Chem. Soc. Rev.* **2021**, *50*, 4259–4298.

72. Kothandaraman, J.; Kar, S.; Goeppert, A.; Sen, R.; Prakash, G.K.S. Advances in Homogeneous Catalysis for Low Temperature Methanol Reforming in the Context of the Methanol Economy. *Top. Catal.* **2018**, *61*, 542–559.

73. Reutemann, W.; Kieczka, H. Formic Acid. In *Ullmann's Encyclopedia of Industrial Chemistry*; Wiley-VCH Verlag GmbH & Co. KGaA: Weinheim, Germany, 2011.

74. Bulushev, D.A.; Ross, J.R.H. Towards Sustainable Production of Formic Acid. *ChemSusChem* **2018**, *11*, 821–836.

75. Wiedner, E.S.; Linehan, J.C. Making a Splash in Homogeneous CO2 Hydrogenation: Elucidating the Impact of Solvent on Catalytic Mechanisms. *Chem. - A Eur. J.* **2018**, *24*, 16964–16971.

76. Preuster, P.; Albert, J. Biogenic Formic Acid as a Green Hydrogen Carrier. *Energy Technol.* **2018**, *6*, 501–509.

77. Albert, J.; Jess, A.; Kern, C.; Pöhlmann, F.; Glowienka, K.; Wasserscheid, P. Formic Acid-Based Fischer–Tropsch Synthesis for Green Fuel Production from Wet Waste Biomass and Renewable Excess Energy. *ACS Sustain. Chem. Eng.* **2016**, *4*, 5078–5086.

78. Laidler, K.J. A glossary of terms used in chemical kinetics, including reaction dynamics (IUPAC Recommendations 1996). *Pure Appl. Chem.* **1996**, *68*, 149–192.

79. Anastas, P.T.; Zimmerman, J.B. The periodic table of the elements of green and sustainable chemistry. *Green Chem.* **2019**, 6545–6566.

80. Zell, T.; Langer, R. From Ruthenium to Iron and Manganese—A Mechanistic View on Challenges and Design Principles of Base-Metal Hydrogenation Catalysts. *ChemCatChem* **2018**, *10*, 1930–1940.

81. Peris, E.; Crabtree, R.H. Key factors in pincer ligand design. *Chem. Soc. Rev.* **2018**, *47*, 1959–1968.

82. Younus, H.A.; Ahmad, N.; Su, W.; Verpoort, F. Ruthenium pincer complexes: Ligand design and complex synthesis. *Coord. Chem. Rev.* **2014**, *276*, 112–152.

83. Van Koten, G.; Gossage, R.A. *The Privileged pincer-metal platform: Coordination chemistry & applications*; 2015; ISBN 9783319229270.

84. Moulton, B.C.J.; Shaw, B.L. 1020 J.C.S. Dalton. **1975**, 1020–1024.

85. Vogt, M.; Langer, R. The Pincer Platform Beyond Classical Coordination Patterns. *Eur. J. Inorg. Chem.* **2020**, *2020*, 3885–3898.

86. Khusnutdinova, J.R.; Milstein, D. Metal-Ligand Cooperation. *Angew. Chemie Int. Ed.* **2015**, *54*, 12236–12273.

87. Eisenstein, O.; Crabtree, R.H. Outer sphere hydrogenation catalysis. *New J. Chem.* **2013**, *37*, 21–27.

88. Piccirilli, L.; Lobo Justo Pinheiro, D.; Nielsen, M. Recent Progress with Pincer Transition Metal Catalysts for Sustainability. *Catalysts* **2020**, *10*, 773.

89. Nielsen, M. Catalyst Kinetics and Stability in Homogeneous Alcohol Acceptorless Dehydrogenation. In *Advanced Chemical Kinetics*; InTech, 2018.

90. Charman, H.B. Hydride transfer reactions catalysed by metal complexes. *J. Chem. Soc. B Phys. Org.* **1967**, 629.

91. Charman, H.B. Hydride transfer reactions catalysed by rhodium–tin complexes. *J. Chem. Soc. B* **1970**, 584–587.

92. Dobscn, A.; Robinson, S.D. Catalytic dehydrogenation of primary and secondary alcohols by Ru(OCOCF3)2(CO)(PPh3)2. *J. Organomet. Chem.* **1975**, *87*, 52–53.

93. Arakawa, H.; Sugi, Y. THE PHOTOCATALYTIC DEHYDROGENATION OF 2-PROPANOL BY USING RhCl(PPh 3) 3. *Chem. Lett.* **1981**, *10*, 1323–1326.

94. Blum, Y.; Shvo, Y. Catalytically reactive (η4-tetracyclone)(CO)2(H)2Ru and related complexes in dehydrogenation of alcohols to esters. *J. Organomet. Chem.* **1985**, *282*, C7–C10.

95. Morton, D.; Cole-Hamilton, D.J. Molecular hydrogen complexes in catalysis: highly efficient hydrogen production from alcoholic substrates catalysed by ruthenium complexes. *J. Chem. Soc. Chem. Commun.* **1988**, 1154.

96. Morton, D.; Cole-Hamilton, D.J.; Schofield, J.A.; Pryce, R.J. Rapid thermal hydrogen production from 2,3-butanediol catalyzed by homogeneous rhodium catalysis. *Polyhedron* **1987**, *6*, 2187–2189.

97. Morton, D.; Cole-Hamilton, D.J. Rapid thermal hydrogen production from alcohols catalysed by [Rh(2,2′-bipyridyl) 2]Cl. *J. Chem. Soc., Chem. Commun.* **1987**, *1*, 248–249.

98. Shinoda, S.; Kojima, T.; Saito, Y. Rh2(OAc)4-PPh3 as a catalyst for the liquid-phase dehydrogenation of 2-propanol. *J. Mol. Catal.* **1983**, *18*, 99–104.

99. Zhang, J.; Gandelman, M.; Shimon, L.J.W.; Rozenberg, H.; Milstein, D. Electron-rich, bulky ruthenium PNP-type complexes. Acceptorless catalytic alcohol dehydrogenation. *Organometallics* **2004**, *23*, 4026–4033.

100. Zhang, J.; Leitus, G.; Ben-David, Y.; Milstein, D. Facile conversion of alcohols into esters and dihydrogen catalyzed by new ruthenium complexes. *J. Am. Chem. Soc.* **2005**, *127*, 10840–10841.

101. Junge, H.; Beller, M. Ruthenium-catalyzed generation of hydrogen from iso-propanol. *Tetrahedron Lett.* **2005**, *46*, 1031–1034.

102. Milstein, D. Discovery of Environmentally Benign Catalytic Reactions of Alcohols Catalyzed by Pyridine-Based Pincer Ru Complexes, Based on Metal–Ligand Cooperation. *Top. Catal.* **2010**, *53*, 915–923.

103. Zell, T.; Milstein, D. Hydrogenation and Dehydrogenation Iron Pincer Catalysts Capable of Metal–Ligand Cooperation by Aromatization/Dearomatization. *Acc. Chem. Res.* **2015**, *48*, 1979–1994.

104. Gunanathan, C.; Milstein, D. Metal-ligand cooperation by aromatization-dearomatization: A new paradigm in bond activation and "green" catalysis. *Acc. Chem. Res.* **2011**, *44*, 588–602.

105. Milstein, D. Metal – ligand cooperation by aromatization – dearomatization as a tool in single bond activation Subject Areas : Author for correspondence : *Phil. Trans. R. Soc. A* **2015**, *373*, 20140189.

106. Nguyen, D.H.; Trivelli, X.; Capet, F.; Swesi, Y.; Favre-Réguillon, A.; Vanoye, L.; Dumeignil, F.; Gauvin, R.M. Deeper Mechanistic Insight into Ru Pincer-Mediated Acceptorless Dehydrogenative Coupling of Alcohols: Exchanges, Intermediates, and Deactivation Species. *ACS Catal.* **2018**, *8*, 4719–4734.

107. Alberico, E.; Lennox, A.J.J.; Vogt, L.K.; Jiao, H.; Baumann, W.; Drexler, H.J.; Nielsen, M.; Spannenberg, A.; Checinski, M.P.; Junge, H.; et al. Unravelling the Mechanism of Basic Aqueous Methanol Dehydrogenation Catalyzed by Ru-PNP Pincer Complexes. *J. Am. Chem. Soc.* **2016**, *138*, 14890–14904.

108. Dub, P.A.; Gordon, J.C. The role of the metal-bound N–H functionality in Noyori-type molecular catalysts. *Nat. Rev. Chem.* **2018**, *2*, 396–408.

109. Dub, P.A.; Gordon, J.C. Metal-ligand bifunctional catalysis: The "Accepted" mechanism, the issue of concertedness, and the function of the ligand in catalytic cycles involving hydrogen atoms. *ACS Catal.* **2017**, *7*, 6635–6655.

110. Dawe, L.N.; Karimzadeh-Younjali, M.; Dai, Z.; Khaskin, E.; Gusev, D.G. The Milstein Bipyridyl PNN Pincer Complex of Ruthenium Becomes a Noyori-Type Catalyst under Reducing Conditions. *J. Am. Chem. Soc.* **2020**, *142*, 19510–19522.

111. Dub, P.A.; Scott, B.L.; Gordon, J.C. Why does alkylation of the N-H functionality within M/NH bifunctional Noyori-type catalysts lead to turnover? *J. Am. Chem. Soc.* **2017**, *139*, 1245–1260.

112. Lei, M.; Pan, Y.; Ma, X. The nature of hydrogen production from aqueous-phase methanol dehydrogenation with ruthenium pincer complexes under mild conditions. *Eur. J. Inorg. Chem.* **2015**.

113. Bertoli, M.; Choualeb, A.; Lough, A.J.; Moore, B.; Spasyuk, D.; Gusev, D.G. Osmium and ruthenium catalysts for dehydrogenation of alcohols. *Organometallics* **2011**, *30*, 3479–3482.

114. Spasyuk, D.; Smith, S.; Gusev, D.G. Replacing phosphorus with sulfur for the efficient hydrogenation of esters. *Angew. Chemie - Int. Ed.* **2013**, *52*, 2538–2542.

115. Leitner, W. The coordination chemistry of carbon dioxide and its relevance for catalysis: a critical survey. *Coord. Chem. Rev.* **1996**, *153*, 257–284.

116. Geilen, F.M.A.; Engendahl, B.; Hölscher, M.; Klankermayer, J.; Leitner, W. Selective Homogeneous Hydrogenation of Biogenic Carboxylic Acids with [Ru(TriPhos)H] + : A Mechanistic Study. *J. Am. Chem. Soc.* **2011**, *133*, 14349–14358.

117. Wesselbaum, S.; Moha, V.; Meuresch, M.; Brosinski, S.; Thenert, K.M.; Kothe, J.; Stein, T. Vom; Englert, U.; Hölscher, M.; Klankermayer, J.; et al. Hydrogenation of carbon dioxide to methanol using a homogeneous ruthenium-Triphos catalyst: From mechanistic investigations to multiphase catalysis. *Chem. Sci.* **2015**, *6*, 693–704.

118. Wesselbaum, S.; Vom Stein, T.; Klankermayer, J.; Leitner, W. Hydrogenation of carbon dioxide to methanol by using a homogeneous ruthenium-phosphine catalyst. *Angew. Chemie - Int. Ed.* **2012**, *51*, 7499–7502.

119. Sordakis, K.; Tsurusaki, A.; Iguchi, M.; Kawanami, H.; Himeda, Y.; Laurenczy, G. Carbon Dioxide to Methanol: The Aqueous Catalytic Way at Room Temperature. *Chem. - A Eur. J.* **2016**, *22*, 15605–15608.

120. Onishi, N.; Laurenczy, G.; Beller, M.; Himeda, Y. Recent progress for reversible homogeneous catalytic hydrogen storage in formic acid and in methanol. *Coord. Chem. Rev.* **2018**, *373*, 317–332.

121. Wang, W.-H.; Ertem, M.Z.; Xu, S.; Onishi, N.; Manaka, Y.; Suna, Y.; Kambayashi, H.; Muckerman, J.T.; Fujita, E.; Himeda, Y. Highly Robust Hydrogen Generation by Bioinspired Ir Complexes for Dehydrogenation of Formic Acid in Water: Experimental and Theoretical Mechanistic Investigations at Different pH. *ACS Catal.* **2015**, *5*, 5496–5504.

122. Himeda, Y. Highly efficient hydrogen evolution by decomposition of formic acid using an iridium catalyst with 4,4′-dihydroxy-2,2′-bipyridine. *Green Chem.* **2009**, *11*, 2018.

123. Sponholz, P.; Mellmann, D.; Cordes, C.; Alsabeh, P.G.; Li, B.; Li, Y.; Nielsen, M.; Junge, H.; Dixneuf, P.; Beller, M. Efficient and Selective Hydrogen Generation from Bioethanol using Ruthenium Pincer-type Complexes. *ChemSusChem* **2014**, *7*, 2419–2422.

124. Loges, B.; Boddien, A.; Junge, H.; Beller, M. Controlled generation of hydrogen from formic acid amine adducts at room temperature and application in H2/O2 fuel cells. *Angew. Chemie - Int. Ed.* **2008**, *47*, 3962–3965.

125. Nielsen, M.; Alberico, E.; Baumann, W.; Drexler, H.J.; Junge, H.; Gladiali, S.; Beller, M. Low-temperature aqueous-phase methanol dehydrogenation to hydrogen and carbon dioxide. *Nature* **2013**, *495*, 85–89.

126. Nielsen, M.; Junge, H.; Kammer, A.; Beller, M. Towards a green process for bulk-scale synthesis of ethyl acetate: Efficient acceptorless dehydrogenation of ethanol. *Angew. Chemie - Int. Ed.* **2012**, *51*, 5711–5713.

127. Nielsen, M. Efficient hydrogen peroxide decomposition to oxygen and water catalysed by a ruthenium pincer complex. *Environ. Chem. Lett.* **2016**, *14*, 359–365.

128. Xie, Y.; Ben-David, Y.; Shimon, L.J.W.; Milstein, D. Highly Efficient Process for Production of Biofuel from Ethanol Catalyzed by Ruthenium Pincer Complexes. *J. Am. Chem. Soc.* **2016**, *138*, 9077–9080.

129. Tseng, K.N.T.; Kampf, J.W.; Szymczak, N.K. Base-free, acceptorless, and chemoselective alcohol dehydrogenation catalyzed by an amide-derived NNN -ruthenium(II) hydride complex. *Organometallics* **2013**, *32*, 2046–2049.

130. Fu, S.; Shao, Z.; Wang, Y.; Liu, Q. Manganese-Catalyzed Upgrading of Ethanol into 1-Butanol. *J. Am. Chem. Soc.* **2017**, *139*, 11941–11948.

131. Wingad, R.L.; Gates, P.J.; Street, S.T.G.; Wass, D.F. Catalytic Conversion of Ethanol to n-Butanol Using Ruthenium P-N Ligand Complexes. *ACS Catal.* **2015**, *5*, 5822–5826.

132. Li, Y.; Nielsen, M.; Li, B.; Dixneuf, P.H.; Junge, H.; Beller, M. Ruthenium-catalyzed hydrogen generation from glycerol and selective synthesis of lactic acid. *Green Chem.* **2015**, *17*, 193–198.

133. Sharninghausen, L.S.; Mercado, B.Q.; Crabtree, R.H.; Hazari, N. Selective conversion of glycerol to lactic acid with iron pincer precatalysts. *Chem. Commun.* **2015**, *51*, 16201–16204.

134. Li, Y.; Sponholz, P.; Nielsen, M.; Junge, H.; Beller, M. Iridium-catalyzed hydrogen production from monosaccharides, disaccharide, cellulose, and lignocellulose. *ChemSusChem* **2015**, *8*, 804–808.

135. Li, W.; Xie, J.-H.; Lin, H.; Zhou, Q.-L. Highly efficient hydrogenation of biomass-derived levulinic acid to γ-valerolactone catalyzed by iridium pincer complexes. *Green Chem.* **2012**, *14*, 2388.

136. Phanopoulos, A.; White, A.J.P.; Long, N.J.; Miller, P.W. Catalytic Transformation of Levulinic Acid to 2-

Methyltetrahydrofuran Using Ruthenium - N-Triphos Complexes. *ACS Catal.* **2015**, *5*, 2500–2512.

137. Wozniak, B.; Spannenberg, A.; Li, Y.; Hinze, S.; de Vries, J.G. Cyclopentanone Derivatives from 5-Hydroxymethylfurfural via 1-Hydroxyhexane-2,5-dione as Intermediate. *ChemSusChem* **2018**, *11*, 356–359.

138. Stadler, B.M.; Puylaert, P.; Diekamp, J.; van Heck, R.; Fan, Y.; Spannenberg, A.; Hinze, S.; de Vries, J.G. Inexpensive Ruthenium NNS-Complexes as Efficient Ester Hydrogenation Catalysts with High C=O vs. C=C Selectivities. *Adv. Synth. Catal.* **2018**, *360*, 1151–1158.

139. Zhang, L.; Raffa, G.; Nguyen, D.H.; Swesi, Y.; Corbel-Demailly, L.; Capet, F.; Trivelli, X.; Desset, S.; Paul, S.; Paul, J.F.; et al. Acceptorless dehydrogenative coupling of alcohols catalysed by ruthenium PNP complexes: Influence of catalyst structure and of hydrogen mass transfer. *J. Catal.* **2016**, *340*, 331–343.

140. Srimani, D.; Balaraman, E.; Gnanaprakasam, B.; Ben-David, Y.; Milstein, D. Ruthenium pincer-catalyzed cross-dehydrogenative coupling of primary alcohols with secondary alcohols under neutral conditions. *Adv. Synth. Catal.* **2012**, *354*, 2403–2406.

141. De Boer, S.Y.; Korstanje, T.J.; La Rooij, S.R.; Kox, R.; Reek, J.N.H.; Van Der Vlugt, J.I. Ruthenium PNN(O) Complexes: Cooperative Reactivity and Application as Catalysts for Acceptorless Dehydrogenative Coupling Reactions. *Organometallics* **2017**, *36*, 1541–1549.

142. Nguyen, D.H.; Trivelli, X.; Capet, F.; Paul, J.F.; Dumeignil, F.; Gauvin, R.M. Manganese Pincer Complexes for the Base-Free, Acceptorless Dehydrogenative Coupling of Alcohols to Esters: Development, Scope, and Understanding. *ACS Catal.* **2017**, *7*, 2022–2032.

143. Das, U.K.; Ben-David, Y.; Leitus, G.; Diskin-Posner, Y.; Milstein, D. Dehydrogenative Cross-Coupling of Primary Alcohols To Form Cross-Esters Catalyzed by a Manganese Pincer Complex. *ACS Catal.* **2019**, *9*, 479–484.

144. Gunanathan, C.; Ben-David, Y.; Milstein, D. Direct Synthesis of Amides from Alcohols and Amines with Liberation of H2. *Science (80-.).* **2007**, *317*, 790–792.

145. Kumar, A.; Espinosa-Jalapa, N.A.; Leitus, G.; Diskin-Posner, Y.; Avram, L.; Milstein, D. Direct Synthesis of Amides by Dehydrogenative Coupling of Amines with either Alcohols or Esters: Manganese Pincer Complex as Catalyst. *Angew. Chemie - Int. Ed.* **2017**, *56*, 14992–14996.

146. Gusev, D.G. Rethinking the dehydrogenative amide synthesis. *ACS Catal.* **2017**, *7*, 6656–6662.

147. Schley, N.D.; Dobereiner, G.E.; Crabtree, R.H. Oxidative synthesis of amides and pyrroles via dehydrogenative alcohol oxidation by ruthenium diphosphine diamine complexes. *Organometallics* **2011**, *30*, 4174–4179.

148. Lane, E.M.; Uttley, K.B.; Hazari, N.; Bernskoetter, W. Iron-Catalyzed Amide Formation from the Dehydrogenative Coupling of Alcohols and Secondary Amines. *Organometallics* **2017**, *36*, 2020–2025.

149. Kuriyama, S.; Arashiba, K.; Tanaka, H.; Matsuo, Y.; Nakajima, K.; Yoshizawa, K.; Nishibayashi, Y. Direct Transformation of Molecular Dinitrogen into Ammonia Catalyzed by Cobalt Dinitrogen Complexes Bearing Anionic PNP Pincer Ligands. *Angew. Chemie Int. Ed.* **2016**, *55*, 14291–14295.

150. Sekiguchi, Y.; Kuriyama, S.; Eizawa, A.; Arashiba, K.; Nakajima, K.; Nishibayashi, Y. Synthesis and reactivity of iron-dinitrogen complexes bearing anionic methyl- and phenyl-substituted pyrrole-based PNP-type pincer ligands toward catalytic nitrogen fixation. *Chem. Commun.* **2017**, *53*, 12040–12043.

151. Kuriyama, S.; Arashiba, K.; Nakajima, K.; Matsuo, Y.; Tanaka, H.; Ishii, K.; Yoshizawa, K.; Nishibayashi, Y. Catalytic transformation of dinitrogen into ammonia and hydrazine by iron-dinitrogen complexes bearing pincer ligand. *Nat. Commun.* **2016**, *7*, 1–9.

152. Eizawa, A.; Arashiba, K.; Tanaka, H.; Kuriyama, S.; Matsuo, Y.; Nakajima, K.; Yoshizawa, K.; Nishibayashi, Y. Remarkable catalytic activity of dinitrogen-bridged dimolybdenum complexes bearing NHC-based PCP-pincer ligands toward nitrogen fixation. *Nat. Commun.* **2017**, *8*, 14874.

153. Kumar, A.; Janes, T.; Espinosa-Jalapa, N.A.; Milstein, D. Manganese Catalyzed Hydrogenation of Organic Carbonates to Methanol and Alcohols. *Angew. Chemie - Int. Ed.* **2018**, *57*, 12076–12080.

154. Langer, R.; Diskin-Posner, Y.; Leitus, G.; Shimon, L.J.W.; Ben-David, Y.; Milstein, D. Low-pressure hydrogenation of carbon dioxide catalyzed by an iron pincer complex exhibiting noble metal activity. *Angew. Chemie - Int. Ed.* **2011**, *50*, 9948–9952.

155. Dubey, A.; Nencini, L.; Fayzullin, R.R.; Nervi, C.; Khusnutdinova, J.R. Bio-Inspired Mn(I) Complexes for the Hydrogenation of CO2 to Formate and Formamide. *ACS Catal.* **2017**, *7*, 3864–3868.

156. Gorgas, N.; Kirchner, K. Isoelectronic Manganese and Iron Hydrogenation/Dehydrogenation Catalysts: Similarities and Divergences. *Acc. Chem. Res.* **2018**, *51*, 1558–1569.

157. Alberico, E.; Sponholz, P.; Cordes, C.; Nielsen, M.; Drexler, H.J.; Baumann, W.; Junge, H.; Beller, M. Selective hydrogen production from methanol with a defined Iron pincer catalyst under mild conditions. *Angew. Chemie - Int. Ed.* **2013**, *52*, 14162–14166.

158. Boddien, A.; Jackstell, R.; Junge, H.; Spannenberg, A.; Baumann, W.; Ludwig, R.; Beller, M. Ortho-metalation of iron(0) tribenzylphosphine complexes: Homogeneous catalysts for the generation of hydrogen from formic acid. *Angew. Chemie - Int. Ed.* **2010**, *49*, 8993–8996.

159. Boddien, A.; Loges, B.; Gärtner, F.; Torborg, C.; Fumino, K.; Junge, H.; Ludwig, R.; Beller, M. Iron-catalyzed hydrogen production from formic acid. *J. Am. Chem. Soc.* **2010**, *132*, 8924–8934.

160. Boddien, A.; Mellmann, D.; Gartner, F.; Jackstell, R.; Junge, H.; Dyson, P.J.; Laurenczy, G.; Ludwig, R.; Beller, M. Efficient Dehydrogenation of Formic Acid Using an Iron Catalyst. *Science (80-.).* **2011**, *333*, 1733–1736.

161. Zell, T.; Butschke, B.; Ben-David, Y.; Milstein, D. Efficient hydrogen liberation from formic acid catalyzed by a well-defined iron pincer complex under mild conditions. *Chem. - A Eur. J.* **2013**, *19*, 8068–8072.

162. Andérez-Fernández, M.; Vogt, L.K.; Fischer, S.; Zhou, W.; Jiao, H.; Garbe, M.; Elangovan, S.; Junge, K.; Junge, H.; Ludwig, R.; et al. A Stable Manganese Pincer Catalyst for the Selective Dehydrogenation of Methanol. *Angew. Chemie - Int. Ed.* **2017**, *56*, 559–562.

163. Ryabchuk, P.; Stier, K.; Junge, K.; Checinski, M.P.; Beller, M. Molecularly Defined Manganese Catalyst for Low-Temperature Hydrogenation of Carbon Monoxide to Methanol. *J. Am. Chem. Soc.* **2019**, *141*, 16923–16929.

164. Bernskoetter, W.H.; Hazari, N. Reversible Hydrogenation of Carbon Dioxide to Formic Acid and Methanol: Lewis Acid Enhancement of Base Metal Catalysts. *Acc. Chem. Res.* **2017**, *50*, 1049–1058.

165. Bielinski, E.A.; Förster, M.; Zhang, Y.; Bernskoetter, W.H.; Hazari, N.; Holthausen, M.C. Base-Free Methanol Dehydrogenation Using a Pincer-Supported Iron Compound and Lewis Acid Co-catalyst. *ACS Catal.* **2015**, *5*, 2404–2415.

166. Bielinski, E.A.; Lagaditis, P.O.; Zhang, Y.; Mercado, B.Q.; Würtele, C.; Bernskoetter, W.H.; Hazari, N.; Schneider, S. Lewis acid-assisted formic acid dehydrogenation using a pincer-supported iron catalyst. *J. Am. Chem. Soc.* **2014**, *136*, 10234–10237.

167. Curley, J.B.; Smith, N.E.; Bernskoetter, W.H.; Hazari, N.; Mercado, B.Q. Catalytic Formic Acid Dehydrogenation and CO2 Hydrogenation Using Iron PNRP Pincer Complexes with Isonitrile Ligands. *Organometallics* **2018**, *37*, 3846–3853.

168. Mellone, I.; Gorgas, N.; Bertini, F.; Peruzzini, M.; Kirchner, K.; Gonsalvi, L. Selective Formic Acid Dehydrogenation Catalyzed by Fe-PNP Pincer Complexes Based on the 2,6-Diaminopyridine Scaffold. *Organometallics* **2016**, *35*, 3344–3349.

169. Zhang, Y.; MacIntosh, A.D.; Wong, J.L.; Bielinski, E.A.; Williard, P.G.; Mercado, B.Q.; Hazari, N.; Bernskoetter, W.H. Iron catalyzed CO2 hydrogenation to formate enhanced by Lewis acid co-catalysts. *Chem. Sci.* **2015**, *6*, 4291–4299.

170. Smith, N.E.; Bernskoetter, W.H.; Hazari, N.; Mercado, B.Q. Synthesis and Catalytic Activity of PNP-Supported Iron Complexes with Ancillary Isonitrile Ligands. *Organometallics* **2017**, *36*, 3995–4004.

171. Marullo, S.; D'Anna, F.; Rizzo, C.; Billeci, F. Ionic liquids: "normal" solvents or nanostructured fluids? *Org. Biomol. Chem.* **2021**, *19*, 2076–2095.

172. Ghandi, K. A Review of Ionic Liquids, Their Limits and Applications. *Green Sustain. Chem.* **2014**, *04*, 44–53.

173. Singh, S.K.; Savoy, A.W. Ionic liquids synthesis and applications: An overview. *J. Mol. Liq.* **2020**, *297*, 112038.

174. Hallett, J.P.; Welton, T. ChemInform Abstract: Room-Temperature Ionic Liquids: Solvents for Synthesis and Catalysis. Part 2. *ChemInform* **2011**, *42*, no-no.

175. Steinrück, H.P.; Wasserscheid, P. Ionic liquids in catalysis. *Catal. Letters* **2015**, *145*, 380–397.

176. Wasserscheid, P.; Keim, W. Ionic Liquids—New "Solutions" for Transition Metal Catalysis. *Angew. Chemie* **2000**, *39*, 3772–3789.

177. Villa, R.; Alvarez, E.; Porcar, R.; Garcia-Verdugo, E.; Luis, S. V.; Lozano, P. Ionic liquids as an enabling tool to integrate reaction and separation processes. *Green Chem.* **2019**, *21*, 6527–6544.

178. Lombardo, L.; Yang, H.; Züttel, A. Study of borohydride ionic liquids as hydrogen storage materials. *J. Energy Chem.* **2019**, *33*, 17–21.

179. Sahler, S.; Sturm, S.; Kessler, M.T.; Prechtl, M.H.G. The Role of Ionic Liquids in Hydrogen Storage. *Chem. - A Eur. J.* **2014**, n/a-n/a.

180. Liu, L. Production of chemicals from marine biomass catalysed by acidic ionic liquids. *Green Chem.* **2021**, *23*, 9800–9814.

181. Mohd, N.; Draman, S.F.S.; Salleh, M.S.N.; Yusof, N.B. Dissolution of cellulose in ionic liquid: A review. In Proceedings of the AIP Conference Proceedings; 2017; Vol. 1809, p. 020035.

182. Xu, A.; Wang, F. Carboxylate ionic liquid solvent systems from 2006 to 2020: thermal properties and application in cellulose processing. *Green Chem.* **2020**, *22*, 7622–7664.

183. Taccardi, N.; Assenbaum, D.; Berger, M.E.M.; Bösmann, A.; Enzenberger, F.; Wölfel, R.; Neuendorf, S.; Goeke, V.; Schödel, N.; Maass, H.J.; et al. Catalytic production of hydrogen from glucose and other carbohydrates under exceptionally mild reaction conditions. *Green Chem.* **2010**, *12*, 1150.

184. Marullo, S.; Sutera, A.; Gallo, G.; Billeci, F.; Rizzo, C.; D'Anna, F. Chemo-enzymatic Conversion of Glucose in 5-Hydroxymethylfurfural: The Joint Effect of Ionic Liquids and Ultrasound. *ACS Sustain. Chem. Eng.* **2020**, *8*, 11204–11214.

185. Wang, B.; Qin, L.; Mu, T.; Xue, Z.; Gao, G. Are Ionic Liquids Chemically Stable? *Chem. Rev.* **2017**, *117*, 7113–7131.

186. Amarasekara, A.S. Acidic Ionic Liquids. *Chem. Rev.* **2016**, *116*, 6133–6183.

187. Marsh, K..; Boxall, J..; Lichtenthaler, R. Room temperature ionic liquids and their mixtures—a review. *Fluid Phase Equilib.* **2004**, *219*, 93–98.

188. Crowhurst, L.; Mawdsley, P.R.; Perez-Arlandis, J.M.; Salter, P.A.; Welton, T. Solvent–solute interactions in ionic liquids. *Phys. Chem. Chem. Phys.* **2003**, *5*, 2790–2794.

189. Ab Rani, M.A.; Brant, A.; Crowhurst, L.; Dolan, A.; Lui, M.; Hassan, N.H.; Hallett, J.P.; Hunt, P.A.; Niedermeyer, H.; Perez-Arlandis, J.M.; et al. Understanding the polarity of ionic liquids. *Phys. Chem. Chem. Phys.* **2011**, *13*, 16831.

190. Lee, J.-M.; Ruckes, S.; Prausnitz, J.M. Solvent Polarities and Kamlet−Taft Parameters for Ionic Liquids Containing a Pyridinium Cation. *J. Phys. Chem. B* **2008**, *112*, 1473–1476.

191. Wang, Y.; He, H.; Wang, C.; Lu, Y.; Dong, K.; Huo, F.; Zhang, S. Insights into Ionic Liquids: From Z-Bonds to Quasi-Liquids. *JACS Au* **2022**, jacsau.1c00538.

192. Ramdin, M.; de Loos, T.W.; Vlugt, T.J.H. State-of-the-Art of CO 2 Capture with Ionic Liquids. *Ind. Eng. Chem. Res.* **2012**, *51*, 8149–8177.

193. Aghaie, M.; Rezaei, N.; Zendehboudi, S. A systematic review on CO2 capture with ionic liquids: Current status and future prospects. *Renew. Sustain. Energy Rev.* **2018**, *96*, 502–525.

194. Torralba-Calleja, E.; Skinner, J.; Gutiérrez-Tauste, D. CO2 capture in ionic liquids: A review of solubilities and experimental methods. *Carbon Capture Storage CO2 Manag. Technol.* **2014**, *2013*, 325–361.

195. Karadas, F.; Atilhan, M.; Aparicio, S. Review on the use of ionic liquids (ILs) as alternative fluids for CO 2 capture and natural gas sweetening. *Energy and Fuels* **2010**, *24*, 5817–5828.

196. Brennecke, J.F.; Gurkan, B.E. Ionic liquids for CO2 capture and emission reduction. *J. Phys. Chem. Lett.* **2010**, *1*, 3459–3464.

197. Sood, A.; Thakur, A.; Ahuja, S.M. Recent advancements in ionic liquid based carbon capture technologies. *Chem. Eng. Commun.* **2021**, *0*, 1–22.

198. Wang, S.; Wang, X. Imidazolium ionic liquids, imidazolylidene heterocyclic carbenes, and zeolitic imidazolate frameworks for CO2 capture and photochemical reduction. *Angew. Chemie - Int. Ed.* **2016**, *55*, 2308–2320.

199. Cui, Y.; He, B.; Liu, X.; Sun, J. Ionic Liquids-Promoted Electrocatalytic Reduction of Carbon Dioxide. *Ind. Eng. Chem. Res.* **2020**, *59*, 20235–20252.

200. Weilhard, A.; Argent, S.P.; Sans, V. Efficient carbon dioxide hydrogenation to formic acid with buffering ionic liquids. *Nat. Commun.* **2021**, *12*, 1–7.

201. Weilhard, A.; Qadir, M.I.; Sans, V.; Dupont, J. Selective CO2 Hydrogenation to Formic Acid with Multifunctional Ionic Liquids. *ACS Catal.* **2018**, *8*, 1628–1634.

202. Wesselbaum, S.; Hintermair, U.; Leitner, W. Continuous-flow hydrogenation of carbon dioxide to pure formic acid using an integrated scCO2 process with immobilized catalyst and base. *Angew. Chemie - Int. Ed.* **2012**, *51*, 8585–8588.

203. Van Doorslaer, C.; Wahlen, J.; Mertens, P.; Binnemans, K.; De Vos, D. Immobilization of molecular catalysts in supported ionic liquid phases. *Dalt. Trans.* **2010**, *39*, 8377.

204. Mehnert, C.P.; Mozeleski, E.J.; Cook, R.A. Supported ionic liquid catalysis investigated for hydrogenation reactions. *Chem. Commun.* **2002**, 3010–3011.

205. Riisager, A. Continuous fixed-bed gas-phase hydroformylation using supported ionic liquid-phase (SILP) Rh catalysts. *J. Catal.* **2003**, *219*, 452–455.

206. Riisager, A.; Eriksen, K.M.; Wasserscheid, P.; Fehrmann, R. Propene and 1-Octene Hydroformylation with Silica-Supported, Ionic Liquid-Phase (SILP) Rh-Phosphine Catalysts in Continuous Fixed-Bed Mode. *Catal. Letters* **2003**, *90*, 149–153.

207. Mehnert, C.P.; Cook, R.A.; Dispenziere, N.C.; Afeworki, M. Supported Ionic Liquid Catalysis − A New Concept for Homogeneous Hydroformylation Catalysis. *J. Am. Chem. Soc.* **2002**, *124*, 12932–12933.

208. Riisager, A.; Fehrmann, R.; Wasserscheid, P.; van Hal, R. Supported Ionic Liquid-Phase Catalysis—Heterogenization of Homogeneous Rhodium Phosphine Catalysts. In; 2005; pp. 334–349.

209. Werner, S.; Szesni, N.; Kaiser, M.; Haumann, M.; Wasserscheid, P. A Scalable Preparation Method for SILP and SCILL Ionic Liquid Thin-Film Materials. *Chem. Eng. Technol.* **2012**, *35*, 1962–1967.

210. Selvam, T.; MacHoke, A.; Schwieger, W. Supported ionic liquids on non-porous and porous inorganic materials - A topical review. *Appl. Catal. A Gen.* **2012**, *445–446*, 92–101.

211. Haumann, M.; Dentler, K.; Joni, J.; Riisager, A.; Wasserscheid, P. Continuous Gas-Phase Hydroformylation of 1-Butene using Supported Ionic Liquid Phase (SILP) Catalysts. *Adv. Synth. Catal.* **2007**, *349*, 425–431.

212. Logemann, M.; Marinkovic, J.M.; Schörner, M.; José Garciá-Suárez, E.; Hecht, C.; Franke, R.; Wessling, M.; Riisager, A.; Fehrmann, R.; Haumann, M. Continuous gas-phase hydroformylation of but-1-ene in a membrane reactor by supported liquid-phase (SLP) catalysis. *Green Chem.* **2020**, *22*, 5691–5700.

213. Riisager, A.; Fehrmann, R.; Flicker, S.; Van Hal, R.; Haumann, M.; Wasserscheid, P. Very stable and highly regioselective supported ionic-liquid-phase (SILP) catalysis: Continuous-flow fixed-bed hydroformylation of propene. *Angew. Chemie - Int. Ed.* **2005**, *44*, 815–819.

214. Hatanaka, M.; Yasuda, T.; Uchiage, E.; Nishida, M.; Tominaga, K. Continuous Gas-Phase Hydroformylation of Propene with CO 2 Using SILP Catalysts. *ACS Sustain. Chem. Eng.* **2021**, *9*, 11674–11680.

215. Moos, G.; Emondts, M.; Bordet, A.; Leitner, W. Selective Hydrogenation and Hydrodeoxygenation of Aromatic Ketones to Cyclohexane Derivatives Using a Rh@SILP Catalyst. *Angew. Chemie Int. Ed.* **2020**, *59*, 11977–11983.

216. Brünig, J.; Csendes, Z.; Weber, S.; Gorgas, N.; Bittner, R.W.; Limbeck, A.; Bica, K.; Hoffmann, H.; Kirchner, K. Chemoselective Supported Ionic-Liquid-Phase (SILP) Aldehyde Hydrogenation Catalyzed by an Fe(II) PNP Pincer Complex. *ACS Catal.* **2018**, *8*, 1048–1051.

217. RUTA, M.; YURANOV, I.; DYSON, P.; LAURENCZY, G.; KIWIMINSKER, L. Structured fiber supports for ionic liquid-phase catalysis used in gas-phase continuous hydrogenation. *J. Catal.* **2007**, *247*, 269–276.

218. Gelesky, M.A.; Chiaro, S.S.X.; Pavan, F.A.; dos Santos, J.H.Z.; Dupont, J. Supported ionic liquid phase rhodium nanoparticle hydrogenation catalysts. *Dalt. Trans.* **2007**, 5549.

219. Wolfson, A.; Vankelecom, I.F.J.; Jacobs, P.A. Co-immobilization of transition-metal complexes and ionic liquids in a polymeric support for liquid-phase hydrogenations. *Tetrahedron Lett.* **2003**, *44*, 1195–1198.

220. Hagiwara, H.; Sugawara, Y.; Isobe, K.; Hoshi, T.; Suzuki, T. Immobilization of Pd(OAc) 2 in Ionic Liquid on Silica: Application to Sustainable Mizoroki−Heck Reaction. *Org. Lett.* **2004**, *6*, 2325–2328.

221. Breitenlechner, S. Solid catalysts on the basis of supported ionic liquids and their use in hydroamination reactions. *J. Mol. Catal. A Chem.* **2004**, *214*, 175–179.

222. Kukawka, R.; Pawlowska-Zygarowicz, A.; Dzialkowska, J.; Pietrowski, M.; Maciejewski, H.; Bica, K.; Smiglak, M. Highly Effective Supported Ionic Liquid-Phase (SILP) Catalysts: Characterization and Application to the Hydrosilylation Reaction. *ACS Sustain. Chem. Eng.* **2019**, *7*, 4699–4706.

223. Riisager, A.; Jørgensen, B.; Wasserscheid, P.; Fehrmann, R. First application of supported ionic liquid phase (SILP) catalysis for continuous methanol carbonylation. *Chem. Commun.* **2006**, 994.

224. Khokarale, S.G.; García-Suárez, E.J.; Fehrmann, R.; Riisager, A. Highly Selective Continuous Gas-Phase Methoxycarbonylation of Ethylene with Supported Ionic Liquid Phase (SILP) Catalysts. *ChemCatChem* **2017**, *9*, 1824–1829.

225. Yamaguchi, K.; Yoshida, C.; Uchida, S.; Mizuno, N. Peroxotungstate Immobilized on Ionic Liquid-Modified Silica as a Heterogeneous Epoxidation Catalyst with Hydrogen Peroxide. *J. Am. Chem. Soc.* **2005**, *127*, 530–531.

226. Joni, J.; Haumann, M.; Wasserscheid, P. Development of a Supported Ionic Liquid Phase (SILP) Catalyst for Slurry-Phase Friedel-Crafts Alkylations of Cumene. *Adv. Synth. Catal.* **2009**, *351*, 423–431.

227. Wolf, P.; Aubermann, M.; Wolf, M.; Bauer, T.; Blaumeiser, D.; Stepic, R.; Wick, C.R.; Smith, D.M.; Smith, A.-S.; Wasserscheid, P.; et al. Improving the performance of supported ionic liquid phase (SILP) catalysts for the ultra-low-temperature water–gas shift reaction using metal salt additives. *Green Chem.* **2019**, *21*, 5008–5018.

228. Werner, S.; Szesni, N.; Kaiser, M.; Fischer, R.W.; Haumann, M.; Wasserscheid, P. Ultra-low-temperature water-gas shift catalysis using supported ionic liquid phase (SILP) materials. *ChemCatChem* **2010**, *2*, 1399–1402.

229. Werner, S.; Szesni, N.; Bittermann, A.; Schneider, M.J.; Härter, P.; Haumann, M.; Wasserscheid, P. Screening of Supported Ionic Liquid Phase (SILP) catalysts for the very low temperature water–gas-shift reaction. *Appl. Catal. A Gen.* **2010**, *377*, 70–75.

230. Yasuda, T.; Uchiage, E.; Fujitani, T.; Tominaga, K. ichi; Nishida, M. Reverse water gas shift reaction using supported ionic liquid phase catalysts. *Appl. Catal. B Environ.* **2018**, *232*, 299–305.

231. Werner, S.; Szesni, N.; Fischer, R.W.; Haumann, M.; Wasserscheid, P. Homogeneous ruthenium-based water–gas shift catalysts via supported ionic liquid phase (SILP) technology at low temperature and ambient pressure. *Phys. Chem. Chem. Phys.* **2009**, *11*, 10817.

232. Kohler, F.T.U.; Popp, S.; Klefer, H.; Eckle, I.; Schrage, C.; Böhringer, B.; Roth, D.; Haumann, M.; Wasserscheid, P. Supported ionic liquid phase (SILP) materials for removal of hazardous gas compounds – efficient and irreversible NH3 adsorption. *Green Chem.* **2014**, *16*, 3560.

233. Haumann, M. Continuous Catalytic Processes with Supported Ionic Liquid Phase (SILP) Materials. In; 2020; pp. 49–67.

234. Schwarz, C.H.; Agapova, A.; Junge, H.; Haumann, M. Immobilization of a selective Ru-pincer complex for low temperature methanol reforming–Material and process improvements. *Catal. Today* **2020**, *342*, 178–186.

235. Schwarz, C.H.; Kraus, D.; Alberico, E.; Junge, H.; Haumann, M. Immobilized Ru-Pincer Complexes for Continuous Gas-Phase Low-Temperature Methanol Reforming-Improving the Activity by a Second Ru-Complex and Variation of Hydroxide Additives. *Eur. J. Inorg. Chem.* **2021**, *2021*, 1745–1751.

236. Nielsen, M.; Kammer, A.; Cozzula, D.; Junge, H.; Gladiali, S.; Beller, M. Efficient hydrogen production from alcohols under mild reaction conditions. *Angew. Chemie - Int. Ed.* **2011**, *50*, 9593–9597.

237. Zhao, G.; Joó, F. Free formic acid by hydrogenation of carbon dioxide in sodium formate solutions. *Catal. Commun.* **2011**, *14*, 74–76.

238. Ziebart, C.; Federsel, C.; Anbarasan, P.; Jackstell, R.; Baumann, W.; Spannenberg, A.; Beller, M. Well-defined iron catalyst for improved hydrogenation of carbon dioxide and bicarbonate. *J. Am. Chem. Soc.* **2012**, *134*, 20701–20704.

239. Treigerman, Z.; Sasson, Y. Generation and Quantification of Formate Ion Produced from Aqueous Sodium Bicarbonate in the Presence of Homogeneous Ruthenium Catalyst. *ACS Omega* **2018**, *3*, 12797–12801.

240. Federsel, C.; Jackstell, R.; Boddien, A.; Laurenczy, G.; Beller, M. Ruthenium-Catalyzed Hydrogenation of Bicarbonate in Water. *ChemSusChem* **2010**, *3*, 1048–1050.

241. Balaraman, E.; Gunanathan, C.; Zhang, J.; Shimon, L.J.W.; Milstein, D. Efficient hydrogenation of organic carbonates, carbamates and formates indicates alternative routes to methanol based on CO2 and CO. *Nat. Chem.* **2011**, *3*, 609–614.

242. Forero-Cortés, P.A.; Marx, M.; Moustakas, N.G.; Brunner, F.; Housecroft, C.E.; Constable, E.C.; Junge, H.; Beller, M.; Strunk, J. Transferring photocatalytic CO 2 reduction mediated by Cu(N^N)(P^P) + complexes from organic solvents into ionic liquid media. *Green Chem.* **2020**, *22*, 4541–4549.

243. Kinzel, N.W.; Werlé, C.; Leitner, W. Transition Metal Complexes as Catalysts for the Electroconversion of CO2: An Organometallic Perspective. *Angew. Chemie - Int. Ed.* **2021**, *60*, 11628–11686.

244. Min, S.; Rasul, S.; Li, H.; Grills, D.C.; Takanabe, K.; Li, L.J.; Huang, K.W. Electrocatalytic Reduction of Carbon Dioxide with a Well-Defined PN3-Ru Pincer Complex. *Chempluschem* **2016**, *81*, 166–171.

245. Tanaka, R.; Yamashita, M.; Nozaki, K. Catalytic hydrogenation of carbon dioxide using Ir(III)-pincer complexes. *J. Am. Chem. Soc.* **2009**, *131*, 14168–14169.

246. Schmeier, T.J.; Dobereiner, G.E.; Crabtree, R.H.; Hazari, N. Secondary coordination sphere interactions facilitate the insertion step in an iridium(III) CO2 reduction catalyst. *J. Am. Chem. Soc.* **2011**, *133*, 9274–9277.

247. Huff, C.A.; Sanford, M.S. Catalytic CO2 hydrogenation to formate by a ruthenium pincer complex. *ACS Catal.* **2013**.

248. Filonenko, G.A.; van Putten, R.; Schulpen, E.N.; Hensen, E.J.M.; Pidko, E.A. Highly Efficient Reversible Hydrogenation of Carbon Dioxide to Formates Using a Ruthenium PNP-Pincer Catalyst. *ChemCatChem* **2014**, *6*, 1526–1530.

249. Kar, S.; Goeppert, A.; Galvan, V.; Chowdhury, R.; Olah, J.; Prakash, G.K.S. A Carbon-Neutral CO2 Capture, Conversion, and Utilization Cycle with Low-Temperature Regeneration of Sodium Hydroxide. *J. Am. Chem. Soc.* **2018**, *140*, 16873–16876.

250. Kothandaraman, J.; Goeppert, A.; Czaun, M.; Olah, G.A.; Surya Prakash, G.K. CO2 capture by amines in aqueous media and its subsequent conversion to formate with reusable ruthenium and iron catalysts. *Green Chem.* **2016**, *18*, 5831–5838.

251. Kuriyama, W.; Matsumoto, T.; Ogata, O.; Ino, Y.; Aoki, K.; Tanaka, S.; Ishida, K.; Kobayashi, T.; Sayo, N.; Saito, T. Catalytic hydrogenation of esters. Development of an efficient catalyst and processes for synthesising (R)-1,2-propanediol and 2-(l-Menthoxy)ethanol. *Org. Process Res. Dev.* **2012**, *16*, 166–171.

252. Liu, Q.; Wu, L.; Gülak, S.; Rockstroh, N.; Jackstell, R.; Beller, M. Towards a sustainable synthesis of formate salts: Combined catalytic methanol dehydrogenation and bicarbonate hydrogenation. *Angew. Chemie - Int. Ed.* **2014**, *53*, 7085–7088.

253. Wu, Y.; Zhao, Y.; Wang, H.; Yu, B.; Yu, X.; Zhang, H.; Liu, Z. 110th Anniversary: Ionic Liquid Promoted CO 2 Hydrogenation to Free Formic Acid over Pd/C. *Ind. Eng. Chem. Res.* **2019**, *58*, 6333–6339.

254. Hull, J.F.; Himeda, Y.; Wang, W.-H.; Hashiguchi, B.; Periana, R.; Szalda, D.J.; Muckerman, J.T.; Fujita, E. Reversible hydrogen storage using CO2 and a proton-switchable iridium catalyst in aqueous media under mild temperatures and pressures. *Nat. Chem.* **2012**, *4*, 383–388.

255. Onishi, N.; Kanega, R.; Fujita, E.; Himeda, Y. Carbon Dioxide Hydrogenation and Formic Acid Dehydrogenation Catalyzed by Iridium Complexes Bearing Pyridyl-pyrazole Ligands: Effect of an Electron-donating Substituent on the Pyrazole Ring on the Catalytic Activity and Durability. *Adv. Synth. Catal.* **2019**, *361*, 289–296.

256. Moret, S.; Dyson, P.J.; Laurenczy, G. Direct synthesis of formic acid from carbon dioxide by hydrogenation in acidic media. *Nat. Commun.* **2014**, *5*, 4017.

257. Jens, C.M.; Scott, M.; Liebergesell, B.; Westhues, C.G.; Schäfer, P.; Franciò, G.; Leonhard, K.; Leitner, W.; Bardow, A. Rh-Catalyzed Hydrogenation of CO 2 to Formic Acid in DMSO-based Reaction Media: Solved and Unsolved Challenges for Process Development. *Adv. Synth. Catal.* **2019**, *361*, 307–316.

258. Shukla, S.K.; Khokarale, S.G.; Bui, T.Q.; Mikkola, J.-P.T. Ionic Liquids: Potential Materials for Carbon Dioxide Capture and Utilization. *Front. Mater.* **2019**, *6*, 1–8.

259. Gurkan, B.E.; de la Fuente, J.C.; Mindrup, E.M.; Ficke, L.E.; Goodrich, B.F.; Price, E.A.; Schneider, W.F.; Brennecke, J.F. Equimolar CO 2 Absorption by Anion-Functionalized Ionic Liquids. *J. Am. Chem. Soc.* **2010**, *132*, 2116–2117.

260. Yu, H.; Wu, Y.-T.; Jiang, Y.-Y.; Zhou, Z.; Zhang, Z.-B. Low viscosity amino acid ionic liquids with asymmetric tetraalkylammonium cations for fast absorption of CO2. *New J. Chem.* **2009**, *33*, 2385.

261. Zhang, Y.; Zhang, S.; Lu, X.; Zhou, Q.; Fan, W.; Zhang, X.P. Dual amino-functionalised phosphonium ionic liquids for CO2 capture. *Chem. - A Eur. J.* **2009**, *15*, 3003–3011.

262. Lv, B.; Jing, G.; Qian, Y.; Zhou, Z. An efficient absorbent of amine-based amino acid-functionalized ionic liquids for CO 2 capture: High capacity and regeneration ability. *Chem. Eng. J.* **2016**, *289*, 212–218.

263. Weisshar, F.; Gau, A.; Hack, J.; Maeda, N.; Meier, D.M. Toward Carbon Dioxide Capture from the Atmosphere: Lowering the Regeneration Temperature of Polyethylenimine-Based Adsorbents by Ionic Liquid. *Energy & Fuels* **2021**, *35*, 9059–9062.

264. Xiao, M.; Liu, H.; Gao, H.; Olson, W.; Liang, Z. CO2 capture with hybrid absorbents of low viscosity imidazolium-based ionic liquids and amine. *Appl. Energy* **2019**, *235*, 311–319.

265. Cadena, C.; Anthony, J.L.; Shah, J.K.; Morrow, T.I.; Brennecke, J.F.; Maginn, E.J. Why Is CO 2 So Soluble in Imidazolium-Based Ionic Liquids? *J. Am. Chem. Soc.* **2004**, *126*, 5300–5308.

266. ZHAO, Z.; DONG, H.; ZHANG, X. The Research Progress of CO2 Capture with Ionic Liquids. *Chinese J. Chem. Eng.* **2012**, *20*, 120–129.

267. Kang, S.; Chung, Y.G.; Kang, J.H.; Song, H. CO2 absorption characteristics of amino group functionalized imidazolium-based amino acid ionic liquids. *J. Mol. Liq.* **2020**, *297*, 111825.

268. Bara, J.E.; Camper, D.E.; Gin, D.L.; Noble, R.D. Room-Temperature Ionic Liquids and Composite Materials: Platform Technologies for CO 2 Capture. *Acc. Chem. Res.* **2010**, *43*, 152–159.

269. Yokozeki, A.; Shiflett, M.B.; Junk, C.P.; Grieco, L.M.; Foo, T. Physical and chemical absorptions of carbon dioxide in room-temperature ionic liquids. *J. Phys. Chem. B* **2008**, *112*, 16654–16663.

270. Shiflett, M.B.; Yokozeki, A. Phase Behavior of Carbon Dioxide in Ionic Liquids: [emim][Acetate], [emim][Trifluoroacetate], and [emim][Acetate] + [emim][Trifluoroacetate] Mixtures. *J. Chem. Eng. Data* **2009**, *54*, 108–114.

271. Carvalho, P.J.; Álvarez, V.H.; Schröder, B.; Gil, A.M.; Marrucho, I.M.; Aznar, M.; Santos, L.M.N.B.F.; Coutinho, J.A.P. Specific Solvation Interactions of CO 2 on Acetate and Trifluoroacetate Imidazolium Based Ionic Liquids at High Pressures. *J. Phys. Chem. B* **2009**, *113*, 6803–6812.

272. Avila, J.; Lepre, L.F.; Santini, C.C.; Tiano, M.; Denis-Quanquin, S.; Chung Szeto, K.; Padua, A.A.H.; Costa Gomes, M. High-Performance Porous Ionic Liquids for Low-Pressure CO 2 Capture**. *Angew. Chemie* **2021**, *133*, 12986–12992.

273. Kelemen, Z.; Péter-Szabõ, B.; Székely, E.; Hollõczki, O.; Firaha, D.S.; Kirchner, B.; Nagy, J.; Nyulászi, L. An abnormal N-heterocyclic carbene-carbon dioxide adduct from imidazolium acetate ionic liquids: The importance of basicity. *Chem. - A Eur. J.* **2014**, *20*, 13002–13008.

274. Besnard, M.; Cabaço, M.I.; Vaca Chávez, F.; Pinaud, N.; Sebastião, P.J.; Coutinho, J.A.P.; Mascetti, J.; Danten, Y. CO 2 in 1-Butyl-3-methylimidazolium Acetate. 2. NMR Investigation of Chemical Reactions. *J. Phys. Chem. A* **2012**, *116*, 4890–4901.

275. Ennis, E.; Handy, S. A Facile Route to C2-Substituted Imidazolium Ionic Liquids. *Molecules* **2009**, *14*, 2235–2245.

276. Edward J. Maginn *DESIGN AND EVALUATION OF IONIC LIQUIDS AS NOVEL CO2 ABSORBENTS*; Pittsburgh, PA, and Morgantown, WV, 2004;

277. Wang, C.; Luo, H.; Luo, X.; Li, H.; Dai, S. Equimolar CO2 capture by imidazolium-based ionic liquids and superbase systems. *Green Chem.* **2010**, *12*, 2019–2023.

278. Rodríguez, H.; Gurau, G.; Holbrey, J.D.; Rogers, R.D. Reaction of elemental chalcogens with imidazolium acetates to yield imidazole-2-chalcogenones: direct evidence for ionic liquids as proto-carbenes. *Chem. Commun.* **2011**, *47*, 3222.

279. Gurau, G.; Rodríguez, H.; Kelley, S.P.; Janiczek, P.; Kalb, R.S.; Rogers, R.D. Demonstration of chemisorption of carbon dioxide in 1,3-dialkylimidazolium acetate ionic liquids. *Angew. Chemie - Int. Ed.* **2011**, *50*, 12024–12026.

280. Nowicki, J.; Muszyński, M.; Mikkola, J.-P. Ionic liquids derived from organosuperbases: en route to superionic liquids. *RSC Adv.* **2016**, *6*, 9194–9208.

281. Wang, C.; Mahurin, S.M.; Luo, H.; Baker, G.A.; Li, H.; Dai, S. Reversible and robust CO2 capture by equimolar task-specific ionic liquid–superbase mixtures. *Green Chem.* **2010**, *12*, 870.

282. Wang, C.; Luo, H.; Jiang, D.; Li, H.; Dai, S. Carbon Dioxide Capture by Superbase-Derived Protic Ionic Liquids. *Angew. Chemie* **2010**, *122*, 6114–6117.

283. Zhu, X.; Song, M.; Xu, Y. DBU-Based Protic Ionic Liquids for CO 2 Capture. *ACS Sustain. Chem. Eng.* **2017**, *5*, 8192–8198.

284. Zhang, Z.; Xie, Y.; Li, W.; Hu, S.; Song, J.; Jiang, T.; Han, B. Hydrogenation of Carbon Dioxide is Promoted by a Task-Specific Ionic Liquid. *Angew. Chemie* **2008**, *120*, 1143–1145.

285. Zhang, Z.; Hu, S.; Song, J.; Li, W.; Yang, G.; Han, B. Hydrogenation of CO2 to formic acid promoted by a diamine-functionalized ionic liquid. *ChemSusChem* **2009**, *2*, 234–238.

286. Weilhard, A.; Salzmann, K.; Navarro, M.; Dupont, J.; Albrecht, M.; Sans, V. Catalyst design for highly efficient carbon dioxide hydrogenation to formic acid under buffering conditions. *J. Catal.* **2020**, *385*, 1–9.

287. Rijksen, C.; Rogers, R.D. A Solventless Route to 1-Ethyl-3-methylimidazolium Fluoride Hydrofluoride, [C 2 mim][F]· x HF. *J. Org. Chem.* **2008**, *73*, 5582–5584.

288. Palgunadi, J.; Hong, S.Y.; Lee, J.K.; Lee, H.; Lee, S.D.; Cheong, M.; Kim, H.S. Correlation between Hydrogen Bond Basicity and Acetylene Solubility in Room Temperature Ionic Liquids. *J. Phys. Chem. B* **2011**, *115*, 1067–1074.

289. Bello, T.O.; Bresciani, A.E.; Nascimento, C.A.O.; Alves, R.M.B. Thermodynamic analysis of carbon dioxide hydrogenation to formic acid and methanol. *Chem. Eng. Sci.* **2021**, *242*, 116731.

290. Federsel, C.; Jackstell, R.; Beller, M. State-of-the-art catalysts for hydrogenation of carbon dioxide. *Angew. Chemie - Int. Ed.* **2010**, *49*, 6254–6257.

291. Rezayee, N.M.; Huff, C.A.; Sanford, M.S. Tandem amine and ruthenium-catalyzed hydrogenation of CO2 to methanol. *J. Am. Chem. Soc.* **2015**, *137*, 1028–1031.

292. Kothandaraman, J.; Goeppert, A.; Czaun, M.; Olah, G.A.; Prakash, G.K.S. Conversion of CO2 from Air into Methanol Using a Polyamine and a Homogeneous Ruthenium Catalyst. *J. Am. Chem. Soc.* **2016**, *138*, 778–781.

293. Kar, S.; Sen, R.; Goeppert, A.; Prakash, G.K.S. Integrative CO2 Capture and hydrogenation to methanol with reusable catalyst and amine: Toward a carbon neutral methanol economy. *J. Am. Chem. Soc.* **2018**, *140*, 1580–1583.

294. Kar, S.; Goeppert, A.; Prakash, G.K.S. Combined CO2 Capture and Hydrogenation to Methanol: Amine Immobilization Enables Easy Recycling of Active Elements. *ChemSusChem* **2019**, *12*, 3172–3177.

295. Kar, S.; Sen, R.; Kothandaraman, J.; Goeppert, A.; Chowdhury, R.; Munoz, S.B.; Haiges, R.; Prakash, G.K.S. Mechanistic Insights into Ruthenium-Pincer-Catalyzed Amine-Assisted Homogeneous Hydrogenation of CO2 to Methanol. *J. Am. Chem. Soc.* **2019**, *141*, 3160–3170.

296. Kothandaraman, J.; Kar, S.; Sen, R.; Goeppert, A.; Olah, G.A.; Prakash, G.K.S. Efficient Reversible Hydrogen Carrier System Based on Amine Reforming of Methanol. *J. Am. Chem. Soc.* **2017**, *139*, 2549–2552.

297. Lane, E.M.; Zhang, Y.; Hazari, N.; Bernskoetter, W.H. Sequential Hydrogenation of CO2 to Methanol Using a Pincer Iron Catalyst. *Organometallics* **2019**, *38*, 3084–3091.

298. Savourey, S.; Lefèvre, G.; Berthet, J.-C.; Thuéry, P.; Genre, C.; Cantat, T. Efficient Disproportionation of Formic Acid to Methanol Using Molecular Ruthenium Catalysts. *Angew. Chemie Int. Ed.* **2014**, *53*, 10466–10470.

299. Kuß, D.A.; Hölscher, M.; Leitner, W. Hydrogenation of CO2 to Methanol with Mn-PNP-Pincer Complexes in the Presence of Lewis Acids: the Formate Resting State Unleashed. *ChemCatChem* **2021**, *13*, 3319–3323.

300. Rayder, T.M.; Adillon, E.H.; Byers, J.A.; Tsung, C.K. A Bioinspired Multicomponent Catalytic System for Converting Carbon Dioxide into Methanol Autocatalytically. *Chem* **2020**, *6*, 1742–1754.

301. Esposito, R.; Melchiorre, M.; Annunziata, A.; Cucciolito, M.E.; Ruffo, F. Emerging catalysis in biomass valorisation: simple Zn(II) catalysts for fatty acids esterification and transesterification. *ChemCatChem* **2020**, *12*, 5858–5879.

302. Zheng, Y.; Zhao, Y.; Tao, S.; Li, X.; Cheng, X.; Jiang, G.; Wan, X. Green Esterification of Carboxylic Acids Promoted by tert -Butyl Nitrite. *European J. Org. Chem.* **2021**, *2021*, 2713–2718.

303. Cole-Hamilton, D.J. Homogeneous Catalysis--New Approaches to Catalyst Separation, Recovery, and Recycling. *Science (80-.).* **2003**, *299*, 1702–1706.

304. Schaub, T.; Paciello, R.A. A Process for the Synthesis of Formic Acid by CO2 Hydrogenation: Thermodynamic Aspects and the Role of CO. *Angew. Chemie Int. Ed.* **2011**, *50*, 7278–7282.

305. Konrath, R.; Sekine, K.; Jevtovikj, I.; Paciello, R.A.; Hashmi, A.S.K.; Schaub, T. Performance enhancing additives for reusable ruthenium-triphos catalysts in the reduction of CO 2 to dimethoxymethane. *Green Chem.* **2020**, *22*, 6464–6470.

306. Scott, M.; Blas Molinos, B.; Westhues, C.; Franciò, G.; Leitner, W. Aqueous Biphasic Systems for the Synthesis of Formates by Catalytic CO 2 Hydrogenation: Integrated Reaction and Catalyst Separation for CO 2 -Scrubbing Solutions. *ChemSusChem* **2017**, *10*, 1085–1093.

307. Reichert, J.; Brunner, B.; Jess, A.; Wasserscheid, P.; Albert, J. Biomass oxidation to formic acid in aqueous media using polyoxometalate catalysts – boosting FA selectivity by in-situ extraction. *Energy Environ. Sci.* **2015**, *8*, 2985–2990.

308. Andrew, R.E.; González-Sebastián, L.; Chaplin, A.B. NHC-based pincer ligands: carbenes with a bite. *Dalt. Trans.* **2016**, *45*, 1299–1305.

309. Ma, Z.; Legrand, U.; Pahija, E.; Tavares, J.R.; Boffito, D.C. From CO2to Formic Acid Fuel Cells. *Ind. Eng. Chem. Res.* **2021**, *60*, 803–815.

310. Eppinger, J.; Huang, K.W. Formic Acid as a Hydrogen Energy Carrier. *ACS Energy Lett.* **2017**, *2*, 188–195.

311. Jiang, K.; Zhang, H.X.; Zou, S.; Cai, W. Bin Electrocatalysis of formic acid on palladium and platinum surfaces: From fundamental mechanisms to fuel cell applications. *Phys. Chem. Chem. Phys.* **2014**, *16*, 20360–20376.

312. Prichatz, C.; Trincado, M.; Tan, L.; Casas, F.; Kammer, A.; Junge, H.; Beller, M.; Grützmacher, H. Highly Efficient Base-Free Dehydrogenation of Formic Acid at Low Temperature. *ChemSusChem* **2018**, *11*, 3092–3095.

313. Sordakis, K.; Tang, C.; Vogt, L.K.; Junge, H.; Dyson, P.J.; Beller, M.; Laurenczy, G. Homogeneous Catalysis for Sustainable Hydrogen Storage in Formic Acid and Alcohols. *Chem. Rev.* **2018**, *118*, 372–433.

314. Wang, X.; Meng, Q.; Gao, L.; Jin, Z.; Ge, J.; Liu, C.; Xing, W. Recent progress in hydrogen production from formic acid decomposition. *Int. J. Hydrogen Energy* **2018**, *43*, 7055–7071.

315. Guan, C.; Pan, Y.; Zhang, T.; Ajitha, M.J.; Huang, K.W. An Update on Formic Acid Dehydrogenation by Homogeneous Catalysis. *Chem. - An Asian J.* **2020**, *15*, 937–946.

316. Onishi, N.; Kanega, R.; Kawanami, H.; Himeda, Y. Recent Progress in Homogeneous Catalytic Dehydrogenation of Formic Acid. *Molecules* **2022**, *27*, 455.

317. Lentz, N.; Aloisi, A.; Thuéry, P.; Nicolas, E.; Cantat, T. Additive-Free Formic Acid Dehydrogenation Catalyzed by a Cobalt Complex. *Organometallics* **2021**, *40*, 565–569.

318. Curley, J.B.; Bernskoetter, W.H.; Hazari, N. Additive-Free Formic Acid Dehydrogenation Using a Pincer-Supported Iron Catalyst. *ChemCatChem* **2020**, *12*, 1934–1938.

319. Zhou, W.; Wei, Z.; Spannenberg, A.; Jiao, H.; Junge, K.; Junge, H.; Beller, M. Cobalt-Catalyzed Aqueous Dehydrogenation of Formic Acid. *Chem. - A Eur. J.* **2019**, *25*, 8459–8464.

320. Haibach, M.C.; Ickes, A.R.; Wilders, A.M.; Shekhar, S. Recent Advances in Nonprecious Metal Catalysis. *Org. Process Res. Dev.* **2020**, *24*, 2428–2444.

321. Nad, P.; Mukherjee, A. Acceptorless Dehydrogenative Coupling Reactions by Manganese Pincer Complexes. *Asian J. Org. Chem.* **2021**, *10*, 1958–1985.

322. Kar, S.; Rauch, M.; Leitus, G.; Ben-David, Y.; Milstein, D. Highly efficient additive-free dehydrogenation of neat formic acid. *Nat. Catal.* **2021**, *4*, 193–201.

323. Iguchi, M.; Himeda, Y.; Manaka, Y.; Kawanami, H. Development of an Iridium-Based Catalyst for High-Pressure Evolution of Hydrogen from Formic Acid. *ChemSusChem* **2016**, 2749–2753.

324. Iguchi, M.; Guan, C.; Huang, K.-W.; Kawanami, H. Solvent effects on high-pressure hydrogen gas generation by dehydrogenation of formic acid using ruthenium complexes. *Int. J. Hydrogen Energy* **2019**, *44*, 28507–28513.

325. Iguchi, M.; Onishi, N.; Himeda, Y.; Kawanami, H. Ligand Effect on the Stability of Water-Soluble Iridium Catalysts for High-Pressure Hydrogen Gas Production by Dehydrogenation of Formic Acid. *ChemPhysChem* **2019**, *20*, 1296–1300.

326. Boddien, A.; Mellmann, D.; Gärtner, F.; Jackstell, R.; Junge, H.; Dyson, P.J.; Laurenczy, G.; Ludwig, R.; Beller, M. Efficient Dehydrogenation of Formic Acid Using an Iron Catalyst. *Science (80-.).* **2011**, *333*, 1733–1736.

327. Agapova, A.; Alberico, E.; Kammer, A.; Junge, H.; Beller, M. Catalytic Dehydrogenation of Formic Acid with Ruthenium-PNP-Pincer Complexes: Comparing N-Methylated and NH-Ligands. *ChemCatChem* **2019**, *11*, 1910–1914.

328. Kumar, A.; Gao, C. Homogeneous (De)hydrogenative Catalysis for Circular Chemistry – Using Waste as a Resource. *ChemCatChem* **2020**, cctc.202001404.

329. Müller, K.; Brooks, K.; Autrey, T. Hydrogen Storage in Formic Acid: A Comparison of Process Options. *Energy and Fuels* **2017**, *31*, 12603–12611.

330. Guo, J.; Yin, C.K.; Zhong, D.L.; Wang, Y.L.; Qi, T.; Liu, G.H.; Shen, L.T.; Zhou, Q.S.; Peng, Z.H.; Yao, H.; et al. Formic Acid as a Potential On-Board Hydrogen Storage Method: Development of Homogeneous Noble Metal Catalysts for Dehydrogenation Reactions. *ChemSusChem* **2021**, *14*, 2655–2681.

331. Sordakis, K.; Tang, C.; Vogt, L.K.; Junge, H.; Dyson, P.J.; Beller, M.; Laurenczy, G. Homogeneous Catalysis for Sustainable Hydrogen Storage in Formic Acid and Alcohols. *Chem. Rev.* **2018**, *118*, 372–433.

332. Loges, B.; Boddien, A.; Gärtner, F.; Junge, H.; Beller, M. Catalytic Generation of Hydrogen from Formic acid and its Derivatives: Useful Hydrogen Storage Materials. *Top. Catal.* **2010**, *53*, 902–914.

333. van Putten, R.; Wissink, T.; Swinkels, T.; Pidko, E.A. Fuelling the hydrogen economy: Scale-up of an integrated formic acid-to-power system. *Int. J. Hydrogen Energy* **2019**, *44*, 28533–28541.

334. Kumar, A.; Daw, P.; Milstein, D. Homogeneous Catalysis for Sustainable Energy: Hydrogen and Methanol Economies, Fuels from Biomass, and Related Topics. *Chem. Rev.* **2021**, acs.chemrev.1c00412.

335. Zhang, Y.; MacIntosh, A.D.; Wong, J.L.; Bielinski, E.A.; Williard, P.G.; Mercado, B.Q.; Hazari, N.; Bernskoetter, W.H. Iron catalyzed CO2 hydrogenation to formate enhanced by Lewis acid co-catalysts. *Chem. Sci.* **2015**, *6*, 4291–4299.

336. Kar, S.; Goeppert, A.; Prakash, G.K.S. Integrated CO2 Capture and Conversion to Formate and Methanol: Connecting Two Threads. *Acc. Chem. Res.* **2019**, *52*, 2892–2903.

337. Montandon-Clerc, M.; Laurenczy, G. Additive free, room temperature direct homogeneous catalytic carbon dioxide hydrogenation in aqueous solution using an iron(II) phosphine catalyst. *J. Catal.* **2018**, *362*, 78–84.

338. Rahman, A.; S-Al-Deyab, S. A review on reduction of acetone to isopropanol with Ni nano superactive, heterogeneous catalysts as an environmentally benevolent approach. *Appl. Catal. A Gen.* **2014**, *469*, 517–523.

339. Rahman, A. Catalytic Hydrogenation of Acetone to Isopropanol: An Environmentally Benign Approach. *Bull. Chem. React. Eng. Catal.* **2011**, *5*, 113–126.

340. Bondue, C.J.; Calle-Vallejo, F.; Figueiredo, M.C.; Koper, M.T.M. Structural principles to steer the selectivity of the electrocatalytic reduction of aliphatic ketones on platinum. *Nat. Catal.* **2019**, *2*, 243–250.

341. Brodt, M.; Müller, K.; Kerres, J.; Katsounaros, I.; Mayrhofer, K.; Preuster, P.; Wasserscheid, P.; Thiele, S. The 2-Propanol Fuel Cell: A Review from the Perspective of a Hydrogen Energy Economy. *Energy Technol.* **2021**, *9*, 2100164.

342. Hauenstein, P.; Seeberger, D.; Wasserscheid, P.; Thiele, S. High performance direct organic fuel cell using the acetone/isopropanol liquid organic hydrogen carrier system. *Electrochem. commun.* **2020**, *118*, 106786.

343. Sievi, G.; Geburtig, D.; Skeledzic, T.; Bösmann, A.; Preuster, P.; Brummel, O.; Waidhas, F.; Montero, M.A.; Khanipour, P.; Katsounaros, I.; et al. Towards an efficient liquid organic hydrogen carrier fuel cell concept. *Energy Environ. Sci.* **2019**, *12*, 2305–2314.

344. Trincado, M.; Bösken, J.; Grützmacher, H. Homogeneously catalyzed acceptorless dehydrogenation of alcohols: A progress report. *Coord. Chem. Rev.* **2021**, *443*, 213967.

345. Trincado, M.; Banerjee, D.; Grützmacher, H. Molecular catalysts for hydrogen production from alcohols. *Energy Environ. Sci.* **2014**, *7*, 2464–2503.

346. Crabtree, R.H. Homogeneous Transition Metal Catalysis of Acceptorless Dehydrogenative Alcohol Oxidation: Applications in Hydrogen Storage and to Heterocycle Synthesis. *Chem. Rev.* **2017**, *117*, 9228–9246.

347. Castro-Amoedo, R.; Csendes, Z.; Brünig, J.; Sauer, M.; Foelske-Schmitz, A.; Yigit, N.; Rupprechter, G.; Gupta, T.; Martins, A.M.; Bica, K.; et al. Carbon-based SILP catalysis for the selective hydrogenation of aldehydes using a well-defined Fe(ii) PNP complex. *Catal. Sci. Technol.* **2018**, *8*, 4812–4820.

348. Pinheiro, D.L.J.; Nielsen, M. Chemoselective Transfer Hydrogenation of Enamides Using Ru Pincer Complexes for the Synthesis of α-Amino Acids. *J. Org. Chem.* **2022**, acs.joc.1c02975.

349. Pinheiro, D.; Nielsen, M. Base-Free Synthesis of Furfurylamines from Biomass Furans Using Ru Pincer Complexes. *Catalysts* **2021**, *11*, 558.

350. Padilla, R.; Koranchalil, S.; Nielsen, M. Homogeneous Catalyzed Valorization of Furanics: A Sustainable Bridge to Fuels and Chemicals. *Catalysts* **2021**, *11*, 1371.

351. Padilla, R.; Jørgensen, M.S.B.; Paixão, M.W.; Nielsen, M. Efficient catalytic hydrogenation of alkyl levulinates to γ-valerolactone. *Green Chem.* **2019**, *21*, 5195–5200.

352. Xu, L.; Li, W.C.; Xin, J.; Zhang, S.J.; Li, B.Z.; Yuan, Y.J. Ethylenediamine Enhances Ionic Liquid Pretreatment Performance at High Solid Loading. *ACS Sustain. Chem. Eng.* **2020**, *8*, 13007–13018.

353. Doherty, T. V.; Mora-Pale, M.; Foley, S.E.; Linhardt, R.J.; Dordick, J.S. Ionic liquid solvent properties as predictors of lignocellulose pretreatment efficacy. *Green Chem.* **2010**, *12*, 1967.

354. Wang, Y.; Wang, M.; Li, Y.; Liu, Q. Homogeneous manganese-catalyzed hydrogenation and dehydrogenation reactions. *Chem* **2021**, *7*, 1180–1223.

355. Zell, T.; Langer, R. From Ruthenium to Iron and Manganese—A Mechanistic View on Challenges and Design Principles of Base-Metal Hydrogenation Catalysts. *ChemCatChem* **2018**, *10*, 1930–1940.

356. Fulmer, G.R.; Miller, A.J.M.; Sherden, N.H.; Gottlieb, H.E.; Nudelman, A.; Stoltz, B.M.; Bercaw, J.E.; Goldberg, K.I. NMR Chemical Shifts of Trace Impurities: Common Laboratory Solvents, Organics, and Gases in Deuterated Solvents Relevant to the Organometallic Chemist. *Organometallics* **2010**, *29*, 2176–2179.

357. Elangovan, S.; Topf, C.; Fischer, S.; Jiao, H.; Spannenberg, A.; Baumann, W.; Ludwig, R.; Junge, K.; Beller, M. Selective Catalytic Hydrogenations of Nitriles, Ketones, and Aldehydes by Well-Defined Manganese Pincer Complexes. *J. Am. Chem. Soc.* **2016**, *138*, 8809–8814.

358. Elliot, S.G.; Tosi, I.; Riisager, A.; Taarning, E.; Meier, S. Response Factors Enable Rapid Quantitative 2D NMR Analysis in Catalytic Biomass Conversion to Renewable Chemicals. *Top. Catal.* **2019**, *62*, 590–598.

359. Riisager, A.; Fehrmann, R.; Haumann, M.; Wasserscheid, P. Supported Ionic Liquid Phase (SILP) catalysis: An innovative concept for homogeneous catalysis in continuous fixed-bed reactors. *Eur. J. Inorg. Chem.* **2006**, 695–706.

360. Langer, R.; Thomas, Z.; Schaub, T. CO2-based hydrogen storage: CO2 hydrogenation to formic acid, formaldehyde and methanol. *Phys. Sci. Rev.* **2018**, *0*, 1–14.

361. Müller, K.; Skeledzic, T.; Wasserscheid, P. Strategies for Low-Temperature Liquid Organic Hydrogen Carrier Dehydrogenation. *Energy and Fuels* **2021**, *35*, 10929–10936.